

The GlueX Experiment Design Report Version 5 A Search for QCD Exotics Using a Beam of Photons

GlueX-doc-xxx — January 2005

The GlueX Collaboration

J. Pinfold

University of Alberta (Edmonton, Alberta, Canada)

D. Fassouliotis, P. Ioannou, Ch. Kourkouvelis

**University of Athens (Athens, Greece)*

G. B. Franklin, Z. Krahn, J. Kuhn, C. A. Meyer (Deputy Spokesperson), C. Morningstar,

B. Quinn, R. A. Schumacher, G. Wilkin

Carnegie Mellon University (Pittsburgh, PA)

H. Crannell, F. J. Klein, D. Sober

Catholic University of America (Washington, D. C.)

D. Doughty, D. Heddle

Christopher Newport University (Newport News, VA)

R. Jones, K. Joo

University of Connecticut (Storrs, CT)

W. Boeglin, L. Kramer, P. Markowitz, B. Raue, J. Reinhold

Florida International University (Miami, FL)

V. Crede, L. Dennis, P. Eugenio, A. Ostrovidov, G. Riccardi

Florida State University (Tallahassee, FL)

J. Annand, D. Ireland, J. Kellie, K. Livingston, G. Rosner, G. Yang

University of Glasgow (Glasgow, Scotland, UK)

A. Dzierba (Spokesperson), G. C. Fox, D. Heinz, J. T. Londergan, R. Mitchell, E. Scott,

P. Smith, T. Sulanke, M. Swat, A. Szczepaniak, S. Teige

Indiana University (Bloomington, IN)

S. Denisov, A. Klimenko, A. Gorokhov, I. Polezhaeva, V. Samoilenko, A. Schukin, M. Soldatov

Institute for High Energy Physics (Protvino, Russia)

D. Abbott, A. Afanasev, F. Barbosa, P. Brindza, R. Carlini, S. Chattopadhyay, H. Fenker,
G. Heyes, E. Jastrzembski, D. Lawrence, W. Melnitchouk, E. S. Smith (Hall D Group Leader),
E. Wolin, S. Wood
Jefferson Lab (Newport News, VA)

A. Klein
Los Alamos National Lab (Los Alamos, NM)

V. A. Bodyagin, A. M. Gribushin, N. A. Kruglov, V. L. Korotkikh, M. A. Kostin,
A. I. Demianov, O. L. Kodolova, L. I. Sarycheva, A. A. Yershov
Nuclear Physics Institute, Moscow State University, Moscow, Russia

E. Solodov
Budker Institute of Nuclear Physics (Novosibirsk, Russia)

P. Mueller
** Oak Ridge National Lab (Oak Ridge, TN)*

D. S. Carman, K. Hicks, S. Taylor
Ohio University (Athens, OH)

M. Barbi, E. J. Brash, G. M. Huber, V. Kovaltchouk, G. J. Lolos, Z. Papandreou
University of Regina (Regina, Saskatchewan, Canada)

T. Barnes, S. Spanier
** University of Tennessee (Knoxville, TN)*

T. Hatziantoniou, Ch. Kanellopoulos, Ch. Petridou, D. Sampsonidis
**University of Thessaloniki (Thessaloniki, Greece)*

(*) Insitutions not yet committed but involved in workshops and planning

GlueX Theory Group

D. B. Leinweber, A. G. Williams
CSSM, University of Adelaide, (Adelaide, Australia)

S. Godfrey
Carleton University (Ottawa, Ontario, Canada)

C. Morningstar
Carnegie Mellon University (Pittsburgh, PA)

R. Kaminski, L. Lesniak
H. Niewodniczanski Institute of Nuclear Physics (Cracow, Poland)

J. Goity
Hampton University (Hampton, VA)

J. T. Londergan, M. Swat, A. Szczepaniak
Indiana University (Bloomington, IN)

A. Afanasev, W. Melnitchouk, A. W. Thomas
Jefferson Lab (Newport News, VA)

M. Pichowsky
Kent State University (Kent, OH)

P. Page
Los Alamos National Lab (Los Alamos, NM)

E. Swanson
University of Pittsburgh (Pittsburgh, PA)

T. Barnes
*University of Tennessee (Knoxville, TN)
Oak Ridge National Lab (Oak Ridge, TN)*

Contents

1	Introduction	1
1.1	History of the project	1
1.2	Synopsis of R&D Efforts	2
1.3	Summary	3
2	Executive Summary	5
2.1	Physics and overview	5
2.2	Photon beam and choice of energy	8
2.3	Detector and solenoid	10
2.4	Electronics	12
2.5	Rates and triggers	13
2.6	Computing	13
2.7	Monte Carlo	13
2.8	PWA	13
2.9	Cassel review	14
2.10	Management plan	14
2.11	NSAC report	14
2.12	Civil construction	14
3	Scientific Goals	15
3.1	Introduction	15
3.2	Conventional light mesons	17
3.3	Gluonic excitations and confinement	18
3.4	Observation of gluonic excitations	22
3.4.1	Glueballs	22
3.4.2	Exotic hybrid mesons	22
3.5	Photoproduction of exotic hybrids	25
3.5.1	Why photoproduction?	25
3.5.2	Current photoproduction data	26
3.6	Complementarity with other searches	29
3.7	Production and analysis of hybrid mesons	29
3.7.1	Kinematics	29
3.7.2	PWA requirements	30
3.7.3	Linear polarization of the beam	30
4	Photon Beam	33
4.1	Choice of Technique	33
4.1.1	Compton Back-scatter	34
4.1.2	Tagged Bremsstrahlung	36
4.1.3	Coherent Bremsstrahlung	36
4.2	Photon Source	37
4.2.1	Essential Features	38
4.2.2	Use of Collimation	39

4.2.3	Choice of Radiator	44
4.2.4	Crystal Quality	46
4.2.5	Crystal Thickness	48
4.2.6	Crystal Mount	51
4.2.7	Crystal Alignment and Monitoring	52
4.2.8	Crystal Lifetime	53
4.3	Electron Beam	55
4.3.1	Beam Polarization	55
4.3.2	Beam Emittance	56
4.3.3	Electron Beam Line Optics	58
4.3.4	Electron Beam Dump	58
4.3.5	Beam Containment and Shielding	58
4.4	Tagging Spectrometer	61
4.4.1	Specifications	61
4.4.2	Magnet	61
4.4.3	Spectrometer Optics	64
4.4.4	Tagger Detectors	66
4.4.5	Beam Dump Optics	68
4.5	Polarimetry Instrumentation	68
4.6	Operating Beam Intensity	70
5	The Superconducting Solenoid	71
5.1	Introduction	71
5.2	Brief Description	71
5.3	Solenoid Refurbishment Activities	72
5.3.1	Detailed Tests of The Coils	72
5.3.2	Refurbishment of Coils One and Two	74
5.3.3	Plans To Complete Coils Three and Four	74
5.3.4	Plans To Complete The Solenoid at JLab	74
5.4	The Magnetic Field of The Solenoid	75
5.4.1	Magnetic Modifications Needed	75
5.4.2	TOSCA Simulations	75
5.4.3	Compensation of the Upstream Plug	78
6	The GlueX Detector in Hall D	81
6.1	Overview	81
6.2	The Target	81
6.3	Calorimetry	84
6.3.1	Global Design	84
6.3.2	The Lead-Glass Calorimeter	84
6.3.3	Barrel Calorimetry	95
6.3.4	Upstream Photon Veto	109
6.4	Charged Particle Tracking	112
6.4.1	Design Considerations	112
6.4.2	Track Reconstruction	114
6.4.3	Straw-tube Drift Chamber	117
6.4.4	Forward Drift Chambers	125
6.4.5	The Start Counter	138
6.5	Particle Identification	138
6.5.1	Overview	138
6.5.2	The Time-of-flight System	143
6.5.3	Čerenkov Counter	148
6.5.4	Acceptance of The Particle Identification System	162
6.6	Detector Integration	168

6.6.1	Assembly and Mounting	170
6.6.2	Survey and Alignment	172
6.6.3	Access	172
6.6.4	Interaction Between Subsystems	173
6.6.5	Cabling	173
7	Readout Electronics	175
7.1	Overview	175
7.2	FADCs for Calorimetry	175
7.2.1	Prototype	177
7.2.2	Additional requirements for final version	178
7.3	FADCs for Tracking	178
7.4	TDCs	179
7.4.1	Jefferson Lab TDC	179
7.4.2	TDC Performance	181
7.4.3	Additional requirements for final version	182
7.5	Track Count	183
7.6	Clock Distribution and Pipeline Synchronization	183
7.7	Discriminators and Amplifiers	183
7.8	High Voltage	183
7.9	Packaging	183
7.10	Readout Bus	185
7.11	Construction	185
7.12	Review	186
8	Rates, Trigger and Data Acquisition	187
8.1	Expected rates	187
8.1.1	Overview	187
8.1.2	Trigger elements	188
8.1.3	Accidental rates	189
8.1.4	Rates in tracking chambers	189
8.2	Trigger	191
8.2.1	Overview	191
8.2.2	Level 1 trigger	193
8.2.3	Trigger simulation	195
8.3	Data acquisition	196
8.3.1	Overview	196
8.3.2	Data flow and rates	196
8.3.3	Level 3 trigger	197
8.3.4	Monitoring and Control	197
9	Computing	199
9.1	Overview	199
9.2	Background	199
9.2.1	Special features of GLUEX	200
9.2.2	CPU, Storage, and Bandwidth Requirements	201
9.3	Computing Strategy	201
9.3.1	Jefferson Lab Computing Resources	203
9.3.2	Off-site Computing Infrastructure	204
9.3.3	Software Model	205
9.4	Organization	206

10 Monte Carlo	209
10.1 Monte Carlo framework	210
10.2 Monte Carlo generators	212
10.3 Detector Geometry	212
10.4 Physics Simulation	213
10.5 Fast simulation	215
10.6 Acceptance studies	216
10.6.1 Acceptance performance	217
10.7 Monte Carlo Study of Photon Energy Resolution	217
10.7.1 Photon Detector Energy Resolution	224
10.8 Physics Event Weighters	226
11 Partial Wave Analysis	229
11.1 Introduction	229
11.2 Beam and final state normalizations	230
11.3 A partial wave analysis study	230
11.3.1 The Role of Linear Polarization	231
11.3.2 The PWA Formalism and Results	232
11.3.3 Joint production of excited baryons and mesons	239
11.4 Leakage studies	240
11.5 Summary	242
A Management Plan	245
A.1 Principles of the management plan	245
A.2 The HALL D collaboration membership	246
A.3 The HALL D governance structure	246
A.3.1 The HALL D collaboration membership structure	246
A.3.2 The working groups	247
A.3.3 The technical review committee	248
A.3.4 The executive group	248
A.3.5 The collaboration board	249
A.4 Summary	251
B The report of the Cassel committee	253
C Report of the Hall D Electronics Review Committee	263
D The GlueX Detector Review	267
D.1 Introduction	267
D.2 Overall Comments	267
D.3 Overview of Subsystem Status	268
D.3.1 Photon Beam and Tagging Spectrometer	268
D.3.2 Forward Calorimeter	269
D.3.3 Barrel Calorimeter	269
D.3.4 Start Counter	269
D.3.5 Upstream Photon Veto UPV	269
D.3.6 Time of Flight Counters	270
D.3.7 Cherenkov Counter	270
D.3.8 Central Drift Chamber	270
D.3.9 Forward Drift Chamber	271
D.3.10 Particle ID	272
D.3.11 Software	273
D.3.12 DAQ and Electronics	274
D.3.13 Integration and Milestones	274

E	The Report of The GlueX Magnet Review	277
F	The Report of the Hall D Tagging Spectrometer and Photon Beamline Review	281
F.1	Charge	281
F.2	Executive Summary	281
F.3	Introduction	282
F.4	Experimental Requirements and Layout	282
F.5	Tagging System Design	283
F.5.1	Optics	283
F.5.2	Magnets	284
F.5.3	Vacuum System	284
F.5.4	Detector System	284
F.5.5	Assembly, Alignment, and Disassembly	284
F.6	Summary	285
F.7	Summary of the Recommendations	285
G	The NSAC Long Range Plan	287
H	Civil Construction	291
H.1	General requirements	291
H.1.1	Compatibility with future upgrades	292
H.2	Personnel protection	293
H.2.1	Failure scenarios	293
H.2.2	Beam containment proposal	293
H.3	Environmental and radiation concerns	294
H.3.1	Site dose limits	294
H.3.2	Beam on radiator	294
H.3.3	Tagger building	294
H.3.4	Tagger hodoscope	294
H.3.5	Electron beam dump	294
H.3.6	Collimator enclosure	295
H.3.7	Detector building	295
H.3.8	Photon beam dump	296
H.3.9	Ground water activation	296
H.4	Geotechnical analysis	296

Chapter 1

Introduction

The primary goal of the GLUEX/HALL D project is the definitive and detailed mapping of the spectrum of a new family of particles called *hybrid mesons* starting with those that carry exotic quantum numbers. Linearly polarized photons produced by electrons from an energy upgraded CEBAF will be the probe used to uncover this spectrum. This experimental information is absolutely critical in finding the answer to an outstanding and fundamental question in physics - a quantitative understanding of the confinement mechanism in quantum chromodynamics.

In addition to the GLUEX detector, the project includes a beam line and an above-ground tagger building and detector building to be located off the stub at the east end of the north linac of the CEBAF accelerator. This project assumes that the electron energy of CEBAF will be increased to 12 *GeV* by about 2008.

1.1 History of the project

The GLUEX plans have evolved over the last five years, starting with a workshop held in July 1997 at Indiana University and the formation of the *Eight+* working group. There then followed workshops at North Carolina State University (November 1997), Carnegie Mellon University (March 1998), Florida State University (October 1998), Rensselaer Polytechnic Institute (March 1999) and at the University of Adelaide (February 2000). At the Rensselaer meeting, the working group officially organized itself into a collaboration, selecting a spokesperson (Alex Dzierba - Indiana), deputy spokesperson (Curtis Meyer - Carnegie Mellon) and Hall D JLab group leader (Elton Smith - JLab). Since that time, the collaboration has held between two and three collaborations meetings per year. The most recent was held at the University of Regina in September 2002.

A Preliminary Design Report appeared in January, 1999 and was presented to the JLab Program Advisory Committee (PAC-15) at its meeting in January, 1999 as a Letter of Intent (LOI). PAC-15 enthusiastically endorsed the physics and recommended the formation of a committee to review the project.

The second version of the Design Report [1] was prepared in August 1999 for the committee which met in December 1999 to review the GLUEX project. The review committee was chaired by David Cassel (Cornell) and consisted of Frank Close (Rutherford Lab), John Domingo (Jefferson Lab), William Dunwoodie (SLAC), Donald Geesaman (Argonne), David Hitlin (Caltech), Martin Olsson (Wisconsin) and Glenn Young (Oak Ridge). Their report provided an extremely strong endorsement for both the physics goal and the technical feasibility of the project. The committee also identified several areas of technical concerns and indicated that an R&D program would need to be carried out to move forward to a full CDR. The technical concerns were quickly resolved by the collaboration and using both University and JLab resources, an aggressive R&D program was started. The full text of the Cassel committee findings are reproduced in Appendix A, but of significance are the following comments on the uniqueness of JLab for this project.

JLab, with the energy upgrade, will be uniquely suited for providing such a beam. In particular, the excellent emittance of the JLab electron beam allows for strong collimation of the coherent bremsstrahlung radiation to enhance the polarization and ratio of tagged to untagged photons in the tagged photon beam. No other facility in the world will be able to provide a beam of this quality, with this combination of energy, duty factor, and emittance. If such a project were pursued at other existing high-energy facilities, either the data taking rate would be dramatically reduced, compromising the physics goals, or a much more complicated detector would be required. We do not see any project at an existing accelerator complex (e.g., SLAC, CESR, DESY) which is likely to be able to compete with the Hall D initiative in this area.

The third version of the Design Report [2] was prepared in November 2000 as part of the NSAC Long Range Planning process. In the process of preparing this report, the collaboration developed a detailed management plan, (appendix B), and established a collaboration board to advise the executive management of the collaboration. The members of this board were elected to two year terms, with the board choosing its own chairperson, (George Lolos - University of Regina). In conjunction with version three of the Design Report, the GLUEX physics case was made at the Electromagnetic and Hadronic NSAC Town meeting held at Jefferson Lab in December of 2000. The JLab upgrade and the GLUEX project were made the top priority of this meeting, and summarized in the resulting white paper. The GLUEX case was then made to the NSAC Long Range Plan Committee at its meeting in Santa Fe in April of 2001. The result of the NSAC meeting was that the upgrade and GLUEX were one of the four recommendations presented to DOE and NSF by NSAC.

We strongly recommend the upgrade of CEBAF at Jefferson Laboratory to 12 GeV as soon as possible.

The 12-GeV upgrade of the unique CEBAF facility is critical for our continued leadership in the experimental study of hadronic matter. This upgrade will provide new insights into the structure of the nucleon, the transition between hadronic and quark/gluon descriptions of matter, and the nature of quark confinement.

The entire plan was published in March of 2002 [3], while a synopsis of the parts relevant to GLUEX are presented in Appendix C.

Since the NSAC meeting, the collaboration has continued to carry out R&D necessary to design and build the GLUEX experiment as well as to make the science case for GLUEX to the community at large. In addition, the collaboration has worked closely with the JLab management in discussions with the DOE and the NSF about moving forward quickly with the entire upgrade project.

1.2 Synopsis of R&D Efforts

Since the publication of the second version of this design report, the collaboration has been carrying out an aggressive R&D program that has been supported both by JLab and individual universities. This program is detailed throughout this report, with more information available on line at <http://www.gluex.org/>. Significant achievements to date include the following.

- The superconducting solenoid will be moved from LANL to the Indiana University Cyclotron Facility (IUCF) by early November 2002 for refurbishment. The total cost of moving the magnet from LANL to IUCF and then to JLab along with the refurbishment is far less than the cost of a new magnet.
- The 3000-element lead-glass electromagnetic calorimeter along with associated electronics from the Brookhaven experiment E852 have been moved to JLab for use in GLUEX.

- 20 μm thick diamond wafers to be used as part of the coherent bremsstrahlung source for GLUEX have been prepared and tested. The wafers were also tested as part of the effort to provide a coherent bremsstrahlung source in Hall B at JLab.
- Prototypes of both the flash-ADC and TDCs necessary for GLUEX have been built and tested. These non-commercial electronics are crucial for GLUEX, but have already found uses in other experiments.
- Construction of prototype sections of the lead-scintillator barrel calorimeter. This work has involved detailed study of both fibers and high-magnetic-field photomultiplier tubes as well as substantial technology transfer from the KLOE collaboration.
- Parts of a full-scale prototype straw-tube drift chamber have been built and tested for use as the central tracking device. Operation studies have also been carried out on a second prototype chamber to understand the behavior of straw-tube devices.
- Prototype time-of-flight elements have been successfully tested using cosmic rays and later particle beams at the proton accelerator in Protvino, Russia. Based on these studies, a design that will achieve the requisite time resolution of 70 ps is in hand.
- Studies of fibers and construction of the infrastructure necessary to build and test the vertex detector have been carried out.
- Detailed studies of the design of the Cherenkov detector have been carried out.
- Development of a fast Monte Carlo has been completed and work on a detailed (GEANT based) Monte Carlo has begun.
- Work has begun on generalized data descriptions based on XML.
- A full scale effort on partial wave analysis (PWA) has been started, and many of the initial tools necessary to carry out this work have been implemented. A double blind study has been performed to demonstrate the ability to pull small signals out of the GLUEX data. Studies have also been made on the effects of detector resolution on our ability to carry out a successful PWA.
- Members of the GLUEX collaboration organized an international workshop on partial wave analysis held in June of 2002 at Carnegie Mellon. This effort has led to a broader interest in developing analysis tools relevant to PWA.
- The GLUEX collaboration is in discussion with members of CLEO-c to identify aspects of PWA that are common to both efforts and attempt to develop a coherent set of tools for analyzing the data from these experiments.
- Work has been carried out to study and soon implement GRID based technology to facilitate data management and transparent access to data for all members of the collaboration.

1.3 Summary

The GLUEX collaboration is ready to move forward quickly with the construction and commissioning of the GLUEX experiment. A strong collaboration has been formed with sufficient expertise to accomplish this. An active R&D effort is quickly creating the knowledge, skills and infrastructure necessary for all tasks at hand, and a vigorous collaboration with theorists is leading to the necessary analysis and theoretical tools that will be necessary to extract timely physics results from the GLUEX data. More information about the physics of the GLUEX project can be found in articles in the September/October 2000 issue of *American Scientist* [4] and in the September 2000 issue of the *CERN Courier* [5]. The collaboration also maintains a detailed web site at <http://www.gluex.org/> that provides detailed information on the project.

Chapter 2

Executive Summary

2.1 Physics and overview

In the early 1970's, evidence that the masses of strongly interacting particles increased as their internal angular momentum increased led the Japanese theorist Yoichiro Nambu to propose that the quarks inside of these particles are tied together by strings [6]. The observed linear dependence of the square of the hadron masses on the spin of the hadrons comes about when the string has a constant mass per length.

Meanwhile, we have learned that the strong interactions are described by quantum chromodynamics (QCD), the field theory in which quarks interact through a *color* force carried by gluons. Numerical simulations of QCD – lattice QCD – have demonstrated that Nambu's conjecture was essentially correct: in chromodynamics, a string-like chromoelectric flux tube forms between distant static color charges, leading to quark confinement and a potential energy between a quark and the other quarks to which it is tied which increases linearly with the distance between them. This linear potential is equivalent to the constant mass per length of Nambu's strings. It qualitatively explains confinement – infinite energy would be needed to separate quarks to infinity. Confinement is the most novel and spectacular feature of QCD.

Figure 3.3 illustrates an estimate of the chromodynamic energy density in the vicinity of a quark and antiquark based on a lattice QCD calculation [7]. The energy peaks at the positions of the quarks and in the space between the quarks the energy is confined to a flux tube. Such flux tubes arise because of the self-interaction of the gluons of QCD. In contrast the photons of QED do not carry electrical charge and thus do not form flux-tubes. The electric field lines between electric charges fill all space.

The ideal experimental test of this new feature of QCD would be to directly study the flux tube of Figure 3.3 directly by anchoring a quark and antiquark several femtometers apart and examining the flux tube that forms between them. In such ideal circumstance, one of the fingerprints of the gluonic flux tube would be the model-independent spectrum characterized by the two degenerate first excited states, which are the two longest wavelength vibrational modes of this system. Their excitation energy is π/r (r is the separation between the quarks) since both the mass and the tension of this relativistic string arise from the energy stored in its color force fields.

Such a direct examination of the flux tube is of course not possible. In real life we have to be content with systems in which the quarks move. Fortunately, we know both from general principles and from lattice QCD that an approximation to the dynamics of the full system which ignores the impact of these two forms of motion on each other works quite well - at least down to the charm quark mass.

To extend the flux tube picture to yet lighter quarks models are required, but the most important properties of this system are determined by the model-independent features described above. In particular, in a region around $2 \text{ GeV}/c^2$, a new form of hadronic matter must exist in which the gluonic degree of freedom of mesons is excited. The unique characteristic of these

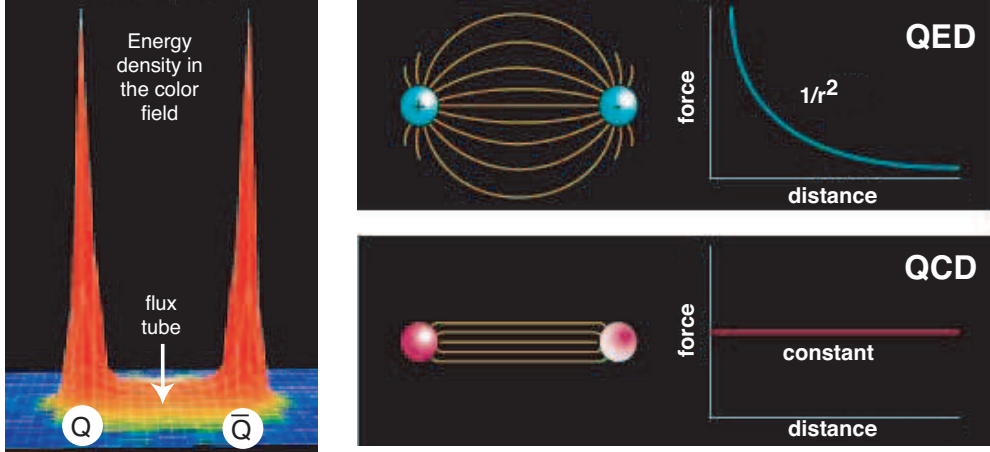


Figure 2.1: (left) A lattice QCD calculation of the energy density in the color field between a quark and an anti-quark. The density peaks at the positions of the quarks and is confined to a tube between the quarks. This calculation is for heavy quarks in the quenched approximation. (right) Field lines associated with the electrical force between two electrically charged particles (top) and the corresponding dependence of force on the distance between the charges and the field lines associated with the color force (bottom) between two quarks and the corresponding dependence of force on distance.

new states is that the vibrational quantum numbers of the string, when added to those of the quarks, can produce a total angular momentum J , a total parity P , and a total charge conjugation symmetry C not allowed for ordinary $q\bar{q}$ states. These unusual J^{PC} combinations, like 0^{+-} , 1^{-+} , and 2^{+-} , are called exotic, and the states are referred to as exotic hybrid mesons.

Not only general considerations and flux tube models, but also first-principles lattice QCD calculations, require that these states be in this $2 \text{ GeV}/c^2$ mass region, while also demonstrating that the levels and their orderings will provide experimental information on the mechanism which produces the flux tube. Moreover, tantalizing experimental evidence has appeared over the past several years for exotic hybrids as well as gluonic excitations with no quarks (glueballs).

Photon beams are expected to be particularly favorable for the production of the exotic hybrids. The reason is that the photon sometimes behaves as a virtual vector meson (a $q\bar{q}$ state with the quark spins parallel, adding up to total quark spin $S = 1$). When the flux tube in this $q\bar{q}$ system is excited to the first excited levels, both ordinary and exotic J^{PC} are possible. In contrast, when the spins are antiparallel ($S = 0$), as in pion or kaon probes, the exotic combinations are not generated. Thus photons are expected to produce exotics more directly than other meson probes. To date, most meson spectroscopy has been done with incident pion or kaon probes. High flux photon beams of sufficient quality and energy have not been available, so there are virtually no data on the photoproduction of mesons below $3 \text{ GeV}/c^2$. Thus, experimenters have not been able to search for exotic hybrids precisely where they are expected to be found.

The GLUEX detector is optimized for incident photons in the energy range from 8 to 9 GeV in order to access the desired meson mass range. The use of a solenoidal spectrometer allows for the measurement of charged particles with excellent efficiency and momentum determination. At the same time, the solenoidal field acts as a magnetic shield, containing the shower of unwanted electron-positron pairs associated with the photon beam. Photons will be produced using the coherent bremsstrahlung technique by passing an electron beam from the CEBAF accelerator through a wafer-thin diamond crystal. At special settings for the orientation of the crystal the atoms of the crystal can be made to recoil together from the radiating electron leading to an enhanced emission at particular photon energies and yielding linearly polarized photons.

Even with only 10% of the eventual photon fluxes of $10^8/\text{sec}$ from the continuous CEBAF

beam, the experiment will accumulate statistics during the first year of operation which will exceed extant published data with pions by at least an order of magnitude. With the GLUEX detector, high statistics, and the linear polarization information, it will be possible to map out the full spectrum of these gluonic excitations.

In order to achieve the required photon energy and flux with coherent bremsstrahlung, an electron beam of 12 GeV is required. Figure 2.2 shows the current accelerator complex with the existing three experimental Halls A, B and C and the planned HALL D. The addition of state-of-the-art accelerating units (*cryomodules*) in the existing space in the linear sections of the accelerator, along with upgrading of magnets in the arcs, will bring the electron energy up from the current maximum of 5.5 GeV to 12 GeV .

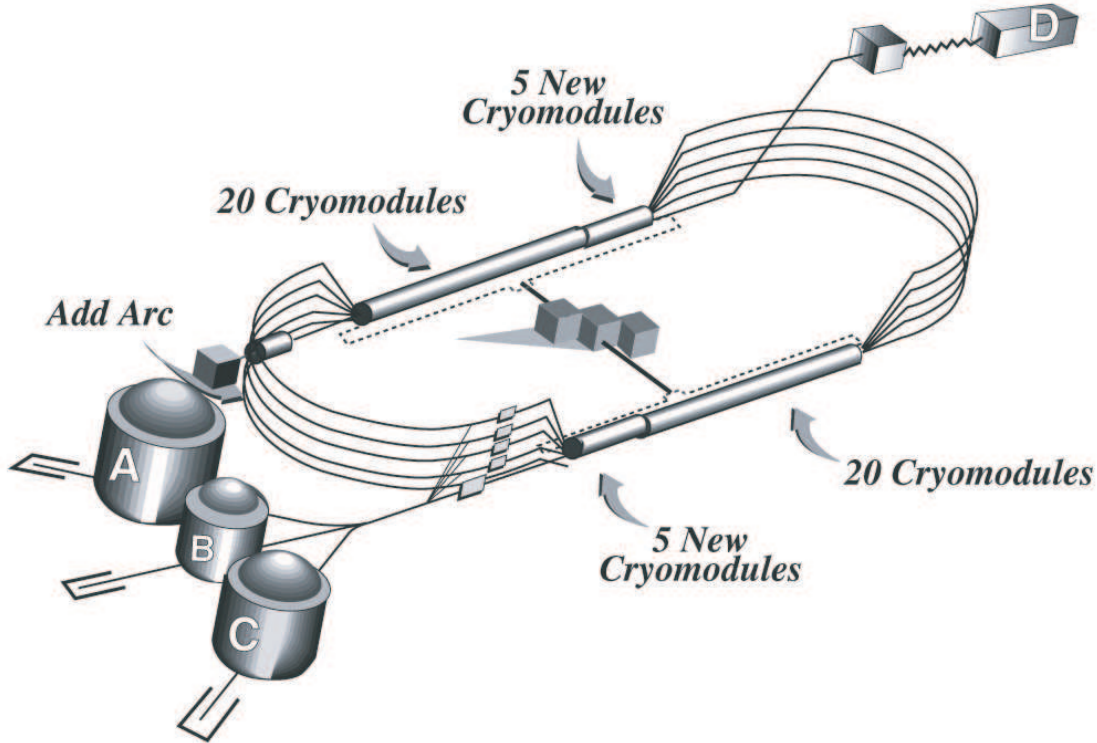


Figure 2.2: The current CEBAF multi-pass electron accelerator at JLab, showing the three existing experimental Halls (A, B and C) and the planned Hall D.

When the spectrum and decay modes of these gluonic excitations have been mapped out experimentally, we will have made a giant step forward in understanding the confinement mechanism in QCD.

In this Design Report we expand on:

1. *Spectroscopy of Light Mesons.* This will include a brief review of the conventional quark model and the status of the light quark meson spectrum.
2. *Gluonic excitations and their role in QCD.* This will include a discussion of how the gluons form flux tubes, and how their excitations lead to QCD mesons, in particular exotic hybrids. This general picture is not restricted to a particular model but follows from the first-principles QCD calculations.
3. *The current evidence for gluonic excitations.* The evidence comes from overpopulation of conventional nonets and from possible glueball and exotic hybrid sightings in $\bar{p}p$ annihilations and π -induced interactions.

4. *Photons are expected to be particularly effective in producing exotic hybrids.* Its spin structure makes the photon a qualitatively different probe from π and K beams. The first excited transverse modes of the flux tube can lead to exotic hybrids only when the quark spins are aligned. This argument is consistent with expectations from models based on phenomenological analysis of existing data that predict cross sections for photoproduction of exotic hybrids comparable to those of normal mesons. And there are essentially no data on photoproduction of light mesons so this is *Terra incognita*. The existing photoproduction data will be discussed.
5. *The complementarity of this study with other planned projects that will study gluonic excitations.* We will compare this to searches in the charm quark or beauty quark sectors or e^+e^- annihilations, in particular the GSI Project and the CLEO-c Project at Cornell.
6. *The importance of the PWA technique in uncovering exotic mesons.* The PWA is a powerful analysis tool that has been successfully employed in experiments to uncover states which are not evident from a simple examination of mass spectra (bump-hunting). PWA is absolutely essential for this project as is the development of the formalism for incident photon beams and an understanding of the phenomenology. The importance of a hermetic detector with excellent resolution and rate capability and sensitivity to a wide variety of decay modes will be discussed.
7. *Linear polarization of the photon beam is essential for this study.* Linear polarization is important in the determination of the J^{PC} quantum numbers and it is essential in determining the production mechanism. Linear polarization can be used as a filter for exotics once the production mechanism is isolated.
8. *The ideal photon energy range.* In order to reach the desired mass range we need to be far enough above threshold so that the decay products of produced mesons can be detected and measured with sufficient precision. Sufficient energies are also required to avoid line-shape distortions of higher-mass mesons. We also want to be high enough in energy to kinematically separate production of baryon resonances from production of meson resonances. This need for higher energies, however is balanced by a need for sufficiently low energy to allow for a solenoid-only-based detector to momentum analyze the highest energy charged particles with sufficient accuracy. These considerations lead to an ideal photon energy in the range from 8 to 9 GeV .
9. *The desired electron energy.* Having established the desired photon beam energy of 9 GeV an electron energy must be sufficiently high compared to the desired photon beam energy to achieve a sufficient degree of linear polarization. With 12 GeV electrons, the degree of linear polarization is 40%. If the electron energy drops to 10 GeV the degree of polarization drops to 5%. The ratio of tagged hadronic rate to total hadronic rate in the detector drops as the electron energy approaches the desired photon energy. The conclusion is that an electron energy of 12 GeV suffices but lower energies will severely compromise the physics goals.

The optimal choice for the photon energy drives the electron energy needed for this study.

2.2 Photon beam and choice of energy

What is the optimal photon beam energy to carry out the GLUEX physics goals? The goal of this experiment is to search for mesons in the mass range up to $2.5 GeV/c^2$ in the reaction $\gamma p \rightarrow Xp$, as shown in Figure 2.3. The minimum beam photon energy to produce a particle of mass m_X in the reaction $\gamma p \rightarrow Xp$ is given by equation 2.1. An incident photon energy of 5.8 GeV is sufficient to produce a meson of mass $2.5 GeV/c^2$. However, it is necessary to operate above this energy to produce mesons with adequate yield and boost so that the decay products can be detected and measured with sufficient precision.

$$E_\gamma = m_X \cdot \left(1 + \frac{m_x}{2m_p}\right) \quad (2.1)$$

The momentum-transfer-squared (t) between the incident photon (γ) and the produced meson (X) in the reaction $\gamma p \rightarrow Xp$ is given by:

$$t = (p_\gamma - p_X)^2 \quad (2.2)$$

and at incident photon energies of several GeV and above, the distribution in t is given by:

$$dN/dt = e^{\alpha t} \quad (2.3)$$

The yield is determined by the value of the minimum value of the momentum-transfer-squared

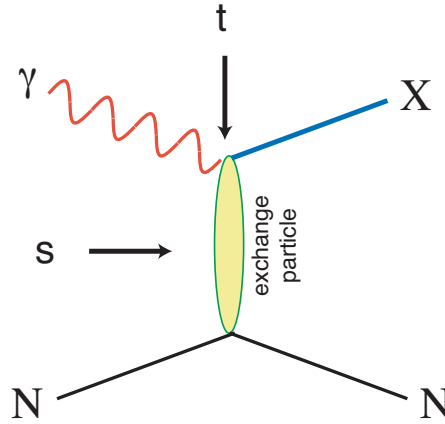


Figure 2.3: Diagram for the photoproduction of particle X . The variables s and t are the center-of-mass energy squared and the momentum-transfer-squared from incoming photon to outgoing particle X . The process shown here proceeds through the exchange of a particle in the t -channel.

from incoming beam to outgoing particle X , $|t|_{min}$, and the exponential falling distribution in $|t|$. For a given photon beam energy, E_γ , $|t|_{min}$ depends on m_X – increasing with increasing m_X for fixed E_γ and decreasing with increasing E_γ for fixed m_X . The variation of $|t|_{min}$ with m_X is rapid for m_X near the kinematic limit leading to a severe damping of the yield of mesons and a distortion of the line shape since the variation of $|t|_{min}$ over the Breit-Wigner width of a resonance can be significant.

Another consideration is the ability to kinematically separate meson resonance production from baryon resonance production. As an example, we considered various reactions leading to a final state: $\pi^+\pi^-\pi^+n$. We enumerate the possibilities:

$$\gamma p \rightarrow X^+n \rightarrow \rho^0\pi^+n \rightarrow \pi^+\pi^-\pi^+n \quad (2.4)$$

$$\gamma p \rightarrow \rho^0\Delta^+ \rightarrow \rho^0\pi^+n \rightarrow \pi^+\pi^-\pi^+n \quad (2.5)$$

$$\gamma p \rightarrow \pi^+N^{*0} \rightarrow \pi^+\pi^-\pi^+n \quad (2.6)$$

Suppose that the first of these is the reaction of interest. We can reduce effects from the other two by requiring that the effective mass of any πn or $\pi\pi n$ combination be outside the baryon resonance region. In this exercise we define the baryon region to include πn or $\pi\pi n$ mass combinations below $1.7 GeV/c^2$. The fraction of events for which we are able to reduce

the offending reactions, as a function of beam momentum and for various m_X masses is a factor in estimating the overall figure-of-merit.

Whereas the considerations mentioned thus far favor larger photon beam energies, other considerations favor a lower photon beam energy. For a given electron energy, the flux of photons and the degree of linear polarization of the photon beam will decrease rapidly as the energy of the photons approaches that of the electrons.

The partial wave analysis (PWA) technique will be used to extract information about the spin and parity of produced states. With a photon beam this process is greatly aided by using photons that are linearly polarized. Linear polarization is essential to correlate characteristics of the exchange mechanism with that of the produced meson. Linear polarization can be achieved by using Compton backscattering or coherent bremsstrahlung off a crystal. The electron energies required and other practical technical limitations involving mirrors and lasers preclude the former for the photon fluxes and energies required. The latter option will be employed and is possible because the stringent requirements placed on the electron beam are realizable with the CEBAF accelerator. The details of how the tagged and collimated coherent beam will be produced are discussed in Chapter 4 of this Design Report.

For the tagged and collimated coherent photon beam the variation in flux, for constant total hadronic rate in the detector, is plotted in Figure 2.4 as a function of photon beam energy for three different values of electron energy. In Figure 2.4 the degree of linear polarization is plotted as a function of photon beam energy for three different values for the electron energy as well.

In Figure 2.5 we plot an overall figure-of-merit which folds in the variation of beam flux and degree of linear polarization with beam energy, as well as the effective yield taking into account $|t|_{min}$ effects and the ability to separate meson resonances from baryon resonances kinematically.

Finally, we note that with a solenoid-only-based detector the maximum photon beam energy is again about 9 GeV. Above that energy, charged products from two-body decays of produced resonances – especially of lower mass – will not be momentum-analyzed with sufficient precision. The solenoid-only geometry is essential for this high-flux photon beam to contain the electromagnetic backgrounds, e.g. e^+e^- pairs, within the beam pipe – the axial field will result in helical trajectories for the electromagnetically produced charged background.

From all this we conclude that the optimum photon beam energy is between 8 and 9 GeV. For this photon energy the maximum electron energy achievable within the confines of the current CEBAF, 12 GeV, is adequate in terms of flux and degree of linear polarization. However the degree of linear polarization at 9 GeV falls rapidly – from 40% at $E_e = 12$ GeV to 5% at $E_e = 10$ GeV.

2.3 Detector and solenoid

The physics goals of the GLUEX project require a full PWA of kinematically identified exclusive reactions producing mesons. The decay products of produced mesons must be identified and measured with good resolution and with full acceptance in decay angles. In many cases, the decays of mesons involve a chain of particle decays. The GLUEX detector must therefore be hermetic with 4π coverage with the capability of measuring energies of neutral particles (γ , π^0 , η) and momenta of charged particles with good resolution. Particle identification is also required.

Figure 2.6 shows a schematic of the GLUEX detector. It is based on solenoid-only detector design – optimal for dealing with the electromagnetic backgrounds produced in the target with the high-flux photon beam. The superconducting solenoidal magnet is the LASS/MEGA magnet. This magnet was built for the Large Aperture Superconducting Solenoid Spectrometer (LASS) at SLAC and later transferred to LANL for use in the MEGA experiment. An assessment team consisting of the originally magnet designers and users, GLUEX personnel and LANL MEGA users visited LANL to review the magnet status. The magnet is in fine shape and will be moved to the Indiana University Cyclotron Facility (IUCF) for refurbishment. The move is scheduled for November, 2002. More details about the magnet are given in Chapter 5.

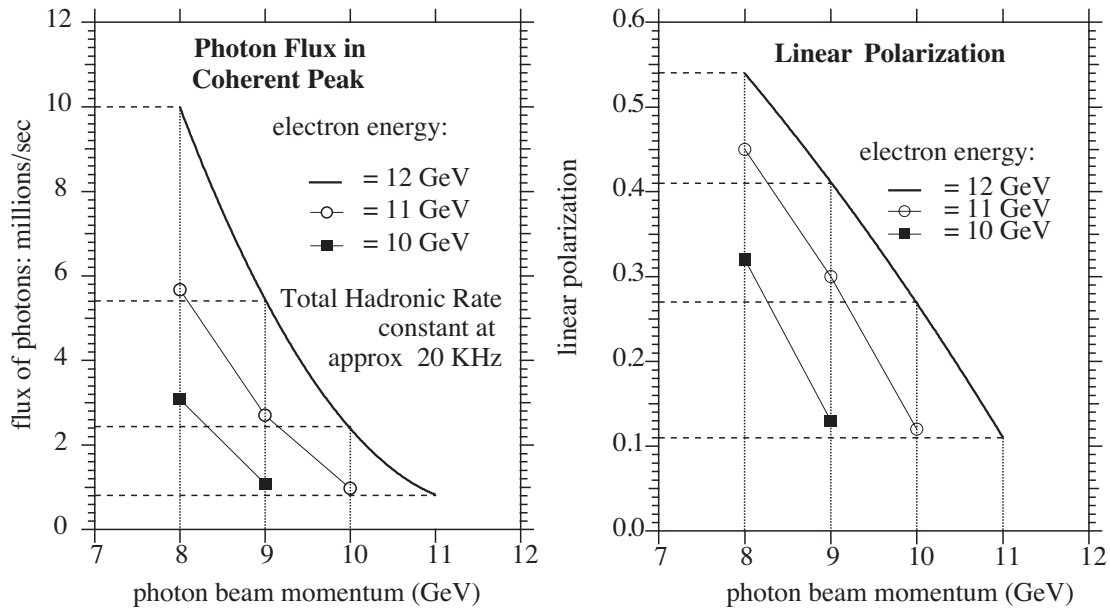


Figure 2.4: (left) The flux of photons in the coherent peak for a constant total hadronic rate in the detector of ≈ 20 KHz as a function of beam photon energy. (right) The degree of linear polarization of photons in the coherent peak as a function of beam energy. In both cases the electron energy is 12 GeV.

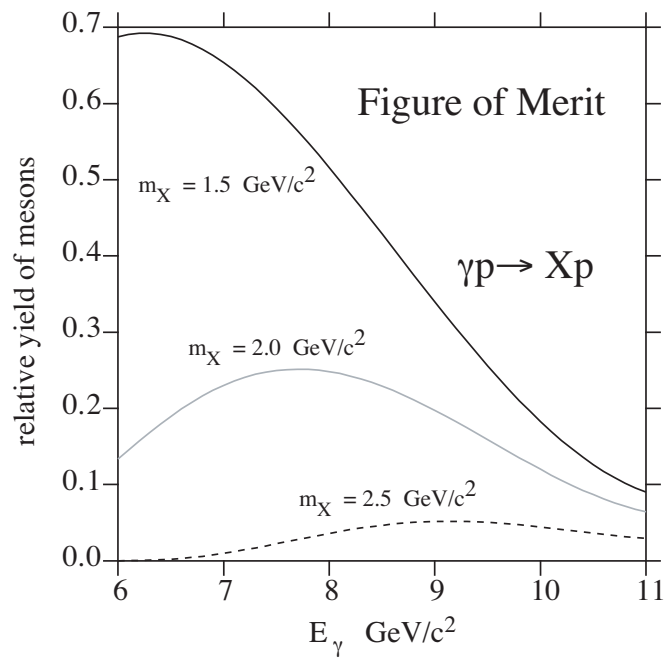


Figure 2.5: An estimate of the overall figure of merit for producing mesons as a function of photon beam energy for three different meson masses.

The GLUEX detector described in Chapter 6 is optimized for photon beam energies between 8 and 9 GeV . The detector consists of a large aperture superconducting solenoid filled with a target, tracking chambers and calorimetry. The calorimetry will also provide time-of-flight information for particle identification. The solenoid will be followed with a threshold Čerenkov counter, particle tracking, a forward TOF and a lead glass electromagnetic calorimeter. The forward electromagnetic calorimeter will be a modified version of the lead glass detector used in Brookhaven experiment E852. That detector has already been moved to JLab.

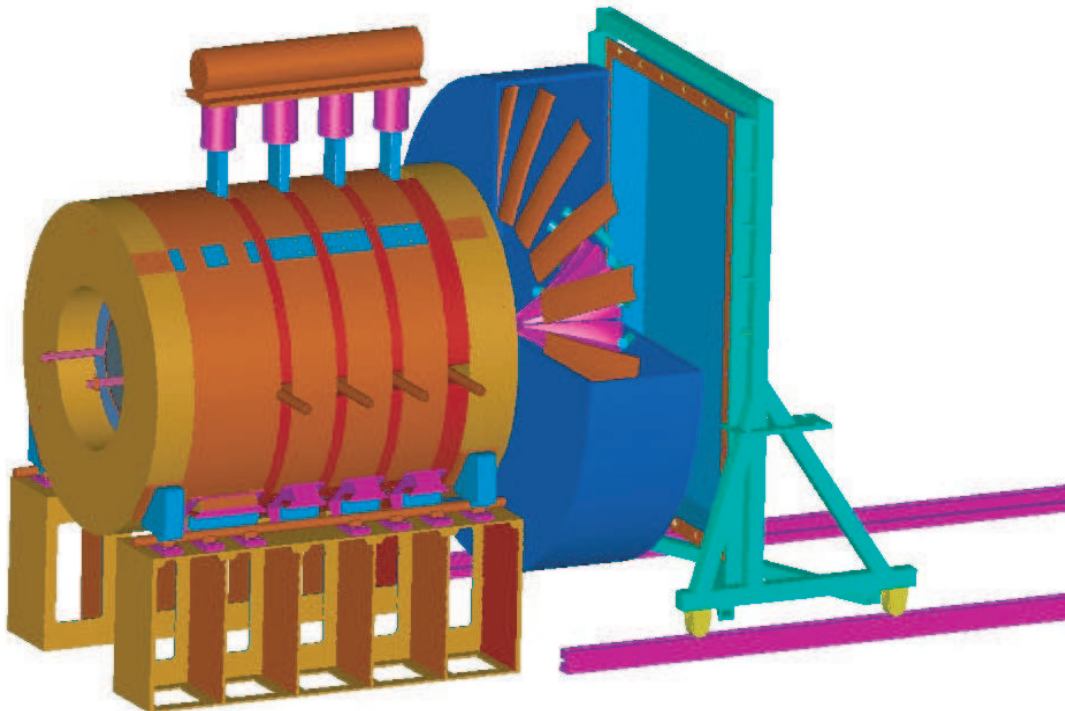


Figure 2.6: The detector for the GLUEX experiment.

2.4 Electronics

The goal of the GLUEX readout electronics system is to digitize and read out the detector signals for level 1 trigger rates of up to 200 kHz without incurring dead time. A pipelined approach is required. The digitized information will be stored for several μs while the level 1 trigger is formed. Multiple events must be buffered within the digitizer modules and read while the front ends continue to acquire new events.

Two basic types of readout electronics will be used in GLUEX, FADCs and TDCs. Detectors which measure energy will be continuously sampled with flash ADCs while detectors which require precise time measurements will use a multi-hit TDC. No currently available commercial solutions exist. These boards will be designed by our collaboration. Prototypes have been constructed, and are being tested.

The number of channels in the GLUEX detector is not large enough to justify the financially risky development of custom integrated circuits. Programmable logic devices are fast enough and available at reasonable cost. Programmable logic also allows for optimization of the data path without redesigning a printed circuit. ICs developed for other experiments will also be used.

Electronics technology is constantly evolving, and the optimum solution for the GLUEX de-

detector depends on when funding becomes available and the construction schedule. A preliminary design that could be implemented with currently available components is presented in Chapter 7.

2.5 Rates and triggers

The GLUEX experiment will begin data taking with an event rate of $\approx 10^7$ tagged γ/s . Using only the hardware, (level 1) trigger, the total rate to tape will be approximately 15,000 events per second, (both interesting physics and backgrounds). As the tagged photon flux is raised toward its ultimate design goal of $10^8 \gamma/s$, a software (level 3) trigger will be implemented to maintain the 15 kHz rate to tape. Details about the trigger design and further discussions about rates and backgrounds are given in Chapter 8.

2.6 Computing

GLUEX will be the first Jefferson Laboratory experiment to generate petabyte scale data sets on an annual basis (One petabyte = $1 \text{ PB} = 10^{15}$ Bytes). In addition, generating physics results in a timely fashion has been identified as a primary goal of our collaboration since its inception. For these reasons, a well-designed, modern, and efficient computing environment will clearly be crucial to the success of the experiment.

Currently, there are a number of particle physics projects world wide which also will produce very large data sets, and which will function with large dispersed collaborations. It seems quite reasonable, then, to expect that over the coming years, many new tools will be developed which will aid in effectively processing and managing these large volumes of data. As a collaboration, we will undoubtedly make effective use of these tools, which will include such things as grid middle ware, distributed file systems, database management tools, visualization software, and collaborative tools.

Nonetheless, it also is clear that the GLUEX collaboration will need to develop a suite of tools which are dedicated to this experiment. This will include data acquisition and trigger software, experiment monitoring and control software, data reduction tools, physics analysis software, and tools dedicated to the partial wave analysis (PWA) effort. The plan is described in Chapter 9.

2.7 Monte Carlo

Monte Carlo simulations of photoproduction reactions and the detector response are an integral part of data analysis for GLUEX. Monte Carlo data sets, which are an order of magnitude larger than the real data for specific channels, must be produced and analyzed within a unified analysis framework. The computer resources needed for this task are discussed in Chapter 9. Chapter 10 describes how the simulation is to be carried out, the specific software components that exist at present, and some preliminary results regarding detector acceptance and resolution.

2.8 PWA

To identify the J^{PC} quantum numbers of a meson it is necessary to perform a *partial wave analysis* (PWA). In the simplest terms, a partial wave analysis determines production amplitudes by fitting decay angular distributions. The fit includes information on the polarization of the beam and target, the spin and parity of the resonance, the spin and parity of any daughter resonances and any relative orbital angular momenta. The analysis seeks to establish the production strengths, production mechanisms and the relative phase motion of various production amplitudes. Phase motion is critical in determining if resonance production is present.

Although the methodology is in principle straightforward, there are issues that complicate the implementation. Mathematical ambiguities must be dealt with. Issues of where to truncate

the series expansion are important. And the theoretical underpinnings, including issues of analyticity, unitarity and S-matrix theory need to be addressed. Chapter 11 discusses both results of detailed PWA analysis carried out to date, and the plans for carrying out the PWA in the experiment.

2.9 Cassel review

A review of the GLUEX/HALL D Project by a committee chaired by David Cassel of Cornell was held in late 1999. The committee, consisting of high energy and nuclear experimentalists and theorists, issued its report in early 2000. The conclusion was that GLUEX is poised to do the definitive search for exotic hybrids and that JLab is unique for this search. Their report is included in Appendix A.

2.10 Management plan

The GLUEX collaboration has adopted a management plan based on the experience of other collaborations at JLab and collaborations in high energy physics. This plan is described in Appendix B.

2.11 NSAC report

In Spring of 2002, the Nuclear Science Advisory Committee (NSAC) released its long-range plan for nuclear physics. One of the four recommendations of this plan is to quickly carry out the 12 GeV CEBAF Upgrade and the physics program of GLUEX. Appendix C summarizes those parts of the long-range plan that are relevant to the upgrade.

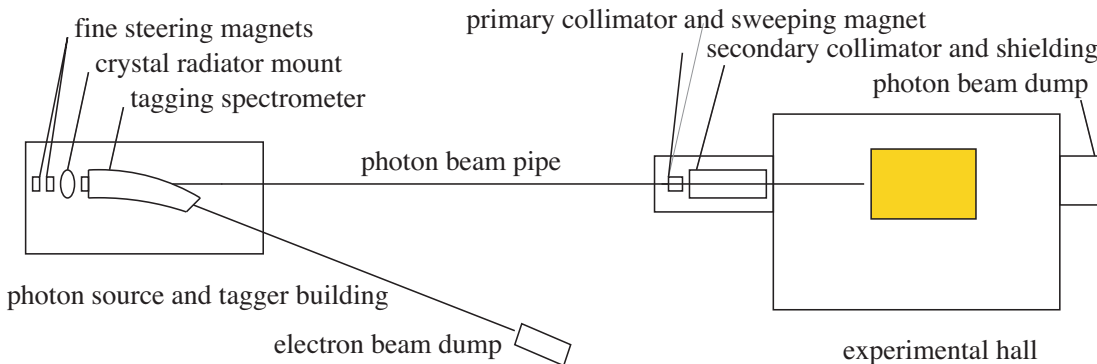


Figure 2.7: Schematic showing the photon beam line into HALL D housing the GLUEX experiment.

2.12 Civil construction

The plan is to site the meson spectrometer in a new experimental hall (HALL D) to be located at the end of a new beam line which would come off the stub at the east end of the north linac of CEBAF. The civil construction includes work associated with breaking through the stub, delivering beam above ground to a tagging spectrometer, a tagger building, HALL D, the counting house, roads, and a parking area. Members of the GLUEX collaboration have been meeting with members of the JLab civil construction team to arrive at a cost estimate and milestones for civil construction. Figure 4.4 shows a schematic of the beam delivery system and HALL D. Details are given in Appendix D.

Chapter 3

Scientific Goals

3.1 Introduction

The primary goal of the GLUOX project is the definitive and detailed mapping of the spectrum of a new family of particles called *hybrid mesons*. Linearly polarized photons produced by electrons from an energy-upgraded CEBAF will be the probe used to uncover this spectrum. This experimental information is absolutely critical in finding the answer to an outstanding and fundamental questions in physics – a quantitative understanding of the confinement mechanism in quantum chromodynamics.

The spectrum of mesons and baryons uncovered during the 1960's led to the quark model within which mesons are bound states of a quark and antiquark, $q\bar{q}$, and baryons are bound states of three quarks, qqq . Further experimental work indicated that quarks are dynamical objects as well and this led to the development of quantum chromodynamics (QCD), the theory of quarks and gluons and their interactions modeled after the very successful theory of quantum electrodynamics (QED). Just as charged particles interact by the exchange of photons, quarks, with their color charge, interact by exchanging gluons. There are however important and fundamental differences between the two theories. There are three types of color charge as opposed to one kind of electrical charge. And the gluons of QCD also carry color charge and can interact with quarks and each other. In contrast, the photons of QED do not carry charge. Bound states involving quarks and gluons or quons alone are thus possible and indeed should exist. QCD also incorporates the experimental fact that the quarks and gluons do not exist as free particles by requiring that only color singlet combinations exist as free particles in nature. In addition to the color singlet combinations $q\bar{q}$ and qqq others are possible, such as $q\bar{q}g$ (*hybrid mesons*) and gg or ggg (*glueballs*). These new states, collectively known as *gluonic excitations*, are fascinating since this is the only case of a theory in which the gauge particle is also a constituent. The analogous states in QED, like atoms of light, cannot exist. Although there is tantalizing evidence for these gluonic excitations, their spectra have not been mapped out.

The confinement of quarks and gluons within the particles of which they are the constituents is a unique feature of QCD. But a quantitative understanding of the confinement mechanism still eludes us. Theoretical progress is being made and lattice QCD, based on first-principle calculations, will ultimately be able to predict a detailed spectrum, including masses and decays, of hybrid mesons and glueballs. The experimental information about the spectrum of this new form of matter as predicted by QCD is an essential ingredient for the ultimate understanding of the confinement mechanism.

The low-lying glueball states will be searched for in the glue-rich J/ψ radiative decays as part of the planned CLEO-c project at Cornell's CESR. However the low-lying glueballs possess J^{PC} quantum numbers that are the same as $q\bar{q}$ states and therefore mixing with conventional $q\bar{q}$ mesons is possible and that can complicate glueball identification. In contrast, hybrid mesons can possess J^{PC} quantum numbers not possible for $q\bar{q}$. These *exotic hybrid mesons* thus have a *smoking gun signature*. Just as nonets of $q\bar{q}$ mesons made of the three light quarks (u , d and

s) exist, nature should also reveal nonets of hybrids with the same flavor quantum numbers but with now with the possibility of exotic J^{PC} . Hybrid mesons should also have widths comparable to conventional mesons. This is supported by theoretical considerations and by the possible sighting of an exotic hybrid in π^- -induced interactions.

Hybrid mesons can be thought of as $q\bar{q}g$ bound states in which the gluon is a constituent. An attractive alternative picture is one in which a gluonic flux tube forms between the q and \bar{q} in a meson. This flux tube forms because of the self-interaction of the gluons and qualitatively accounts for confinement. It leads to a linear potential, or a force that is constant as the distance between the quark and anti-quark varies. Infinite energy is required to separate the quarks to infinity, thus qualitatively accounting for confinement. This notion of a relativistic string or flux tube between the quarks was introduced in the 1970's to account for the observed linear dependence of particle mass-squared (m^2) on spin (J). The flux tube concept is supported by lattice QCD studies. Within this picture conventional mesons result when the flux tube is in its ground state. Hybrid mesons arise when the flux tube is excited. The lack of information on this spectroscopy is due in part to the complicated decay modes favored by these states. Another is due to the apparent suppression of exotic hybrid mesons in production mechanisms with π or K probes. On the other hand production of exotic hybrid mesons is expected to be favored using beams of photons and essentially no data exist on the photoproduction of light mesons. The GLUEX project will remedy this situation.

In addition to providing for a linearly polarized photon beam of sufficient energy, the GLUEX project includes construction of a hermetic detector to allow for particle identification and momentum and energy determination sufficient to allow for complete kinematic reconstruction of events with a wide variety of final states. This is essential for the spin analysis – partial wave analysis (PWA) – needed to determine the J^{PC} quantum numbers, to map out the flavor quantum numbers of the hybrid nonets and to test assumptions about the details of confinement that would lead to predicting specific decay modes.

In this chapter we expand on the following:

1. *Spectroscopy of Light Mesons.* This will include a brief review of the conventional quark model and the status of the light quark meson spectrum.
2. *Gluonic excitations and the role in QCD.* This will include a discussion of how the gluons form flux tubes, and how their excitations lead to QCD mesons, in particular exotic hybrids. This general picture is not restricted to a particular model but follows from the first-principles QCD calculations.
3. *The current evidence for gluonic excitations.* The evidence comes from overpopulation of conventional nonets and from possible glueball and exotic hybrid sightings in $\bar{p}p$ annihilations and π -induced interactions.
4. *Photons are expected to be particularly effective in producing exotic hybrids.* Its spin structure makes the photon a qualitatively different probe from π and K beams. The first excited transverse modes of the flux tube can lead to exotic hybrids only when the quark spins are aligned. This argument is consistent with expectations from models based on phenomenological analysis of existing data that predict cross sections for photoproduction of exotic hybrids comparable to those of normal mesons. And there are essentially no data on photoproduction of light mesons so this is *terra incognita*. The existing photoproduction data will be discussed.
5. *The complementarity of this study with other planned projects that will study gluonic excitations.* We will compare this to searches in the charm quark or beauty quark sectors or e^+e^- annihilations, in particular the GSI Project and the CLEO-c Project at Cornell.
6. *The importance of the PWA technique in uncovering exotic mesons.* The PWA is a powerful analysis tool that has been successfully employed in experiments to uncover states which are not evident from a simple examination of mass spectra (bump-hunting). PWA

is absolutely essential for this project as is the development of the formalism for incident photon beams and an understanding of the phenomenology. The importance of a hermetic detector with excellent resolution and rate capability and sensitivity to a wide variety of decay modes will be discussed.

7. *Linear polarization of the photon beam is essential for this study.* Linear polarization is important in the determination of the J^{PC} quantum numbers and it is essential in determining the production mechanism. Linear polarization can be used as a filter for exotics once the production mechanism is isolated.
8. *The ideal photon energy range.* In order to reach the desired mass range we need to be far enough above threshold so that the decay products of produced mesons can be detected and measured with sufficient precision. High enough energies are also important to avoid line-shape distortions of higher-mass mesons. We also want to be high enough in energy to kinematically separate production of baryon resonances from production of meson resonances. This need for higher energies, however is balanced by a need for sufficiently low energy to allow for a solenoid-only-based detector to momentum analyze the highest energy charged particles with sufficient accuracy. These considerations lead to an ideal photon energy in the range from 8 to 9 GeV .
9. *The desired electron energy.* Having established the desired photon beam energy of 9 GeV an electron energy must be sufficiently high compared to the desired photon beam energy to achieve a sufficient degree of linear polarization. With 12 GeV electrons, the degree of linear polarization is 40%. If the electron energy drops to 10 GeV the degree of polarization drops to 5%. The ratio of tagged hadronic rate to total hadronic rate in the detector drops as the electron energy approaches the desired photon energy. The conclusion is that an electron energy of 12 GeV suffices but lower energies will severely compromise the physics goals.

3.2 Conventional light mesons

The early version of the quark model described the observed mesons as bound states of a quark and antiquark, where the quarks were assumed to be the u , d and s quarks. Thus mesons were grouped in families with nine members – a nonet – characterized by a given J^{PC} determined by the relative spin of the two quarks and their relative orbital angular momentum. Within the nonet three are members of an isotriplet with zero strangeness. Two are members of an isodoublet with positive strangeness and another two with negative strangeness. And the remaining two members have zero strangeness and isospin. This flavor pattern holds for all the nonets. Radial excitations are also allowed.

The rules for allowed values of J^{PC} follow from the requirements of a fermion-antifermion system: the quark spins can be parallel ($S = 1$) or antiparallel ($S = 0$) with relative orbital angular momentum (L), $\vec{J} = \vec{L} + \vec{S}$, $P = (-1)^{L+1}$ and $C = (-1)^{L+S}$. Thus the low-lying nonet with $\vec{L} = 0$ and $\vec{S} = 0$ leads to $J^{PC} = 0^{-+}$, the pseudoscalar nonet, including the π , K , η and η' mesons. The nonet with $\vec{L} = 0$ and $\vec{S} = 1$ leads to $J^{PC} = 1^{-}$, the vector mesons, including the ρ , K^* , ω and ϕ mesons. The combination $\vec{L} = 1$ and $\vec{S} = 1$ leads to three nonets: scalar ($J^{PC} = 0^{++}$), axial vector ($J^{PC} = 1^{++}$) and tensor ($J^{PC} = 2^{++}$).

Using the rules for determining J^{PC} for a fermion-antifermion system, certain J^{PC} combinations are not allowed for $q\bar{q}$ systems and these include $J^{PC} = 0^{--}$, 0^{+-} , 1^{-+} , 2^{+-} , \dots . Such combinations are referred to as *exotic* quantum numbers. Indeed, that such combinations were not initially observed gave credence to the quark model.

Figure 3.1 shows our current knowledge of conventional $q\bar{q}$ states. The exact association of an observed meson with a particular $q\bar{q}$ state within a nonet depends on a good understanding of the various decay modes of the meson as well as its mass, width and production characteristics. Figure 3.1 also shows the expected range of masses for glueballs, hybrid mesons and meson-meson molecular states. These will be described in more detail below.

The range of masses of the known conventional meson nonets and their radial excitations extend from the π mass up to about $2.5 \text{ GeV}/c^2$. Figure 3.2 shows the spectrum of $q\bar{q}$ states in more detail including radial excitations. There is also now clear evidence that the observed meson spectrum includes states which cannot be accommodated within the naive quark model. For example, there are at least five scalar states reported with masses below $2 \text{ GeV}/c^2$. These, along with indications of exotic J^{PC} sightings will be discussed below.

3.3 Gluonic excitations and confinement

The Standard Model of elementary particles includes electroweak theory and QCD, the latter describing the strong interactions among the quarks and gluons. At short distances – the regime of asymptotic freedom – perturbative techniques are applicable and QCD describes high energy experimental phenomena and data both qualitatively and quantitatively. At large distance scales – the confinement regime – the situation is far different. Here the successful calculational techniques of the perturbative regime cannot be used. We must rely on first-principles lattice QCD calculations or QCD-inspired models. There has been significant theoretical effort in this area recently and more progress can be expected in the near future, especially as multi-teraflop lattice QCD centers come into operation.

Understanding confinement in QCD requires a detailed understanding of the role of gluons. QCD is distinct from QED in that the force carriers of the former (gluons) carry color charge whereas for the latter the photons are electrically neutral. As illustrated in Figure 3.3, the force between two electrically charged particles falls off like the inverse square of the distance between the charges. The number of field lines intersecting a unit area midway between the charges and perpendicular to the line connecting them would decrease as the inverse square of the distance between the charges. In contrast, the color field lines between a quark and an anti-quark do not fill all of space as in the case with electrical charges. Rather the field lines form flux tubes. A unit area placed midway between the quarks and perpendicular to the line connecting them intercepts a constant number of field lines, independent of the distance between the quarks. This leads to a constant force between the quarks – and a large force at that, equal to about 16 metric tons. The potential associated with this constant force is linear and grows with increasing distance. It takes infinite energy to separate the quarks to infinity and thus, qualitatively at least, this accounts for confinement.

Lattice QCD calculations support this notion of the formation of a flux tube between the quark and anti-quark. Figure 3.4 shows the energy density in the color field between a quark and an anti-quark in a meson with a separation of 1.2 fermi . The density peaks at the positions of the quarks and is confined to a tube between the quarks. This calculation is for heavy quarks in the quenched approximation. Figure 3.4 also shows the corresponding potential between the quarks. The ground state potential has a $1/r$ dependence at small distances and is linear for large distances.

This notion of the formation of flux tubes was first introduced in the 1970's by Yoichiro Nambu [6] to explain the observed linear Regge trajectories – the linear dependence of mass squared, m^2 , of hadrons on their spin, J . This linear dependence results if one assumes that massless quarks are tied to the ends of a relativistic string with constant mass (energy) per length with the system rotating about its center. The linear m^2 versus J dependence only arises when the mass density per length is constant, which is equivalent to a linear potential.

Within this picture, conventional mesons arise when the flux tube is in its ground state. Excitations of the flux tube lead to hybrid mesons that exhibit both the quark and gluonic degrees of freedom. The first excited state of the flux tube is a transverse excitation. The flux tube, or string, spins clockwise or counter-clockwise around the $q\bar{q}$ line leading to two degenerate states – degenerate since the energy should not depend on which way the flux tube is spinning. Lattice QCD and flux tube models both indicate that the lowest excited flux tube has $J = 1$ [8, 9, 10]. The linear combinations of the clockwise or counter-clockwise rotations are eigenstates of parity and charge conjugation leading to two possibilities for the excited flux

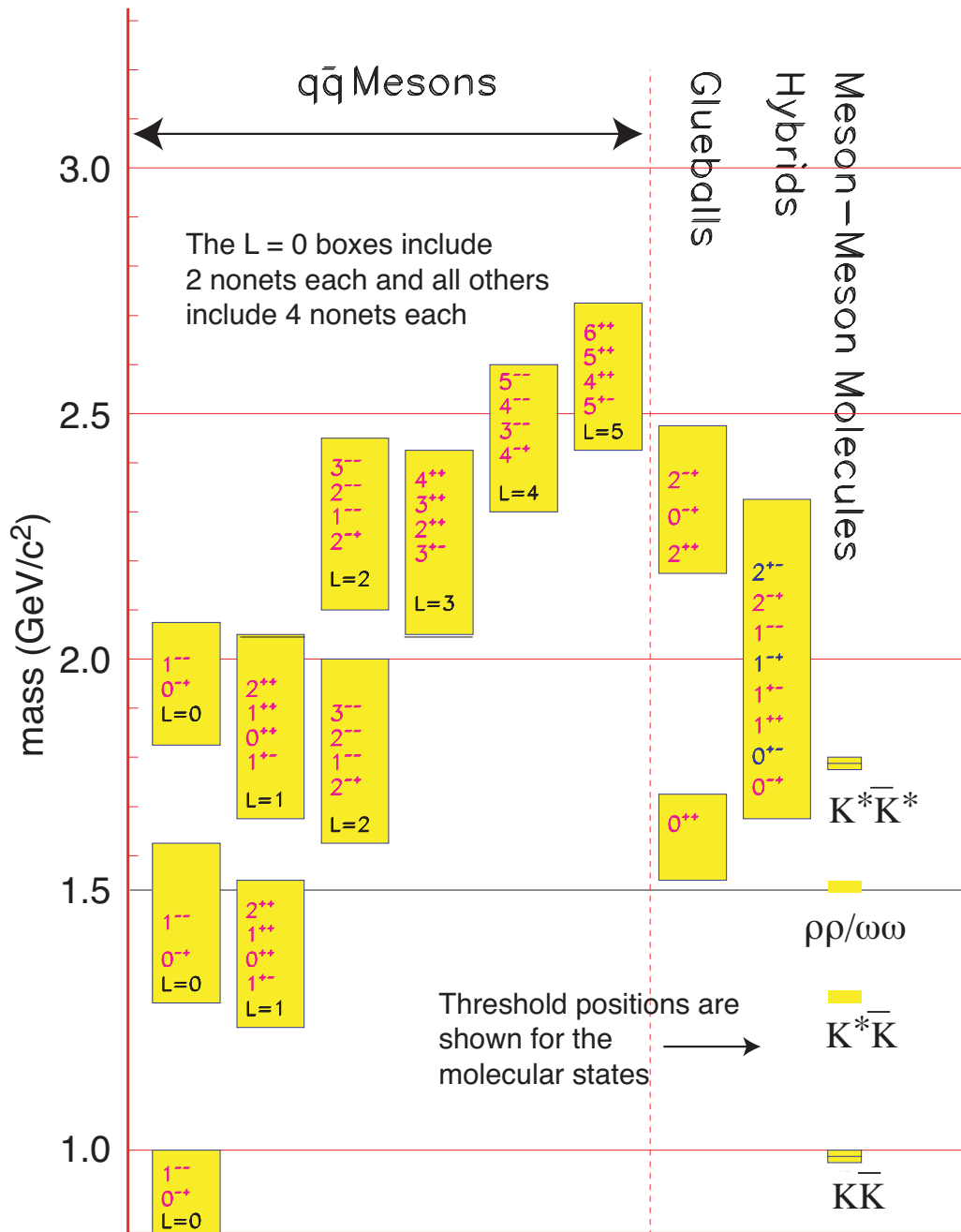


Figure 3.1: A level diagram showing conventional nonets and expected masses of glueballs, hybrids and molecular thresholds. The vertical axis is in units of GeV/c^2 . For the $q\bar{q}$ boxes the L refers to the angular momentum between the quarks and each J^{PC} refers to a nonet of mesons. Note also that exotic J^{PC} , - 0^{+-} , 1^{+-} , 2^{+-} - occur only among the hybrids for the range of masses shown.

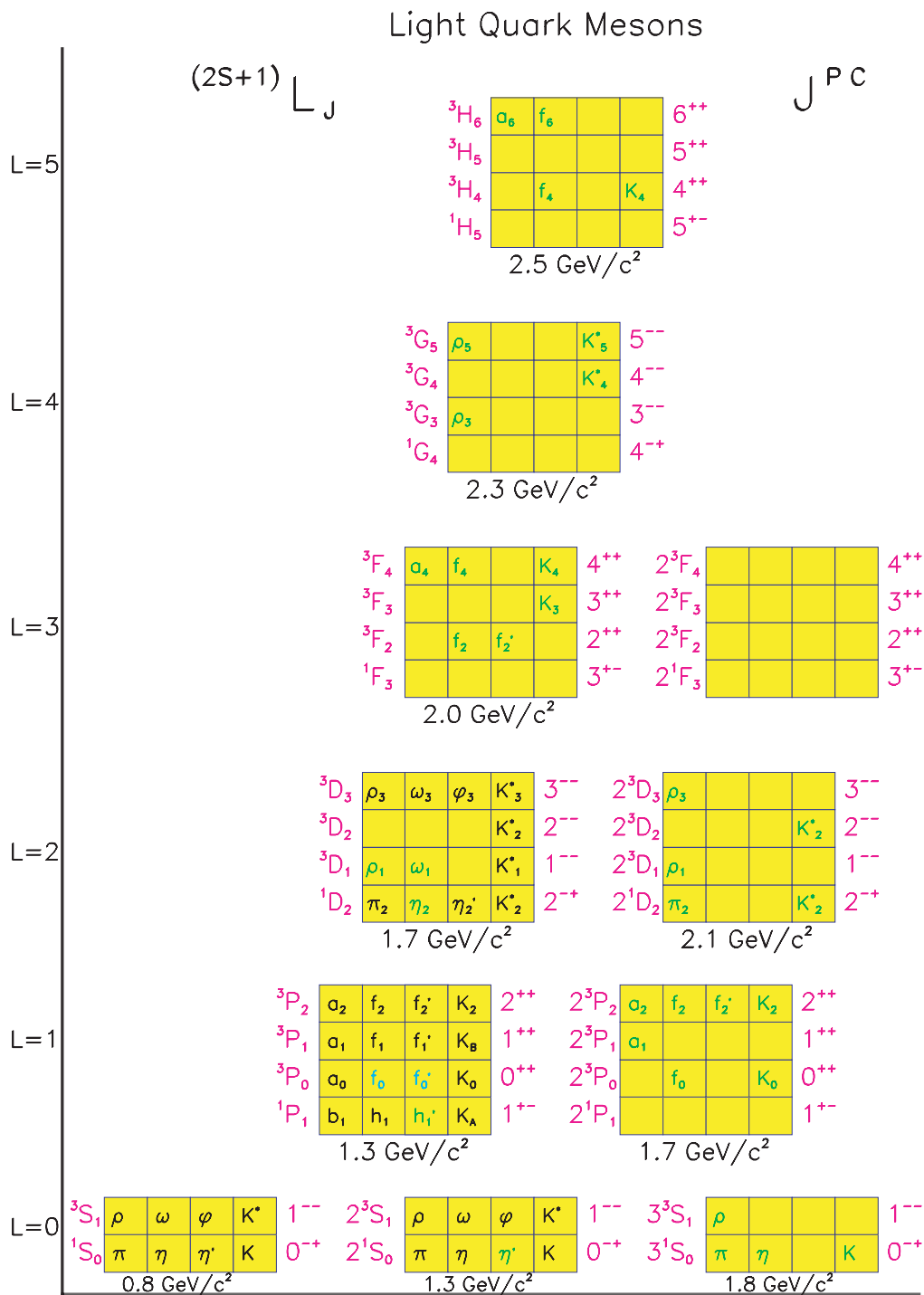


Figure 3.2: The $q\bar{q}$ spectrum of states. The assignments of the light colored states are speculative, while the empty boxes are missing states. The orbital angular momentum of the nonet is plotted on the vertical axis, while the towers of radial excitations are shown along the horizontal axis.

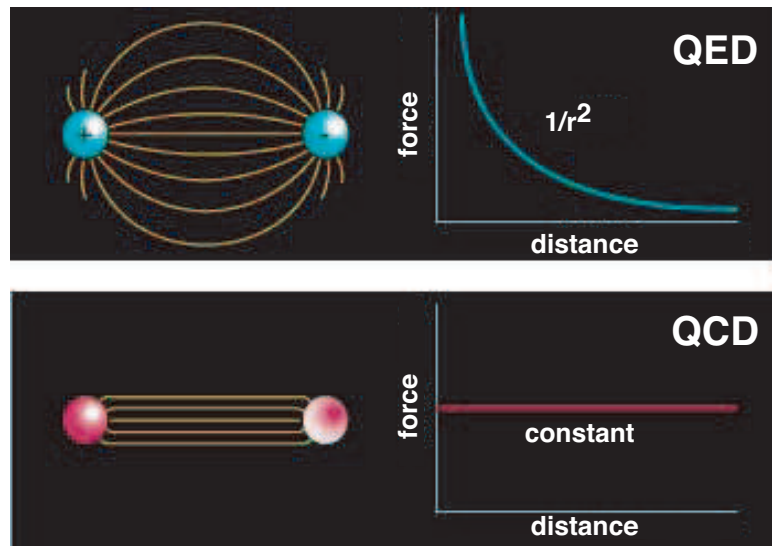


Figure 3.3: Field lines associated with the electrical force between two electrically charged particles (top) and the corresponding dependence of force on the distance between the charges and the field lines associated with the color force (bottom) between two quarks and the corresponding dependence of force on distance.

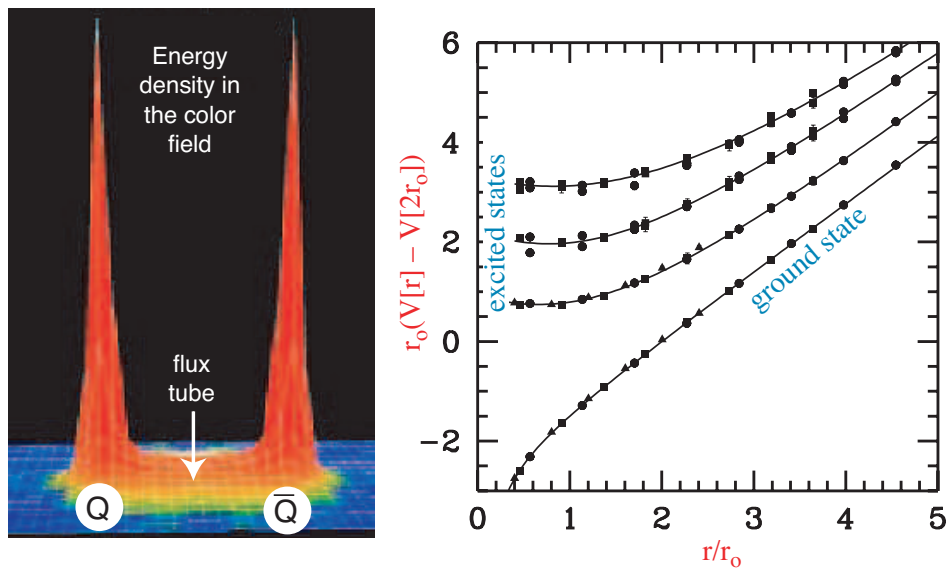


Figure 3.4: (left) A lattice QCD calculation of the energy density in the color field between a quark and an anti-quark. The density peaks at the positions of the quarks and is confined to a tube between the quarks. This calculation is for heavy quarks in the quenched approximation. (right) The corresponding potential between the quarks. The ground state potential has a $1/r$ dependence at small distances and is linear for large distances.

tube: $J^{PC} = 1^{-+}$ or $J^{PC} = 1^{+-}$. Suppose we start with the $q\bar{q}$ in the $S = 0$ and $L = 0$ (or $J^{PC} = 0^{-+}$ – the π or K) configuration. Combining this with $J^{PC} = 1^{-+}$ or $J^{PC} = 1^{+-}$ of the excited flux tube results in hybrid mesons with $J^{PC} = 1^{++}$ or $J^{PC} = 1^{--}$. These are non-exotic quantum numbers. If, however, we start with $q\bar{q}$ in the $S = 1$ and $L = 0$ (or $J^{PC} = 1^{--}$ – the vector photon) configuration, the resulting hybrid meson can have $J^{PC} = [0, 1, 2]^{+-}$ for the flux tube with $J^{PC} = 1^{-+}$ and $J^{PC} = [0, 1, 2]^{-+}$ for the flux tube with $J^{PC} = 1^{+-}$. We note that of these six possible J^{PC} combinations, three are exotic: $J^{PC} = 0^{+-}$, $J^{PC} = 1^{-+}$ and $J^{PC} = 2^{+-}$. These states will not mix with $q\bar{q}$ and thus have unique signatures.

Meson production proceeds with an incoming probe interacting with the target particle and one result of the scattering can be the excitation of the flux tube. If the probe is a $q\bar{q}$ in $L = 0$ and $S = 0$ (π or K), production of exotic hybrids will not be favored. But if the $q\bar{q}$ probe has $L = 0$ and $S = 1$, for example a photon, one expects exotic hybrids to be produced readily.

Finally we consider the expected masses for hybrid mesons. We would expect the mass difference between the ground state (conventional) mesons and hybrid mesons to be given by the level spacing between the ground state of the flux tube and the first excited transverse mode and that is simply given by π/r where r is the quark separation. When translated to appropriate units this corresponds to about $1 \text{ GeV}/c^2$.

In this discussion the motion of the quarks was ignored, but we know from general principles [11] that an approximation that ignores the impact of the flux tube excitation and quark motion on each other seems to work quite well.

3.4 Observation of gluonic excitations

3.4.1 Glueballs

Lattice QCD calculations indicate that lightest glueball is a scalar with a mass in the range from 1.5 to $1.7 \text{ GeV}/c^2$ [12, 13, 14, 15]. Indeed there is evidence from the Crystal Barrel experiment, which studied $\bar{p}p$ annihilations at CERN, that the $f_0(1500)$ is a leading candidate for a glueball [16, 17]. There are, however, indications that this state is not a pure glueball but is mixed with conventional $q\bar{q}$ [18]. There are also strong indications that the scalar meson sector contains one or more glueballs since there are several more observed states than can be accommodated in the simple $q\bar{q}$ model. However, the unique identification of a glueball is exacerbated by the possibility of mixing with $q\bar{q}$. Lattice QCD indicates a rich spectrum of glueballs, all with non-exotic quantum numbers, from 1.5 to $2.5 \text{ GeV}/c^2$. The lightest glueball with exotic quantum numbers is predicted to have $J^{PC} = 2^{+-}$ and to have a mass of $4 \text{ GeV}/c^2$ [12].

3.4.2 Exotic hybrid mesons

After about two decades of experimental searches there have been reports of experimental observations of states with exotic $J^{PC} = 1^{-+}$ by the Brookhaven E852 collaboration in π^-p interactions at $18 \text{ GeV}/c$. One of these has a mass of $(1593 \pm 8_{-47}^{+29}) \text{ MeV}/c^2$ and width of $(168 \pm 20_{-12}^{+150}) \text{ MeV}/c^2$ and decays into $\rho^0\pi^-$ [19].

This state was observed in the reaction $\pi^-p \rightarrow \pi^+\pi^-\pi^-p$ at a beam momentum of $18 \text{ GeV}/c$. In Figure 3.5, the acceptance-corrected (average acceptance was 25%) distributions of the $\pi^+\pi^-\pi^-$ and $\pi^+\pi^-$ effective masses are shown. The positions of well-established meson states are shown, including the $a_1(1260)$, which does not show up as a prominent peak in the overall mass distribution. The partial wave analysis (PWA) performed on these data assumes an *isobar model* – a parent decaying into a $\pi\pi$ state and an unpaired π followed by the decay of the $\pi\pi$ state. The resulting decomposition into various waves is shown in Figure 3.6. The decomposition clearly shows the $\pi(1800)$ in the 0^{-+} wave, the $a_1(1260)$ in the 1^{++} wave, the $\pi_2(1670)$ in the 2^{-+} wave, and the $a_2(1320)$ in the 2^{++} wave. Evidence for the exotic 1^{-+} $\rho\pi$ is shown in Figure 3.7. If an isovector $\rho\pi$ resonates in an $L = 1$ wave, it has $J^{PC} = 1^{-+}$. Also shown in this figure is the effect of leakage of non-exotic waves. Finally in Figure 3.8 a coupled fit to the wave intensities and phase difference between the 1^{-+} and 2^{-+} waves is shown.

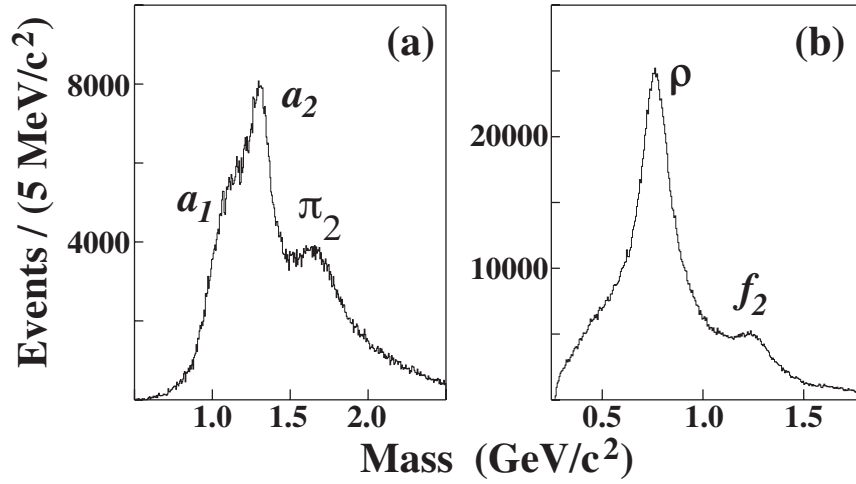


Figure 3.5: Acceptance corrected effective mass distributions for the (a) $\pi^+\pi^-\pi^-$ combination and (b) $\pi^+\pi^-$ combination (two entries per event) from E852 [19].

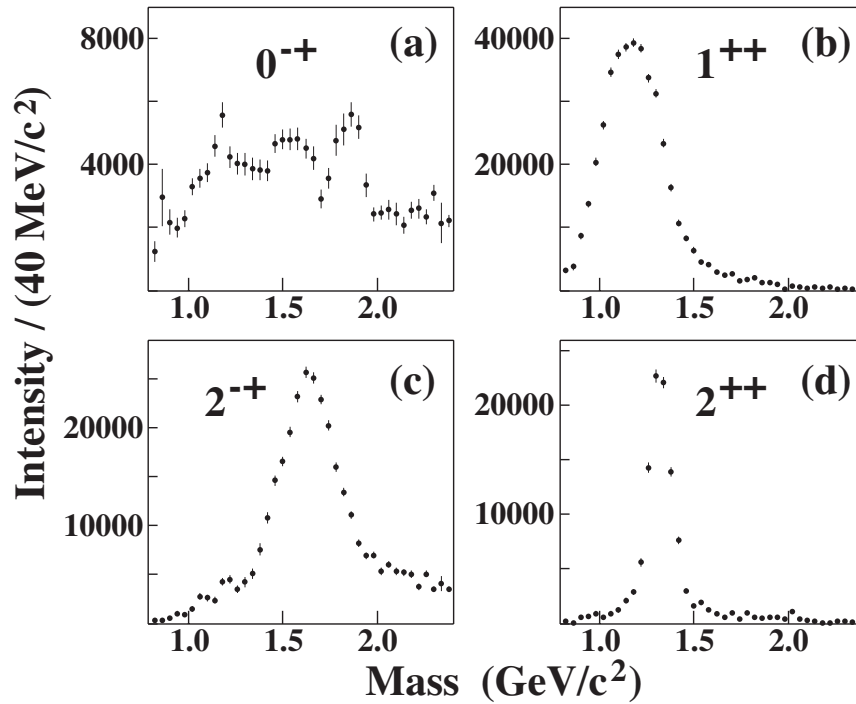


Figure 3.6: Combined intensities for all (a) 0^{-+} waves; (b) 1^{++} waves; (c) 2^{-+} waves; and (d) 2^{++} waves from E852 [19].

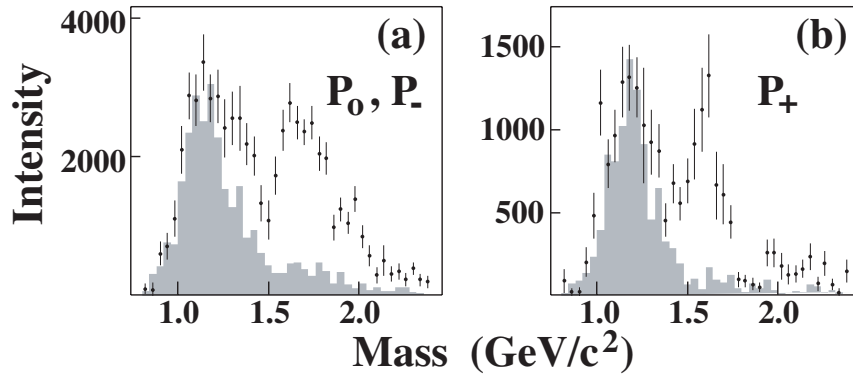


Figure 3.7: The intensities for the waves corresponding to 1^{-+} into $\rho\pi$. The shaded distributions are an estimate of leakage due to non-exotic waves – from E852 [19].

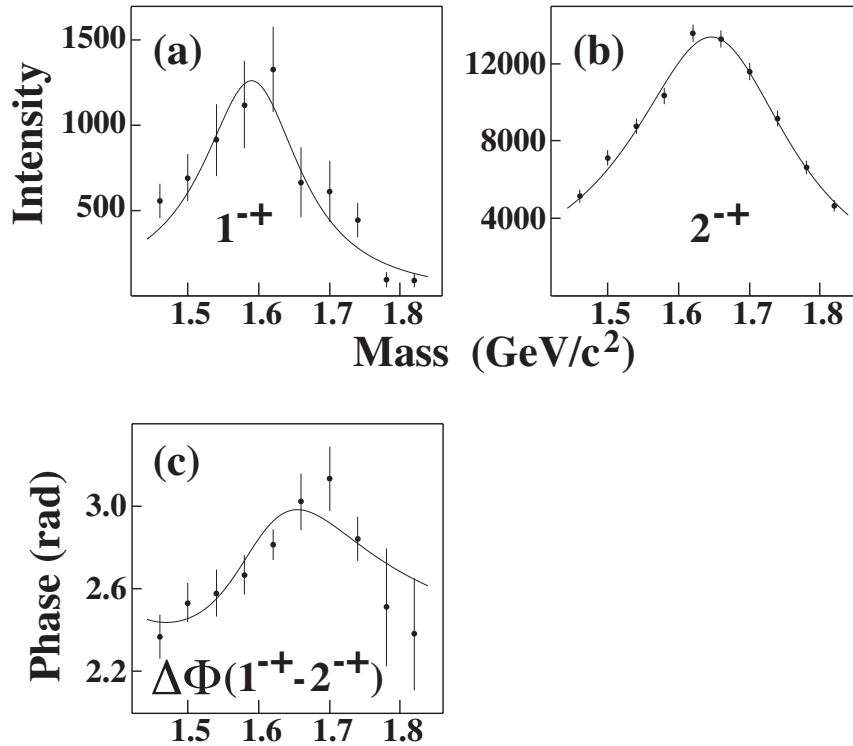


Figure 3.8: Results of a coupled mass-dependent Breit-Wigner fit of the 1^{-+} and 2^{-+} waves showing the phase difference as well – from E852 [19].

Another state reported by E852 has a similar mass, $(1597 \pm 10^{+45}_{-10}) \text{ MeV}/c^2$, but with a significantly larger width, $(340 \pm 40^{+50}_{-50}) \text{ MeV}/c^2$, and decays into $\eta'\pi^-$ [20]. It has not been determined whether these represent two decay modes of the same state or whether they are due to two different mechanisms.

The E852 collaboration also reported observation of another $J^{PC} = 1^{-+}$ state with mass $(1370 \pm 16^{+50}_{-30}) \text{ MeV}/c^2$ and a width of $(385 \pm 40^{+65}_{-105}) \text{ MeV}/c^2$ decaying into $\eta\pi^-$ [21]. If an $\eta\pi$ system is in a P wave, the resulting J^{PC} quantum number combination is exotic (1^{-+}). In these studies the dominant state observed in the $\eta\pi$ channel is the $J^{PC} = 2^{++}$ $a_2(1320)$ seen in the D -wave. Critical to the identification of this state is not only showing the presence of a P -wave, but also that the resulting line shape is consistent with a Breit-Wigner and that the phase motion of the P , as determined by its interference with the dominant D -wave, cannot be due solely to the $a_2^-(1320)$ resonance. Soon after the E852 report, the Crystal Barrel Collaboration reported an exotic $J^{PC} = 1^{-+}$ state produced in $\bar{p}n \rightarrow \pi^-\pi^0\eta$ obtained by stopping antiprotons in liquid deuterium [22]. They reported a mass of $(1400 \pm 20^{+20}_{-20}) \text{ MeV}/c^2$ and a width of $(310 \pm 50^{+50}_{-30}) \text{ MeV}/c^2$.

The first claim of an exotic meson decaying into $\eta\pi^0$ with a mass of $1400 \text{ MeV}/c^2$ was made by the GAMS collaboration in the reaction $\pi^-p \rightarrow \eta\pi^0n$ [23] but a later analysis by the group [24] led to ambiguous results. The VES collaboration also presented evidence for a P -wave contribution in $\eta\pi$ [25] and at KEK a claim was made for an exotic $\eta\pi$ state [26] as well, but with a mass and width close to that of the $a_2(1320)$; leakage from the dominant D wave could not be excluded.

In all the observations in π -induced reactions, the $\eta\pi$ P -wave enhancements have cross sections that are substantially smaller than the dominant $a_2(1320)$ so this leakage, usually due to an imperfect understanding of experimental acceptance, is a source of concern. In contrast, the observed yield of the $\pi_1(1400)$ yield in $\bar{p}p$ annihilations is of the same magnitude as the $a_2(1320)$. Apart from these experimental issues, the interpretation of the nature of low-mass $\eta\pi$ P -wave amplitude and phase motion should be guided by the principle of parsimony – less exotic interpretations must also be considered. In a recent analysis of the $\eta\pi^0$ system in the reaction $\pi^-p \rightarrow \eta\pi^0n$ from data using the E852 apparatus, a P -wave is observed but it is not consistent with a Breit-Wigner resonance. The observed P -wave phase motion is consistent with $\eta\pi^0$ final state interactions. This could explain the relatively wide width of the observed $\eta\pi^-$ state and could also explain the broad $\eta'\pi^-$ enhancement. The $\pi^-p \rightarrow \eta\pi^0n$ and $\pi^-p \rightarrow \eta\pi^-p$ have some notable differences. For the former charge conjugation (C) is a good quantum number but not for the latter and for the former both the $a_0(980)$ and $a_2(1320)$ are prominently present but for the latter only the $a_2(1320)$ is strongly produced. This is an important factor in selecting the physical solutions among mathematically ambiguous solutions.

The conclusion from these studies is that there indeed are tantalizing hints of gluonic excitations in both the glueball and hybrid sectors but the results are not conclusive. The large statistics samples of high quality data to be collected with the GLUEX detector will provide the definite resolution of the murky situation. Furthermore there is good reason to believe that whereas exotic hybrids may be suppressed in π production, they are enhanced in photoproduction where essentially no data exist. In the glueball sector, the large samples of glue-rich radiative J/ψ decays should shed light on the spectrum of these gluonic excitations.

3.5 Photoproduction of exotic hybrids

3.5.1 Why photoproduction?

Based on the arguments presented above, the photon is expected to be particularly effective in producing the *smoking gun* signature for gluonic excitations: hybrids with exotic J^{PC} . In this regard, we will compare the effectiveness of the π or K as a probe with that of the photon. In the former case, the meson is a $q\bar{q}$ with spins anti-aligned ($S = 0$) and in the latter, the photon is a virtual $q\bar{q}$ with spins aligned ($S = 1$). In both cases, the relative orbital angular

momentum is zero ($L = 0$) and the flux tube connecting the quarks is in its ground state. Figure 3.9 illustrates the differences between a π probe and a γ probe. If the scattering results in excitation of the flux tube, one expects exotic hybrid mesons to be suppressed in π -induced interactions and enhanced in photoproduction.

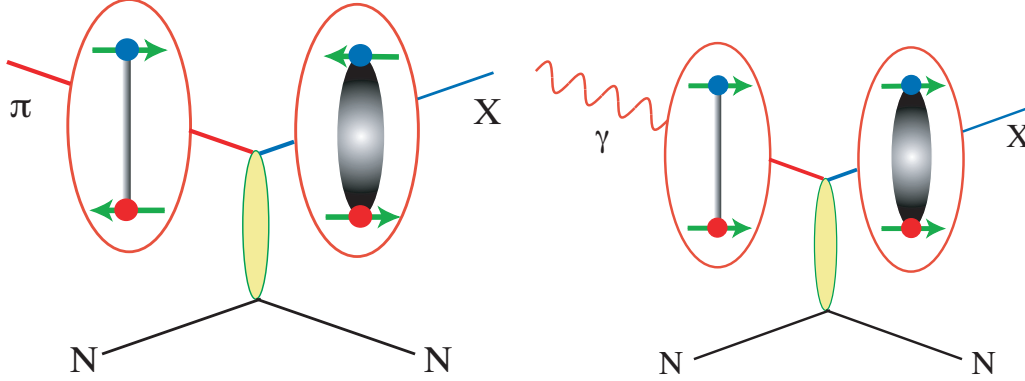


Figure 3.9: (left) With a π probe the incoming quarks have $L = 0$ and $S = 0$. The excited flux tube from the scattering results in hybrid mesons with non-exotic quantum numbers. (right) With a photon probe the incoming quarks have $L = 0$ and $S = 1$. When the flux tube is excited, hybrid mesons with exotic quantum numbers are possible.

Current phenomenology also supports the notion that photons should be more effective at producing exotic hybrids [27, 28]. Figure 3.10 shows an estimate of the photoproduction cross sections at 8 GeV for the $a_2(1320)$ and the exotic $\pi_1(1600)$ [28]. The model uses as input the ratio of $\pi_1(1600)$ to $a_2(1320)$ as observed in E852. The model is compared with photoproduction of the $a_2(1320)$ at 5 GeV . Whereas in E852, with a π beam, the $\pi_1(1600)$ is produced at about 5% of the rate for $a_2(1320)$, in photoproduction the rates for $\pi_1(1600)$ are expected to be comparable for that of the $a_2(1320)$. In the case of the incident π , the $\pi_1(1600)$ is produced by ρ exchange and the suppression at very low- $|t|$ due to angular momentum – spin 0 in and spin 1 out – decreases the cross section. This is to be compared to photoproduction of the $\pi_1(1600)$ with π exchange where there is no suppression at very low- $|t|$ since now we have spin 1 in and spin 1 out. Furthermore the $N\rho N$ coupling at the baryon vertex in the incident π case is lower by a factor of 4 compared to the $N\pi N$ in the photoproduction case.

To underscore the differences between existing photoproduction and π production, the corresponding largest data sets on 3π production are compared in the plots of Figure 3.11. The 3π mass spectrum from the reaction $\pi^- p \rightarrow \pi^+ \pi^- \pi^- p$ at 18 GeV/c from E852 at Brookhaven is shown. Also shown is the 3π mass spectrum from the reaction $\gamma p \rightarrow \pi^+ \pi^+ \pi^- n$ at 19 GeV from SLAC. We note the large difference in statistics between the two and we also note the differences in the structure of the spectra.

3.5.2 Current photoproduction data

Table 3.1 is a partial compilation of known photoproduction cross sections and the numbers of events from the existing experiments. The typical cross sections range from of order $0.1 \mu b$ up to of order $10 \mu b$, with most measurements involving rather small numbers of events, typically on the order of a few thousand. The extant data from photoproduction are far too meager to perform the analysis necessary to unambiguously identify gluonic excitations. For example, after one year of low intensity running at 10^7 photons/sec, the yield of $a_2(1320)$ in GLUEX will be five orders of magnitude greater than the same collected in the SLAC photoproduction experiment. The yield of the exotic $\pi_1(1600)$ in the published E852 results will be increased by four orders of magnitude by GLUEX after one year of running.

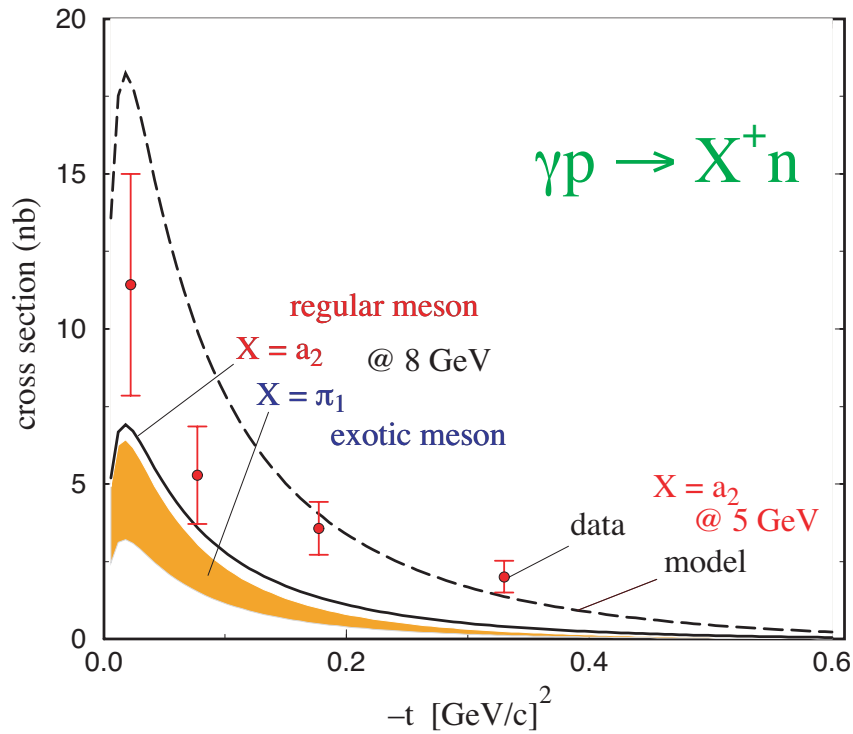


Figure 3.10: Estimates of the photoproduction cross sections for $a_2(1320)$ and the exotic $\pi_1(1600)$ at 8 GeV based on a phenomenological analysis described in [28]. The model uses as input the ratio of $\pi_1(1600)$ to $a_2(1320)$ as observed in E852. The model is compared with photoproduction of the $a_2(1320)$ at 5 GeV.

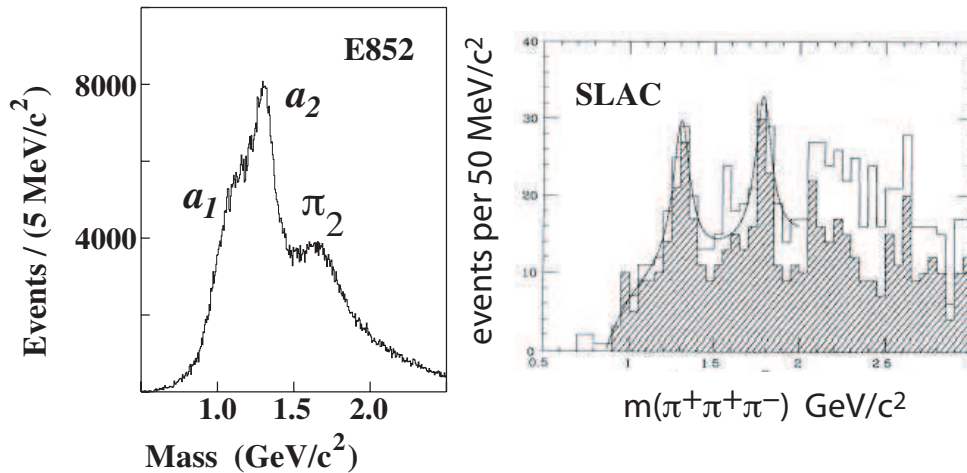


Figure 3.11: (left) The 3π mass spectrum from the reaction $\pi^- p \rightarrow \pi^+ \pi^- \pi^- p$ at 18 GeV/c from E852 at Brookhaven. (right) The 3π mass spectrum from the reaction $\gamma p \rightarrow \pi^+ \pi^+ \pi^- n$ at 19 GeV from SLAC.

<i>Reaction</i>	E_γ <i>GeV</i>	σ (μb)	<i>Events</i>	<i>Ref.</i>
$\gamma p \rightarrow p\pi^+\pi^-$	9.3		3500	[29]
$\gamma p \rightarrow p\pi^+\pi^-$	19.3		20908	[30]
$\gamma p \rightarrow p\pi^+\pi^-\pi^0$	2.8		2159	[29]
$\gamma p \rightarrow p\pi^+\pi^-\pi^0$	4.7		1606	[29]
$\gamma p \rightarrow p\pi^+\pi^-\pi^0$	9.3		1195	[29]
$\gamma p \rightarrow p\pi^+\pi^-\pi^0$	4.7–5.8	$13.5 \pm 1.5 \mu\text{b}$	3001	[31]
$\gamma p \rightarrow p\pi^+\pi^-\pi^0$	6.8–8.2	$11.8 \pm 1.2 \mu\text{b}$	7297	[31]
$\gamma p \rightarrow n\pi^+\pi^+\pi^-$	4.7–5.8	$4.6 \pm 1.4 \mu\text{b}$	1723	[31]
$\gamma p \rightarrow n\pi^+\pi^+\pi^-$	6.8–8.2	$4.0 \pm 1.2 \mu\text{b}$	4401	[31]
$\gamma p \rightarrow n\pi^+\pi^+\pi^-$	16.5–20		3781	[32]
$\gamma p \rightarrow p\pi^+\pi^-\pi^0$	20–70		14236	[33]
$\gamma p \rightarrow p\pi^+\pi^-\pi^+\pi^-$	4–6	$4.0 \pm 0.5 \mu\text{b}$	~ 330	[34]
$\gamma p \rightarrow p\pi^+\pi^-\pi^+\pi^-$	6–8	$4.8 \pm 0.5 \mu\text{b}$	~ 470	[34]
$\gamma p \rightarrow p\pi^+\pi^-\pi^+\pi^-$	8–12	$4.5 \pm 0.6 \mu\text{b}$	~ 470	[34]
$\gamma p \rightarrow p\pi^+\pi^-\pi^+\pi^-$	12–18	$4.4 \pm 0.6 \mu\text{b}$	~ 380	[34]
$\gamma p \rightarrow p\pi^+\pi^-\pi^+\pi^-$	15–20		6468	[35]
$\gamma p \rightarrow p\pi^+\pi^-\pi^0\pi^0$	20–70		8100	[36]
$\gamma p \rightarrow p\pi^+\pi^+\pi^-\pi^-\pi^0$	19.5		2553	[37]
$\gamma p \rightarrow \Delta^{++}\pi^-\pi^+\pi^-$	4–6	$1.65 \pm 0.2 \mu\text{b}$	~ 200	[34]
$\gamma p \rightarrow \Delta^{++}\pi^-\pi^+\pi^-$	6–8	$1.8 \pm 0.2 \mu\text{b}$	~ 200	[34]
$\gamma p \rightarrow \Delta^{++}\pi^-\pi^+\pi^-$	8–12	$1.1 \pm 0.2 \mu\text{b}$	~ 200	[34]
$\gamma p \rightarrow \Delta^{++}\pi^-\pi^+\pi^-$	12–18	$1.15 \pm 0.2 \mu\text{b}$	~ 200	[34]
$\gamma p \rightarrow p\omega$	4.7–5.8	$2.3 \pm 0.4 \mu\text{b}$	< 1600	[31]
$\gamma p \rightarrow p\omega$	6.8–8.2	$2.0 \pm 0.3 \mu\text{b}$	< 1200	[31]
$\gamma p \rightarrow p\omega$	4.7	$3.0 \pm 0.3 \mu\text{b}$	1354	[29]
$\gamma p \rightarrow p\omega$	9.3	$1.9 \pm 0.3 \mu\text{b}$	1377	[29]
$\gamma p \rightarrow p\phi$	4.7	$0.41 \pm 0.09 \mu\text{b}$	136	[29]
$\gamma p \rightarrow p\phi$	9.3	$0.55 \pm 0.07 \mu\text{b}$	224	[29]
$\gamma p \rightarrow na_2^+$	4.7–5.8	$1.7 \pm 0.9 \mu\text{b}$		[31]
$\gamma p \rightarrow na_2^+$	6.8–8.2	$0.9 \pm 0.9 \mu\text{b}$		[31]
$\gamma p \rightarrow na_2^+$	19.5	$0.29 \pm 0.06 \mu\text{b}$	~ 100	[32]

Table 3.1: A sample of measured photoproduction cross sections from several references. Note the small numbers of events in any given channel.

There are reasonable sized data sets in 2π and 2π photoproduction from the CLAS detector at JLab that are currently under analysis. However, these arise from unpolarized photon beams and are produced from an incoherent bremsstrahlung spectrum that peaks at around 5 GeV .

3.6 Complementarity with other searches

Gluonic excitations include both exotic and non-exotic hybrid mesons and glueballs. Hybrid mesons exist in both the light quark (u , d and s) and heavy quark (c and b) sectors. Clearly, existing data collected with incident π beams, central collisions, $\bar{p}p$ annihilations and e^+e^- collisions have not uncovered a wealth of information about these states. As discussed earlier, the focus of the GLUOX project is in the light-quark hybrid sector. The initial benchmark states will be the exotic hybrids, which cannot mix with $q\bar{q}$ and therefore have a *smoking gun* signature. There are good reasons to expect that photoproduction will be particularly effective at uncovering the exotic hybrid mesons. And the existing photoproduction data are meager indeed.

The glueball and heavy hybrid sectors are not accessible to GLUOX. Glueballs are not preferentially produced in photoproduction because they do not couple to photons. Moreover, according to lattice QCD, the lightest exotic glueball has a mass of $4\text{ GeV}/c^2$. One fruitful area of investigation are J/ψ radiative decays since the system recoiling from the photon should be rich in two-gluon states. The planned CLEO-c project at CESR will collect a billion J/ψ radiative decays.

The direct production of exotic hybrids in e^+e^- collisions is complicated by the fact that the angular momentum barrier (the excited flux-tube carries $J = 1$) suppresses this production mode.

Lattice QCD predictions about heavy-quark exotic hybrids are as reliable as for the light-quark hybrids but the experimental situation is far more problematic. The photoproduction cross-sections are a few orders of magnitude lower. At the higher energies needed to produce these more massive states many other uninteresting processes can contribute to background. Finally, to unambiguously tag a charm or beauty hybrid one must identify detached vertices, further complicating the experimental challenge.

3.7 Production and analysis of hybrid mesons

3.7.1 Kinematics

Consider a specific exclusive photoproduction reaction:

$$\gamma p \rightarrow X p \quad (3.1)$$

The center-of-mass energy squared, s , and the momentum-transfer-squared, t , between the incoming beam and outgoing X are defined in terms of the four-vectors of the particles:

$$s = (p_\gamma + p_p)^2 \quad (3.2)$$

$$t = (p_\gamma - p_X)^2 \quad (3.3)$$

The dependence of the cross section on s and t depend on the production mechanism, which is usually described in terms of the particle or particles which can be exchanged as shown in Figure 3.12. For example, if the exchange particle is the pomeron (diffractive process) the cross section is nearly constant in s . For meson-exchange processes, cross sections typically fall off with increasing s . The dependence on t is typically exponential:

$$\frac{dN}{dt} \propto e^{-\alpha|t|} \quad (3.4)$$

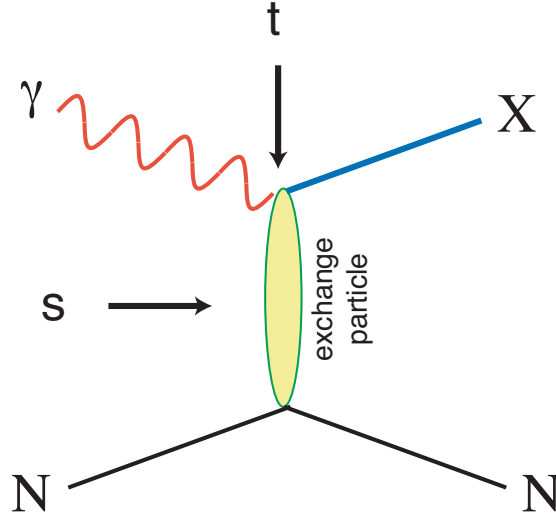


Figure 3.12: Diagram for the photoproduction of particle X . The variables s and t are the center-of-mass energy squared and the momentum-transfer-squared from incoming photon to outgoing particle X . The process shown here proceeds through the exchange of a particle in the t -channel.

For the process (3.1) at high enough photon beam energy, E_γ , we can make the approximation $s \approx 2 \cdot E_\gamma$ where E_γ is in GeV and s is in GeV^2 . For fixed s and mass of X , m_X , there is a minimum value of $|t|$, or $|t|_{min}$, needed to produce X . This $|t|_{min}$ increases with increasing m_X for fixed E_γ and decreases with increasing E_γ for fixed m_X . Coupled with the steep dependence implied in equation (3.4), the dependence of $|t|_{min}$ on m_X will affect event yields. In addition, the line shape of a resonance can be distorted if there is too rapid a variation of $|t|_{min}$ across the width of a resonance.

Figure 3.13 shows an example of how the dependence in t is correlated with particle exchange. The distribution is in $|t'|$ where $t' = t - t_{min}$ for the D -waves after a PWA of the $\eta\pi^0$ system from the reaction $\pi^-p \rightarrow \eta\pi^0n$ at $18 GeV/c$. The curves are fits to expected Regge exchanges for the various D -waves.

3.7.2 PWA requirements

The PWA technique is described in a later chapter. It is important to stress here that the detector design focuses on hermeticity and resolution to insure nearly uniform coverage with well-understood acceptance functions for various decay angles for particle X . Kinematic fitting will also be used to identify exclusive processes. The design focuses on the requirements of the PWA. The existence of well established resonances will be used as benchmarks for the PWA. They also provide benchmarks for the phase variation of candidate exotic states. Furthermore, candidate exotics can appear with multiple decay modes which should give consistent results. As an example, a meson which decays into $\eta\pi$ should be observed in channels where $\eta \rightarrow \pi^+\pi^-\pi^0$, $\eta \rightarrow 3\pi^0$, and $\eta \rightarrow 2\gamma$. Each of these modes leads to different acceptances and systematics. This provides a powerful check on PWA results.

3.7.3 Linear polarization of the beam

Linear and circular polarization

We start with a review of the relationship between linear and circular polarization. A right-handed-circularly ($|R\rangle$) polarized photon has $m = 1$ while for a $|L\rangle$ photon $m = -1$. These

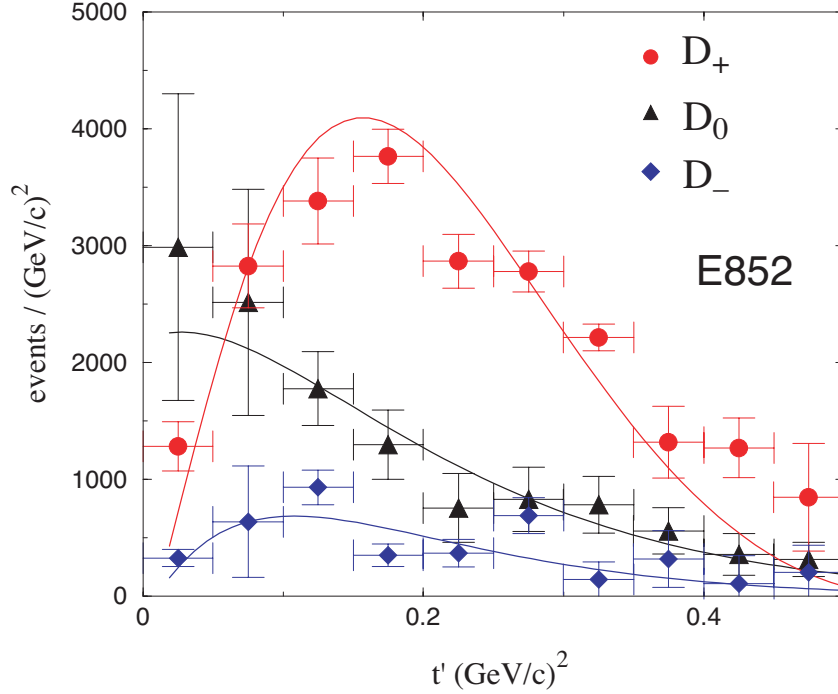


Figure 3.13: The distribution in $|t'|$ where $t' = t - t_{min}$ for the D -waves after a PWA of the $\eta\pi^0$ system from the reaction $\pi^- p \rightarrow \eta\pi^0 n$ at $18 \text{ GeV}/c$. The curves are fits to expected Regge exchanges for the various D -waves.

are related to the linear polarization states, $|x\rangle$ (in production plane) and $|y\rangle$ (perpendicular to production plane) by:

$$|x\rangle = \frac{1}{\sqrt{2}} (|L\rangle - |R\rangle) \quad (3.5)$$

$$|y\rangle = \frac{i}{\sqrt{2}} (|L\rangle + |R\rangle) \quad (3.6)$$

States of linear polarization are eigenstates of parity. We will use these relations in several straightforward cases to show how linear polarization:

1. can provide information on decays in lieu of statistics,
2. is essential in isolating production mechanisms, and
3. can be used as an exotics filter if the production mechanism is known.

Linear polarization and statistics

To illustrate how linear polarization provides useful information in the PWA, consider the case of the photoproduction of a vector meson which subsequently decays into two pseudoscalar mesons. Possible examples are $\rho \rightarrow \pi\pi$ or $\phi \rightarrow K\bar{K}$. Suppose the production mechanism produces the vector with the same helicity as the incident photon (or s -channel *helicity conservation*). In the rest frame of the vector the two-pseudoscalar wave function is described by

$$Y_1^m(\theta, \phi) \propto \sin\theta \cdot e^{im\phi} \quad (3.7)$$

For circularly polarized photons (either $m = 1$ or $m = -1$) the square of this amplitude carries no ϕ information while for in-plane photons there is a $\cos^2 \phi$ dependence and out-of-plane a $\sin^2 \phi$ dependence in the decay angular distribution, since in these cases we have the sum or difference of Y_1^{+1} and Y_1^{-1} according to equations (3.5) and (3.6). Although not essential in determining spin, a gain of statistics is needed to recover a drop in the degree of linear polarization. For example, our Monte Carlo simulation studies indicate that when the degree of linear polarization decreases from 0.40 to 0.2 a factor of two increase in statistics is needed to achieve the same relative error in determination of spin amplitudes.

Linear polarization and production mechanism

This is best illustrated by considering a specific example. Suppose we produce a vector particle ($J^P = 1^-$) by the exchange of a scalar particle ($J^P = 0^+$ – natural parity exchange) or a pseudoscalar particle ($J^P = 0^-$ – unnatural parity exchange). We wish to determine whether the vector is produced by natural (amplitude A_N) or unnatural (amplitude A_U) parity exchange. In the center-of-mass of the vector particle, the momentum vectors of the beam photon and exchange particle are collinear. For circularly polarized photons, the m of the vector is the same as that of the photon. From parity conservation, the orbital angular momentum between the photon and exchange particle is $L = 0$ or $L = 2$ for natural parity exchange and $L = 1$ for unnatural parity exchange. So for circularly polarized photons, with $m = +1$, the total amplitude is $A_N + A_U$ whereas for $m = -1$, the total amplitude is $A_N - A_U$. This follows simply from the addition of angular momenta. Circularly polarized photons allow us to measure only the sum or difference of the two exchange amplitudes. If however, we have linearly polarized photons along the x -direction, we extract A_N using equation (3.5) and for polarization along the y -direction, we extract A_U using equation (3.6).

Linear polarization as an exotics filter

Using arguments similar to those above, it has been shown [38] that linear polarization can be used as a tool to filter exotics. For example, a $\rho\pi$ system with $I = 1$ has $C = +$. Suppose that one can determine the naturality of the exchange particle by selecting data within a range of $|t|$. For a produced $C = +$ particle with spin one we can have natural parity ($J^{PC} = 1^{-+}$ – exotic) or unnatural parity ($J^{PC} = 1^{++}$ – non-exotic). In the case of natural parity exchange the in-plane polarization selects the $J^{PC} = 1^{-+}$ wave while out-of-plane polarization selects $J^{PC} = 1^{++}$. For unnatural parity exchange the reverse is true. Note that in this case, we are specifying the naturality of the exchange and using linear polarization to select the naturality of the produced particle. In the previous section, we specified the naturality of the produced particle and used linear polarization to select the naturality of the exchanged particle.

Chapter 4

Photon Beam

One of the unique opportunities presented by a CEBAF upgrade to energies of 12 GeV and beyond is the possibility of generating high-intensity continuous photon beams for high-energy photoproduction experiments. In this regime, photon beams represent an interesting extension to the meson spectroscopy program that has been actively pursued using beams of pseudoscalar mesons at hadron accelerator laboratories: with high energy photons one has essentially a beam of *vector* mesons. It is difficult, in fact, to conceive of any other way to obtain such a vector beam.

The requirements for photon beam energy and polarization were described in Chapter ???. This chapter describes a design for a real photon source that meets these requirements. Starting with a beam of monochromatic electrons, it provides an intense beam of high-energy photons with an energy spectrum that is dominated by a single peak. A significant fraction of the total power in the beam is concentrated inside this peak, which has a width of less than 10% f.w.h.m. At a fixed electron beam energy E_0 , the peak energy of the photon beam can be varied anywhere up to 90% E_0 simply by rotating a crystal. The photon spectrum inside the intensity peak has a large degree of linear polarization. The precise energy of an individual photon inside the peak is determined (“tagged”) from the momentum of the recoil electron measured in a dedicated “tagging” spectrometer. The design is formed around the expected parameters for the CEBAF beam following the energy upgrade to 12 GeV , although nothing prevents its operation at lower energies before the time that 12 GeV beams are available.

This chapter begins with a survey of the techniques for producing high-energy photons that were considered in the development of this design, and the reasons for the choice of coherent bremsstrahlung. The coherent bremsstrahlung source is then described in greater detail, followed by a discussion of the requirements that the design places on the electron beam that feeds the source. The tagging spectrometer design is described next, and the chapter concludes with a discussion of the considerations that govern the choice of beam intensity for particular measurements.

4.1 Choice of Technique

Two basic methods have been considered for producing photons of the highest possible energy, flux and polarization from electrons of $E_0 = 12\text{ GeV}$. The methods are bremsstrahlung and Compton scattering of light. Both are well-established methods of producing photon beams. Both techniques are actually described by the same Feynman diagrams, shown in Fig. 4.1. In the case of Compton scattering the incoming photon is real, whereas it is virtual for the case of bremsstrahlung.

Each of these techniques has its own limitations and advantages. In order to be suitable for GLUEX, the photon source must be capable of producing photons of energy at least 80% E_0 , (9 GeV). The photon beam should have linear polarization. The energy resolution for individual photons in the beam should be as high as possible, *i.e.* on the order of the energy

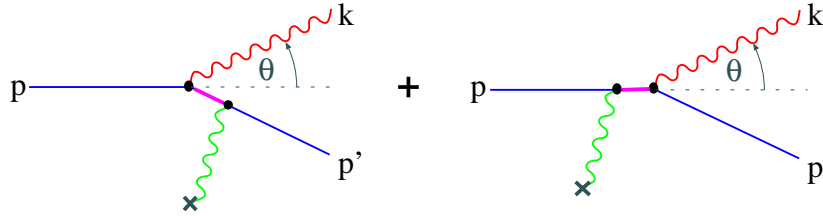


Figure 4.1: Generic diagrams for hard photon production from a high energy electron beam. The symbol \times represents either a static charge distribution, in the case of virtual photons in the initial state (i.e. bremsstrahlung), or an optical cavity, in the case of real photons in the initial state (i.e. Compton scattering).

spread of the electron beam itself. It should be capable of producing intensities up to $10^8/\text{s}$. The contamination of the beam with photons outside the desired energy band should be as low as possible. It is also important that the source be reliable and require a minimum of down-time for maintenance. The suitability of each approach is discussed below in the light of these criteria.

4.1.1 Compton Back-scatter

A Compton source begins with a beam of visible or ultraviolet light, typically from a laser that is aligned to intersect the incident electron beam at close to 180° . Some of the photons undergo Compton scattering with the beam electrons. In the lab frame, the scattered photons come out in a narrow cone about the incident electron direction and carry a significant fraction of the electron energy.

The basic design of the Compton back-scatter source for this study was put forward by C. Keppel and R. Ent [39]. The design entails the use of a four-mirror high-gain cavity pumped by a 10 kW argon-ion laser putting out 2 ps pulses at a frequency of 100 MHz. The pulses in the cavity are synchronized so that the light pulses intercept an electron bucket each time they pass through the beam. The total length of the cavity is 2 m with a crossing angle of 1° . Both cavity and electron beam are focused to a tiny spot of 10 μm r.m.s. radius at the crossing point. A small spot size is necessary in order to get as high a scattering rate as possible. The gain of the cavity is 10^4 , which is conservative in view of recent advances in mirror technology. The wavelength of the light is 514 nm. The rate spectrum of the back-scattered beam from this source is shown in Fig 4.2a for a 1 μA electron beam at 12 GeV.

From the point of view of flux, this source is marginal. With a few μA of beam and mirror improvements, it might produce 10^8 photons/s in the upper third of its energy spectrum. However, its maximum photon energy of 3.7 GeV is far short of the 80% E_0 needed for GLUEX. To remedy this one must decrease the wavelength of the laser beam. This can be done by the use of a frequency-doubling crystal that absorbs the green light from the laser and produces ultraviolet light at 257 nm. Storing this light in a cavity of similar design to that described above yields the back-scatter rate spectrum shown in Fig. 4.2b. The major reason for the drop in rate is the decrease in the cavity gain from 10000 to 250. This is imposed by the diminished reflectivities of mirrors in the UV. Other factors are the inefficiency of the doubling crystal, a factor of two in rate from the doubling itself, and the decreasing Compton cross section with energy. The maximum photon energy is still under 50% E_0 and the flux is three orders of magnitude below the desired rate.

In order to reach photon energies of 80% E_0 , initial photons of 20 eV are needed. The brightest source of these would be a synchrotron light source or a free electron laser (FEL). Mirrors that operate at these wavelengths typically have reflectivities around 70%. With these one could conceive of a scheme that uses a wiggler to extract energy from the 12 GeV beam before it enters the dump. This light would have the same time structure as incident beam, and so it could be reflected back and made to cross the incident beam at a small angle for a Compton back-scatter source. An indication of the level of flux that could be achieved with

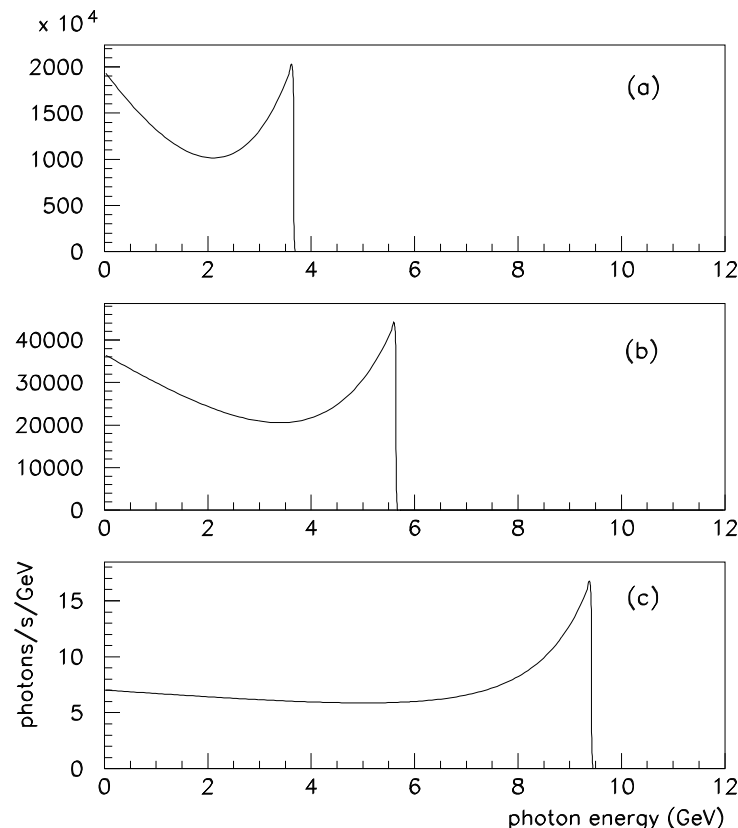


Figure 4.2: Photon energy spectrum from the Compton back-scatter source described in the text and a 12 GeV electron beam at 1 μA . (a) cavity of gain 10000 driven by a 10 kW Argon-ion laser (514 nm) at 100 MHz. (b) cavity of gain 250 driven by 3 kW frequency-doubler (257 nm) pulsed at 100 MHz. (c) cavity of gain 1 driven by a hypothetical FEL source operating at 20 eV with the same time structure as CEBAF beam, peak power 1 kW.

such a source can be obtained by using the laser cavity model described above, setting the gain to 1, the wavelength to 62 nm, and assuming 1 kW peak (1 W average) of synchrotron light. The back-scatter rate is shown in Fig 4.2c. This plot shows that even if the full power of a 1 μA on a 12 GeV beam were converted into 20 eV photons and back-scattered from the incoming beam, the rate would still fall far short of the requirements for GLUEX.

From the point of view of polarization, the Compton back-scatter source would be ideal. The polarization of the back-scattered beam is controlled by that of the laser, and can be essentially 100%. This source is also virtually background-free because the spectrum below any desired cutoff can be eliminated by collimation. The energy of the remaining beam can be measured to within the resolution of the electron beam by tagging. However the the combination of sufficient energy and sufficient flux for the purposes of the GLUEX experiment in HALL D cannot be achieved using this source.

4.1.2 Tagged Bremsstrahlung

A bremsstrahlung source consists of a thin piece of material (the radiator) that is placed in the electron beam and converts part of the energy of the beam into bremsstrahlung radiation. Bremsstrahlung offers the only practical way, starting with an electron beam at CEBAF energies, to produce a photon beam with a significant flux in the vicinity of the end point. It produces a naturally collimated photon beam with a characteristic angular spread of m/E_0 . This allows the low emittance of the CEBAF beam to be effectively transferred into the secondary photon beam.

Bremsstrahlung does not suffer from the kind of flux limitations that were encountered in the examination of Compton back-scatter sources. The radiator thickness must be kept below 1% of a radiation length in order to maintain good energy resolution in the tagger. Keeping the thickness below 10^{-3} radiation lengths ensures that multiple scattering in the radiator does not significantly broaden the divergence angle of the photon beam. A 10^{-3} radiator and 1 μA of electrons would produce much more than sufficient flux for GLUOX.

A bremsstrahlung source is, however, deficient in some other respects. Averaged over the bremsstrahlung cone, the photon beam has zero linear polarization. Circular polarization can be achieved by polarization transfer from a polarized electron beam, but for the purposes of GLUOX it is linear polarization that is desired. A bremsstrahlung source also suffers from a large low-energy flux in the beam. The power spectrum of a bremsstrahlung beam is approximately uniform from zero up to the energy of the incident electrons. This means that an experiment that uses the high-energy part of the beam must operate in a background of low-energy photons that are many times more frequent. The tagger is helpful in eliminating many of the false starts in the detector that arise from the background, but this technique becomes ineffective at rates above a few 10^7 tagged photons/s. For the typical experiment using tagged bremsstrahlung and open detector geometry, background from low-energy beam particles limits the rate at which the experiment can run to less than $5 \cdot 10^7$ tagged photons/s. The goal for GLUOX pushes that limit to 10^8 /s by employing tagged *coherent* bremsstrahlung.

4.1.3 Coherent Bremsstrahlung

The source described in the previous section meets most of the requirements for GLUOX, but is deficient in the areas of polarization and backgrounds. Both of these deficiencies can be remedied by replacing the conventional amorphous or polycrystalline radiator with a thin mono-crystalline wafer. At special settings for the orientation of the crystal, the atoms in the radiator can be made to recoil together from the radiating electron. When they do this they produce a coherent enhancement at particular energies in the radiation spectrum, which correspond to the reciprocal lattice vectors of the crystal. The kinematics are such that a randomly oriented lattice vector would make a tiny peak located up at the end point of the energy spectrum, where the coherent gain factor is negligible. By careful orientation of the crystal, however, one of the lattice vectors can be aligned with the favored kinematics for bremsstrahlung, at which point its coherent peak appears well below the end point, and its coherent gain can be large enough that it contributes a large fraction of the total radiated power.

This is illustrated in Fig. 4.3. This plot shows the intensity (dP/dE) or power spectrum of the coherent bremsstrahlung beam after collimation. The sequence of secondary peaks above the primary correspond to integral multiples of the fundamental reciprocal lattice vector and so they are always present. By careful choice of orientation angles it is possible to suppress all other vectors and isolate just one primary peak in the energy band of interest, as shown in the figure. By a small rotation of the crystal, the position of the peak can be moved from one end of the spectrum to the other. Note that the coherent peaks appear as enhancements on top of the incoherent bremsstrahlung continuum.

Unlike those from the incoherent process, coherent bremsstrahlung photons have significant net linear polarization in the plane given by the beam direction and the crystal lattice vector. This polarization is enhanced by collimating the photon beam below its intrinsic angular spread, as discussed in the next section. The loss in flux from collimation can be recovered by increasing

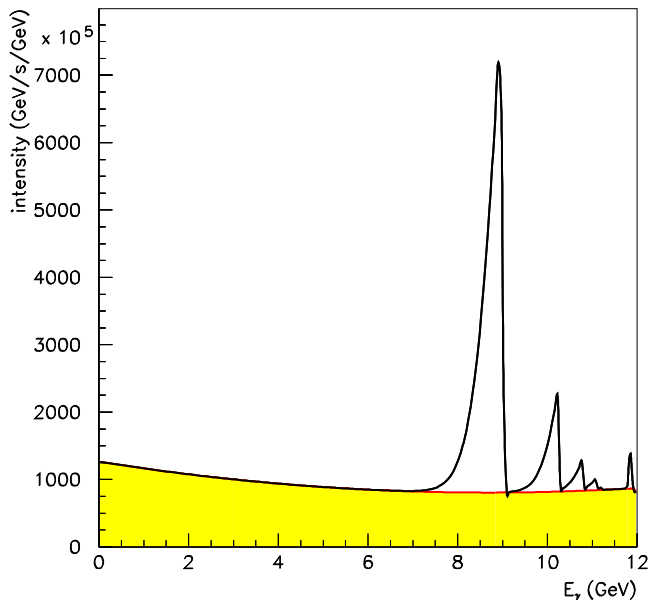


Figure 4.3: Photon power spectrum from an oriented diamond radiator. The y axis is dP/dE with power P expressed in GeV/s and E in GeV . The radiator thickness is 10^{-4} radiation lengths and the electron beam current is $1 \mu A$. Shown is what emerges after the photon beam passes through a collimator 3.4 mm in diameter located 80 m downstream from the radiator.

the electron beam current. As will be shown in the following section, even in the case of very thin crystals and severe collimation, quite modest electron beam currents are needed to produce the required photon flux.

The use of coherent bremsstrahlung improves the background conditions of the beam by enhancing the spectral intensity in the desired energy band relative to the incoherent continuum. For measurements that do not require polarization, a crystal radiator can be used without collimation to reduce the low-energy beam background for a given rate of tagged photons. Where polarization is required, coherent bremsstrahlung is indispensable.

4.2 Photon Source

A horizontal plan view of the photon beam line is shown in Fig. 4.4 with the major components labeled. The electron beam enters the figure from below ground at the left and is bent into the horizontal plane to enter the tagger building. There it passes through two small dipoles to impinge upon the bremsstrahlung radiator. After its exit from the radiator, the electron beam passes into the tagging spectrometer where the primary beam is bent in the direction of the electron beam dump. The radiator crystal is thin enough that the average energy loss by the electrons in traversing the radiator is less than the intrinsic energy spread of the incident beam. Those electrons which lose a significant fraction of their initial energy inside the radiator do so by emitting a single bremsstrahlung photon. These degraded electrons are bent out of the primary beam inside the tagger magnet and exit the vacuum through a thin window, passing through air for a short distance to strike the focal plane of the spectrometer. The primary electron beam is contained inside vacuum all the way to the dump.

The photons that are produced in the radiator pass through a small hole bored in the return

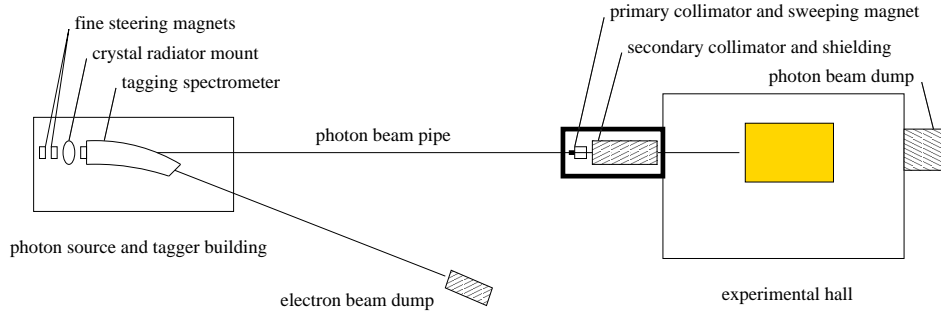


Figure 4.4: Schematic plan view of the photon beam line, shown in the horizontal plane as viewed from above. The objects in this figure are not drawn to scale.

yoke of the tagger magnet in the forward direction. They then pass into an evacuated photon beam pipe and travel to the experimental hall. Just before entering the hall the photon beam passes through a system of collimators and sweeping magnets. They are housed in a separate enclosure for shielding purposes. The primary collimator is first. It defines the part of the photon beam that is allowed to reach the target. Debris from interactions along the inside surface of the collimator bore forms a halo around the photon beam that exits the primary collimator. The charged component of the halo is deflected away from the beam axis by a dipole “sweeping” magnet just downstream of the collimator. A secondary collimator follows the sweeping magnet to stop the deflected shower particles and block the halo of secondary photons generated by the first collimator. The secondary collimator is of a larger diameter than the primary and so sees a reduced rate of secondary interactions on the inner surface of the hole. What new showers are generated there are cleaned up by a second sweeping magnet. The beam then passes through a block of shielding material into the experimental hall. This triple-collimation system is similar to the setup at the SLAC coherent bremsstrahlung beam line [40].

The collimated photon beam, now only a few mm in diameter, is delivered to the experimental target. After passing through of order 3% radiation lengths of target, the photon beam passes through the detector and into the photon beam dump at the back of the hall. Based upon a design upper limit of 60 kW ($5\ \mu A$ at 12 GeV) being delivered to the electron beam dump, the total power in the photon beam is not more than 1.5 W in the experimental hall and not more than 15 W in the collimator enclosure.

4.2.1 Essential Features

The adjective ‘coherent’ in coherent bremsstrahlung does not indicate that the photons in the beam are in a coherent state, as is light from a laser. Rather it refers to the coherent effect of multiple atoms in a crystal lattice in absorbing the recoil momentum from a high energy electron when it radiates a bremsstrahlung photon. In X-ray spectroscopy one encounters the same thing in the Mössbauer effect, except in that case the chief physical consequence is the disappearance of the recoil Doppler shift from the photoabsorption/emission spectrum. Here the chief consequence is the enhancement of bremsstrahlung at those particular kinematics for which the recoil momentum matches one of the reciprocal lattice vectors of the crystal.

Another useful way to view the process of coherent bremsstrahlung is as virtual Compton scattering. To the high energy electron, the atoms in the radiator appear as clouds of virtual photons. For a disordered radiator material, the virtual photon spectrum is given simply by the atomic form factor squared, averaged over the different species in the material. If the radiator is a single crystal, however, the atomic form factor gets multiplied by the form factor of the crystal, which in the ideal case looks like a series of delta-functions located at the sites of the reciprocal lattice. In effect, the crystal provides a set of virtual laser beams, each one a standing wave tuned to a specific reciprocal lattice vector. In this view the process of hard bremsstrahlung is seen to be the same as Compton back-scattering of laser light. For a more detailed discussion

of the physics of coherent bremsstrahlung there are a number of good references [40, 41, 42, 43].

The use of Compton back-scattering of laser light as a photon source was earlier noted as ruled out by the limitation of high-power lasers and cavities to wavelengths above $100 \mu m$. The characteristic wavelength of the crystal photons is a few Angstroms, three orders of magnitude shorter. In this case, 180° scattering would result in essentially 100% of the electron beam momentum being transferred to the photon in the lab frame. However, the Compton cross section contains a factor of $1/(\vec{q} \cdot \vec{p})^2$ where \vec{q} is the virtual photon momentum and \vec{p} is that of the electron, which strongly favors incident photons with \vec{q} nearly orthogonal to \vec{p} . With reciprocal lattice vectors pointing in almost every direction, only those nearly perpendicular to the beam contribute appreciably to the scattering rate. This fact applies equally to ordinary bremsstrahlung; in fact, to a first approximation the bremsstrahlung spectrum from a single crystal is the same as from a disordered radiator. The reason is that, if the sum over crystal momenta were replaced with a continuous integral, one would recover the ordinary bremsstrahlung result for isolated atoms. Beyond a few unit cells from the origin in reciprocal lattice space, the atomic form factor and kinematic factors become slowly varying on the scale of the lattice spacing, and the sum becomes indistinguishable from the integral. Besides that, the uncertainty principle requires that atoms localized at the sites in a crystal undergo fluctuations about their mean position. This has the effect of attenuating the discrete peaks in the crystal form factor at progressively higher-order crystal momenta, eventually washing them out and filling in the gaps between them, so that the sum deforms smoothly into the integral at high momentum transfer. Hence, the sum over crystal indices that yields the final photon spectrum can be separated into two parts: a discrete sum over a limited set of small crystal indices and an integral over the continuum of momentum transfer values beyond. The latter appears in the coherent bremsstrahlung beam as an ordinary $1/k$ bremsstrahlung spectrum, while the former appears as a set of peak structures superimposed upon it. The $1/k$ continuum, referred to as the incoherent component, is invariant as the crystal is rotated, whereas the coherent peaks change in position and intensity, depending on crystal orientation.

A typical coherent bremsstrahlung spectrum is shown in Fig. 4.5. The distinction between incoherent and coherent components in the figure is artificial; it is there to show the part of the spectrum that shifts as the crystal is rotated. The vertical scale in the figure gives the photon rate for the given beam current and crystal thickness. Note that the intensity of the incoherent background is less than what would be obtained with an amorphous carbon radiator of the same thickness, because a part of the momentum transfer integral in the Bethe-Heitler formula has been moved into the discrete sum and contributes to the coherent part. The radiation length of diamond is actually an average over all orientations of the crystal. In the calculation for Fig. 4.5 the leading 400 lattice sites were included in the discrete part of the calculation, although it can be seen that, at the chosen crystal orientation, only two or three of them contribute with sufficient intensity to be individually visible in the spectrum.

4.2.2 Use of Collimation

The presence of the large incoherent continuum in Fig. 4.5 presents a significant handicap to a photoproduction experiment. Not only do the continuum photons produce background in the detector, but they diminish the polarization of the beam. The entire beam polarization appears in the coherent component; the underlying incoherent flux only serves to dilute the polarization. There is another difference between the two components that allows them to be separated to some extent. The kinematics of bremsstrahlung confines most of the intensity of the photon beam to forward angles within m/E radians of the incident electron direction. This is true both for the incoherent and coherent components. In the lab this is a small angle, but in the rest frame of the electron-photon system it subtends all angles in the forward hemisphere. The difference lies in the fact that a peak in the coherent component corresponding to a single reciprocal lattice vector has two-body kinematics, so there is a well-defined relation between the emission angle and the energy of the emitted photon in the lab: emission at 0° yields a maximum energy photon, with energy decreasing with increasing angle. This accounts for the

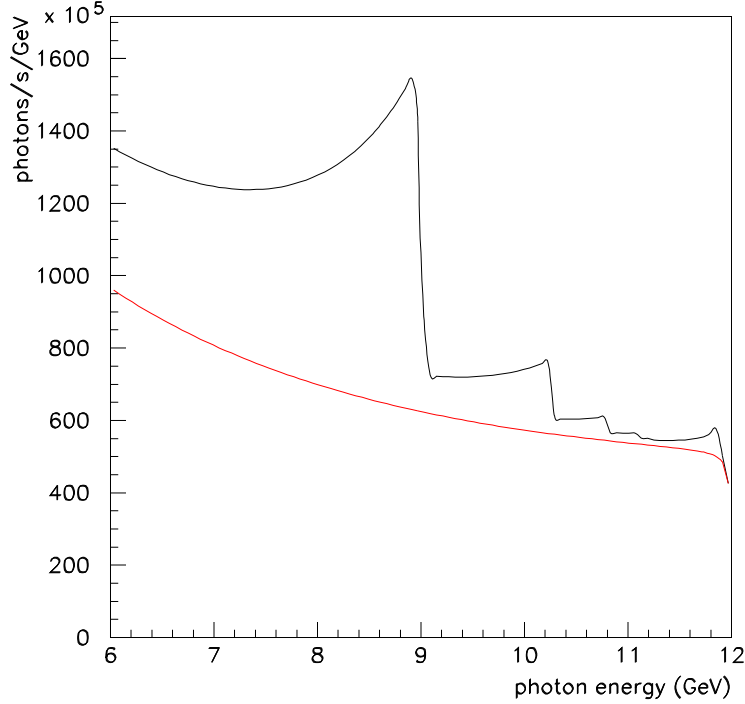


Figure 4.5: Uncollimated coherent bremsstrahlung spectrum, calculated for a diamond crystal radiator 15 μm thick and a 1 μA electron beam of 12 GeV energy. Typical values are used for beam emittance and crystal mosaic spread.

shape of the coherent peaks in Fig. 4.5, with the sharp right-hand edge corresponding to 0° emission and the tail to lower energies corresponding to emission at higher angles.

The incoherent component, because it comes from a sum over momentum transfers at all angles, has essentially no correlation between photon energy and emission angle. This means that collimating away all photons beyond some angle $\theta_{max} < m/E$ uniformly attenuates the incoherent spectrum at all energies, whereas it preserves all of the coherent photons from the maximum energy for the given peak down to some cutoff. The kinematic relations for coherent bremsstrahlung are as follows,

$$\theta^2 + 1 = \left(\frac{1-x}{x} \right) \left(\frac{x_{max}}{1-x_{max}} \right) \quad (4.1)$$

$$x_{max} = \frac{2\vec{p} \cdot \vec{q}}{2\vec{p} \cdot \vec{q} - m_e^2} \quad (4.2)$$

where x is the photon energy in units of the incident electron energy and θ is the lab emission angle of the photon relative to the incident electron momentum axis, in units of m/E .

The effects of collimation are demonstrated in the calculated spectra shown in Fig. 4.6. First, note that the collimation angles are very small, which requires a long flight path of order 100 m in order that the collimator can be larger than the intrinsic beam spot size, otherwise the collimator is cutting in transverse coordinate instead of in angle. This distance is, in fact, a sensitive function of the electron beam emittance from the machine, and must be increased in inverse proportion to the beam emittance if the effectiveness of collimation is held constant.

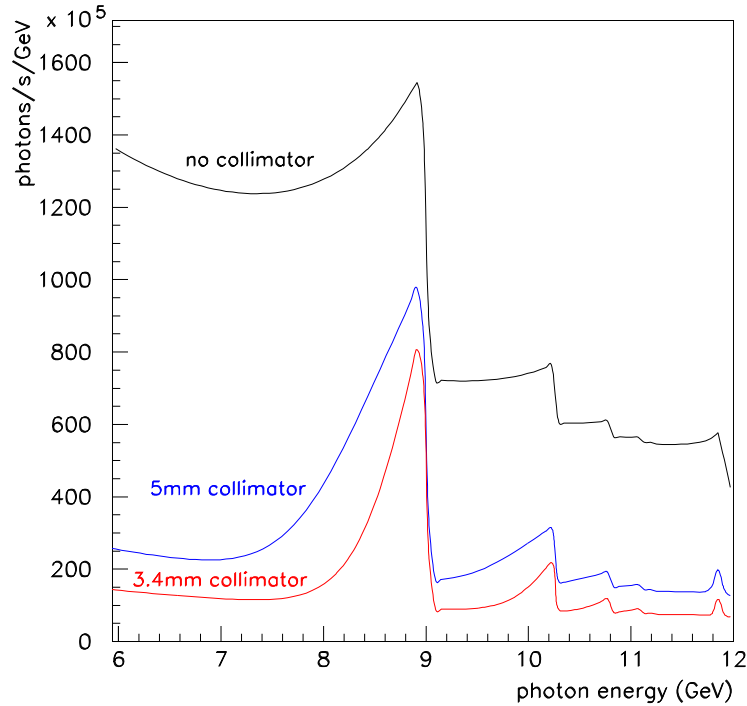


Figure 4.6: Coherent bremsstrahlung spectrum, calculated under the same conditions as in Fig. 4.5, after collimation. The upper curve is the uncollimated spectrum from Fig. 4.5. The middle curve corresponds to a 5 mm diameter collimator placed 80 m downstream of the radiator, or approximately $0.75 m/E$ in collimator half-angle. The lower curve corresponds to a 3.4 mm collimator in the same position, approximately $0.50 m/E$. For the 3.4 mm collimator there are approximately $3.3 \times 10^7 \gamma/s$ in the primary peak for a nominal electron beam current of 1 μA and crystal thickness of 15 μm .

This issue, along with the associated demands placed on beam alignment and position stability, are taken up in more detail in the following section on the electron beam line.

Second, note that the cut imposed on the coherent peak by collimation does not produce a perfectly sharp edge as would be expected from two-body kinematics. This is because the collimator cuts on radius at some fixed distance which translates into a cut on emission angle only in an approximate way. Thus the curves in Fig. 4.6 are labeled by their collimator size and distance individually, rather than their ratio, which is the nominal collimation angle. Multiple scattering by the electron in the radiator prior to emission, and beam spot size and divergence are the major contributors to the error involved in translating a collimator radius into a cut on emission angle. All of these effects have been incorporated into the analytical calculation of the yields from a collimated coherent bremsstrahlung source that has been used in preparing this report. Crystal imperfections, which amount to an intrinsic spread in the direction of the incoming virtual photon, are also taken into account in the calculation.

Third, note that the relatively weak collimation at 5 mm reduces the incoherent background without significantly affecting the coherent flux near the maximum, and thereby almost doubling the polarization of the beam at the peak relative to the uncollimated case. Further reducing the collimator diameter continues to narrow the peak and reduce the incoherent flux relative to the peak, albeit at some cost in peak intensity.

The 3.4 mm collimator diameter has been chosen for this design because it provides for a maximum reduction in the incoherent flux while transmitting 95% of the coherent flux at the peak. Most of the total photon beam energy coming from the crystal is absorbed by the collimator. For this reason the collimator is located in a separate enclosure outside the experimental hall, and must be surrounded by a considerable amount of shielding. The peak in Fig. 4.6 for a 3.4 mm collimator contains 33M photons/s for an electron beam current of 1 μA , which will be increased by a factor of 3 for full-intensity running of the GLUEX experiment in HALL D.

Fourth, note that the rate seen in the focal plane of the tagging spectrometer corresponds to the upper curve in Fig. 4.6, regardless of the collimation. This means that collimating the bremsstrahlung beam increases the rate in the tagger focal plane relative to what is seen at the detector. For full-intensity running at 10^8 photons/s on target in the coherent peak, Fig. 4.6 implies a rate of 240 MHz in the focal plane within a 600 MeV window around the peak. Combining this rate with the beam pulse spacing of 2 ns leads to an accidental tagging rate of about 50% and to a fraction of ambiguous tags of 40%. Even with ideal electronics the per-second yield of single-tag events is close to saturation at this intensity. The detector and tagging spectrometer design are based upon a maximum rate of 10^8 photons/s on target and 400 MHz per GeV in the tagger. A novel focal plane design is currently under study, to be discussed below in section 4.4, which may enable the focal plane rate to be reduced by about a factor of two without any decrease in the collimated flux.

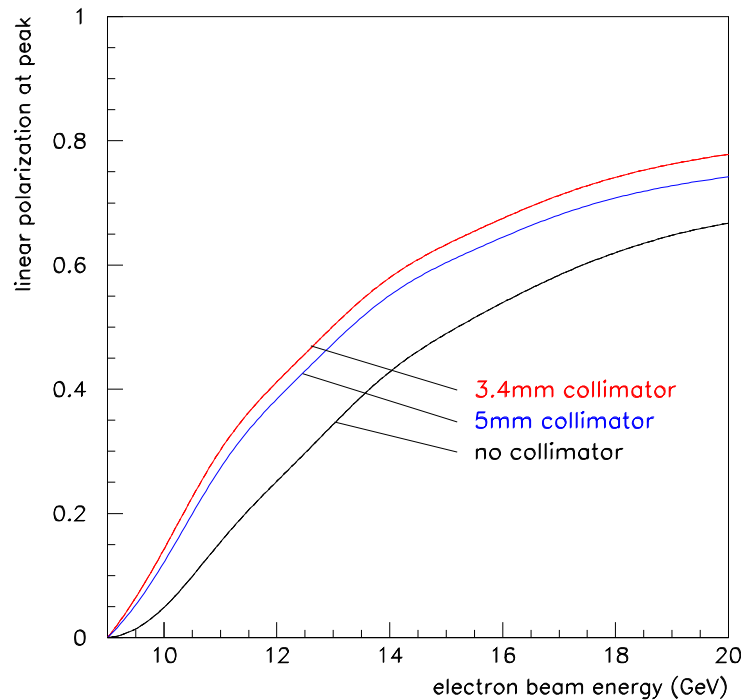


Figure 4.7: Linear polarization in the coherent bremsstrahlung peak as a function of electron beam energy keeping the energy of the coherent peak fixed at 9 GeV. The calculation is performed under the same conditions as in Fig. 4.6.

The linear polarization of the photons in the coherent peak is shown in Fig. 4.7 as a function of the energy of the electron beam. This figure demonstrates why it is essential to have electrons of as high energy as possible, even though photon energies of no more than 9 GeV are required.

The intensity of the coherent peak, not shown in the figure, has a similar dependence on the electron beam energy in this region.

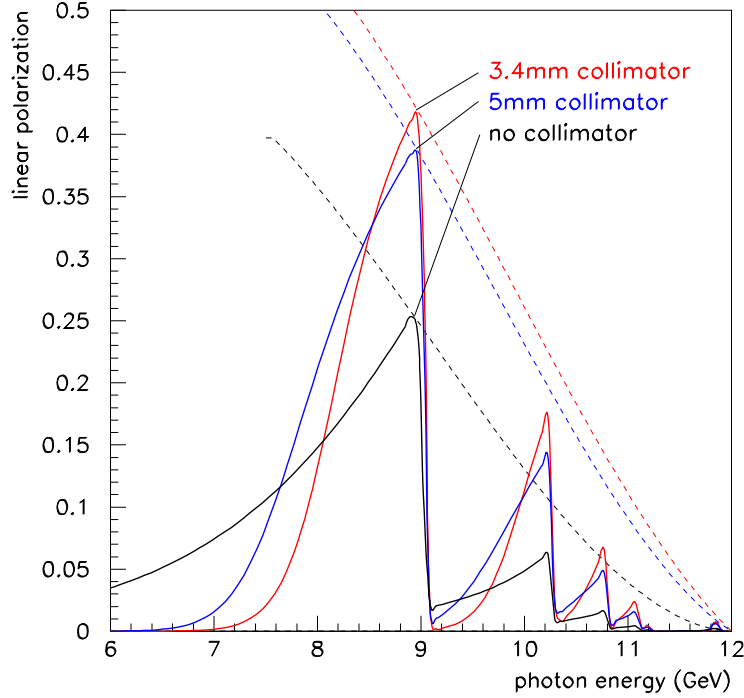


Figure 4.8: Linear polarization of the coherent bremsstrahlung beam for a fixed electron beam energy of 12 GeV, calculated under the same conditions as in Fig. 4.6. The dashed lines indicate the trajectory of the peak polarization as the peak energy is swept across the focal plane by rotating the crystal.

Shown in Fig. 4.8 is the linear polarization of the photon beam *vs* photon energy for fixed electron beam energy. The dashed curves show how the maximum polarization in the primary peak varies as the peak energy is changed by rotating the crystal. The polarization in all cases is zero at the end-point. Without collimation it rises as $(E_0 - k)^2$, one power coming from the intensity of the coherent peak relative to the incoherent component, and the other from the intrinsic polarization of the coherent photons. Collimation allows one to essentially isolate the coherent component, so that the polarization available to the experiment rises from zero at the end-point in a linear fashion. The dashed curves in Fig. 4.8 demonstrate this point.

In order to obtain the full polarization enhancement from collimation, it is necessary to have a distance between the radiator and collimator on the order of 100 *m*. This distance scale is set by the requirement that the collimator aperture must be large compared to the virtual electron beam spot on the collimator but small compared to the actual photon spot size. The virtual electron beam spot is defined as the profile that the electron beam would have at the entrance to the collimator if it were allowed to propagate freely instead of being bent into the beam dump.

The size of the virtual spot at the collimator is determined by the beam emittance combined with an upper limit of 20 μr on the angular spread of the electron beam at the radiator. The latter value was chosen to match the spread in the beam incidence angle to the mosaic spread of the crystal because it is the combination of the two that limits the definition of the coherent peak. Taking this value together with an emittance of 10^{-8} *m* · *r*, which has been projected for

the CEBAF beam at 12 GeV leads to a virtual spot size of 0.5 mm r.m.s. (1.2 mm f.w.h.m.). Note that this scale does not depend on the radiator-collimator distance. The size of the real photon spot is given by one characteristic angle m/E which defines a circle on the collimator containing approximately 50% of the total photon intensity. The real spot size is proportional to the radiator-collimator distance. At a distance of 80 m the ratio of spot sizes is 6, sufficient to allow collimator apertures that satisfy both of the above inequalities.

Fig. 4.9 shows the peak polarization of the beam as a function of radiator-collimator distance for a coherent peak at 9 GeV . In this calculation the collimator diameter is held constant at 3.4 mm to make sure that the virtual beam spot of 1.2 mm f.w.h.m. is well-contained within the aperture, which is the main condition for effective collimation. At zero distance the collimator has no effect except to attenuate the beam, and so the uncollimated polarization from coherent bremsstrahlung is obtained. At 100 m separation distance the polarization enhancement from collimation has saturated. The design for GLUEX calls for a radiator-collimator distance of approximately 80 m . However from the figure one can see that the performance of the photon source is not a very sensitive function of this variable.

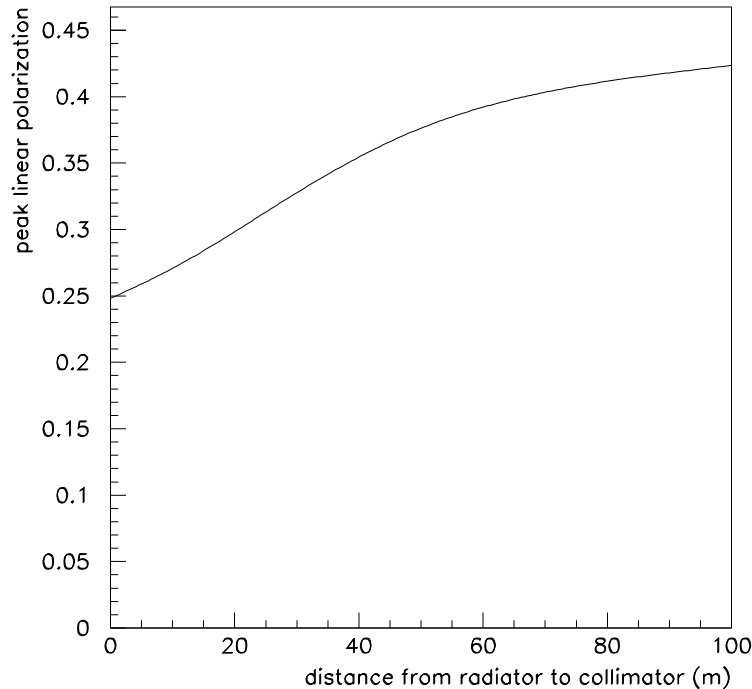


Figure 4.9: Maximum polarization *vs* radiator-collimator distance for a coherent peak at 9 GeV . The collimator diameter is held fixed in this calculation to keep a constant ratio between the sizes of the virtual electron spot and the collimator.

4.2.3 Choice of Radiator

The ideal radiator would be a layered structure with strong transverse fields that alternate between layers spaced about 50 nm apart, thus simulating the standing wave in a cavity driven by a 15 eV laser. While it is possible to construct ordered materials with unit cells as large as this, the self-shielding of atoms means that beyond the atomic length scale the residual

crystal	best reciprocal vector	P/P _{diamond}
diamond	2,-2,0	1.00
beryllium	0,0,2	0.86
boron	2,0,8	0.38
silicon	2,-2,0	0.19
Be ₂ C	2,2,0	1.10

Table 4.1: Figure of merit for various materials that might be used as a coherent bremsstrahlung radiator. This table is reproduced from Table 2 in Ref. [41].

fields are comparatively weak. Hence heterogeneous structures are not viable for use as a coherent radiator. Since the strong fields inside a solid are revealed at the atomic scale, the first requirement for a good radiator is that the unit cell be compact and closely packed. The best radiators are those with the smallest unit cells because these provide the best match between the atomic and the crystal form factors. This match is best for the light elements, and essentially prohibits the effectiveness of any materials heavier than carbon. An extensive survey of possible radiator materials is presented in Ref. [41]. In Table 4.1 is shown the figure of merit that those authors report for favored crystalline materials. The figure of merit is the product of the atomic times the crystal form factor evaluated at the leading peak, normalized to the value for diamond.

Table 4.1 shows that the list of viable materials for a crystal radiator is relatively short. Silicon would be an excellent choice from the point of view of price and fabrication, but unfortunately it is far inferior in terms of performance. Beryllium carbide is not a material that is familiar to the crystal growth industry, and nothing is known at present concerning its suitability for the growth of single crystals of large area. In general compound materials are more susceptible to radiation damage than are pure elements, which would argue in favor of diamond and beryllium metal. These two materials are comparable in terms of their performance.

Most of the experience to date with coherent bremsstrahlung has been with diamond radiators. Extensive expertise with large diamond crystals, such as would be required for the production of coherent bremsstrahlung radiators, already exists within the gem industry. However such capabilities are typically treated in that highly competitive business as sensitive corporate information, particularly as they pertain to the creation of large gem-quality synthetics. Researchers at the University of Glasgow have established contacts within the gem industry for procuring single-crystal diamonds of high quality and large surface area [44]. The techniques used for selecting and assessing the quality of the diamonds are discussed in the next section.

In general terms, diamonds are classified as type I or type II, where type II have been subjected to greater stresses during their formation than type I. Commonly, type II exhibit substantial plastic deformation. Diamonds are also classified according to the form in which nitrogen atoms are present in the crystal lattice. In type *a* the nitrogen is aggregated into clusters of atoms, whereas in type *b* the nitrogen is almost uniformly distributed throughout the crystal. For coherent bremsstrahlung radiators, type Ib diamonds are the most suitable. Unfortunately, type Ib natural diamonds are very rare and probably the most reliable source of Ib diamonds will be synthetics. At present synthetic diamond mono-crystals typically have nitrogen concentrations around 100 ppm.

Synthetic diamonds are made using either vapor deposition (CVD) or high pressure high temperature (HPHT) techniques. CVD diamonds have an extensive mosaic and are unsuitable for coherent bremsstrahlung. However HPHT synthetics look very promising, and the Glasgow group have recently acquired a $5 \times 5 \text{ mm}^2$ synthetic diamond less than $18 \mu\text{m}$ thick which has a [100] orientation. It produces a very good coherent bremsstrahlung spectrum and X-ray measurements show it has rocking curve widths of less than $10 \mu\text{r}$, quite close to the ideal value for diamond.

Beryllium is another material that might be used as a crystal radiator. Beryllium metal is

widely used in industry, being preferred for its high strength-to-weight ratio and robustness, in addition to its transparency to X-rays. Thin films of high-purity beryllium are routinely produced for vacuum window applications, which use some of the same vacuum deposition techniques that would be used for the growth of single crystals. As a radiator material, beryllium is distinguished as the metal with the highest Debye temperature, around 1400°K. The Debye temperature measures the temperature at which the thermal motion of the atoms in the lattice reaches the level of the zero-point motion due to their confinement in the lattice. A high Debye temperature indicates a stiff crystal lattice, in which the atoms have little liberty to move and so have large momentum fluctuations, as dictated by the uncertainty principle.

A high Debye temperature is important for a bremsstrahlung radiator material for three reasons. First, the cross section for coherent bremsstrahlung from a discrete crystal momentum vector \vec{q} contains a factor $e^{-q^2/4M\theta_D}$ which reflects the fact that position fluctuations of atoms in the lattice diminish the coherent effect. This factor is near unity for the low-order crystal momenta provided that the Debye temperature θ_D is sufficiently large. Second, the Debye temperature is, roughly speaking, a measure of the stability of the crystal structure and hence its capacity to survive significant doses of radiation. Third, the radiator material will inevitably be heated by the beam, and will normally operate in vacuum well above the ambient temperature. A high Debye temperature means that there is a large range of temperatures over which the material may operate without degraded performance as a crystal radiator. The Debye temperature of diamond is about 2200° K.

Past experience has shown that diamond meets all of the requirements for a good crystal radiator. Beryllium remains a second choice, to be investigated further in the case that affordable sources of large-area diamond crystals at some point are no longer available.

4.2.4 Crystal Quality

In the calculation of the coherent bremsstrahlung spectrum it is necessary to take into account the fact that even the very best crystals have some dislocations and other defects. Besides locally disrupting the regularity of the crystal, these defects impose stresses which produce small ripples in the crystal planes. If these ripples were amplified, the surface of a crystal would appear like a mosaic of planar regions with approximately parallel surfaces. The scale of deviations from planarity across the face of a single crystal is termed the *mosaic spread* of the crystal. The mosaic spread contributes in the same way as electron beam divergence to the blurring of the exact energy-angle relation for coherent photons.

Besides dislocations, there are other kinds of crystal defects. The presence of foreign atomic species during the crystal growth process can result in the substitution of impurities at some lattice sites, or the formation of voids where impurities tend to collect in clusters of several atoms. In the growth of diamond crystals under conditions of high pressure and temperature, the growth rate is greatly enhanced by the presence of a small amount of nitrogen. Thus it is normal that small amounts of nitrogen impurities should exist even in the best natural stones, as well as in the synthetics created by the HPHT process.

The ideal conditions for growth of a perfect synthetic crystal require pre-existing mono-crystalline diamond with clean planar facets cleaved along the major crystal planes, upon which new layers of carbon are deposited in succession. If conditions are right, the registry of the atoms with the original crystal is preserved over millions of deposited layers, starting from the original seed. In principle, the expansion of the regular lattice should continue to match up perfectly at the boundaries between the different growth surfaces that originated on the facets of the seed, but in practice the strains from small imperfections that occur during the growth process tend to accumulate there, forming recognizable patterns of concentrated defects known as *growth boundaries*. If the stresses grow too large then new strain regions may develop, leading to a more pronounced mosaic pattern in the subsequent layers.

Unfortunately the growth process has proved difficult to control in a reproducible fashion. As a result, out of several dozen stones examined, only one or two may be of sufficient quality for use as a coherent bremsstrahlung radiator for HALL D. The selection process described below

was formerly developed by the Glasgow group to supply crystals for the coherent bremsstrahlung source at Mainz, Germany and subsequently for the Hall B source at Jefferson Lab. The requirements for HALL D are very similar to those of Mainz and Hall B, except that the electron beam current will be higher by about an order of magnitude and the crystals will be cut much thinner.

The diamond ingots from the synthetic process are sliced into sections at the laboratory where they are produced. From these, thin wafers of about $100\ \mu\text{m}$ thickness are cleaved along the (1,0,0) axis and provided to the Glasgow group for assessment. The samples are first examined under a microscope with polarized light. Many of the stresses in the crystal lattice can be revealed in this way, particularly those which exhibit plastic deformation. If the diamond appears clear and featureless under polarized light then it is examined with X-rays. Two types of X-ray measurements are performed.

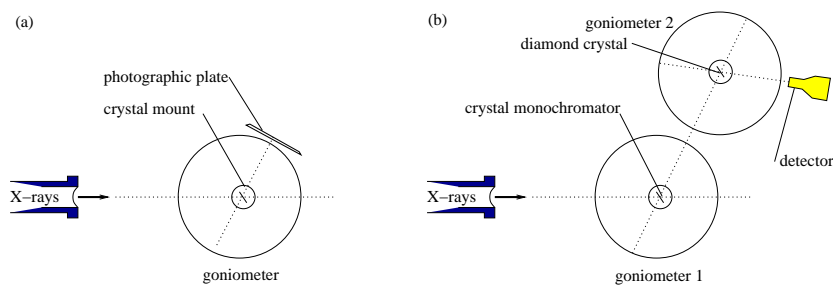


Figure 4.10: Experimental setup for assessment of diamond crystals at the Synchrotron Light Source beam line, configured for topograph measurements (a), and rocking curves (b).

1. Topographs

A topograph is a real-space image of a diamond formed from X-rays that Bragg-scatter from a particular set of planes in the crystal, as shown in Fig. 4.10a. Using the highly-parallel X-ray beam from the Synchrotron Light Source (SRS) and setting the detector at twice the Bragg angle for a known set of planes for diamond, X-rays of the appropriate wavelength to satisfy the Bragg condition are scattered at a precise angle θ into the detector. The X-ray image formed on the plane of the detector is a simple real-space projection of the crystal, called a *projection topograph*. If the vertical slits defining the X-ray beam are narrowed forming the incident beam into a thin ribbon a few μm wide, then the image at the detector reveals a slice through the crystal, called a *section topograph*. Projection topographs reveal any large-scale imperfections in the crystal. Section topographs can be used to examine the depth profile of imperfections. Topographs sample the whole volume of the crystal. Hence, by measuring projection and section topographs, a 3-dimensional picture of the diamond can be obtained. It is also possible to differentiate between screw and edge dislocations. The topograph image reveals dislocations, growth boundaries and any feature which suppresses or enhances Bragg scattering at the selected angle. In principle, topographs taken at different angles provide independent views of the crystal structure. In practice, however, the imperfections that are revealed with one set of planes appear in a similar fashion when viewed from other orientations.

2. Rocking curves

A rocking curve is a plot of Bragg-scattering intensity *vs* angle between the incident X-ray beam and the normal to the crystal planes. A diagram of the setup is shown in Fig. 4.10b. First the broad-band X-ray beam from the SRS is monochromated by scattering at a known fixed angle from a reference crystal, in this case silicon. This beam is then directed at the diamond crystal under study, from which it scatters a second time and is detected. The scattering is appreciable only when the diamond is at just the right angle with respect to the incident beam such that the Bragg condition is satisfied at both crystals. The

variation in the scattering intensity with angle as the diamond wafer is rotated through the resonance is called the *rocking curve* for that diamond. A perfect crystal exhibits a rocking curve consisting of a single peak whose width is called the *natural width* and depends on the material. The natural width for diamond is about $5 \mu r$. Instead of a single peak, for actual crystals one typically sees a number of peaks spread out over a region in angle over known as the rocking curve width. Rocking curves widths, for a selected set of crystal planes, measure quantitatively how any defects or dislocations distort the crystal lattice. By adjusting the slits it is possible to examine the rocking curve of a region of the crystal or to examine the entire crystal at once. Using rocking curves it is possible to measure how close to ideal is the lattice structure of the diamond being investigated.

Figs. 4.11-4.12 show some of the results that were obtained at the SRS laboratory in Daresbury, England in January, 2002. At the left of the figures is shown a projection topograph taken using the (0,4,0) planes, the second harmonic of the (0,2,0) planes used for coherent bremsstrahlung. At the right is shown the corresponding rocking curve taken in combination with a silicon crystal set to reflect from the (3,3,3) planes at a wavelength of 1 \AA . The two diamond wafers had been cut from the same original type Ib stone, with Fig. 4.11 coming from the end close to the seed, and Fig. 4.12 coming from near the middle of the ingot. The topographs are negatives, meaning that the image is dark in regions where the X-ray intensity was largest.

The first thing to notice from the topographs is that both wafers are mono-crystalline; there are no regions where X-rays do not scatter. Even so, there are important differences between the two samples. The growth boundaries (the picture-frame pattern) which are visible in Fig. 4.11 spread out and become less pronounced in slice 2 which was taken further from the seed. It is interesting that the strain pattern appears mostly as dark regions rather than light, which indicates stronger scattering in the defects than in the ordered regions, the opposite from what one might naively expect. It should be recalled that both crystals appeared clear and featureless under polarized light at visible wavelengths. The requirement for a diamond radiator useful for HALL D is that the rocking curve width be of the same order of magnitude as the divergence of the electron beam at the radiator, which when folded with multiple-scattering is about $25 \mu r$ r.m.s. The conclusion is that slice 2 is a good candidate for use in the GLUEX experiment, and that slice 3 is not. Having confirmed the quality of slice 2, it should now be possible for the manufacturer to cut a dozen or more wafers of similar quality from that region of the original stone.

4.2.5 Crystal Thickness

The range of permissible thicknesses for a crystal radiator is bounded both from above and below. It is bounded from above by multiple scattering of the electron beam as it passes through the radiator, which causes the divergence of the incident beam to grow, thereby enlarging the photon beam spot on the collimator face and degrading the degree to which collimation discriminates against the incoherent component in favor of the coherent part. It is bounded from below by the fact that the crystal must have some minimum thickness in order to achieve the full coherent gain. In the calculation of the coherent bremsstrahlung process one begins by assuming an infinite crystal, although practically it is presumed to mean only that the crystal is large compared to some characteristic scale. It is important to identify what the characteristic scale is in this problem in order to know how thin one can make the crystal without hurting performance. In the analogous case of the Mössbauer effect, one can estimate the number of atoms participating in the collective absorption by looking at the emission time of the photon (lifetime of the radiating transition) and asking how many nuclei lie within the envelope of the photon wave packet. In the coherent bremsstrahlung process, the lifetime of the radiating system is given in the lab system by the uncertainty principle and by how far the electron energy deviates from its on-shell value between absorbing the virtual photon and emitting the real one. The latter quantity is almost exactly given by q_z , the virtual photon momentum component along the incident electron axis, which means that the electron travels a distance $\lambda = \hbar c/q_z$ during the interaction. For a given

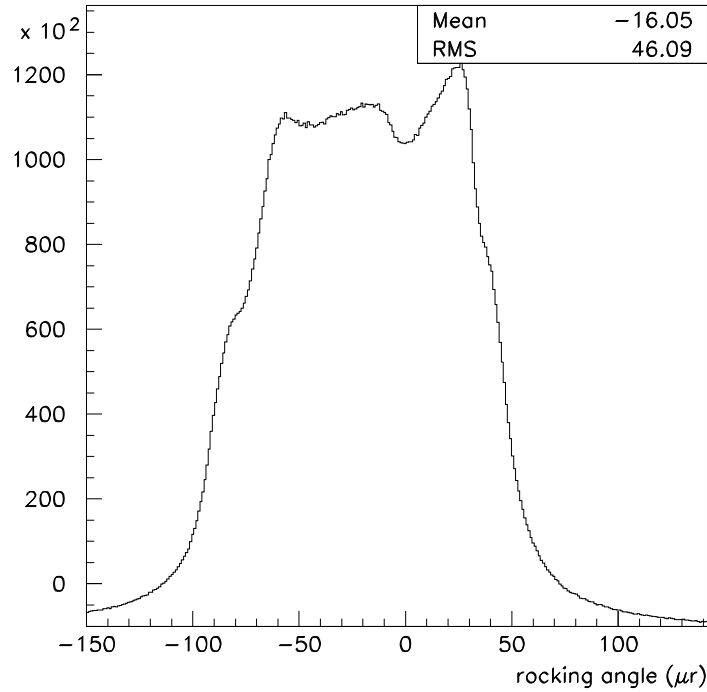
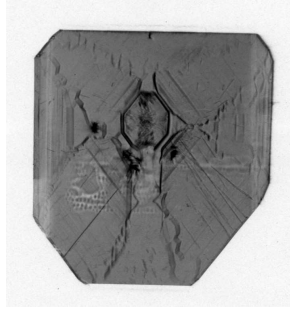


Figure 4.11: Experimental data collected using highly-parallel X-rays from the SRS light source for stone 1482A slice 3 (close to the seed). At the top is shown a projection topograph of the wafer taken using the broad-band X-ray beam and a Polaroid film placed at the angle for reflection from the (0,4,0) planes. The image is a magnified by a factor of 5. The graph shows the rocking curve for the same set of planes, taken using a NaI counter and 1 Å X-rays monochromated by a silicon crystal.

coherent peak at normalized energy x in the photon spectrum, the coherence length is given by

$$\lambda = \frac{2E(1-x)}{xm^2} \quad (4.3)$$

in units of $\hbar c$. From this simple argument one sees that the coherent gain goes linearly to zero at the end-point, a result that is borne out by the full QED calculation. One also sees that the lower limit on crystal thickness imposed by the coherence length depends upon both the electron beam energy and the photon energy. For a 12 GeV beam energy and a 6 GeV coherent photon the coherence length is 18 nm, or about 50 unit cells for diamond. This shows that the coherence length does not impose a practical limit on how thin the radiator should be.

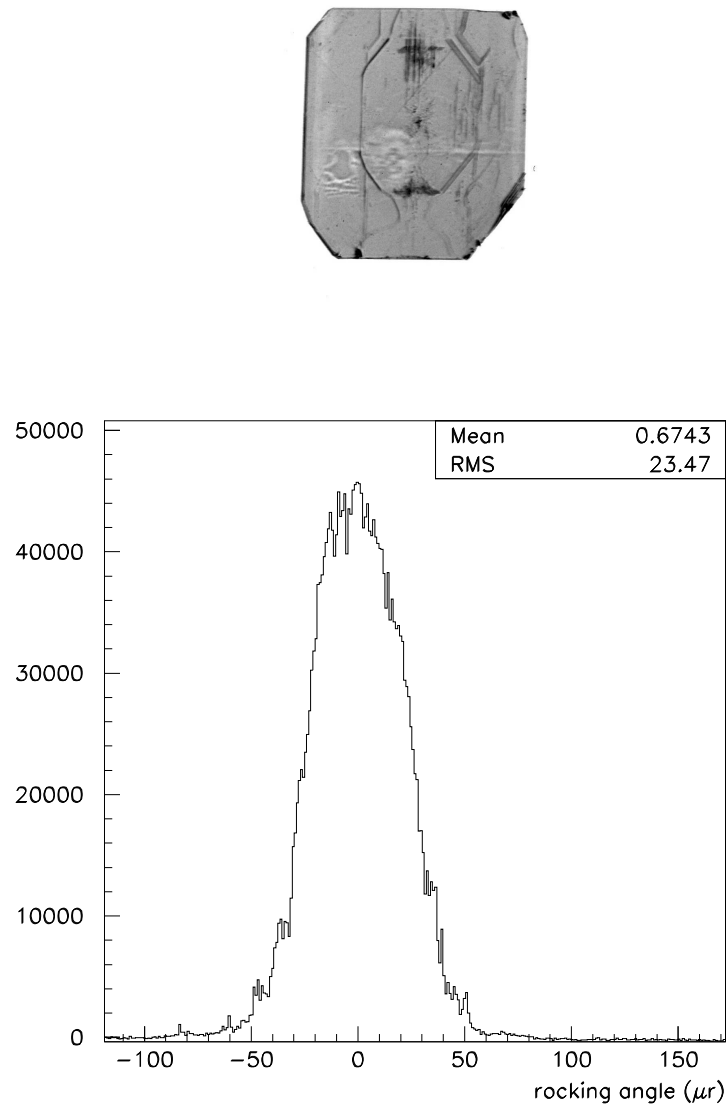


Figure 4.12: Experimental data collected using highly-parallel X-rays from the SRS light source for stone 1482A slice 2 (further from the seed). At the top is shown a projection topograph of the wafer taken using the broad-band X-ray beam and a Polaroid film placed at the angle for reflection from the (0,4,0) planes. The image is magnified by a factor of 5. The graph shows the the rocking curve for the same set of planes, taken using a NaI counter and 1 Å X-rays monochromated by a silicon crystal.

The effects of multiple scattering are best presented by showing the calculated spectra for various radiator thicknesses. In Fig. 4.13 is shown the photon spectrum for a 10^{-4} and a 10^{-3} radiation-lengths radiator to demonstrate the effect. The 10^{-3} radiator spectrum is scaled down by a factor of 10 to facilitate the comparison. The calculation assumes a 3.4 mm collimator located 80 m downstream of the radiator. The loss in normalized intensity with the thicker radiator, as well as the broadening of the left edge of the peak, is due to the enlarging of the photon beam spot on the collimator face from multiple scattering of the electron beam in the crystal prior to radiation. A 10^{-4} diamond radiator is 15 μm thick. The goal for GLUEX is to

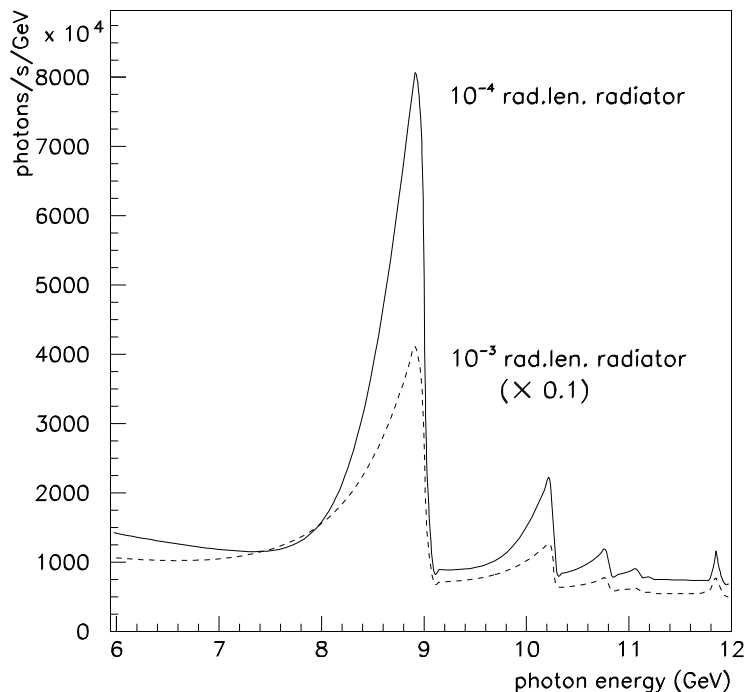


Figure 4.13: Collimated coherent bremsstrahlung spectrum from a $1\mu\text{A}$ electron beam at 12 GeV using diamond radiators of two different thicknesses. The calculation assumes a 3.4 mm collimator located 80 m from the radiator, and typical values for beam emittance and crystal quality.

run with crystals of thickness in the range $10\ \mu\text{m}$ to $20\ \mu\text{m}$.

4.2.6 Crystal Mount

It has already been shown that in order to achieve appreciable coherent gain the crystal must be oriented so that the coherent peaks appear well below the end point. Equation 4.2 then implies that the orientation must be such that the crystal momentum dotted with the beam momentum be of order m^2 . Given a p of 12 GeV and q of 10 keV , this requires that the two vectors must be within $100\ \mu\text{r}$ of perpendicular to each other and that, within a range of angles of that order, the coherent peak sweeps out nearly the full range in x from 0 to 1.

Hence, to have a stable photon beam with the coherent peak positioned at the right energy, the angle between the incident electron beam and the crystal radiator must be adjustable in steps of a few μr and remain stable at this level. Since the angle of the incident beam is fixed by the beamline optics and the position of the photon collimator, all adjustments must be made by changing the orientation of the crystal. This is achieved with a precision goniometer (shown schematically in Fig. 4.14) which should provide motion on at least 5 axes. Rotation about the azimuthal axis ϕ sets the orientation of the polarization plane, rotations about the θ_v, θ_h axes set the angle of the crystal relative to the beam, and x, y translations select the position of the beam spot on the crystal. Estimates of the approximate range and step size for each of the axes are given in Table 4.2.

In practice several targets need to be mounted in the goniometer. The minimum requirement

this maximum tilt occurring at an azimuthal angle ϕ_t . In addition, the 022 vector will be offset by ϕ_0 with respect to the horizontal. Any motion about the azimuthal axis ϕ changes the angle of the 100 axis (C) relative to the beam. The angle of the polarization plane is set by adjusting the azimuthal angle of the crystal ϕ . Hence when a new crystal is installed, the default value ϕ_0 needs to be measured. Furthermore, to position the coherent peak at the required photon energy, the angle (or *offsets*) between the beam and 100 crystal axis (C) at the chosen value of ϕ must also be established.

Feedback on the relative angle between the crystal and the beam is obtained from a photon energy spectrum derived from the tagger focal plane counters, either via scalers or a TDC hit pattern. The scaler spectrum does not show the effect of collimation (unless the scalers are gated with a downstream photon detector), but can be obtained very quickly since it does not require a triggered data acquisition system. The scaler readout is essential for the alignment process, where the offsets are measured by carrying out a series of scans in which 2d histograms of photon energy vs. crystal angle are built up by moving the goniometer in a sequence of small angular steps and reading the tagger scalers. In addition to providing the feedback required for alignment, the focal plane counters provide essential online diagnostics to monitor drifts in angles caused by the beam tuning, or thermal effects in the crystal mount. If necessary a feedback system could be implemented via the slow control system, where any drift in the position of the coherent peak could be corrected by periodically adjusting the goniometer within predefined limits.

The spectrum obtained from the tagger focal plane can also provide online monitoring of the photon polarization to within 5% by fitting with an analytic bremsstrahlung code. A more detailed discussion of polarimetry appears in the following sections.

4.2.8 Crystal Lifetime

The best information regarding crystal degradation comes from X-ray studies performed by the Glasgow group of a diamond which had been used in the MAMI coherent bremsstrahlung source at Mainz for several years. The electron beam on the Mainz crystal had a diameter of about $100 \mu\text{m}$ and it was estimated that around 10^{20} electrons had passed through the diamond during its use in the source. There was a small greenish black spot where the beam had hit the diamond.

The X-ray rocking curve measurements showed that considerable damage had occurred to the integrity of the crystal structure in the center of the beam spot. However 2 mm away from the damage center the width of the diffraction peak was the same as it had been for the pristine crystal, which indicates that the lifetime of the crystal could be extended by occasionally moving the beam spot on the face of the crystal.

The area of the MAMI beam spot on the radiator is two orders of magnitude smaller than what is being planned for GLUEX in HALL D. A larger spot means a longer crystal lifetime before radiation damage substantially degrades its crystal properties. Appropriately scaled, the exposure of the Mainz crystal would correspond to 15 years of running in HALL D at the full intensity of $3 \mu\text{A}$ without a spot move. Plans for the HALL D source are to keep the exposure about three orders of magnitude less than this. At the SLAC coherent bremsstrahlung beam line it was found that the performance of their diamond radiators had degraded noticeably after a total charge of 3 Coulombs had been accumulated over a spot of size roughly 2 mm r.m.s., leading to a limit of about $0.25 \text{ Coulomb}/\text{mm}^2$ [45]. Taking this as a conservative estimate for the allowed exposure, the source can run at a full intensity of $3 \mu\text{A}$ for 60 hours before it is necessary to move the spot on the crystal. If it had no bad zones, a square crystal of $5 \times 5 \text{ mm}^2$ would accommodate 5 spot moves before the crystal would need to be replaced. SLAC researchers were able to recover a good performance for the damaged crystals by putting them through an annealing process. Further research and development will be required to determine whether crystal recovery through annealing is an effective way to reduce the operating costs of the HALL D source.

Another issue related to crystal degradation is that of heat dissipation for very thin crystals.

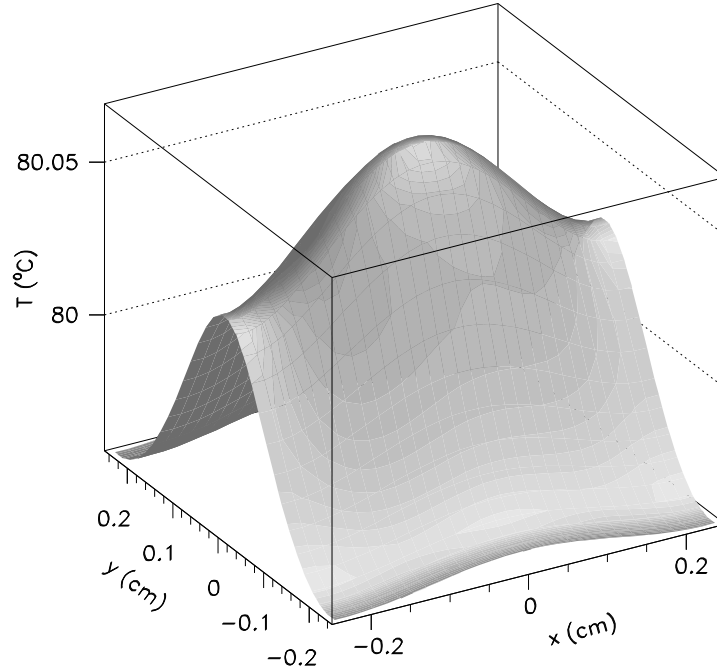


Figure 4.15: Calculated temperature profile of diamond crystal with a 12 GeV beam at 3 μA . The crystal dimensions are 5 mm \times 5 mm \times 15 μA . The ambient room temperature was taken to be 27° C (300 K). The x-y asymmetry is caused by the elliptical shape of the electron beam spot on the radiator.

The heat comes from the ionization energy loss of the beam as it passes through the crystal. Although this is small compared to the bremsstrahlung energy loss, it is not entirely negligible at these beam currents. It can be calculated using the restricted energy loss formula, which yields 21 mW for a 15 μm (10^{-4} radiation lengths) crystal at a current of 3 μA . This is not much power, but the crystal is very thin. Heat dissipation is through radiation and conduction. Diamond has a very high melting point; at low pressures it sublimates at about 4027° C. However at normal pressures it begins to transform into graphite above 707° C, at a rate that depends on temperature. It is therefore important that the crystal at the center of the beam spot stay well below this limit.

The diffusion equation including a heating term and one for radiative cooling can be written as

$$C_P a \frac{dT}{dt} = h(x, y) - 2\sigma (T^4 - T_0^4) + \kappa a \nabla^2 T$$

where the heating term $h(x, y)$ has units of power/area, σ is the Stefan-Boltzmann constant, C_P is the heat capacity and κ the coefficient of conduction for diamond, and a is the thickness of the crystal. T_0 is the ambient temperature of the environment and T is the local crystal temperature, a function of space and time coordinates. After a certain time, T converges to the steady-state solution shown in Fig. 4.15. The calculation used a crystal of dimensions 5 \times 5 \times 15 μm^2 and a beam current of 3 μA . This calculation shows that the conductivity of diamond is sufficient to prevent significant temperature gradients across the crystal even for very thin wafers, and that radiative cooling alone is sufficient to dissipate the heat being generated by the beam passing

parameter	design goals	design results
energy	12 <i>GeV</i>	12 <i>GeV</i>
electron polarization	not required	available
minimum useful current	100 pA	100 pA
maximum useful current	3 μ A	5 μ A
r.m.s. energy spread	< 10 <i>MeV</i>	7 <i>MeV</i>
transverse <i>x</i> emittance	10 <i>mm</i> $\cdot\mu$ r	10 <i>mm</i> $\cdot\mu$ r
transverse <i>y</i> emittance	2.5 <i>mm</i> $\cdot\mu$ r	2.3 <i>mm</i> $\cdot\mu$ r
x-dispersion at radiator	none	negligible
y-dispersion at radiator	none	< 1 cm
<i>x</i> spot size at radiator	1.7 <i>mm</i> r.m.s.	1.55 <i>mm</i> r.m.s.
<i>y</i> spot size at radiator	0.7 <i>mm</i> r.m.s.	0.55 <i>mm</i> r.m.s.
<i>x</i> image size at collimator	0.5 <i>mm</i> r.m.s.	0.54 <i>mm</i> r.m.s.
<i>y</i> image size at collimator	0.5 <i>mm</i> r.m.s.	0.52 <i>mm</i> r.m.s.
distance radiator to collimator	80 m	75 m
position stability	± 200 μ m	

Table 4.3: Electron beam properties that were asked for (column 2) and obtained (column 3) in a preliminary optics design for the transport line connecting the accelerator to the HALL D photon source.

through the crystal so that the crystal mount does not need to act as a heat sink.

4.3 Electron Beam

The performance of the photon source is dependent upon the parameters of the electron beam in several important areas. These parameters are listed in Table 4.3. The first column of numbers gives the set of parameters that have been adopted as the design goals for the source. These are the values that have been taken as input in calculating the characteristics of the coherent bremsstrahlung source. The second column of numbers was obtained from a concrete design of the HALL D beam line [46] that was carried out by members of the Jefferson Lab Accelerator Division. The exact choice of the final parameters has not yet been made, but the preliminary design shows that all of the design goals can be met within the available real estate. The reduction of the radiator-collimator distance from 80 to 75 *m* does not significantly affect the performance of the source.

The following sections highlight the particular properties of the electron beam which have a special impact on the performance of the source.

4.3.1 Beam Polarization

It has already been stated that to generate bremsstrahlung photons with linear polarization it is necessary to use an oriented crystal radiator. However photons with circular polarization are produced by ordinary incoherent bremsstrahlung any time the incident electrons are longitudinally polarized. In fact for 9 *GeV* photons produced by 12 *GeV* electrons, the transfer from electron beam longitudinal polarization to photon beam circular polarization is greater than 80%. This raises the question of what happens when one has longitudinally-polarized electrons incident on an oriented crystal radiator. What happens in this case is that the photon beam is elliptically polarized; it carries both circular and linear polarization. There is a sum rule that limits the sum of the squares of the linear plus circular polarizations to be no greater than 1. Hence one sees the linear polarization in coherent bremsstrahlung going to zero as one approaches the end-point energy (see Fig. 4.8) while at the same time the circular polarization goes to 1 at the end-point (assuming electrons of 100% longitudinal polarization).

The statement in Table 4.3 that electron beam polarization is not required for the GLUEX experiment in HALL D is correct, but it is not correct to assume that the photon source is independent of the state of polarization of the electron beam. The presence of a non-zero circular polarization in the HALL D photon beam will, in principle, produce observable effects in the angular distributions measured in photoproduction reactions. This means that there will be an important coupling between the GLUEX program and the other experimental halls whose programs sometimes require them to have control over the beam polarization. This coupling can be eliminated by setting up the tune of the electron beam line to HALL D such that the longitudinal component of the electron beam polarization is rotated to zero at the crystal radiator. Whether the decision is made to rotate it away or simply to measure its value periodically, this consideration underlines the importance of having a means to measure photon beam polarization in a way that does not rely on *a priori* knowledge of the properties of the electron beam.

Although the ability of the source to produce photon beams with both circular and linear polarization complicates operation when one of them is desired without the other, it does increase the versatility of the source. The two kinds of polarization are controlled independently of one other, and together they give access to a more complete set of polarization observables than would be possible with only one or the other.

4.3.2 Beam Emittance

The values for the electron beam emittances shown in Table 4.3 are estimates based upon the parameters of the current machine projected to 12 *GeV*[46]. The definition of emittance used here is the product of the r.m.s. widths of the beam in transverse position and divergence angle. Because synchrotron radiation inside the accelerator occurs mainly in the horizontal plane, the emittance values in x are generally larger than those for y . The two vertical bends required for bringing the 12 *GeV* beam from the level of the accelerator up to beam height in HALL D do increase the vertical emittance a small amount over its value inside the machine; this effect has been included in computing the vertical emittance shown in Table 4.3.

The longitudinal emittance of the beam is important as it is the limiting factor in determining the ultimate energy resolution of the tagger. The design goal of 0.1% photon energy resolution is well matched to the energy spread expected for the CEBAF beam at 12 *GeV*.

The place where transverse emittance plays a critical role is at the photon collimator. For optimum effectiveness in collimation it is important that the virtual electron beam spot at the collimator position be as small as possible. The electron beam does not actually reach the photon collimator, being bent into the dump by the tagger magnet shortly after the radiator. But considering the optics of the electron beam as if the tagger dipole were switched off, the electron beam at the radiator can be projected forward to form a virtual image on the collimator entrance plane. The position and size of this virtual spot determines the definition of 0° emission angle for the photons. If this spot is small compared to the collimator aperture and is correctly centered then the bremsstrahlung photons of a given emission angle α intersect the entrance plane of the collimator in a well-defined ring of radius $D\alpha$ concentric with the collimator aperture, where D is the distance between the radiator and the collimator entrance plane. In this way a collimator of diameter d passes only those photons of emission angle $\alpha \leq d/2D$. If however the size of the virtual spot is comparable to or larger than the collimator aperture then the ring image of photons of a given emission angle α is smeared out, so that the effect of collimation is simply to reduce the intensity of the beam but not to enhance the coherent component.

Note that this analysis does not place any specific limits on the size of the beam at the radiator. The beam spot can and should be larger there to increase the lifetime of the crystal between spot moves. For the SLAC coherent bremsstrahlung source the beam spot at the radiator was about 2 *mm* r.m.s., focused down to a 1 *mm* r.m.s. virtual spot at the primary collimator positioned 91 *m* downstream of the radiator.

The superior emittance characteristics of the CEBAF beam allow the transverse dimensions to be somewhat smaller than this for the HALL D source, more so in the vertical than the horizontal

dimension. The difference between the horizontal and vertical emittance of the CEBAF beam implies that making the spot round at the radiator implies an elliptical virtual spot at the collimator, and *vice versa*. It is difficult to construct a collimator with an elliptical aperture, so the choice was made to make the virtual spot round. This is why the beam spot on the radiator is asymmetric.

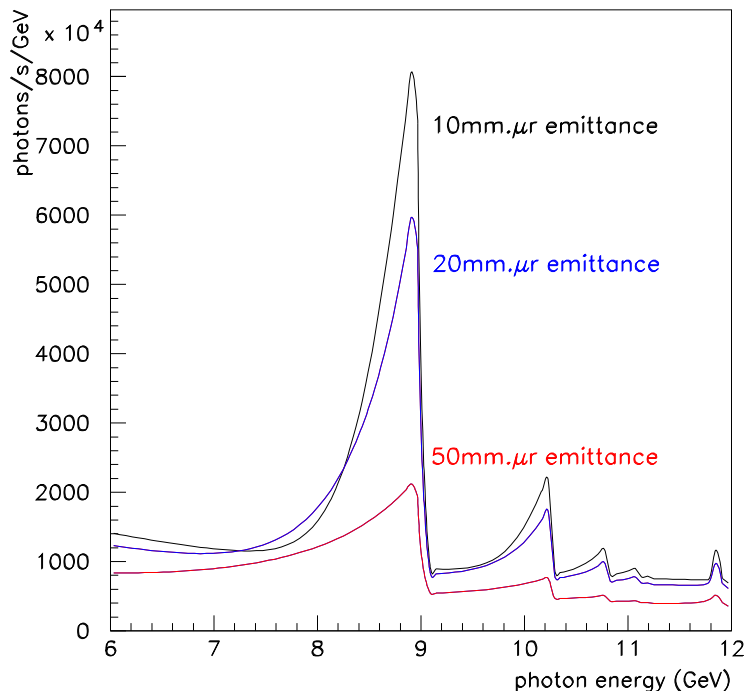


Figure 4.16: Coherent photon spectrum for three different values of the electron beam transverse emittance. The horizontal (shown on the plot) and vertical emittances are assumed to scale together. A 3.4 mm collimator located 80 m from the radiator was used for this calculation.

Figure 4.16 shows how the collimated photon spectrum depends upon the transverse emittance of the electron beam. To generate this plot the increases in emittance were simply translated into an increased virtual spot size on the collimator. This was done because it was assumed that the spot size of the electron beam on the radiator, already close to 2 mm r.m.s., cannot be further inflated and stay contained within the limits of the crystal. When the virtual spot size becomes comparable with the collimator aperture then the collimation is rendered ineffective, and the photon spectrum and polarization revert to their uncollimated values. There is another connection between focal spot size and beam emittance that is connected with the requirement that all electrons enter the radiator at the same incidence angle with respect to the planes of the crystal. Practically, the divergence does not broaden the coherent peak provided that it is kept below the mosaic spread of the crystal. A conservative value for the allowable angular divergence δ in the electron beam at the radiator would then be $20 \mu r$. Taken together with a 500 μm r.m.s. spot size at the focus, this leads to an emittance of 10 mm· μr at 12 GeV. This corresponds to the upper curve in Fig. 4.16.

4.3.3 Electron Beam Line Optics

Translating the beam emittance into r.m.s. values for the beam radius and divergence requires the knowledge of the β function of the transport line between the accelerator and the radiator, defined as the ratio of the beam size to its angular divergence.

The preliminary optics design [46] of the HALL D beam line (see Table 4.3) is shown in Fig. 4.17. The horizontal and vertical beta functions are shown in the upper and lower panels, respectively. Between the two panels is shown a schematic of the transport lattice. The design begins at the exit of the beam from the end of the linac and ends at HALL D. The z coordinate is measured along the axis of the linac, with its origin at the mid-point of the accelerator. Fig. 4.18 shows the beta functions translated into r.m.s. beam size and shifted to place the radiator at the origin. The design allows the ratio of the spot sizes at the radiator and collimator to be adjusted over about an order of magnitude simply by changing the current in the beam line elements. In this way it will be possible to optimize the optics for a given size of crystal and collimator after beams are delivered to the hall, and more precise values for the emittances are in hand.

Not only must the virtual electron spot be small enough to fit within the collimator aperture, but it must also be centered on the aperture and stable. In order to maintain a stable beam position on the collimator, the SLAC experiment [40] instrumented the collimator with a secondary-emission detector. The detector was of the “pin-cushion” design and was installed between segments of the collimator near the position of the shower maximum. The readout was divided into four quadrants, which read equal currents when the beam was properly aligned on the collimator. The readout was connected via a feedback loop to the last steering elements on the electron beam line prior to the radiator. Over that distance a bend of only $10 \mu r$ results in a shift of 1 mm at the collimator position. The small deflections that are necessary to keep the beam centered on the collimator do not produce appreciable walk in the beam-crystal angle. This means that an active feedback system can be set up between the instrumented collimator and deflection coils just upstream of the radiator, that can operate independent of the crystal alignment system to keep the electron beam aimed at the center of the collimator.

The experimental program in parity violation at Jefferson Lab has already demonstrated a position stabilization circuit that is able to keep the beam position steady to within $20 \mu m$ over a 20 m lever arm. A less sophisticated version of this circuit will meet the position stability requirements for the HALL D photon source.

4.3.4 Electron Beam Dump

The electron beam is dumped in the horizontal plane, as shown in figure 4.4. The horizontal bend offers several advantages over dumping the beam into the ground. The tagger magnet is easier to support if it sits in the horizontal position. It is also easier to mount and service the focal plane instrumentation in this position. The dump itself is also more accessible in case it needs to be serviced. An above-ground dump also affords the possibility of running parasitic beam dump experiments that do not interfere with the operation of the experimental hall.

The primary design requirement for the electron beam dump is that it has a sufficiently high capacity to handle beams of the highest intensities foreseen for the GLUEX experiment in HALL D. A 60 kW design would provide a healthy margin for operation of a 12 GeV beam at $3 \mu A$ and sufficient capacity to handle $3 \mu A$ at 20 GeV in the case of a further upgrade.

4.3.5 Beam Containment and Shielding

There are three factors that must be taken into account in the design of the shielding for the HALL D beam line. The first is the constraint on the background radiation level that is allowed outside the beam enclosure. The second factor is the level of radiation in the experimental hall which can generate background in the detector during normal running. The third factor is the control of hazards which may occur in the event of a failure of one or more of the beam delivery systems. The first issue has been studied by the Jefferson Laboratory Radiation Controls Group, and will be discussed further in the chapter on Civil Construction. The latter two

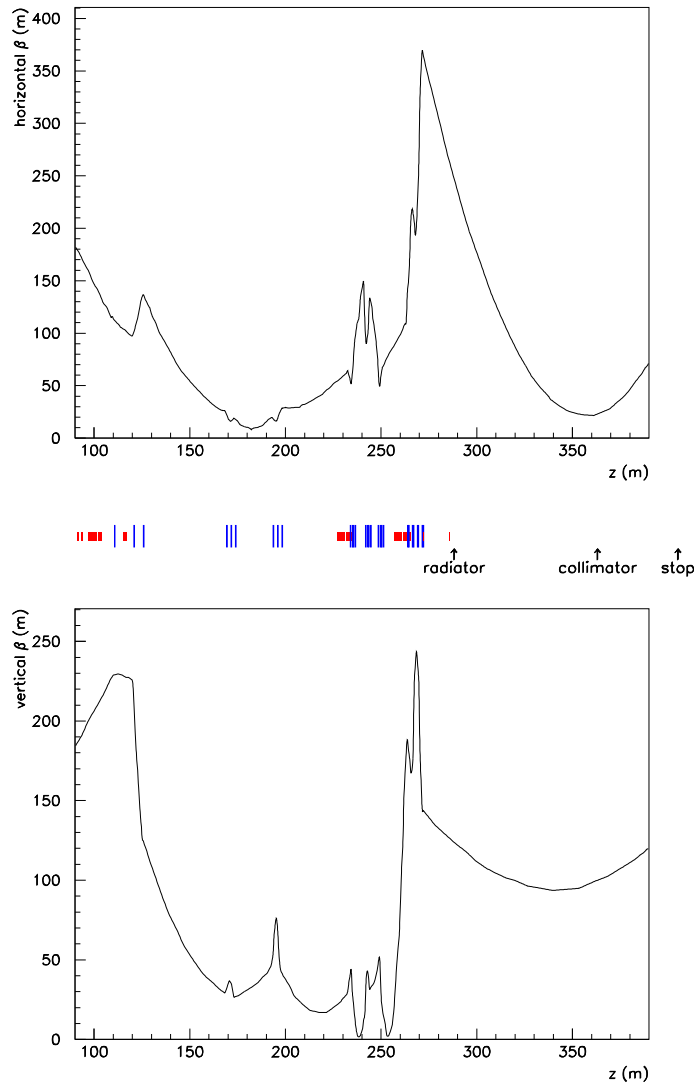


Figure 4.17: Horizontal (upper panel) and vertical (lower panel) beta functions from the preliminary optics design for the transport line from the accelerator to the HALL D photon source. The beam line lattice is shown schematically between the two panels, with dipole magnets represented by the short boxes and quadrupoles by the taller lines. The z coordinate is equal to the flight path length of the electrons starting at the center of the linac, up to an error of a few cm from the vertical motion of the beam.

considerations have been studied by a working group headed by L. Keller (SLAC). A summary of their recommendations [47] follows.

Assuming that the electron beam dump is shielded to the requirements of radiation safety, the next source of background radiation in the experimental hall is the photon collimator. The most penetrating forms of radiation from the collimator are muons and neutrons. A Monte Carlo simulation, assuming a 13 radiation lengths tungsten collimator followed by a sweeping magnet and 5 m of iron shielding, predicted a flux of $1.4 \times 10^3 \mu^\pm/s$ incident on the detector at full operating beam intensity. This is a negligible rate compared with the trigger rate from photon interactions in the target. The flux of neutrons from the collimator is more difficult to calculate, but some fraction of 1 m of concrete shielding will be needed surrounding the collimator enclosure to shield the hall from energetic neutrons.

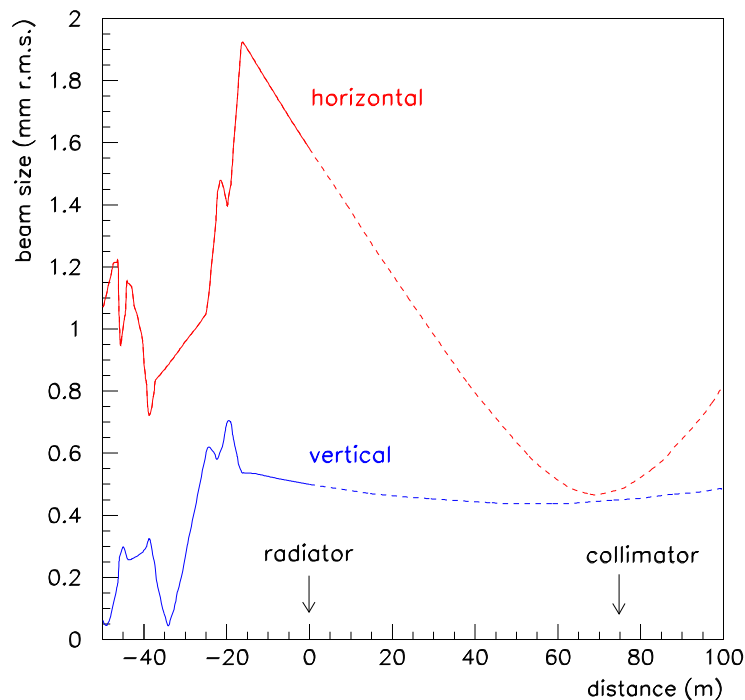


Figure 4.18: Horizontal and vertical r.m.s. envelopes for the electron beam in the region of the photon source, as derived from the beam emittance and beta functions of Fig. 4.17. The origin of the z coordinate has been placed at the radiator. In the region between the radiator and the collimator the envelope refers to the projected image of the electron beam, and does not describe the size of a physical beam that exists in that region.

With regard to hazards associated with the accidental failure of beam line elements or controls, the following measures were recommended in the Keller study [47] and have been incorporated into the HALL D design. The dipole string that bends the electron beam up towards the surface from the below ground and then bends it back horizontal will be connected in series so that failure of a magnet supply or current control electronics cannot result in the beam being steered into the ceiling of the tagger building. The power supply feeding this string of magnets will be protected by a meter relay that shuts off if the current varies from its desired value outside a predefined tolerance. A similar meter relay will also be used on the power supply of the tagger magnet. An electron beam collimator with a burn-through monitor will be located just upstream of the radiator to prevent a mis-steered beam from using radiator support structures as a bremsstrahlung target. Permanent magnets will be located in the upstream region of the photon beam line to bend an errant electron beam into the ground in the case that beam is present while the tagger magnet is off. An emergency beam stop will be installed in the bottom of the photon beam line to catch the errant beam deflected by the permanent magnets. It will be equipped with a current monitor to shut down the primary beam any time electrons are sensed in the photon beam line. Ion chambers located upstream of the photon collimator, and also at the entrance to the photon beam dump behind the experiment, will monitor the total flux in the photon beam and shut off the beam if the flux exceeds a safe value.

4.4 Tagging Spectrometer

4.4.1 Specifications

To satisfy the needs of the GLUEX physics program, the tagged photon spectrometer should meet the following specifications:

1. Photon energy detection from 70% to 75% of E_0 with energy resolution of about 0.1% r.m.s. Percentages refer to the primary beam energy E_0 , i.e. “0.1%” means 12 MeV energy resolution for a 12 GeV beam.
2. A detector system which allows a counting rate of at least 5×10^6 electrons per second per 0.1% over this range of photon energies.
3. An additional capability for photon energy detection from 25% to 90% of E_0 , with less stringent resolution and count rate requirements .
4. A quadrupole magnet between the radiator and dipole spectrometer which images the beam spot on the radiator onto a line on the focal plane. This feature makes it possible to envision the use of focal plane counters with two-dimensional readout, with which one could enhance the tagging efficiency of the source. Focal plane detectors with two-dimensional readout are considered as a possible upgrade beyond the baseline design presented in this chapter. Any improvements obtained using this technique would be over and above the performance figures presented in this report.

The system described below, based on a room-temperature design, meets all of these criteria. The option of a superconducting design was also studied. With a superconducting magnet, the spectrometer could operate at much higher fields, offering the possibility of some space savings in the size of the tagger focal plane array and larger head-room for future possible energy upgrades beyond 12 GeV. An iron yoke design was found which would clamp the 5 T field sufficiently to make it possible to operate normal phototubes on the nearby tagger focal plane. However, as shown below, rate considerations require a degree of segmentation in the tagging counters such that it is impractical to increase the dispersion along the focal plane above what is provided by a 1.5 T room temperature magnet. That being the case, it was decided that considerations of upgrade margin and electrical power alone do not justify the additional cost and complexity of a superconducting magnet.

4.4.2 Magnet

The original design of the tagger spectrometer, which incorporated a single, long dipole magnet ~ 6.1 m in length weighing about 100 tons, has been changed to replace the single dipole with a configuration consisting of two identical dipoles in series with each other.

The main reasons for this change are:

1. It will be difficult to find a supplier of ~ 6.5 m lengths of high quality magnetic iron at a reasonable cost.
2. Since the weight of the top and bottom yoke pieces for a single dipole tagger will weigh more than 20 tons, either a crane with a capacity of more than 20 tons or heavy duty lifting equipment will be necessary to install the magnet or undertake any future repairs or modifications.
3. The long structure of a single dipole tagger will be difficult to install.
4. Since the energy degraded bremsstrahlung electrons exit a tagger along the whole of its length, it is necessary to have the exit completely open. Due to the attractive magnetic force between the poles, the aperture along the exit will distort when the field is present.

The effect of this distortion will probably be less for two smaller dipoles than for a single long dipole.

5. The smaller magnets can be made by more manufacturers and will probably be cheaper.
6. Building costs will be less for the two dipole option - cheaper crane, smaller access doors etc.

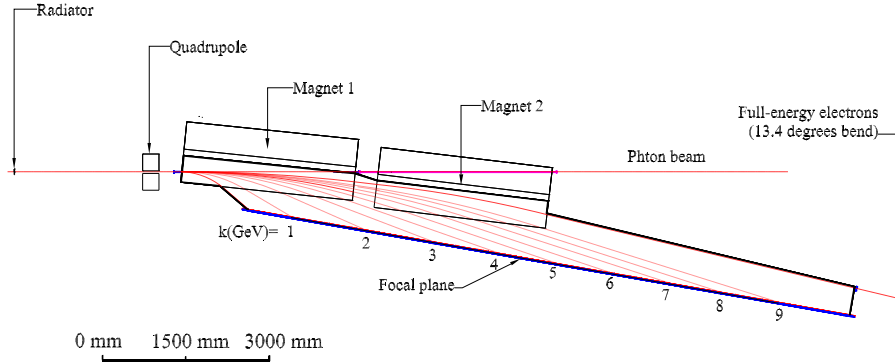


Figure 4.19: A plan view of the tagging spectrometer from above, showing the path of the primary beam and the trajectory of post-bremsstrahlung electrons of various recoil momenta.

The parameters of the two dipole tagger are shown in Table 4.4. The object distance is listed explicitly since it has been increased from 1.5 *m* to 3.0 *m*. This improves the resolution by around 30% and gives more room for the goniometer vacuum chamber, the quadrupole and monitoring devices. A plan view of the layout of the spectrometer is shown in Figure 4.19.

Radius of curvature	26.7 m
Full-energy deflection	13.4°
Object distance	3 m
Field at 12 <i>GeV</i>	1.5 Tesla
Gap width	3.0 cm
Length of each pole	3.1 m
Weight of each dipole	38 tons
Length of focal plane (25% to 90% of E_0)	~ 9.0 m
Coil power	30 kW

Table 4.4: Design parameters for the two dipole tagging spectrometer.

The coils for the two dipole tagger will be run in series from a single power supply.

The first dipole magnet analyzes electrons from 1 to 4.3 *GeV* corresponding to photon energies of 7.7 to 11 *GeV*, and the second magnet analysis electrons from 4.3 to 9 *GeV*, corresponding to photon energies of 3 to 7.7 *GeV*. This is ideally matched to GlueX which requires photons in the energy range covered by the first dipole. It is also clear that a two dipole magnet system is optimum, since with more magnets, the energy range required by GlueX would probably have to be shared between different dipoles.

The pole gap has been increased from 2.0 to 3.0 *cm*. The larger gap is more accessible, and is less susceptible to any changes to the pole gap caused by the magnetic field. Furthermore since only ~ 30 *kW* are required for the 3.0 *cm* gap -compared to ~ 17.6 *kW* for the 2.0 *cm* gap - the coil power consumption remains modest.

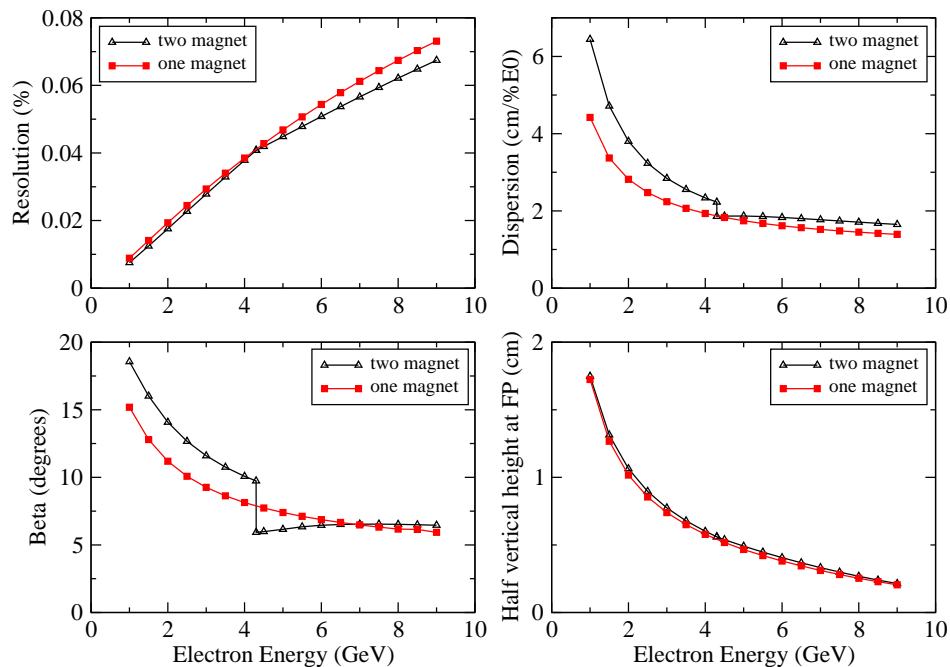


Figure 4.20: Comparison of optics properties between the one dipole and the two dipole tagger.

The two dipole magnet configuration was only adopted after extensive investigations into the magnetic optics confirmed it is possible to design such a system with a continuous focal plane. First order TRANSPORT calculations of the dispersion, resolution and vertical height along the focal plane, as well as beta, the angle at which the analyzed electrons cross the focal plane, are compared for the single and two dipole magnet systems in Figure 4.20.

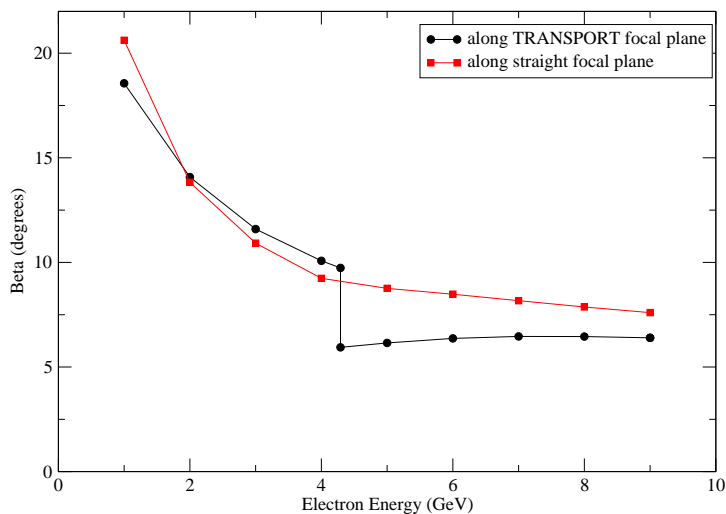


Figure 4.21: Comparison between the beta for the focal plane calculated using TRANSPORT and the beta for the straight focal plane determined according to the TOSCA results.

The resolution and vertical height are essentially unaltered. Although the dispersion shows a small discontinuity at an electron energy ~ 4.3 GeV, which is where the focal planes from the dipoles join, along the whole extent of the focal plane the dispersion from the two dipole tagger is slightly larger. However, beta shows a significant discontinuity at the join of the focal planes. This apparent effect was examined in more detail by ray tracing electron trajectories through a 3-D magnetic field obtained from TOSCA. The ray tracing calculations were also used to find an acceptable location for a straight focal plane which is displaced slightly from the curved TRANSPORT focal plane. Figure 4.21 compares the variation of beta along the straight focal plane obtained using TOSCA, and along the first order TRANSPORT focal plane. It shows that the realistic field computed by TOSCA leads to a smooth variation for beta and also shows that beta is larger for the higher energy section of the focal plane. The magnetic optics parameters, calculated by TRANSPORT along the straight focal plane, are shown in section 4.4.3.

Several designs have been considered for the vacuum system. The most promising approach is to use the magnet poles as part of the vacuum chamber. Either the poles could be welded to a stainless steel vacuum chamber, or the seals between the vacuum chamber and the poles could be made by compressing a viton O-ring between the top and bottom lids of the vacuum chamber and a lip machined round the pole shoes.

A reasonably detailed design for a two dipole magnet tagger, which incorporates a vacuum chamber using O-ring seals, has been completed. The design has been sent to Russian groups within the GlueX collaboration who will examine the technical feasibility of the design and investigate if ISTC funding can be obtained to construct the tagging spectrometer. It should be possible to assemble and test the complete spectrometer in Russia since a feature of the design which uses O-ring seals is that the spectrometer can be fully assembled and tested in the factory where it is built, and then be taken apart and subsequently re-assembled in Jefferson Lab.

The detector package is divided into two parts: a set of 141 fixed scintillation counters spanning the full energy range from 25% to 95%, and a movable “microscope” of more finely-segmented counters designed to span the region of the coherent peak.

The fixed array provides access to the full tagged photon spectrum, albeit at a modest energy resolution of 0.5% and reduced photon spectral intensity. These detectors are well suited for running with a broadband incoherent bremsstrahlung source. They enable experiments to be performed with the highest photon energies possible with the source. When running with a coherent source they play an essential role in the crystal alignment procedure, and provide a continuous monitor of the performance of the source. The microscope is needed in order to run the source in coherent mode at the highest polarization and intensities, and whenever energy resolution better than 0.5% is required. Using the microscope, the source is capable of producing photon spectral intensities in excess of 2×10^8 photons/GeV, although accidental tagging rates will limit normal operation to somewhat less than this.

4.4.3 Spectrometer Optics

Table 4.5 and Table 4.6 give some of the tagger optics parameters as functions of the photon energy. They were calculated for the one-magnet spectrometer option, but the differences between the optics of the two-magnet and one-magnet designs are not very significant, as shown in Figs. 4.20-4.21. The energy resolution and transverse position resolution were calculated assuming the beam properties listed in Table 4.3. The intrinsic energy resolution (i.e. the energy resolution independent of detector size) is limited in most cases by the 0.08% energy spread of the primary electron beam.

At the focal plane, the characteristic bremsstrahlung angle corresponds to a few millimeters of transverse displacement. The vertical beam spot size at the radiator (0.5 mm r.m.s.) contributes a comparable amount because of the large transverse magnification in the dipole transport matrix. However, placing a quadrupole magnet between the radiator and the tagger dipole magnet reduces this magnification nearly to zero over a substantial range of photon energies without substantially changing the other optical properties. Including the quadrupole in the design makes possible a future upgrade of the photon source to employ tagging detectors with

k	Bend	Drift	Angle	cm/% E_0	cm/% E_0
(GeV)	(deg)	(m)	(deg)	perp.to ray	along FP
6	17.270	3.7790	6.035	1.467	13.956
7	17.664	3.2039	6.428	1.568	14.008
8	18.28	2.6276	6.992	1.716	14.096
9	19.108	2.0485	7.872	1.954	14.264
10	20.695	1.4626	9.459	2.407	14.644
11	24.608	0.8560	13.372	3.668	15.860

Table 4.5: Geometrical parameters of the tagging spectrometer for $E_0 = 12$ GeV: Bend = deflection angle; Drift = distance from exit edge to focal plane; Angle = angle between electron path and focal plane; $cm/\%E_0$ = dispersion in units of cm per percent of the incident energy

k	(x x)	(y y)	(y y')	Δk_{beam}	Δk_{spot}	Δk_{tot}	Δy_{tot}	y_{char}
(GeV)	(mm/mm)	(mm/mm)	(mm/mr)	(% E_0)	(% E_0)	(% E_0)	(mm)	(mm)
Without quadrupole:								
6	-0.701	2.737	18.882	0.080	0.081	0.114	1.372	0.804
7	-0.667	2.708	16.538	0.080	0.072	0.108	1.357	0.986
8	-0.625	2.670	14.178	0.080	0.062	0.101	1.337	1.207
9	-0.569	2.617	11.788	0.080	0.050	0.094	1.310	1.506
10	-0.494	2.539	9.341	0.080	0.035	0.087	1.270	1.989
11	-0.389	2.402	6.745	0.080	0.018	0.082	1.201	3.159
With quadrupole: (length = 50 cm, gradient = -0.4 kGauss/cm)								
6	-0.628	0.451	17.622	0.080	0.073	0.108	0.242	0.750
7	-0.583	0.348	15.121	0.080	0.063	0.102	0.190	0.901
8	-0.526	0.202	12.535	0.080	0.052	0.095	0.119	1.068
9	-0.449	-0.024	9.792	0.080	0.039	0.089	0.050	1.251
10	-0.338	-0.427	6.699	0.080	0.024	0.083	0.216	1.426
11	-0.162	-0.416	2.474	0.080	0.008	0.080	0.708	1.159

Table 4.6: Optical properties and resolutions of the tagging spectrometer at the focal plane, for $E_0 = 12$ GeV: (x x),(y y),(y y') = first-order transport matrix elements where x and y are radial and transverse coordinates respectively; the focal plane is defined by (x x')=0.; Δk_{beam} = r.m.s. energy resolution due to beam energy uncertainty; Δk_{spot} = r.m.s. energy resolution due to spot size on radiator; Δk_{tot} = total r.m.s. energy resolution excluding detector size; Δy_{tot} = transverse r.m.s. position resolution due to spot size on radiator; y_{char} = transverse size corresponding to one characteristic electron angle $\theta_{Ce} = (m/E_0)(k/(E_0 - k))$.

two-dimensional readout.

4.4.4 Tagger Detectors

Fixed Focal Plane Array

Tagging of photons over the full range from 25% to 95% of E_0 is not required as part of the physics program here proposed for GLUEX, but is desirable for two separate reasons. First, it will increase the flexibility of the source by providing a broad-band incoherent bremsstrahlung tagging mode, enabling access to photons of the highest energy possible at Jefferson Lab. Second, the process of aligning the crystal radiator for coherent bremsstrahlung requires rotation about several axes and rapid observation of the resulting energy spectra, as described in section 4.2.7. The low-energy portion of the spectrum, between about 25% and 50% of E_0 , is most sensitive to these rotations, and experience with the coherent bremsstrahlung beam at Mainz [48, 49] indicates that the alignment process would be severely compromised if photon energies below $0.5 E_0$ were not measurable.

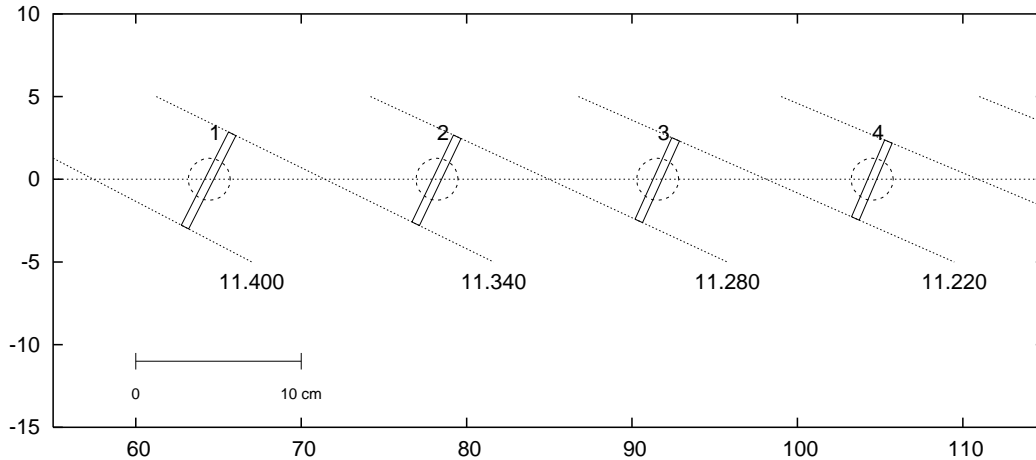


Figure 4.22: Layout of the tagging counters on the high-energy end of the tagger focal plane, corresponding to the lowest-energy electrons from the spectrometer. The view is from above.

The design for the fixed tagger focal plane array consists of 141 non-overlapping scintillation counters. The scintillators are 0.5 *cm* thick and 4 *cm* high and are read out by 1-inch phototubes located below the mid-plane of the spectrometer. The scintillator paddles are oriented perpendicular to the scattered electron rays and are distributed along the focal plane to give essentially 100% coverage of the range from 25% to 95% of E_0 . The size and spacing of the counters varies along the focal plane, according to the dispersion and crossing angle listed in Table 4.5. The high-energy end of the array is shown in Fig. 4.22, which corresponds to the lowest-energy electrons from the spectrometer.

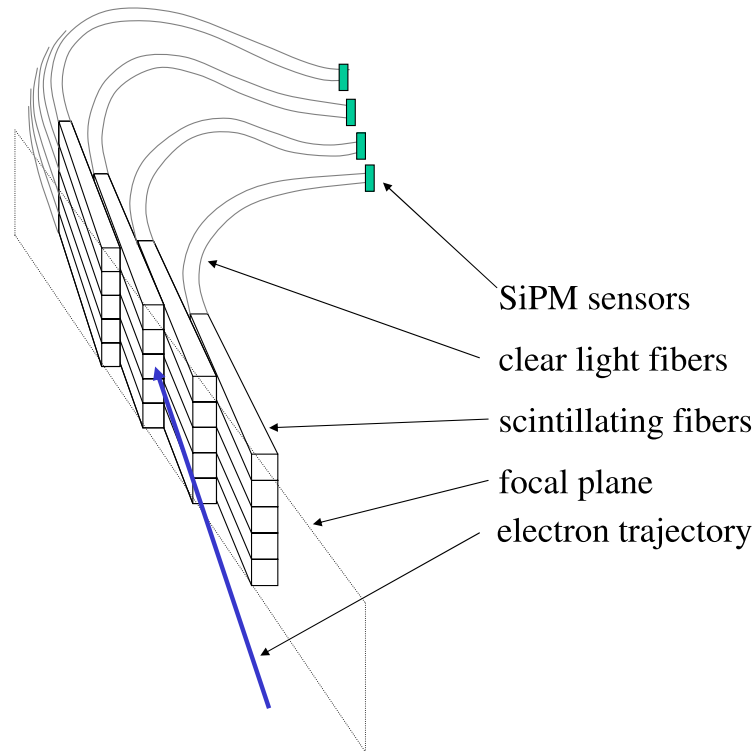


Figure 4.23: Conceptual design of a segment of the tagger microscope, showing the two-dimensional array of scintillating fibers and the clear fiber light guides that couple the light to the silicon photomultipliers.

Focal Plane Microscope Detectors

The design energy resolution of 0.1% r.m.s. (see Table 4.6) is met by non-overlapping detectors which span an energy range of 0.1% each. The principal limitation on detector size is imposed by the design goal of tagging collimated photons at rates up to 100 MHz over the coherent peak. The nominal collimated coherent peak has its highest intensity between about 8.5 and 9 GeV (see Fig. 4.6). However, the the tagger sees both collimated and uncollimated photons, and the total tagging rate in this region is more than twice the collimated rate (see Fig. 4.6), about 250 MHz. The nominal position of the microscope on the focal plane is spanning the region 70% - 75% of E_0 . Dividing this range into 80 bins of equal size limits all channels to less than 5 MHz, which is well within the operating range of the silicon photomultiplier (SiPM) devices foreseen to be used for this detector.

The detector is composed of a two-dimensional array of square scintillating fibers of cross section 1 mm^2 , as shown in Fig. 4.23. Electrons from the spectrometer follow a path approximately parallel to the axis of the fibers, creating a large light yield which effectively suppresses omnidirectional background in the hall and permits the operation of the SiPM detectors with a high discriminator threshold where their dark rate is low. Multiple scattering of electrons in the fiber material effectively produces some degree of overlap between the channels, but does not appreciably degrade the energy resolution of the device. Clear fibers attached to the back end of the scintillating fibers transport the light out of the spectrometer mid-plane to a region with low radiation where the SiPM detectors are located, each with an active area of 1 mm^2 . The microscope will be located immediately in front of the fixed array.

In the baseline operating mode, all five fibers in a column shown in Fig. 4.23 will be summed into one electronics channel. The vertical segmentation of the device also permits its operation in an enhanced mode, where only one fiber in each column is active. In the enhanced mode with the tagger quadrupole switched on, the detector counts only a narrow band of scattered electrons that lies close to the spectrometer mid-plane. This has the advantage that the tagger is blind to those electrons which scatter at large vertical angles in the radiator, whose corresponding photon will be lost on the photon collimator. This can be accomplished efficiently by delivering the power to the SiPM devices independently by row. Simply by selectively powering the individual rows of the array, the readout can be switched from tagging the full vertical range of the beam to counting only a central stripe which corresponds to the size of the photon collimator.

4.4.5 Beam Dump Optics

Although the full-energy beam leaving the tagger magnet is diverging in both directions, the range of angles is small enough that the beam does not blow up rapidly. For a dump distance of 30 *m* the r.m.s. beam size is 6.3 *mm* horizontal (dominated by the 0.08% beam energy spread) and 0.7 *mm* vertical (combination of vertical spot size and multiple scattering in a 10^{-4} radiation length radiator.)

These values scale approximately linearly with distance from the magnet to the dump, and are not very sensitive either to the quadrupole or to small rotations of the exit edge of the tagger magnet. Thus the beam dump design is quite insensitive to the beam optics, and depends only on the lateral and longitudinal spread of the shower in the absorber.

4.5 Polarimetry Instrumentation

The majority of bremsstrahlung photons produced in the radiator are absorbed in the collimator system. If the radiator and collimator system are well aligned, the photon spectrum behind the collimators is dominated by the coherent peak. The beam parameters can be determined by using the intensity spectra from the tagger.

Nevertheless, in order to monitor the polarization parameters – degree (P_γ) and direction (ϵ_γ) – of the collimated photon beam it is crucial to have an independent method, either a photon polarimeter detecting the asymmetry of a process that is well understood within theory (QED) or a well known hadronic process so that the measured beam asymmetry can be compared with theoretical (or experimental) expectations. At photon energies above 5 *GeV*, the forward production of vector mesons is described by vector meson dominance (VMD), resulting in a $\sin^2\theta_{hel}\cos(2\psi)$ dependence of the vector meson's decay distribution where θ_{hel}, ϕ_{hel} are the polar and azimuthal decay angles in the helicity frame and $\psi = \phi_{hel} - \epsilon_\gamma$. With ρ^0 production accounting for about 10% of all hadronic triggers in the detector, this method suffers no lack of statistics. It is limited only by the accuracy of the VMD approximation, roughly 5 – 10% at these energies.

The other method, measuring the photon polarization by means of a polarimeter, can be realized by a pair polarimeter or a triplet polarimeter. It involves additional hardware components on the beamline between the collimator system and the spectrometer magnet. Both types of polarimeter require a thin radiator and a detector in a field free area followed by a dipole magnet and counters for the trigger. Space is available upstream of the spectrometer in HALL D for the insertion of a polarimeter.

QED based calculations for the latter process show that the angle and energy of the soft (triplet) electron is almost independent of the energy of the incident photon ($\bar{E}_{triplet} \approx 0.7 - 0.9\text{MeV}$). The low rate of this process and the technical challenge for a counter device measuring accurately the angular distribution of low energy electrons do not favor this type of polarimeter.

For pair production, on the other hand, the opening angle between the produced electron and positron decreases with increasing energy making the measurement more complicated at higher energies. A magnetic separation is not desirable because the deflection cannot be determined

very accurately. The proposed polarimeter consists of a thin scintillator ($d = 50 \mu m$) as an active target, 1.5 m in front of a silicon microstrip detector arrangement, followed by a dipole magnet and two scintillators 10 cm apart from the beamline for triggering on symmetric e^+e^- pairs. The microstrip detector consists of four layers having 512 channels each of silicon wafers with a spatial width for a single channel of $25 \mu m$. The second and third layer are oriented at $\pm 60^\circ$ with respect to the first layer, the fourth perpendicular to one of the previous layers, thus allowing to measure the full angular range of produced e^+e^- -pairs without any gap in the acceptance. A Monte Carlo simulation of this device including multiple scattering in the target, the microstrip detector, and foils in the vacuum system (using GEANT) shows that an analyzing power of 25% is achievable (cf. fig 4.24). QED calculations predict an angular distribution for pair production proportional to $(1 + P_\gamma \alpha \cos 2(\phi - \epsilon_\gamma))$ with an analyzing power of $\alpha = 0.28$ for incident photons in the range of 6-10 GeV. Because of the thickness of the microstrip layers ($300 \mu m$) it is convenient to measure the beam polarization for fifteen minutes every time the orientation of the crystal radiator or the electron beam parameters have changed. The scintillator target as well as the detector device have to be mounted on motor driven stages so that they can be removed from the beamline.

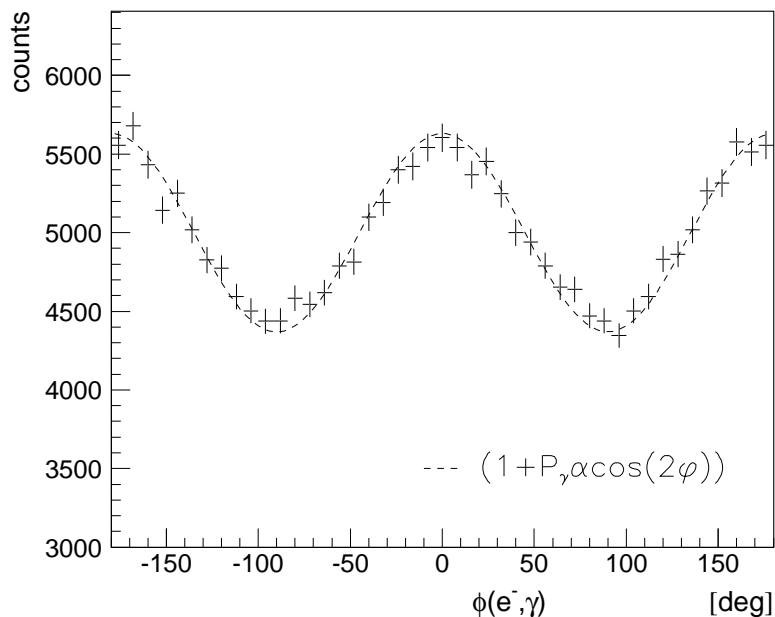


Figure 4.24: Angular distribution for pair production by linearly polarized photons as measured by a polarimeter in comparison with theoretical prediction (*dashed line*). The count rate corresponds to 15 minutes of data taking.

A research and development program is underway at the Yerevan Physics Institute to test these ideas using the 2 GeV coherent bremsstrahlung beam line at YerPhi (Yerevan, Armenia). This 2-year program is funded by the U.S. Civilian Research and Development Fund, and supports a collaboration of Armenian and U.S. collaborators from the University of Connecticut. One of the primary goals of this project is to show the accuracy with which the polarization of a coherent bremsstrahlung beam can be calculated based upon QED and the measured shape of the intensity spectrum.

E of peak	8 GeV	9 GeV	10 GeV	11 GeV
N_γ in peak	185 M/s	100 M/s	45 M/s	15 M/s
peak polarization	0.54	0.41	0.27	0.11
(f.w.h.m.)	(1140 MeV)	(900 MeV)	(600 MeV)	(240 MeV)
peak tagging efficiency	0.55	0.50	0.45	0.29
(f.w.h.m.)	(720 MeV)	(600 MeV)	(420 MeV)	(300 MeV)
power on collimator	5.3 W	4.7 W	4.2 W	3.8 W
power on target	810 mW	690 mW	600 mW	540 mW
total hadronic rate	385 K/s	365 K/s	350 K/s	345 K/s
tagged hadronic rate	26 K/s	14 K/s	6.3 K/s	2.1 K/s

Table 4.7: Operating parameters for an experiment using the coherent bremsstrahlung beam. The calculation assumes a 12 GeV electron beam energy and a 3.4 mm collimator 80 m downstream from a radiator of thickness 10^{-4} radiation lengths. The electron beam current is taken to be 3 μA . The rates in the detector (last two rows) are calculated for a 30 cm liquid hydrogen target and an open hadronic trigger.

4.6 Operating Beam Intensity

Table 4.7 brings together the diverse set of parameters that must be considered in evaluating the optimum beam intensity at which an experiment using the coherent bremsstrahlung beam should operate. All four columns of numbers were obtained for the same beam conditions, except that the crystal orientation was adjusted to align the coherent intensity peak at the energy listed in row one. The second row, labeled N_γ , gives the integrated rate of beam photons in the coherent peak downstream of the collimator. Note the sharp decrease in the intensity of the coherent peak as the energy approaches the end point. By contrast, the incoherent bremsstrahlung flux is approximately constant over this range of energies. The third and fourth row show the height and width of the peak in the polarization spectrum of the beam. Rows five and six report the height and width of the peak in the tagging efficiency spectrum. The tagging efficiency is defined as the number of beam photons of a particular energy reaching the target divided by the corresponding rate in the tagging focal plane. Large tagging efficiencies are required in order to make effective use of tagging. The width of the peak in the tagging efficiency spectrum determines the width of the focal plane that would be active when running with collimation. The peak integral reported in row two is summed within the f.w.h.m. tagging efficiency window. Rows seven and eight give the photon beam power that is incident on the experimental target (and photon beam dump) and the photon collimator, respectively.

The last two rows in Table 4.7 give the inclusive and tagged rates for hadronic triggers from a 30 cm liquid hydrogen target placed in the beam following the collimator. Note that the total hadronic rate is dominated by background (*i.e.* non-tagged) events associated with the low-energy component of the beam. This is why the total trigger rate is essentially constant while the flux in the coherent peak varies with peak energy over an order of magnitude. This table illustrates the value of having an electron beam energy well above the photon energy needed for the experiment.

Chapter 5

The Superconducting Solenoid

5.1 Introduction

Momentum analysis in GLUOX will be provided by a 2.24 T superconducting solenoid magnet. This solenoid was built at SLAC ca. 1970 for the LASS spectrometer and was subsequently moved to LAMPF in 1985 for inclusion in the MEGA spectrometer. The MEGA experiment and the solenoid were decommissioned in place in 1995. The MEGA experimental equipment was dismantled and preparations for shipment started in the spring and summer of 2002. The solenoid was shipped from LANL to the Indiana University Cyclotron Facility (IUCF) for coil refurbishment and testing in October 2002. Currently all four coils have been extensively tested and coils one and two have been completely refurbished. Refurbishment efforts on coils three and four will start in the fall of 2004.

The magnet employs a cryostatically stable design and uses cryostats that were designed to be easily opened for service with hand tools. The inspection of the magnet performed at LANL in 2000 concluded that the solenoid was still in excellent condition and worthy the time and cost involved in relocation and refurbishment. Nevertheless, the magnet support systems are now 30 years old. Even though the magnet is in good condition, it still requires repairs, maintenance, updating, and modifications for use as part of the GLUOX experiment.

5.2 Brief Description

The magnet is described in a technical note [50] and some relevant portions of that description are quoted below. Table 5.1 summarizes important magnet parameters. The refrigeration units are not currently available and new ones are required.

The LASS solenoid magnet provides a 22.4 kG magnetic field parallel to the beam direction. The clear bore inside diameter of the magnet is 73 inches and its final - as modified overall length - is 195 inches. Within the clear bore region the field homogeneity is $\pm 3\%$. Along the beam axis the field homogeneity improves to $\pm 1\%$. The solenoid is constructed of four separate superconducting solenoidal coil-cryostat units [51] and uses a segmented 232 ton iron flux return path that surrounds and supports the coil assemblies. A common liquid helium reservoir is located on top of the solenoid providing the gravity feed of the liquid to the coils.

The liquid helium vessel is surrounded by a liquid nitrogen cooled radiation shield and this assembly is centered in the vacuum tank by a circumferential series of tie bolts designed for minimum conductive heat flux to the helium bath. Radial centering and support are achieved by four low conductance hangers arranged in a spiral pattern. Various tie rods and hangers are instrumented with stress bolts to measure the tremendous forces on the assembly caused by the magnetic fields.

The inductance of the coil is 22 Henries, and the magnet is run at 1800 Amperes. The liquid helium volume is ≈ 5000 liters and the heat load is ≈ 50 watts. Refrigeration at Hall D

Inside winding diameter of SC coils	80 <i>inches</i>
Clear bore diameter	73 <i>inches</i>
Overall length (iron)	195 <i>inches</i>
Inside iron diameter	116 <i>inches</i>
Outside iron diameter	148 <i>inches</i>
Coil-to-coil separation	11 <i>inches</i>
Total iron weight	232 <i>tons</i>
Central field	22 <i>kG</i>
Conductor current	1800 <i>A</i>
Total stored energy	36 <i>MJ</i>
Inductance	22 <i>H</i>
Total helium volume (including reservoir)	5000 <i>liters</i>
Operating heat load (liquid He)	30 <i>liters/hour</i>
Operating heat load (liquid nitrogen)	30 <i>liters/hour</i>
Cool-down time	2 <i>weeks</i>
Copper to superconductor ratio	20 : 1 (grade A) 28 : 1 (grade B)
Total conductor length	117,600 <i>feet</i>
Total conductor weight	29,000 <i>lbs</i>
Turn on time	20 <i>minutes</i>
Turn off time (normal)	20 <i>minutes</i>
Axial load per coil due to magnetic forces	280 <i>tons</i>

Table 5.1: Summary of characteristics of the solenoid as used in the LASS configuration.

will be supplied by a small local refrigerator of 200 watt capacity. This over-engineered nature of the design of the magnet, cryostat and the superconductor itself, has produced a stable, reliable and safe superconducting magnet.

5.3 Solenoid Refurbishment Activities

The LASS/MEGA solenoid was inspected in April 2000 by a team from the GLUEX collaboration, JLab staff and two of the original designers of the magnet. This team met at Los Alamos with the MEGA staff and inspected the MEGA magnet installation and the fourth coil. The fourth coil was found sealed in its original shipping crate. The fourth coil iron yoke ring, yoke stand and coil insertion tool were all found in storage. Magnet documentation and spare parts were also found. Jefferson Lab subsequently entered into negotiation with Los Alamos and the DOE to transfer ownership of the magnet to Jefferson Lab. The solenoid was next dismantled by a heavy rigging contract crew and shipped to IUCF in October 2002.

Currently, two coils have been refurbished and the other two are expected to be completed in early 2005. The first two are expected to be moved to JLab in early 2005. After the all coils are completely refurbished at IUCF, the remainder of the solenoid will be moved to JLab for addition of new support systems including the DC system, control system and cryogenic interface. Testing of individual coils at 4.5 Kelvin and a full solenoid recommissioning test are planned prior to installation in HALL D.

5.3.1 Detailed Tests of The Coils

The detailed examination of the solenoid's four coils began in May 2003. The goal of this detailed testing was to accurately determine the leak rates, verify pressure ratings and verify operation of all internal instrumentation. The solenoid has had a 30 year history of large internal leaks which complicated operations and raised the cryogenic heat load. The internal instrumentation

Coil	N2 shield 10 ⁻⁵ torr-liter/s	He Vessel 10 ⁻⁵ torr-liter/s	External Vessel	Over Pressure
1	5	ok	12in bellows	ok
2	ok	0.2	12in bellows	ok
3	4	ok	12in bellows	ok
4	0.4	ok	12in bellows	ok

Table 5.2: Status of leak and pressure testing. To date, coils one and two have been tested and show no leaks. The status of “ok” indicates a leak rate of less than 10⁻⁹ torr-liter/s

was known to have deteriorated and accurate checks of coil electrical properties needed to be confirmed.

Coil	Resistance Across coil (Ω)	Resistance LH Lead-Ground (Ω)	Resistance RH Lead-Ground (Ω)	Inductance (mH)
1	4.9	2.2	6.4	372
2	3.2	open	open	244
3	2.7	2.6	0.2	172
4	5.2	open	open	763

Table 5.3: Measured electrical properties of the four coils.

One of the goals of this effort was to carefully perform calibrated leak rate measurements of the four coils’ helium spaces, nitrogen spaces and vacuum spaces. This was necessary to quantify the leaks to guide the decision to repair. A decision was reached early on - when good leak detection sensitivity could not be achieved - to install 8 conflat on each of the four coils. This resulted in achieving leak detection sensitivity of 1×10^{-9} torr-liter per second. At this sensitivity the leaks were quickly identified and quantified. The complication due to 18 inch bellows failure was corrected by replacing the bellows. Coil four, which was not part of the MEGA experiment at LANL, had a non-standard vacuum pump-out flange that required replacing. The coil electrical properties and internal instrumentation were measured during this time also. The instrumentation operability was confirmed and the wiring was verified and documented. The results of the testing are summarized in Tables 5.2, 5.3 and 5.4.

The work at IUCF to test the four coils in detail and to perform such repairs as to permit the testing was concluded in February 2004. At the conclusion of this work all four coils had been extensively tested, and the leak position had been determined in coils one and two.

Coil	Voltage Taps	Carbon Resistance Thermometer (4 to 300K)	Thermocouple (80 to 300K)	Platinum Resistance (40 to 300K)	Strain Gauge (new)
1	ok	7 of 8 ok	removed	30 new	6 new
2	ok	ok	removed	30 new	6 new
3	ok	ok	TBD	TBD	TBD
4	ok	4 of 7 ok	TBD	TBD	TBD

Table 5.4: Table of internal instrumentation and voltage taps. Each coil has voltage taps (VT) and Carbon Resistance Thermometers (CRT) in the Helium vessel and Thermocouples (TC) on the N2 shield and strain gauges (SG) on the support posts.

5.3.2 Refurbishment of Coils One and Two

Following the conclusion of the initial investigations, a contract was negotiated with IUCF to perform all repairs and proof testing on coils one and two. The scope of work of this effort included localizing and repairing all leaks. Replacement of all strain gauges as most had failed. To replace the thermal couples shield thermometers with Platinum resistance thermometers (PT100). The replacement of all wiring, and finally to replace the aluminized mylar multi layer insulation (MLI). A decision was made to retain the original Liquid Nitrogen shields due to their good state of repairs and functionality. The new PT100 thermometers were installed in small copper blocks soldered to the copper shield panels for good thermal contact and reliable mounting. The new strain gauges were installed on the outermost of the three nested cylinders of the cold to warm supports.

Coil one was previously determined to have a shield leak only. The most difficult part of completing coils one and two was reconnecting the shields and plumbing due to the out of sequence reassembly. This necessitated replacing the simple joints with more complex junctions that had only forward facing welds. This technique was used extensively on a magnet in JLABs Hall C namely the HMS Dipole. Both coils were cooled to approximately 120 Kelvin and no leaks were found. A side benefit of this testing was the confirmation of proper operation of the new shield PT100 thermometers and the wiring correctness. Both coils were pressure tested to 100 psi successfully. This concluded the testing and internal repair phase of coils one and two. The next step was to replace all the shield MLI insulation and perform a final evacuation as preparation for placing the coils in storage. Both coils one and two achieved vacuum in the range of 1×10^{-5} , passed a final leak check and were subsequently backfilled with N₂ gas, sealed and moved to an inside storage location at IUCF.

5.3.3 Plans To Complete Coils Three and Four

As of September 2004, coils three and four have been moved into the working area at IUCF and contract negotiations for their refurbishment are underway. This work is expected to begin in the fall of 2004 and be completed before summer 2005.

5.3.4 Plans To Complete The Solenoid at JLab

The remaining work to upgrade and re-assemble and test the solenoid is planned to occur at JLab. Activities during 2005 include securing a test and assembly space in the Test Lab at JLab, moving coils one and two to the space in the test lab and preparing the coils for cool-down to 4.5 Kelvin. This testing effort requires equipping and staffing the solenoid test area in the test lab and designing and fabricating a new single coil test interface. The original SLAC-designed test interface was never found so a replacement is required to support testing. The replacement will have connections matching JLab standards. A set of temporary cryogenic connection lines for use in the Test Lab will also need to be designed and fabricated. These two design and fabricate items will become the highest priority of the JLab HALL D design and engineering staff in FY 2005. This is to support the cool-down and test of one single coil by the end of FY 2005. This test would consist of cool down and fill at 4.5 Kelvin with helium, LN₂ shield cool down and fill and only limited low current operation of the coil.

The solenoid also requires an entirely new control system. The original solenoid had only manual controls and instrument data were recorded in paper log books. The cryogenic control of the solenoid was completely absent and all cooling was achieved by manipulating a small Helium refrigerator. The replacement of the controls on the HMS SC magnets at JLAB at this time and the similarity of many systems and identical nature of others leads to common solutions. The prototype for the solenoid new controls is being tested as this is written. A full system of the prototype is planned for January and February 2005. Following debugging and commissioning of the HMS Dipole prototype system a clone will be prepared for the Hall D solenoid. The current plan calls for a more complete test of coil two using the new solenoid controls, new power supply

(already on site) and would operate a single coil at full current. Test and re-assembly of the entire solenoid are pending and depend significantly on the year of availability of HALL D.

5.4 The Magnetic Field of The Solenoid

5.4.1 Magnetic Modifications Needed

The original SLAC configuration of the solenoid allowed for gaps in the return yoke so that wire chambers could be inserted from the outside. Further, in the LASS and MEGA installations the Cerenkov detector had to be located at large radius due to the presence of high magnetic fields near the downstream end of the solenoid. The source of these high fields has been investigated using a 3D TOSCA model of the yoke and coil and various methods to reduce these “stray” fields have been explored.

The following yoke modifications will reduce the saturation in the pole cap and lower the stray field in the region where the GLUEX Cerenkov will be located:

1. Replace the air gaps with iron rings. This lowers the required operating current to achieve the same central field. The lowering of the local fields especially around coil seventeen helps reduce pole cap saturation.
2. Increase the distance in “Z” between the seventeenth coil and the downstream pole cap. This lowers the local field near the pole cap and thus lowers the saturation.
3. Increase the thickness of the pole cap by adding an iron disk to dilute the pole cap field and reduce saturation.

These yoke modifications will reduce the stray field levels in the Cerenkov region from ~ 700 gauss down to ~ 50 gauss, low enough to be shielded by thin iron and Mu-metal shields.

5.4.2 TOSCA Simulations

The original solenoid magnet was designed without the benefit of modern 3D magnetic modeling, yet the magnet has worked long and well in two experiments. But there has been a persistent difficulty with downstream stray fields, as noted above. Thus we have created a 3D TOSCA model of the solenoids fields to study the problem in detail and design a remedy.

TOSCA Model

The yoke and coils have been modeled using the TOSCA 3D magnetic analysis software. This model was prepared with geometry that allowed simulating the effect of closing the yoke gaps or creating new gaps, or opening or closing the ends by simply changing materials definitions.

The solenoid magnetic field as currently modeled is based on the actual distribution of current within the four coil cryostats and the actual details of the yoke construction. The yoke modifications for the benefit of the GLUEX experiment have also been included. The current distribution of the solenoid can not be modified and therefore the details must be included to accurately model the magnetic fields for experiment simulation taken and to test the effect of various modifications. The TOSCA model also provides valuable design information about the magnetic environment as seen by each detector system. The modifications to the yoke are a mix of requirements from GLUEX physics, the need to lower external fields, and modifications to provide better access for the GLUEX detectors. The TOSCA model is designed to evaluate the yoke modifications needed to lower the external fields. The TOSCA modeled internal fields have already been valuable as the source of magnetic fields for the Geant simulations. Further magnetic simulation work will be performed to study more carefully the effect of all the above changes on the exact B vs I excitation curve, the inductance and stored energy and the forces on the coils. Generally filling in the yoke gaps will lower all of these quantities but the exact values remain to be confirmed.

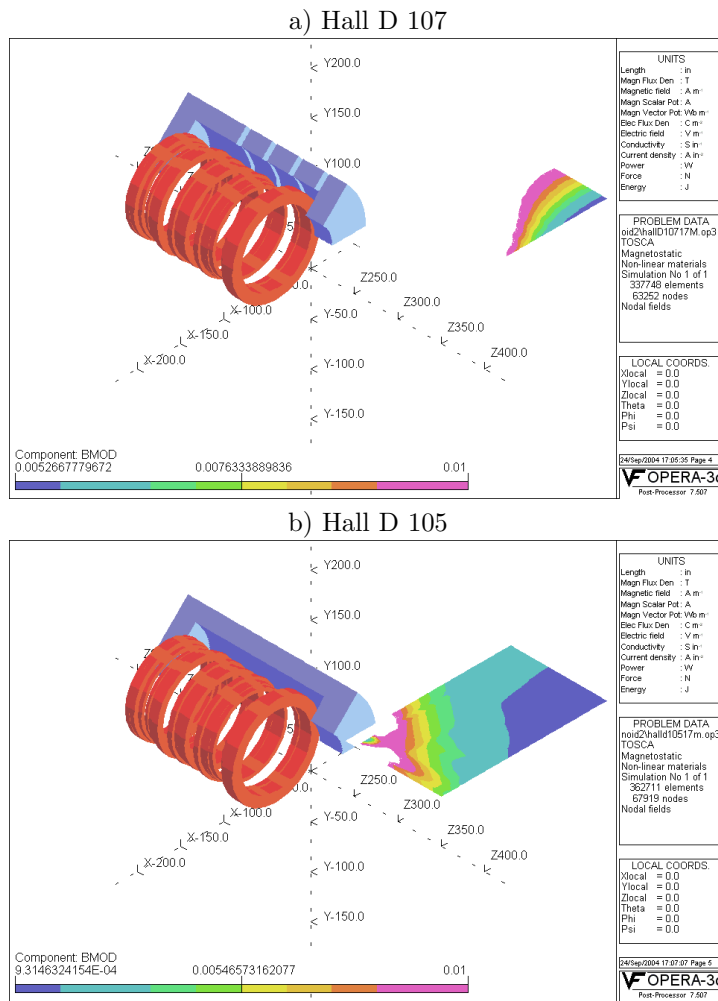


Figure 5.1: TOSCA models for a) the original magnet configuration and b) configuration that fills the gaps with iron, extends the fourth gap and thickens the pole. Both figures show the model for the coils (solenoid and 13th coil ring) and a 45 degree pie slice of the yoke iron. Also shown is a contour plot of fields which are less than 100 G in the region of 50 to 240 in radially and 190 to 300 in along the axis. This is a region that could be considered acceptable for placing photomultiplier tubes. Note that in the bottom configuration the region of low field begins at the iron, allowing detectors to be mounted near the solenoid. The magnetic field scale is in Tesla.

Preliminary Results

Four GLUEX models were investigated. The original and last configurations are shown in Figure 5.1. All four models use identical coil models and identical current densities. The integral field increases by 2.6 % as a result of filling the gaps. The other modifications have no significant effect on the total field. This effect can be easily understood since most of the flux must return through the original gaps. Thus filling them with iron must have a large effect on the field integral while only some of the flux is effected by the other changes, and thus a minimal effect on field integral is seen.

Model Number	Max Field (G)	Min Field (G)	Low-Field Area (%)	$\int B \cdot dl$ (T·Inches)
Hall D 107	1067	523.0	none	302.8
Hall D 106	351	82.5	none	311.0
Hall D 103	241	56.7	17	311.3
Hall D 105	158	45.7	50	310.8

Table 5.5: Field parameters for the region between 50 and 80 in radially, where Cerenkov photomultiplier tubes might be placed. The entries correspond to the maximum and minimum B fields, and fractional area with field below 75 Gauss. Also given is the on-axis field integral for each TOSCA model.

We briefly describe each configuration:

Hall D 107 has the iron yoke and coil configuration of the original LASS solenoid as it was used at SLAC. This model is to provide a baseline for comparison and to compare with historical calculations and measurements. The model has the original segmented yoke with the four original 6 inch air gaps. *This model should be used to measure the effectiveness of the yoke changes which are the subject of the other three models.*

Hall D 106 has the SLAC yoke but with the four 6 inch gaps filled with the same iron as the rest of the yoke. This was a requested change and it has the effect of lowering the external fields. You can clearly see that the external fields are in general lower, especially in the regions where it would be desirable to locate photo tubes.

Hall D 103 has the four gaps filled with steel and gap four extended from 6 inches to 12 inches. This modification was selected because of the extreme saturation in the yoke that was observed around the 13th coil. Fields as high as 3 Tesla are observed near the 13th coil. Moving the yoke further away from the 13th coil will lower the yoke saturation and thus make the yoke more effective in collecting external flux and channeling it back within the yoke iron.

Hall D 105 has the down stream “pole cap” thickened from 20 inches to 26 inches. This is in addition to filling the gaps and extending the fourth gap. This modification was selected to further reduce saturation levels in the yoke and thus reduce further the external fields.

We studied the external fields in the region where Cerenkov photomultiplier tubes may be located. The region extends in z for 20 inches and in R from 50 to 80 inches. The model Hall D 105 has a substantial volume ($\sim 50\%$) with fields between 46 and 74 gauss (see Table 5.5). These fields can be shielded by a combination of soft iron and Mu-Metal tubes. As this region extends from 65 to 80 inches in radius, the photomultiplier tubes for the Cerenkov could be located much closer to the detection volume. A maximum distance of about 2 meters (~ 80 inches) is certainly possible. Figure 5.2 plots the computed fields for the four models as a function of radial distance in the area where we expect to place sensitive detectors, and Table 5.5 summarizes the characteristics for each case. Clearly there are large regions close to the detection volume where tubes could be located. It is also obvious that simply moving further

out can have the same effect. Indeed the original solution chosen at SLAC was to locate the tubes at 4 meters where the fields are ~ 75 gauss for the original SLAC /LASS geometry. The modifications computed above can achieve these field levels in a much more efficient manner.

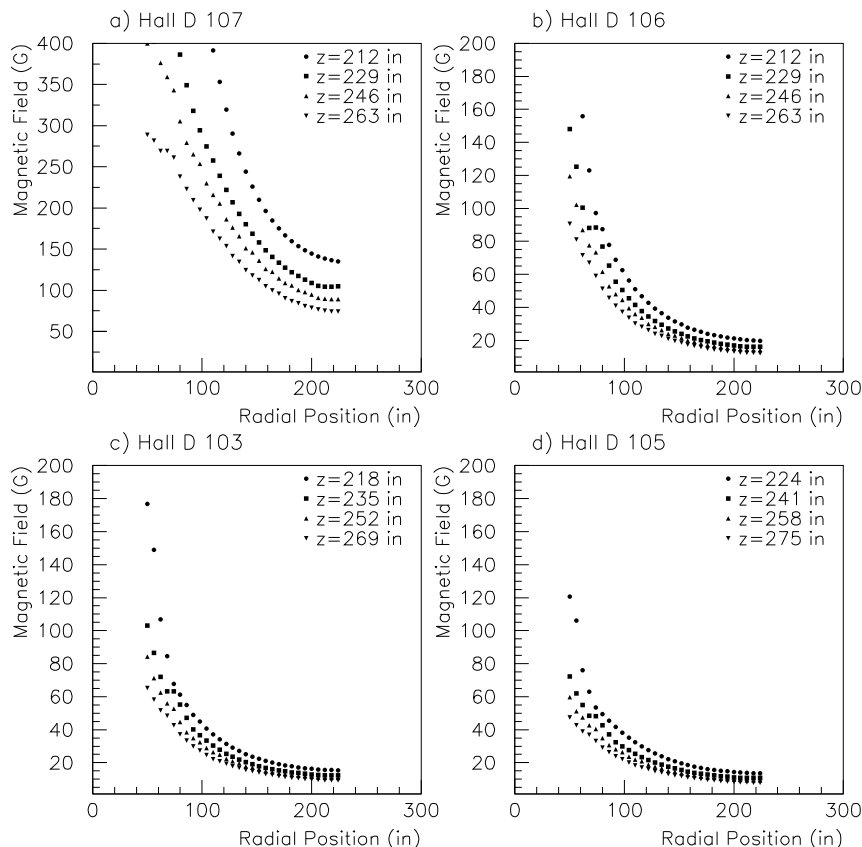


Figure 5.2: Magnetic field as a function of radial distance at constant distance along the z axis for the four different configurations of the solenoid. Note the scale change for plot a).

5.4.3 Compensation of the Upstream Plug

The collaboration desires a matching full aperture hole (73 inch diameter) in the upstream yoke to provide access to the detector volume for service, installation and support, and also to provide a route for cables to exit the upstream end of the magnetic volume. This upstream hole has the same effect on the internal field quality as the downstream hole and thus must be studied carefully. The downstream hole in the yoke is the same diameter as the cryostat inner diameter, 73 inches. This opening is equivalent in magnetic effect to boring a large hole in the center of the pole of a dipole magnet because the end yoke pieces for the solenoid are in fact the poles. The designers of the solenoid compensated for this large hole by increasing the current density in coil # 4, which has four times the average number of Amp-turns of the other 16 coils. This compensates for the missing iron and also contributes to the nearby yoke saturation and stray fields that we dealt with in the previous sections.

We examined four options to deal with the loss of field integral and flatness caused by the new opening: a) no action, b) creating a gap in the upstream yoke and c) increasing the current by 15% in all the coils of cryostat # 1 Figure 5.3 and show the on-axis magnitude of

the field through the solenoid for the various options discussed above. The first is the nominal configuration with the upstream plug in place and the second is with the new upstream hole. All other modifications mentioned earlier are included. The loss of field integral in the backward direction is not a significant problem, but the reduction of flatness has the effect of increasing the computation requirements for analysis. Clearly, an improvement in the upstream field flatness is desirable. We detail the three options considered.

New upstream yoke gap

Creating a new upstream yoke gap was examined in the first round of magnetic simulations and the conclusion was that this creates more of a problem than it solves. The new gaps make a lot of exterior field that can get into phototubes and it adds the complication to the assembly that cables, the yoke and detectors are now linked. The new gaps do not cause a loss of good field region but it does reduce the integral on axis.

Increase current in cryostat # 1

Increasing the current in the 7 coils inside cryostat # 1 by approximately 15% has the effect of increasing the local Amp-turns to boost the field back up and replace the flux lost by enlarging the upstream yoke hole. This can easily be accomplished by stacking a floating DC power supply across cryostat # 1 to enhance the current relative to the main current. The main current power supply provides 1800 A to all 4 cryostats in series. In this way all 17 internal coils are in series and have the same charging and discharging. The small biasing DC power supply that floats across cryostat # 1 permits a local current increase and is adjustable. This method if selected requires that a low amperage (≈ 300 A) current lead be added to the new cryo-reservoir during the solenoid refurbishment. The new DC biasing supply is simply connected between one of the main current leads and the low current biasing current lead. This is an adjustable, low cost, and reliable method to boost the field back up and is identical in principal to the method used to boost the down stream field. Instead of adding turns, which is difficult, one just adds some extra current to the existing turns. The magnet control and quench protection stems are marginally more complex as a result of this solution. Precautions must be taken to guarantee that there can never be a current path through the biasing lead and power supply that conducts the main 1800 A solenoid current. Figure 5.3 is a graph of the central field with extra current in the 7 coils of cryostat #1.

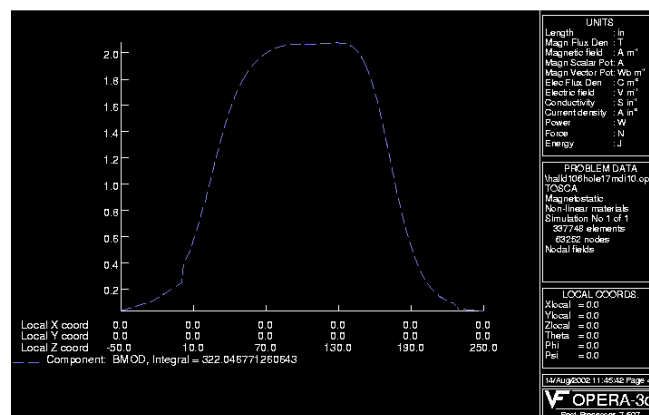
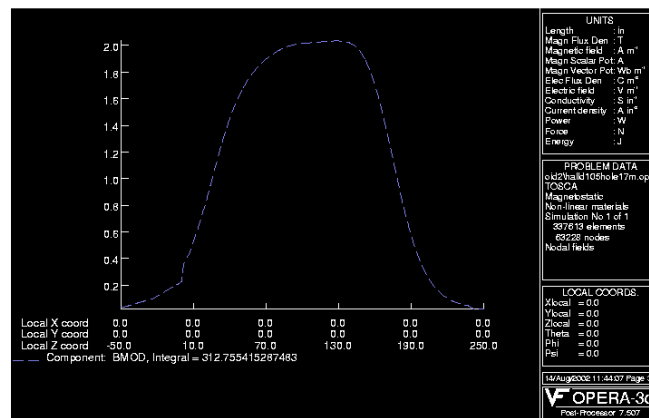
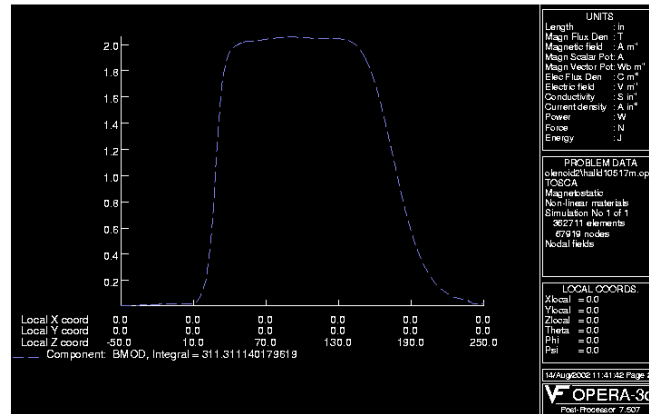


Figure 5.3: Upper) Standard configuration. Middle) Standard configuration without upstream plug. Lower) No upstream plug, nominal current in coils 2-4 (14000 A/in^2), but current in coils 2-4 increased by 10% (15400 A/in^2).

Chapter 6

The GlueX Detector in Hall D

6.1 Overview

The goal of the GLUEX experiment is to search for gluonic excitations with masses up to $2.5 \text{ GeV}/c^2$. The identification of such states requires knowledge about their production mechanism, the identification of their quantum numbers J^{PC} and their decay modes. The production mechanism and J^{PC} determination require a partial wave analysis which in turn depends on the kinematic identification of exclusive reactions. The decay products of produced mesons must be identified and measured with good resolution and with full acceptance in decay angles. In many cases the decays of mesons involve a chain of particle decays. The GLUEX detector (see Figure 6.1) must therefore be hermetic with 4π coverage and have the capability of measuring directions and energies of photons and momenta of charged particles with good resolution. Particle identification is also required.

The partial wave analysis technique depends on high statistics and in the case of incident photons, also requires linear polarization. The latter is needed to identify the production mechanism. The linear polarization is achieved by the coherent bremsstrahlung technique. The degree of linear polarization and flux of photons in the coherent peak fall dramatically as the photon energy approaches the endpoint energy. On the other hand, it is desirable to have photon energies high enough to produce the required masses with sufficient cross section and with sufficient forward boost for good acceptance. For a fixed incident momentum and a fixed resonance mass, it is also desirable to have a fairly constant $|t|_{min}$ over the natural width of the resonance. This also requires sufficiently high incident photon energy.

An operating photon energy 9.0 GeV produced from a 12.0 GeV electron beam represents an optimization of beam flux, cross-section and degree of polarization. The GLUEX detector is therefore optimized for this energy range. Figure 6.1 is a schematic representation of the proposed GLUEX detector. The individual subsystems are discussed in more detail below.

6.2 The Target

The main physics program for the GlueX experiment will be conducted with a low-power liquid hydrogen or liquid deuterium target. We propose a design which is very similar to the cryogenic target presently in use in Hall B. This target should fit comfortably into the detector geometry. Solid targets, required for various calibrations, can easily be incorporated into this design.

The maximum power deposited in the target by the beam is 100mW . In such low-power targets, natural convection is sufficient to remove heat from the target cell and a circulation pump is not required. These targets frequently employ mylar target cells. The mylar cell is often mounted on a metal base to provide for liquid entry ports and a reliable means of positioning the cell. The beam enters through a thin window mounted on a reentrant tube at the base of the cell. The diameter of this entrance window must be sufficiently large to allow

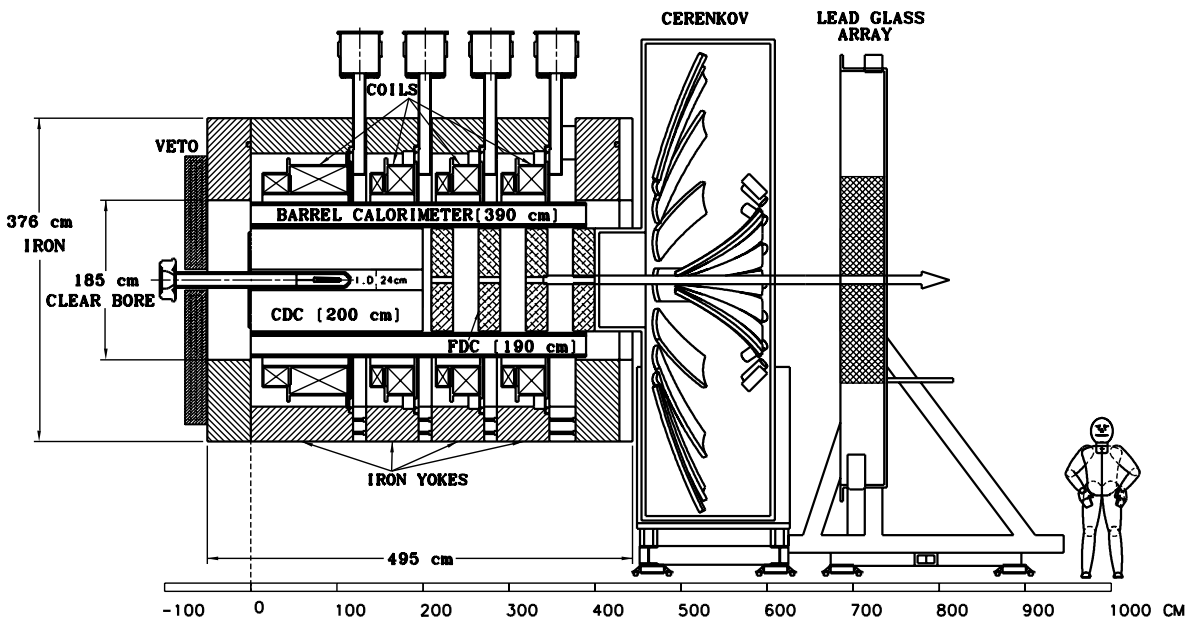


Figure 6.1: An overview of the GLUEX detector. The major subsystems are labeled and are discussed individually in the text.

the beam to enter the cell without scraping; taking into consideration the uncertainties that will be present in aligning the cell. The area between the reentrant window and the outer wall of the cell must be sufficiently large to allow for convection and to prevent bubbles from being trapped. A target cell diameter of three to six centimeters would seem reasonable. A smaller diameter cell would be possible with more stringent alignment requirements. A system such as this, containing a few hundred cm^3 of liquid hydrogen, would be considered “small” by Jefferson laboratory standards and the safety requirements would not place any significant constraints on the target design or operation.

The target cell is connected to a condenser located upstream of the cell. In the Hall B target the condenser is formed by concentric cylindrical shells with the axis of the cylinders lying along the beam line. The heat exchanger should be sized to allow the target to be condensed in a reasonable period of time (a few hours). In some target systems the condenser is cooled by a separate refrigerator. In other systems liquid helium at 4.5K is used as the refrigerant. Because the magnet in Hall D will require liquid helium there seems little reason to operate a separate refrigerator for the target. The standard CEBAF delivery system supplies 5K 3 atmosphere fluid through a 1-3/8” diameter bayonet. This gas is expanded through a JT valve to produce liquid. This system is somewhat cumbersome for small loads. It would be much more convenient to supply the target with low-pressure 4.5K liquid through a small transfer line. It would be possible to draw liquid from the magnet if a port is available. In Hall B it was found convenient to draw liquid helium for the target from a buffer dewar which is filled by a JT valve. To allow for a similar arrangement in Hall D, a 4.5K supply bayonet and a 5K cold return bayonet should be provided.

The extent to which target components shadow the veto counter must be considered. Some shadowing of the veto counter will be unavoidable, since the cell must be supported. As we are relying on convection to remove heat from the target cell it would be favorable to locate the heat exchanger as close to the target cell as possible. This would result in increased shadowing of the veto counter. It is not clear that convection alone would be sufficient if the condenser were located outside the veto detector. This design could easily be tested using the Hall B test cryostat.

The hydrogen cell is located inside of a scattering chamber to provide an isolation vacuum.

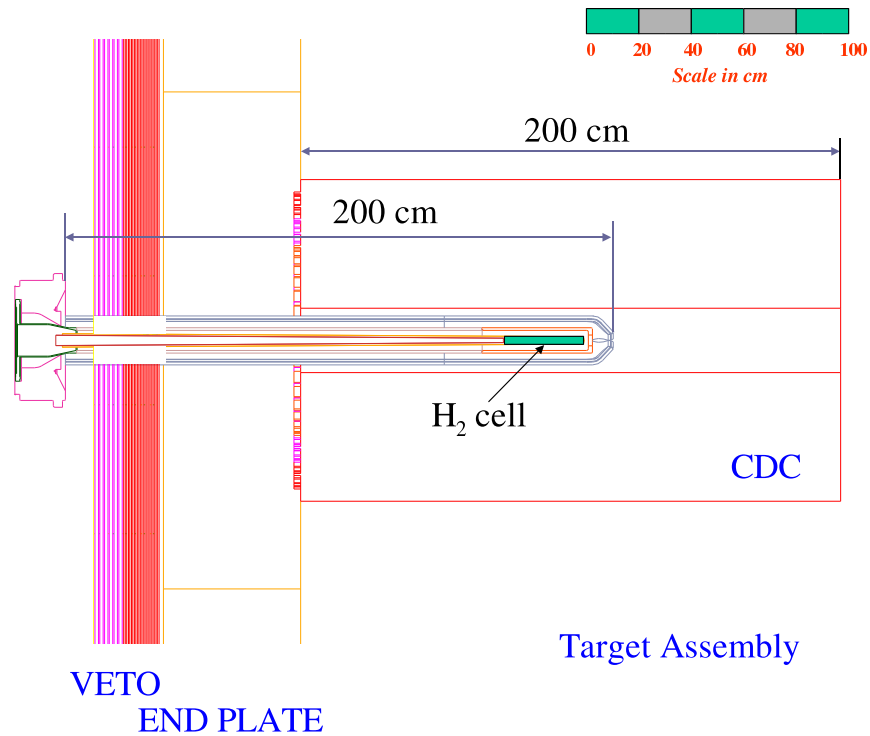


Figure 6.2: Target region including target cell, vacuum scattering chamber, start counter. Sufficient room exists for a vertex detector. Also shown for reference are the CDC and thickness of the magnet iron and upstream veto.

The walls of this chamber should be kept as thin as possible. In Hall B, plastic foam chambers have been used successfully. The target vacuum is likely to be shared with the upstream and downstream beam-lines. The target vacuum chamber would include a service port for the refrigerant, target gas and instrumentation connections.

Solid targets are required for purposes of calibration and studying detector response. It may be desirable to replace the target cell with a multi-foil “optics target” from time to time. Installing the target and bringing it into operation will probably require two days. A mechanism to introduce solid targets either upstream or downstream of the hydrogen cell would be possible. Consideration should be given to the number of different targets required and to their placement.

Attaching the vertex detector and veto counter to the target vacuum chamber will locate those detectors accurately with respect to the vacuum chamber, but may complicate target assembly and disassembly. The cool-down and vacuum motion of the target cell relative to the vacuum chamber will remain major sources of uncertainty in the target cell position. The alignment requirements for this are not severe but should be considered early in the design stage. It is likely that a rail system would be used to position the target inside the magnet, as the insertion cart is used to position the cryogenic target in Hall B. Figure 6.2 illustrates a target cell similar to one which has been used in Hall B positioned inside the GlueX detector. In this design the cell incorporates an extended reentrant window to place all metallic components upstream of the veto detector.

6.3 Calorimetry

6.3.1 Global Design

The electromagnetic (EM) calorimetry for the GLUEX experiment is divided in three parts, each handled by a different detector sub-system.

The very forward angles ($\theta < 14^\circ$) of the HALL D detector will be covered by an existing lead glass detector (LGD) used in the E852 experiment at BNL and re-stacked to meet the geometrical acceptance criteria for HALL D. The approximate polar angular range $14^\circ < \theta < 138^\circ$ will be subtended by the barrel calorimeter. Finally, the upstream, large-polar angle region ($\theta > 138^\circ$) will be the domain of the upstream photon veto.

Each of these three sub-systems is treated individually in a dedicated subsection within this chapter.

6.3.2 The Lead-Glass Calorimeter

The most downstream subsystem of the GLUEX experiment is the lead glass detector (LGD), an electromagnetic calorimeter consisting of nearly 2500 lead glass blocks. The purpose of the LGD is to detect and measure forward-going photons from the decays of π^0 , η and other mesons. The LGD will also provide a fast energy sum to be used in the level-1 trigger.

Each block has dimensions of $4 \times 4 \times 45 \text{ cm}^3$ and they are arranged in a nearly circular stack. The radius ($\approx 1 \text{ m}$) is matched to the aperture of the GLUEX solenoid magnet. The type of glass used in E852 and RADPHI and proposed for use in GLUEX was produced in Russia and is called type F8-00. Its chemical composition is 45% PbO, 42.8% SiO₂, 10.4% K₂O and 1.8% Na₂O. This glass has an index of refraction of 1.62, a density of 3.6 gm/cm^3 , a radiation length of 3.1 cm and a nuclear collision length of 22.5 cm. The blocks were machined to a precision of about 25 microns in transverse dimensions and flatness so stacking the array does not result in gaps. The Cerenkov light from each block is viewed by a FEU-84-3 Russian PMT. The PMT bases are of a Cockcroft-Walton (CW) design [52]. The PMT's will be registered with respect to the glass using a cellular wall that includes soft-iron and μ -metal shielding. The signal from each block will be digitized with an 8-bit 250 MHz FADC. A schematic of the calorimeter is shown in Figure 6.3.

Several of the GLUEX collaborating institutions have been involved in the design, construction and operation of calorimeters of a design similar to that presented here and in the analyses of data from those calorimeters. The first of these calorimeters was a 3000-block calorimeter used in the E852 experiment at Brookhaven Lab (BNL) which used an $18 \text{ GeV}/c \pi^-$ beam and the multiparticle spectrometer (MPS). Details of the design and operation of prototype calorimeters and the one used in E852 have been published [53, 54]. Several physics results based on measurements with the E852 LGD will be discussed here.

An LGD was also used in the RADPHI experiment [55, 56] at JLab that was located downstream of the CLAS detector in HALL B and used in a bremsstrahlung photon beam produced with 5.4 GeV electrons. The goal of RADPHI was a measurement of the radiative decay modes of the ϕ meson resulting in five-photon final states. The experience gained with the RADPHI LGD is extremely valuable for GLUEX. As will be discussed below, the π^0 and η mass resolutions based on measurements from the LGD improve as the distance from the production point of photons (the target) to the LGD increases. The resolutions also improve as the mean photon energy increases and thus as the beam energy increases. Photons produced in RADPHI resulted from interactions of beam photons of energies distributed almost uniformly in the range from 3 to 5.4 GeV and the target to LGD distance was $\approx 1 \text{ m}$. For GLUEX the photon energy is 9 GeV and the target to LGD distance is $\approx 5 \text{ m}$.

Based on the experience with the LGD's used in E852 and RADPHI we expect the GLUEX LGD to provide the granularity and resolution required to carry out the amplitude analysis needed to map the spectrum of gluonic excitations, the goal of this experiment.

In what follows we also address several technical issues regarding the GLUEX LGD including issues of the assessment of the E852 and RADPHI glass and PMT's that will be used in GLUEX,

curing of radiation-damaged glass, electromagnetic backgrounds in the beam region, shielding PMT's from the fringe field of the solenoid, calibration and monitoring.

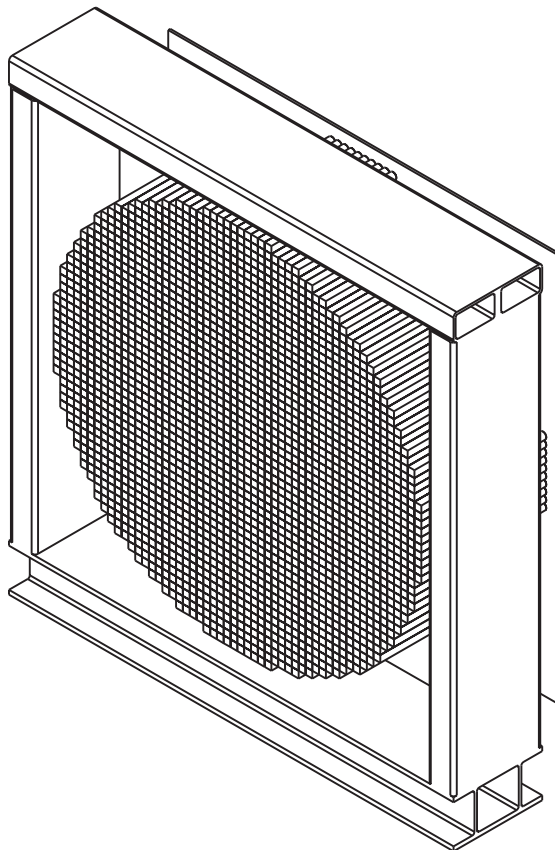


Figure 6.3: The lead glass detector as modified for GlueX . 2500 lead glass blocks will be arranged in a nearly circular stack of radius ≈ 1 m.

The E852 Experience

The goal of E852 was a search for mesons with unusual quantum numbers using the MPS at BNL with a Lead-Glass Calorimeter. The E852 LGD was located 5.4 m from a liquid H_2 target located mid-way inside a large dipole spectrometer magnet. E852 detected and measured both charged particles as well as photons from π^0 and η mesons. The measured mass resolution for π^0 and η mesons was 10 and 25 MeV/c^2 respectively.

Several physics results from amplitude analyses based solely on data from the LGD have been published. Events in which four photons were identified in the all-neutral final state $4\gamma n$ led to analyses of the $\pi^0\pi^0$ [57, 58] and $\pi^0\eta$ systems [59, 60, 61]. Figure 6.4 shows a scatterplot of one $\gamma\gamma$ effective mass combination versus the other $\gamma\gamma$ effective mass from the reaction $\pi^-p \rightarrow 4\gamma n$. Clusters associated with the $\pi^0\pi^0n$ and $\pi^0\eta n$ final states are clearly observed.

The $\pi^0\pi^0$ effective mass spectrum for the $\pi^-p \rightarrow \pi^0\pi^0n$ reaction is shown in Figure 6.5. The prominent feature in this spectrum is the $f_2(1275)$ tensor meson. The spectrum also shows a sharp dip at $\approx 1 GeV/c^2$ that is understood as evidence for the scalar meson $f_0(980)$ interfering with the S -wave background. A partial wave analysis (PWA) of these data set was performed [57, 58] for events in various ranges in momentum transferred from the target proton to the recoil neutron and some of the results for the lowest momentum transfer range are shown in Figure 6.6. Plots show open and filled circles corresponding to mathematically ambiguous solutions with

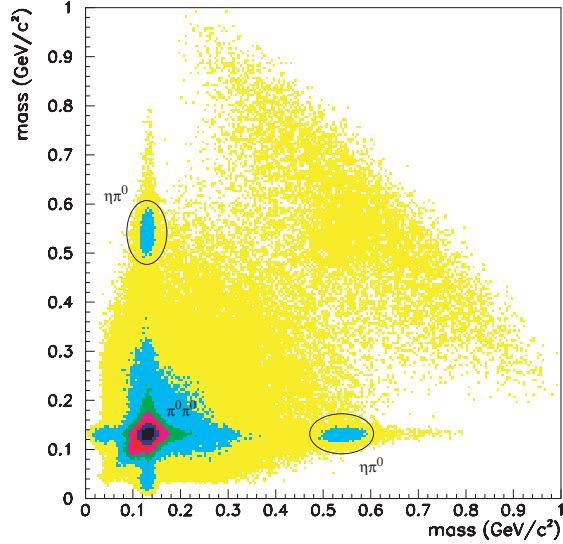


Figure 6.4: Scatterplot of one $\gamma\gamma$ effective mass combination versus the other $\gamma\gamma$ effective mass from the reaction $\pi^-p \rightarrow 4\gamma n$. These measurements were made using the E852 LGD.

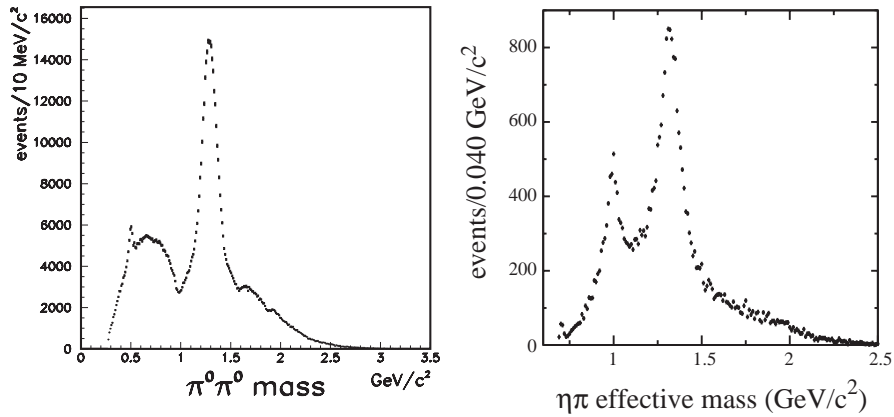


Figure 6.5: left: Distribution of the $\pi^0\pi^0$ effective mass in the E852 reaction $\pi^-p \rightarrow \pi^0\pi^0n$. right: Distribution of the $\eta\pi^0$ effective mass in the E852 reaction $\pi^-p \rightarrow \eta\pi^0n$.

the filled circles indicating the physical solutions based on other criteria. The S -wave shows evidence for the $f_0(980)$ scalar meson via its interference with a broad background, the D_0 -wave shows the $f_2(1275)$ and the phase difference between the S -wave and D_0 -waves show the classic motion expected of a resonance.

Figure 6.5 also shows the $\eta\pi^0$ effective mass spectrum for the $\pi^-p \rightarrow \eta\pi^0n$ reaction. This spectrum features both the scalar $a_0(980)$ and the tensor $a_2(1320)$. A partial wave analysis of this system has also been performed [59, 60, 61].

Figure 6.7 shows the $\eta\pi^+\pi^-$ and $\eta\pi^0\pi^0$ effective mass distributions where well known meson states are clearly observed. The $\eta\pi^0\pi^0$ system requires the reconstruction of six-photons in the LGD. Other analyses involving photons and charged particles have also been published including a study of the $a_0(980)$ in the $\eta\pi^+\pi^-$ and $\eta\pi^0$ spectra [62] and a partial wave analyses of the $\eta\pi^+\pi^-$ [63], $\omega\eta$ [64], $\omega\pi^-$ [65] and $\eta\pi^+\pi^-\pi^-$ [66] systems.

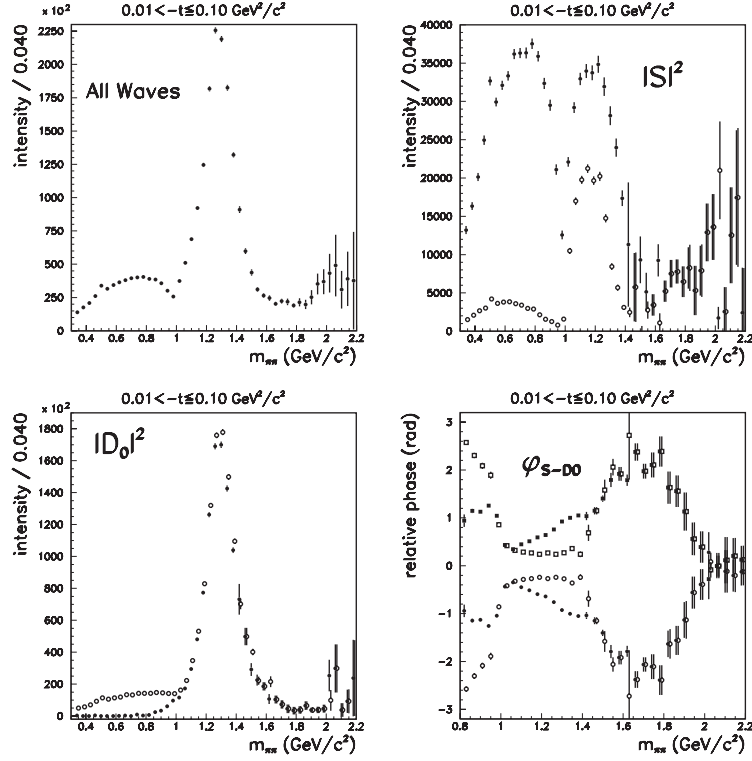


Figure 6.6: Results of a partial wave analysis of the $\pi^0\pi^0$ system in the E852 reaction $\pi^-p \rightarrow \pi^0\pi^0n$ for low momentum transfer events. The sum of all waves (upper left), the S -wave (upper right), the D_0 -wave (lower left) and the phase between the S -wave and D_0 -wave (lower right) are shown. Plots show open and filled circles corresponding to mathematically ambiguous solutions with the filled circles indicating the physical solutions based on other criteria.

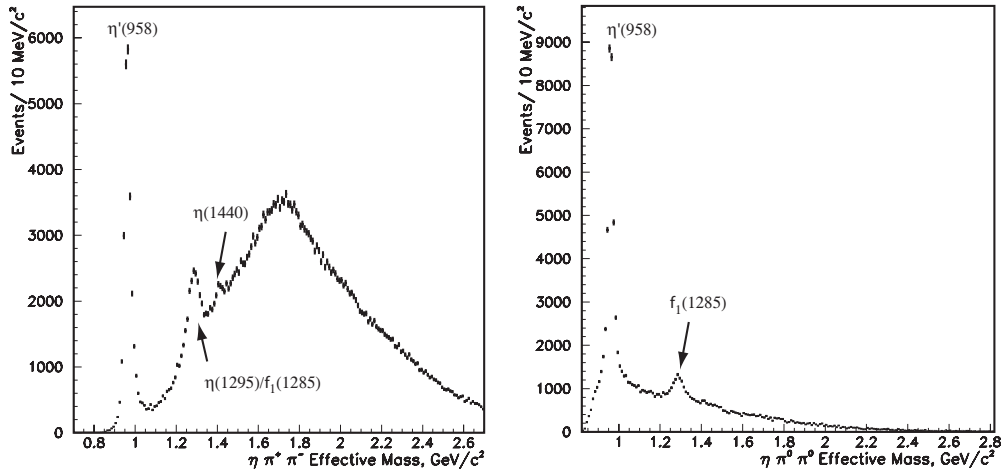


Figure 6.7: left: Distribution of the $\eta\pi^+\pi^-$ and right: $\eta\pi^0\pi^0$ mass distributions observed in E852.

The Radphi Experience

The RADPHI detector is shown schematically in Fig. 6.8. This detector was operated downstream of the CLAS detector in HALL B. The beam was incident on a 2.66-cm diameter, 2.54-cm long

beryllium target. Surrounding the target and extending forward to 30° from the beam axis was a cylindrical scintillator detector (BSD) which provided nearly full angular coverage for recoil protons. Surrounding the BSD was a cylindrical lead-scintillating fiber photon detector (BGD) which served to reject events (off-line) with large angle photons. The primary detector component was a 620-channel lead-glass wall (LGD) assembled to approximate a circle around the beam line with a $8 \times 8 \text{ cm}^2$ central hole for the passage of the beam. The lead-glass detector was positioned 1.07 m downstream of the target and subtended an angle of approximately 27° from the beam line.

The RADPHI experiment provides an opportunity to understand the operation of a lead glass calorimeter in a bremsstrahlung photon beam. Two important issues are understanding the energy and spatial resolution of the detector (relevant for the reconstruction of π^0 and η mesons) and electromagnetic backgrounds.

Lacking a source of electron or photon showers of a well-defined energy, the RADPHI experiment had to rely on the observed width of known mesons to deduce the energy resolution of the lead-glass calorimeter. The observed width of narrow mesons such as the π^0 and η that undergo 2γ decay is determined by the single-shower energy and position resolutions of the LGD. In cases where the spatial contribution can be neglected, the single shower energy resolution was extracted by selecting pairs with one of the two showers in a narrow energy window and examining the energy spectrum of the other, for a given cluster-separation angle. This energy spectrum shows peaks that correspond to the masses of the π^0 and η and whose line-shapes are convolutions of the energy response functions for the two showers plus contributions from uncertainties on the shower centroid positions. The contribution from spatial resolution to the width of the peaks was minimized by focusing first on the η , which is associated with pairs of showers that are well separated on the face of the calorimeter. By analyzing the dependence of the peak width on the energies of the individual showers, the convolution was inverted to obtain the r.m.s. resolution for single showers as a function of shower energy without introducing a model for the energy dependence. Once the energy resolution had been determined in this way, the spatial resolution was then examined by looking at the excess width of the π^0 peak over what was expected based upon energy resolution alone. In the end, a unified analysis including both energy and spatial resolution effects was able to reproduce both the π^0 and η profiles.

Assuming that the spatial resolution is not important for $\eta \rightarrow 2\gamma$ decays, the r.m.s. shower energy resolution can be extracted without assuming any functional form for its dependence on shower energy. This model-independent solution was then compared with the standard parametrization [67] of the lead glass energy resolution given in Eq. 6.1.

$$\frac{\sigma_E}{E} = \frac{B}{\sqrt{E}} + A. \quad (6.1)$$

The first term on the right contains the effects of photoelectron statistics, while the second term wraps up all of the systematic block-to-block differences and calibration errors which prevent the width of the response function from collapsing to a delta function in the high-energy limit. In order to describe the π^0 peak with the same parameters it is necessary to introduce a model for the shower spatial resolution, which itself depends upon shower energy. The energy dependence is proportional to $1/\sqrt{E}$ with a proportionality constant that depends on the size of the LGD block [68]. Eq. 6.2 is adopted for showers at normal incidence, with the constant C expected to be around $7 \text{ mm} \cdot \text{GeV}^{-\frac{1}{2}}$.

$$\sigma_x = \frac{C}{\sqrt{E}}. \quad (6.2)$$

In the RADPHI geometry many of the showers are far from normal incidence and so the shower depth fluctuations of roughly one radiation length also contribute to the centroid position resolution along one of the spatial axes. This was taken into account in the analysis by projecting one radiation length from along the shower axis onto the transverse plane and adding it in quadrature to the base term in Eq. 6.2. The final values for all parameters were determined by simultaneous analysis of the η and π^0 data where all of the above effects are included for both.

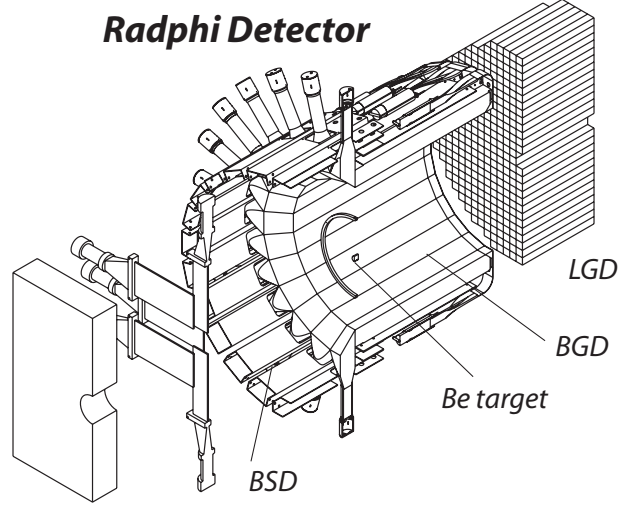


Figure 6.8: The RADPHI detector.

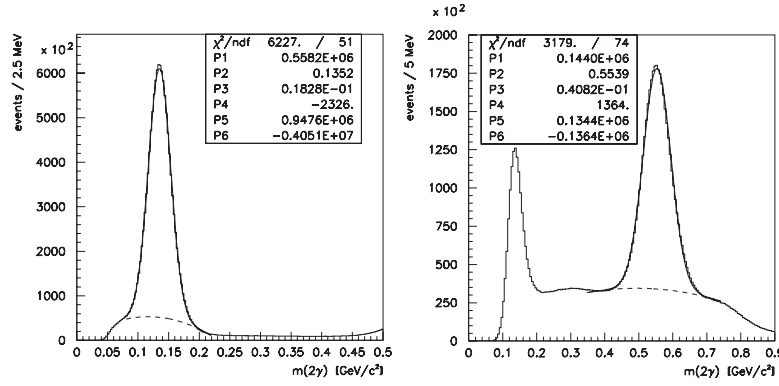


Figure 6.9: Invariant mass distribution of $\pi^0 \rightarrow 2\gamma$ (left) and $\eta \rightarrow 2\gamma$ (right). The parameters shown are the height (P1), mean (P2) and sigma (P3) of the Gaussian peak fitted to the data over a polynomial background described by parameters P4-P6.

Estimating the GlueX π^0 and η Mass Resolutions

The experience with the E852 and RADPHI detectors allows us to reasonably interpolate to expected GLUEX performance. Based on the discussion above and that of reference [69] we assume the energy resolution given by:

$$\frac{\sigma_E}{E} = 0.036 + \frac{0.073}{\sqrt{E}} \quad (6.3)$$

and the spatial resolution is given by:

$$\sigma_\rho = \sqrt{\left(\frac{7.1}{\sqrt{E}}\right)^2 + (X_0 \sin \theta)^2} \text{ mm} \quad (6.4)$$

where ρ locates the shower position in the plane of the LGD measured from the center of the LGD, θ is measured from the normal to the LGD plane, X_0 is the radiation length of glass (31 mm in this case) and E is the photon energy in GeV.

A Monte Carlo simulation of forward π^0 and η production for RADPHI, E852 and GLUEX assumed:

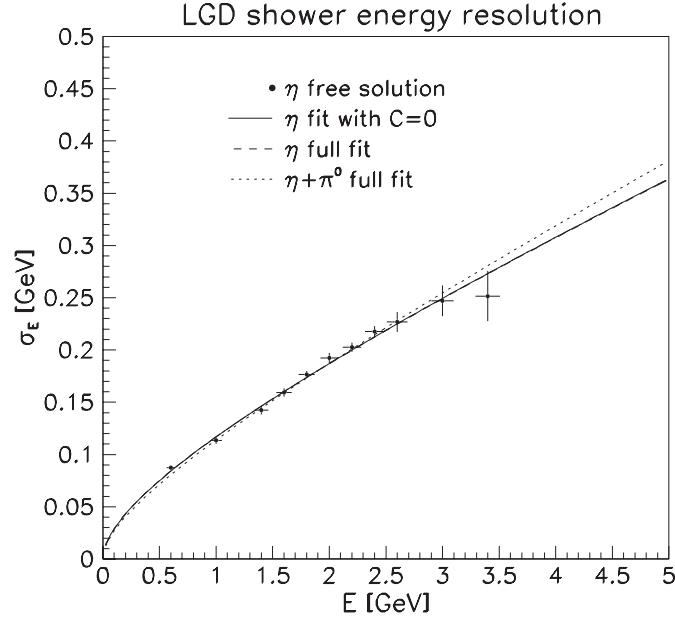


Figure 6.10: Energy resolution of showers in the LGD obtained from analysis of the 2γ sample.

1. A uniform photon beam between 3.0 and 5.4 GeV for RADPHI, 18.0 GeV for E852 and 9 GeV for GlueX;
2. A target to LGD distance of 1.0 m, 5.4 m and 5.0 m for the three experiments respectively.
3. Transverse LGD dimensions characterized by circular stacks of radii 0.5 m for RADPHI and 1.0 m for GLUEX and a 1.68 by 2.8 m rectangular stack for E852.
4. A minimum photon energy of 150 MeV and a minimum photon separation of 8 cm.

Simulation results are shown in the plots of Figure 6.11. We obtain π^0 mass resolutions of 16 MeV for RADPHI and 8 MeV for E852 compared to measured resolutions of 18 and 10 MeV. For GLUEX we predict 9 MeV. For the η we obtain mass resolutions of 40 MeV for RADPHI and 27 MeV for E852 compared to measured resolutions of 40 and 25 MeV. For GLUEX we predict 30 MeV.

Electromagnetic Backgrounds

The experience with the RADPHI LGD also allows us to compare estimates of electromagnetic backgrounds as calculated using GEANT with measured rates. Such a comparison is shown in Figure 6.12. The histogram in the figure is the Monte Carlo estimate for the LGD rates arising only from electromagnetic background. Note that for individual blocks, the expected hadronic rate is negligible on this scale. The simulation includes the principal components of the Hall B photon beam line starting at the radiator and including the (empty) CLAS target and downstream yoke aperture. Note that in Figure 6.12 a marked depression appears at small radius, relative to the observed rates. These blocks are in the vicinity of the beam hole and, in addition to suffering from the highest rates, these blocks also suffered from radiation damage. The eight blocks closest to the beam axis (first data point) are the most affected, but some effects can be seen at neighboring points.

Radiation Damage

Online monitoring of the LGD during the RADPHI experiment indicated that the 8 blocks immediately adjacent to the beam hole were becoming progressively reduced in gain as the run

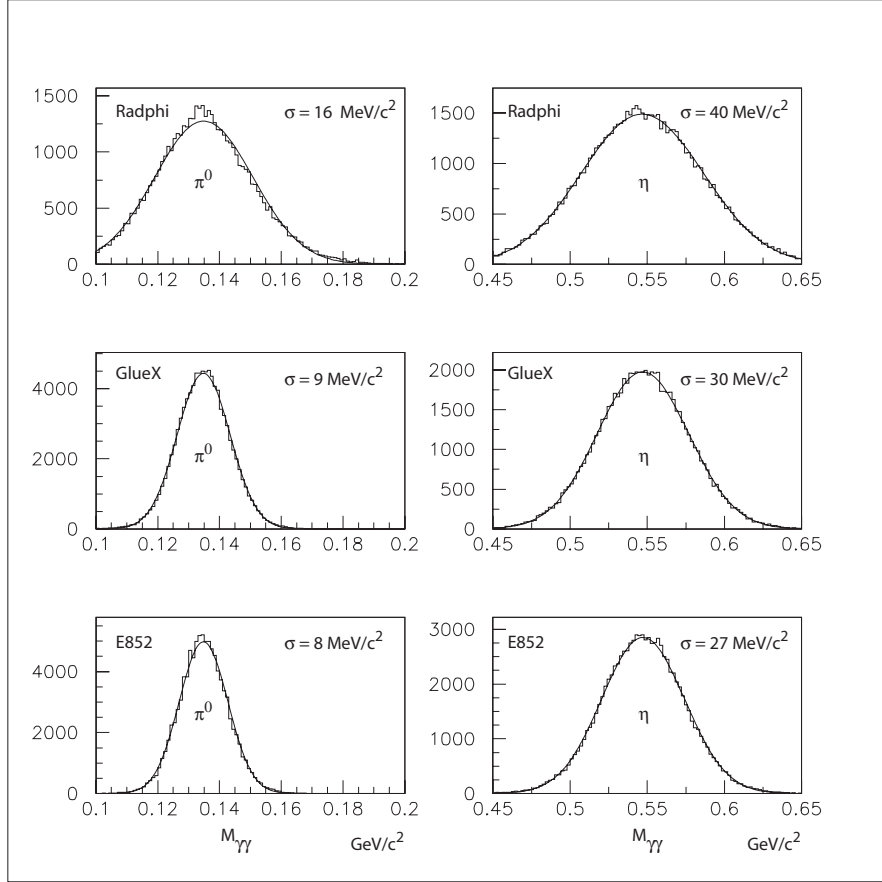


Figure 6.11: Simulated diphoton mass for the π^0 and η using the Radphi, GlueX and E8652 geometry.

progressed. This observation was based upon the laser monitor system, the raw pulse-height distributions, and the channel gains which were periodically recalibrated during the run. A similar effect was seen, but to a lesser degree, for the next layer of blocks once removed from the beam hole. During a pause in the experiment, visual inspection of the blocks indicated that the glass was darkening, a well-known effect of radiation damage on lead glass. Figure 6.13 illustrates the gain reduction with beam time (roughly proportional to integrated radiation dose) for a typical block adjacent to the beam hole. It is apparent that the gain change is a gradual, cumulative effect rather than a sudden change which might be characteristic of a beam mis-steering event.

The magnitude of the gain loss (order 40%) was such that it could be compensated by adjustments of the PMT high voltages. This was done periodically during the experiment. The last datum in Figure 6.13 shows the result of one adjustment. However, this is only a partial solution, since the module suffers a loss of photoelectrons due to the radiation damage, and thus a degraded resolution. Thus it was desirable to ‘heal’ the radiation damage as much as possible.

Radiation damage in lead glass is known to be temporary, and to largely heal itself on the time scale of a few months. The healing can be accelerated by the use of ultraviolet (UV) light. This approach was adopted for the most affected blocks. During an extended down-time in the run, the PMT and base for selected modules were removed and a UV light guide attached to a quartz envelope Mercury vapor lamp was inserted. The output of the lamp was 5 W/cm^2 in the range 300 to 480 nm, with a peak intensity at 365 nm. The affected blocks were each illuminated for periods of 6-8 hours. These blocks showed a gain increase of 30% following this treatment, nearly recovering their initial gains.

It should be noted that the change in the response of the modules due to radiation damage

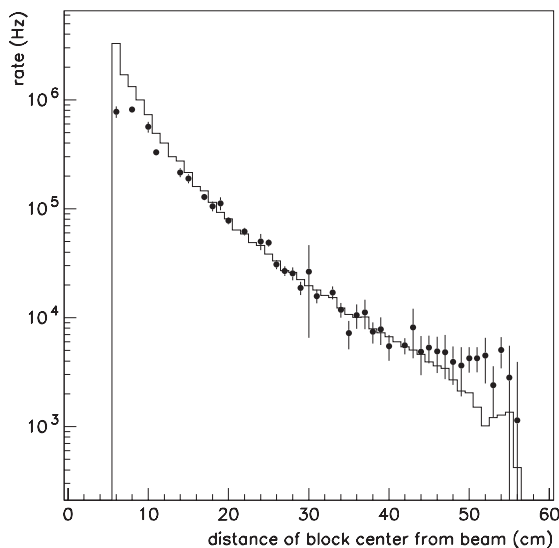


Figure 6.12: Characteristics of unbiased flux observed in individual blocks in the LGD as a function of distance from the beam. The points are derived from data and the histograms from a Monte Carlo simulation of the electromagnetic background coming from the beam and target. All hits over 15 MeV are recorded.

and the gain recovery following UV treatment was even more dramatic in the data from the laser monitoring system (typically a factor of two change). The difference between the shift in the pulser response and that seen in the gain constants from the calibration can be qualitatively understood by noting that the laser illuminates the front of the block and thus measures the transmission of the entire block, while the showers seen in the calibration data create Cerenkov light throughout the volume of the block, and are therefore less sensitive to attenuation effects in the upstream region of the block. The radiation damage is now known, from measurements, to be within 11 *cm* of the front surface of the detector, and this was confirmed by visual inspection, in qualitative agreement with the difference between the laser monitor data and the calibration data.

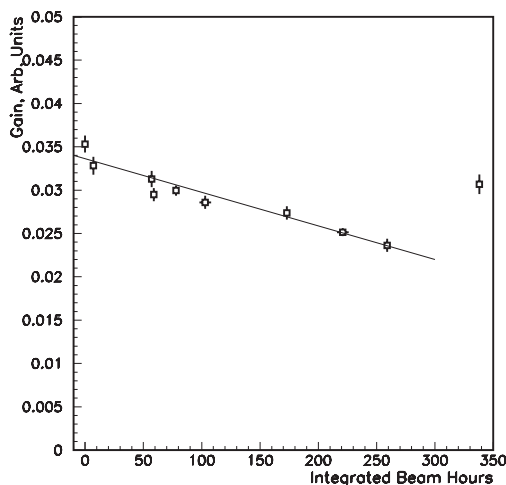


Figure 6.13: The effect of radiation damage on the central part of the detector. The last point shows the gain after an adjustment of the PMT high voltage.

Heat Curing of Damaged Blocks As part of the program to assess the glass used in E852 and RADPHI for use in GLUEX a spectrophotometer (Shimadzu UV-160) was modified to allow a lead glass bar to be automatically moved along its long axis to measure transmission through the 4 cm thickness. Based on the transmission dependence on wavelength, the transmission of the bar as a function of length was measured at 410 nm. Figure 6.14 shows the dependence of transmission as a function of length along the block for a block that visibly shows radiation damage. An alternative to UV curing, heating blocks in an oven has also been studied. The plot also shows the transmission curve for the same block after heating the block for several hours in an oven at 260 °C.

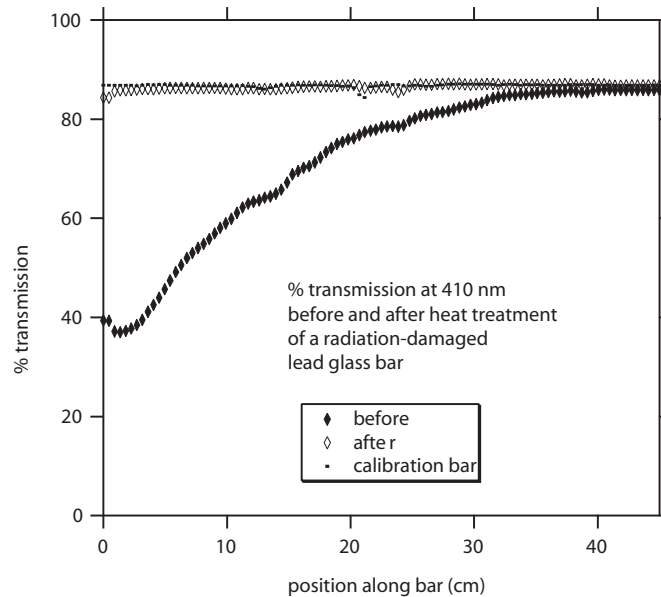


Figure 6.14: The effect of heat curing.

Assessing Lead Glass Blocks and PMT's

Lead glass block evaluation Some of the lead glass blocks used in the E852 experiment were used in the RADPHI experiment. All of the blocks are being examined for mechanical and radiation damage – the latter being assessed using the spectrophotometer described above.

The transmission at a wavelength of 410 nm as a function of length along the block will be measured and recorded for each block. The reason for measuring the transmission at this wavelength can be understood from the data presented in Figure 6.15 where the transmission as a function of wavelength is measured for a block that suffered radiation damage and a block with no damage. The measurement was made approximately 2.5 cm from the upstream end of block where *upstream* refers to the orientation of the damaged block in the beam. At about 410 nm the undamaged glass reaches a transmission plateau.

PMT Evaluation The PMT's available for GLUEX were used in E852 starting in 1994. There is some concern about the aging of the PMT's so a program of testing the 3200 PMT's (including spares) has already started. A similar process was used prior to constructing the E852 LGD for rating PMT's and is described in reference [53]. For the current test a light-tight box will accommodate 25 PMT's at a time. The tubes will view a diffusing plate that is illuminated by two blue LEDs that will be pulsed. Under computer control the gain as a function of high-voltage will be recorded and random noise and correlated noise rate will be measured. The correlated noise rate will be measured within a fixed gate delayed by a few hundred nanoseconds after the

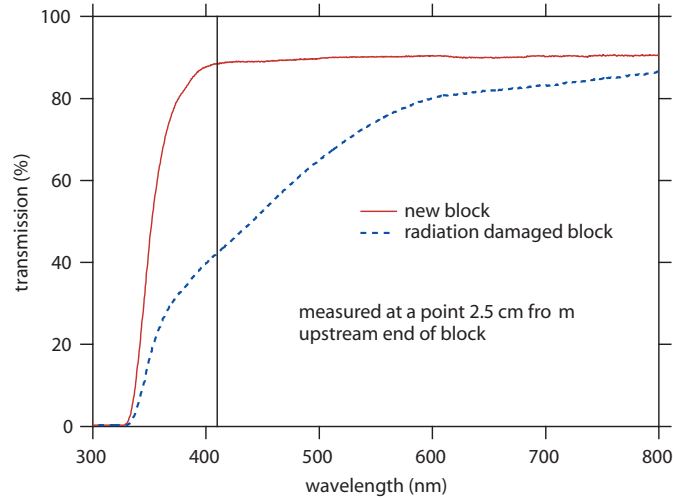


Figure 6.15: Transmission as a function of wavelength for radiation-damaged lead glass and undamaged glass. At about 410 nm the undamaged glass reaches a transmission plateau.

LED's are pulsed. Preliminary measurements with a random selection of PMT's indicate that the PMT's performance has not degraded.

Other Issues

Electromagnetic Rates in the LGD The RADPHI experience has forced us to deal with the issue of high rates in the central part of the detector and also how to use GEANT to estimate those rates. Those studies are currently underway for the GLUEX arrangement. We are also exploring the option of using another medium in the central region of the LGD, such a radiation hard lead glass, lead tungstate or another material. This will of course impact on shower reconstruction – especially for those showers that cross the boundary between media. Another option under investigation is to place a thin sheet of lead in front of the LGD blocks in danger of damage. The impact this has on resolution is also being studied.

Magnetic Shielding In E852 a cellular wall was used to register the PMT's to the glass wall. That cellular wall consisted of two aluminum plates with holes into which cylindrical soft iron tubes were squeezed (the tubes were sandwiched between the plates). Epoxy was injected the space between the tubes and between the plates through small holes in the plates. Additional μ -metal shields surrounded individual PMT's before insertion into the soft iron tubes. The PMT's were positioned against the glass blocks with an air gap in between. This entire cellular wall structure was surrounded by a thick iron frame to provide further shielding. The structure is described in reference [54]. A similar wall was used for RADPHI. In E852 the PMT's were shielded from the fringe field of the BNL MPS dipole magnet.

Simulations of the fringe field of the GLUEX solenoid are currently underway for various assumptions about the structure and material in the vicinity of the LGD. More details about magnetic shielding are also discussed in the section on the TOF – the forward time-of-flight system.

For the LGD we plan to have the PMT photocathode recessed inside the iron shielding tube by about the diameter of the photocathode and we plan to study the use of short cylindrical glass segments to couple the lead glass to the PMT with proper index of refraction matching.

Monitoring The E852 and RADPHI LGD's were monitored [54, 55] by using light from a nitrogen laser illuminating a block of scintillator. The scintillator light was transported by several optical fibers coupled to the sides of a Plexiglass sheet large enough to cover the front face of

the glass stack. This system was used for initial gain setting and to monitor gains throughout the run.

Calibration GLUEX will base its LGD calibration system on the extensive experience gained with calibrating the E852 and RADPHI LGD's that is described in references [54] and [55].

Triggering An energy sum trigger was provided by the E852 and RADPHI LGD's [54, 55]. In addition the E852 LGD had a trigger processor that provided an estimate of the total effective mass of photons striking the LGD and this was used in the trigger.

6.3.3 Barrel Calorimetry

The barrel calorimeter (BCAL) will be positioned immediately inside the solenoid, which constrains the outer radius to be 90 *cm* and results in an outer surface area of approximately 23 *m*². This leaves a 2.7 *cm* space radially for supports and installation. This device is a key component of a hermetic system, and is crucial for both fully reconstructing all the photons in many physics reactions and providing accurate time-of-flight measurements for charged particles. In addition, it may be possible to get some *dE* information on charged particles as well. The large size of this device implies that it will be a challenge to build and instrument it at reasonable cost. The main parameters of the BCAL are given in Table 6.1.

A principle goal of GLUEX calorimetry is to detect and to measure photons from the decays of π^0 's and η 's which, in turn, can come from the decays of produced mesons or possibly from excited baryons (N^* or Δ). The positions and energies of the photons must be determined to sufficient accuracy to allow for a complete kinematic reconstruction of the event. Detailed Monte Carlo studies [70] [71] indicate that the BCAL should be sensitive down to as close to 20 *MeV* as possible and up to a few *GeV* in energy. The BCAL is also required to provide timing information for charged particles. The BCAL, in conjunction with *dE/dx* measurements in the CDC, will be the primary PID device for most of the protons detected in GLUEX. Monte Carlo studies [72] [73] show that in order to carry out this function, the BCAL needs to have close to 200 *ps* timing resolution. For events with only charged particles, it is essential to be able to veto on neutral missing energy. Here, nearly hermetic coverage is critical. For selected triggers, neutral energy requirements (or vetoes) are relatively easy to implement. A secondary function for this device is to be able to provide *dE* information to further aid the central tracking system in particle identification.

Table 6.1: Main parameters of the Barrel Calorimeter.

Parameter	Size
Length	390 <i>cm</i>
Inner radius	65 <i>cm</i>
Outer radius	90 <i>cm</i>
Fiber diameter	1 <i>mm</i>
Lead Sheet thickness	0.5 <i>mm</i>
Number of Fibers	1,000,000
Number of Readout Channels	~1000-5000
Weight	35 metric tons

Design Considerations

For the tracking elements inside the magnet to perform optimally, the BCAL must be thin, no more than 25 *cm*. This and the 4.5 *m* length of the solenoid lead to a long, narrow, tube-like design. In this geometry, readout is easiest at the ends where space exists. The choice of readout device must bear in mind the considerable magnetic field (22.4 *kG*) inside the bore

and the rapidly varying fringe field at the ends. Conventional photo-multiplier tubes (PMTs) will work only outside of the solenoid and even there considerable attention must be paid to shielding.

While the collaboration initially looked at several potential designs, it was quickly realized that the only viable, cost-effective solution is one which utilizes scintillating fibers embedded in a lead matrix. The Pb/SciFi is used to make a relatively high-resolution sampling calorimeter. This solution is based on proven technology from other experiments.

Unfortunately, the very strong magnetic field in the immediate vicinity of the SciFi ends make the options for readout less clear. We initially looked at hybrid PMT (HPMT) which have been developed for CERN applications. These devices are immune to magnetic fields up to 2 T and their power supplies are very compact due to the fact that they draw virtually no current even under maximum bias. The HPMT's have a fast rise time of 6 ns or less, very good energy resolution, modest timing resolution, but low gain and as such require amplification. An additional drawback is their high cost. After careful study [74], these were rejected as an option because no suitable circuit could be devised to provide adequate pulse amplification and good timing simultaneously.

The option that is currently under investigation involves Silicon photo-multipliers (SiPM's). These devices offer gain and timing resolution comparable to that of a PMT, superior energy resolution, require a simple electronic circuit and are not sensitive to magnetic fields. These are discussed later in this report.

A more conventional option is to use magnetic field resistant PMTs coupled to fiber optic light guides to place the PMTs in regions of reduced field and with an appropriate orientation to further minimize signal loss. This option has the drawback that there is a loss of light associated with the long (probably fiber) light guides, as well as an increased mechanical complexity due to their placement. While this option would certainly work, it is being reserved as a backup.

Pb/SciFi Barrel Calorimeter

Scintillating fibers embedded in a matrix of lead (Pb/SciFi) or other high- Z materials have been used in calorimeter design and operation for more than a decade. The ratio of the active scintillator to the passive high- Z material, as well as the diameter of the fibers, can be tuned to enhance resolution, to determine the radiation length, and to achieve uniformity in the electromagnetic to hadronic response (the e/h ratio).

For high-resolution EM performance, the Jetset detector used such a calorimeter which was developed at Illinois [75]. This was the first detector designed specifically to optimize EM resolution. The recipe produced a detector comparable to lead glass at a considerably lower cost and with approximately half the radiation length. It utilized 1 mm fibers spaced uniformly (close packed) on specially grooved plates of lead. The lead was alloyed with 3 – 6% antimony to provide mechanical stiffness.

Of more relevance to the GLUEX experiment is the calorimeter built for the KLOE experiment at DAΦNE. The KLOE collaboration has taken the development of Pb/SciFi a step further than JetSet. They developed better tooling for the production of long grooved plates, have pushed the technology for excellent fibers with long attenuation lengths [76] and have built a device with larger radius than needed in GLUEX and 4.3 m in length. This device is currently operating and results on its actual performance are available. Like Jetset, the KLOE design utilizes 1 mm diameter scintillating fibers embedded in a lead matrix with a fiber to lead to glue ratio of approximately 48 : 42 : 10.

Both the JetSet and the KLOE calorimeter exhibit similar energy resolutions. An array of JetSet prototypes subjected to electrons in the range 0.3 – 1.5 GeV was represented by the function

$$\sigma/E = 6.3\%/\sqrt{E}$$

with E in GeV. The constant term was negligible. In the Jetset Forward Calorimeter, the beam entered nearly parallel to the fiber direction. The energy resolution was also measured with tagged photons below 0.1 GeV and improved to $\approx 5\%/\sqrt{E}$; the detector gave a resolvable

signal all the way down to 0.02 GeV. A KLOE prototype modules, 2 m in length was produced with conventional PMT readout at both ends. Such readout was possible due to the lower field and more favorable field gradient of KLOE compared to GLUEX. An excellent energy resolution parametrization of

$$\sigma/E \approx 4.4\%/\sqrt{E}$$

was extracted. The final energy resolution for KLOE [77] was

$$\frac{\sigma(E)}{E} = \frac{5.4\%}{\sqrt{E(\text{GeV})}} + 0.7\%,$$

and this number serves as a benchmark for the GLUEX Barrel Calorimeter.

Because of the ~ 4 m module length in KLOE, special efforts needed to be made to develop and test scintillating fibers with very long attenuation lengths. Tested fibers had attenuation lengths in the range from $2.3 < \lambda < 3.2$ m which is far superior to the average λ of 1 m for the JetSet fibers. This aspect of the design is critical because there exists a significant coupling between the position of impact (essentially the polar angle, θ) and the interpreted energy. Light collected at each end must be corrected for attenuation length before conversion to energy units.

Another important feature of scintillating fibers is the signal rise time and overall duration. Because fast plastic scintillator is used (Decay times are 2.0–2.5 ns), integrated signal time can be kept below 100 ns, with shorter times possible if deemed necessary for rate considerations. No problems are anticipated at the expected maximum luminosity of GLUEX. With rise times of a few ns, excellent timing can be expected for each of the devices involved in collecting the light from a shower. The time difference from the two ends produces the z coordinate of the hit.

Because we will use an array of such devices on each end (segmented in azimuth and depth), redundant measurements are made of the z coordinate. These measurements of z correspond to different average radii and therefore help to establish the angle of the incoming photon.

The fractional volume of scintillator in the detector naturally makes it efficient for detecting charged hadrons. The mean light collection time of the two readout ends can be used to determine the particle time-of-flight (TOF). TOF coupled with the track length and momentum then yields particle mass. Therefore, this design for a Barrel Calorimeter is expected to play an important role in the overall barrel PID scheme. KLOE achieved an operational time resolution of

$$\sigma_t = \frac{56 \text{ ps}}{\sqrt{E(\text{GeV})}} \oplus 133 \text{ ps},$$

which yields a nearly constant $\sigma_t \approx 180$ ps for photon energies above 150 MeV, and a diverging time resolution for $E_\gamma < 75$ MeV. The first term is the sampling fluctuation term, and can be reduced by improving the calorimeter light collection. The constant term is mostly due to the intrinsic time spread due to the finite length in the z direction of the luminous point. Improvements on this are possible. A similar figure can be expected for GLUEX as long as readout devices and discriminator chains are selected carefully.

The GlueX BCAL

Pb/SciFi calorimeters have been built that satisfy the physics requirements of GLUEX. By using the knowledge gained in the KLOE construction, members of the GLUEX collaboration expect to improve on this for the GLUEX experiment.

For GLUEX, we expect to build 48 modules each ~ 4 m in length and 20–25 cm deep. The readout scheme takes advantage of the fact that all fibers run parallel to the axis of symmetry of the solenoid and therefore all light piped to the ends of the modules retains its azimuthal and radial information. The polished ends of the detectors will be coupled with multiple independent light guides.

Because the EM showers spread across these azimuthal boundaries, algorithms for finer positioning of the shower are employed. In JetSet, one finds a typical weighted position resolution of $\delta x \approx 5 \text{ mm} / \sqrt{E}$. For the GLUEX design, this would lead to an azimuthal resolution of

≈ 8.5 mrad. Using the z position resolution of approximately 4 cm obtained from the time difference leads to a polar angular resolution at 45° of ≈ 7 mrad. As the design of the BCAL is further refined, it will be important to keep these numbers balanced.

The transverse size of each of the 48 modules is approximately 8.5 cm at impact. A further subdivision of the readout can reduce this number by half or more. In Figure 6.16, ten (two in width times five in depth) segments per azimuthal slice are shown as a minimal example of the readout subdivision. Each such segment would contain approximately 1200 fibers. In effect, this subdivision could be made smaller whether PMT's or SIPM's are used. The former would require a (clear) fiber-to-fiber mask to carry the light outside the magnetic field, whereas the latter would need a Winston cone with a light mixer or a diffuser, and wavelength shifting fibers (WLSF's) or ordinary fibers to further guide the light to the small surface of each SIPM. The investigation into the optimal readout scheme is now underway and will couple Monte Carlo simulations of the expected light produced to R&D trials in the lab with different geometries using SIPM's and PMT's.

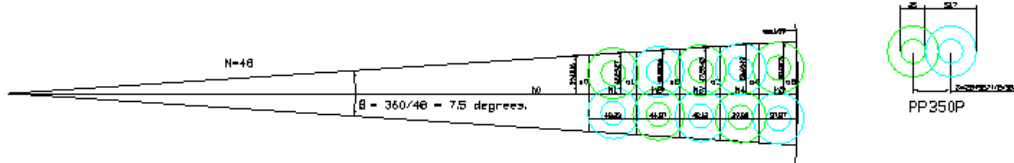


Figure 6.16: Sketch of Barrel Calorimeter readout ends. The subtended angle of each module corresponds to two azimuthal slices. Each slice has five readout devices on either end. As an example, the dimensions of DEP PP00350G HPMTs were used. The outer circles represent the boundary of the devices, assuming a 5.27 cm outer diameter. The devices have been closely packed so as to not shield each other's active area, which is indicated by the smaller circles (diameter of 2.5 cm). The readouts have been staggered axially to allow the closest packing.

Each channel requires high voltage, a flash ADC, discriminator, TDC and cabling. A calibration system is critical and can be based in part on the use of Nichia blue (or green) LEDs glued directly to a short light guide stub at the end of each module. An LED driver system is also required. The choice of ADC and TDC systems depends on the overall readout coordination for GLUEX.

Construction of Prototype Modules

In order to form grooved plates and construct modules 4 m long, we have studied and used the KLOE tooling techniques. GLUEX physicists visited Frascati and Pisa and were trained in the use of the KLOE 15 cm-wide lead swaging machine (a.k.a. *Francesca*). In May 2002, the GLUEX physicists successfully swaged 0.5 mm thick lead sheets, and glued 10 layers of lead and 1 mm optical fibers together, producing the first Pb/SciFi test module with dimensions 100 cm x 14 cm x 1.25 cm at LNF/Frascati. Francesca (total weight of 200 kg) was then moved to Canada on a two-year loan from Frascati, where four prototypes have been built:

1. 1 m x 13 cm x 5.0 cm, *Baby-0 Module*
2. 2 m x 13 cm x 17.0 cm, *Module-0*
3. 4 m x 13 cm x 23.7 cm, *Module-1*
4. 1 m x 13 cm x 5.0 cm, *Baby-1 Module*

As is reported below, the construction of all modules was met with success, with only minor faults resulting in the uniformity of each of the three matrices. The construction method has

been adjusted to avoid these in the production phase. Francesca has been returned to LNF; we will design and build a similar machine for our production phase.

Production of Lead Sheets The initial stages of construction for the 4m module calorimeter took place in February-April 2004 at the University of Regina. The main focus was to produce the needed lead rolls for the first full-length module (Module-1) of the Barrel Calorimeter at Hall D. A total of 240 rolls were cut, swaged and shipped to the Centre for Subatomic Research (CSR) at the University of Alberta where this module would be constructed.

The lead came from the manufacturer¹ on a giant roll, 27" wide. Five sheets (width-wise) could be extracted from each length of lead. The quality of lead used for this module was superior to that used for the 2 m module. The lead used for Module-1 had a lower percentage of copper than the roll used in the 2 m module (Module-0) and was consequently softer and easier to ply. *Bananas* (curved sheets resulting from uneven pressure of the rollers during the swaging process, or from impurities in the lead itself) were a continuous problem for Module-0. Bananas rarely occurred for the lead used in Module-1: out of 240 sheets there were only three irreversible bananas.

The wide lead sheets were placed under a special cutter that consists of two parallel blades, separated by 12.93 cm, attached to a roller on tracks. This cutter greatly reduced the cutting time over the mask and box cutters used in the previous modules. A few improvements in the design (easier exchange of blades, smoother insertion/extraction of lead sheets) are planned for the production phase, as well as a multi-track enhancement to allow cutting of 4-5 sheets at the same time. The lead was then swaged with Francesca to have 96 lengthwise grooves on both sides and trimmed to 404 cm.

The time required to cut and swage a sheet of lead, where one sheet contains 4-5 rolls of lead, changed with experience. Once a rhythm was established, on a good day with four workers, the time had reduced to approximately 9 min/roll with a daily total of about 30 rolls. After several trials of methods to lay the fibers in the lead grooves, a detailed method was developed [78]. This led to the successful construction of Module-1.

Module Construction During the summer of 2004 the University of Regina sent a team of undergraduates to Edmonton to build a 4m calorimeter module. Composed of 210 alternating layers of lead and scintillating fiber the module measured 4.04 m in length, 12 cm in width and 24 cm high. Over 80 km of fibers and 12 kg of epoxy was used in the four weeks of construction. The process itself was a learning experience, as much of the facility was custom built for the occasion.

The first stage of construction included the machining, assembly and installation of an electro-pneumatic press, used to press the matrix as it is being stacked with alternating layers of lead sheets and fibers. It consisted of steel bed, two tilting pistons that raised/lowered a group of 20 pistons to the top surface of the matrix, and the associated electronics and pneumatics.

The second stage of construction consisted of building the clean room where the module would be constructed. This was a 7 m x 5 m x 3 m room lined with Tyvek sheathing and black polyethylene sheets along its walls, and clear poly and UV filters as its ceiling. The room was ventilated with a variable speed fan and was equipped with an air exhaust. An airlock provided access to the room. The third stage of construction was the building of the 4 m module. A five member crew built this module working two three-hour shifts each day. This resulted in module growth of two centimeters each day. The fourth and final stage of the production was the construction of a one-meter Baby-1 module that was only 5 cm thick. This module is to be used for testing various readout systems.

Most tasks in the construction process are simple ones that are repeated each layer. A comprehensive report (how-to manual) and training video were prepared to simplify the training of personnel during the production phase and to document the methods employed [79].

¹Vulcan Lead Inc, <http://www.vulcanlead.com/>

The optimum size of the construction team turned out to be five people. Accurate documentation of all stages of the construction over a five week period show that just over 300 man hours are needed for each module, or a total of almost 15 thousand man hours for the construction of 48 modules. The construction of a second press and operations with two crews would allow the completion of the production phase in well under 24 months.

The Summer 2004 construction was a successful practice of full scale production. There were unanticipated problems and useful discoveries. The full set of recommendations for improving the construction technique is described in [79]. The GLUEX Collaboration believes that all R&D issues on the Pb/SciFi matrix construction have been resolved and that we are ready to proceed to the production phase.

Following the completion of the construction, Module-1 was craned out of the clean area and its ends machined and polished to final dimensions of $400\text{ cm} \times 13\text{ cm} \times 23.7\text{ cm}$ and was moved to Regina. A picture of one end of the module is shown in Fig. 6.17. A jump in the tracks of a single fiber layer is visible only on this end; the fibers are sitting properly at the other end. This was a result of having to lift the lead to realign it, something that had to be done several times and only once is resulted in misaligned fibers. This mishap has no effect on the light collection and integration of the module and will be tested for potential delamination. The testing of Module-1 with cosmic rays is underway at Regina and in 2005 the module will be tested in beam conditions at Serpukhov and latter at Jefferson Lab (Hall-B). Baby-1 will be cut into two equal length pieces that will be shipped to CERN and Athens for front end readout tests.

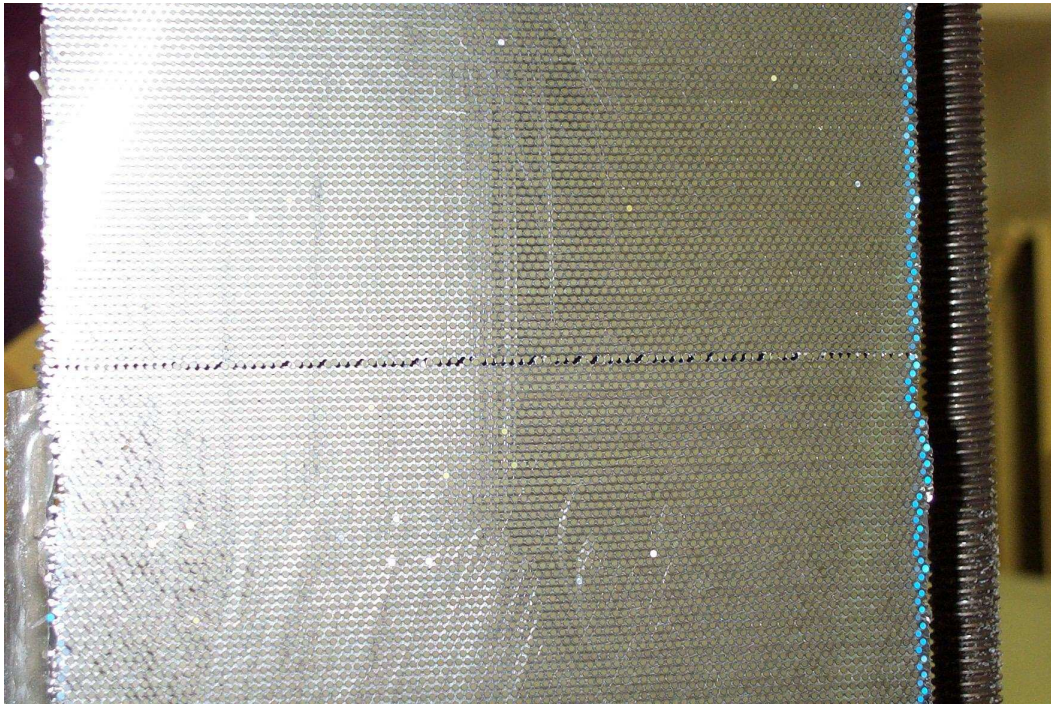


Figure 6.17: Module-1 end. Note the layer that has jumped its tracks. See text for a detailed description.

Scintillating Fiber Tests

Clearly, the inherent properties of scintillating fibers play a crucial role for the Barrel Calorimeter function. The criteria which must be evaluated include:

- Light collection efficiency (cladding),

- Amount of scintillation light produced (doping), and
- Loss of the light as it travels down the fiber (attenuation length) and decomposition of intensity as a function of wavelength.
- UV damage of fibers when exposed to sunlight or fluorescent lights.

To address the first three points, different types of fibers from two different manufacturers were procured and tested first with cosmics and then a pion beam at TRIUMF, Vancouver, in connection to their light attenuation and timing resolution. Specifically, the tested fibers were Kuraray SCSF-81 single-clad², Pol.Hi.Tech.0046 single- and multi-clad³. All fibers were 1 mm in diameter and were procured in the summer of 2000. In addition, a second bundle of single-clad Kuraray fibers was procured in 2001. Beam tests of these fibers are reported in reference [80], whereas tests of newer (2002 batch) Kuraray multi-clad and Pol.Hi.Tech. multi-clad fibers have been conducted using a spectrophotometer and the light output has been analyzed as a function of wavelength.

To evaluate the attenuation length of the various fibers tested, it is necessary to evaluate first the ratio of the means of the left and right PMT ADC values at each position along the beam. To understand this, consider that the attenuation of light as it travels along the fiber is given by

$$I(z) = I_0(z)e^{-z/\lambda} \quad (6.5)$$

where z is the distance from the point of impact of the beam along the fiber to the appropriate PMT, λ is the attenuation length, and $I_0(z)$ is the amount of light produced at the interaction point.

In practice, it is found that the amount of light produced at the interaction point is a function of z . Consequently, the ADC values for the two PMT's in question may be expressed as

$$ADC_{left} = f(z)e^{-z/\lambda} \quad \text{and} \quad ADC_{right} = f(z)e^{z/\lambda}, \quad (6.6)$$

where $f(z)$ is the geometric mean calculated from

$$f(z) = \sqrt{(ADC_{left}ADC_{right})}. \quad (6.7)$$

Thus, a reliable method to extract the attenuation length value is to take the ratio between the two ADC values above:

$$\ln(ADC_{left}/ADC_{right}) = -2z/\lambda. \quad (6.8)$$

Plotting the ADC ratio values at different positions on a semi-log scale results in a straight line with a slope of $-2/\lambda$. This is what is shown in Fig. 6.18 for all fiber bundles, where the curves have been shifted along the y-axis for clarity.

It is evident that the attenuation lengths of the Kuraray fibers are quite reproducible between different fiber samples, as well as different geometrical configurations. The Pol.Hi.Tech. multi-clad fibers had an attenuation length of $\lambda = (234 \pm 3)$ cm, considerably shorter than the Kuraray fibers. All the results are in broad agreement with those of KLOE and are presented in Table 6.2. It should be mentioned that the KLOE Collaboration also tested BICRON⁴ scintillating fibers, but recent price quotes from BICRON revealed that these are too costly for the HALL D project and so were excluded from testing for this reason.

To determine the timing resolution of the fiber bundles, the software mean time and the left-right timing difference must be computed. These quantities should have constant values at any given point along the fiber. However, there are some uncertainties associated with these values, which arise from inherent timing resolution of PMTs involved and photon statistics.

The timing resolution was determined with two methods that yielded consistent results. Statistically it appears that Kuraray fibers have superior timing resolution to the Pol.Hi.Tech.

²Kuraray Co., Ltd., 3-1-6, Nihonbashi, Chuo-ku, Tokyo 103-8254, Japan.

³Pol.Hi.Tech. s.r.l.O, Carsoli, Italy.

⁴BICRON Corporation, Newbury, Ohio, USA.

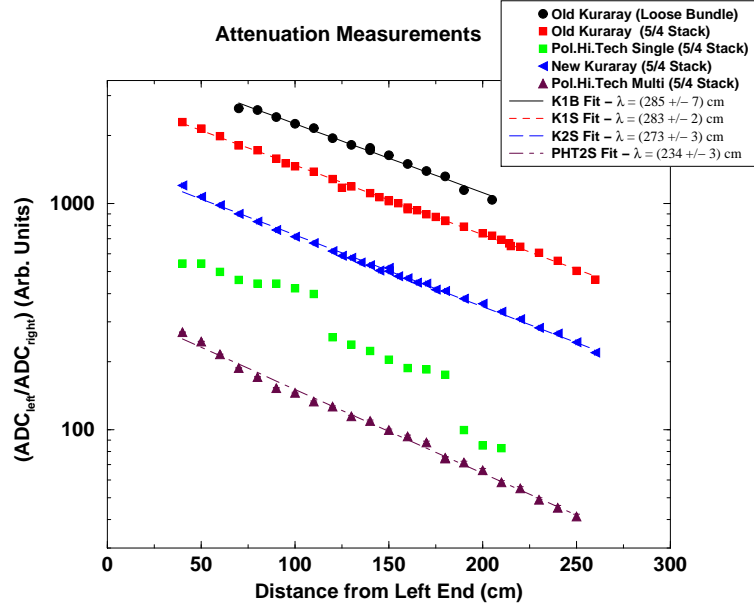


Figure 6.18: Attenuation length measurements for various fibers. The Pol.Hi.Tech. single-clad fibers appear to have been broken or stressed at the locations where the discontinuities appear in their curve (unconnected squares).

fibers which implies that the former fibers have better light production and light collection capabilities. All fiber bundles gave $\sigma = 550 - 700 ps$. This is consistent with the KLOE results which had $\sigma = 300 ps$ for the Pol.Hi.Tech. and Kuraray fibers and $400 ps$ for the Bicon fibers, when the number of photo-electrons collected was $N(p.e.) = 30$. These numbers rise to $500-800 ps$ for $N(p.e.) \leq 10$. From the TRIUMF measurements, fitting of the ADC spectra yielded $N(p.e.) \leq 4$. Thus, the TRIUMF results are consistent, at least qualitatively, with those from KLOE. Additional details can be found in reference [80].

The Kuraray fibers showed a consistently better performance as per the light attenuation coefficient and timing resolution. However, the Pol.Hi.Tech. multi-clad fibers performed better in terms of light yield, based simply on the observation that for the same bias and gain the mean of the ADC spectra for these fibers was higher. These fibers had more than adequate performance for the requirements of the GLUEX experiment and are considerably cheaper (by a factor of 2) than the Kuraray fibers. For this reason, Pol.Hi.Tech. multi-clad fibers have been used in the construction of all prototype modules, except Baby-0.

Fiber Light Transmission Tests

Light-transmission tests of the scintillating fibers have been conducted using a dedicated optical testing system that employs LED light sources with different wavelengths, transport light guide fibers, optical filters, and is coupled to a dual-channel spectrophotometer and ADC. The system is sensitive to wavelengths from $350 nm$ to $1000 nm$, is connected to the USB port of a laptop, and is read out by means of commercial software.

Preliminary tests had indicated that exposing scintillating fibers to UV light caused degradation in transmission intensity. This agreed with test results from KLOE [76]. The next step was to understand the reason for this decrease in light emission. One possibility was that UV exposure created cloudiness in the fiber, causing a decrease in attenuation length. Another theory was that after exposure, the fibers were absorbing light in different regions, shifting the output spectrum away from the PMT's peak efficiency. Using an Ocean Optics Inc.

Batch	Fiber Type (mode)	Attenuation Length (cm)		
		Cosmics	TRIUMF	KLOE
1992	Bicron BCF-12			226 ± 3
1993	Bicron BCF-12			286 ± 8
N/A	Kuraray SCSF-81 single-clad			321 ± 5
1992	Pol.Hi.Tech.0046 single-clad			284 ± 5
1993	Pol.Hi.Tech.0046 single-clad			267 ± 6
2000	Kur.SCSF-81 single-clad (loose)	321 ± 22	285 ± 7	
2000	Kur.SCSF-81 single-clad (5/4)		283 ± 2	
2001	Kur.SCSF-81 single-clad (5/4)		273 ± 3	
2000	P.H.T.0046 single-clad (loose)	259 ± 20		
2000	P.H.T.0046 multi-clad (loose)	247 ± 47		
2000	P.H.T.0046 single-clad (5/4)		Broken	
2000	P.H.T.0046 multi-clad (5/4)		234 ± 3	

Table 6.2: Attenuation length determined using 2" PMT's following the cosmics runs and the TRIUMF beam tests. The results are compared to those from the KLOE Collaboration [76, 81].

(OOI) ⁵ SD2000 spectrometer coupled successively to UV (380 *nm*), Blue (470 *nm*) and Tungsten ($\lambda = 350 - 1100$ *nm*) diodes, scintillating fibers were exposed to UV light emitted from normal fluorescent room lights while periodically measuring the fibers' output spectra.

Light from the diodes was divided into two channels. The master channel passed through a clear reference fiber that allowed us to monitor the stability of the diode. The sample scintillating fibers were placed into the slave channel. Five scintillating fibers and one Bicron (clear) light-guiding fiber were chosen at random to be tested. The six fibers were placed parallel to each other on a table and irradiated by leaving the room lights on for long periods of time. During the measurement of the output spectra of the fibers, all room lights were turned off and only lamps with UV filters were on.

Data reproducibility was a major concern for our experiment. If the fibers were not coupled into the OOI system in a consistent fashion, it would be impossible to compare recorded spectra from one hour to the next. Furthermore, it had been discovered that small rotations in the reference fiber at the connection point to the spectrometer could change the intensity of the reference spectrum by up to fifty percent.

A method that eliminated coupling as a contributing factor was sought. It was decided to perform the experiment one fiber at a time, leaving it connected to the OOI system even during exposure. One fiber was placed into the system and left unexposed over night. When re-tested in the morning, the results were found to be nearly identical. This gave a degree of confidence in the data to be collected. The light source used was the 470 *nm* LED. The results are shown in Fig. 6.19. A key observation in this figure is the effective "shift" of the spectra to higher values of λ . This is a result of a significant reduction of spectral strength in the blue region, precisely where PMT's are the most sensitive.

An additional interesting feature of these fibers can be gleaned from measurements of their light output as a function of length. These measurements are shown in Fig. 6.20. The reader is directed to notice the $\lambda=400-480$ *nm* region. Clearly, a reduction in intensity is observed with increasing fiber length. It should be mentioned that these measurements were done on a single fiber, starting with a 410 *cm* fiber that was successively trimmed to shorter lengths with its cut end being polished each time. As it turns out, such a light response is more suited for collection by SIPM's whose overall efficiency peaks in the yellow-green region. However, this renders yellow-green WLSF's useless when coupled to SIPM's; red WLSF's would have to be used instead and these suffer from poor timing resolution. The effect is pronounced enough to be visible by eye, as displayed in Fig. 6.20.

These measurements were repeated using a UV diode (380 *nm*) and the results are being an-

⁵<http://www.oceanoptics.com/>

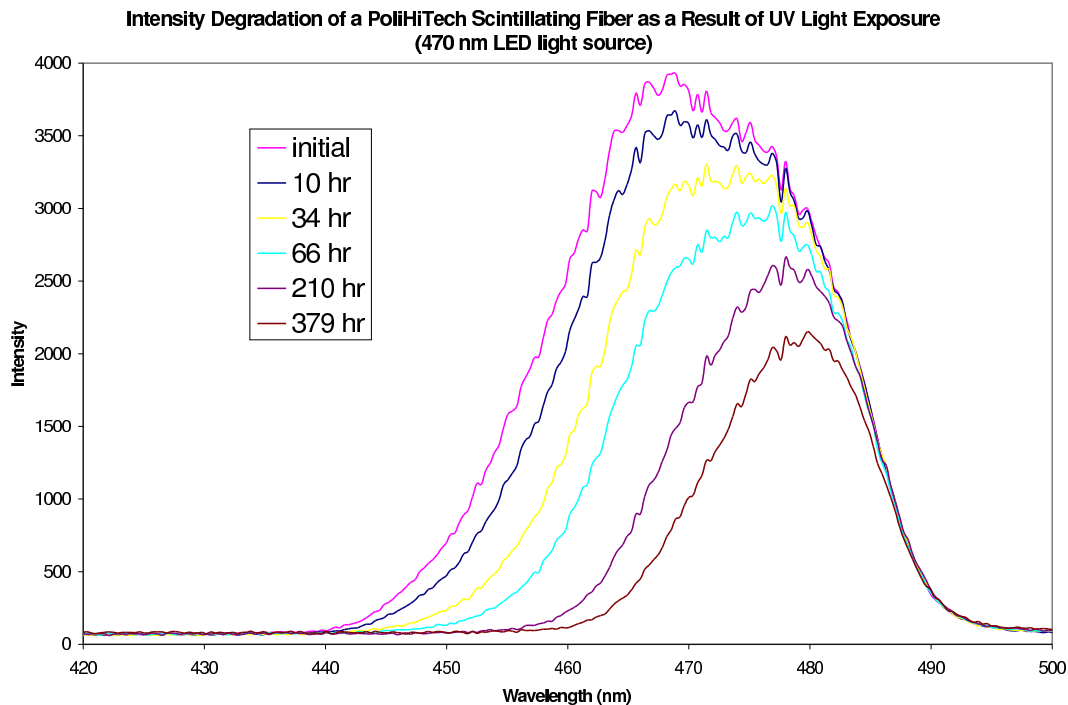


Figure 6.19: Degradation of fiber intensity as a function of UV exposure time. These are the final measurements using the 470 nm LED.

alyzed. Several lessons were learned that will help future measurements of the spectral response of scintillating fibers [82]. In the future, the long term effects of cosmic rays on scintillating fibers should be studied to give an idea of the longevity of the Barrel Calorimeter. This can be achieved by placing a select group of fibers into a tube made of UV filter and measuring the spectra every few months. Due to the extreme length of this investigation, it is not feasible to study one fiber at a time. In this case, plenty of care must be given to ensuring consistent coupling between the fibers and the OOI system.

Silicon Photomultiplier Tests

Although single-pixel Geiger mode devices (Avalanche Photo Diodes - APDs) were developed in the mid sixties, the SIPM is a novel type of APD [83]. It is a promising device for our application in GlueX, since it is insensitive to magnetic fields, has a high gain ($\sim 10^6$), good quantum efficiency, provides excellent timing resolution (~ 120 ns for single photo electron detection) and a fast risetime (sub-ns), achieves good dynamic range ($\sim 10^3/\text{mm}^2$), and does not suffer from nuclear counter effects when operated in Geiger mode. Finally, it has a solid performance at room temperature (in contrast to VLPCs) and does not exhibit any serious radiation damage effects, other than perhaps from neutrons [84].

The SIPM is a multi-pixel photo diode with a large number of micro pixels (500-1500 each with a typical size of 20–30 μm) joined together on a common substrate and under a common load. The total number of pixels defines the dynamic range of the photodetector. The photodiode has a multi-layer structure with different doping levels. As a result, within the thin depletion region between p^+ and n^+ layers, a very high electric field of about 5×10^5 V/cm is created, with the right conditions for a Geiger discharge mode to take place. The operational bias voltage is 10–20% higher than breakdown voltage, with typical supplied bias voltage of 50–60 V.

The single pixel gain is approximately 10^6 , roughly the same order of magnitude as that of a traditional PMT. While each pixel operates digitally as a binary device – because all SIPM pixels work together on a common load and there is a large number of pixels – the output signal is a

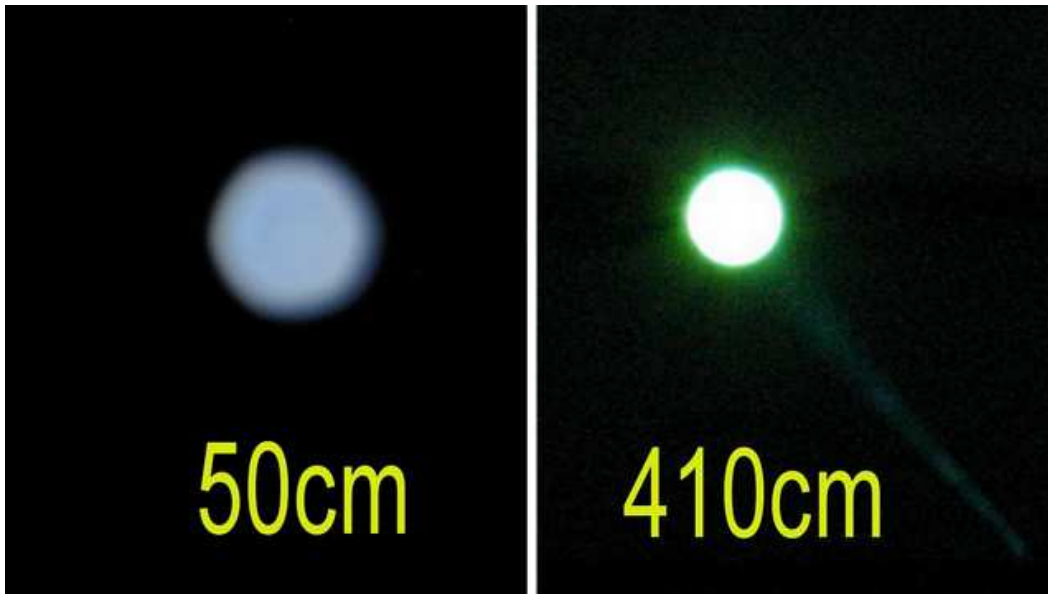
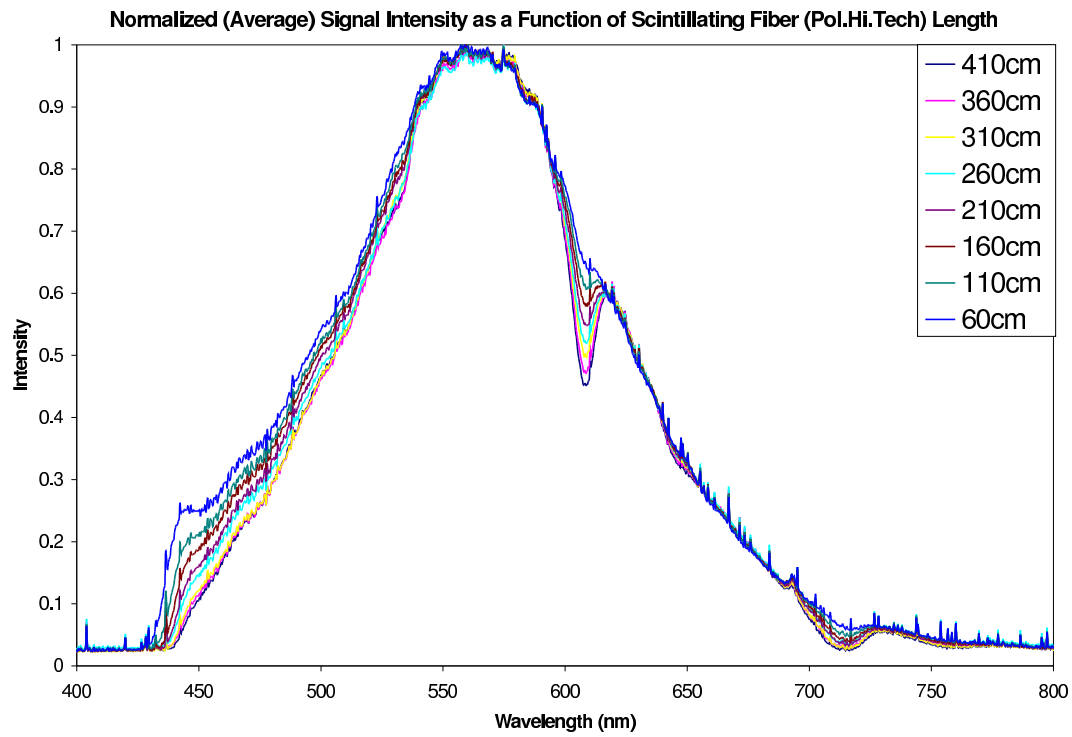


Figure 6.20: Fiber intensity as a function fiber length. These are the final measurements using the 470 nm LED. The shift in color from blue to green is evident even visually.

sum of the signals from all pixels registering a “hit”. Thus, the SiPM, as whole, is an analogue detector that can measure the incident light intensity. The distribution of the voltage across the depletion depth of 4–6 μm is such that for only a fraction of the depth ($\sim 1\text{--}2\ \mu\text{m}$) the former exceeds a value sufficient for Geiger discharge creation, and therefore, the Geiger discharge is contained within this limited region. As a result, its duration is very short, a few hundreds of ps, resulting in typical rise times of 1 ns.

The SiPM’s photon detection efficiency, η , is given by $\eta = QE \cdot \varepsilon$, where η is the photon detection efficiency, QE is the quantum efficiency and ε is a geometrical factor. The latter is a ratio of the sensitive area (as defined by the total active pixel area) to the total area. This value does not depend on wavelength and is a constant for each SiPM. The devices used in our particular tests had geometrical factors of 0.3/1.0 for all SiPM’s/PMT’s investigated, respectively.

The SiPM’s used in our tests were developed and produced by the Moscow Engineering and Physics Institute (MEPHI) in cooperation with a state enterprise (PULSAR). The specific SiPM’s had 1000 pixels in each detector covering the 1 mm² sensitive area and the supplied bias voltage was 50–60 V. Although the geometrical factor for these SiPM’s was 0.3, efforts are underway at MEPHI/PULSAR to increase this to as much as 0.7. Competitors at the University of Obninsk in cooperation with a private firm (CPTA) [85] claim that their device has 50% higher photon detection efficiency in the green region and fewer constraints on mechanical performance. Moreover, the Obninsk/CPTA is investigating the construction of larger areas by connecting SiPM’s in a matrix configuration [85]. We have recently obtained 60 1 mm² CPTA units and these are currently undergoing evaluation at Regina. In addition, negotiations are underway with experts at CERN and DESY to allow for future testing of these devices with sophisticated setups and for testing with beam.

Tests of the MEPHI SiPM’s were conducted in order to investigate their use as front-end detectors for the Barrel Calorimeter readout system. The results of this work have been accepted for publication in Nuclear Instruments and Methods. Specifically the SiPM’s were investigated under the following two conditions: a) detection of incident light of high flux intensity, where about 200–500 SiPM pixels registered a hit but the signal was not saturated, and b) Detection of light of lower photon flux intensity in which case only few pixels registered a hit. This regime corresponds to a few-photon-counting condition.

An Optitron nanosecond broad spectrum optical pulse radiator (Model NR-1A) with a Nitrogen Plasma Discharge Tube⁶ was used as a source of light for the SiPM investigation under high photon flux conditions. The light pulses had a 1 ns rise time and a few ns pulse duration, and were measured with the SiPM as well as with a 2” Burle PMT (model 8575). A clear, pure fused silica fiber of 5 m length was used to transport the light from the Optitron plasma discharge tube to the sensitive surface of the SiPM. The light intensity emitted from was monitored by the PMT.

Pulses from the SiPM and the PMT were measured with a Tektronix TDS-5104 digital oscilloscope. The detected signal amplitude for the SiPM was ~ 300 mV, corresponding to $\sim 200\text{--}300$ pixels registering a hit. Whereas the timing distributions have a similar structure with risetimes of 1 ns and 4 ns for the SiPM and PMT, respectively, the former has a σ that is less than half of the latter’s: $\sigma = 140$ ps vs. 375 ps.

In order to investigate the energy resolution of the SiPM, we measured the pulse amplitude distribution under low photon flux conditions employing the Optitron unit and a neutral-density attenuation filter that reduced the light to 1% of its initial value. The amplitude of the signals in the SiPM, in this case, was 5–10 mV, and this necessitated the use of a fast amplifier (LeCroy 612A). Under such conditions it was not possible to eliminate completely the noise pick-up from electronic equipment present in the area. Nevertheless, the pulse amplitude distribution shown in Fig. 6.21 exhibits five well separated peaks corresponding to single photon detection and good separation for emission of up to five photoelectrons.

Next, we evaluated the performance of the SiPM used as a front-end detector for light signals produced by minimum ionization particles traversing a 4-m-long Kuraray SCSF-81 single-clad

⁶Optitron Inc. 23206 Normandie Ave. #8, Torrance, CA 90502, USA.

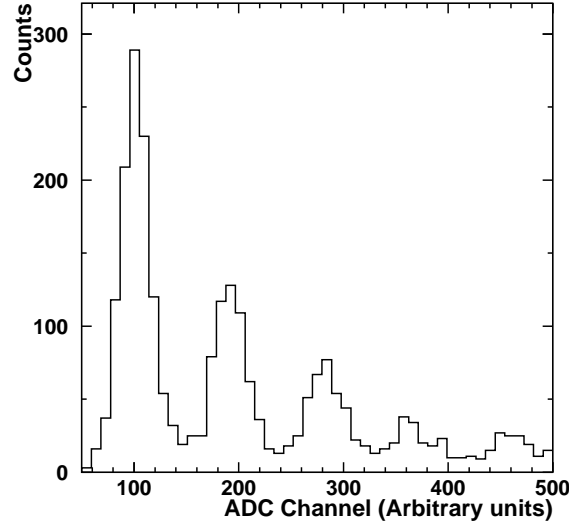


Figure 6.21: SIPM pulse height spectrum for low intensity light pulses.

SciFi. Fibers with similar parameters will be used in the Barrel Calorimeter for GLUEX detector system.

Kuraray SCSF-81 SciFi's have an emission spectrum range of 400–550 nm, peaking at 437 nm, with a 2.4 ns scintillation decay time and an attenuation length of ~ 3.5 m. The fiber was in direct contact with the surface of the PMT window, while it had a 0.3–0.5 mm air gap between the end of the fiber and the sensitive surface of the SIPM in order to prevent damage to the SIPM. It should be noted that the Burle 8575 PMT has a 25% efficiency at the peak of the Kuraray emission wavelength while the SIPM's efficiency for that region is about 15%. As a result, for the the same light intensity from the scintillating fiber, the SIPM exhibits a photon detection efficiency that is 60% of the PMT's. The comparison in efficiency between the two devices is summarized in Table 6.3.

λ	Device	ϵ	QE	η
550 nm	SIPM	0.3	60%	20%
	PMT	1.0	5%	5%
437 nm	SIPM	0.3	45%	15%
	PMT	1.0	25%	25%

Table 6.3: Detection efficiency, $\eta = QE \cdot \epsilon$, for the SIPM's and PMT's.

The scintillating fiber was excited using a $^{90}\text{Sr}(^{90}\text{Y})$ beta source that has a 2280 keV maximal and 935 keV average energy of beta particles. The difference in the distributions of ionization energy loss in the scintillating-fiber core, as calculated by a Monte-Carlo simulation for the triggering beta particles and compared to the minimum ionization particles, is only a few percent on average [86]. The TDC and ADC spectra were accumulated and analyzed to extract the dependence of the detected light and timing resolution as a function of distance of the source from the respective readout end of the fiber. The mean values of the distributions were used in the calculation of the attenuation length.

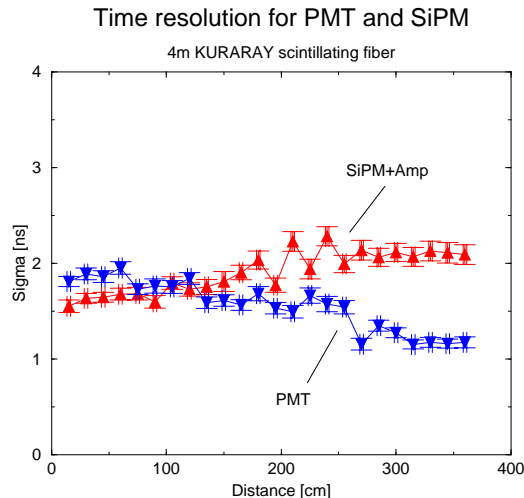


Figure 6.22: The timing resolution as a function of the distance from the v detector.

The experimental data were fit with an exponential curve, $y = I \cdot \exp(-x/L)$, where I is the amount of light produced at the interaction point, L is the attenuation length and x is the distance to the ionization source. The ratios of the mean values for the two identical positions of an ionization source are larger for the PMT in comparison with the SiPM. As a result, two different attenuation lengths were obtained for the same fiber, $L_{SiPM} = 251$ cm and $L_{PMT} = 146$ cm for the SiPM and the PMT data, respectively, stemming from the difference in the spectral sensitivity of these two devices. The SiPM is more sensitive to longer values of λ where the transmission loss for the Kuraray fiber is lower. Therefore, the SiPM “realizes” a longer attenuation length compared to the PMT. Obviously, the SiPM-fiber combination provides a clear advantage over the PMT-fiber one, in applications where long fibers must be used.

The TDC peak location (the mean value of the Gaussian fit) was plotted versus the distance from the front-end detector. The slopes of the linear fits for the SiPM and the PMT agree with each other within the error of measurement, and are equal to 1.32 ± 0.01 ch/cm and 1.33 ± 0.01 ch/cm for the v and the PMT experimental data, respectively. The TDC conversion factor was 47 ps/ch. The calculation of the velocity of light propagation gives $v = (1.60 \pm 0.03) \times 10^8$ m/s, a value that agrees with the Kuraray SciFi specifications sheet.

The timing resolution is presented in Fig. 6.22 as a function of the distance of the ionization source from each front-end detector. The data presented in Fig. 6.22 have not been corrected for the time jitter of the trigger detector or the jitter connected with the LeCroy 612 amplifier. The smallest values of sigma were 1.5 ns and 1.1 ns for the SiPM and the PMT, respectively, corresponding to the minimal distance between the ionization source and the front-end detector. Finally, the timing resolution depends on the number of detected photoelectrons. The average number of photoelectrons detected for the closest position of the ionization source from each front-end detector was $\sim 3-5$ for the SiPM and $\sim 5-8$ for the PMT. The resultant timing resolutions for the SiPM and for the PMT were comparable.

The properties of a SiPM working in Geiger limited mode have been measured and compared with a standard 2” vacuum PMT. The measurement with the nitrogen plasma discharge unit shows that the SiPM can achieve better time and energy resolutions under high photon flux. To evaluate the possibility of using the SiPM as a front-end detector for an electromagnetic calorimeter readout system, we measured the ADC/TDC spectra from the SiPM for 4 m scintillating fiber irradiated by ^{90}Sr beta source. Coupled to the performance attributes of SiPM’s, the results of these investigations demonstrated that SiPM’s satisfy the basic requirements for such an application.

Although SiPM’s appear to satisfy all the performance criteria of timing and energy resolu-

tions - and they also eliminate the need for high voltage supplies and associated cabling - one serious issue remains, namely their small active areas. Conventional coupling methods between the polished area of the fiber-lead composite and the SIPM's are not possible. Embedded wave shifting fibers in plexiglas light-guides or tiles will not suffice either, due to the loss scintillation light of low λ . One solution under investigation is the use of small light guides to collect the light from an area of the read-out face of the modules, a Winston cone to increase the light density and embedded clear fibers viewed head-on to collect the light to a number of SIPM's. Preliminary calculations indicate an adequate amount of light collected by each SIPM and a matrix of a number of them will combine into one output. We expect to have the first matrix of 16 SIPM's with common voltage supply and output within a few months and testing to begin.

6.3.4 Upstream Photon Veto

Studies of the photon angular distribution for the GLUEX experiment have shown the need for photon detection in the backward or upstream direction [70]. Several exclusive reactions, listed below, contain photons in the final state originating from both the meson and baryon decay vertexes, and were simulated to study the emission angles of the decay particles within the HALL D detector. These reactions were simulated using the GENR8 [87] phase space event generator assuming a photon beam energy of 9 GeV and a t dependence of $e^{-5|t|}$. The Monte Carlo events were then tracked through a simulation of the detector assuming the production and decay vertex coincided with the center of the target region, and analyzed for three different detector regions: the lead glass detector, barrel calorimeter, and the backward region upstream of the target (see Figure 6.23).

$$\begin{aligned} \gamma p &\rightarrow N^*(1500)\pi^+ \rightarrow (n\eta)\pi^+ \rightarrow n\pi^+\gamma\gamma \\ \gamma p &\rightarrow X^+(1600)\Delta^0 \rightarrow (\pi^+\pi^+\pi^-)(n\pi^0) \rightarrow \pi^+\pi^+\pi^-n\gamma\gamma \\ \gamma p &\rightarrow X^+(1600)n \rightarrow (\eta\pi^+)n \rightarrow n\pi^+\gamma\gamma \\ \gamma p &\rightarrow X(1600)p \rightarrow (\pi^+\pi^-\pi^0)p \rightarrow p\pi^+\pi^-\gamma\gamma \end{aligned}$$

In addition to the importance of keeping the energy threshold of the barrel calorimeter and the lead glass as low as possible, it was found that the reactions with photons emanating from the baryon decay vertex have shown that approximately 10% of the photons miss detection by either the barrel calorimeter or the lead glass detector. These photons go undetected by escaping out the upstream hole, which corresponds to emission angles greater than 117° .

Figure 6.24 displays where these lost photons hit the plane at the upstream end of the solenoid. The ring at 117° is the current barrel calorimeter limit. Several rings are shown at other angles, indicating the geometrical losses from each. In order to detect the escaping backward photons and provide nearly hermetic photon coverage it is necessary to implement an Upstream Photon Veto counter (UPV).

Design Considerations

The UPV is a lead scintillator sampling veto calorimeter located directly upstream of the CDC and in place of the solenoid's original field-shaping mirror plate. In the current GLUEX design, this mirror plate is modified by removing all of the soft iron within the inner solenoid radius. This modification effectively removes the upstream mirror plate leaving only a soft iron annulus the size of the magnet coils. This modification has several benefits. First, it allows for upstream access to the target region, cylindrical drift chamber, and the upstream end of the barrel calorimeter. More importantly, it allows for the addition of an upstream photon veto.

The UPV is designed to detect soft photons of energy 20 MeV and greater emerging from the target region. The counter is able to detect multiple photons with fast detection and with timing information that may be utilized at the trigger level.

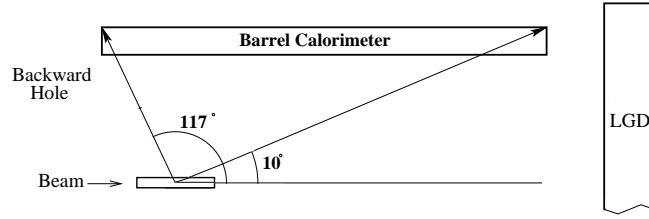


Figure 6.23: Angular distribution, in degrees, from the center of the target to various reference points, for various simulated reaction channels. Tracks more forward than 10° miss the barrel calorimeter and will hit the LGD. Between 10° and 117° the photons will enter the barrel calorimeter. Photons produced at angles larger than 117° miss both calorimeter detectors, and necessitate the construction of an upstream veto detector to achieve near hermeticity.

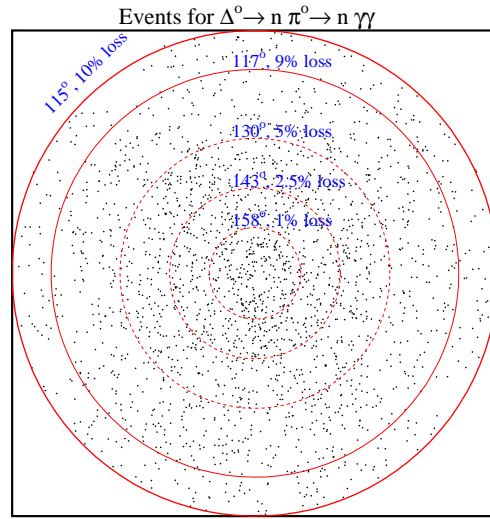


Figure 6.24: The tracked photon intersections on the x-y plane at the upstream end of the barrel calorimeter. The 117° circle is the end of the barrel calorimeter. Various other photon-loss percentages, and their corresponding angles are plotted as well.

As shown in Figure 6.25, the UPV consists of 18 layers of 1 cm thick scintillator alternating with first 12 layers 0.185 cm thick lead sheets ($0.36X_0$ each) then 6 layers of 0.370 cm thick lead sheets ($0.72X_0$ each). This design was simulated using the GEANT 4 package to study the expected performance of the UPV calorimeter. The study uses a photon beam of various energies incident normal to the detector face. The results, summarized in Figure 6.26, ignore quantum fluctuations and express an optimal resolution of $\frac{\sigma}{E} = 5\% + \frac{8\%}{\sqrt{E(\text{GeV})}}$.

Each scintillator layer consists of seven $34\text{ cm} \times 238\text{ cm}$ paddles forming a plane. The central paddle has a 10 cm hole to allow for the passage of the beam. The effective area of each plane is approximately $238\text{ cm} \times 238\text{ cm}$. The total counter thickness is 22.4 cm or $8.91X_0$. The layers are arranged into three alternating orientations: x , u , and v ($\pm 45^\circ$, respectively) as shown in

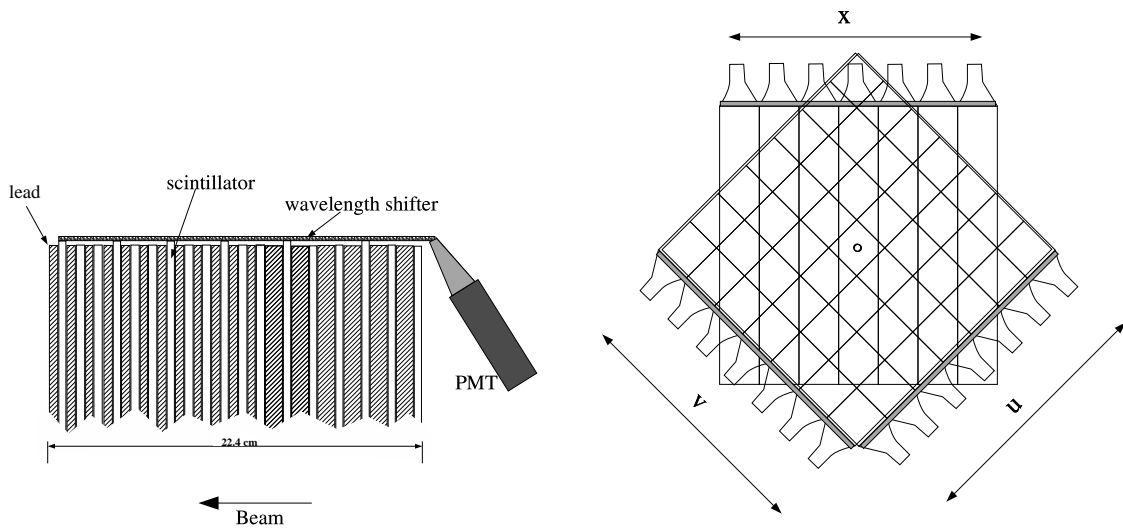


Figure 6.25: The left-hand figure is a sketch of a UPV segment. The 18 scintillator layers are arranged into 3 alternating orientations: x , u , and v . Shown is the light collection for one such orientation. The light-collecting ends of the scintillators are joined together via a wavelength shifter which is oriented perpendicular to the scintillators. The wavelength shifter is used to redirect the light through 90° and out the upstream end of the solenoid to PMTs. The right-hand figure is a sketch of an upstream photon veto counter orientation. The layers are arranged into three alternating orientations: x vertical, u $+45^\circ$ and v -45° layers.

Figure 6.25.

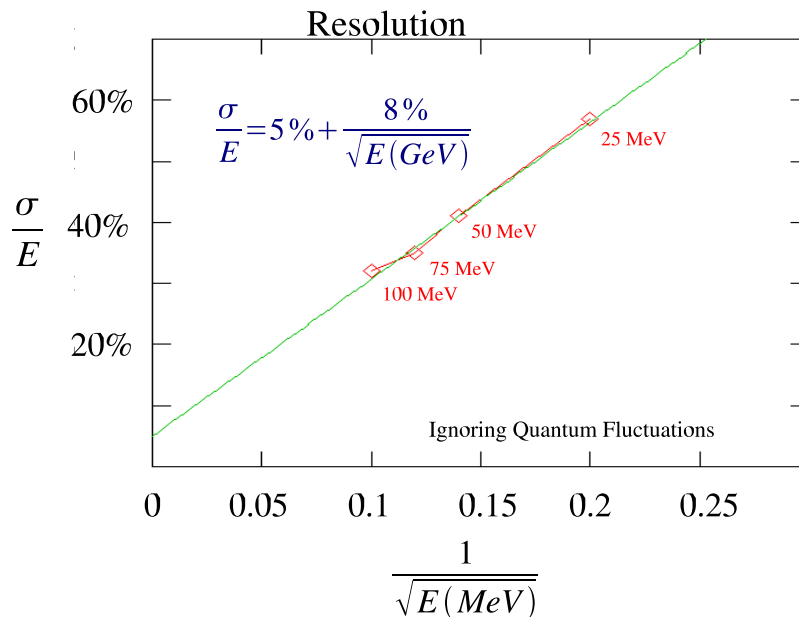


Figure 6.26: Simulation using the GEANT 4 package to study the expected performance of the UPV calorimeter. The study uses a photon beam of various energies incident normal to the detector face. The results, ignoring quantum fluctuations, express an optimal resolution of $\frac{\sigma}{E} = 5\% + \frac{8\%}{\sqrt{E(\text{GeV})}}$.

The scintillation light collection is realized at one end of each paddle only. The opposite end is coated with an opaque material to eliminate reflections. For each orientation, the light collecting ends of the scintillators are join together via a wavelength shifter which is oriented perpendicular to the scintillators. The wavelength shifter is used to redirect the light through 90° and out the upstream end of the solenoid to photo-multipliers tubes (PMT). Each PMT is protected from any fringe magnetic field with soft steel casing and mu-metal shield.

6.4 Charged Particle Tracking

The system of tracking chambers in the GLUEX detector must cover as close to a 4π solid angle as possible over a wide range of particle momenta and must have sufficient momentum resolution to be able to identify missing particles. All tracking devices are located inside the barrel calorimeter which is in turn inside the $2.24 T$ solenoid. The barrel calorimeter defines a maximum keep-out radius of about $65 cm$. The physical radius of all chambers has been limited to $59 cm$. This provides $6 cm$ of space for support and installation rails, and cables and gas feeds for the forward chamber packages. In the forward region, the chambers need to extend as close to the beam line as possible. In the initial detector design, there is no vertex chamber around the liquid hydrogen target. A possible upgrade to the system would be the addition of a device which could achieve sub- $100 \mu m$ resolution. Very accurate vertex information from such a device could be important in identifying secondary vertexes from decaying particles (e.g. K_S , Λ , Σ , ...). In the forward region, it is important to be able to reconstruct fast, small-angle particles (down to nearly 0°). Finally, there is a small hole in the particle identification for particles that spiral and do not reach the barrel calorimeter. It is necessary that in the central region, the tracking should have sufficient dE/dx information to aid in the separation of π 's, K 's and p 's up to momenta of about $0.45 GeV/c$ — a regime where dE/dx measurements work extremely well.

6.4.1 Design Considerations

In order to achieve the desired goals in the GLUEX tracking, the LASS detector [50] design was used as our starting point. This device used several different tracking elements each optimized for a particular region in the detector. Figure 6.27 shows the GLUEX tracking regions. Surrounding the target is a cylindrical straw-tube drift chamber (CDC) which provides very good $r - \phi$ and good z resolution. In addition, it is necessary for this detector to provide some dE/dx information. In the forward region, round planar drift chambers (FDC) will be arranged in four identical tracking packages. There are still background studies underway to determine exactly how to handle the beam-line region. One option is to have the chambers physically fill the space, but to deaden the active elements that are in the beam line. This could be accomplished by placing Styrofoam around them. An alternative would be to add small support structures around the beam hole and physically remove all material. The final decision will be based on the results of background studies. A summary of the tracking chamber parameters are given in Table 6.4.

System	Radius		Length		Resolution	
	r_{min}	r_{max}	z_{min}	z_{max}	$\sigma_{r-\phi}$	σ_z
CDC	13.0 cm	59.0 cm	10 cm	210 cm	150 μm	1.5 mm
FDC	3.5 cm	59.0 cm	230 cm	400 cm	150 μm	fixed

Table 6.4: A summary of the tracking chamber parameters. The z values under *Length* indicate the smallest and largest z of the combined system. The z origin is at the upstream end of the magnet. The z resolution for the CDC comes from $\pm 6^\circ$ stereo layers. The z resolution of the planar chambers is assumed to be given by their position in space.

The charged-particle system within the solenoid must be optimized for both overall ac-

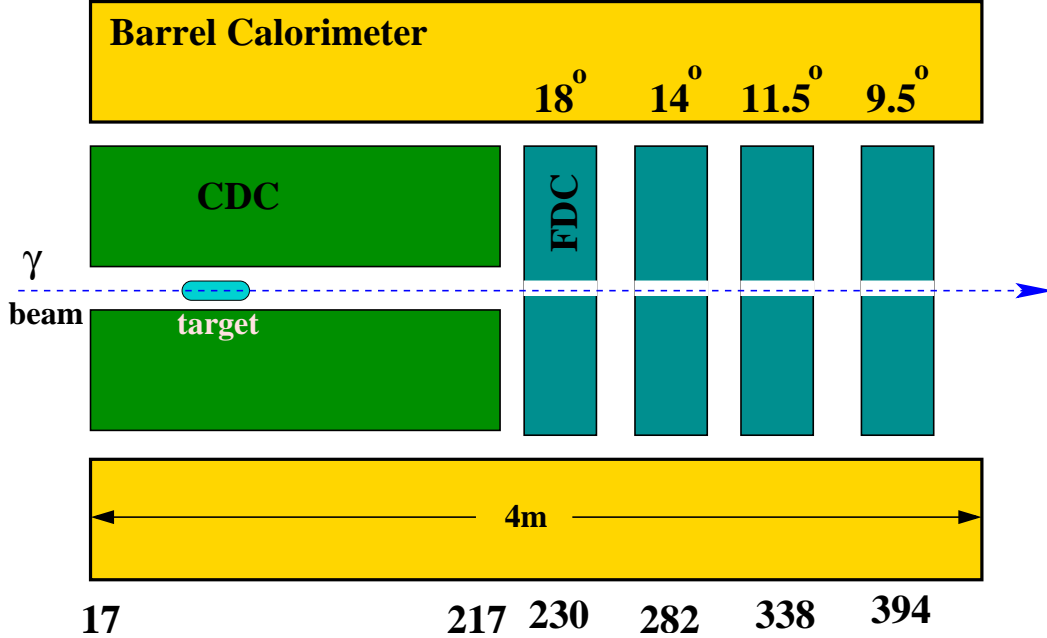


Figure 6.27: The GLUEX detector. The tracking is composed of two elements: a straw-tube chamber called the cylindrical drift chamber (CDC) and circularly-shaped planar chambers designated as the forward drift chambers (FDC). The small gap indicated in the middle of the FDCs is due to wires that will not be instrumented. If background studies merit, we could also consider a physical hole. The distances labeled along the bottom of the figure are the z coordinate of the upstream and downstream ends of the CDC, and the center of each FDC package. The angles labeled above the FDC packages are from the center of the target to the center of the outer edge of the chamber.

ceptance and momentum resolution. A detailed study using the *HDFast* framework has been performed to examine this [88]. The results of this study indicate that the above combination of the straw-tube chamber and planar drift chambers with typical $r - \phi$ position resolutions of $150 \mu m$ will satisfy our requirements. A plot of resolution as a function of angle is shown in Fig 6.28 where we have zoomed in on the forward angles in the left panel of the figure. Note that the current Monte Carlo does not fully deal with the degradation in resolution as the tracks become parallel to the CDC wires. A couple of features of these plots are worth commenting on. The rapid degradation in resolution as one goes to very forward angles is driven by the distance (in z) between the first and fourth FDC packages. The most forward numbers can be decreased by about 0.01 for each additional 25 cm of length. Unfortunately, moving the fourth FDC package further down-stream moves it into a non-uniform field region. This tends to cancel the improved resolution due to the larger length. The degradation in resolution from about 10° to 20° corresponds to the transition region from mixed FDC-CDC tracks to all CDC tracks. It is due to the successive loss of FDC packages being linked to the tracks. It is possible to somewhat shorten the CDC and move the first FDC package upstream. However, if the CDC is shortened by as much as 50 cm , then the transition region degrades significantly. An optimum length for the CDC is between 170 and 200 cm and is currently understudy. Such a small perturbation in length has little effect on construction of the chamber.

The $22.4 kG$ solenoid field determines the physically measurable quantities, and hence, the momentum resolution. The transverse momentum, p_\perp and the dip-angle, λ , ($\lambda = \frac{\pi}{2} - \theta$) are measured from the curvature of the tracks and their initial direction. The total momentum and the longitudinal momentum are then obtained from these as $p_{total} = p_\perp \sec \lambda$ and $p_\parallel = p_\perp \tan \lambda$. The accuracy of the p_\perp measurement is completely dominated by the $r - \phi$ resolution of the

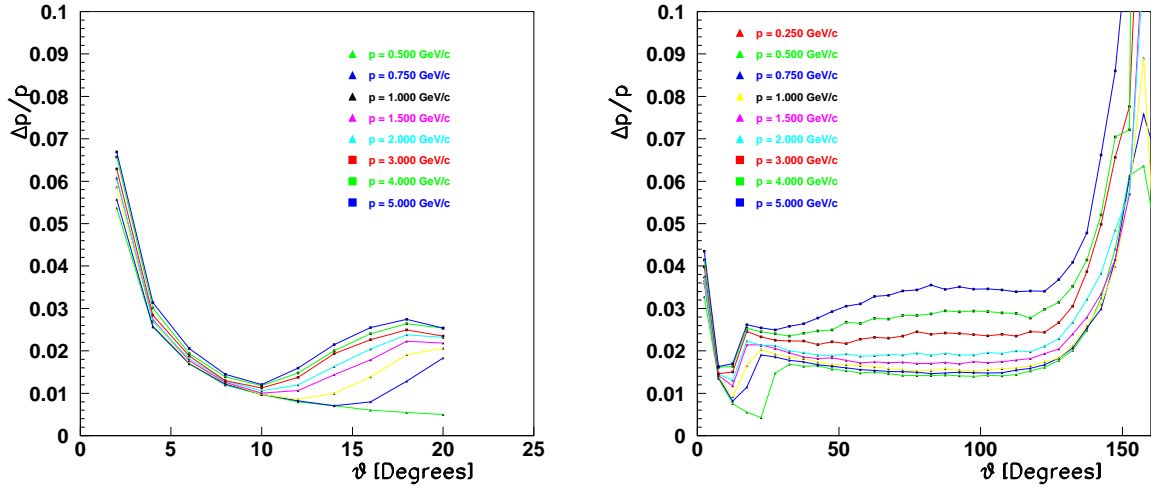


Figure 6.28: The resolution as a function of angle is plotted for several total momenta. The plots correspond to the detector design shown in Figure 6.27. For polar angles larger than 70° , the maximum detected momentum will be well under $1\text{GeV}/c$ so even though the resolution for high-momentum tracks is poor in this large-angle region, it will not affect the overall tracking of physics events.

tracking chambers, while the λ measurement relies on an accurate measurement of both z and the distance traveled.

6.4.2 Track Reconstruction

Track reconstruction effects play a very important role in the design of the combined system. In particular, track matching between different detectors and the associated inter-calibration problems often limit the ultimate resolution. In addition, the high magnetic field strength of 22.4 kG means that tracks may spiral significant distances between measurement planes in the forward direction. This means that one would like as much information as possible from each measured hit in the detector. Other complicating issues are that the magnetic field is non-uniform near the ends of the magnet, and in the region between the end of the solenoid and the forward calorimeter. However, particle identification will require projecting charged tracks forward through this non-uniform field region. Tracking near the end of the solenoid needs to be as good as possible.

An example showing the typical charged particle momentum that needs to be measured comes from reaction 6.9. This final state consisting entirely of charged particles is fairly typical of the typical exotic-hybrid channel that will be studied.

$$\gamma p \rightarrow \eta_1(1800) p \rightarrow \pi^+ \pi^- \pi^+ \pi^- p \quad (6.9)$$

The exotic spin-one $\eta_1(1800)$ is produced with a mass of $1.8\text{ GeV}/c^2$ and a typical t distribution. The incident photon energy is $9\text{ GeV}/c^2$. Figure 6.29 shows the transverse and longitudinal components of momentum from the π 's in this reaction while Figure 6.30 shows the same distributions for the protons.

From the two sets of plots, several important features can be seen. The charged pions from the decay of the meson system are fairly forward peaked. Once θ_π is larger than about 40° , there are almost no pions with a momentum larger than about $1\text{ GeV}/c$. Additionally, there are almost no pions with θ larger than 100° . The protons almost all fall within the angular

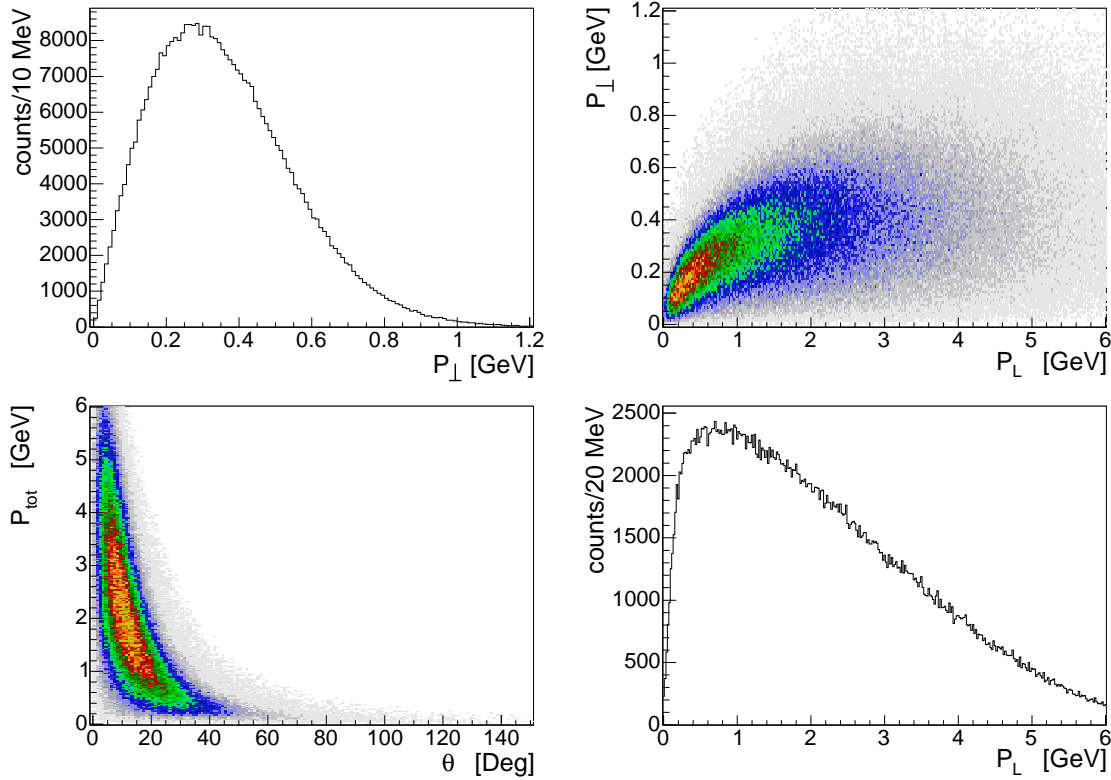


Figure 6.29: The momentum distribution of charged pions from the reaction $\gamma p \rightarrow \eta_1(1800)p \rightarrow 2\pi^+2\pi^-p$. The upper left-hand figure shows the momentum perpendicular to the beam direction. The upper right-hand figure shows the perpendicular versus the longitudinal momentum. The lower left-hand figure shows the total momentum versus the polar angle θ and the lower right-hand figure shows the momentum along the beam direction.

range of 20° to 60° degrees. This is almost entirely covered by the CDC. Many of these protons will need to be identified by either time-of-flight for the BCAL or using dE/dx in the CDC. Good tracking resolution for high-momentum particles in the backward angle region is not required, so the rapid degradation of momentum resolution for these large angles as seen in Figure 6.28 is not a real issue for the detector's overall performance. In addition, most events have at least one particle moving in the forward direction at high momentum. The momentum versus angle for all particles in each event is displayed in Figure 6.29. Good tracking will be needed as close to the beam line as possible, hopefully extending down to 2° .

Another tracking issue is that many of the charged particles in GLUEX will produce spiraling tracks in the solenoid. Figure 6.31 shows the p versus θ plane for tracks in the solenoid. Tracks which fall above the hyperbolic curve cannot spiral in the 59 cm radius region containing the tracking chambers. Below the hyperbola are a series of approximately horizontal lines. Tracks below these lines spiral the number of times indicated. Based on the p versus θ distributions in Figures 6.29 and 6.30, it is clear that most tracks at angles larger than 50° will always spiral at least once in the detector.

Pattern recognition is an important part of track reconstruction as well. This process requires finding local clusters of hits and associating them into small track segments that can be combined into larger tracks. In order for this procedure to work well, it is desirable to have sufficient hits in close proximity such that they will be easily associated. One useful comment on this issue is when the LASS experiment ran in similar conditions, they had severe pattern recognition issues due to the large magnetic field. They resolved it by building chambers with both anodes and cathodes which were read out, with the cathodes and anodes being arranged such that together

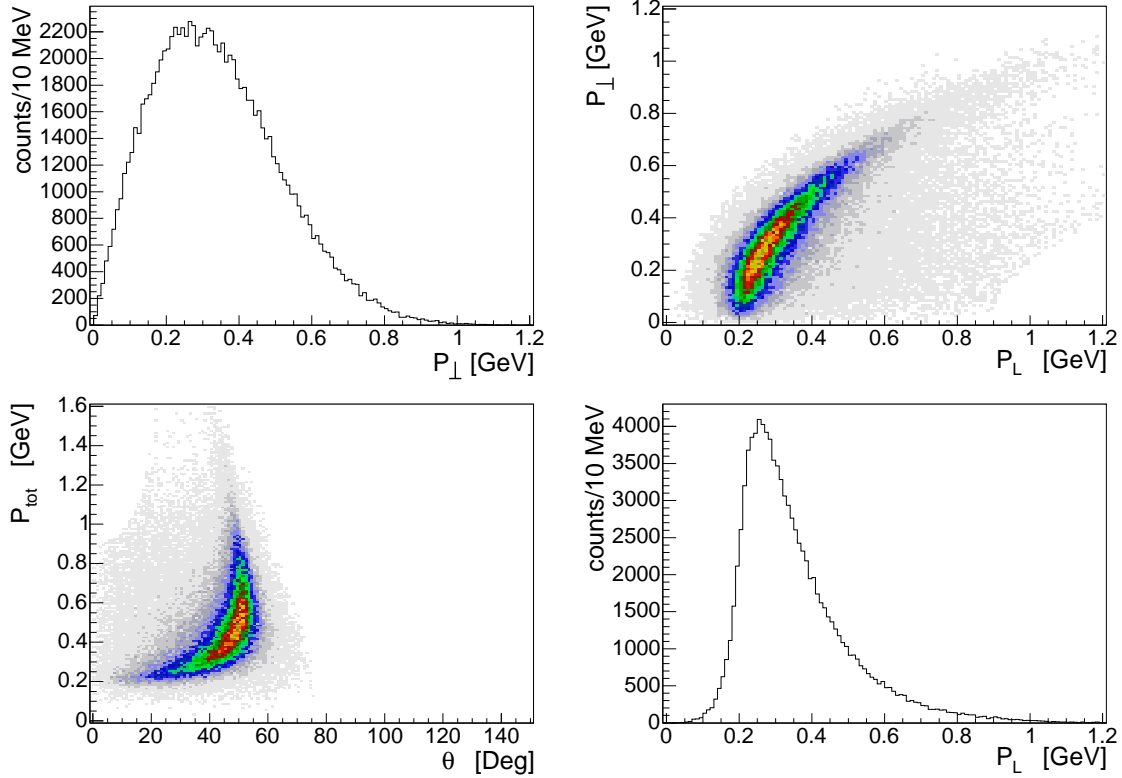


Figure 6.30: The momentum distribution of protons from the reaction $\gamma p \rightarrow \eta_1(1800)p \rightarrow 2\pi^+ 2\pi^- p$. The upper left-hand figure shows the momentum perpendicular to the beam direction. The upper right-hand figure shows the perpendicular versus the longitudinal momentum. The lower left-hand figure shows the total momentum versus the polar angle θ and the lower right-hand figure shows the momentum along the beam direction.

they provided a 3-dimensional point. The GLUEX detector is trying to build on this experience by reading out both cathodes and anodes in the forward direction. We are also planning packages that consist of six closely spaced planes. Such packages will allow local identification of track segments with a reasonable measure of curvature. This has then been repeated four times to provide sufficient segments for high efficiency track-segment linking. In the CDC, the pattern recognition issue is dealt with by creating three sections containing several adjacent straight tube. These are then interleaved with two sets of crossed stereo layers.

The resolution necessary in the photon beam energy has been matched to the expected momentum resolution in the tracking elements of the GLUEX detector. This has been done by looking at the missing mass resolution. As an example, consider reaction 6.10.



It is also assumed that the π^0 in 6.10 is not detected. Using the reconstructed charged tracks, the known beam energy, and the assumption that the reaction took place on a proton target, the square of the missing mass is computed and shown in Figure 6.32(a) for a nominal 0.1% beam energy resolution. The distribution is centered at the square of the π mass, but it has a non-negligible width. In Figure 6.32(b) the width of the peak in (a) is plotted as a function of the beam energy resolution. For this particular reaction with a missing π^0 , a beam energy resolution of 0.1 to 0.2% is well matched to the $200 \mu m$ resolution of the tracking system.

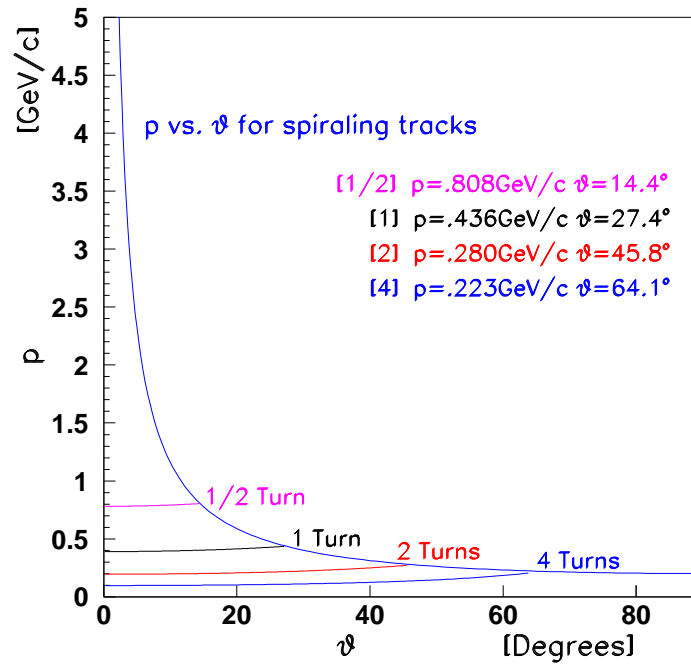


Figure 6.31: This figure shows the number of full circles made by charged particles in the magnetic field. The limit line corresponds to $p_{\perp} = 0.2 \text{ GeV}/c$ tracks. The approximately horizontal lines indicate when the particle can make the indicated number of turns without leaving the magnet.

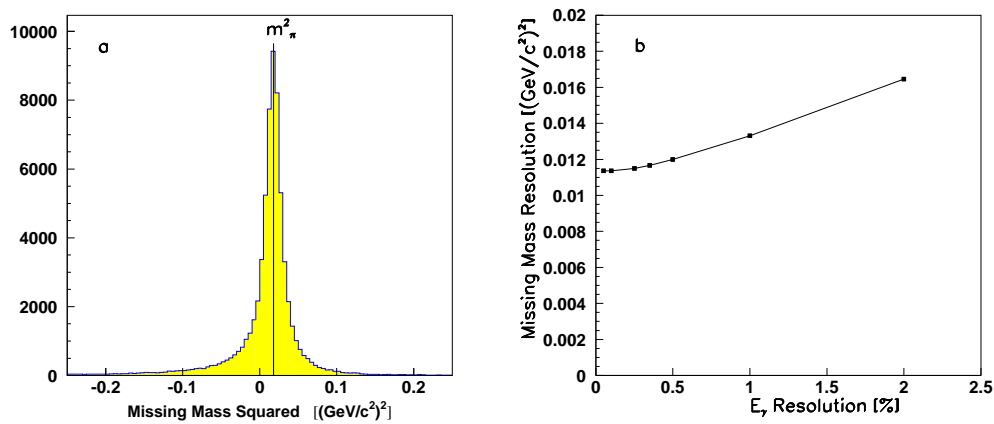


Figure 6.32: Missing mass squared from the reaction 6.10 where the π^0 is assumed missing. (a) is for 0.1% beam energy resolution, while (b) is a plot of the missing mass resolution as a function of the beam energy resolution.

6.4.3 Straw-tube Drift Chamber

The straw-tube drift chamber (CDC) is used to track particles coming from the GLUOX target with polar angles between 6° and 155° with optimal coverage from about 20° to 140° , (see

Figure 6.33). Tracks moving more forward than about 20° will be tracked by both the CDC and the FDC systems. These tracks will need to travel through the downstream end plates of the CDC, so minimizing the material in these plates is extremely desirable. The use of a straw-tube chamber in this region allows us to accomplish this goal as the straws can easily support the $\sim 50 g$ of tension on each of the 3240 anode wires in the chamber. If one were to go with a wire-cage geometry using field wires, one would need to support about $3000 kg$ of tension between the the end plates. This would require thick end plates as well as thick shell material at both the inner and outer radius of the chamber. In addition to minimizing material, the straw-tube designs also allows for an extremely well defined electric field through which the ionization drifts. This is especially important given the $2.24 T$ magnetic field. With straw-tubes, the time-to-radius relation is extremely simple, (see Figure 6.36). In the case of field wires, there are always regions between the field wires where the field is poorly defined. This in turn leads to a significant deterioration in resolution for tracks passing near the edge of such cells.

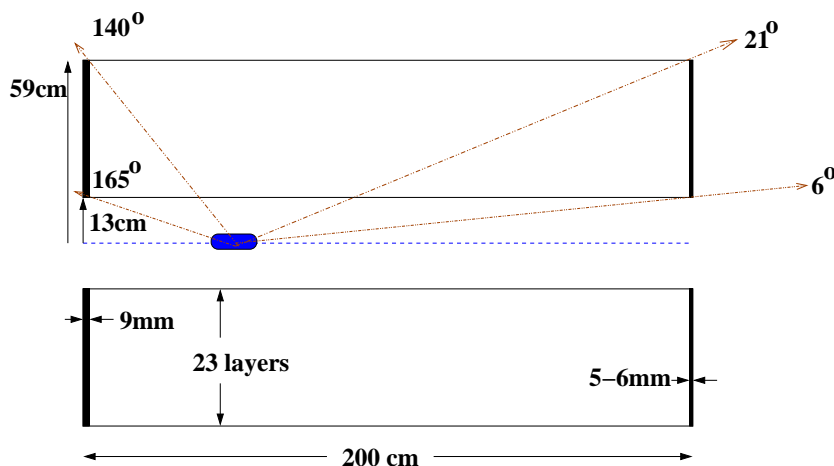


Figure 6.33: A side view sketch of the CDC.

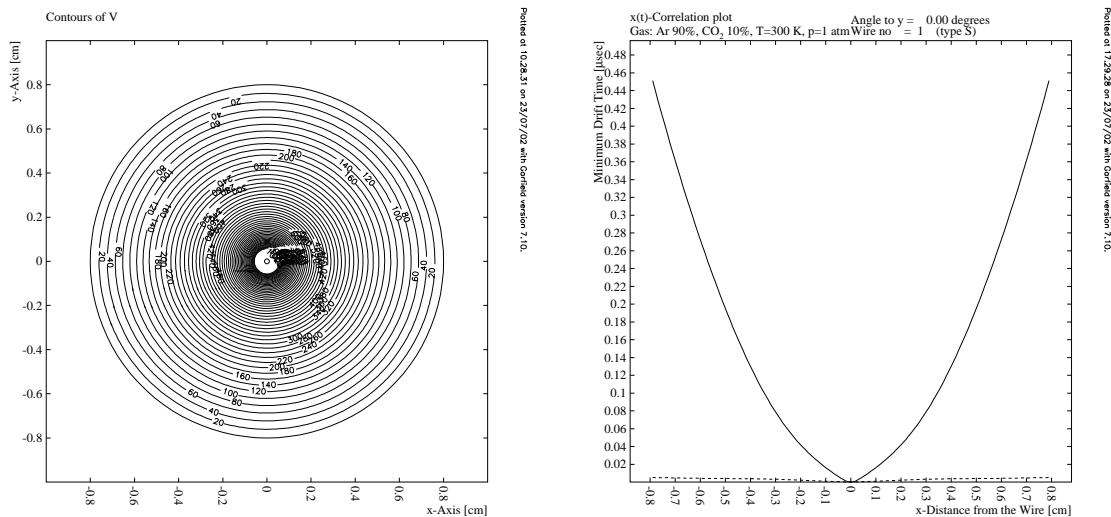


Figure 6.34: The left-hand plot shows a GARFIELD [89] calculation of the electric field in the straw tube. The right-hand figure shows a typical time-to-distance plot calculated for the straw-tube geometry in the $2.24 T$ magnetic field.

The major disadvantage of a straw-tube design is that it adds additional material in the tracking region. However, by careful use of thin straws, this material can be minimized. An additional concern is the measurement of dE/dx using straw-tube chambers. This has been done once [90], but is typically not something that straw-tube chambers are asked to do. In order to do this, one has to be able to accurately compute the tracks path length within the ionization volume. Fortunately, the particles for which the dE/dx measurements are to separate π s, Ks and ps whose total momentum is under $0.45 \text{ GeV}/c$. A region where dE/dx does not need to be particularly good to have a big impact.

Table 6.5 lists the material type and approximate thickness of all materials used in the CDC. The upstream end plate is about 9 mm thick aluminum. However, the down stream will be either $5-6 \text{ mm}$ thick aluminum or 9 mm thick G10. The minimum thickness of the downstream end plate is controlled by machining that needs to be done to support the stereo layers. However, in addition to the end plate themselves, the feed throughs in the down stream end do not need to be conductive. The use of plastic (DELRIN) will help to minimize the material. The exact choice between aluminum and G10 will be based of structural studies that are currently underway. It is anticipated that in the CDC, the amount of material in the down-stream end plate will be between $\frac{1}{3}$ and $\frac{1}{2}$ of that in the up-stream plate.

Part	Material	Thickness	
		r	z
Upstream End plate	Al		9 mm
Downstream End plate	Al		$5-6 \text{ mm}$
	G10		9 mm
Inner Shell	Carbon Fiber	0.7 mm	
Outer Shell	Fiberglass	6 mm	
Upstream Feed Through	Al		1.5 cm
Downstream Feed Through	Delrin		1.0 cm
Wire	Au-W	$20 \mu\text{m}$	
Straw Tubes	Kapton	$100 \mu\text{m}$	
	Al	$15 \mu\text{m}$	
Upstream Gas Plenum	Lucite		5 mm
Downstream Gas Penum	Lucite		3 mm

Table 6.5: The anticipated material to be used to build the CDC. See the text for discussion.

The CDC will contain 3240 straws, each of which is 1.6 cm in diameter and 2 m long. The straws are arranged in 23 layers (see table 6.6). Eight of the 23 layers will be stereo, tilted by $\pm 6^\circ$ from the straight tubes. The tubes are assumed to have an $r - \phi$ resolution of $150 \mu\text{m}$, while resolution along the wire length will be obtained using the 8 stereo layers. This will yield a resolution along the length of the wire of about $150 \mu\text{m}/\sin(6^\circ)$ or about 1.4 mm . The straws will be at ground potential, while the $20 \mu\text{m}$ diameter gold-plated tungsten wire will be at a positive high voltage between 1.5 and 2.5 kV such that they provide a gain of about 10^4 . The exact voltage will depend on the final choice of gas mixture. The wires will be read out only at the upstream end of the detector. This will also minimize material between the CDC and FDC chambers and improve the overall momentum resolution.

We are also considering the possibility of connecting pairs of wires together on the down stream end and using the effective two-ended readout to provide a charge division measurement. While the resulting z -resolution would be on order of 10 cm , this may be useful in pattern recognition. It would also provide a hardware measurement of the transit time correction in the anode wire. A final decision awaits both completion of the prototype and initial work on pattern recognition software. However, the only impact in chamber design is in the choice of anode wires. A second small design change that may also improve pattern recognition is the arrangement of stereo layers. Table 6.6 shows the two stereo super-layers containing both $+6^\circ$ and -6° layers. Changing them so that all of one super layer of $+6^\circ$ and the other -6° is likely to make track

finding in these groups easier. The major concern with this is the mechanical torques extorted by the stereo layers will no longer be completely balanced. A careful engineering study needs to be done to determine how to prevent an induced twist in the chamber.

Layer	No. of Tubes	Radius <i>cm</i>		Stereo Radians
		Center	Plate	
1	58	14.777	14.777	0.000
2	65	16.559	16.559	0.000
3	72	18.340	18.340	0.000
4	79	20.122	20.122	0.000
5	86	21.905	24.295	0.105
6	93	23.687	25.913	0.105
7	100	25.469	27.552	-0.105
8	107	27.251	29.207	-0.105
9	121	30.816	30.816	0.000
10	128	32.598	32.598	0.000
11	135	34.381	34.381	0.000
12	142	36.163	36.163	0.000
13	149	37.945	37.945	0.000
14	156	39.728	41.094	0.105
15	163	41.510	42.820	0.105
16	170	43.293	44.550	-0.105
17	177	45.075	46.284	-0.105
18	189	48.131	48.131	0.000
19	196	49.913	49.913	0.000
20	203	51.696	51.696	0.000
21	210	53.478	53.478	0.000
22	217	55.261	55.261	0.000
23	224	57.043	57.043	0.000

Table 6.6: Geometrical data about the CDC. There are a total of 3240 straw tubes in the CDC. The listed radii are at the center (length-wise) of the chamber and at the end plates. It should be noted that the stereo wires have a smaller radius at the center than at the end plates.

The choice of gas also plays a significant role in the chamber's performance due to the 2.24 T magnetic field. In order to study this, the GARFIELD program [89] has been used to compute electrostatic properties of the straw tubes, both with and without the magnetic field. The results of this work can be summarized in reference [91]. Figure 6.34 shows an electrostatic calculation for a tube with the wire well-centered in it. Figure 6.35 shows GARFIELD calculations for two tracks going through a straw tube in three different gas mixtures. The three gas mixtures are Ar(30%)-C₂H₅(20%)-CO₂(50%), Ar(90%)-CO₂(10%) and Ar(50%)-C₂H₅(50%). While in all three cases the time-to-distance relationship is well defined, the longer drift distances of the spiraling tracks introduce a large diffusion contribution to the total resolution. The diffusion resolution, σ_L is also dependent on the gas. Pure argon has an extremely poor resolution, while pure carbon dioxide has a very good resolution. Finally, it is desirable to collect the electrons as quickly as possible. A slow gas, or a very long drift distance can easily push the collection time over a micro second. For this reason, the Argon-Ethane mixture shown in the lower two plots of Figure 6.35 is an inappropriate mixture. Investigations are ongoing to identify mixtures that will satisfy the all of the requirements. To indicate the advantage of good electrostatics, Figure 6.36 shows what happens to the time-to-distance relation as one goes from zero magnetic field to full magnetic field.

In order to achieve the desired 150 μm resolution in the CDC, we need to account for all possible contributions to the resolution. Table 6.7 summarizes these. Clearly the most important is the diffusion term, which depends on the gas. In order to achieve this, a gas mixture that

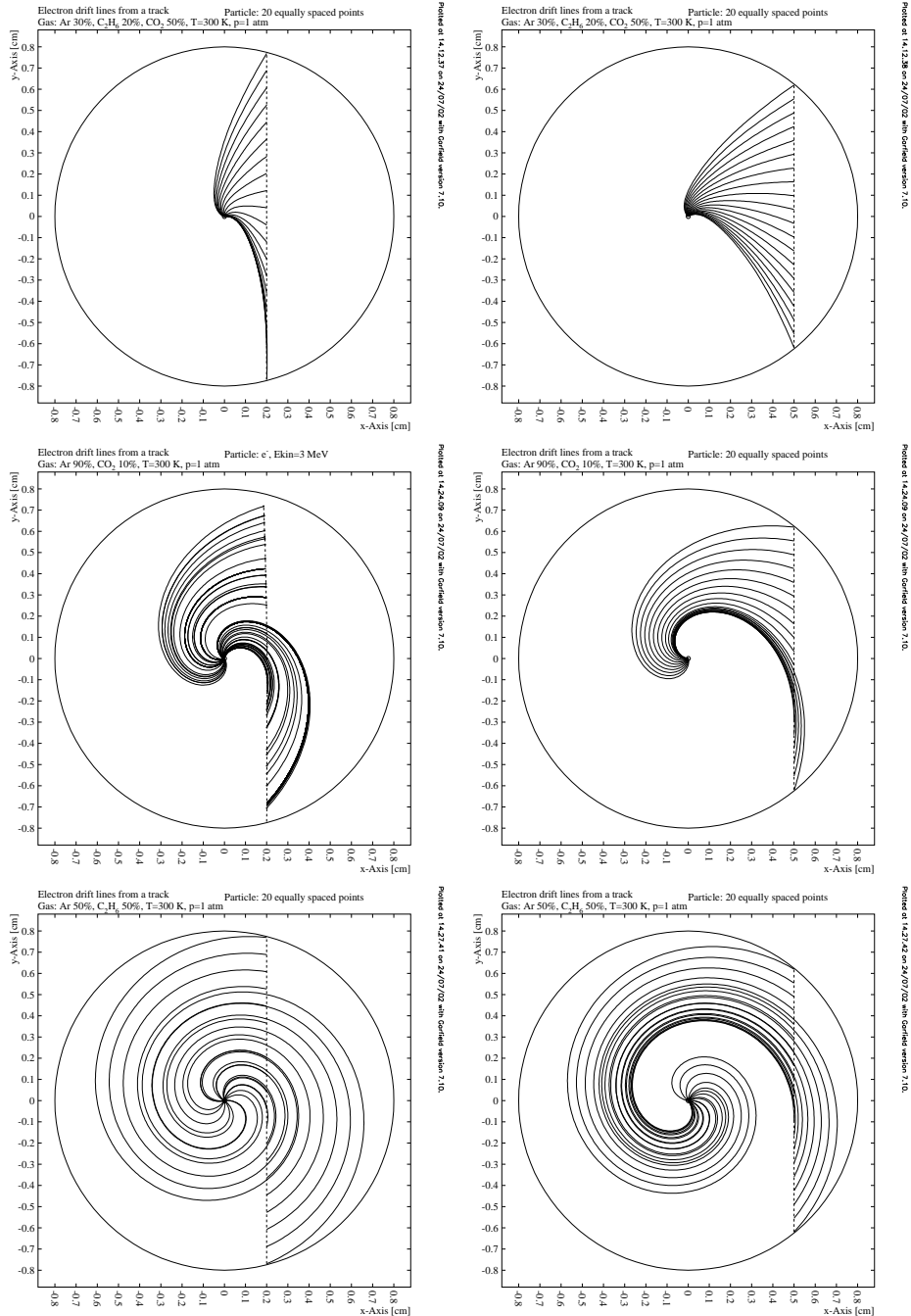


Figure 6.35: Garfield simulations of electrons drifting through a straw tube in the CDC. The curved shape of the tracks is due to the Lorentz angle induced by the 2.25 T magnetic field.

contributes about 120 μm for an average 5 mm drift in a $\sim 2.5 \text{ kV/cm}$ electric field needs to be used. Many gas mixtures satisfy this requirement. The next largest contribution is the gravitational sag. This scales with the length squared, and will go down if the chamber is shorter than 2 m. The timing resolution of 45 μm assumes that the signal is digitized using 125 MHz flash ADCs and that a timing algorithm that yields times to about $\frac{1}{3}$ of the digitization are used. Time fitting algorithms that are matched to the pulse shape in chambers usually yield intrinsic time resolutions around 20% of the time bin width.

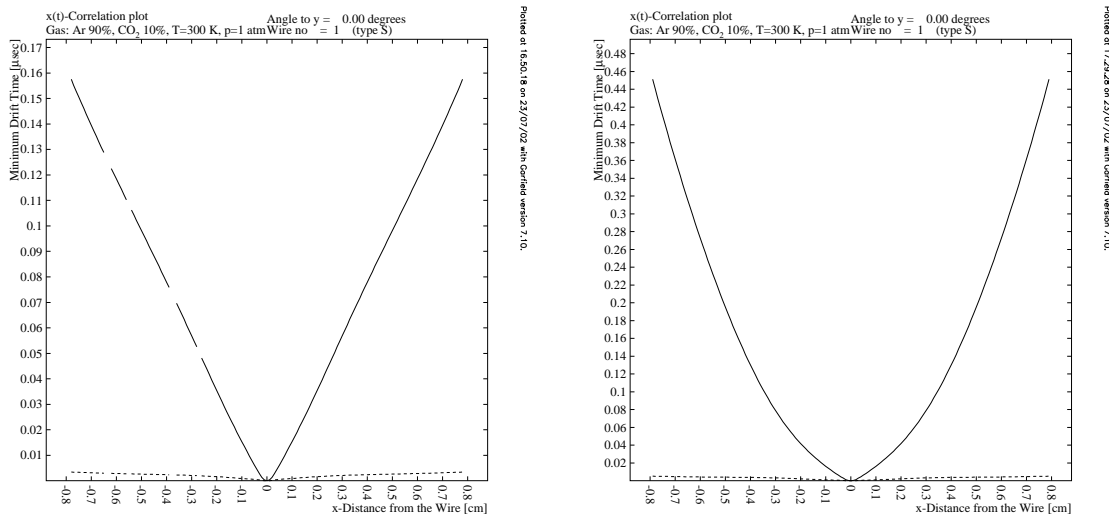


Figure 6.36: Calculated time versus distance in 90% Argon, 10% Carbon Dioxide mixture. **left:** No magnetic field, **right:** full magnetic field.

Effect	Resolution μm
Diffusion σ_L	50 to 200 μm
Geometrical Precision	40 μm
Gravitational Sag	56 μm
Electrostatic Deflection	10 μm
Timing Resolution	45 μm
Quadrature Total	96 to 216 μm
Design Resolution	150 μm

Table 6.7: The estimated contributions to the ultimate chamber resolution from various known effects. These numbers are based on 2 m long, 20 μm diameter, Au-W wires under 50 g tension.

In the construction of the straw-tube chamber, the most technically difficult part involves the stereo layers. Several aspects contribute to this. The holes for these layers need to be drilled at a layer-dependent compound angle. The outside of the tube inserts need to rest flush against the end plates as shown in Figure 6.37 for both the straight-through and the stereo tubes. Such work either requires a multi-axis CNC machine, or a rotary table stacked on top of three sine plates. This machining also limits the minimum thickness of a plate.

There are also difficulties in mounting the straw tubes for the stereo layers. In the final chamber, the tubes are glued to adjacent tubes in the same layer, and adjacent layers are glued together. In order to do this gluing, clam-shell holders need to be built that match the spacing in each layer and hold the tubes in position while they are glued. For the stereo layer, these clam shells need to be built with the same compound angles as the end plates.

In order to understand the issues involved in the building and operating the straw-tube chamber, the Carnegie Mellon (CMU) group has gone through several steps in prototyping the chamber. They are currently completing a full-scale prototype of $\frac{1}{4}$ of the chamber.

To study the behavior of straw tube chambers, a 2 m long chamber with 2 cm diameter tubes has been acquired from the EVA experiment at Brookhaven [92]. A setup which reads out four tubes in the chamber using a 4-channel digital oscilloscope, and then transfers the data to a local computer for analysis has been built. Signals are produced from a $^{44}Ru_{106}$ source, (see Figure 6.38). The β 's from the source are collimated through a 1 mm diameter, 1 cm long tube. The source is placed about 30 cm below the chamber and aligned as shown in the figure. The

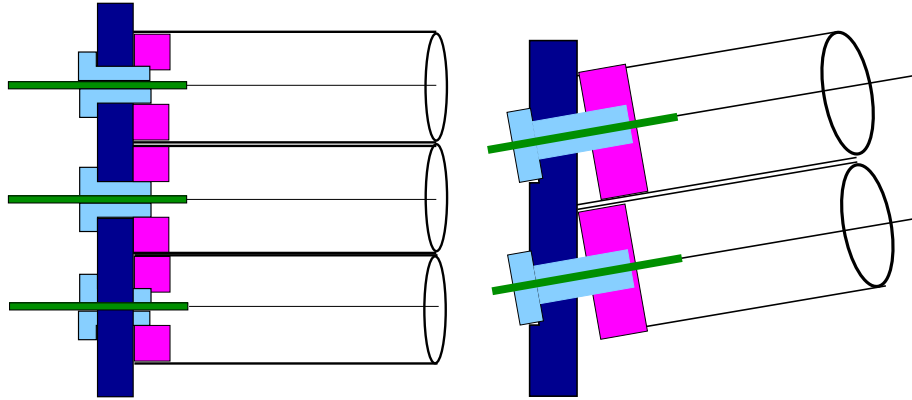


Figure 6.37: Schematic drawings of the feed throughs for both the normal (**left**) and stereo (**right**) wires.

system is triggered on a signal in the upper tube, and events with signals in all four tubes are read out. Gas mixtures can be varied using a locally built three-component gas-mixing system. This allows for detailed studies of the chamber performance in different gas mixtures [93].

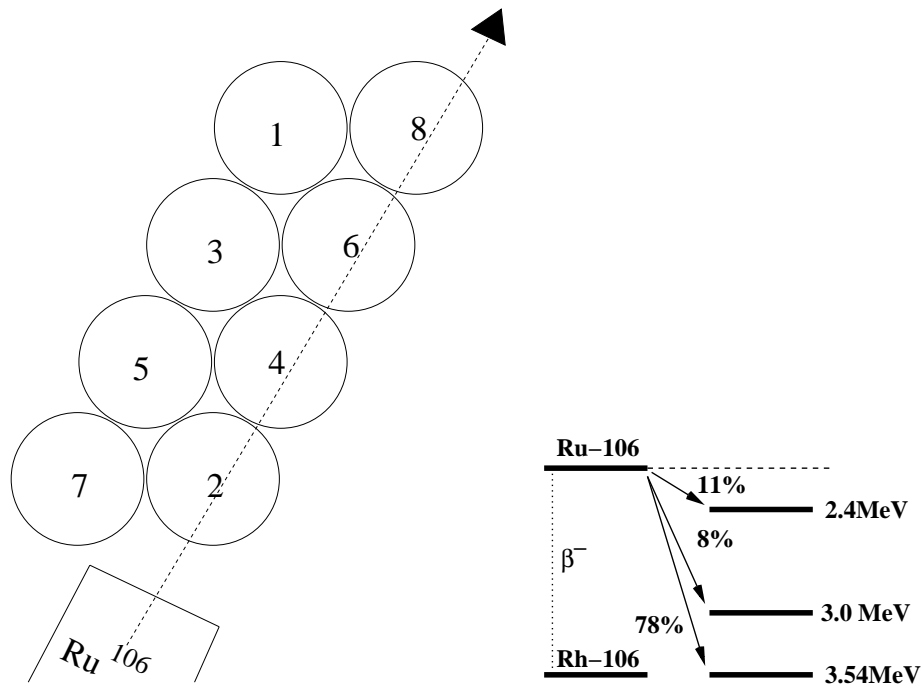


Figure 6.38: Setup of the straw-tube prototype chamber used in studying signals and gas properties. Note the ^{106}Ru source emits primarily 3.54 MeV electrons but there are also up to 1.14 MeV photons.

Figure 6.39 shows signals measured in two different gas mixtures. Currently, there is no way of applying a large magnetic field to the straw tubes. This makes detailed studies of the Lorentz angle only possible through simulation which is currently underway using the GARFIELD [89] program.

In order to build the full-scale prototype, software was written that computes the necessary compound angles at each end plates, and then turns them into machining instructions. An example of the visual output of this program is shown in Figure 6.40 which shows the drilling

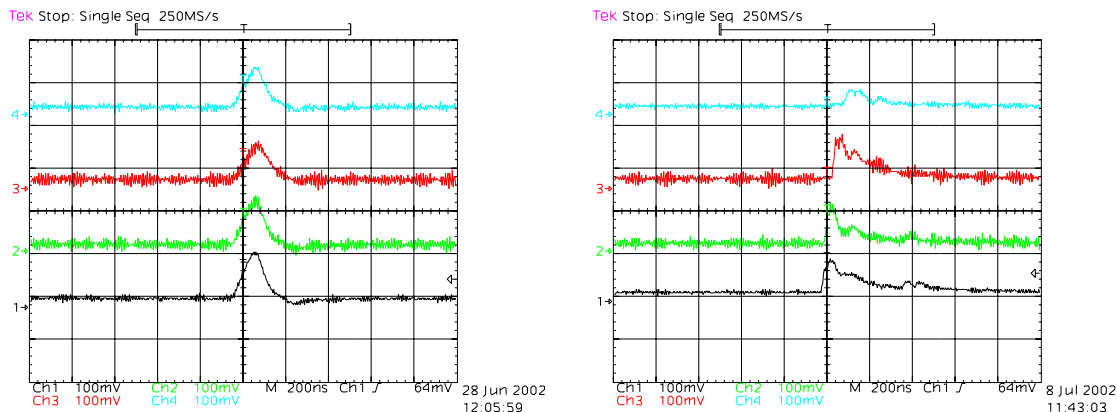


Figure 6.39: Signals observed in the straw-tube chamber for two different gas mixtures. **left:** 50% Argon, 50% Ethane at 2050 V **right:** 90% Argon, 10% Carbondioxide at 1800 V.

pattern for the down-stream end plate. Due to the mills available at CMU, two end plate sections each representing $\frac{1}{8}$ of the chamber were made. These were then connected together and the resulting quarter-end-plate sections were sent to JLab to be measured [94]. While this process led to a number of improvements in the construction technique, it was finally concluded that maintaining sufficient accuracy over eight sections that needed to be connected together would probably not be possible, and it would make more sense to contract out the end plate fabrication to industry.

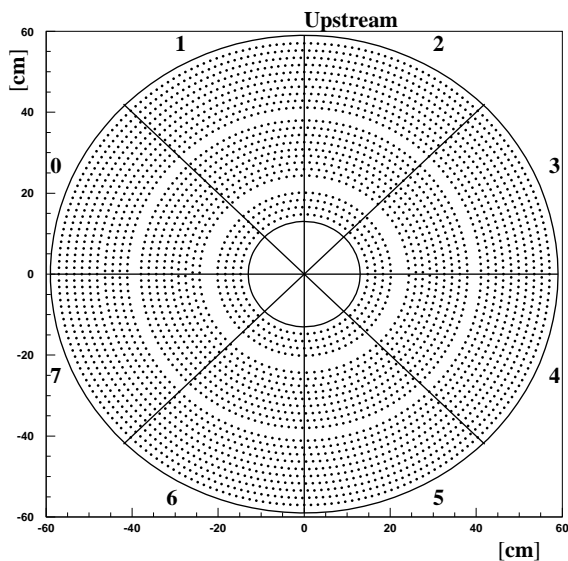


Figure 6.40: The position of the 3240 holes that need to be drilled in the downstream end plate of the CDC. The gaps in radius after layers 4 and 13 are due to the layers just beyond these being stereo wires.

An problematic issue that is common with straw-tube chambers is the conductive glue joints that both hold the straws to the feed throughs as well as the feed throughs to the chamber end plates. Careful examination of an existing straw tube chamber from the Brookhaven EVA experiment showed that all of these joints tend to develop leaks over time. In order to try to alleviate this leak problem, a detailed study of many conducting and non-conducting epoxies

was carried out to see if a good glue could be found. The conclusion of this work was that the particular choice of glue did not matter. Instead, the act of inserting one part of a feed through into another part tended to scrape much of the epoxy off the contact surface. This led to a joint with many weak spots that over a short period of time, developed leaks.

Upon careful study of this, it was decided that the only way to guarantee a good glue connection was to develop a system in which one is certain the glue is actually making solid contact with both surfaces. The result of this is a feed through system as shown in Figure 6.41. The *donut* is a small tube with a small *glue trough* machined into its perimeter. From one end of the donut, a small *glue port* is drilled from the outside to the *glue trough*. Once the donut has been inserted into the straw tube, a known amount of conducting epoxy can be injected through the *glue port* into the *glue trough*. The strength of the resulting glue joint is solid, independent of the tested epoxies. In fact several test sells have maintained several psi overpressure for nearly nine months without leaking.

Into the donut, it is necessary to glue the insert that both holds the straw tube the chamber end plate and holds the crimp pin. In order to guarantee a good glue joint between the donut and the insert, a small *glue lip* has been machined on the tip of the insert. If a uniform coat of glue is applied to the outside of the *insert*, then when it is inserted into the donut, the epoxy tends to collect in both the *glue lip* and between the *insert* and the chamber end plate. Exactly where we need it to guarantee a good epoxy seal. Using these specially designed feed through systems, we are able to obtain a conducting gas-tight joint with all conducting epoxies that we have tried.

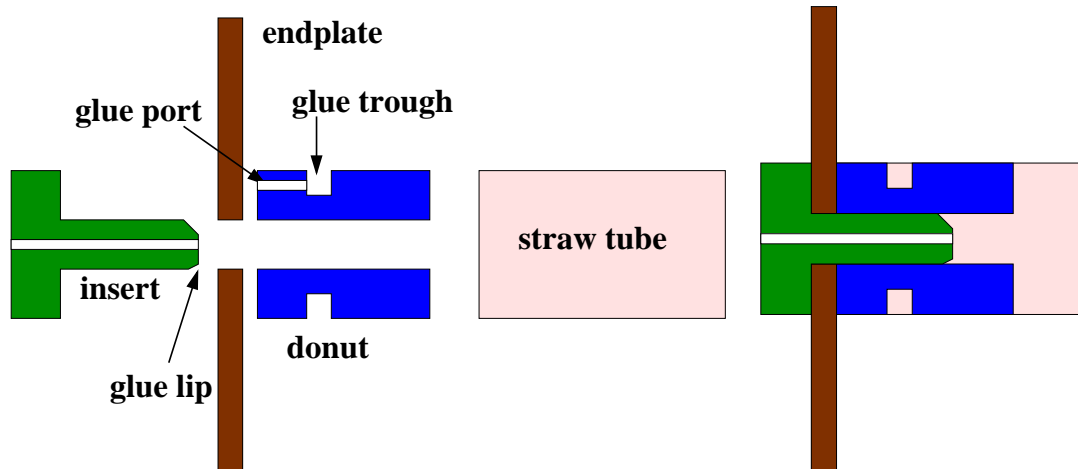


Figure 6.41: The CMU designed feed throughs which provide a solid glue joint between the straw-tube and the end plate. The left-hand figure shows an expanded view, while the right-hand shows the feed throughs in the chamber end plates.

Figure 6.42 shows several photographs of the prototype straw-tube chamber being built at CMU. Four tubes per layer are being put into this chamber, with particular emphasis on making sure that we have both the transition from straight to stereo and from stereo back to straight layers. During construction, wire tension has been carefully monitored. Summaries of tests that have been performed during the construction of the CDC can be found in reference [95].

6.4.4 Forward Drift Chambers

The Forward Drift Chamber system (FDC) is used to track charged particles coming from the GLUEX target with polar angles up to 30° . Tracks at angles greater than 10° also pass through the CDC detector and its associated downstream endplate. Due to the spiraling trajectories of the charged particles and the high multiplicity of charged tracks passing through the FDC, it is crucial for this system to be able to provide a sufficient number of measurements with

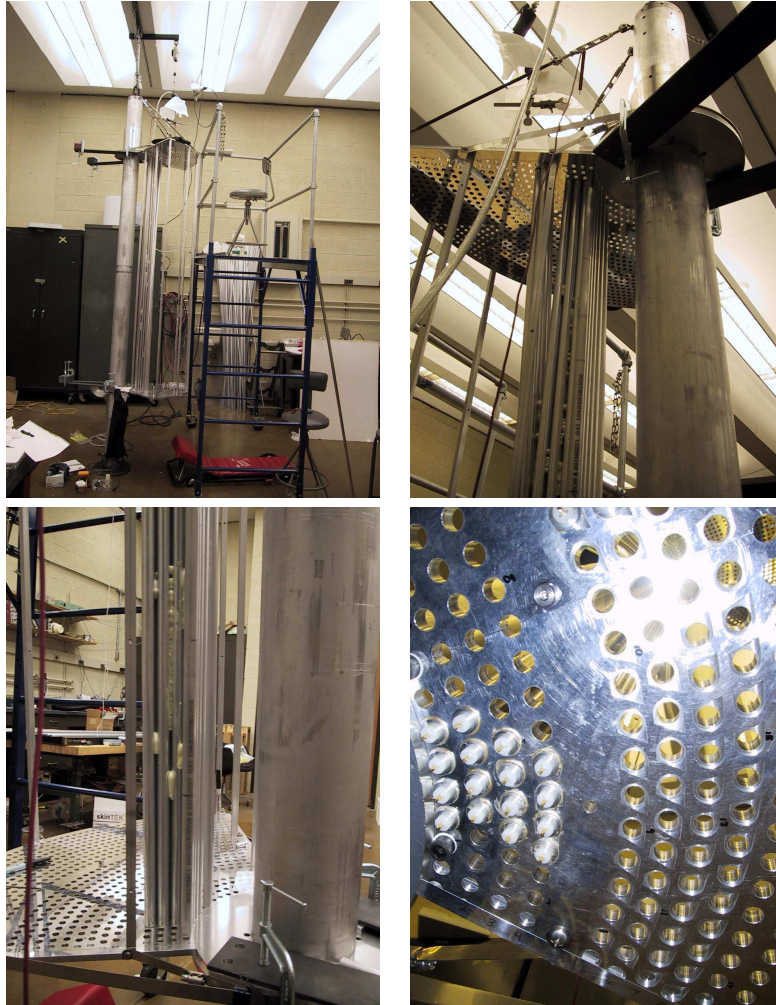


Figure 6.42: The upper-left picture shows the prototype chamber suspended and in position to string wires. The upper-right picture shows several partial layers of tubes glued into the prototype CDC. The lower-left picture shows the same tubes at the lower plate. The lower-right picture is taken from under the lower plate showing several crimped wires in the chamber.

appropriate redundancy to enable linking of the hits from the different tracks with high accuracy, while providing good spatial resolution with reasonable direction information. Current studies with the *HDFast* Monte Carlo program indicate that track hit coordinates should be measured to an accuracy of $150\ \mu\text{m}$ in order to achieve the desired momentum resolution for the charged tracks in the final state.

In the current detector design, the FDCs include four separate but identical disk-shaped planar drift chambers (MWDC's) as shown in Fig. 6.27. Each package will include six layers of alternating anode and field-shaping wires sandwiched between planes of cathode strips. The total thickness of each package is estimated to be roughly $0.15\ \text{gm}/\text{cm}^2$. Neighboring wire planes will be rotated by 60° with respect to each other in order to improve track reconstruction decisions on the corresponding anode wire left/right ambiguities, hence improving the overall resolution. By charge interpolation of the electron avalanche image charge in the cathode strip readout, spatial resolutions at the cathode planes are expected of better than $150\ \mu\text{m}$.

The orientation of the cathode strips on either side of the wires has yet to be decided. The optimal resolution of the hit coordinate along the wire direction is obtained when the cathode strips are perpendicular to the anode wires. In this configuration there is no quantization of the

position measurement resulting from the discrete nature of the anode wires (i.e. the cathode measurement in the coordinate perpendicular to the wires simply locates the wire position). The issue of the optimal electrode configuration for the FDC chambers will ultimately be answered for GLUEX from studies of a prototype cathode readout chamber that is currently being tested at Jefferson Laboratory (discussed later in this section). In the current FDC system design, the cathode strips on either side of the anode plane are arranged in a U and V geometry at $\pm 45^\circ$ with respect to the wires. This technique of employing a stereo angle may prove valuable in separating and assigning multiple hits within a chamber to the different tracks.

The basic chamber element is a disk of outer radius 60 cm, where the wires are strung as cords across the chamber as shown in Fig. 6.43. With a wire-to-wire spacing of 5.0 mm, each chamber plane will contain 119 anode wires. In addition, there will be double this number of cathode strips on each cathode plane. This amounts to 595 channels per FDC chamber element and 3570 channels per FDC chamber package.

The cathode readout as presently planned will employ 125 ps F1 TDCs for the anode wire drift time readout and 125 MHz FADCs for the cathode readout. This would enable commonality with the readout electronics planned for the other GLUEX detector subsystems. Note that with a clock rate of 125 MHz on the FADCs, time fitting algorithms matched to the chamber pulse shape can be employed to provide a time resolution of ~ 2 ns (amounting to $\sim 40\%$ of the time bin width). This timing information from the cathode signals would aid in pattern recognition of multiple tracks passing through the chamber volume. We are also exploring options with FADCs with slower clock rates. This could in principle reduce the electronics costs significantly if we can accept the poorer time resolution.

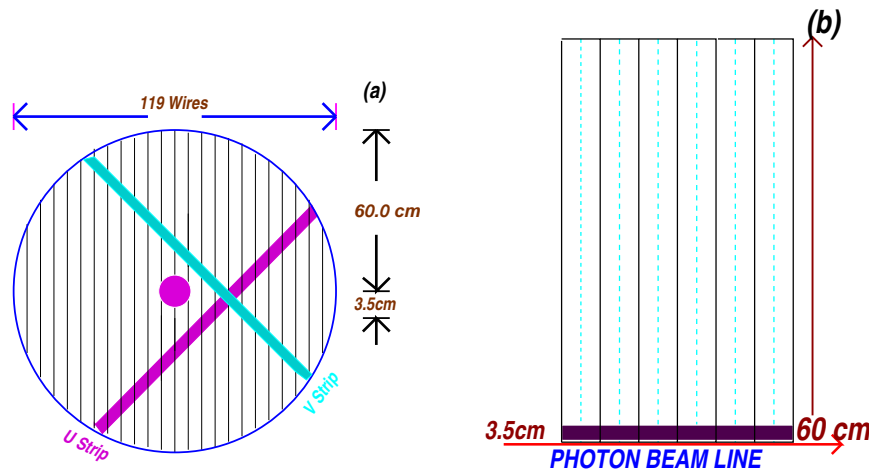


Figure 6.43: A front (a) and side (b) sketch of an FDC package. In (a) the wires are schematically indicated as the vertical lines. The U cathode strips are in front of the wires and the V cathode strips are behind the wires. The field-shaping wires are not shown. In (b) a side view of the upper half of a six-chamber package is shown. The wire planes are shown as the dashed lines, while the cathode planes are shown as the solid line. Ground planes between adjacent chambers are not shown.

The wires that cross through the beam line require special treatment to handle the otherwise unmanageable rates. Several possibilities are currently being considered. The first is to deaden the wires out to a radius of ~ 3.5 cm by placing a material such as Styrofoam around them or to include support structures around the beam line to remove the wires entirely from this vicinity. The final decision will be based on background and design studies.

The primary development issues associated with the FDCs that must be addressed are factors affecting the intrinsic resolution of the chambers, along with the mechanical and electronics

layout. The goal is to construct a tracking detector that meets the required design specifications and has a long life time, a uniform and predictable response, a high efficiency, and is serviceable in case of component failure.

FDC Monte Carlo Studies

The initial specifications for the layout of the FDC system have been studied within the framework of the *HDFast* Monte Carlo. The goals of these studies were to consider the basic number of FDC chamber packages within the solenoid and to consider the number of wire planes per package.

For these studies, pions with momenta between 0.25 and 4.0 GeV and angles from 5-10° were generated and the momentum uncertainty in the form of $\delta P/P$ was studied as a function of momentum. Fig. 6.44(a) shows results comparing a 3-package vs. a 4-package configuration (with packages equally spaced along the beam line). Here the preliminary results make it apparent that the single track resolution, if all cathode and anode positions can be resolved to 150 μm , is improved by roughly a factor of 2 (for pion momenta above 2 GeV/c) with the 4-package configuration. Although the resolution decreases with increasing momentum, it worsens at a noticeably slower rate for the 4-package configuration. The tracking system design parameters can be met with such a 4-package configuration. However, it is the redundancy that the fourth package provides that will be crucial in disentangling multiple charge particle hits and background within the readout time window.

Fig. 6.44(b) shows results for a 4-package FDC system with each package containing either 4, 5, or 6 wire planes. Here the 4-layer design yields a resolution about 20% worse than for the 5 and 6-layer designs. Although the resolution of the 5 and 6-layer packages are about the same, the 6-layer design has been shown to improve pattern recognition for multiple hits within a chamber.

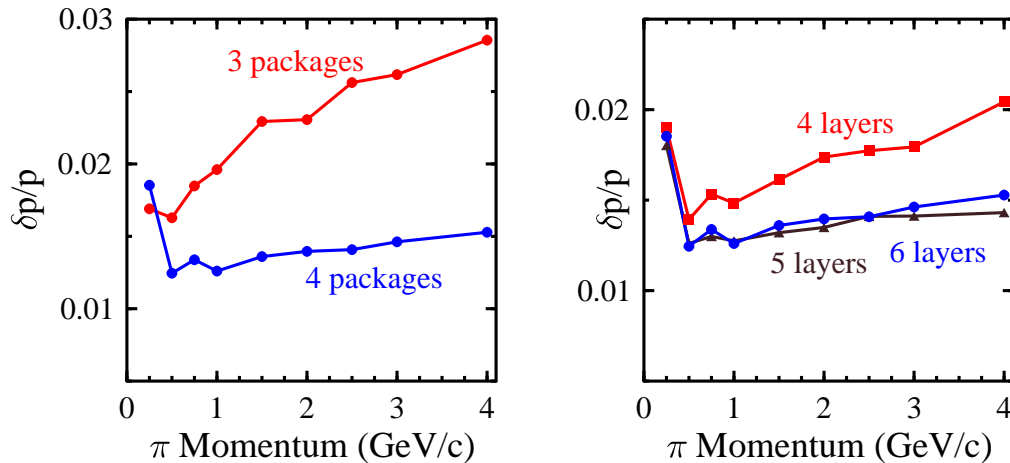


Figure 6.44: Monte Carlo studies comparing the FDC resolution in (a) a configuration with three packages vs. four packages and (b) a 4-package configuration with 4, 5, and 6 wire planes per package.

At the present time the Monte Carlo work is proceeding in earnest to perform detailed systematic studies of the FDC design with realistic backgrounds in the chambers. This will enable final decisions to be made regarding the number of chamber packages, the number of wire planes, the optimal rotation between neighboring planes, the number of cathode strips and their segmentation, and the optimal z -positions of the chambers. Also note that as discussed in Section 6.4.1 for the CDC, the final z -extent of the straw tube chamber has not been finalized. In this case and others, the design of the CDC and FDC systems must be considered in concert. Of course the final resolution for charged tracks is firmly connected to the design and performance of *both* the CDC and the FDC tracking packages.

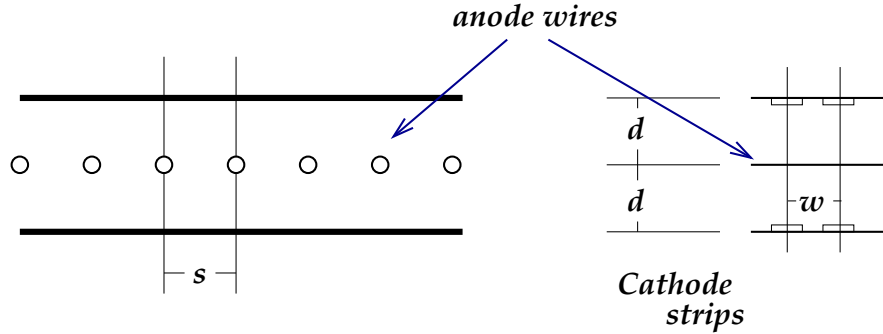


Figure 6.45: Schematic diagram of a typical cathode strip chamber.

Cathode Strip Chambers

Cathode strip chambers (CSC) are typically multiwire proportional chambers (MWPCs) with a symmetric drift cell in which the anode-cathode spacing d is equal to the anode wire pitch s (see Fig. 6.45). In these chambers the spatial resolution of the anode readout is limited to roughly $s/\sqrt{12}$ (RMS). In a CSC the precision coordinate is obtained by measuring the charge induced on a segmented cathode by the electron avalanche formed on the anode wire as shown in Fig. 6.46(a). For the case of multiple tracks, a second segmented cathode rotated at an angle with respect to the first cathode can also help to reduce multi-hit ambiguities as shown in Fig. 6.46(b). The stereo technique is superior to the alternative of reading out only one cathode plane and a hit wire number in that multiple hits on a single wire may be resolved.

The optimum cathode readout pitch w is determined by the width of the induced charge distribution. It has been shown by several groups that minimal differential non-linearity ($\sim 1\%$) is achieved when $w/d \approx 1$ (e.g. [96]). This ratio is employed in the current FDC design, although optimization studies are underway with our prototype cathode chamber. Other groups [97] have been able to construct cathode chambers with larger w/d ratios while maintaining acceptable resolution and minimal differential non-linearity by using intermediate strips between cathode readout nodes that are capacitively coupled to their adjacent readout strips as shown in Fig. 6.47. This option, which can significantly reduce the associated readout costs, is also being considered in the FDC design studies.

Simulations from Ref. [96] have shown that resolutions of $25 \mu\text{m}$ for the precision coordinate in a CSC could be achieved for minimum-ionizing tracks if the electronics and readout could be provided with noise and inter-channel gain variations of less than 0.5% of the nominal pulse height. The primary factor limiting the spatial resolution of a cathode chamber is the electronic noise of the preamplifier. Other factors such as the uncertainty in the gain calibrations and cathode plane distortions should also be considered as well. The precision in the determination of the position of the induced charge depends linearly on the signal-to-noise ratio. Note that preamplifier noise is dominated by the input capacitance and that optimal capacitive coupling requires that the inter-strip capacitance be much larger than the capacitance of a strip to ground [97]. Operation within a realistic experimental environment will result in resolutions much closer to our design goal of $150 \mu\text{m}$.

An interesting question regarding cathode chambers is the change in system resolution when they are also employed as drift chambers (MWDCs), specifically horizontal drift chambers. The principles of operation of a MWDC are such that the best position resolution is achieved when the first electrons that reach the anode wire drift along field lines in the plane of the wires. If we consider a GARFIELD calculation [89] of the field lines for such a chamber (see Fig. 6.48(a)), the first electrons to reach the anode wire will most certainly arise from other locations within the drift cell. This gives rise to non-linearities in the space-time correlation that strongly degrade the position resolution. In order to improve the field configuration for the MWDC operation, field-shaping wires can be included within the anode plane between each anode wire. This can

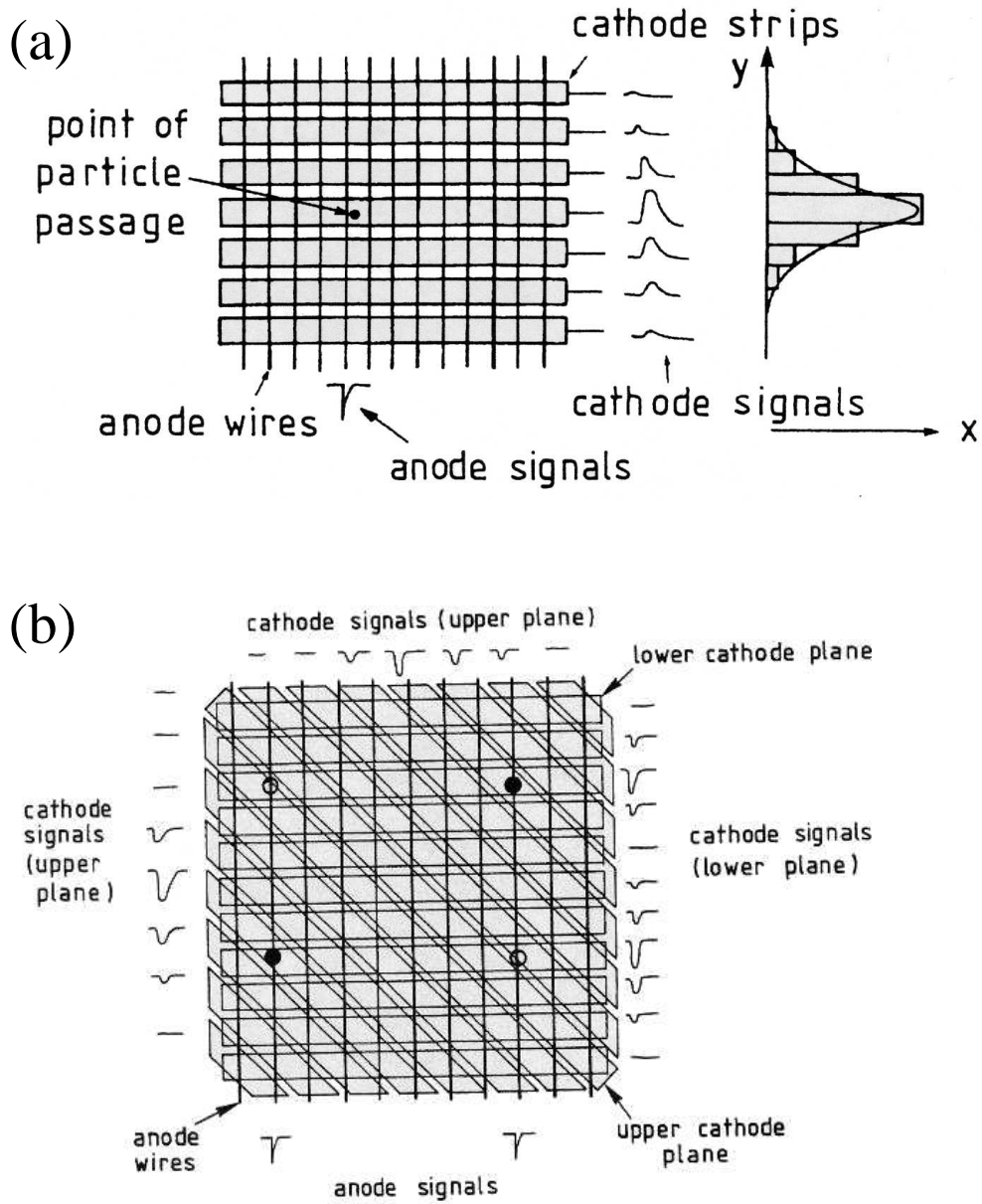


Figure 6.46: Illustration within a typical MWPC of (a) the cathode readout and (b) the resolution of ambiguities within a CSC for two particle hits.

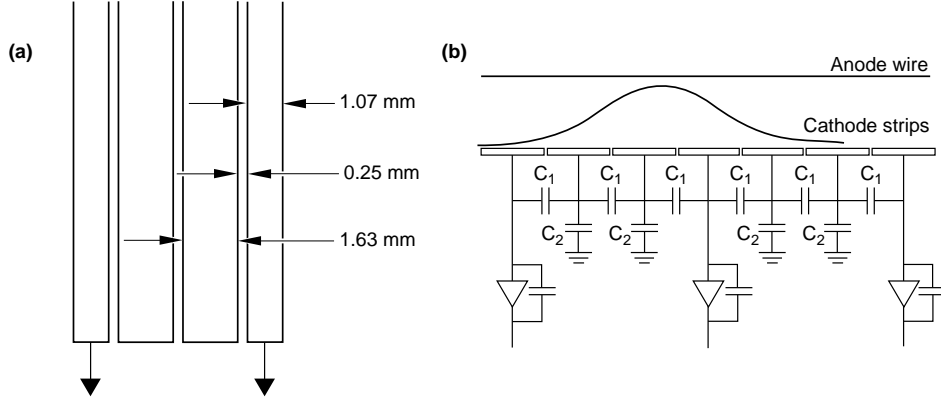


Figure 6.47: (a). CSC layout with a modified cathode strip layout using readout and intermediate strips (from the ATLAS detector). (b) The equivalent circuit highlighting the capacitive interpolation using the two intermediate strips.

clearly improve the field configuration as shown in Fig. 6.48(b).

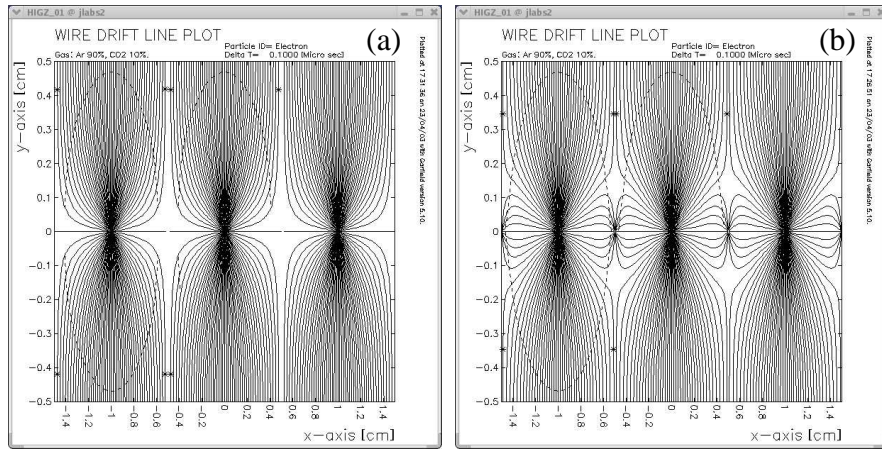


Figure 6.48: GARFIELD calculations of electric field lines (for a $B = 0$ field configuration) within a square drift cell for a 90% argon - 10% CO_2 gas mixture for electrode configurations without (a) and with (b) field-shaping wires.

It is not known at the current time how inclusion of field-shaping wires will affect the cathode position resolution. One of the central questions that we are investigating through our R&D program for the FDC system regards the optimal electrode structure in our cathode chambers. Specifically we are seeking to fully understand the trade-offs between timing resolution from the wire planes and spatial resolution from the cathode planes. However, with inclusion of the field-shaping wires and maintaining a square drift cell, in order to achieve optimal resolution, the number of cathode strips on each cathode plane increases by a factor of two relative to an anode wire only plane design.

The basic algorithm to determine the cathode position of the charged track is to fit the charge distribution across the cathode plane. This amounts to determining the position of the center of gravity using the ratio of the first and second moments of the charge distribution on the plane of the strips from [97]:

$$x_{c.g.} = \frac{\sum_{i=1}^N x_i q_i}{\sum_{i=1}^N q_i}, \quad (6.11)$$

where N is the number of strips involved, $x_i=iw$ is the strip coordinate, and w is the pitch of the cathode readout. If the charges q_i on each strip are measured with an RMS error of σ , then with $Q = \sum_i q_i$, the uncertainty in $x_{c.g.}$ is given by:

$$\sigma_{c.g.} = \frac{\sigma}{Q} \sqrt{2 \sum_i x_i^2} \quad (6.12)$$

or

$$\sigma_{c.g.} = \frac{\sigma}{Q} \sqrt{2w^2 + 2(4w^2) + 2(9w^2) + \dots} \quad (6.13)$$

Therefore the resolution depends on the number of strips used. Monte Carlo simulations and operational experience from different groups have shown that the optimum number lies between three and five strips. The position resolution is poor when only one or two strips are present as there is not enough information, while it increases slowly when more than five strips are used. The resolution function in this case also includes the additional electronic noise from each strip. Here there must be an optimization of chamber resolution factoring in the desire to minimize the number of readout channels to contain costs.

Resolution Effects

Resolution degradation of cathode chambers comes primarily from two sources, tracks inclined from the normal to the face of the chamber and Lorentz angle effects. In both cases the spatial resolution is degraded because the avalanche charge is distributed non-uniformly along the anode wire due to the energy loss fluctuations in the gas. The cathode position resolution is optimum when the avalanche is formed at a single point along the wire. A finite spatial extent of the anode charge results in a resolution degradation \mathcal{D} . Studies of the PHENIX cathode chamber [98] have shown that \mathcal{D} goes as:

$$\mathcal{D} = 0.16d \tan \theta, \quad (6.14)$$

where d is the anode-to-cathode spacing and θ is the angle from the normal to the face of the chamber.

Skewed or non-local charge distributions along the anode wire can also be caused by a Lorentz force along the anode wire from the presence of magnetic field components that are not collinear with the electric field of the chambers. The Lorentz effect itself does not result in a systematic shift of the measured coordinate in the cathode plane. It simply results in a degradation of the resolution because of the spread of the charge along the wire.

Gas Considerations

There are several basic requirements that need to be met by the chamber gas that will be used for the FDC system. These include a high drift velocity (50-60 $\mu\text{m}/\text{ns}$), low Lorentz angle ($< 10^\circ$), and for safety, we much prefer a non-flammable mixture. It is important to understand that the performance of a cathode chamber in terms of cathode position resolution is reasonably insensitive to the exact values of the gas parameters. Here variations of the drift velocity or non-uniform drift velocities as a function of E/p (i.e. electric field/pressure) are relatively unimportant. For the same reason, the cathode readout operation is immune to modest variations of temperature and pressure. Variations in gas gain on the order of 20% do not strongly affect the cathode resolution since a relative charge measurement in adjacent strips is involved.

However, the gas mixture and its control are essential to consider carefully for the operation of the MWDC. In order to enable accurate calibrations of the drift times, it is essential that the gas mixture is stable, which amounts to constructing a gas handling system that carefully controls the gas mixture, as well as hall controls to fix the temperature and relative humidity as much as possible.

Detailed studies of chamber performance will be performed with our prototype cathode chamber employing various gas mixtures. A number of gas mixtures have been studied by various groups that have proven suitable for cathode chambers. Most of these gases contain CF_4 in combination with isobutane (C_4H_{10}) or CO_2 . The Lorentz angle is similar for each gas and is about 5° at 0.5 T magnetic field. One chamber-safe gas mixture that has worked well with the PHENIX cathode chambers consists of 30% argon, 50% CO_2 , and 20% CF_4 [98].

Readout Electronics

The primary design issue for the front-end electronics for the FDC system is to maintain a signal-to-noise ratio of better than 100:1 in the presence of a large detector capacitance. Capacitance measurements in detectors are very important because they serve to determine the performance of the detector in terms of the charges induced on the cathodes, gain variations, detector efficiency, etc. They also play an important role in determining the characteristics of the readout electronics. For the FDC chambers the dominant contribution to the capacitance seen by the preamplifiers will be the strip-to-strip capacitance. The capacitance between adjacent strips is given approximately by [98]:

$$C(\text{pF/cm}) = 0.12t/w + 0.09(1+k)\log_{10}(1 + 2w/s + w^2/s^2), \quad (6.15)$$

where t is the strip thickness, w is the strip width, s is the strip separation, and k is the dielectric constant of the backing material (here it is envisioned to be kapton). For the FDC design that is presently considered, this capacitance is roughly 1 pF/cm. Accounting for the total capacitance of the system then forms a basic requirement for the input capacitance for the front-end electronics performance. An additional concern for this design is the coupling of the signals between adjacent strips. Studies of the PHENIX CSCs have shown that appropriate setting of the integration times of the electronics is important to decrease sensitivity to distortions in the induced charge distribution due to inter-strip coupling.

The chamber-mounted electronics for the cathode strip readout will consist of a charge-sensitive preamplifier that drives a pulse-shaping amplifier. The pulse shape will be chosen as a compromise between noise and pileup, both of which degrade the resolution. The electronics must also be designed to minimize cross-talk, particularly to non-adjacent channels. R&D efforts related to selection of the preamplifier and pulse-shaper are just now beginning. However we expect to develop contacts with outside groups who have more experience. We will also work with the Fast Electronics group at Jefferson Laboratory to explore potential options. The preamplifier circuits employed for the prototype cathode chamber employ the same preamplifiers used with the CLAS drift chambers. This choice was made mainly for convenience, and their performance will provide a benchmark for comparison.

FDC Cathode Chamber Prototype

The FDC prototype cathode chamber has been designed primarily to provide us experience with cathode strip chambers. Through detailed study of this prototype we hope to be able to better understand which electrode structure and layout will fulfill the design requirements for the final FDC chambers. The prototype will also provide important insights into the mechanical design, tolerances, construction and assembly techniques, noise immunity, and calibrations that will be important for the final FDC detector design. Some of the elements of the FDC prototype design have descended from the cathode chambers employed in the original LASS spectrometer [99].

A schematic of the FDC prototype chamber is shown in an exploded view in Fig. 6.49. The basic chamber layout consists of two cathode planes with strips oriented at $\pm 45^\circ$ sandwiching a single wire plane. The gas volume is defined by two outer aluminum frames that each include an aluminized mylar window. The active area of the prototype chamber is roughly 20 cm \times 20 cm, and the chamber is about 8 cm thick.

The test chamber has purposefully been designed to act as a test bed for any number of electrode configurations. So far we have wound wire planes consisting only of anode wires

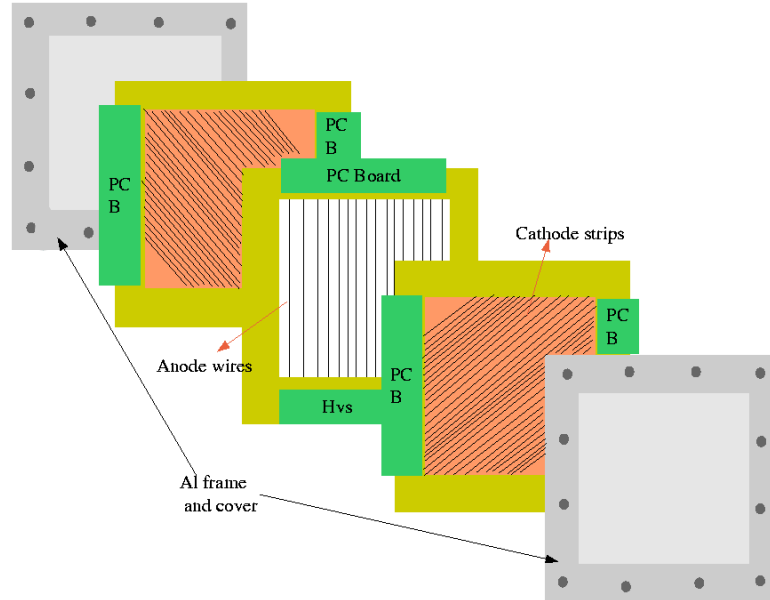


Figure 6.49: Schematic representation of the FDC prototype chamber in an exploded view showing the wire plane, two cathode planes, and the two aluminum window frames.

and planes consisting of alternating anode and field-shaping wires. We have also designed cathode planes of varying rotation angle, varying cathode strip pitch, and varying cathode strip separations. Ultimately each configuration will be studied in order to come to an understanding of the optimal electrode structure for our purposes.

The U and V cathode planes are mirror symmetric with respect to each other. The cathode planes are copper-clad kapton sheets (~ 2 mil thickness) mounted onto 5-mm thick G10 frames. The chamber is designed to operate with the anode wires at positive high voltage, the field wires at negative high voltage, and the cathode strips at ground.

The printed circuit board for the wires was designed to capacitively decouple high voltage from the signals and to route the signals to the output connector. The printed circuit board for the cathodes routes the signals directly to the output connector. The basic circuits on the boards are shown in Fig. 6.50. Small signal routing circuit boards attach to the output connectors on the wire and cathode circuit boards and contain the preamplifiers for each readout channel. The output connects to a shielded twisted-pair line that routes the signals to the readout electronics (FASTBUS 1877 TDCs and 1881 ADCs). The signal readout boards used for the cathodes are essentially the same as those used for the anode wire readout. The only difference in the design is a polarity switch of the cathode signals before sending the signals to the amplifier and the ADC.

Each readout channel has its own associated ‘‘SIP’’ preamplifier. These single-channel transimpedance preamplifiers were originally designed for the Hall B CLAS detector. They have complementary outputs designed to amplify signals by a factor of $2.25 \text{ mV}/\mu\text{A}$. Besides high gain, characteristics of the SIPs include: fast rise and fall times (3 to 4 ns), wide frequency bandwidth, wide dynamic range, and low noise and power dissipation (65 mW).

In total the prototype chamber includes 16 $20\text{-}\mu\text{m}$ diameter sense wires alternated with $80\text{-}\mu\text{m}$ diameter field wires, with a wire-to-wire separation of 5 mm and a strip-to-strip separation of 1 mm. The cathode planes are located 5 mm away from the wire plane. They each include 32 copper strips with a pitch of 5 mm. Three different sets of U and V cathode planes have been designed with strip separations of 0.25 mm, 0.50 mm, and 1.0 mm to allow for the optimal configuration to be determined. Presently the chamber is operating with a 90% argon - 10% CO_2 gas mixture. Photographs of the prototype cathode chamber and the cathode plane itself

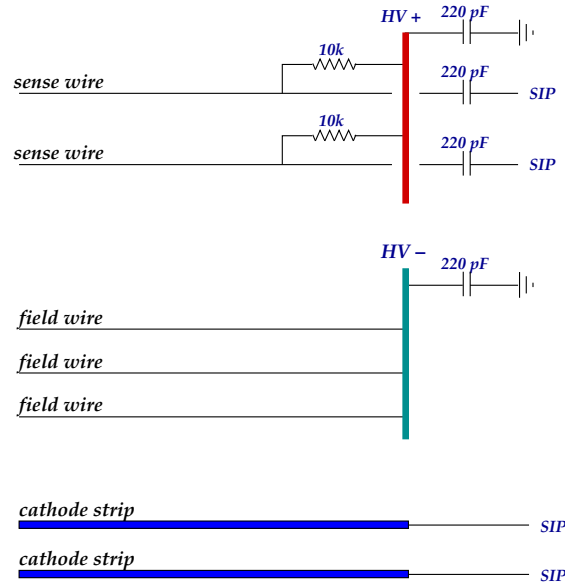


Figure 6.50: Circuit board electronics for the sense and field wires, along with the cathode strips.

are shown in Fig. 6.51.

A set of 19 wire chambers have been borrowed from IUCF in order to assemble a cosmic ray test stand at Jefferson Laboratory. This test stand is being used to define tracks through the FDC prototype chamber. A schematic drawing of the layout of the cosmic ray test stand is shown in Fig. 6.52. This system employs multiple layers of drift chambers above and below the FDC prototype chamber to precisely define the trajectory of an incident charged particle track that can be used to compare against the position measured in the FDC prototype. The configuration of the test stand includes two X layers and two Y layers above the FDC prototype and a matching set of four layers below. This system, once properly calibrated, should be capable of defining a track to roughly $200 \mu\text{m}$ at the location of the FDC prototype. A photograph of the test setup is shown in Fig. 6.53.

At the present time the cosmic ray test stand has been crudely calibrated and we have succeeded in getting readout of the cathode chamber. A look at the first anode and cathode signals from this chamber is shown in Fig. 6.54. So far the detector is operating quite nicely and an initial characterization of its performance and resolution is in progress.

Based on the results of studies of the first cathode chamber prototype, as well as continued Monte Carlo studies of both the detector and the physics, we will begin working on the design for a second prototype for the FDC system. One of the primary purposes of the second prototype chamber will be to test mechanical support designs for the full-scale chamber and wire planes. This is necessary to avoid electrostatic instabilities and non-uniformities that are known to affect resolution. To illustrate the issue at hand, the gain \mathcal{G} in a proportional counter is given in general by:

$$\mathcal{G} = Ke^{CV}. \quad (6.16)$$

For an operational voltage V , the gain is dependent on the capacitance of the detector C . Thus any variation on the flatness of the cathode plane changes the capacitance of the detector and hence the gain. It also creates field non-uniformities that affect the cathode position resolution. For gain variations of less than 5%, a rough calculation shows that the cathode plane must have less than a ± 5 mil flatness variation.

Various schemes have been employed by different groups to provide mechanical support for the cathode planes in large area chambers. For example, in the so-called *Plug Chambers* used

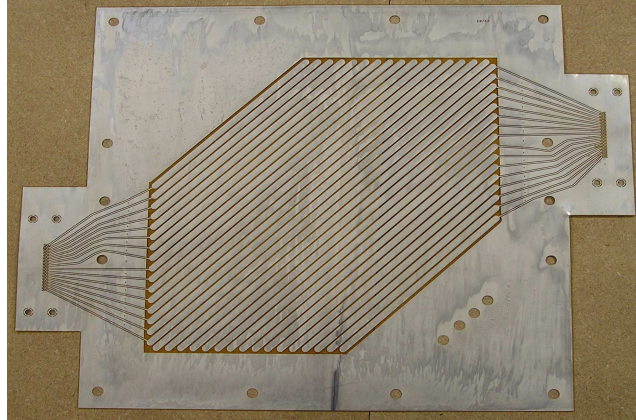
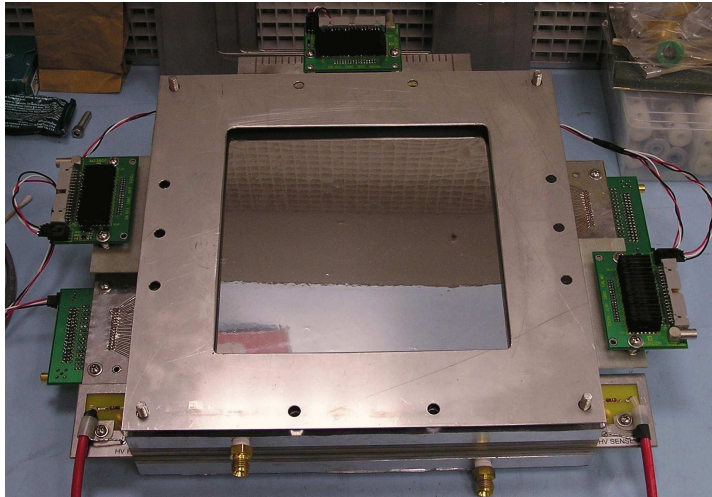


Figure 6.51: (Top) Photograph of the prototype FDC cathode chamber constructed to optimize chamber electrode structures. (Bottom) Photograph of a cathode plane showing the cathode strips.

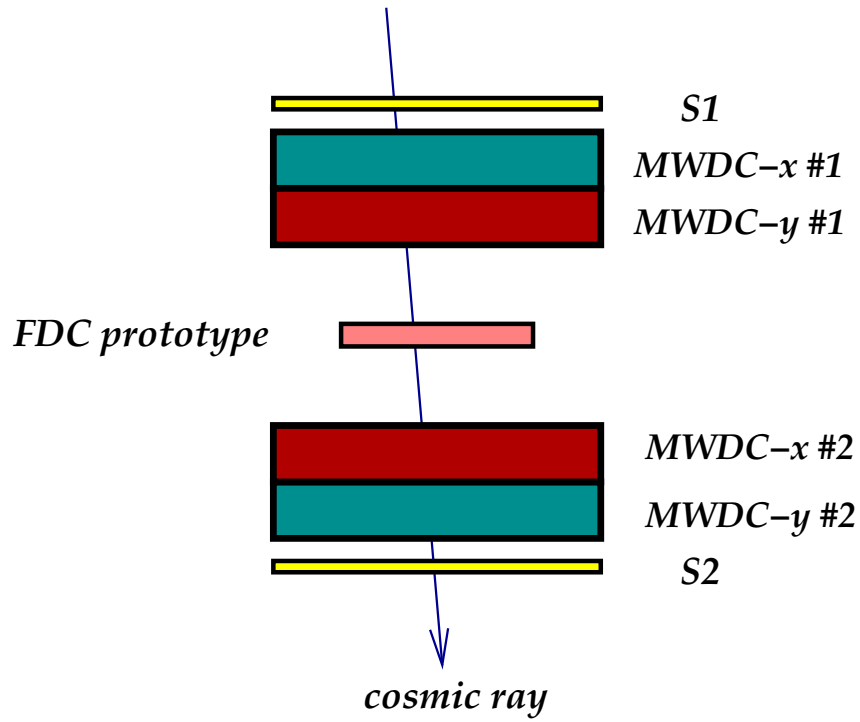


Figure 6.52: Schematic drawing of the cosmic-ray telescope used for FDC prototype resolution studies.

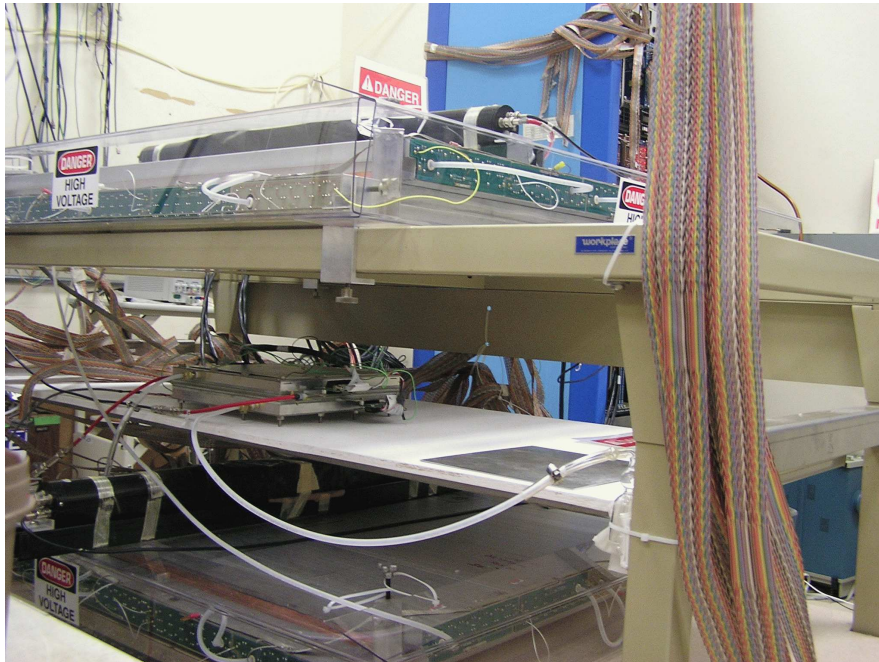


Figure 6.53: Photograph of the cosmic ray test stand set up at Jefferson Laboratory to study resolution characteristics of the cathode strip chambers.

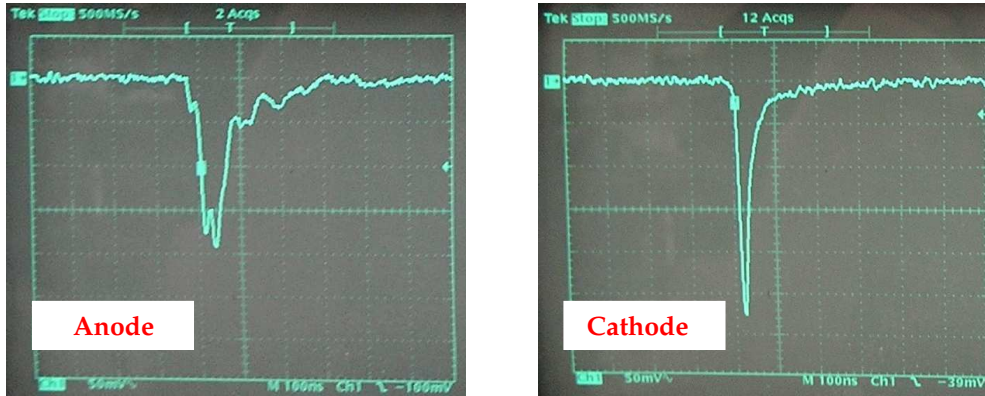


Figure 6.54: Anode (left) and cathode (right) signals from our prototype cathode strip chamber. The electrode structure and layout of this prototype is expected to be very similar to the final FDC design.

in the LASS experiment [99], polyurethane spacers were epoxied onto the cathodes to fix the anode-cathode gap spacing. This and other options are currently being explored.

Another important role for the second prototype chamber is to give us a design test bed for the circuit boards associated with both the cathode and wire planes. We will again seek out contacts with other groups who have constructed chambers of similar design as well as work with the Fast Electronics Group at Jefferson Laboratory in order to minimize R&D lead times.

6.4.5 The Start Counter

The START counter will provide a fast signal which is used in the level-1 trigger of the experiment. For this purpose the time resolution cannot be worse than 4 - 5 ns. As an element of the level-1 trigger, this detector needs an excellent solid angle coverage and a high degree of segmentation for background rejection. Using tracking information the start counter will be able to provide a time resolution of better than 0.5 ns thus allowing us to identify the electron beam pulse associated with the event.

The start counter will consist of a cylindrical array of 40 scintillator paddles (see figure 6.55). The scintillators have a thickness of 5 mm. This will provide a good light output and therefore a good timing signal. The downstream side of the scintillators will be bent toward the beam line in order to increase the solid angle coverage while minimizing multiple scattering.

Each paddle will be coupled at the upstream end to a light guide leading out of the very high magnetic field region. Photo-tubes which can be operated in magnet fields of the order of one to two kilo gauss will be used for readout. Tests with the Hamamatsu system H6614 have shown that the required time resolution can be achieved routinely. As scintillation material we plan to use Eljen Technology EJ200 which is fast and has a large absorption length. The time resolution (σ) for a EL204 scintillator bar, directly coupled to a H6614-01 system, is shown in figure 6.56 as a function of distance from the PMT. This detector is similar to the start detector currently used in CLAS in HALL B at Jefferson Lab.

6.5 Particle Identification

6.5.1 Overview

Particle identification in the GLUEX detector (i.e., the separation of pions, kaons, and protons) will incorporate information from at least four different subsystems – two subsystems in the central region and two in the forward region.

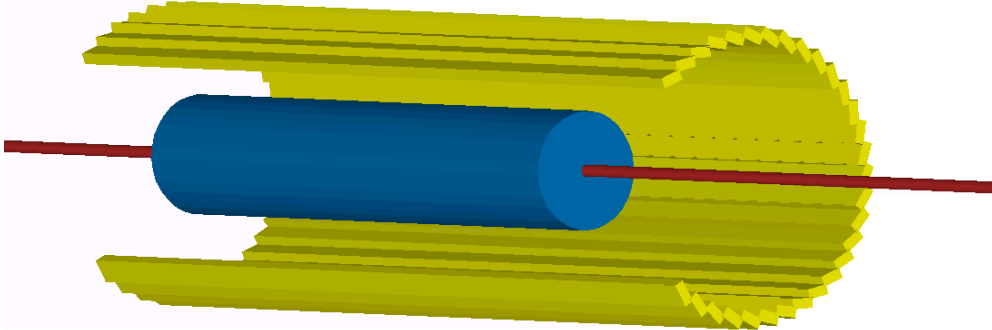


Figure 6.55: Central drift chamber (CDC) with a cylindrical array of scintillator.

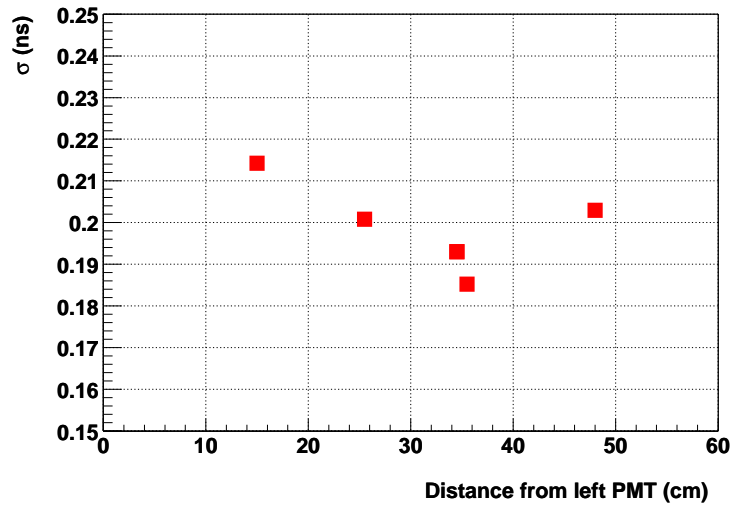


Figure 6.56: The Start Counter time resolution (σ) as a function particle trajectory position along a EJ204 bar with the dimensions $0.5 \times 3 \times 70 \text{ cm}^3$.

1. Low momentum central tracks will be identified using dE/dx measurements from the Central Drift Chamber (CDC).
2. A time of flight measurement from the barrel calorimeter (BCAL) will also provide identification information for central tracks. The CDC and the BCAL working in conjunction will provide an excellent means for identifying recoiling protons from the target.
3. Higher momentum forward-going kaons and pions will be distinguished using a Cerenkov detector. Two possibilities for this detector exist – a threshold gas option (CKOV) using C_4F_{10} , and a Quartz-based DIRC option; each will be discussed in detail in a later section.
4. Time of Flight (TOF) information for forward-going tracks with momenta less than around $2.5 \text{ GeV}/c$ will be provided by a scintillator wall 500 cm downstream of the target.

Once information is gathered from each of these four elements, the information will be combined into likelihoods in order to provide a unified way of making a particle identification decision. The likelihood method will be discussed in section 6.5.4.

To illustrate the overall features of the particle identification, consider the reaction $\gamma p \rightarrow K^* \bar{K}^* p$. This reaction has kinematics that are typical of the reactions to be studied by the GlueX experiment. The $K^* \bar{K}^*$ system is produced peripherally with a t dependence of e^{-10t} . The proton recoils predominantly in the central region with a momentum below $2 \text{ GeV}/c$. The central kaons from the K^* decays range in momentum up to $5 \text{ GeV}/c$; central pions range up to $3.5 \text{ GeV}/c$. Forward kaons and pions have higher momenta, in general, than those in the central region, kaons ranging up to $7 \text{ GeV}/c$, and pions up to $5 \text{ GeV}/c$.

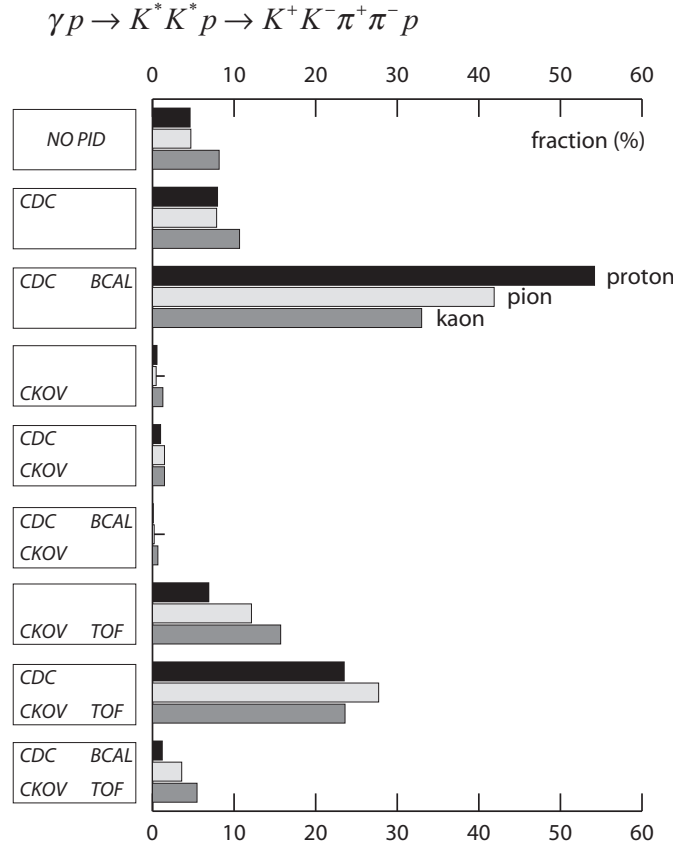


Figure 6.57: The fraction of tracks from the reaction $\gamma p \rightarrow K^* \bar{K}^* p$ detected by different combinations of particle identification elements.

Each of the five tracks in the final state can be categorized according to the particle identification elements it encounters. Figure 6.57 shows the percentage of tracks from $\gamma p \rightarrow K^* \bar{K}^* p$ encountering each of the eight possible combinations of PID detectors. Cases 1 (CDC) and 2 (CDC,BCAL) are purely central tracks; cases 6 (CKOV,TOF) and 7 (CDC,CKOV,TOF) are the dominantly forward tracks. Notice that the proton usually lands in the central region, and larger fractions of the pions and kaons go forward.

In the central region, the CDC and BCAL effectively work together to identify the recoiling proton. Figure 6.58 shows the momentum spectrum of the central protons from $\gamma p \rightarrow K^* \bar{K}^* p$ overlaid with K/p and π/p separations from the CDC and BCAL. For the dE/dx measurements from the CDC, an Argon-based gas was assumed and the resolution was estimated to be 10%. A 250 ps time resolution was assumed for the BCAL, and a typical path length of 2 m was used for the figure. The entire range of the central proton momentum spectrum is well covered. Protons in the forward region also have low momenta and are easily identified by the TOF wall.

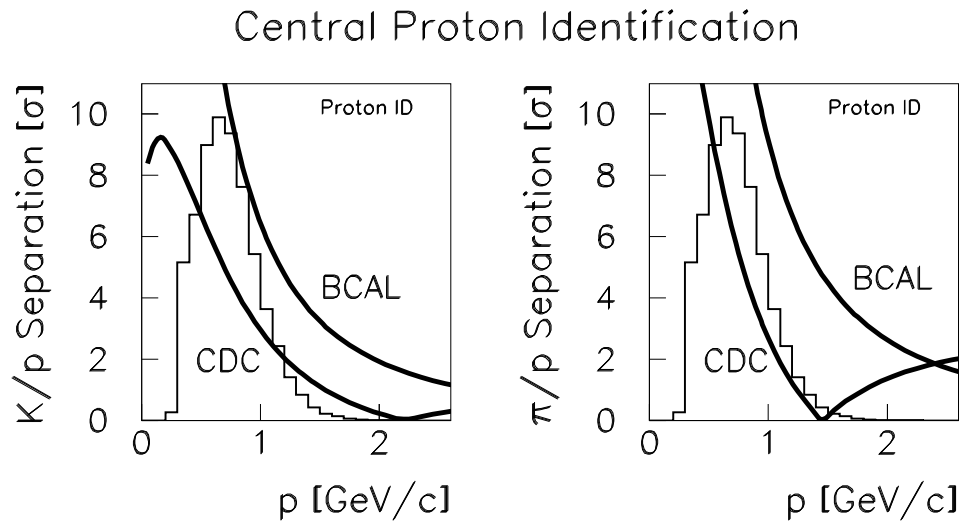


Figure 6.58: Identifying protons in the central region of the detector. The left plot shows K/p separation; the right shows π/p . The histogram in each is the momentum distribution for central protons from the reaction $\gamma p \rightarrow K^* \bar{K}^* p$. The curves are estimates of the separating power (in numbers of sigma) of the CDC dE/dx and the BCAL time of flight measurements.

Central Pion/Kaon Identification

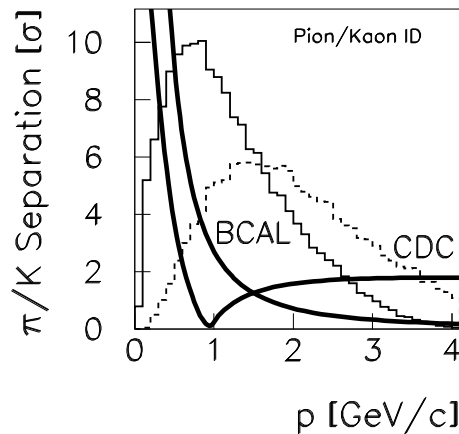


Figure 6.59: Identifying pions and kaons in the central region of the detector. The solid histogram is the central pion momentum spectrum; the dashed histogram is the momentum spectrum of central kaons. The curves are estimates of the separating power (in numbers of sigma) of the CDC dE/dx and the BCAL time of flight measurements.

In addition to the recoiling proton, however, a fraction of the pions and kaons in the reaction $\gamma p \rightarrow K^* \bar{K}^* p$ end up in the central region. Figure 6.59 shows estimated π/K separation curves (using the same detector parameters as above) overlaid on the pion and kaon momentum

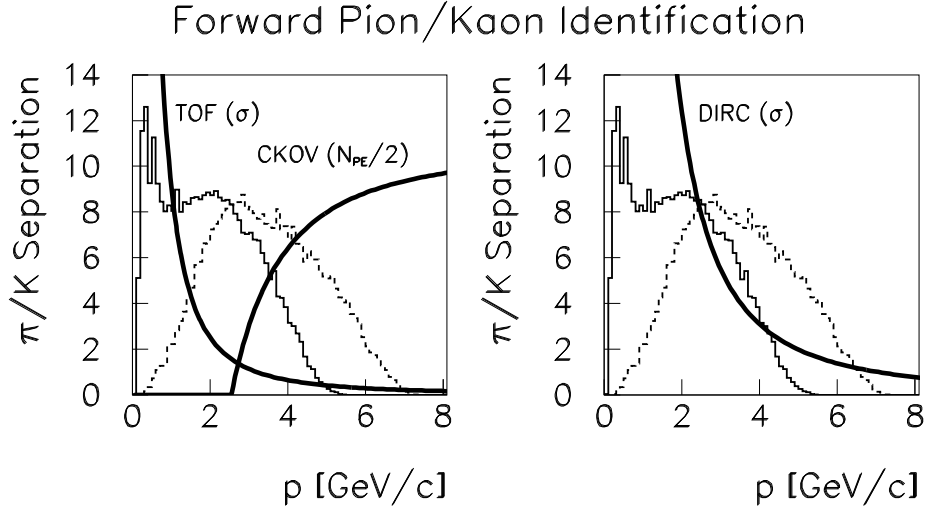


Figure 6.60: Identifying pions and kaons in the forward region of the detector. The left plot shows the gas Cerenkov option; the right plot is for the DIRC option. In each case, the solid histogram is the forward pion momentum distribution; the dashed is the forward kaon distribution. The curves of the left plot are the estimated π/K separations of the TOF and CKOV systems. The TOF π/K separation is expressed in numbers of sigma; the CKOV performance is plotted as the number of expected photoelectrons divided by two. The right plot shows the DIRC π/K separation in numbers of sigma. (Note the TOF will be used in conjunction with either option but is shown only in the left plot.)

distributions. Some fraction of the higher momentum tracks cannot be identified, but the strong separations in the forward region compensate.

The momentum spectra of forward-going pions and kaons from the $\gamma p \rightarrow K^* \bar{K}^* p$ reaction are shown in Figure 6.60. These will be identified by a time of flight measurement from the forward TOF wall in conjunction with either a gas Cerenkov system (CKOV) or a DIRC. The expected π/K separations from each option are overlayed on the momentum spectra. Typical TOF parameters were used in generating the time separation: a detector time resolution of 70 ps, a typical flight length of 5.0 m, and a conservative momentum resolution of 1% and length resolution of 1% added on when projecting different particle hypotheses to the wall.

The performance of the gas Cerenkov system is expressed in terms of the average number of photoelectrons, N_{pe} , for π mesons traversing 80 cm of C_4F_{10} gas with index of refraction $n = 1.0015$. The momentum threshold for π and K mesons are 2.5 and 9.0 GeV/c respectively and the light yield per radiator length is given by:

$$\frac{dN_{pe}}{dx} = N_o \cdot \sin^2 \theta_c = N_o \cdot \left(1 - \frac{1}{\beta^2 n^2}\right) \quad (6.17)$$

and since $n \approx 1$, in the relativistic limit $\beta \rightarrow 1$:

$$\frac{dN_{pe}}{dx} \approx N_o \cdot 2(n - 1) \quad (6.18)$$

N_o is the figure of merit of a Čerenkov counter taking into account all efficiencies in the system and for a counter of reasonably good design $N_o \approx 90 \text{ cm}^{-1}$. Based on this, the average photoelectron yield for the Čerenkov counter will be about 21 in the relativistic limit.

The gas Cerenkov option leaves a significant gap in momentum where the π/K separation is restricted. The TOF separating power falls below 3σ at a momentum near 2 GeV/c , while the pion threshold in the C_4F_{10} gas is 2.5 GeV/c .

The DIRC option, on the other hand, will use a higher index of refraction (Quartz) to make a measurement of the Čerenkov opening angle:

$$\cos \theta = \frac{1}{\beta n} \quad (6.19)$$

The estimated π/K separation of figure 6.60 assumed a resolution on the opening angle measurement of 2.1 mrad. More details on the DIRC will be given in a later section.

Required Design Parameters For the Čerenkov counter, assuming that the inefficiency for detection is given by $e^{-N_{pe}}$, then the efficiency for detecting pions exceeds 95% when the π momentum is above 3 GeV/c . At this momentum the TOF difference is about 210 ps . For 95% (3σ) efficiency to separate pions and kaons with the TOF at this momentum, the time resolution, σ_t should be less than about 70 ps .

dE/dx in the chambers

As described above, there is a subset of the low momentum charged particles which will not reach a time of flight counter, or will reach them after spiraling so many times in the magnet that the TOF information will be very difficult to use. For these particles, dE/dx information from the CDC chamber will be the primary source of identification. Fortunately, these particles all have momenta smaller than about 450 MeV , which is exactly where dE/dx will work the best. This detector has been discussed in an earlier section.

6.5.2 The Time-of-flight System

Barrel Time-of-flight Measurement

The design of the barrel calorimeter is dictated primarily by the available space inside the magnet and the method chosen for photon conversion. Charged particles emitted at large angles to the beam often have low velocity so even moderate time resolution is sufficient to distinguish pions from kaons. The lead/fiber design of the barrel calorimeter provides a large number of scintillator samples as a particle traverses the individual fibers. The KLOE collaboration has demonstrated [100] an RMS time resolution of 252 ps for minimum ionizing particles traversing 19 layers of lead and fiber. This value will be used as an estimate of the performance that can be achieved in the TOF measurement from the calorimeter in HALL D. This detector has been discussed in an earlier section of this report.

The Lead Glass Forward Calorimeter

Located just upstream of the forward electromagnetic calorimeter, the LGD, and downstream of the Čerenkov counter will be the forward time-of-flight system, the TOF. The goal of the forward TOF is to separate K^\pm from π^\pm among forward-going charged particles. The TOF will also provide a forward multiplicity count to be used in the level-one trigger.

Assuming a momentum resolution of about 1% and a particle path length resolution of 1% an overall TOF time resolution of 80 ps should allow for K/π separation at the 3σ level up to a momentum of 2.5 GeV/c . The TOF will consist of two planes of scintillation counters, each 2.5 m long, 6 cm wide and 1.25 cm thick. Each counter will be read out at both ends. The counters in one wall will be oriented perpendicular to the other wall. The total module count is 84 modules and the total channel count is 168 for the number of FADC's, constant fraction discriminators and TDC's.

The scintillator bars need to be 2.5 m long to cover the active regions of the Čerenkov counter. The 6 cm width of the bars is set by the requirement that the overlap of charged particles from the same event at the TOF in any one bar be acceptably small ($< 2\%$). From Monte Carlo simulations of $\gamma p \rightarrow K^* \bar{K}^* p$ it was found that a 6 cm width satisfies the occupancy requirement. (We studied four reactions, but are most vulnerable to this one because of its low

Q value.) Specifically we find a probability of 0.22% that two charged particles go through just one bar in both the front and back planes. The thickness of the scintillation bars, the dimension along the beam direction, is set by the requirement that sufficient light be produced to meet the time resolution requirements, while at the same time minimizing the amount of material in front of the LGD.

Prototype Studies

Extensive prototype studies have been carried out to optimize the TOF system design. Data using scintillation bars of various dimensions and manufacture and various phototubes were collected using a cosmic ray test facility at Indiana University. Data were collected in several data runs with hadron beams at the Institute for High Energy Physics (IHEP) in Protvino, Russia. During the data runs we also explored the possibility of using Čerenkov light in Plexiglas (non-scintillating) bars to exploit prompt Čerenkov light to build a TOF system. Results of the IHEP tests have been presented at various instrumentation conferences and publications [101, 102, 103, 104]. Further beam tests at IHEP are planned using 2.5 m scintillator bars with four elements in each of two walls in early 2005.

Cosmic Ray Test Facility Figure 6.61 shows part of the cosmic ray test facility. A large light-tight box was prepared to accommodate a 2-m long scintillator bar and a cosmic ray telescope consisting of two small scintillation counters that can be positioned along the bar. The scintillation bar under test is read out at both ends with Phillips XP2020 PMT's and their signals are read into separate channels of a TDC and ADC. Trigger electronics use signals from the telescope to define the passage of a cosmic ray particle and define the start signal for the TDC and gate for the ADC.

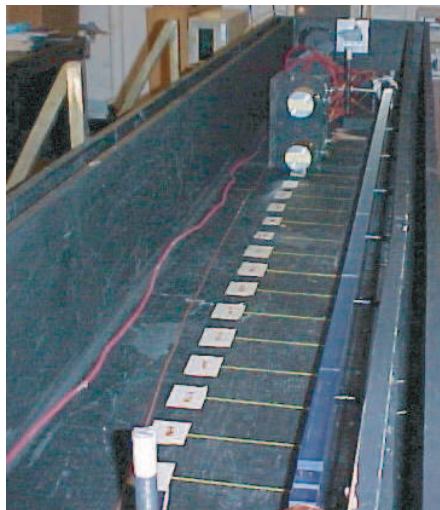


Figure 6.61: Part of the cosmic ray test facility showing a light-tight box inside of which is a 2-m long scintillator bar, read out at both ends, as well a trigger telescope with two small scintillation counters that can be positioned along the bar.

Measurements Made in a Hadron Beam at IHEP Several data runs testing TOF prototype modules were made at the IHEP accelerator. The setup for these runs is shown in Figure 6.62. The two bars under test were coupled to PMTs T1 through T4 at their ends. The bars could be moved transverse to the beam. We define x as the position of the center of the long scintillator relative to the beam with $x=0$ at the center of the bar.

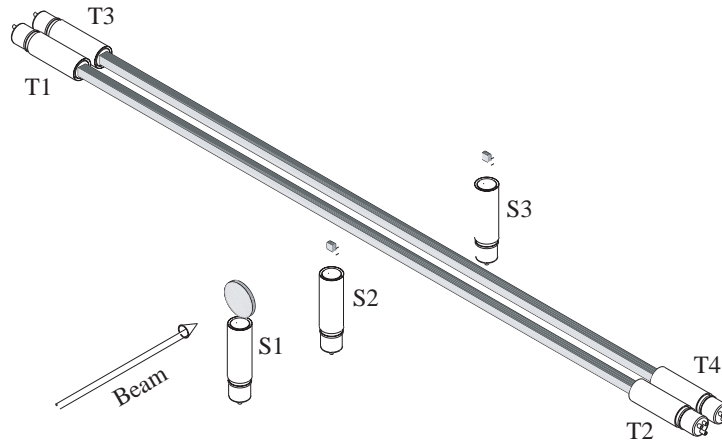


Figure 6.62: The setup for the beam tests at IHEP at Serpukhov.

Table 6.8: Time resolution for various phototubes.

Phototube	T_{av} Time Resolution (ps)
2.5 cm Bar	
XP2020	102
FEU 115	172
Hamamatsu R5506	167
Hamamatsu R5946	102
5.0 cm Bar	
XP2020	89
XP2020/UR	82

The beam defining counters shown in Figure 6.62 are S1, S2, and S3. The cross sectional size of the beam was large compared to the 2 cm by 2 cm size of S2 and S3. S2 and S3 were each 1.25 cm thick and both coupled to an XP2020 phototube with a 5 cm air gap. S1 was not used for timing purposes, nor to define the effective size of the beam.

The first data run at IHEP was used to test 2-m long counters with square cross sections of $2.5 \times 2.5 \text{ cm}^2$ and $5.0 \times 5.0 \text{ cm}^2$. The scintillator is type EJ-200, produced by the Eljen Corporation. This scintillator has a decay time of 2.1 ns, a bulk attenuation length of 4 m, an index of refraction of 1.58, a peak in the emission spectrum at 425 nm, and a light output equal to 64% of that of Anthracene. The surfaces of two of the four long sides of each bar were in contact with the casting form and had no other preparation. The other two long sides and the two ends of each bar were diamond fly-cut in order to minimize losses due to surface imperfections. A phototube was placed on each end of each bar. The two bars, with their phototubes, were placed in a light-tight box. The beam was a 3 to 40 GeV/c positive beam with variable energy.

Table 6.5.2 shows the results for average time resolution measured for various combinations of scintillation bars and PMTs. Figure 6.63 shows the variation of time resolution as a function of position of the beam along the bar ($x=0$ at the center) for the two types of bars.

In a later data run 2 m-long bars of cross sections $2.5 \times 6.0 \text{ cm}^2$ were tested using a 5 GeV/c beam. A typical PMT pulse observed after a 40 m cable is shown in Figure 6.64. These

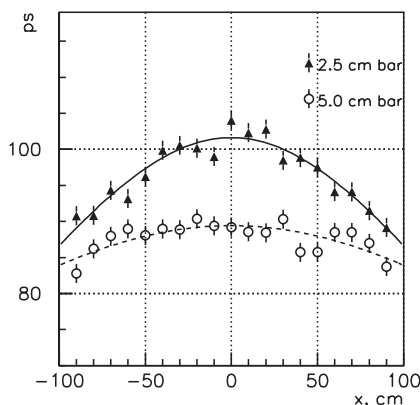


Figure 6.63: The average time resolution for a 2 m-long scintillation counter read out at both ends with Phillips XP2020 PMTs as a function of position of a charged particle beam along the bar ($x=0$ at the center of the bar). Bars of square cross section $2.5 \times 2.5 \text{ cm}^2$ and $5.0 \times 5.0 \text{ cm}^2$ were tested.

signals went to constant fraction discriminators (CFD) to eliminate time corrections associated with variations of signal amplitude. Measurements using leading edge discriminators (LED) and Analog to Digital Converters (ADC) were also made. In this case a time vs. amplitude correction was made using measured signal pulse heights. Custom made Time to Digital Converters (TDC) with 26.5 ps least count were used for time measurements. The S3 signal was used as the common start and signals from the other beam counters and the bars under test were used as stop signals. The intrinsic time resolution of the electronics was 18 ps (r.m.s.) as measured by using the S3 signal to both to start and to stop the TDC. The measured time resolution of S2 and S3 was 70 ps.

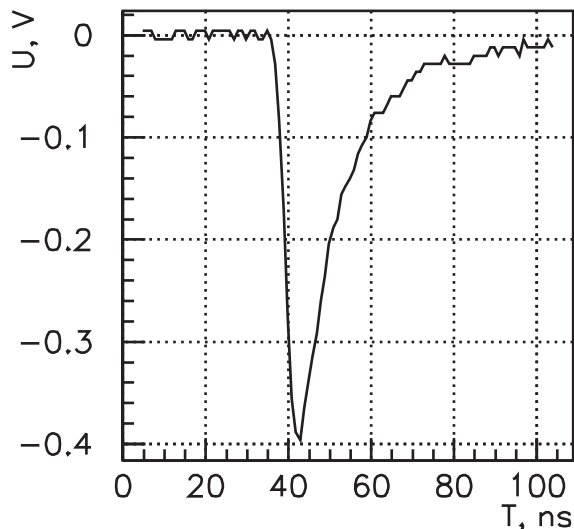


Figure 6.64: A typical pulse a Phillips XP2020 PMT attached to a 2 m long scintillation bar after the signal passed through a 40 m delay cable.

Figure 6.65 shows the average time resolution as a function of the position of the beam along the 2 m-long scintillator bar ($x=0$ at the center of the bar). In Figure 6.65a and figure 6.65b the open circles show resolution using a single bar and the closed circles show resolution using

information from both bars. In (a) the beam passed through 2.5 cm of scintillator and in (b) through 6.0 cm of scintillator. In (a) and (b) a constant fraction discriminator was used and in (c) pulse height information was used to do the time-walk correction for the case when the beam passed through 2.5 cm of scintillator.

Using constant fraction discriminators the time resolution for two bars was measured to be less than 40 and 60 ps when particle cross 6.0 cm and 2.5 cm of scintillator respectively. The results obtained with leading edge discriminators and corrected for time walk effect were similar to those measured with CFDs.

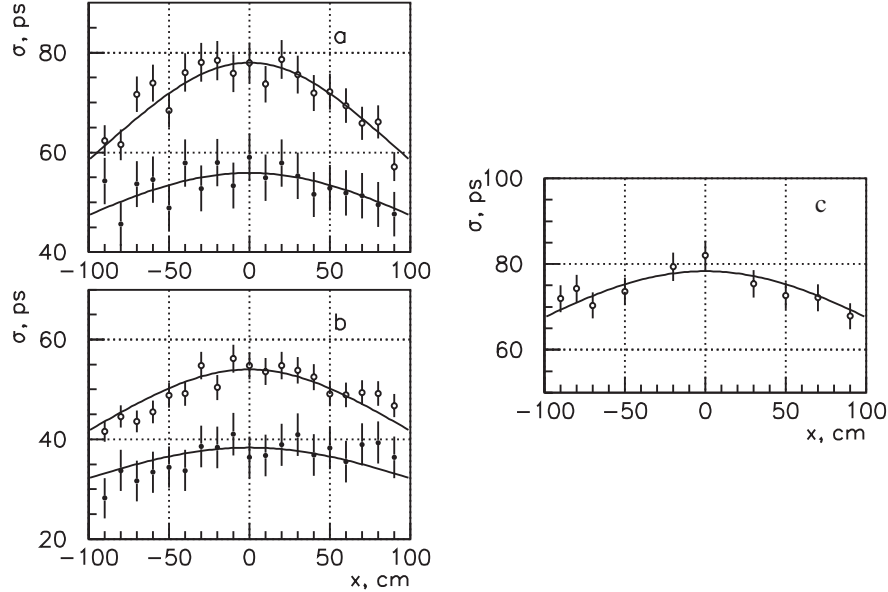


Figure 6.65: Average time resolution as a function of the position of the beam along the 2 m-long long scintillator bar ($x=0$ at the center of the bar). In (a) and (b) the open circles show resolution using a single bar and the closed circles show resolution using information from both bars. In (a) the beam passed through 2.5 cm of scintillator and in (b) through 6.0 cm of scintillator. In (a) and (b) a constant fraction discriminator was used and in (c) pulse height information was used to do the time-walk correction for the case when the beam passed through 2.5 cm of scintillator.

The tests described above in the hadron beam are described in more detail in references [101, 102]. In order to minimize the amount of material in front of the LGD bars of 1.25 cm thickness were tested and compared and those measurements were reported in reference [103].

Comparison of timing properties for the $1.25 \times 6.0 \text{ cm}^2$ and $2.5 \times 6.0 \text{ cm}^2$ bars shows that the time resolutions at the center of the bar are better by factor of ≈ 1.4 for the $2.5 \times 6.0 \text{ cm}^2$ bar. But the time resolutions at the bar edges are the same in both cases indicating that near the PMT's the time resolution does not depend on photoelectron statistics.

Conclusions and remaining issues

Based on the results presented above, therefore, we have chosen the 1.25 cm thick, 6 cm wide bar for the TOF wall. As shown in Figure 6.65a, the time resolution for two bars of this size is 80 ps or less at all point on the bar – satisfying our design criterion.

In addition to optimizing the time resolution, a practical consideration in the choice of bar geometry is the ability to accommodate magnetic shielding for the approximately 200 G magnetic field in the vicinity of the XP2020s. For a 6 cm wide bar the phototubes can simply be attached

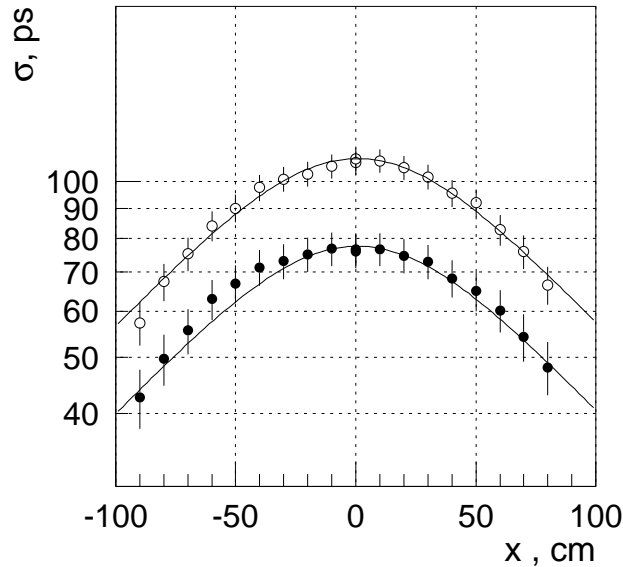


Figure 6.66: The time resolution for one (○) and two (●) $1.25 \times 6.0 \text{ cm}^2$ bars viewed by XP2020 PMT's.

to scintillator snouts and then surrounded by magnetic shielding; this cannot be done for bars less than 6 cm wide.

6.5.3 Čerenkov Counter

The Čerenkov detector for GLUEX is unfortunately not as well defined as the rest of the equipment. This is due to the fact that the first group to express interest in this detector pulled out of GLUEX because of the long time scales involved and detector became an *orphan* for several years. After the granting of CD0 to the JLab upgrade and GLUEX in the spring of 2004, a pair of groups from Tennessee approached the collaboration about joining GLUEX and taking on a large detector responsibility. The natural piece of hardware was the orphaned Čerenkov system.

Based on this interest, it was felt that a completely fresh look should be taken at the system. This should consider both the physics of GLUEX and technological developments that have occurred over the last several years. The result of this effort is a proposal to build a DIRC detector rather than the gas Čerenkov system that had been proposed earlier. Because this proposal is so new, and the collaboration is still evaluating its implications, we have presented both the newer DIRC material and the older gas Čerenkov material here. A final decision on this clearly depends on many factors including physics, manpower, costs and timescales. The collaboration is currently evaluating these.

In the case of both Čerenkov designs, it is possible for the GLUEX experiment to start taking quality data without this system in place. There is a very solid physics program with pions that does not need the Čerenkov. However, as the collaboration begins to study final states with both hidden and open strangeness, the Čerenkov system will be crucial. What follows are first a discussion of the DIRC option followed by the earlier work on the gas Čerenkov detector.

A DIRC Čerenkov Detector

The Čerenkov detector, DIRC, of the BABAR experiment at the PEP-II asymmetric B -factory of SLAC has proven to be a successful novel technique for pion and kaon identification [105]

[106][107]. The DIRC (acronym for **D**etection of **I**nternally **R**elected **C**herenkov (light)) is a ring imaging Cherenkov detector. It provides the identification of pions, kaons, and protons for momenta up to 4.5 GeV/c with high efficiency. This is needed to reconstruct CP violating B -decays and to provide B -meson flavor tagging for time-dependent asymmetry measurements. The DIRC radiators consist of long rectangular bars made of synthetic fused silica and the photon detector is a water tank equipped with an array of 10,752 conventional photo-multiplier tubes (PMT). By the summer 2004, BABAR had recorded about 227 million $\bar{B}B$ pairs, exceeding the design luminosity of $3 \cdot 10^{33}/\text{cm}^2\text{s}$. The observation of direct CP violation with more than 4 standard deviations in the decay $B^0 \rightarrow K^+\pi^-$ [108], which has to be distinguished from B^0 decays into $\pi^+\pi^-$ and K^+K^- , is a successful demonstration of the DIRC's capabilities.

Similar to the physics program of BABAR, the spectroscopy program of GlueX depends on the capability to identify charged kaons. We discuss the possibility to adapt the DIRC concept for the GlueX detector to complement the particle identification information of the tracking chambers and the time-of-flight (TOF) detector for momenta above 1.5 GeV/c.

The BABAR DIRC

The physics program of the BABAR [109] detector is to observe CP violation and to probe the Standard Model of Particle Physics by collecting enough B -meson decay channels to over-constrain predictions. The source of B mesons is the PEP-II asymmetric e^+e^- collider [110][111][112], where 9 GeV electrons strike 3.1 GeV positrons producing $\Upsilon(4S)$ resonances with a boost of $\gamma\beta \simeq 0.56$. The $\Upsilon(4S)$ resonance decays nearly exclusively in a pair of B and anti- B mesons. This allows precise measurements of time-dependent asymmetries in B meson decays which can be related to the CP violation phase in the Cabbibo-Kobayashi-Maskawa (CKM) matrix [113].

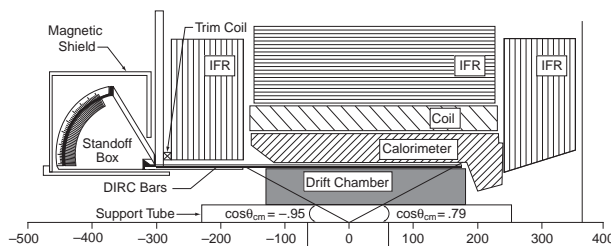


Figure 6.67: The side-view of the BABAR detector with the components of the DIRC indicated (units in cm).

BABAR is a typical collider detector but asymmetrically placed around the interaction point to ensure nearly full solid angle coverage in boost (forward) direction (see Fig. 6.67). The location of the particle identification system is radially between the drift chamber and a CsI(Tl) crystal calorimeter. Therefore, a small radiation length is preferred to avoid deterioration of the excellent energy resolution of the calorimeter. The DIRC minimizes the radial dimension and keeps the amount of required calorimeter material (cost) small. Up to a momentum of 700 MeV/c, the drift chamber can provide pion-kaon separation based on the dE/dX measurement. Only if pion-kaon separation up to 4.5 GeV/c particle momentum is available can one distinguish the channels $B^0 \rightarrow \pi^+\pi^-$ from $B^0 \rightarrow K^+\pi^-$ or $B^\pm \rightarrow \phi\pi^\pm$ from $B^\pm \rightarrow \phi K^\pm$, interesting for the measurement of indirect or direct CP violation. Moreover, the flavor content of the recoil $B(\bar{B})$ needs to be tagged by identifying kaons in its successive decays with momenta below 4 GeV/c. In addition, τ , charm-, and light-quark meson spectroscopy profit from kaon identification.

The difference in the Cherenkov angle between a pion and a kaon at 4.0 GeV/c momentum is 6.5 mrad. Therefore, a 3 standard deviation π/K separation requires resolution of the Cherenkov angle for given a track of 2.2 mrad or better (see Fig. 6.68). Finally, to operate successfully in the high-luminosity environment of PEP-II, the Cherenkov detector has to be radiation hard,

fast, and tolerant of background.

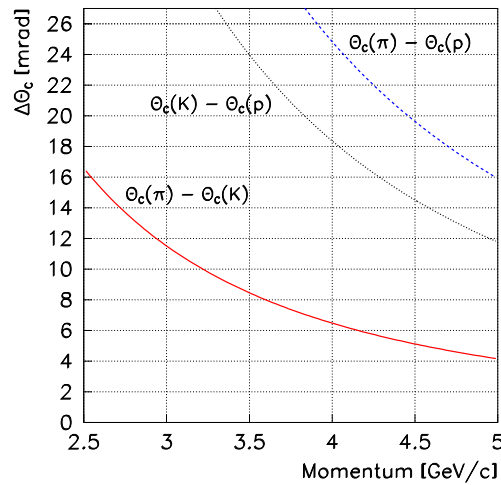


Figure 6.68: The difference in the Cherenkov angles between pions, kaons, and protons in synthetic quartz.

Principle of the BABAR DIRC

The DIRC uses thin, long rectangular bars made of synthetic fused silica (quartz) [114] ($H \times W \times L = 17 \text{ mm} \times 35 \text{ mm} \times 4900 \text{ mm}$) both as Cherenkov radiators and light guides (refractive index $n_1 \approx 1.47$). Bars are glued together from four pieces, each 1225 mm long. All together, 144 bars are arranged in a 12-sided polygonal barrel with a radius of about 84 cm around the beam axis. The DIRC bars extend 178 cm forward from the interaction point of BABAR covering 87% of the polar solid angle in the center-of-mass frame. The azimuthal coverage is 93%, since there are gaps between the bars at the 12 sides of the radiator polygon. Every 12 bars are housed in a bar-box surrounded by nitrogen at STP (index $n_2 \approx 1$). The box is built mostly of aluminum honeycomb material. The radiation length (X_0) of the bars is 14%, and 19% for the full assembly at perpendicular incidence. A schematic view is presented in Fig. 6.69.

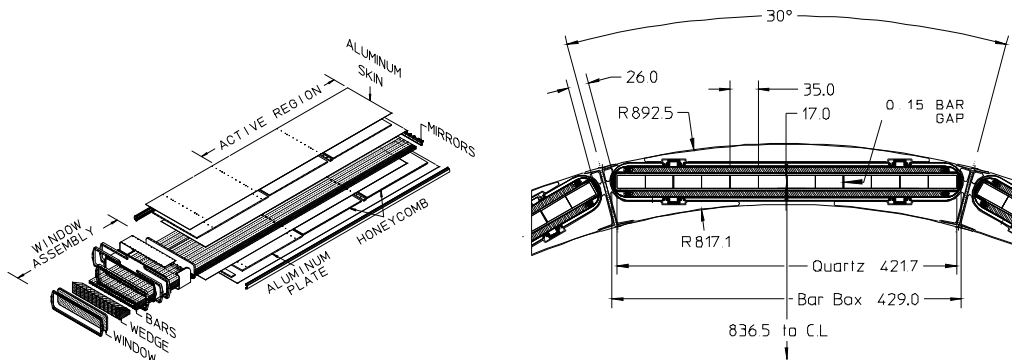


Figure 6.69: Left: View of a bar-box assembly. 12 bar-boxes surround the drift chamber. Right: Placement of the bar-box in the BABAR detector above the cylindrical drift chamber.

The principle of the DIRC is shown in Fig. 6.70. The DIRC imaging works like a pinhole focus camera with the bar cross section small compared to the imaging plane.

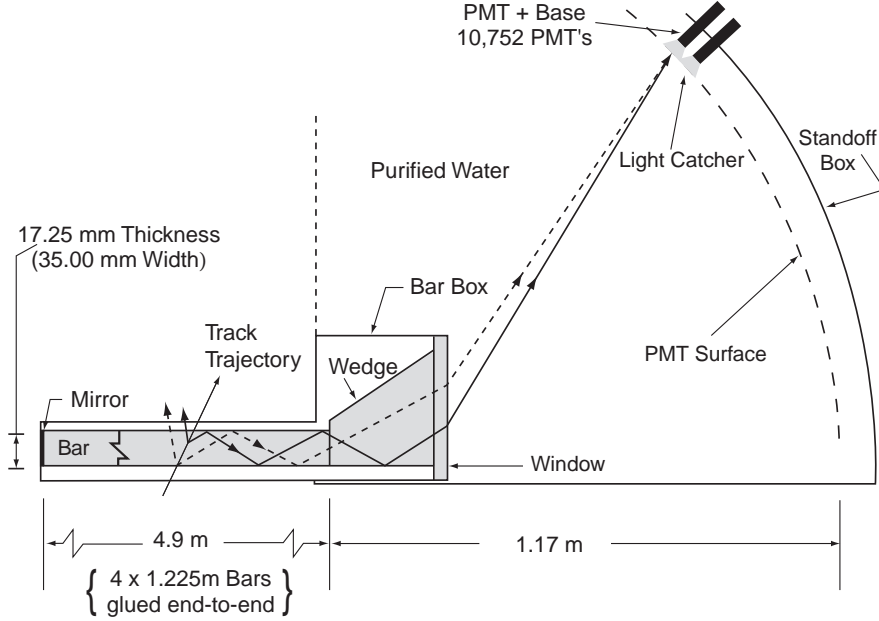


Figure 6.70: The principle of the BABAR DIRC.

Since the refractive index of the radiator bar n_1 is larger than $\sqrt{2}$, a certain fraction of the Cherenkov photons produced by a relativistic charged particle traversing the quartz bar will be totally internally reflected, regardless of the incidence angle of the track, and propagate along the length of the bar. Only one side is viewed by the PMT array and a mirror (reflectivity $\approx 92\%$) is placed perpendicular to the bar axis on the other end, where positrons enter the BABAR detector. Due to the boost of the $\Upsilon(4S)$ there is a higher density of charged tracks towards the mirror side and hence it is less preferable for the readout. Since the rectangular bar is of high optical precision (mean surface reflectivity $\approx 99.96\%$ per bounce at 442 nm photon wavelength), the initial direction of the photon is preserved throughout its propagation, modulo left/right, up/down and forward/backward ambiguities. The latter is resolved by the measurement of the photon arrival time. The bars have very high light transmission (99.9% at 442 nm photon wavelength) required for the typical photons path-lengths of 6 to 20 m.

Photons exiting the bar in the downward direction, or with large exit angles with respect to the bar length axis, are partly recovered into the instrumented area by a prism (wedge). This optical element is 91 mm long and the top side has a 30° opening angle. The bottom side is slightly tilted upwards by 6 mrad. It reduces the required photon-sensitive area by more than a factor of two.

A thin (9 mm) quartz window separates the prism from the so called standoff box (SOB), a water tank filled with 6000 liters of purified water ($n_3 \approx 1.33$) in a toroidal shape. The backplane of the SOB is divided into 12 sectors, each equipped with 896 conventional photo-multiplier tubes [115] ($\approx 25\%$ quantum efficiency at 400 nm wavelength, 250 nm – 650 nm spectral range), facing the wedge of a corresponding bar box. Hexagonal reflectors (light catchers) with water-resistant rhodium surfaces surround the PMT cathodes improving the detection efficiency by about 20%. The ratio of refractive indices n_1/n_3 is nearly wavelength independent. It reduces internal reflection at the bar-box wedge. Furthermore, the exit angle is magnified by this ratio, increasing the position resolution of the photons.

The detector provides a three dimensional measurement of the photon in the variables (α_x, α_y) , the photon exit angles with respect to the bar axis, and the arrival time of the photon t_a . The spatial position of the bar through which the track passed and the particular PMT hit

within a certain readout time interval is used to reconstruct the photon vector pointing from the center of the bar end to the center of the tube. This vector is then extrapolated back into the quartz bar using Snell's law, where the photon exit angles (ϕ_C, θ_c) with respect to the track are calculated. Most of the photon phase space $(\alpha_x, \alpha_y, t_a)$ is mapped onto the Cherenkov angles (ϕ_C, θ_c) with less than a three-fold average ambiguity.

The timing information apart from the resolution of the forward-backward propagating photons, is not competitive with the position information, but it is crucial for suppression of beam background. The expected arrival time of the Cherenkov photon is a sum of the time-of-flight of the charged particle from its origin to the quartz bar (typically 2-3 ns), the photon propagation time in the quartz bar and the wedge along its reconstructed path, and the traveling time through the water before reaching the surface of the PMT. Applying the reconstructed mean arrival time of the photons in an event as correction for the uncertainty in the bunch-crossing time yields a precision of about 1.5 ns in the time between photon creation and photon arrival, which is close to the intrinsic time resolution of the PMTs. This allows restriction of the event time interval to 8 ns.

Particle identification uses likelihood ratios for different particle hypotheses based on the number of photons above and below threshold and the Cherenkov angle. Another way to use the information is to compare the ring pattern in the PMT plane with expected patterns for the different particle hypotheses.

Imaging with Synthetic Fused Silica

The Cherenkov angle separation between particle types is the Cherenkov angle difference in Fig. 6.68 divided by the Cherenkov angle resolution σ_C . This resolution, in turn, depends primarily on the precision of the track angle of incidence as provided by the tracking detectors, σ_t , and the single photon Cherenkov angle resolution in the DIRC, $\sigma_{C,\gamma}$, and the number of photo-electrons contributing to the measurement, N_γ , as follows:

$$\sigma_C = \sqrt{\sigma_t^2 + \sigma_{C,\gamma}^2 / N_\gamma}. \quad (6.20)$$

The dominant contributions to the error of the single photon measurement are

chromatic	5.4 mr
imaging (bar size) and detection (PMT size)	7.5 mr
transport (through the bar)	1.0 mr .

These add in quadrature to $\sigma_{C,\gamma} = 9.3$ mr. The number of Cherenkov photons per track for di-muon events versus the track polar angle with respect to normal incidence is shown in Fig. 6.71 b). The number varies between 25 and 60 photons. Therefore, with negligible tracking resolution, σ_C decreases from 1.9 mr to 1.2 mr in the extreme forward direction where tracks have the highest momenta in BABAR due to the boost. The imaging and detection error can be improved by extending the distance between bar end and PMT plane. For instance, with a distance of 1.4 m we obtain a single photon angle resolution of about 8.3 mr. With a slightly increased bar thickness and shorter bars the minimum number of photons per track can be increased to 25 or higher.

Features of the BABAR DIRC

Here we summarize the main advantages of the BABAR DIRC type Cherenkov detector:

- The BABAR DIRC separates kaons from pions to better than 3 standard deviations below $4 GeV/c$. It is an imaging device in the required momentum range with high photo-electron yield (25 or more). It also works as a threshold detector for different particle types with momenta below 0.92 times the particle's mass.
- Compact: The total thickness between tracking and calorimeter is less than 5 cm. The total radiation length (X_0) for a full assembly is 19%.

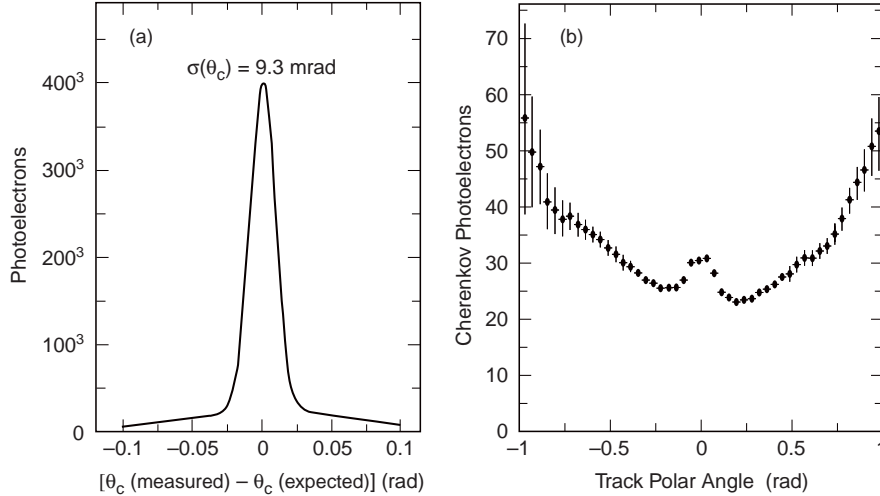


Figure 6.71: (a) The Cherenkov angle resolution for single photons associated with a particle track. (b) The number of Cherenkov photons per track versus the track polar angle with respect to normal incidence. The slightly lower efficiency in forward direction is due to the reflection in the mirror and the increased photon path-length in the bar.

- **Radiation robust:** It has been demonstrated that there is no efficiency loss in the wavelength regime above 280 nm after irradiation with 250 krad [116].
- **Fast device:** The photon collection time is less than 100 ns.
- **Insensitive to background:** The BABAR DIRC is a 3-dimensional device; the photon arrival time and the location of the PMT are correlated, allowing reconstruction of the true arrival time of the Cherenkov photons originating from the same track with a precision of 1.5 ns. Therefore, the event time interval can be smaller than 10 ns.
- **Robust device:** The radiator is passive and needs only to be kept in a dry atmosphere. Conventional photo-multiplier tubes are used which can be easily accessed. The DIRC is the subsystem within BABAR that requires the least maintenance.

Requirements for GlueX

In the previous design a gas-Cherenkov detector is placed behind 4 layers of FDCs and before the TOF system. It extends into the inner cylinder of the solenoid and has an effective length along the beam axis (z -axis) of 1.4 m. Instead of this detector a DIRC system can be positioned at some short distance behind the solenoid opening. To evaluate the situation with GEANT simulations [117] we place a virtual (xy) plane perpendicular to the beam direction at $z = 450$ cm, which is about 10 cm behind the solenoid opening. Without modification of the bar-imaging concept of the DIRC detector, the bars would line up along one axis in that plane and leave a gap for the beam to pass through.

Particle Momenta and Angle of Incidence In a typical reaction $\gamma p \rightarrow (\text{mesons}) p$ with strangeness production, 50% of the pions and kaons (somewhat fewer protons) produced with momenta between 1 GeV/c and 5 GeV/c arrive at the Cherenkov detector plane. In many cases strangeness conservation can be used to recover the final state if the remaining particles are identified with high efficiency. Highly efficient and redundant kaon identification is required to access a large variety of final states and to reduce combinatorial background in the search for new signals. A particle identification coverage with constant efficiency and low mis-identification rate over the full momentum range is essential to perform angular analysis of their decays.

Figure 6.72 shows the momentum spectra for the pions, kaons, and protons which arrive at the Cherenkov-detector plane for the two reactions:

$$\begin{aligned} \gamma p &\rightarrow K^{*0}(892)K^{*0}(892)p & (6.21) \\ &\rightarrow K^+\pi^-K^-\pi^+p \end{aligned}$$

$$\begin{aligned} \gamma p &\rightarrow K_1(1270)K^-p & (6.22) \\ &\rightarrow K^{*-}\pi^+K^-p \\ &\rightarrow K^-\pi^0\pi^+K^-p. \end{aligned}$$

These are typical reactions with more than two final state pions and kaons. In these final states kaon-pion separation is required up to a momentum of $5 \text{ GeV}/c$. Based on dE/dX and TOF a 3 standard deviation separation is obtained up to $1.5 \text{ GeV}/c$ momentum, while with the kaon threshold in a DIRC at $0.45 \text{ GeV}/c$ enough photo-electrons are created for efficient Cherenkov imaging. The proton spectrum extends to $2 \text{ GeV}/c$ and below $1 \text{ GeV}/c$ a DIRC detector acts as a threshold Cherenkov detector for this particle type.

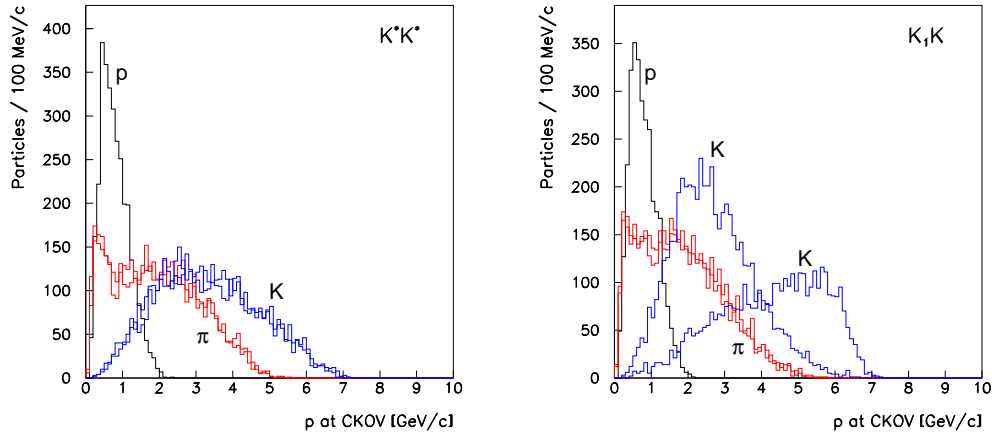


Figure 6.72: The particle momenta at the Cherenkov detector plane ($z = 450 \text{ cm}$) for the two reactions described in the text (π :pions, K :kaons, p :protons).

Figure 6.73 shows the polar angle with respect to the z -axis for the charged final state particles in the reactions Eq. 6.21. This angle typically does not exceed 15 degrees. Pions with polar angles greater than 15 degrees typically have momenta below $1 \text{ GeV}/c$.

Beam Background We assume an electron beam current of $3 \mu\text{A}$. This is the high-luminosity scenario for the Hall-D project. We use a full GEANT simulation of the GlueX detector [117] to track primary and secondary particles. The charged particle background which can create Cherenkov light consists mostly of electrons and positrons coming from upstream or from photon conversions in the Cherenkov detector.

Figure 6.74 shows the combined electron-positron rate along the y -axis in our virtual detector plane at $z = 450 \text{ cm}$. We obtain rates below 100 kHz per cm (200 kHz per 2 cm) at distances of about 6 cm from the beam axis. The total rate integrated over all of x and from $\pm 6 \text{ cm}$ to $\pm 65 \text{ cm}$ (the hole radius) of y is at the most 900 kHz . The integration from $\pm 10 \text{ cm}$ to $\pm 65 \text{ cm}$ of y yields a total rate of 580 kHz .

Figure 6.75 shows the photon rate per cm along the y -axis integrated over all of x in the virtual detector plane at $z = 450 \text{ cm}$. We expect $600 \text{ kHz}/\text{cm}$ photons at distances near $y = 6 \text{ cm}$. The total rate integrated over all of x and from $\pm 6 \text{ cm}$ to $\pm 65 \text{ cm}$ of y is 29.6 MHz ; from $\pm 10 \text{ cm}$ to $\pm 65 \text{ cm}$ of y it is 24 MHz .

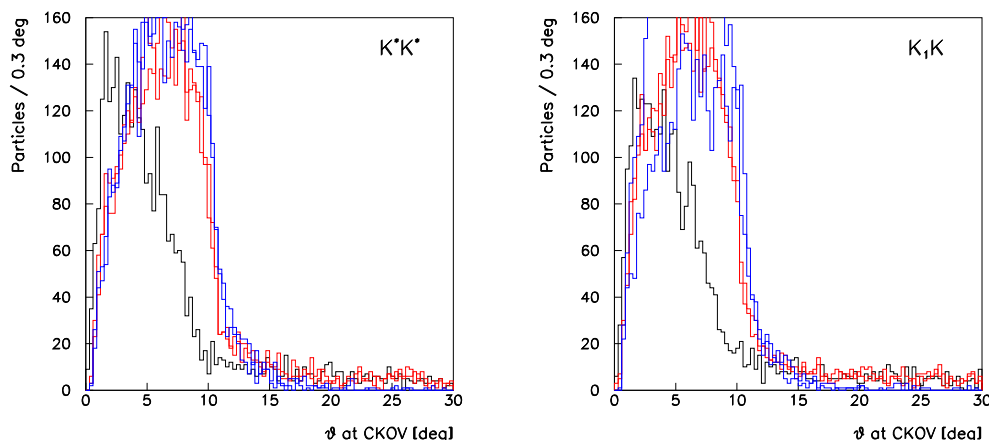


Figure 6.73: The polar angle with respect to the normal incidence at the Cherenkov detector plane ($z = 450$ cm) for pions, kaons, and protons in the two reactions described in the text.

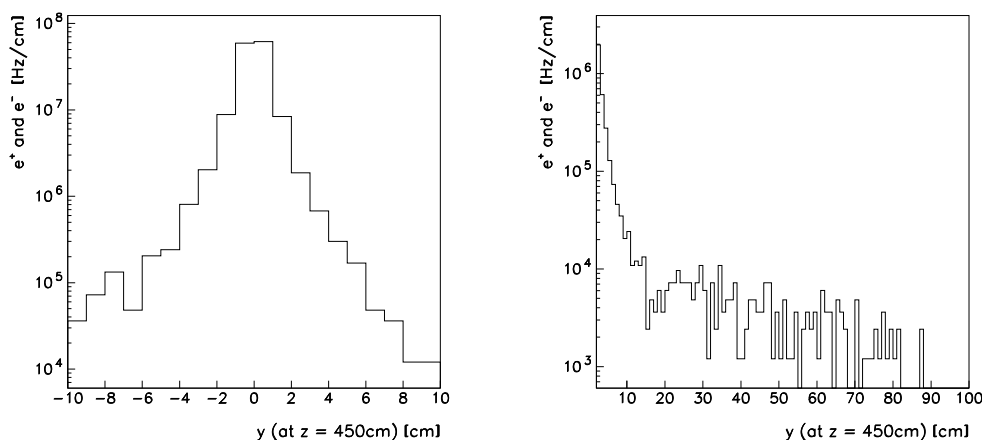


Figure 6.74: The rate of electrons and positrons per cm along the y -axis integrated over all of x at the location $z = 450$ cm. Left: rate/cm below ± 10 cm in y . Right: rate/cm versus y . The innermost 3 cm are omitted.

Each electron or positron potentially creates 30 detected photons in the struck bar. A beam photon converts with a probability of about 15% into an electron-positron pair somewhere inside the DIRC generating an average of 20 photons per lepton track. We estimate, that a DIRC placed at a distance of ± 6 cm away from the beam axis produces Cherenkov light into the readout tank at a rate of 210 MHz. If the DIRC has a central gap of ± 10 cm the total rate is 160 MHz. The time to collect photons out of the bars is less than the 100 ns for the long BABAR DIRC bars. We estimate the number of beam-background related Cherenkov-photons within 100 ns for a gap in the plane along the y -axis of ± 6 cm (± 10 cm) to be 21 (16). After reconstruction we can reduce the time window for the photon arrival to less than 10 ns, which reduces the background photons to 2, while we expect 25 or more signal Cherenkov photons in a limited region of the readout plane.

The hit rate in a single PMT depends also on the optics at the bar end (opening angle of the wedge) and the profile of the background shown in Fig. 6.74 and Fig. 6.75. Assuming that

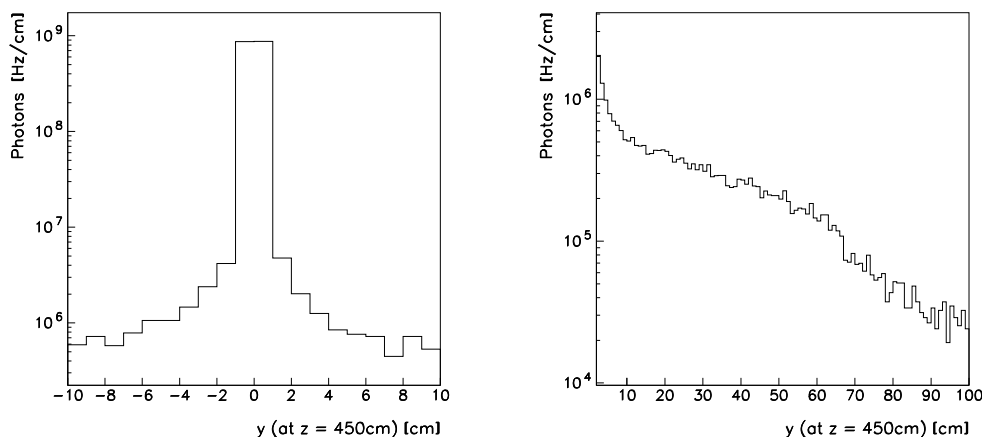


Figure 6.75: The rate of photons per cm along the y axis integrated over all of x at the location $z = 450$ cm. Left: rate/cm below ± 10 cm; Right: rate/cm versus y . The innermost 3 cm are omitted.

typically 1000 PMTs are randomly hit, the rate per tube is 210 kHz. This is the average rate encountered by PMTs in the BABAR DIRC which tolerates up to 1 MHz.

Magnetic Field The solenoid has strong fringe fields. We simulate the situation with the TOSCA program [118]. At a distance of about 3 m left or right of the solenoid center the field strengths are below 100 Gauss. Efficient operation of conventional photo-multiplier tubes requires shielding. In BABAR a magnetic field strength transverse to the PMTs of less than 0.2 Gauss is achieved with metal shielding and bucking coils.

Irradiation From the penetration rate with charged particles we estimate the radiation dose per year. We assume that the dominant component is secondary electrons and positrons created upstream or in the bars by photon conversions. The flux versus radius is shown in Fig. 6.76. It stays below 100 kHz/cm^2 for radii greater than 3 cm. For a flux of 100 kHz/cm^2 and a minimum ionizing $dE/dx = 1.6 \text{ MeVcm}^2/\text{g}$ we estimate a yearly dose of 51 krad. This rate is well below the negligible dose of 250 krad tested with a ^{60}Co source [116].

Conceptual Design

At this point we discuss a geometry and imaging concept similar to that in the BABAR DIRC. In fact, we can even envision the use of four of the DIRC bar-boxes which would only need the design of a new support and a new shielded readout tank.

However, for a new design the bar dimensions can be optimized. Because azimuthal and polar angles of incidence are comparable and we expect a higher background rate per bar closer to the beam compared to BABAR, a width of 2 cm is more appropriate than 3.5 cm. The thickness can be increased from 1.7 cm to 2 cm to increase the photon yield and the structural stability. The modularity should be kept, with say, 14 bars in a box. Altogether four boxes provide a geometrical match. In principle, the bars could follow the circular boundary of the magnet opening. Also, the gap can be partly covered from the readout side. This would result in bars with different lengths.

The water tank should be placed on the side of the magnet, shielded, and away from secondary tracks which are produced in the forward direction in the central calorimeter or in the magnet yoke. This may also require that the bars be somewhat farther downstream (greater z). Hence, the length of the bars and their z position is a matter of further optimization. We

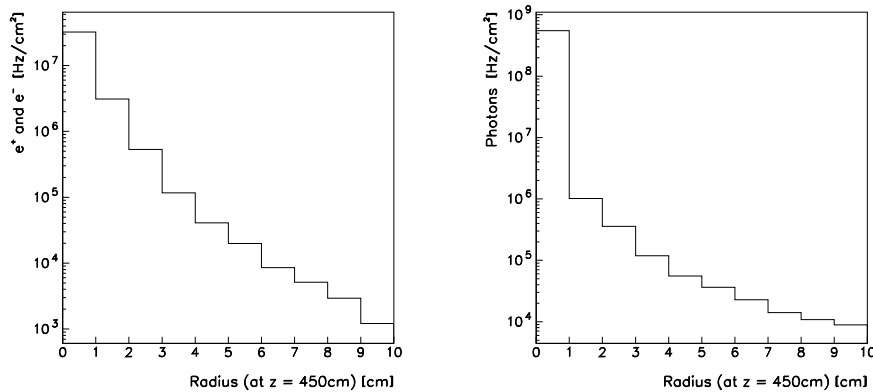


Figure 6.76: Left: The rate of electrons and positrons together per cm^2 versus radial distance from the beam axis in the virtual plane at $z = 450$ cm. Right: The same for photons.

explore the possibility that the purified water can be kept sealed in the tank for several years without maintenance.

In our first approach we allow the bars to extend into a region where there are no spatial restrictions and the transverse magnetic field [118] at the location of the PMTs is about 10 Gauss, while the longitudinal field drops below 45 Gauss. This corresponds to about 3 lengths of BABAR DIRC bars. Figure 6.77 shows the technical drawing of a first draft design of the bar arrangement with bars of 1.225 m length and a front area of 2×2 cm^2 . We have not optimized the bar length to follow the circular shape of the hole. Each 14 bars are housed in a separate bar-box. Two bar-boxes are placed below and two above the center leaving a gap for the beam to pass through. The readout side is shown in Figure 6.78. The maximum upward opening angle at the readout is 52 degrees. The sides open up with an angle of 30 degrees. Each tube covers an angle of 2 degrees. In this scenario the number of photo-tubes is 1512. A three-dimensional view of the half open bar-boxes and the readout tank is presented in Fig. 6.79.

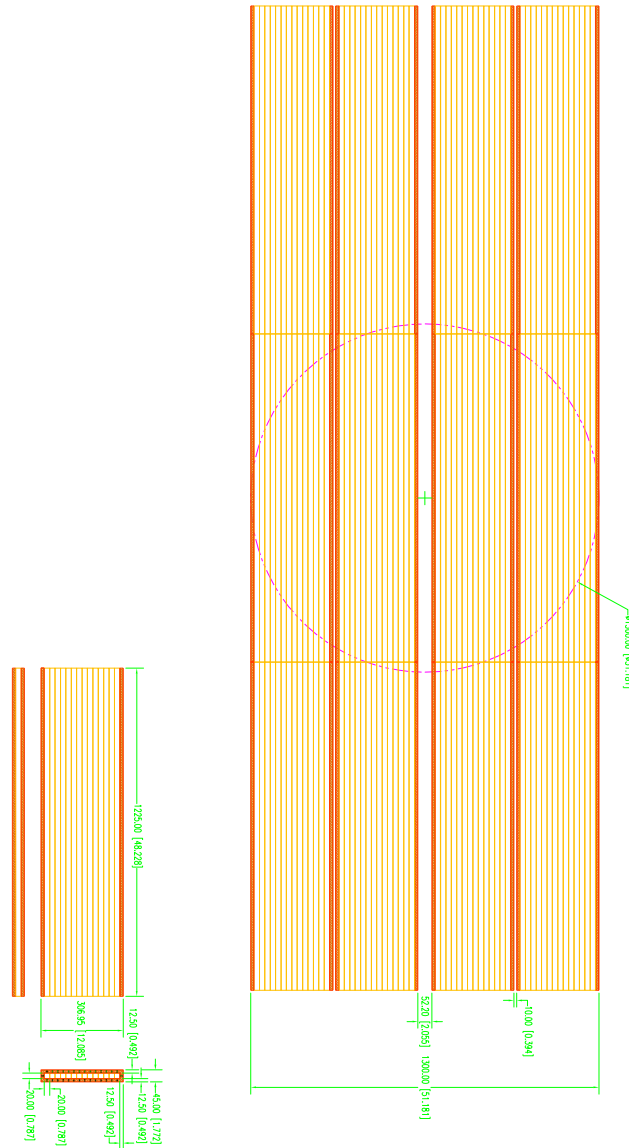


Figure 6.77: Arrangement of the bar-boxes in front of the solenoid. The circle indicates the size of the inner radius of the cylindrical calorimeter inside the solenoid. The bar-boxes will be placed asymmetrically with respect to that hole.

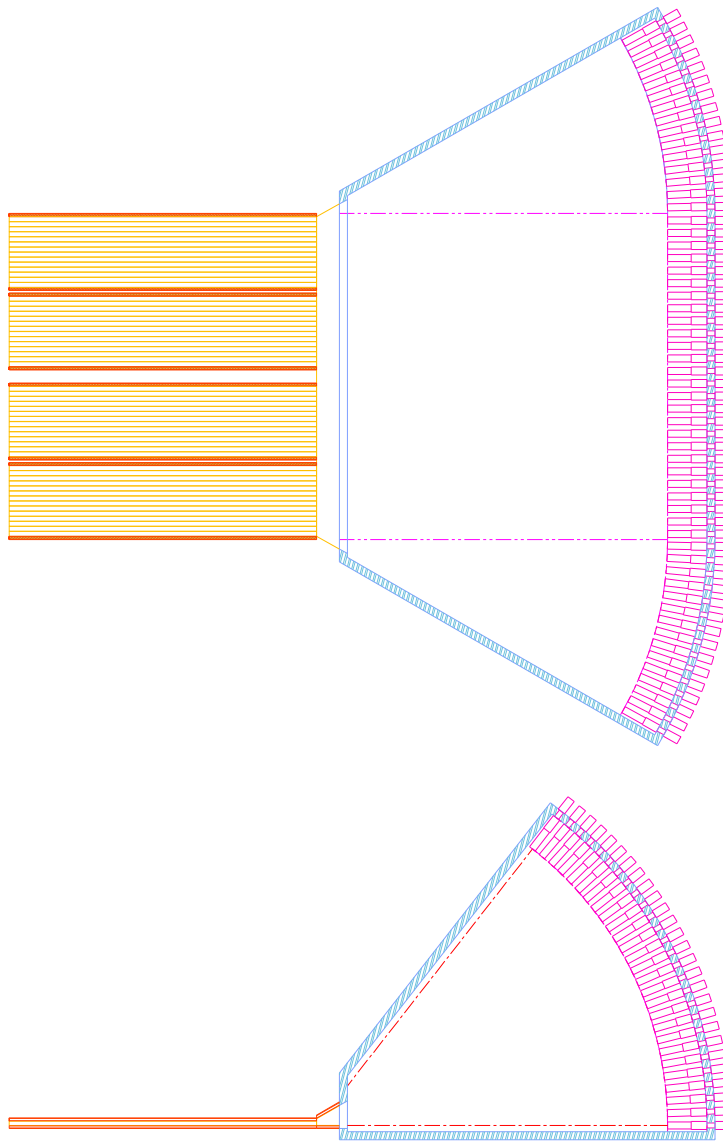


Figure 6.78: The readout side of the bars. The volume will be filled with water and the photomultiplier tubes will be immersed in the water as in the BABAR DIRC.

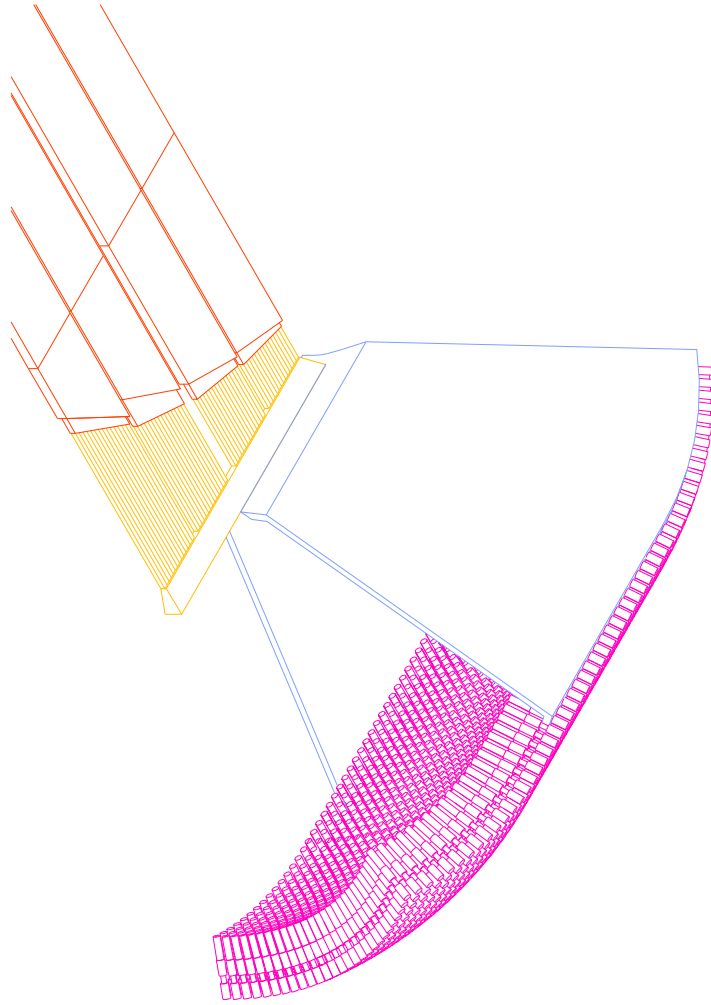


Figure 6.79: A 3-D view into the four half open bar-boxes and the readout tank.

The Gas Čerenkov Counter System

TOF measurements alone will not provide particle identification above $3 \text{ GeV}/c$, and thus TOF does not suffice for typical reactions of interest. Therefore a threshold Čerenkov detector has been included in the HALL D design. The primary function of this detector is to signal the presence of pions over a large part of the expected momentum range (see Figure 6.80).

Several radiator materials have been considered for the design. A pressurized gas radiator has the advantage of allowing one to match the index of refraction to the desired momentum range. A prototype of such a detector was developed for CLEO-III [119]. However this method requires the use of thick gas containers in the downstream detector region. This results in unwanted photon conversions and hadronic interactions, as well as safety concerns. Two atmospheric-pressure radiators were found to produce high acceptance rates: aerogel ($n = 1.008$), and C_4F_{10} gas ($n = 1.00153$). The C_4F_{10} gas radiator has been chosen for HALL D because it has a threshold momentum of $2 \text{ GeV}/c$ for pions, which complements the TOF system's useful range of $3 \text{ GeV}/c$ and below. The kaon threshold of $9 \text{ GeV}/c$ in this gas is nicely above the momenta that will be encountered in the experiment, overlapping less with the TOF system.

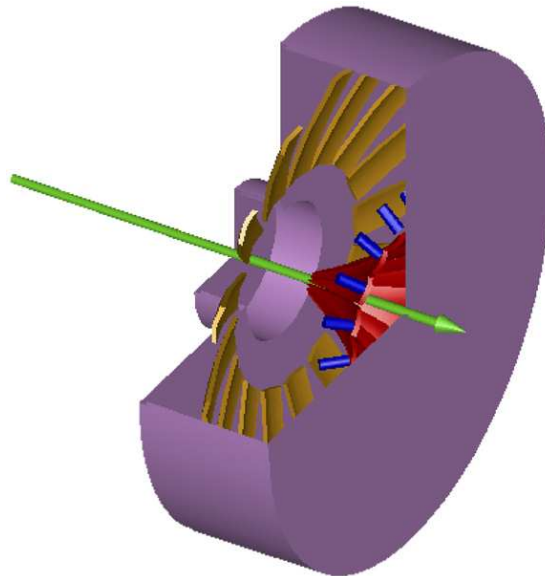


Figure 6.80: A schematic drawing of the HALL D Čerenkov detector system. The particles enter from the left into the gas volume in the center. The Čerenkov light is then reflected off the mirrors in the center (shown in dark) into the phototubes at the outer rim (shown as dark cylinders).

Gas-filled Čerenkov detectors have been used in many particle physics experiments. The original LASS spectrometer [50] used a freon radiator in a design similar to the one in HALL D. The primary changes we will make in the LASS design are the use of an environmentally friendly gas (freon is no longer available) and mirrors made of low-density carbon-fiber composite materials. The gas handling system will be patterned after a similar system now in use on the JLab CLAS spectrometer. The detector will be segmented into sixteen azimuthal regions, each housing a single mirror that focuses light onto its own photomultiplier tube. Light emitted into the region within 10 cm of the beam axis will not be collected in order to suppress accidental coincidences in the detector. A sketch of the optical design is shown in Figure 6.80. The minimum radiator thickness encountered by a particle traversing the detector is approximately 90 cm . The measured performance of the JLab CLAS Čerenkov detector was used to estimate the photoelectron yield of the HALL D design, adjusting for radiator length and the number of mirror reflections. This results in an expected average yield of 5.0 (3.3) photoelectrons for 5.0 (2.9) GeV/c pions.

Particles that traverse thicker regions of the detector will register proportionately larger signals.

The optical design of the detector (two ellipsoidal mirrors) was chosen to produce a strong focus at the photomultiplier tubes. This produces small linear magnification and allows good light collection from the wide range of particle trajectories exiting the solenoid. Prototype mirrors were constructed and tested for their focal properties. These were found to be mechanically and optically stable after cutting to shape. Having two mirrors in the design also offers flexibility as to the placement of the photomultipliers. This freedom was used to place the axis of the tubes perpendicular to the ambient magnetic field. This was done to optimize the effectiveness of the passive magnetic shields surrounding the photomultipliers.

A finite-element analysis of the shielding requirements was performed with the FLUX-3D computer code. A four-layer shield with axial symmetry was found to produce adequate reduction in the magnetic field. The predicted transverse field at the photocathode is less than 0.1 gauss. Burle 8854 photomultipliers were chosen for their high detection efficiency and low noise level.

A Monte Carlo simulation of the Čerenkov detector efficiency was made for the events in the following reaction:

$$\gamma p \rightarrow X p \rightarrow K^* \bar{K}^* p \rightarrow K^+ \pi^- K^- \pi^+ p \quad (6.23)$$

The geometry, mirror reflectivity, kinematics and photomultiplier response were modeled in the simulation, which yielded the detector efficiency as a function of pion momentum (see Figure 6.81).

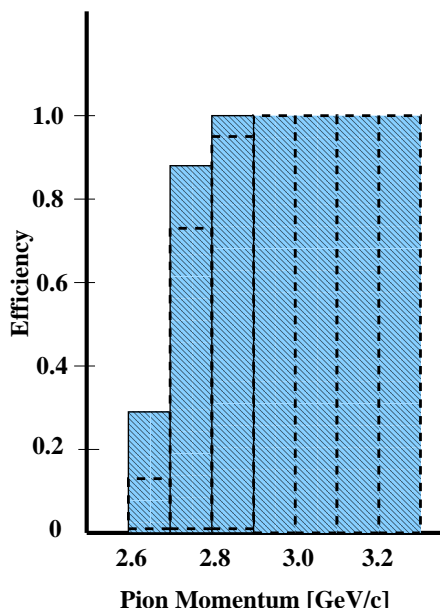


Figure 6.81: Predicted pion detection efficiency as a function of average pion momentum. The solid histogram is for a one-photoelectron detection threshold and the dashed line is for a two-photoelectron threshold.

6.5.4 Acceptance of The Particle Identification System

Since each of the particle identification subsystems works most effectively in different regions of momentum and different regions of particle production, and since no subsystem alone can provide particle identification for all the events necessary for GLUEX analyses, it is crucial to integrate the information from the different subsystems in the most effective way possible. An algorithm based on assigning likelihoods to different particle hypotheses using information from all the relevant subsystems is one natural and straightforward way to proceed.

Given a track with a measured momentum, the basic idea is to use information from the different particle identification elements (dE/dx from the CDC, times from the BCAL and forward TOF, and Cerenkov photoelectrons or Cerenkov opening angle) to assign this track a set of likelihoods, each likelihood corresponding to a different particle hypothesis. For example, $L(\pi)$ and $L(K)$ are the likelihoods a given track is a pion or a kaon, respectively. Once these likelihoods are known, a statistical test can be performed to discriminate between hypotheses. One of the most convenient tests, the likelihood ratio test, works by forming the χ^2 statistic $R(i)$ for each particle hypothesis i ($i = \pi, K, p$):

$$R(i) = -2 \ln \frac{L(i)}{L(\pi) + L(K) + L(p)}. \quad (6.24)$$

Making the requirement

$$R(i) > 2.7 \quad (6.25)$$

rejects hypothesis i at the 90% confidence level.

This method lends itself well to the GlueX environment since separate likelihoods can be calculated for each subdetector individually and then combined into overall likelihoods. For example, the likelihood a given track is a kaon is computed from individual detector likelihoods as:

$$L(K) = L^{CDC}(K)L^{BCAL}(K)L^{CKOV}(K)L^{TOF}(K). \quad (6.26)$$

To illustrate how likelihoods are calculated for specific detector elements, consider the forward TOF system. Start with a track with measured momentum p . The expected time required for this particle to traverse a distance L from the target to the TOF wall can be calculated under different assumptions for the particle mass:

$$t_i = \frac{L}{c} \left(\frac{m_i^2}{p^2} + 1 \right)^{\frac{1}{2}}, \quad (6.27)$$

where $i = \pi, K, p$. This time will have an associated error σ_i , which can be obtained by combining the inherent resolution of the scintillator and electronics (≈ 70 ps) with the effects of momentum resolution and the uncertainty in the path length. Assuming the time measurement follows a gaussian distribution, the likelihood for hypothesis i is then:

$$L^{TOF}(i) = \frac{1}{\sigma_i \sqrt{2\pi}} \exp \frac{-(t - t_i)^2}{2\sigma_i^2}, \quad (6.28)$$

where t is the measured time the particle spent between the target and the TOF wall. The closer the measured time t is to a calculated expected value t_i the more likely the particle being considered is of type i . Likelihoods for the other detectors are calculated in a similar way, using predicted and measured dE/dx for the CDC, predicted and measured time at the BCAL, and the expected and observed numbers of photoelectrons in the gas Cerenkov (or the predicted and measured Cerenkov angle in a DIRC detector).

A simulation of the integrated GlueX particle identification system using the likelihood methodology was carried out for $\gamma p \rightarrow K^* \bar{K}^* p$ events. The properties of these events have already been described at the beginning of this chapter (see figures 6.57 to 6.60). The generated events were sent through a full GEANT simulation and hits were recorded at each of the subdetectors associated with particle identification.

Relevant track measurements were smeared at each subdetector according to their expected resolutions. The dE/dx measurement of the CDC was smeared by 10%; the time of flight at the BCAL by 250 ps; and the time of flight at the forward TOF wall by 70 ps. In addition, the momentum and path length of each track was perturbed randomly by 1% to simulate uncertainties in the tracking. For the simulation using the Gas Cerenkov option (CKOV), the generated number of photoelectrons were distributed according to a Poisson distribution with an 80 cm C_4F_{10} radiator length with index of refraction $n = 1.0015$ and efficiency $N_0 = 90 \text{cm}^{-1}$ (see equation 6.17). The Cerenkov opening angle of the DIRC option was smeared by its estimated

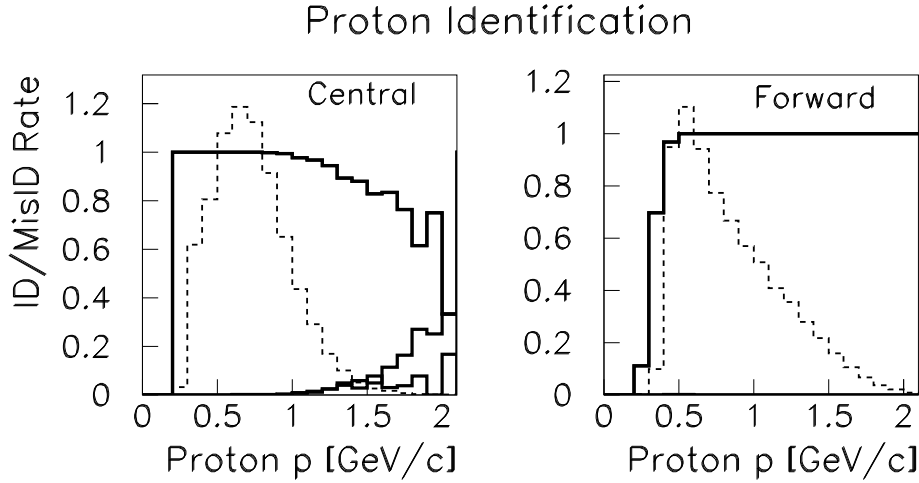


Figure 6.82: The acceptance of proton tracks in the reaction $\gamma p \rightarrow K^* \bar{K}^* p$. The left plot shows central tracks and the right plot shows forward tracks. The top curve is the correct identification rate; the bottom is the misID rate. The starting momentum spectra for proton tracks in the central or forward regions are shown in the background.

resolution, 2.1 mrad. The particle separations in numbers of sigma versus momentum using these parameters were shown previously (figures 6.58 to 6.60).

Likelihoods were then calculated for each track at each detector and combined into total likelihoods according to the method described above. Particles were identified by rejecting hypotheses at the 90% confidence level, as prescribed in equation 6.24. A particle is called a pion if the kaon hypothesis is rejected and the pion hypothesis is not rejected:

$$R(K) > 2.7, R(\pi) < 2.7.$$

Similarly, a particle is identified as a kaon if:

$$R(\pi) > 2.7, R(K) < 2.7.$$

Finally, to find protons, both the pion and kaon hypotheses must be rejected, but the proton hypothesis is not rejected:

$$R(\pi) > 2.7, R(K) > 2.7, R(p) < 2.7.$$

This is perhaps the most basic algorithm possible for this situation. Certainly improvements could be made, such as incorporating strangeness conservation.

The results of this exercise can now be studied in several different pieces. Case 1(CDC) and case 2(CDC,BCAL) tracks are referred to as “central” (see figure 6.57); case 6(CKOV,TOF) and case 7(CDC,CKOV,TOF) tracks are “forward.”

First consider proton identification. Figure 6.82 shows a nearly perfect proton identification rate for both the central region and the forward region; there is a drop in efficiency for central tracks above 1 GeV/c, but it has little effect on the overall identification rate. In addition, only a small fraction of tracks are misidentified.

Next, pion and kaon identification rates in the central region of the deceptor are shown in figure 6.83. Tracks less than 1 GeV/c are identified reliably; above that the efficiency drops to around 60%. Higher momentum central tracks are relying entirely on dE/dx information from the CDC in the relativistic rise region. With a dE/dx resolution of 10% this should be achievable

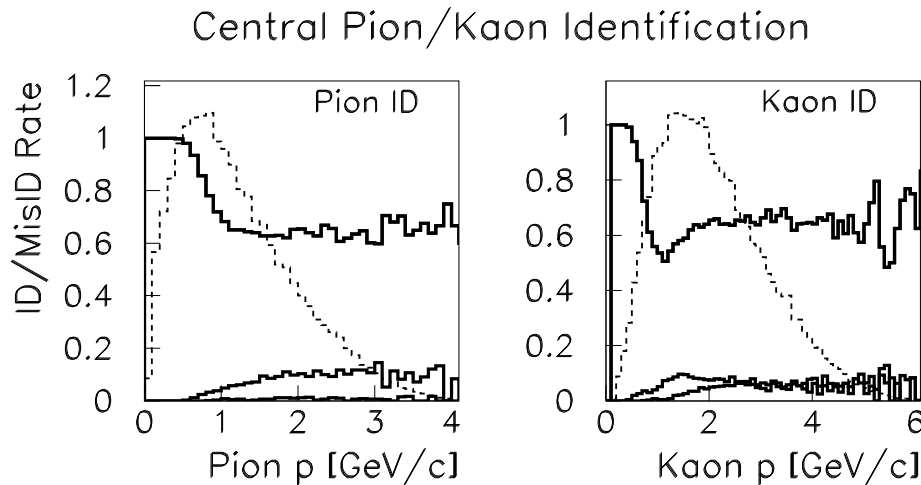


Figure 6.83: The acceptance of pions and kaons in the central region of the detector. The left plot is for pions; the right for kaons. The histograms in the background are the starting momentum spectra for pions and kaons in the central region. Each plot shows the identification and misidentification rates.

	π	K	p
Starting Number	50368	43665	62581
ID Rate	76.4%	64.0%	99.2%
MisID Rate	5.6%	10.1%	0.6%

Table 6.9: Particle identification in the central region for $\gamma p \rightarrow K^* \bar{K}^* p$ events. The statistics are for case 1(CDC) and case 2(CDC,BCAL) tracks. The starting number is the number of π , K , or p in the central region out of 100,000 total events generated.

at the 2σ level (also see figure 6.59). Table 6.9 tabulates all the particle id results for central tracks.

Results for tracks in the forward region of the detector are shown in figure 6.84. The top two plots use the gas Cerenkov option. Notice the drop in efficiency between 2 and 3 GeV/c where the momentum is too high for the TOF wall to be effective, but still not high enough to reliably measure photoelectrons from pions in the Cerenkov detector. The DIRC option solves this problem; its results are shown in the bottom two plots. Table 6.10 summarizes the efficiency numbers of forward tracks under the two different Cerenkov options. Finally, the central and forward cases are combined into overall pion and kaon identification rates in figure 6.85. The overall rates are tabulated in table 6.11.

	Gas Option			DIRC Option		
	π	K	p	π	K	p
Starting Number	38793	38789	30267	38793	38789	30267
ID Rate	94.4%	91.4%	99.1%	98.6%	90.3%	99.2%
MisID Rate	1.5%	4.8%	0.02%	0.3%	2.0%	0.8%

Table 6.10: Particle identification in the forward region for $\gamma p \rightarrow K^* \bar{K}^* p$ events. The statistics are for case 6(CKOV,TOF) and case 7(CDC,CKOV,TOF) tracks. The starting number is the number of π , K , or p in the forward region out of 100,000 total events generated.

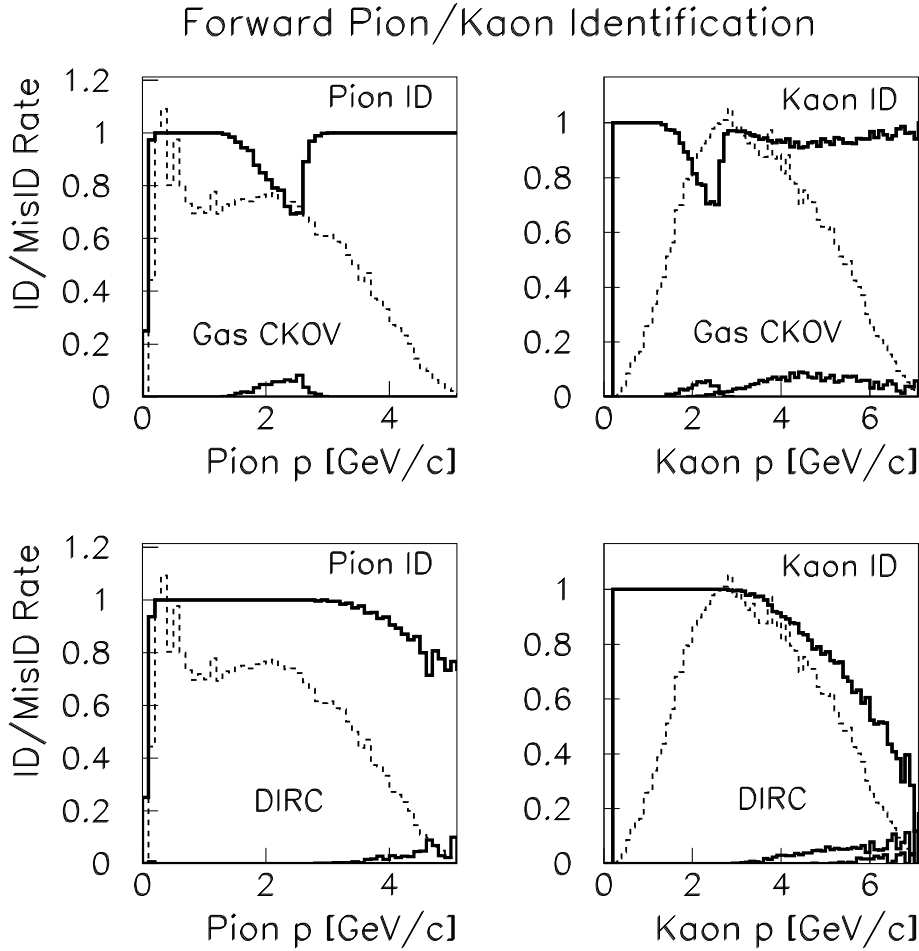


Figure 6.84: The acceptance of pions and kaons in the forward region of the detector. The top two plots are for the gas Cerenkov option; the bottom two are for the DIRC option. The left plots show pions; the right kaons. The histograms in the background are the starting momentum spectra for pions and kaons in the forward region. The curves in each plot represent the identification and misidentification rates.

	Gas Option			DIRC Option		
	π	K	p	π	K	p
Starting Number	100000	100000	100000	100000	100000	100000
ID Rate	80.4%	71.2%	94.3%	82.9%	71.9%	94.7%
MisID Rate	3.5%	6.8%	0.4%	2.9%	5.3%	0.8%

Table 6.11: Overall particle identification for the reaction $\gamma p \rightarrow K^* \bar{K}^* p$. The statistics are for all track cases.

It should be remembered that one of the crucial design parameters of the GLUEX experiment – in addition to, and perhaps more important than, the total efficiency numbers – is the uniformity of acceptances in the angles that will be used in Partial Wave Analyses. Efficiencies based on identification rates for the Gottfried-Jackson $\cos\theta$ angle of the $K^* \bar{K}^*$ system are shown in figure 6.86. This acceptance rises at $\cos\theta \approx \pm 1$ and falls at $\cos\theta \approx 0$ for the gas Cerenkov

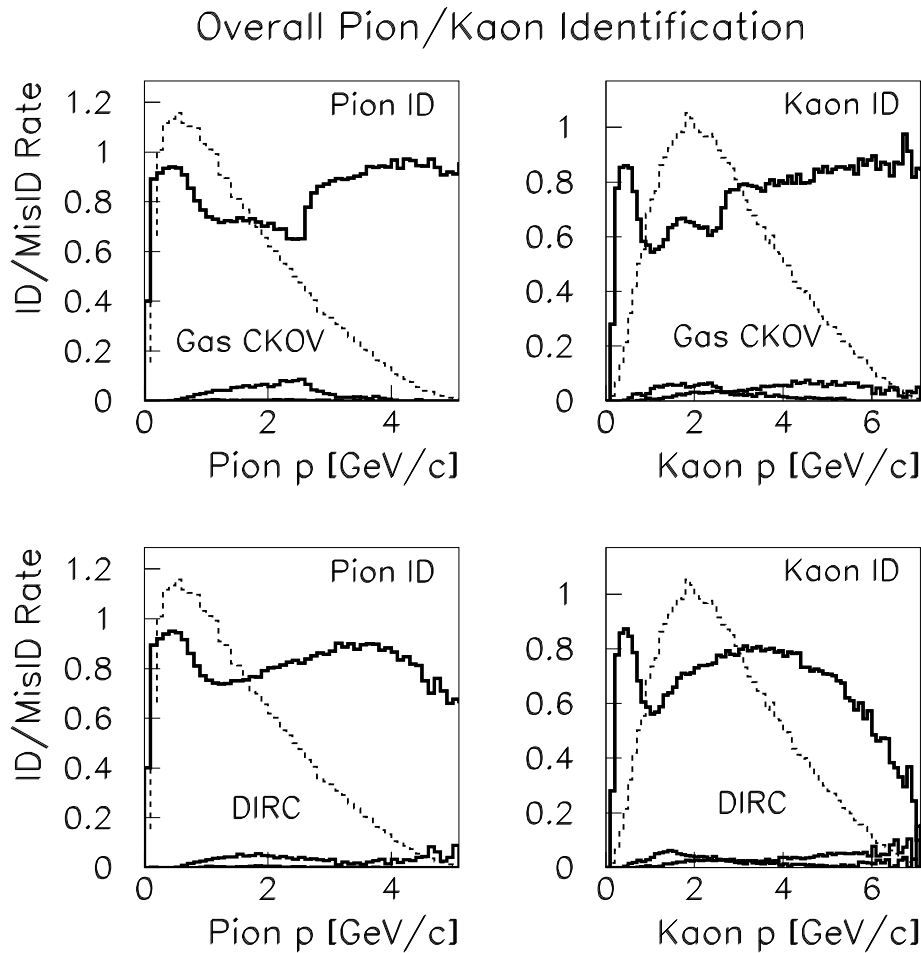


Figure 6.85: The overall acceptance of pions and kaons in all regions of the detector in the reaction $\gamma p \rightarrow K^* \bar{K}^* p$. The top two plots are for the gas Cerenkov option; the bottom two are for the DIRC option. The left plots show pions; the right kaons. The histograms in the background are the overall starting momentum spectra for pions and kaons. Each plot shows the identification and misidentification rates.

option for the following reason. When $\cos\theta$ is near its extremes, the final state particles are typically divided into high momentum (along the decaying resonance direction) and low momentum (against the decaying resonance direction) cases. The high momentum tracks are above pion threshold and are identified by the gas Cerenkov system; the low momentum tracks are effectively identified by the TOF wall. On the other hand, when $\cos\theta$ is near zero, final state tracks tend to fall in the momentum region where neither the TOF nor the gas Cerenkov is effective.

The DIRC option avoids this problem. Consequently, the $\cos\theta$ acceptance of the second plot of figure 6.86 is significantly more uniform.

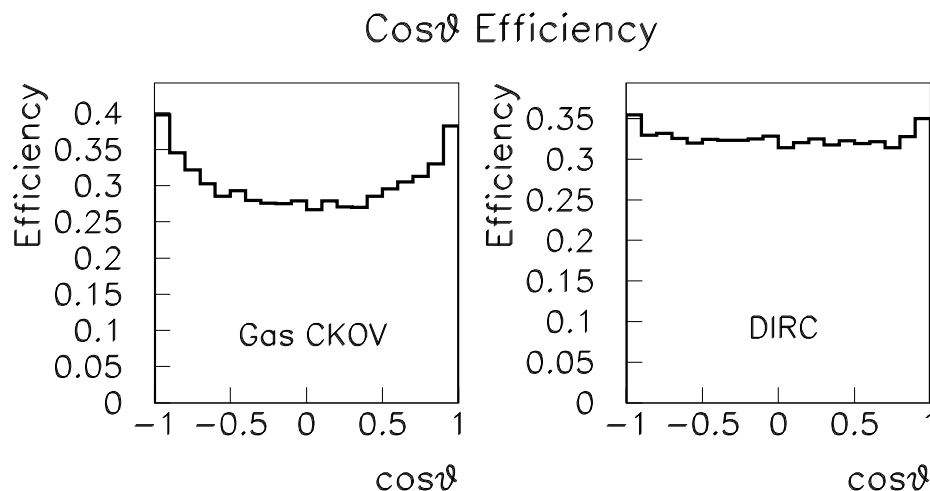


Figure 6.86: Angular efficiencies for $\cos\theta$ in the Gottfried-Jackson coordinate system for $\gamma p \rightarrow K^*K^*p$ events. The left plot is for the Cerenkov option, the right for the DIRC option.

6.6 Detector Integration

The assembly and integration of each of the detector subsystems into the GLUEX detector requires careful coordination and attention to many diverse issues. The magnetic field configuration outside the magnet dictates the location and orientation of standard PMTs and/or use of high field devices such as HPMTs and SiPMs. The field distribution can be affected by magnetic materials used for support structures such as iron and, therefore, care must be taken in choosing common materials for the various support systems. The magnetic field in the vicinity of the Čerenkov counter is estimated to be approximately over 1 kG at the location of the readout devices and between 0.300 kG and 0.160 kG at the position of the PMTs for the forward LGD. The mounting and assembly of detectors must allow for the delivery of services required for their

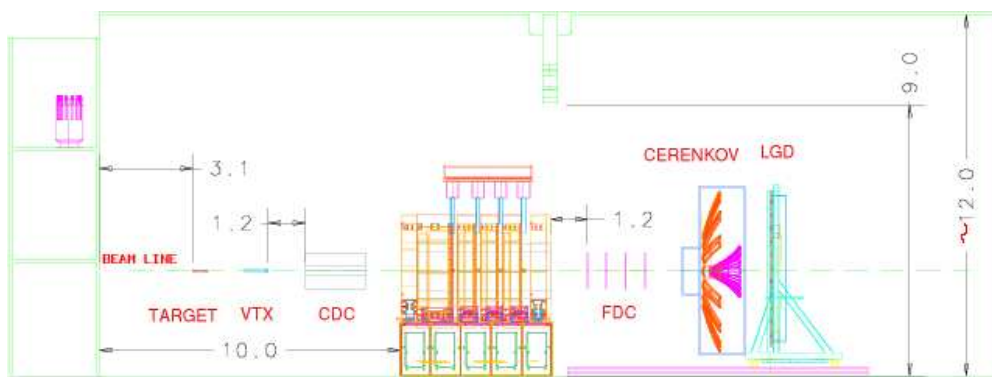


Figure 6.87: Exploded view of detector showing the detector subsystems in their extracted positions. The magnet does not move and detectors are inserted both from upstream and downstream into their nominal positions for normal operation.

operation, including cryogenics, cooling, electrical power, ventilation, gas connections, high voltage and signal and monitoring cables for all detectors. Moreover, access to each sub-system must be facilitated for purposes of maintenance or repair.

The detector sub-systems are shown in Figure 6.1 while the general layout of HALL D with all detectors extracted is shown in Figure 6.87. As the detector will need to be in its extracted position for both installation and servicing, it is important that its layout in the HALL D building accommodate access to the detector. Figure 6.88 shows a sketch of the detector in HALL D. The cryogenic connections to the solenoidal magnet are brought in from the north-west corner of the building, opposite the ramp used for truck access. This permits a large staging area in front of the door and minimal blocking of crane movement by the cryogenic lines. These lines can also be used to feed other cryogenic systems such as the liquid hydrogen target and potentially VLPCs used in the start counter. Gas lines from external mixing systems can also be run along this common path to minimize obstructions for crane and assembly operations.

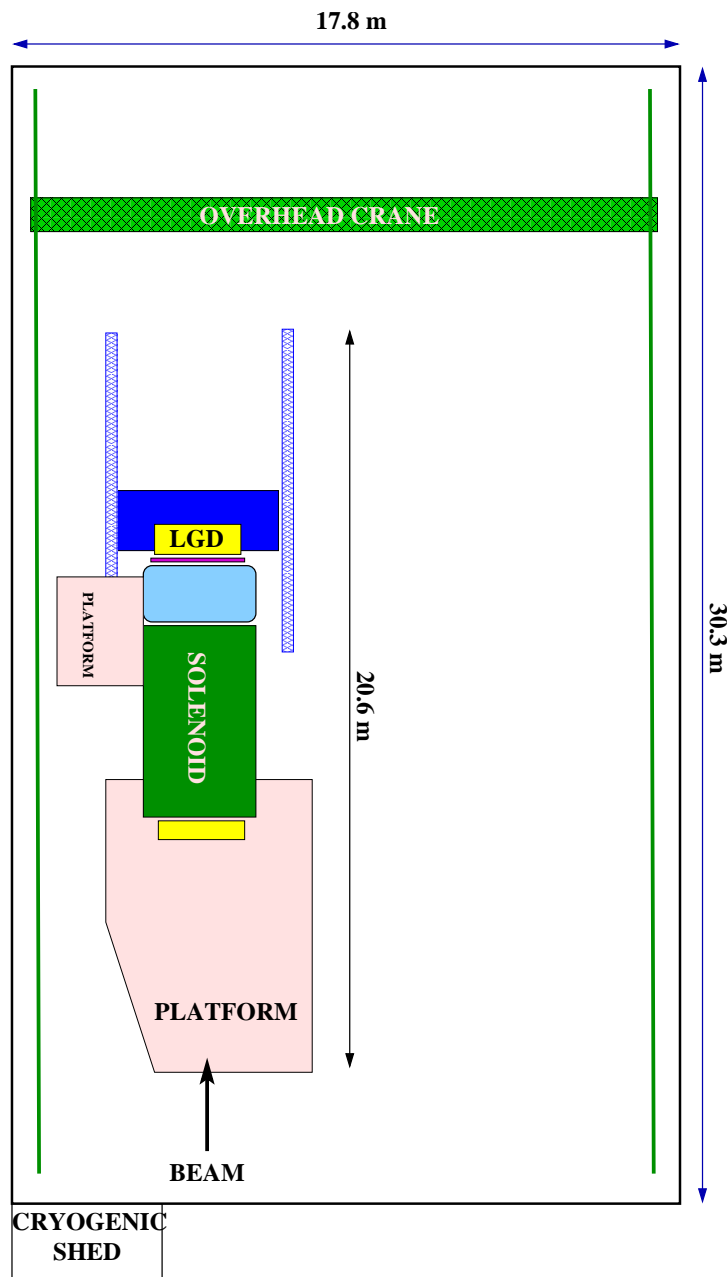


Figure 6.88: Plan view of the GLUEX experiment in HALL D.

Electrical power will be most likely delivered in trenches in the floor from breaker panels located on the north wall of the building. Clean power will be provided to detector electronics using isolation transformers as close to the detector as possible. As an example, the estimated power consumption of the forward calorimeter is 30 KW. All detector frames will be connected to the building ground network both for safety and to minimize electrical noise.

In terms of installation, most of the detector is fairly open and can be quickly accessed with minimal disruption of operations. However, the limited space inside the solenoidal magnet deserves special attention. This space contains the BCAL and its support structure, the Straw-tube Chamber, CDC, the Forward Drift Chambers, FDC, and the structures which both align and support these chambers as well as the mechanisms for extracting them. Finally, inside the CDC is space for the liquid hydrogen target, the beam pipe and the Start counter. Space allocation also needs to be made to assure that signals cables can be brought out from the detectors, while voltage and monitoring cables as well as gas, cryogenics and cooling lines can be brought to the appropriate detectors. Table 6.12 shows the radial space allocation inside the solenoid. The spaces labeled *keep out* are reserved for support, installation structures, signal and power cables, and other necessary services to the detectors such as gas and cooling.

Detector Name	r_{min}	r_{max}
Solenoid	92.7 cm	
Keep Out	90 cm	92.7 cm
Barrel Calorimeter	65 cm	90 cm
Keep Out	59 cm	65 cm
Straw Tube Chamber	13 cm	59 cm
Forward Drift Chambers		59 cm
Keep Out		12 cm

Table 6.12: A radial space allocation map for the space inside the GLUEX solenoid.

6.6.1 Assembly and Mounting

As much of the GLUEX detector will need to be assembled in HALL D, the construction of the building is critical to any time line of the experiment. It is absolutely necessary that JLab do everything possible to guarantee early construction of this building. Once the building can be occupied, the assembly of the detector can begin. The first item will be the solenoidal magnet. It is transported in sections and will need to be re-assembled inside HALL D. It is also expected that both the BCAL and the LGD calorimeters will be assembled in HALL D. The assembled LGD will not fit through the door. It is also possible that parts of other detectors would be assembled in the HALL D building as well.

Of all the in-hall assemblies, the BCAL is likely to be another time line bottle neck. The time from start of construction until delivery at JLab is estimated at three years, but it is likely that the detector would arrive in several shipments spread out over the 3-year time frame. There are currently two possible assembly scenarios. The first follows what was done with the KLOE detector. This would have the BCAL being assembled inside the solenoid. The draw back to this plan is that the assembly of th BCAL cannot begin until the solenoid is fully installed. A second scenario would be to assemble the BCAL in a vertical orientation outside the solenoid, and then rotate it to horizontal and roll it into the solenoid as a single unit. This latter scenario both allows assembly to proceed in parallel with the solenoid and requires less service space between the outside of the BCAL and the inside of the solenoid. In both scenarios, the BCAL would be held in place with bolts that come through ring girders in the gaps between the magnet coils. These would connect to the 2.5 cm thick Aluminum backing plates on the BCAL modules as shown in Figure 6.89. In both installation scenarios, an assembly and installation jig will need to be designed and built. These options are currently under study by the engineering staff at JLab.

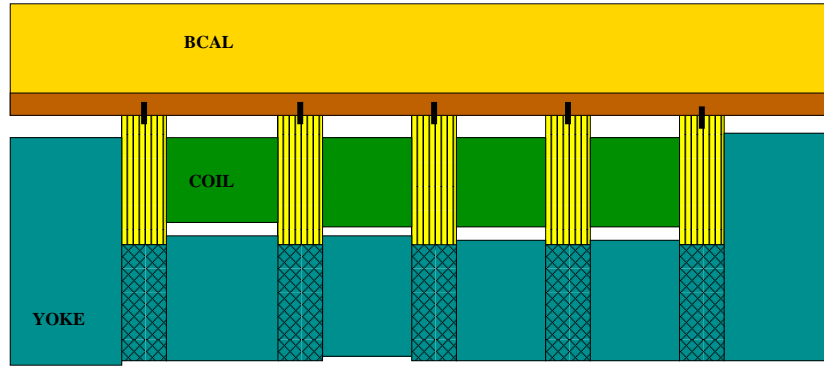


Figure 6.89: The Barrel Calorimeter bolted to the inside of the solenoid.

Once the BCAL has been mounted on the inside of the magnet, only the readout electronics will be accessible. Because of its design, it is anticipated that once it has been installed, it will not be removed. If for some reason it became crucial to replace a module, a fairly extensive down time would need to be scheduled. However, given that there is nothing that can be serviced except for the readout electronics, such an event is considered highly unlikely over the lifetime of the experiment. Finally, to facilitate the installation of the tracking devices inside the solenoid, we anticipate placing a protective cover over the inner face of the BCAL. This will both protect the calorimeter and provide a surface to which the chamber supports can be mounted.

After the BCAL has been mounted in the solenoid, it will be necessary to install a pair of rails along the length of the detector. These rails will be used to support the CDC and FDC packages. Extensions can be added to allow for installation and extraction of the chambers. There is some possibility of the lead in the barrel calorimeter settling slightly over time. While we are currently investigating this, we also recognize that the rails will need to be fitted with bearings that have some play to prevent things from locking up due to small shifts in the *bed rock*. Both because of the difficulty of maintaining precision alignment between two rails over the 4 m length of the magnet and the possibility of settling in the BCAL, we anticipate no more than one precision rail, with the 2nd rail being used for load bearing.

The CDC will be inserted from the up-stream end of the magnet, while FDC will be inserted from down-stream end. On the down-stream end, the Čerenkov, TOF and LGD detectors will be rolled back to make room for the FDC packages. On the up-stream end, the UPV will need to be put in place after the CDC has been installed. Then the START counter and target will be inserted into the CDC from the upstream end. They will be mounted on an independent cantilever system.

The Čerenkov counter and forward calorimeter will be mounted on independently movable support frames which can be moved in and out of their nominal location for access to the FDC. The TOF detectors will be mounted on the frame for the forward calorimeter. Each support structure will be self-contained, including electrical power and the appropriate readout electronics. Access platforms will be provided to allow easy access to the PMTs and readout electronics.

6.6.2 Survey and Alignment

In order to achieve the physics goals of the experiment, a system must be devised that can measure and maintain at least $100\ \mu\text{m}$ relative alignment of all of the tracking packages inserted into the magnet. The locations of the drift chamber wires relative to each other and the magnetic field are the most critical alignment tasks for the experiment. In addition, for ease of maintenance, the positions of the chambers should be either reproducible at that level, or a system needs to be established that can easily survey them into position at this accuracy. It will also be important to have an on-line monitoring system in place to dynamically correct for time dependent shifts in alignment. Such shifts might arise due to settling of the BCAL, thermal expansion and contracting of the chambers themselves, or accidental moving of the chambers when other detectors are being serviced. The collaboration is currently exploring the use of a system used by ATLAS for maintaining alignment.

As the CDC and FDC are inserted from opposite ends of the magnet, the mating and initial alignment are blind. The z positions of these chambers can be accurately registered at a single point by surveying in stops along the guide rail. We will also need a remote adjustment system that allows for correction of possible *pitch*, *roll* and *yaw* of the chamber packages.

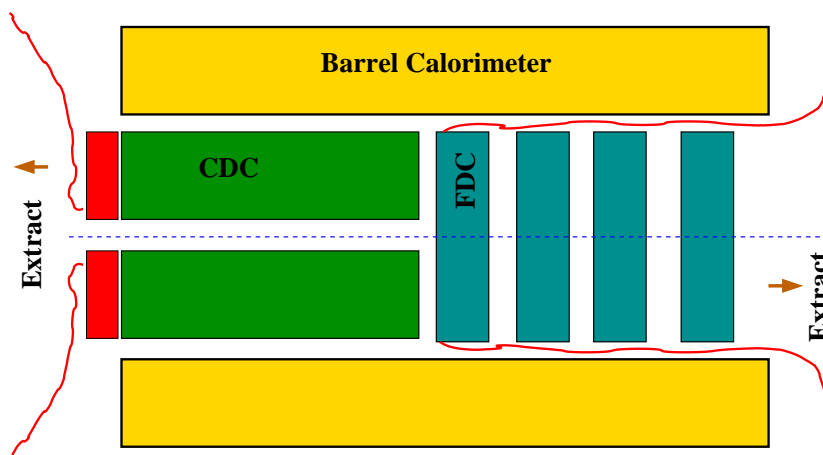


Figure 6.90: The insertion of the Central and Forward Tracking chambers inside the Barrel Calorimeter.

6.6.3 Access

Ease of access to the detector for maintenance ensures short commissioning and debugging times. Our goal is to allow maintenance of all detector components in less than one day. In order to maintain or check the upstream BCAL readout, the UPV will have to be removed and the service platform must be designed in a way to allow access to readout both above and below the horizontal scattering plane of the detector. To service the CDC, the UPV, the target and START detectors must be moved out of the way. All serviceable elements are located on the up-stream end of the CDC. To access the FDC and/or the downstream BCAL readout, the Čerenkov and forward calorimeter must be moved on their rail systems, as shown in the exploded view in Figure 6.87. Service to the FDC is likely to be the most involved operation. Once the downstream detector packages are moved out of the way, a support structure will need to be craned in, and the chambers extracted from the solenoid.

The readout electronics for all the systems will be accessible without having to move any detector component. The PMTs for the Čerenkov, TOF and LGD will be accessible by at most moving the forward calorimeter carriage. Access to the LGD enclosure will in principle be easy, but radiation levels must be measured and deemed to be at a safe level prior to any access.

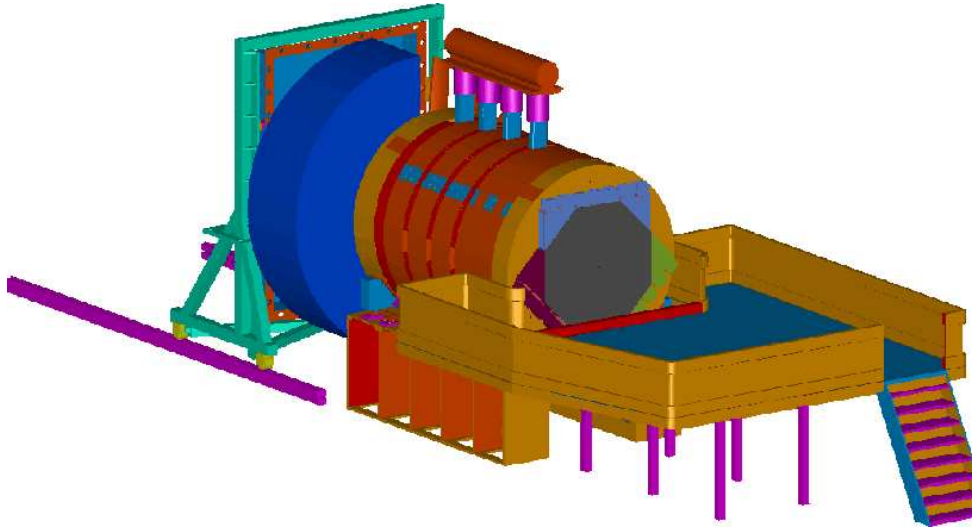


Figure 6.91: Detector and upstream platform for service of the inner detector packages.

6.6.4 Interaction Between Subsystems

The detectors in the forward direction (Čerenkov, TOF and LGD) are relatively isolated mechanically and operate independently of other systems. The detectors inside the magnet, however, are in close proximity and mounted on the same mechanical frames that are anchored on the BCAL and/or the solenoid. Therefore, cabling, power consumption, and access for maintenance must be coordinated carefully.

6.6.5 Cabling

All detector electronics will be located near the detector itself. This will minimize cable lengths and eliminate the need for large cable runs from the detector to electronic racks far from the detector. The racks of electronics servicing the inner detectors will be located on a platform upstream of the magnet with ample space for access. A possible *Access Platform* is shown in Fig.6.91 with the primary aim being that detectors can be operated both inside and outside the solenoid without making any disconnections. This implies that either the cabling for START detector, CDC and FDC will have enough slack so that they can be moved in or out of the magnet without any disconnections, or that the electronics will themselves move along with the detector elements. It is crucial that the detectors can be operated in the extracted position for testing and the installed position during normal operation without wiring changes.

Chapter 7

Readout Electronics

7.1 Overview

The goal of the GLUEX readout electronics system is to digitize and read out the detector signals for level 1 trigger rates of up to 200 *kHz* without incurring downtime. A pipelined approach is required. The digitized information will be stored for several μs while the level 1 trigger is formed. Multiple events must be buffered within the digitizer modules and read out while the front ends continue to acquire new events.

A summary of the GLUEX detector subsystems from an electronics viewpoint is shown in figure 7.1.

Two basic types of readout electronics will be used in GLUEX, FADCs and TDCs. Detectors which measure energy will be continuously sampled with flash ADCs while detectors which require precise time measurements will use a multi-hit TDC. No currently available commercial solutions exist. These boards will be designed by our collaboration. Prototypes have been constructed, and are being tested.

The number of channels in the GLUEX detector is not large enough to justify the financially risky development of custom integrated circuits. ICs developed for other experiments will be used as well as commercially available chips. Programmable logic devices will be extensively used for data path, memory, and control functions.

Technology is constantly evolving, and the optimum solution for the GLUEX detector depends on when funding becomes available and the construction schedule. Presented here is a preliminary design which could be implemented with currently available components.

7.2 FADCs for Calorimetry

The calorimeters will be read out with 8-bit, 250 *MHz* FADCs. The 250 *MHz* sampling clock will be derived from the 1499 *MHz* accelerator clock. This sampling rate and bit depth is well matched to the FEU84-3 PMTs used in the Forward Calorimeter, and is adequate for the silicon PMTs used in the Barrel Calorimeter. Additional FADC channels will read out the Photon Tagger, Backwards Veto, Start Counter, Čerenkov Detector, and time-of-flight PMTs.

Figure 7.2 shows an FEU84-3 PMT pulse digitized by the prototype FADC described in section 7.2.1. Note that the sum of the samples from 120 to 180 *ns* is 1429; for this PMT the 8-bit FADC is equivalent to a 10 or 11-bit conventional charge-integrating ADC. To address resolution concerns, simulations were performed to show that the proposed FADC provides an adequate measurement. Pulses measured with a digital oscilloscope were fitted to determine their functional form. The response of the FADC was simulated using this functional form and the time integral of the function was compared to the summed output of the simulated FADC for many pulses. Since the relationship between deposited energy and pulse height in this type of calorimeter is known, direct comparison of the resolution due to the FADC and the resolution of

Summary of GlueX Detector Subsystems

Detector	Photon tagger	Upstream Photon veto	Start counter	Central drift	Forward drifts	Cerenkov	Time-of-flight	Barrel calorimeter	Forward calorimeter
Type	Scintillator	Scintillator	Scintillator	Straw tube	Planar chamber	Gas	Scintillator	Sci fibers	Lead glass
Energy resolution	0.1% (segmentation)	10%/√E	N/A	20%	N/A	N/A.	N/A	10% @ 1 GeV	3.6% + 7.1%/√E
Channel count	192	20	40	3240	2900 anode 11,400 cathode	40	168	960	2500
Signal source	PMT	PMT	PMT	Straw tube	anode wires cathode strips	PMT	PMT	SiPMT	PMT
Physics signal	100 pe	100 pe	100 pe	25 e	25 e	5 pe	500 pe	100 pe/GeV	250 pe/GeV.
Gain in detector	10°	10°	10°	10°	10°	10°	10°	10°	10°
Typical charge	16 pC	16 pC	16 pC	40 fC	40 fC anodes 4 fC cathodes	1 pC	80 pC	16 pC/GeV	40 pC/GeV
Preamp gain	no	no	no	10 ³	10 ³ anodes 10 ³ cathodes	10 ²	no	no	no
Discrimination	constant fraction	no	constant fraction	no	yes (anode) no (cathode)	no	constant fraction	constant fraction	no
Time resolution	100 ps	1 ns	350 ps	1 ns	1 ns	3 ns	80 ps	200 ps	400 ps
Dynamic range	5	100	100	1000	100 anodes 1000 cathodes	10	10	1000	1000
FADC	8 bits 250 Msps	8 bits 250 Msps	8 bits 250 Msps	10 - 12 bits 125 Msps	Cathodes: 10 - 12 bits 62.5 Msps	8 bits 250 Msps	8 bits 250 Msps	8 bits 250 Msps	8 bits 250 Msps
TDC	62 ps	no	62 ps	no	Anodes: 125 ps	no	31 ps	62 ps	no
Level 1 trigger	yes (low rate runs)	no	track count	no	no	no	track count	track count	energy sum

Figure 7.1: Detector subsystems

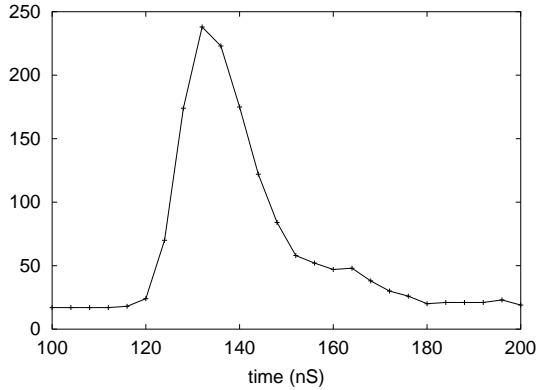


Figure 7.2: Digitized FEU84-3 pulse.

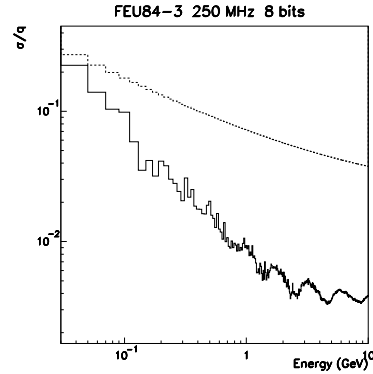


Figure 7.3: Dashed - calorimeter resolution, Solid - FADC resolution.

the calorimeter is possible. Figure 7.3 shows the result of this comparison. Clearly, above 0.15 GeV the resolution of the FADC is small compared to the intrinsic resolution of the calorimeter.

The FADCs will also give a measurement of the time a photon arrived at the calorimeter. Previous work [120, 121] indicates that a time resolution better than the FADC sampling interval can be achieved by fitting the FADC waveform. To study how well this time could be determined a “library” of pulses from phototubes of the type to be used was created using a digital oscilloscope with a 2.5 GHz sampling frequency. The leading edge of these sampled pulses were fitted to a 9th order polynomial to determine the location of various “features” of the pulses. The features considered were the time the pulse achieved 10, 25, 50, 75, 90 and 100% of its maximum value. These features carry the arrival time information of the pulses and were used as reference times.

To determine how well the FADC could determine the pulse arrival time, the samples from the digital oscilloscope (2.5 GHz) were averaged over 10 samples (to 250 MHz) and quantized to 8 bits. These transformed samples are what would be expected from the FADC system proposed here. Using only the bin containing the pulse maximum and the two samples preceding it and a simple algorithm, it was found that the 50% crossing time could be determined with a resolution of 160 ps compared to the time determined by the detailed fitting described above. This resolution is sufficient to determine if a pulse is in time with an event (rejecting background) or to determine the time of the event sufficiently well to select the beam “bucket” that initiated the event.

7.2.1 Prototype

A single channel prototype of the calorimeter FADC has been designed and built at Indiana University. A block diagram is shown in Fig. 7.4 and a photo in Fig. 7.5.

A differential amplifier inverts the negative PMT signal and shifts the voltage levels to match the input range of the digitizer integrated circuit. The digitization is performed by an SPT7721 integrated circuit manufactured by Fairchild Semiconductor [122]. This IC costs about US\$20. An 8-bit value is produced internally every 4 ns; two samples are output every 8 ns (125 MHz).

All digital functions are performed in a Xilinx [123] XC2S50 programmable gate array. This IC costs about US\$10. A dual port RAM configured as a circular buffer stores the data for 8 microseconds. Upon receipt of a trigger signal the data from the time window of interest is copied to an output FIFO which can buffer the data from multiple events. This FIFO is interfaced to a 32 bit, 33 MHz PCI bus. More information on this prototype is available [124].

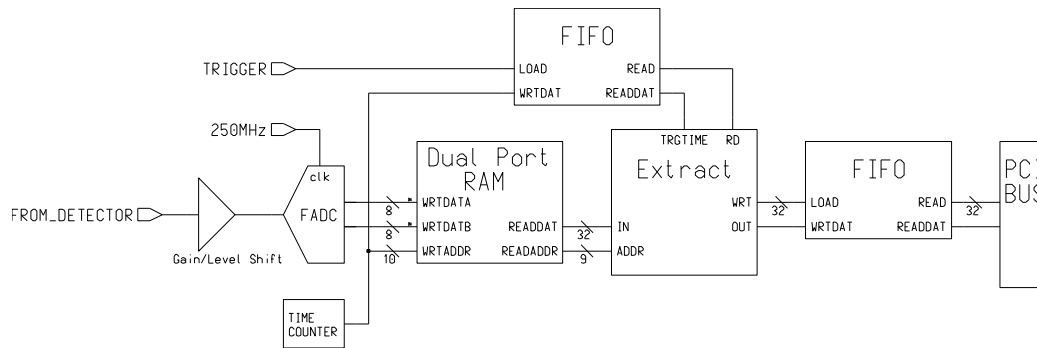


Figure 7.4: Block diagram of prototype FADC board.

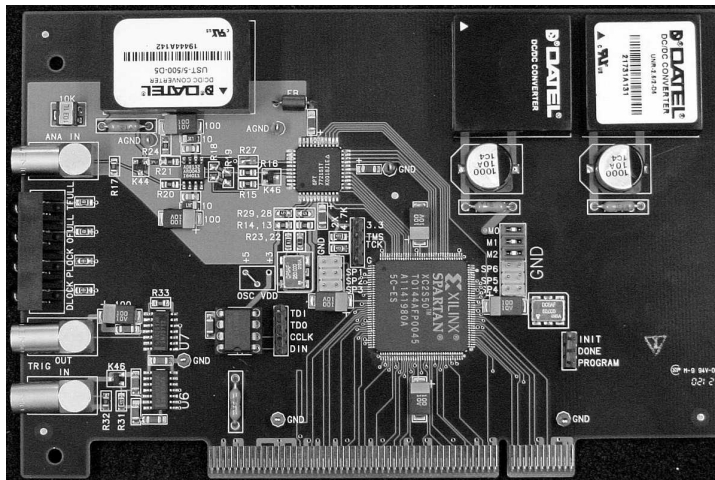


Figure 7.5: Photograph of prototype FADC board.

7.2.2 Additional requirements for final version

The final version of the calorimeter FADC board will include pipelined adders operating at the 125 MHz digitizer output clock which continuously sum the digitized information from all channels on a board. Additional pipelined adders will sum the information from all boards in a crate, and then sum the information from all the crates associated with a detector. The sum of all channels will be passed through a shift register giving a time history. Successive samples within a programmable time window will be summed, analogous to the gate in a conventional charge sensitive ADC. Energy sums from the Forward and Barrel Calorimeters will be used in the level 1 trigger. A block diagram is shown in Fig. 7.6.

Assuming a 100 ns time window, each FADC channel will produce 25 bytes of data per level 1 trigger. In the final version of the FADC we will want to suppress the readout of channels with no data. The FADC data will be processed in real time to provide an energy and time measurement. We believe that the raw FADC data can be reduced to about 10 bytes per channel. This zero suppression and pulse shape processing may be done at the channel level in the gate array, at the board level, the crate level, the detector system level, or in some combination of these levels.

7.3 FADCs for Tracking

The Central Tracking Drift Chamber anodes will be read out with 10 or 12-bit, 125 MHz FADCs. The additional dynamic range is required for the dE/dx measurement. The Forward Tracking

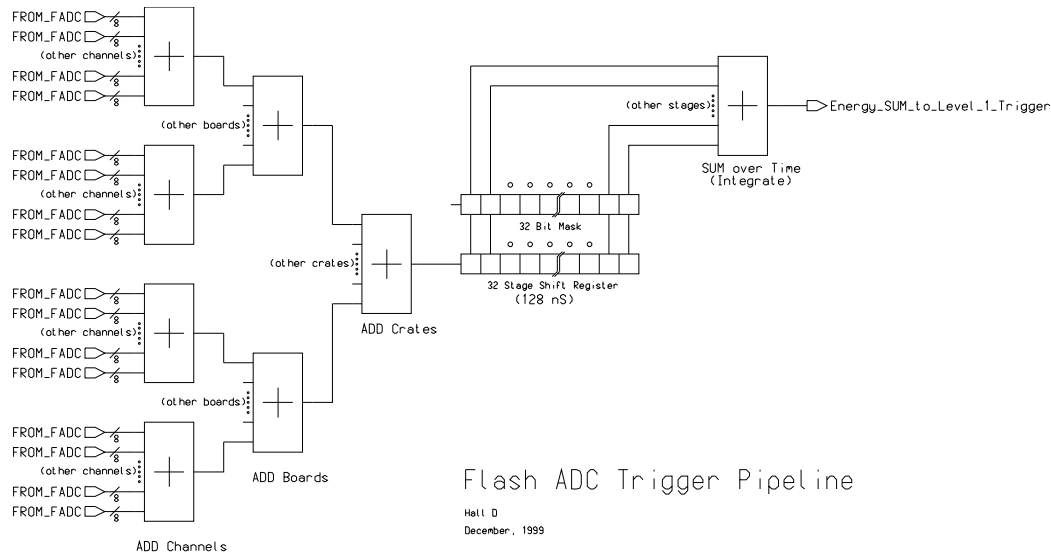


Figure 7.6: Block diagram of energy sum.

Drift Chamber cathodes will be read out with 10 or 12-bit 62.5 *MHz* FADCs. The exact read out electronics requirements for these detectors is the subject of ongoing R&D efforts.

7.4 TDCs

The Photon Tagger, Start Counter, Forward Drift Chamber anodes, Čerenkov Detector, Barrel Calorimeter, and Time of Flight detectors will be read out by multi-hit TDCs.

7.4.1 Jefferson Lab TDC

A high resolution pipeline TDC module has been developed for use at Jefferson Lab. The design is targeted to meet the requirements of current experiments, as well as to serve as a prototype for future experiments at Jefferson Lab, including Hall D. The design is implemented as a VME-64x module. This bus standard was chosen because it is already in use at Jefferson Lab, has good (and evolving) data transfer capabilities, and reasonable channel densities are possible.

The module is built around the TDC-F1 integrated circuit from acam- messelectronic gmbh [6]. The TDC-F1 chip was designed for the COMPASS experiment at CERN [7], and costs about \$130 each in small quantities. The chip utilizes purely digital delay techniques to measure time. In normal mode the TDC-F1 chip provides 8 input channels with resolution of 120 ps (LSB). In high resolution mode channels are combined in pairs to yield a resolution of 60 ps for 4 input channels. The dynamic range for measurement is 16 bits. The resolution of the chip is tunable about its nominal value. A PLL circuit adjusts the core voltage of the chip to compensate for temperature and supply voltage variation, assuring stability of the resolution value. On-chip buffering for input channels, triggers, and output data allows for multihit operation with nearly zero downtime. The chip also has a complex trigger matching unit that can filter out hits unrelated to the input trigger. When enabled, only hits that are within a programmed timing window and latency from the trigger time are kept. The trigger matching feature is used in common start and synchronous measurement modes. In common start mode, an external start signal resets the internal measurement counter and a delayed trigger signal sets the measurement window. In synchronous mode, an external 'sync reset' signal is used to reset the internal measurement counter and clear internal buffers. Internal start signals are then automatically generated at a programmable rate.

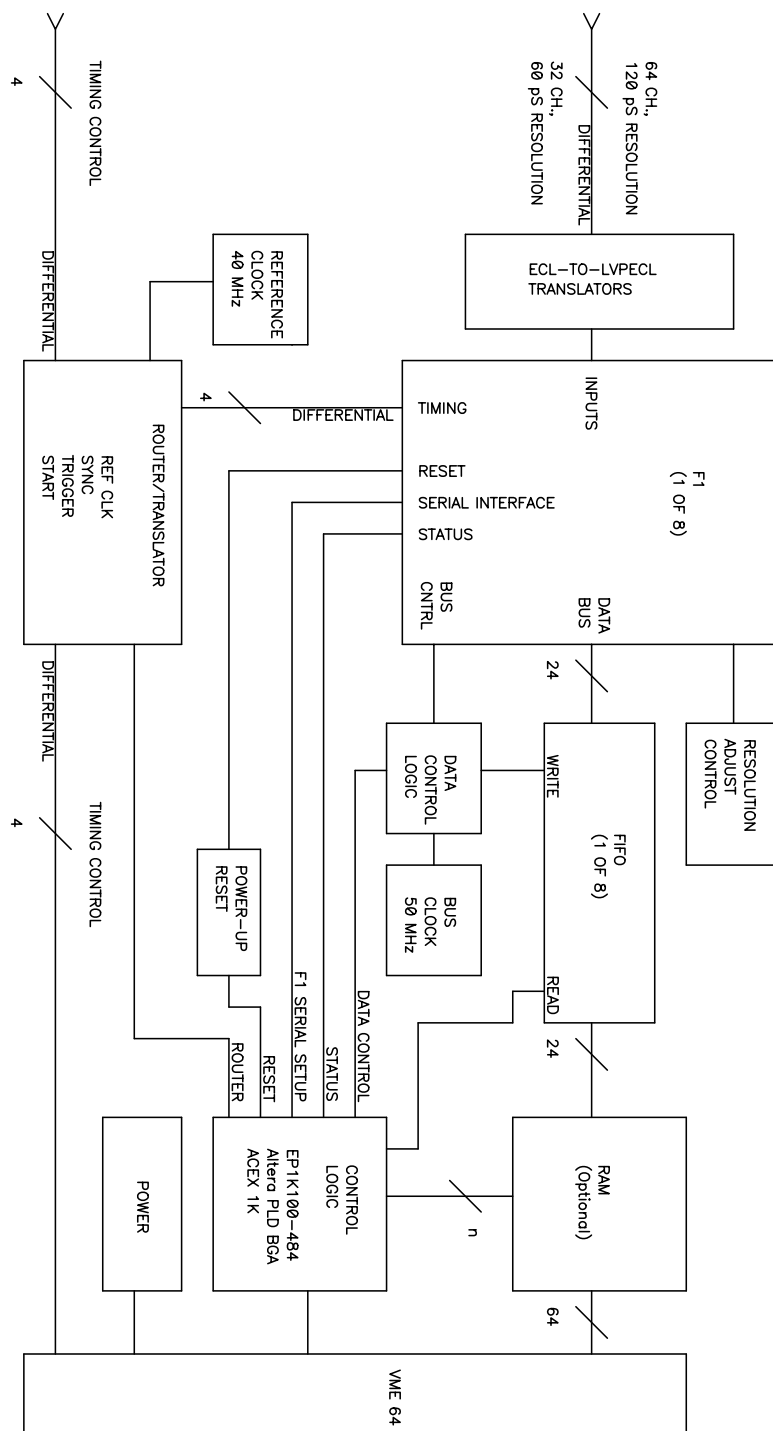


Figure 7.7: Block diagram of TDC board.

Figure 7.7 shows a block diagram of the TDC module. The 8 TDC-F1 chips on the module provide 64 channels in normal mode, or 32 channels in high resolution mode. Front panel input signal levels are differential ECL to be compatible with existing systems a Jefferson Lab. Timing control signals are also available through backplane connections for ease of system integration. A 128K word deep FIFO is attached to each TDC-F1 chip to buffer its output data. In addition, a global 1K word FIFO buffer is implemented within the single FPGA that controls the module.

The external RAM shown in the figure is not present on this version. The module can be set up to interrupt the crate controller after a programmable number of triggers have been received. During read out the module will provide a block of data associated with a programmed number of triggers, and then terminate the transaction. To enhance system performance a set of TDC modules may be read out as a single logical read using a multiblock read protocol. This involves passing a token between modules along a private daisy-chain line. In this setup, only the first module in the chain will generate the interrupt, and only the last module in the chain will terminate the transaction. Configuration parameters for the 8 TDC-F1 chips are stored in non-volatile memory on the module and may be updated by the user. The configuration process is automatic at power up.

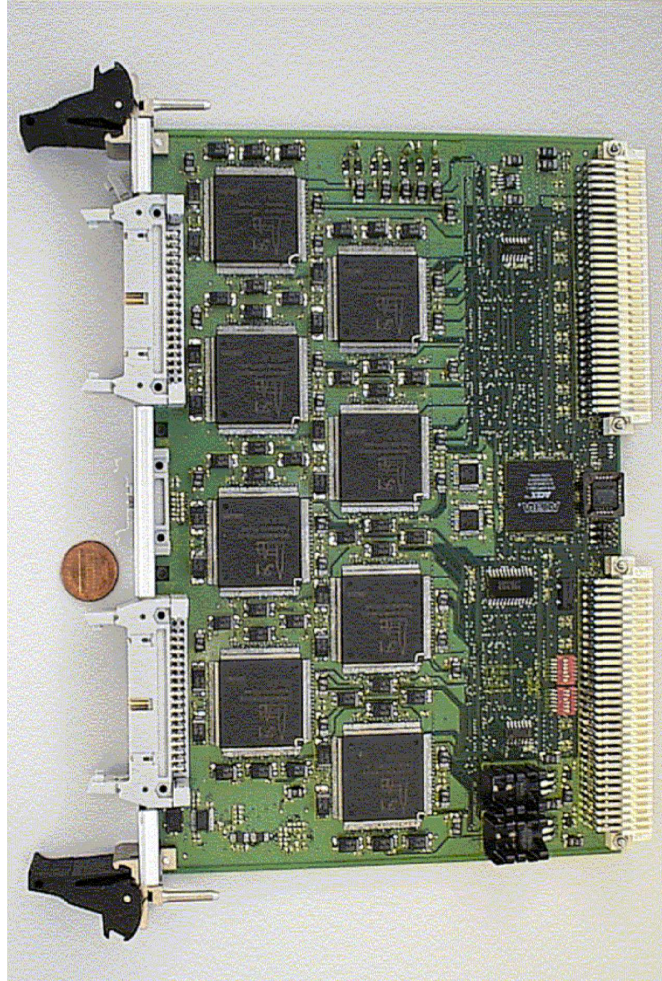


Figure 7.8: Photograph of TDC board.

A photograph of the module is shown in Figure 7.8. Fifty TDC modules have been produced and are currently being installed into Jefferson Lab experiments in Halls B and C.

7.4.2 TDC Performance

Figure 7.9 shows the timing distribution for an input signal that has a fixed time relationship to the start signal. The TDC was operated in high resolution mode. Unfolding the uncertainty of the input signal (33 ps) from the measured distribution yields a TDC resolution (RMS) of 61.2 ps. Figure 7.10 shows the equivalent distribution for a TDC operated in normal resolution mode. The resolution is 86.2 ps. These resolutions were confirmed across the entire dynamic

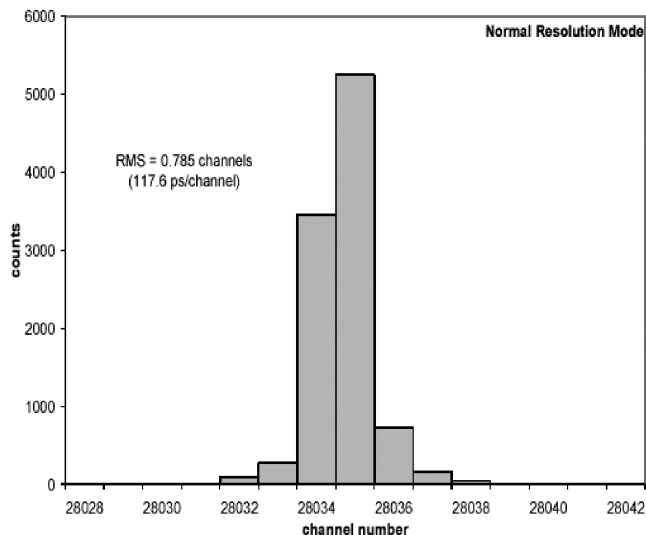


Figure 7.9: TDC performance in low resolution. (resolution=86.2ps)

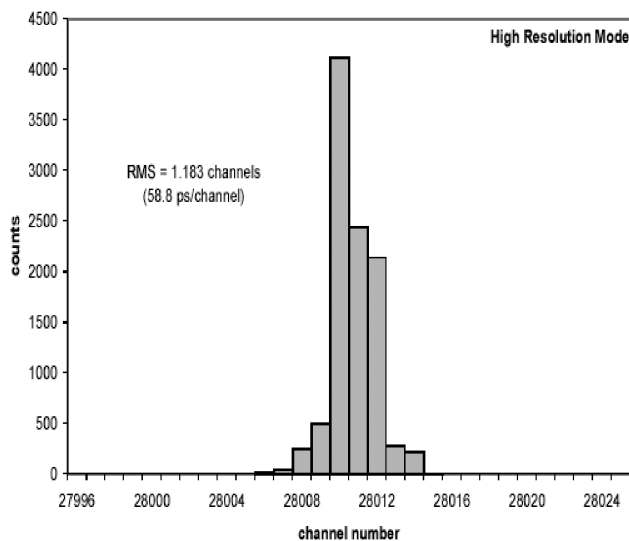


Figure 7.10: TDC performance in high resolution. (resolution=61.2ps)

range of the TDC, and for trigger rates up to 200 KHz. Full crate tests have been performed using the multiblock readout protocol. Sustained data transfer rates of 40 Mbytes/s over the VME bus have been achieved.

7.4.3 Additional requirements for final version

A 62.5 MHz clock phase-locked to the accelerator will be distributed to all TDC modules so that every channel has the same time calibration. With this clock frequency, LSB resolutions will be 125 ps for the standard version and 62.5 ps for the high resolution version.

A commercial TDC module, the CAEN[125]v1290, based on the HPTDC chip developed at CERN, is being evaluated by Jefferson Lab. It might be possible to use this type of TDC to provide 31 ps LSB resolution for the time-of-flight counters.

7.5 Track Count

The Start Counter, Barrel Calorimeter, and Time of Flight detectors will require pipelined adders to implement a track count for use in the level 1 trigger.

7.6 Clock Distribution and Pipeline Synchronization

A 62.5 MHz global front end clock will be phase-locked to the 1499 MHz accelerator clock. This global clock will be distributed to all readout electronics crates and used directly by the TDCs and Forward Drift chamber cathode FADCs. The Calorimeter and Central Drift chamber FADCs will phase-lock their higher frequency clocks to the global front end 62.5 MHz clock. A global reset will be distributed to synchronize all pipelines. The level 1 trigger as well as calibration and other special triggers will also be distributed globally.

7.7 Discriminators and Amplifiers

Detectors which provide precise timing (Photon Tagger, Start Counter, Barrel Calorimeter, and Time of Flight counters) will require “constant fraction” discriminators. The Forward Drift Chamber anodes require leading-edge discriminators mounted on the chambers inside the solenoid. The Central Drift Chamber anodes and Forward Drift Chamber cathodes will need an amplifier to drive their FADC inputs. These amplifiers should be located on the chambers. ICs developed for the Atlas [126] detector are being considered for all chamber mounted electronics.

7.8 High Voltage

The Forward Calorimeter PMTs will be powered by Cockcroft-Walton voltage multipliers [52] which will be built at Indiana University. This type of base provides for the very low power consumption necessary for such a tightly packed array and is controlled over a CAN communication link. One hundred prototypes of these bases have been built at Indiana University and are being tested. The other GLUEX PMTs will likely use conventional resistive divider bases powered by commercial HV power supplies. The Tracking Chambers will use commercial HV power supplies with sensitive current monitoring.

7.9 Packaging

The calorimeter FADC circuit requires about 50 cm^2 of board space and adjacent channels will need to be about 2 - 3 cm apart. This implies a density of about 8 channels on a 6U board or possibly 16 channels on a 9U board.

The tracking FADCs will be designed at Jefferson Lab. Sixteen channels of 125 MHz FADC for the Central Drift chamber should fit on a 9U board. The exact requirements for the Forward Drift cathode FADCs have not been determined; it should be possible to put 64 channels of 62.5 MHz FADC on a 9U or possibly even a 6U board.

In the low resolution (125 ps) version of the TDC 64 channels fit on a 6U board. This version of the TDC is used for the Forward Drift Chamber anodes.

The Photon Tagger, Start Counter, Barrel Calorimeter, and Time of Flight counters require the high resolution (62.5 ps) version of the TDC; the density is 32 channels per 6U board.

Assuming a maximum of 18 boards in a crate, and 3 9U or 4 6U crates in a 7 foot tall rack, figure 7.11 summarizes the space required for the readout electronics. Estimated counts for high voltage, gas handling, level 1 trigger, and other necessary racks are also included.

The readout electronics will be located as close to the detector as possible to minimize signal cable runs. Note that the Tagger electronics will be located in a separate building 80 m upstream of the main detector. The Time of Flight and Forward Calorimeter electronics will

Summary of GlueX Rack Space

Detector	Type	Channels	Modules	Crates	Racks
Photon Tagger	6U, 8 channel, 8 bit, 250 Msps FADC	192	24	2	
	6U, 32 channel, 62 ps TDC	192	6	1	
	High voltage	192		1	1
Upstream Photon Veto	6U, 8 channel, 8 bit, 250 Msps FADC	20	3		
Start Counter	6U, 8 channel, 8 bit, 250 Msps FADC	40	5		
	6U, 32 channel, 62 ps TDC	40	2	1	
	High voltage (includes UPV)	60		1	1
Central Drift	9U, 16 channel, 125 Msps FADC	3240	203	12	4
	High voltage			1	1
	Gas				2
Forward Drift anodes	6U, 64 channel, 125 ps TDC	2900	46	3	1
Forward Drift cathodes	9U, 64 channel, 10 bit, 62.5 Msps FADC	11,400	179	10	4
	High voltage			1	1
	Gas				2
Time of Flight	6U, 8 channel, 8 bit, 250 Msps FADC	168	21	2	
	6U, 16 channel, 31 ps TDC	168	11		
Cerenkov	6U, 8 channel, 8 bit, 250 Msps FADC	40	5	1	1
	High voltage (includes TOF)	208		1	1
	Gas				2
Barrel Calorimeter	6U, 8 channel, 8 bit, 250 Msps FADC	960	120	7	
	6U, 32 channel, 62 ps TDC	960	30	2	3
Forward Calorimeter	6U, 8 channel, 8 bit, 250 Msps FADC	2500	313	18	5
	Cockcroft Walton control, misc				1
Level 1 Trigger				4	1
Totals				68	31

Figure 7.11: Rack space

be downstream of these detectors. Cabling from detectors inside the solenoid will exit at the upstream and downstream ends of the magnet and connect to nearby electronics. Fiber optic cables will transport the data from the crate readout processors to the level 3 trigger processor farm in the GLUEX counting house.

7.10 Readout Bus

FASTBUS crates are no longer being manufactured, and FASTBUS is not being considered for GLUEX. CAMAC crates are fairly slow and have limited board space and power available. Some legacy devices like discriminators, trigger logic or HV supplies which are not part of the data readout may be packaged in CAMAC, but not the bulk of the readout electronics.

VME is popular at Jefferson Lab and the TDC prototype is constructed on a VME64x card. Compact PCI is used extensively in the telecommunications industry and can be driven directly by typical FPGA ICs without the need for bus interface ICs. Predefined PCI interface “cores” are available, minimizing design time. One disadvantage of cPCI is that bridges are required for a system with more than 8 slots, although commercial bridges which consume no slots are available. VXI and PXI are “instrumentation” extensions to VME and cPCI. Shielding, triggering, clock distribution, and additional power are added to the basic bus standard.

The FADCs require a low skew fanout of the 250 MHz clock, a synchronization signal, and the level 1 trigger. The need to form a digital global energy sum for the level 1 trigger will probably drive the choice of packaging for the calorimeter FADCs. Some sort of custom backplane will be required to support the trees of adders which form the energy sum and track counts.

The telecommunications industry is moving towards “Switched Serial Fabrics.” This adds a high speed serial connector to the backplane which can support Ethernet and other high speed serial technologies. For VME the applicable standard is VXS (VITA 41) and for cPCI the standard is cPSB (PICMG 2.16). For a 16 channel FADC module producing 25 bytes per channel per level 1 trigger; a level 1 trigger rate of 200 kHz; and a 2% occupancy the data readout bandwidth required for a module is 16 Megabits per second, well within the capability of a 100baseT Ethernet connection.

7.11 Construction

Indiana University has experience building large electronic systems for experiments at Fermilab, Brookhaven, and Jefferson Lab. The GLUEX experiment is larger and more complex than past experiments and will require the development of new techniques. High reliability is crucial to the success of the GLUEX experiment. We plan to begin long term tests of GLUEX electronics as soon as they are produced giving early identification of problems and failure modes.

A robotic electronic assembly machine[127] shown in figure 7.12 was purchased and used to construct 100 prototype Forward calorimeter Cockcroft-Walton PMTbases. This device dispenses solder paste, picks and places components, and uses infrared lasers to selectively solder components without disturbing nearby devices. This facilitates building a board in stages and testing partial assemblies, a technique especially useful in producing the Cockcroft-Walton PMT bases. The infrared lasers are particularly useful for removing and replacing defective components.

Producing electronics assemblies in house has several advantages over having a commercial firm doing the assembly. To achieve the lowest cost, a commercial service would assemble a large batch all at once. This risks learning about problems after it’s too late to change anything. Assembling smaller batches in house allows immediate feedback to the assembly process.

The lifetime of the GLUEX experiment will be long enough that we must plan for maintenance and repair of the custom electronics. Sufficient spare parts must be purchased at construction time to avoid the risk of a component manufacturer discontinuing some crucial part. Spreading the purchase of components over too long a time also risks some components becoming unavailable.



Figure 7.12: Selective assembly robot.

Jefferson Lab used a commercial board assembly contractor to build the 50 TDC boards used in Hall C. No major problems were associated with this contract assembly, although it was necessary to quickly test the first few units before committing to assembling the remainder.

7.12 Review

The GLUEX electronics were reviewed by one internal and two outside reviewers in July of 2003. The report of this review is attached as an appendix. The review was scheduled at an early stage in the development of GLUEX so that their recommendations could be incorporated into final designs. The guidance of the committee has been extremely useful in the continued prototyping and design of the system.

The present design for the GLUEX electronics differs in a few ways from the reviewers recommendations:

At the time of the review it was believed that a single FADC module could be used for all detectors. The detector characteristics have been further defined since the review and it seems unlikely that one type of FADC is optimal for all detectors. The channel count for the Forward drift cathodes has grown substantially; the overall system cost will likely be lowered by designing a module specifically for this detector. The different types of FADC will be as similar as possible; it may be possible to use a common printed circuit board stuffed with different components.

The reviewers recommended locating the readout electronics in a radiation free area. The collaboration believes the advantages of shorter signal cables outweigh the access considerations and is planning to locate the electronics in crates adjacent to the detector. Access to the above ground GLUEX detector should be easier than access to the existing underground experiments at Jefferson lab.

Chapter 8

Rates, Trigger and Data Acquisition

8.1 Expected rates

8.1.1 Overview

We estimate trigger and background rates in GLUEX using measurements of the hadronic cross section combined with the CLAS experience. The hadronic rate between any two photon energies E_1 and E_2 can be written as

$$R = \int_{E_1}^{E_2} n\sigma(E) \frac{dN}{dE} dE$$

where n is the number of target protons per unit area, $\sigma(E)$ is the hadronic cross section as a function of energy, and dN/dE is the photon energy spectrum. The photon flux is composed of a coherent and incoherent sum as detailed in Chapter 4. Background rates are dominated by the broad-band incoherent flux. The signal rates result from the photon flux in the coherent peak, which will depend on the radiator crystal structure and its orientation. The coherent peak will be optimized to the specific physics program. For our rate estimates, we use the typical case for the flux computed on a diamond radiator with the coherent peak at $E_\gamma = 9 \text{ GeV}$.

Both coherent and incoherent fluxes are proportional to the electron beam current and radiator thickness. Multiplying the number of electrons per second by the radiator thickness in radiation lengths gives the product N_0 which we will use in the following calculations. For conditions which we will refer to as “low intensity” (300 nA beam on a 10^{-4} radiator), $N_0 = 1.9 \times 10^8/\text{s}$. For the coherent peak at 9 GeV the tagged photon flux between 8.4 and 9.0 GeV is $R_{tag} = 0.14 N_0$. The average tagging efficiency over this interval is 0.375 , so the tagged photon flux on target is $1.0 \times 10^7/\text{s}$. “High intensity” running, where the tagger becomes ineffective as part of the level 1 trigger, nominally corresponds to $N_0 = 1.9 \times 10^9/\text{s}$ and yields $10^8/\text{sec}$ tagged photons on target.

The total hadronic γp cross section¹ is plotted in Fig. 8.1. For the experimental conditions defined above and a 30 cm liquid hydrogen target, the total hadronic rate in the detector is

$$R_0 = 2 \times 10^{-4} N_0 \tag{8.1}$$

and a tagged hadronic rate

$$R_T = 7.4 \times 10^{-6} N_0 \tag{8.2}$$

For low intensity, the expected total hadronic rate is 37 kHz and the tagged hadronic rate is 1.4 kHz .

¹We use measured cross sections [128, 129] with actual data obtained from the Durham Data Base [130]

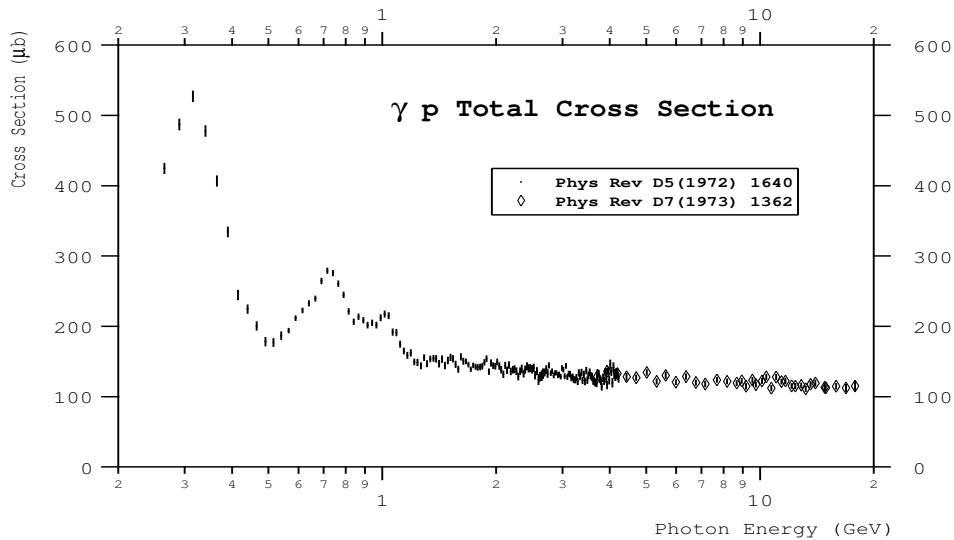


Figure 8.1: Total cross section for $\gamma p \rightarrow \text{hadrons}$ as a function of photon energy.

8.1.2 Trigger elements

We make some rudimentary assumptions about the trigger elements in order to estimate various rates. These assumptions are discussed further in the Trigger section of this document. Initial commissioning of the detector at low rates will use a level 1 trigger to select events of interest. At higher rates a sophisticated level 3 software trigger² is required. We concentrate here on discussion of rates at lower photon beam fluxes.

The trigger consists of coincidences between several counter elements of the detector. It must select the tagged hadronic rate in the presence of accidentally coincident backgrounds. The first trigger element is the photon tagger, essentially a segmented scintillation counter. The rate in this counter is determined by N_0 , which is controllable (within limits) by the experiment.

The second trigger element is the start counter/vertex chamber. This detector package will provide position and timing information with sufficient resolution for track reconstruction. In comparing the demands of the GLUEX start counter to the CLAS experience, it is useful to note that the GLUEX target is inside a solenoidal magnetic field which will protect the start counter from the flux of low-energy Compton scattered electrons emerging from the target. The CLAS start counter does not enjoy this protection.

The tagger and start counters are small, and are therefore the best candidates for determining the precise event timing. For this discussion, we will assume that coincidences between them can be identified within a time window $\Delta T_1 = 15 \text{ ns}$.

Interesting events will have particles in the final state other than the one that satisfied the start counter requirement. These particles may be energetic, forward-going charged particles, forward or large angle photons, and/or charged particles with sufficient transverse momentum to reach the bore of the solenoid. Any particles of this type will be registered in other elements of the detector and these signals can be used as further requirements in the trigger. This refines the loose interaction definition given above. We refer to this collection of signals as the global level 1 trigger. As its elements are counters of extended size, we take a coincidence time window $\Delta T_2 = 100 \text{ ns}$ when the global level 1 trigger is required.

²We are reserving level 2 for a possible intermediate level hardware trigger

8.1.3 Accidental rates

The rate of interesting events given by Eq. 8.2 is 1.4 kHz ($N_0 = 1.9 \times 10^8/\text{s}$) and 14 kHz ($N_0 = 1.9 \times 10^9/\text{s}$) for low and high intensity beams respectively. However, various other processes will form accidental coincidences at the different trigger stages, and we need to recognize these. It is most important that these do not form the bottleneck for the data acquisition system, regardless of our ability to reject them offline.

We consider two sources of accidental background. They are not entirely mutually exclusive, but we consider them separately for ease of explanation. The first (A_1) of these comes from purely random time coincidences between the trigger elements, in which case we compute the time overlap based on the various counter singles rates. The second (A_2) is more “physical”, considering hadronic photoproduction that is outside the tagging range, but in accidental coincidence with the tagging system.

First consider purely random coincidence events. A coincidence between the tagger and start counter loosely defines an interaction in the target. The rate A_0 of this coincidence is given by

$$A_0 = SR_{tag}\Delta T_1 \quad (8.3)$$

where S is the total rate in the start counter. Based on the experience in CLAS, we take $S = 0.03N_0$, scaled using appropriate factors for collimation and beam intensity. This is most certainly an upper limit because of the solenoidal shielding effect. For $R_{tag} = 2.7 \times 10^7/\text{s}$ we find $A_0 = 2.3 \times 10^6/\text{s}$, considerably larger than the tagged hadronic rate $R_T = 1400/\text{s}$. Further refinements are achieved by the global level 1 trigger.

The rate of the global level 1 trigger, $f_{L1} \times R_0$, is taken to be the total hadronic rate³ reduced by the rate for single pion production for $E_\gamma \leq 0.5\text{ GeV}$ ($f_{L1} = 0.5$). A loose trigger which uses a charged particle track count in the start counter and requires neutral energy in the barrel and/or forward calorimeter (see Section 8.2.2 below) should easily be able to eliminate these low energy events. The accidental rate using both the interaction and global level 1 triggers is

$$A_1 = A_0 f_{L1} R_0 \Delta T_2 = S f_{L1} (0.28 \times 10^{-4}) N_0^2 \Delta T_1 \Delta T_2 \quad (8.4)$$

where we have substituted from Eqs. 8.1 and 8.3 and used $R_{tag} = 0.14 \times N_0$. The second accidental background comes from true hadronic events, and therefore would pass the global level 1 trigger. They are out of time with the precise RF signal, but that is much smaller than the online resolving time ΔT_1 of the interaction coincidence. Ignoring the “true” events that are part of this rate, one calculates

$$A_2 = f_{L1} R_0 R_{tag} \Delta T_1 = f_{L1} (0.28 \times 10^{-4}) N_0^2 \Delta T_1 \quad (8.5)$$

In order to evaluate the total accidental contribution numerically, correlations must be taken into account. This reduces the sum of the above estimates. For $N_0 = 1.9 \times 10^8/\text{s}$, the accidental contribution to the trigger is 7.3 kHz , and the tagged hadronic rate is $R_T = 1.4\text{ kHz}$. We note that as the photon flux increases, the start counter and tagger lose their effectiveness in reducing trigger rates, so the trigger rate asymptotically becomes proportional to the hadronic rate. At higher currents, a DAQ system with a software level 3 trigger is required. A summary of the rates is shown in Fig. 8.2 as a function of electron beam current.

8.1.4 Rates in tracking chambers

At the high photon flux anticipated for GLUEX, one concern is that the occupancy rates in the drift chambers may be too high to allow reconstruction. In order to estimate these occupancies, a test of high intensity running with photons was performed in the CLAS detector.⁴ Measurements were taken at 10, 80, 250 and 320 nA with a 10^{-4} radiator, and rates were measured in the forward TOF scintillators (7.5-12.5 deg), the electromagnetic calorimeter (8-45 deg), and the drift chambers. The drift chamber occupancies at the highest current (320 nA) are given in Table 8.1.

³The cosmic-ray rate is small and has been neglected.

⁴This information is taken from CLAS-NOTE-2000-004 High-Rate-Test by Elton Smith.

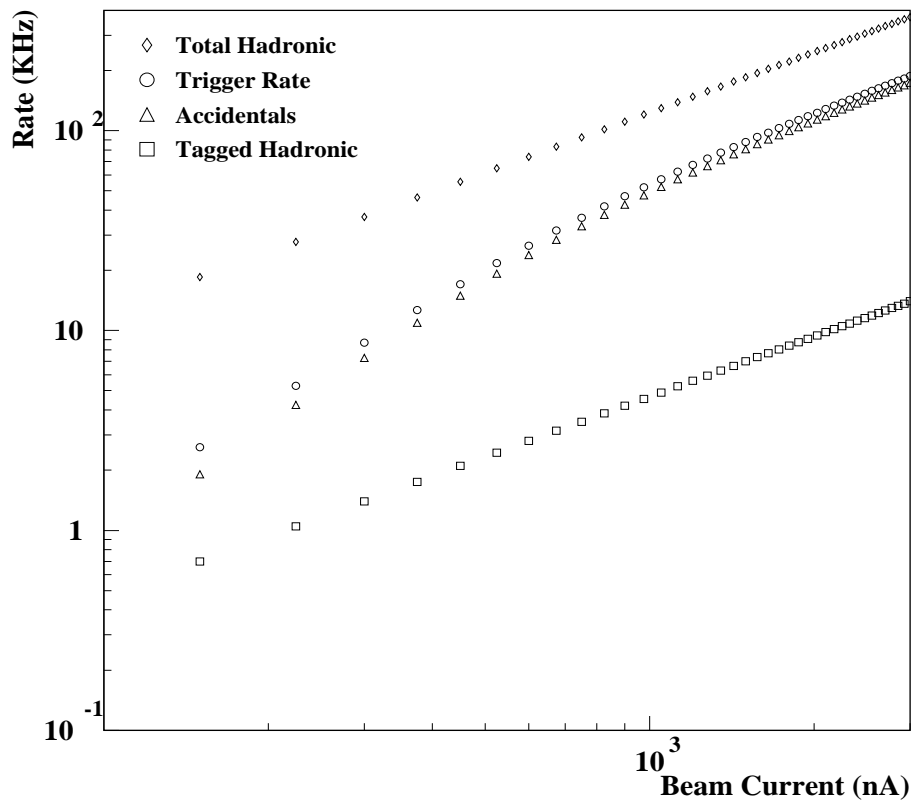


Figure 8.2: Estimated rates as a function of electron beam current. Plotted is the total hadronic rate and the estimated trigger rate, which is the sum of accidental coincidences and the tagged hadronic signal.

Beam	Region 1 S1	Region 1 S2	Region 2 S3	Region 2 S4	Region 3 S5	Region 3 S6
Photon	2.3%	2.3%	0.3%	0.4%	0.7%	0.9%

Table 8.1: Drift chamber occupancies for each superlayer (in percent) for run 21998 at the maximum beam current of 320 nA (logbook entry #7031).

Although the conditions of the test did not duplicate precisely the conditions expected in GLUEX, reasonable estimates can be made by appropriate scaling. In Table 8.2 we compare the differences in target, collimation and beam energy. As the majority of background results from lower energy photons, we assume the energy dependence of the measured rates is small. The rates are scaled by a factor of 1.7 (ratio of target lengths) and the beam current is scaled up by a factor of 5.33, which is the expected collimation ratio. The drift chambers in region 1 are completely unshielded by any magnetic field in CLAS, whereas the drift chambers in region 2 are shielded by the field of the CLAS torus. The 2.2 T solenoidal field for GLUEX is expected to be at least as effective as a shield as the CLAS torus. Therefore, we expect the occupancies in the GLUEX drift chambers to be as low or lower than those in CLAS for comparable granularity.

	Hall B Test	Hall D
Beam Current	80 nA \rightarrow 320 nA	300 nA \rightarrow 3 μ A
Radiator	10^{-4}	10^{-4}
Collimation keeps	80%	15%
Target Length	18 cm	30 cm
Beam Energy	2.4 GeV	12 GeV
Trigger	Restricted	Open

Table 8.2: Comparison between conditions in Hall B during high rate test and anticipated running parameters for GLUEX. A current of 3 μ A in GLUEX corresponds to 10^8 photons/s in the coherent peak.

Extrapolating measured occupancies in region 2 to a current of 3 μ A (GLUEX with 10^8 photons/s in the coherent peak), we expect an occupancy of 0.6%. The rates are plotted versus electron current scaled to GLUEX in Figure 8.1.4. This is well below the typical operational limits of 2.3% imposed for the region 1 drift chambers in CLAS during electron beam running, a rate at which tracks can still be reconstructed with reasonable efficiency. We note that the extrapolated rates in region 1 for a beam current of 3 μ A is approximately 5%, exceeding usual operational limits by a factor of 2, but this figure is for a configuration which is completely unshielded by any magnetic field whatsoever and thereby represents an absolute maximum to the expected rates. We note that the operation of a polarized target in Hall B (which replaces the mini-toroid with a solenoidal field) allows running at twice the normal luminosity. Thus we expect that for comparable segmentation, raw rates in the GLUEX detector at the maximum design current will be similar to the current experience with CLAS. The conclusion is that the GLUEX detector should be able to handle rates up to 10^8 photons/s.

8.2 Trigger

8.2.1 Overview

In order to achieve the roughly 20-1 reduction in event rate, GLUEX will use a two-stage trigger, combining a hardware-based level 1 trigger with a software (reconstruction) based level 3 trigger. An essential feature of the GLUEX design is to build pipelining into the entire trigger, digitizer,

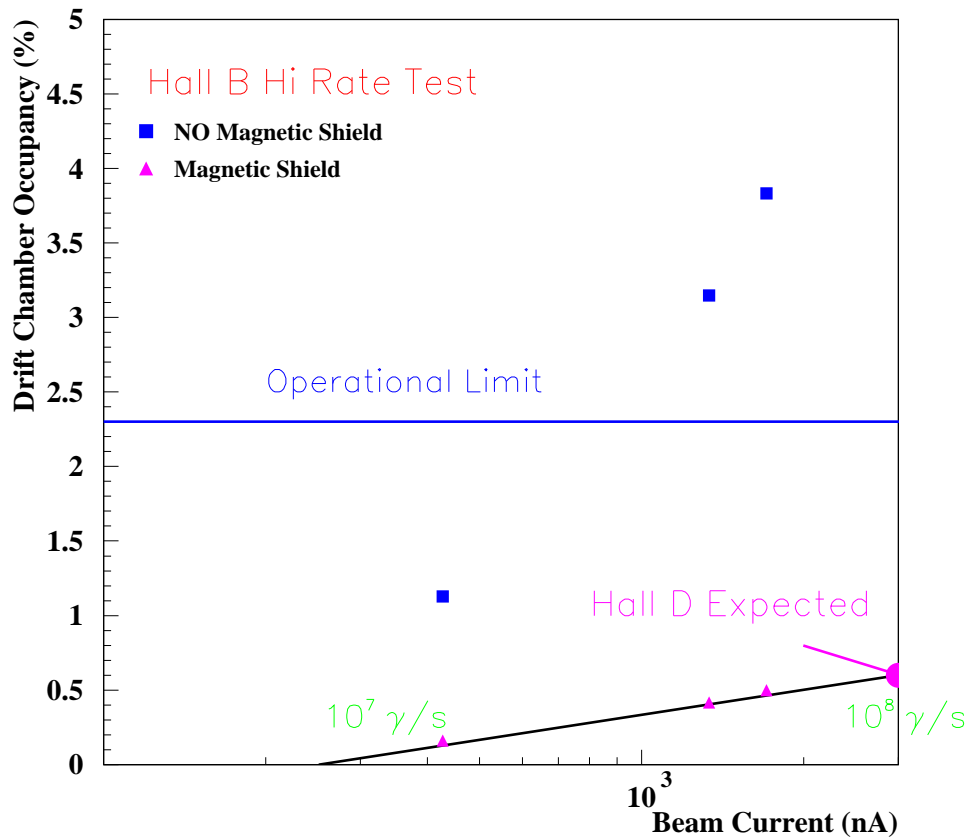


Figure 8.3: Drift chamber occupancies (scaled by target thickness = 1.7) plotted versus beam current (scaled by collimation factors = 5.33) expected for HALL D operation. The drift chambers in region 1 (squares) are completely unshielded by any magnetic field in CLAS, whereas the drift chambers in region 2 (triangles) are shielded from backgrounds by the main torus field. The nominal low current operation in GLUEX (10^7 photons/s in the coherent peak) corresponds to 300 nA. The 2.2 T solenoidal field for GLUEX is expected to be at least as effective as a shield as the CLAS torus.

and data acquisition systems at the outset. This has the twin virtues of allowing adequate time for the level 1 trigger to do its job, while eliminating signal degradation involved in delaying the signals while the trigger operates. Pipelining in this way also allows us to upgrade from initial photon fluxes of 10^7 photons/sec to eventual fluxes of 10^8 photons/sec without any significant changes to the trigger/DAQ architecture. Eliminating conversion deadtimes will allow us to acquire events which occur very close together in time.

Figure 8.4 shows a schematic of the implementation of the GLUEX level 1 trigger. The level

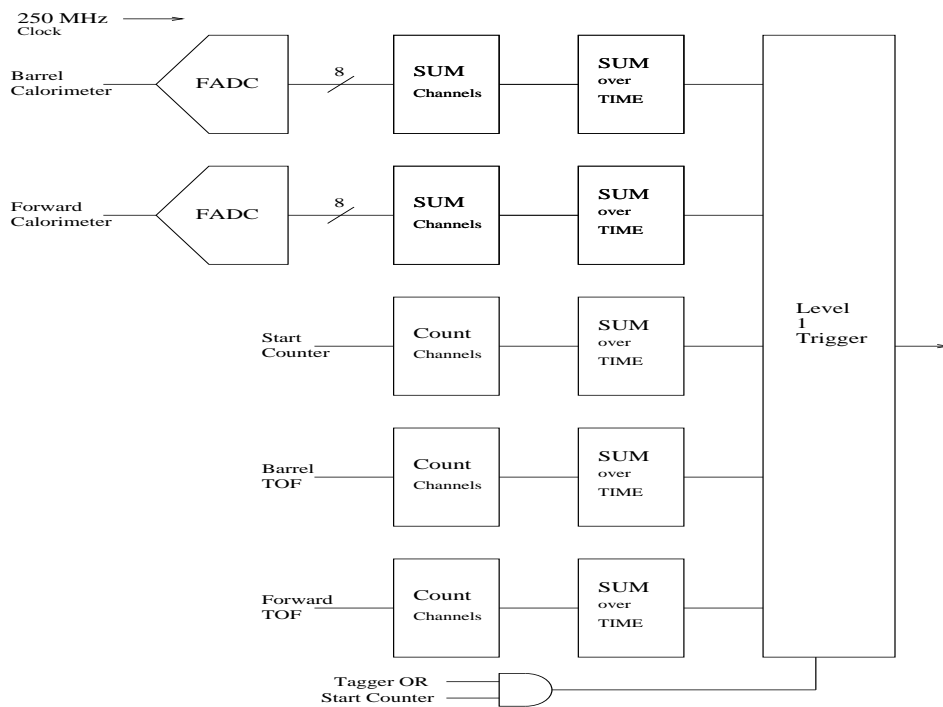


Figure 8.4: A schematic diagram of the GLUEX trigger.

1 trigger makes a decision based on detector elements which measure hadronic multiplicities (track counts) and energies. In the schematic shown, the start counter and barrel calorimeter and forward TOF detectors provide the track count while the barrel and forward calorimeters determine the energy. A tight tagger OR/start counter coincidence is used as input to the level 1 trigger for low photon fluxes of $\approx 10^7$ photons/sec.

For high photon fluxes ($\approx 10^8$ photons/sec), the tagger OR/start counter coincidence is not a useful requirement, and the level 1 trigger will probably only be able to cut the rate down from 385 KHz to around 180 KHz. Most of this background comes from multi-pion events caused by untagged (low energy) photons. In order to reduce this rate by a factor of 10, a very accurate reconstruction of the photon energy is required. Because of the complexities involved in accurately determining track momenta and then linking information from the different detectors, we believe the best approach is to use a software level 3 trigger embedded in the DAQ architecture, rather than to build a series of specialized level 3 trigger processors. This level 3 trigger will do a simplified full reconstruction of the event, using all of the data, in order to throw out events from low energy photons.

8.2.2 Level 1 trigger

The level 1 trigger consists of five subsystems, and a global trigger processor (GTP) which combines these five outputs into the global level 1 trigger. Each of the subsystems continuously (via a digital pipeline) computes a parameter, then compares it against a number of programmed

value/function pairs. The trigger pipeline would sample input data at the rate of the FADC clock (250 MHz) or possibly at half that rate (125 MHz). A value/function pair might be an energy value and a $<$, $=$, or $>$ function. When any of the value/function requirements is satisfied, the subsystem sends a timestamped subsystem event report (SER) to the GTP. The GTP is programmed with a number of different level 1 trigger configurations, each combining different value/function pairs from the subsystems, along with a trigger coincidence window (TCW) specifying the maximum time window for coincidence of the different trigger requirements.

The five level 1 trigger subsystems are:

1. **A track count** - obtained from the start counter. The start counter discriminator signals are used to create the prompt OR for coincidence with the tagger, but are also sent into a *track count pipeline* to determine the number of tracks. Two different track counts may be programmed, each with a $<$, $=$, or $>$ criterion attached.
2. **A track count** - obtained from the barrel calorimeter. The discriminator signals from the central calorimeter are sent into another *track count pipeline* which determines the number of tracks. This pipeline runs synchronously with the start counter track count pipeline. Two different track counts may be programmed, each with a $<$, $=$, or $>$ criterion attached.
3. **An energy sum** - obtained from the barrel calorimeter. The barrel calorimeter will be digitized by 8 bit, 250 MHz flash ADCs (FADC). All channels are then digitally added together (in a pipeline tree) to form the barrel calorimeter energy sum. The energy sum then passes through a shift register thus making available a time window. Successive samples within this time window are added together. This is analogous to the gate width in a conventional charge sensitive ADC. Two different energy values may be programmed, each with a $<$, $=$, or $>$ criterion attached.
4. **A track count** - obtained from the forward TOF. Discriminator signals from the forward TOF are sent into a *track count pipeline* which determines the number of tracks. This pipeline runs synchronously with all the other level 1 pipelines. Two different track counts may be programmed, each with a $<$, $=$, or $>$ criterion attached.
5. **An energy sum** - obtained from the forward calorimeter. This sum is constructed in the same manner as for the central calorimeter, except that the selection of which digitized analog sums are added together to form the forward energy sum, is programmable. Two different energy values may be programmed, each with a $<$, $=$, or $>$ criterion attached.

As mentioned above, the GTP may be programmed with several different triggers. Programming a single trigger means selection of

1. Either a minimum, maximum, or exact number of tracks in the start counter.
2. A minimum, maximum, or exact number of tracks in the barrel calorimeter.
3. A minimum, maximum, or exact number of tracks in the forward TOF.
4. A minimum or maximum for the global energy in the barrel calorimeter.
5. A minimum or maximum for the global energy in the forward calorimeter. Certain areas might be programmed out of this sum.
6. The appropriate boolean combination of elements 1-5.

The trigger will have the capability to have at least eight simultaneously defined triggers. This trigger is very flexible and can be programmed to be very loose (say one track in the start counter) or very tight and complex (specific track counts and energy thresholds in each detector). Examples of triggers which can be programmed in this model include:

1. At least two tracks in the start counter AND at least one track in the downstream TOF.

2. At least one track in the start counter AND a minimum energy in the downstream calorimeter.
3. At least two tracks in the start counter AND at least one track in the barrel calorimeter AND a minimum requirement of energy in the barrel calorimeter AND a minimum requirement in the forward calorimeter.

All subsystems will run synchronously and will be timed so that the time stamps from average momentum tracks ($\sim E_{\text{beam}}/3$) will match at the GTP. Higher and lower momentum tracks will be slightly out of time, but this effect should be less than 20 ns , and this is compensated for by programming the TCW value. The synchronous output of the level 1 trigger will then be ANDed with the coincidence of the tagger OR and the start counter OR. This allows the timing to be determined by the tagger and start counter, and removes the synchronous nature of the trigger.

The rate of the global level 1 trigger, $f_{L1} \times R_0$, is taken to be the total hadronic rate⁵ reduced by the rate for single pion production for $E_\gamma \leq 0.5 \text{ GeV}$ ($f_{L1} = 0.5$). A loose trigger which uses a charged particle track count in the start counter and requires neutral energy in the barrel and/or forward calorimeter should easily be able to eliminate these low energy events. The resultant level 1 trigger rate is about 180 kHz . We note, however, that 80% of the hadronic rate comes from photons with energies below 2 GeV . This energy cut, which would require a more sophisticated trigger, would reduce the level 1 rate to 70 kHz .

8.2.3 Trigger simulation

As mentioned above, background events are typically due to low energy photons, resulting in low energy events. Not only are these background events lower in energy, but they are also less forward, due to reduced Lorentz boost. Thus, good events typically deposit a larger fraction of their energy in the forward calorimeter, and have more tracks and hits in the forward time-of-flight. The goal of the Level 1 trigger is to use these differences to cut as large a fraction as possible of the background events, while minimizing the number of good events lost. The goal for the data reduction in the level 1 trigger is to remove at least 50% of the background events, without losing more than 0.5% of the good events.

In order to test the the trigger, the six reactions listed in Table 8.3 were simulated and studied. The simulated events include two low energy delta production channels, and four interesting physics channels at low (background) and high energies. Reaction events were generated using *Genr8* [87]. After generation the events were then run through *HDGeant* [131] for simulation. This provided the necessary data needed. For each reaction 10,000 events were generated giving 120,000 events.

A function of the form given in Eq. 8.6 was used as the basis for deciding cuts. When the calculation is less than Z the event is cut. A genetic algorithm was used to optimize the coefficients and Z . The fitness function was weighted such that keeping good events was given a higher score than cutting background events. If good events were cut then it would be penalized and if it cut too many then the score received was zero. As shown in Table 8.3 the best set of coefficients cut nearly all of the delta's and most of the low energy background events. On average 72% of the background events are cut, while no single good event channel lost more than 0.5%.

$$\begin{aligned}
 Z >= & A * [NumberTracksForwardTOF] \\
 & + B * [EnergyForwardCal] \\
 & + C * \frac{[EnergyForwardCal + 1]}{[EnergyBarrelCal + 1]}
 \end{aligned} \tag{8.6}$$

⁵The cosmic-ray rate is small and has been neglected.

Reaction	Energy(GeV)	Percent Cut
$\gamma p \rightarrow \rho^0 \pi^+ n \rightarrow n \pi^+ \pi^- \pi^+$	1	67.99%
	2	41.68%
	9	0.05%
$\gamma p \rightarrow \rho p \rightarrow p \pi^+ \pi^-$	1	70.48%
	2	54.82%
	9	0.50%
$\gamma p \rightarrow X^*(1600)n \rightarrow (\eta^0 \pi^+)n \rightarrow n \pi^+ \gamma \gamma$	1	90.10%
	2	56.24%
	9	0.11%
$\gamma p \rightarrow X^+(1600)\Delta^0 \rightarrow (\pi^+ \pi^+ \pi^-)(n \pi^0) \rightarrow \pi^+ \pi^+ \pi^- n \gamma \gamma$	9	0.23%
$\gamma p \rightarrow \Delta \rightarrow n \pi^+$	0.337	99.99%
$\gamma p \rightarrow \Delta \rightarrow p \pi^0$	0.337	98.75%

Table 8.3: Trigger cut rates for reactions and their energies.

8.3 Data acquisition

8.3.1 Overview

The GLUEX data acquisition system is being designed to accept a 200 KHz Level 1 input rate, and will be pipelined so as to incur no deadtime. Front-end boards will continually digitize and store several microseconds worth of data to allow time for the Level 1 trigger decision. When a Level 1 accept arrives the boards will extract the appropriate time slice of data from the digitizing memory and move it into a large secondary memory store. Readout controllers will collect data from many boards over a backplane, then transmit the data to event building processors over a network. Note that the readout controllers likely will not need to run a hard real-time operating system (e.g. VxWorks) due to the large memories on the digitizing boards, an important simplification.

Complete events will be shipped from the event builders via a network to a large farm of Level 3 processors. The Level 3 farm will reduce the event rate by approximately a factor of 10 before shipping the remaining events to event recording processors, which will then write the events to a staging disk in preparation for transfer to tape. We are designing the system to handle a recording rate of 100 Mb/s. During initial running at low luminosity (10^7) this system will be able to record all events to disk, and no Level 3 rejection will be needed.

Most of the hardware components needed to build the DAQ system described above are available now or will be available soon, so there should be no problem finding hardware a few years from now. The main challenge will be to develop the DAQ, online, monitoring, and controls software.

8.3.2 Data flow and rates

GLUEX will have approximately 12500 FADC channels. Assuming a typical occupancy of 2%, a 250 MHz, 8-bit FADC, a time window of 100 nanoseconds, and readout of the full time window, the total amount of FADC data would potentially be: $12500 \text{ channels} * 0.02$ (occupancy) $* 25$ bytes/channel = 6.25 Kbytes per event.

The 25 bytes/FADC channel will be used to extract an energy and a time signal. Previous work [120, 121] indicates that a time resolution better than the FADC sampling interval can be achieved by fitting the FADC waveform (see also Chapter 7). Thus we plan to reduce the FADC data to an energy, time, and channel identifier in real-time using special on-board hardware. The amount of data per hit will drop from 25 bytes to 10 bytes per FADC channel, thereby lowering the total FADC data to a more manageable 2.5 Kbytes per event.

In GLUEX there will be approximately 8000 TDC channels so the data volume for the TDCs will be: 8000 channels *0.02 (occupancy) *4 bytes/channel = 640 bytes per event.

There will be little data from devices other than TDCs and ADCs (scalers, latches, etc.) so the total event size will be about 4 Kbytes per event. Taking 5 Kbytes per event as the design goal gives 5 Kbyte/event *200 KHz = 1 Gbyte/sec off the detector. Assuming 100 front-end VME crates (cPCI will need more) gives a backplane rate of 10 Mbytes per second, easily handled by current technologies.

Event building will be done in parallel on 8-16 event building processors. Event analysis will be performed in parallel on 50-200 Level 3 farm processors (see below). Event recording will be done in parallel on 2 to 8 event recording processors. In all cases existing network switches can easily route the volume of data between stages. Note that we are investigating use of advanced (e.g. layer 7 routing) network switches to further simplify transfer of data between stages.

8.3.3 Level 3 trigger

If the Level 1 trigger rate for low intensity running (10^7 tagged photons/s) is less than 20 KHz, or 100 Mbytes/sec, the Level 3 trigger farm will not have to cut any events since the DAQ system is being designed to handle this rate to disk. In high intensity mode, where the Level 1 rate may be as high as 200 KHz, the Level 3 trigger must be able to reduce the event rate by a factor of ten.

Most of the unwanted events result from an untagged, mostly lower energy photon interacting in coincidence with a tagged photon. To reject these events Level 3 must be able to estimate the energy of the photon which produced the event. This involves reconstructing tracks, matching them with the calorimeters, and adding additional energy deposited by neutral particles in the calorimeters. This is most simply and easily done in a commodity processor Level 3 farm, rather than in specialized hardware.

We estimate the required processing power required as follows. The Hall B online hit-based event reconstruction system obtains 3% momentum resolution using about 5 milliseconds of cpu time on a 20 SPECint processor, or about 0.1 SPECint per event (full reconstruction with better than 1% resolution takes about 45 milliseconds). Assuming the same for GLUEX gives 20000 SPECints total for the full Level 3 farm at 200 KHz event rate. Assuming 50% processor utilization (due to I/O overhead, etc.), approximately 40000 SPECints or 200 processor boxes at 200 SPECint each are needed (150 SPECint boxes are currently running in the JLab farm system). Depending on the improvement in cpu performance over the next few years, far fewer boxes will likely be required, perhaps 1/4 as many.

Table 8.4 shows the rates, sizes, and processing requirements for the Level 3 trigger.

8.3.4 Monitoring and Control

Monitoring and control tasks include hardware configuration and control (“slow controls”), bookkeeping, online event monitoring, alarm systems, and messaging systems. These are less demanding tasks than data acquisition in GLUEX, and should not present unusual challenges. We plan to follow some examples from Hall B, but to also make use of lessons learned there. In particular, we plan to integrate offline data analysis tools with the online software at the outset to reduce the total cost of software development.

The framework for slow controls will be uniform for all subsystems in GLUEX, but the framework choice is not obvious. VME-based EPICS works in Hall B, but does not mesh well with the online requirements and has proven to be manpower intensive. In fact, a number of Hall B systems do not use EPICS or VME, but instead resort to CAMAC or other options. We believe that an open, message-based system that takes advantage of commodity hardware and software, and that implements a uniform user interface to diverse underlying hardware is best. The JLab Data Acquisition group is currently developing an agent-based system meeting these requirements.

	Low Rate	High Rate
Event Size	5 KB	5 KB
Event Rate to Farm	20 KHz	200 KHz
Data Rate to Farm	100 Mbytes/s	1000 Mbytes/s
Num Links to Farm	1	10
Data Rate per Link	100 Mbytes/s	100 Mbytes/s
Link Technology	Gigabit Ethernet	Gigabit Ethernet
Events/s per Link	20000	20000
SPECints/ev for L3	0.1	0.1
Num SPECints/link	2000 SPECints	2000 SPECints
Num SPECints/link x 2	4000 SPECints	4000 SPECints
Num 200 SPECint processors/link	20	20
Total Num 200 SPECint processors	20	200

Table 8.4: Rates, sizes, and processing requirements for the Level 3 trigger.

Bookkeeping tasks include all recordable activities of the experiment other than raw and calibration data. We expect this will be done using object/relational databases. Current commercial and public domain database technology should be adequate.

The alarm and messaging framework allows sub-systems to communicate their state to monitoring programs and operators. This system needs to be integrated across the entire online, DAQ, and database systems in a simple, uniform manner. The scale and performance requirements of this system are modest, and similar to other systems running or in development at Jefferson lab.

Chapter 9

Computing

9.1 Overview

GLUEX will be the first Jefferson Laboratory experiment to generate petabyte scale data sets on an annual basis (One petabyte, $1 PB = 10^{15}$ Bytes). In addition, the need to generate physics results in a timely fashion has been identified as a primary goal of the GLUEX collaboration since its inception. For these reasons, a well-designed, modern, and efficient computing environment will clearly be crucial to the success of the experiment.

Currently, there are a number of particle physics projects world wide which also will produce very large data sets, and which will function with large dispersed collaborations. It seems quite reasonable, then, to expect that over the coming years, many new tools will be developed which will aid in effectively processing and managing these large volumes of data. As a collaboration, GLUEX will undoubtedly make effective use of these tools, which will include such things as grid middle ware, distributed file systems, database management tools, visualization software, and collaborative tools.

Nonetheless, it also is clear that the GLUEX collaboration will need to develop a suite of tools which are dedicated to this experiment. This will include data acquisition and trigger software, experiment monitoring and control software, data reduction tools, physics analysis software, and tools dedicated to the partial wave analysis (PWA) effort.

The rest of this chapter outlines in some detail the approach taken by the GLUEX collaboration. First, a review the approaches taken by current experiments with similar computing requirements, along with the GLUEX specific features and numerical constraints is given. Then an outline of the GLUEX strategy to meet these demands, and also the specific tasks that will be divided up among the collaboration members. Finally, a summary of computing milestone within the GLUEX collaboration will be presented. By keeping abreast of developments and new technologies that may be applicable to the GLUEX software environment, the collaboration will be able to carry the computing effort through from design to implementation and into the steady state running through a steady evolution of the system.

9.2 Background

In developing the GLUEX computing design, one can draw from two experiences, both of which are ongoing activities. These are the experiments using the CLAS detector in Hall B at JLab, and the CERN LHC experiments.

CLAS is of course particularly relevant, as it is also a multi-particle spectrometer arrangement at JLab, and is a good measure of how one may best use the existing infrastructure at the laboratory. An important difference, however, between CLAS and GLUEX is the volume of data acquired and analyzed. Based on the most recent numbers achieved in CLAS, the trigger rates and data volume are still a factor of three less than those projected for GLUEX. (See Sec. 9.2.2).

It is clear then that the JLab computing infrastructure will need to be significantly upgraded in support of GLUEX.

As the CERN/LHC experiments, CMS and ATLAS, began to take shape in the 1990's, it was realized that these large international collaborations would be acquiring previously unheard of amounts of data. It was further realized that all members of the worldwide collaborations would need ready access to this data, and that recent advances in computing could in fact make this possible. CERN commissioned the MONARC[132] (“Models of Networked Analysis at Regional Centres for LHC Experiments”) project in 1998, to study various configurations of distributed data analysis, based on “regional centers”. The results of this study were published in 2000, and it was concluded that a multi-tier system of regional centers was the best solution to the problem.

CMS and ATLAS are now, in fact, following this model in their own computing efforts. Indeed, several large scale collaborations, mainly connecting physicists and computer scientists, have appeared in the U.S. and elsewhere, to realize this computing model for nuclear and particle physics in general. These include the DoE/SciDAC funded Particle Physics Data Grid [133] (PPDG), and the NSF/ITR funded Grid Physics Network [134] (GriPhyN) and International Virtual Data Grid Laboratory [135] (iVDGL). These collaborations are devoted to developing the tools needed to realize the promise of large scale distributed computing and data handling, as it pertains to nuclear and particle physics.

The PPDG, GriPhyN, and iVDGL projects are based on the concept of a “virtual data grid”. This concept, which takes its name from the analogy with the public electrical utility network, aims to provide the user with an invisible layer of “middle ware” so that data sharing is carried out straightforwardly and quickly, regardless of the geographic separation of the actual physical data. Grid technology relies on the observation that the rate of increase of deployed network bandwidth is faster than the rate of increase in affordable computing power, and the assumption that these relative trends will continue for a number of years to come. This appears well founded based on historical trends [136], and are presumably driven by economics and the needs of society.

9.2.1 Special features of GlueX

There are important differences between GLUEX and the CERN LHC experiments ATLAS and CMS, which can be traced to the primary physics goals. Events in ATLAS or CMS will be very complicated, with very large amounts of data per event, and these will consequently consume a lot of CPU time to reduce. By comparison, GLUEX events will be simpler to disentangle. However, the subsequent analysis of GLUEX events will be both computationally and data intensive, requiring sophisticated visualization and data handling tools, as large amounts of both “real” and Monte Carlo data are brought together in order to carry through an amplitude decomposition analysis.

The primary goal of GLUEX is the systematic identification and categorization of short-lived meson states, unraveled from the raw, multi-particle reaction data using the techniques of “Partial Wave Analysis” (PWA). Achieving this goal requires simultaneous access to two large and independent data sets, namely the actual reduced experimental data and the simulated Monte Carlo data, each sorted for the particular multi-particle reaction(s) under consideration. It is quite probable that these data sets will be distributed physically over multiple locations, and that the access will be from other separated sites, associated with the group who has undertaken that particular analysis.

This not only impacts the structure of the data grid, but also implies that new analysis tools need to be developed. This especially includes visualization tools, as one searches for the appropriate combination of partial waves which best describe the reaction. That is, as one fits the parameters associated with a certain set of partial waves, some visual inspection mechanism is needed to evaluate how well the fit reproduces distributions in angles and invariant mass, for the many possible combinations. A universal set of tools is important in order to come to a more or less standard set of measures that would be applied by the analysis groups.

9.2.2 CPU, Storage, and Bandwidth Requirements

The GLUEX computing requirements are driven primarily by the projected data volume. GLUEX will use a multi-level triggering system, and it is projected that at the peak tagging rate, GLUEX will acquire 15,000 physics events per second which pass the Level 3 trigger requirement, or 1.5×10^{11} events in a live year, (assumed to be 10^7 seconds). The event size will be ≈ 5 kB. Consequently, the data acquisition system must handle 100 MB/sec, which corresponds to storing 1 PB of raw Level 3 data per year.

It is important that the Level 3 raw data be reconstructed somewhat faster than real time, for the purposes of monitoring the detector performance as well as the experiment setup. It takes on the order of 250 msec to process a multi-track event in a detector with complex geometry, on a standard workstation computer available in 2000. Using a conservative interpretation of Moore's Law, i.e. CPU speed doubling every two years, this is reduced to 15 msec by 2008, so 2.25×10^9 CPU-sec to process one year's running. A reasonable goal is to process these data in one-third the time it took to acquire it, i.e. 1.0×10^7 sec. Consequently, 225 circa 2008 CPU's will be required to process the raw data.

An accurate and detailed simulation will be critical for successful partial wave analysis. For any given reaction channel, one needs a greater number of simulated events than actual events, so that the result is not limited by the statistical precision of the generated sample. The goal will be to generate a factor of three times more simulated events than actual actual events for the data sample representing the final states for which one carries out a more detailed analysis. At the same time, one will, at least initially, be interested in analyzing a specific set of reaction channels. Taking both of these factors into account, and assuming a similar event size for reconstructed data, we estimate that the simulations will produce an additional 1 PB/year of simulated data.

Significant CPU resources will be required to generate the Monte Carlo sample. Ideally, one would generate only those events which in fact are accepted by the apparatus, correcting for the fraction of phase space assumed at the beginning. It is very difficult in practice, however, to achieve this optimal "importance sampling". A reasonable assumption is that only 1/2 of the events generated events will actually be accepted by the simulated experimental trigger. Consequently, one must generate a number of events

$$N_{\text{gen}} = 2 \times (N_{\text{anal}})$$

where $N_{\text{anal}} = 1.5 \times 10^{11}$ is the number of (fully) analyzed hadronic events per year from the data stream. Consequently, $N_{\text{gen}} = 3 \times 10^{11}$ events. Generating Monte Carlo events requires detailed simulation of various detector components, and then these events must pass through the same analysis program as the raw data. Thus, more CPU time is required per simulated event than for real data. A starting assumption is to use a factor of two, namely 30 msec, or 1.0×10^{10} CPU-sec for a year's worth of simulated data. to generate this data in one-half of a calendar year, ($\approx 1.5 \times 10^7$ sec), translates to approximately 700 circa 2008 CPU's necessary for generating and processing the Monte Carlo data set. Table 9.1 summarizes the CPU and storage requirements for computing in GLUEX.

Physics analysis for GLUEX will be carried out by a worldwide collaboration, which will require access to both the reconstructed data, as well as the processed Monte Carlo data. It is probable that the reconstructed data, simulated data, and as well the CPU's upon which the physics analysis is carried out, will physically reside at locations separate from one another, and also separate from the typical user. Sufficient bandwidth is necessary to connect the user to these resources in order to make appropriate use of the data grid.

9.3 Computing Strategy

In Fig. 9.1, we show a conceptual plan of the GLUEX data processing and computing environment. In the following sections, we will discuss the important features of this plan.

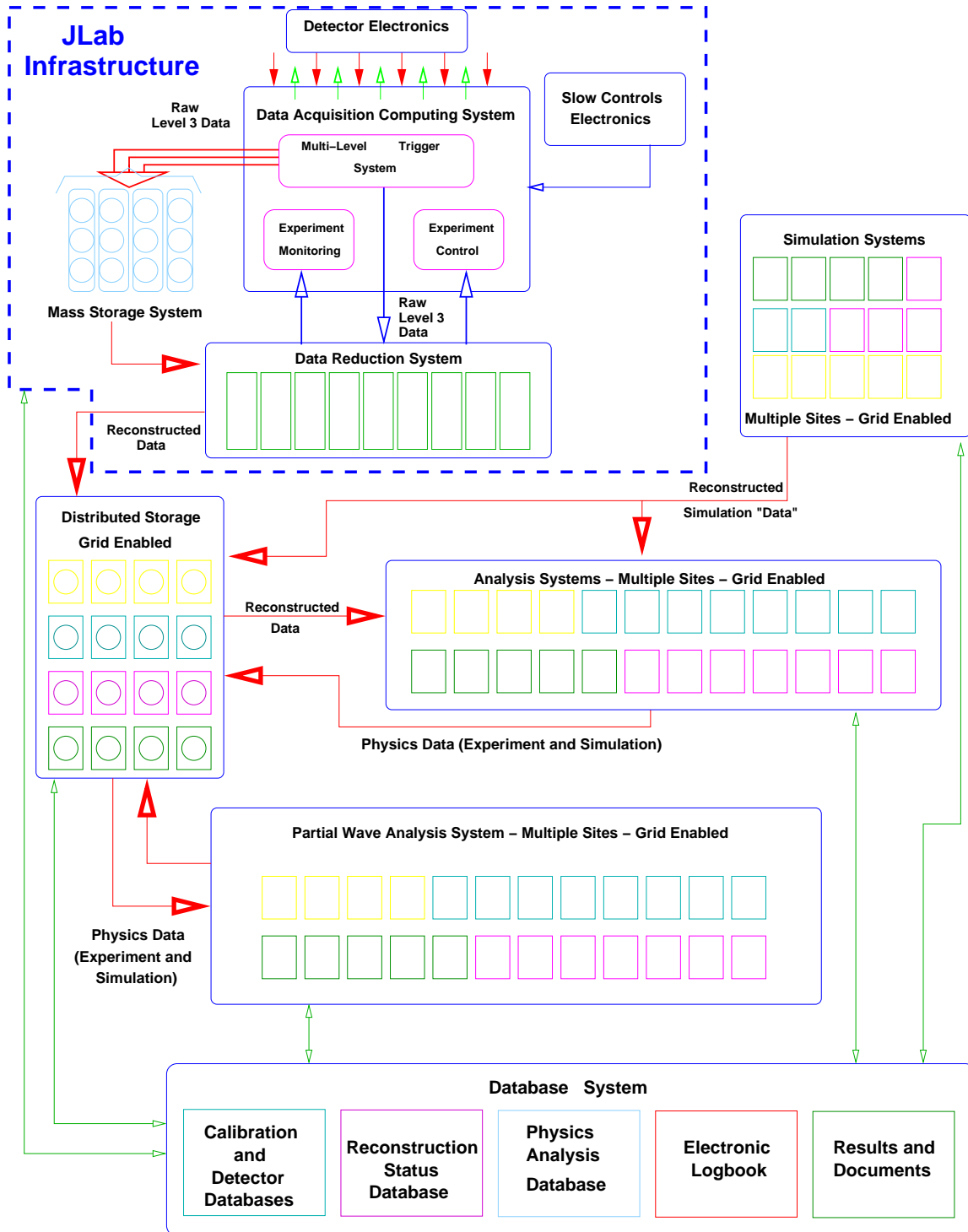


Figure 9.1: The GLUEX Computing Environment

Table 9.1: CPU, Storage, and Bandwidth Requirements for GLUEX

Raw Data Processing		Monte Carlo Data Processing	
Level 3 Data Rate	100 MB/sec	Simulated data	1 PB/year
Raw data storage	1 PB/year	Generation CPU's	700
Reconstruction CPU's	450		

9.3.1 Jefferson Lab Computing Resources

Clearly, the nature of this experiment dictates that a significant computing infrastructure must exist at Jefferson Lab. As shown in Fig. 9.1, the computing facilities at JLab will coordinate the experiment monitoring and control, data acquisition, Level 3 raw data storage, slow controls monitoring, and data reduction.

Data Storage

Currently, at JLab, raw data from experiments are written to tapes housed in a tape silo in the JLab computer center, and this is one option that we have considered for the GLUEX Level 3 raw data. Current tape speeds are 30 MB/sec onto 200GB cassettes, and should exceed 100 MB/s onto 1 TB cassettes when GLUEX data taking begins. At a data rate of 100 MB/s, and accounting for tape mount times and redundancy, GLUEX would need three to four tape drives dedicated to on-line data recording.

A tape silo typically holds 6000 tapes, or 6000 TB at 1 TB/tape. Thus, JLab would need to purchase one tape silo to store GLUEX raw and processed data, and would need adequate tape archive and storage facilities. Tape costs should be less than for CLAS, as much of CLAS data was written to low capacity tapes, and tape costs remain constant independent of capacity.

One should also note that at the present time, the relative prices of tape and disk storage are scaling in such a way that by the time GLUEX is in the data taking phase, it may be more practical to store the raw data directly on disk. Even with current RAID technology, high reliability disk storage may be achieved with mirroring or optical archiving techniques.

It is also important to note that while not explicitly shown in Fig. 9.1, the reconstructed data will almost certainly be stored primarily at JLab, and will therefore comprise a significant portion of the grid-enabled mass storage system.

Data Acquisition and Interface to Electronics

The projected raw data rate into the Level 3 trigger system from the detector is 1 GB/sec ($5 \text{ kB/Event} \times 200 \text{ kEvent/s}$). Our goal is a reduction factor of 10 in the Level 3 trigger, resulting in a Level 3 recorded raw data rate of up to 100 MB/sec. There can be no software, or otherwise computing related, impediments to this goal. The computer center staff, working closely with the data-acquisition group, will be responsible for assembling a system that allows direct transfer of the data from the acquisition electronics to the mass storage media, while providing for adequate experiment monitoring and control. It must also provide a natural interface to the data reduction software, which would be used on line for at least a subset of the monitoring activities.

Speed is a premium, and this software will be dedicated to on-site operation at JLab. Consequently, there are few constraints on the software model used to build it. However, we should also keep in mind that we must have the ability for detector and hardware experts located remotely to monitor detector performance and provide diagnostic information.

Experiment Calibration and Detector Monitoring

The calibration database will be an important input to both the raw data reduction and to the event simulation. Good indexing will be necessary to track any changes in the detector or its performance over time, and correlate that to analysis and simulation. The database records themselves will be used to monitor detector performance over time, including both long term drifts as well as failure modes.

The calibration procedure will also involve the use of a set of raw data dedicated to detector calibration. It is important that these data have high availability, and thus the calibration data sets would be replicated at multiple sites to achieve this.

Data Reduction: Reconstruction from Raw Data

Event reconstruction will be a CPU intensive task. It will include, for example, accurate particle tracking through the (approximately) solenoidal field to determine the momentum vectors of the individual particles; the event vertex and any secondary vertexes; conversion of time-of-flight and Čerenkov information to particle identification confidences; identification of electrons and photons from the electromagnetic calorimeters; and determination of the corresponding tagging event, with confidences.

The computing hardware requirements for the data reduction facilities at JLab were discussed in detail in the previous section, with the principal motivation being that the Level 3 raw data be reconstructed in approximately real time. To reiterate, it is anticipated that we will require 450 Year 2008 CPU's for this task.

We require this code to be portable, as the same code used for reconstruction of the raw data will be used for reconstruction of the simulated data. These tasks will almost certainly be carried out at different sites with different computers.

Other Tasks

Jefferson Lab needs to extend their high speed network to Hall D, and to establish specific computing resources to acquire and process the raw data from GLUEX. This includes storage capacity for the raw data, CPU power to reduce it, and the ability to store the resulting reduced data. A high speed network, capable of sustaining the necessary bandwidth to support the connections to off-site analysis and simulation centers, must be established at the laboratory.

9.3.2 Off-site Computing Infrastructure

Again referring to Fig. 9.1, the distributed computing facilities associated with GLUEX will comprise both distributed mass storage, as well as computational resources devoted to physics analysis and simulation. It is envisioned that the facilities located at these distributed centers will be matched to the specific data-intensive activities, such as detector calibrations, Monte Carlo simulation, and the various stages of physics analysis that are being pursued by the groups located at these institutions. The storage capacity that needs to exist at a center will depend on the specific activity it represents. For example, a typical analysis of 100 GB of reconstructed data may require 300 GB Monte Carlo of simulated data to be loaded and stored at the center simultaneously.

Distributed Data Storage Considerations

The distributed mass storage system (data grid) which we envision is a powerful concept, but it relies on both high speed networks between the centers, as well as networks which are reliable and available. For the purposes of this discussion, we refer to the OC standard for network bandwidth; OC-1 = 51.85 Mbit/second and OC-N = $N \times$ OC-1 rate. Of critical importance will be the connection to JLab, which will be dispensing the reconstructed data to possibly several analysis sites at any one time; and the Monte Carlo center, which would dispense simulated

data at about four times the rate of reconstructed data. For example, it takes approximately two days to transfer a 400 GB simulation data set at 20Mbits/sec (13% of an OC-3 connection). With several analysis running at once, it seems clear that we would saturate the currently available OC-3 bandwidth. *It is likely that we would need an OC-24 (1244 Mbits/second) or better connection between the Monte Carlo simulation center, and the physics analysis sites.* Even with high speed networks coming into the universities, it can often be problematic to move the data through the universities' internal networks. However, the few examples that we have within the GLUEX collaboration have found that the university computer centers have been very interested in resolving these problems. Nevertheless, this may not always be true, particularly for smaller universities, where the "last mile" problem may still be an issue.

Physics and Detector Simulations

An accurate Monte Carlo simulation will be crucial to the success of the detailed partial wave analysis that are the goal of GLUEX. This will begin with some physical model for the final states to be studied, followed by "swimming" charged particles through the (nearly) solenoidal magnetic field and then simulating the signal on the various detector components. This will be a CPU intensive task, which will then be followed by the event reconstruction code. The collaboration needs to establish the Monte Carlo farm for generation, reduction, and storage of the simulated data sets. These are critical sites, and the connection bandwidth to JLab and to other users must be realized.

It is likely that event generation will take place at either one physical site, or perhaps a small number of sites, so the portability of the code will not be a large constraint. However, this activity may well benefit from distributed computing, and in that sense, portable code may prove to be a significant asset.

Partial Wave Analysis: Methodology and implementation

The PWA code must be flexible enough to allow for a large number of different final states within the same framework. Further, it is a CPU intensive task, involving the minimization of a complicated, multi-parameter function, as part of the extended maximum likelihood fit. New visualization tools, which need to be interfaced to the raw and simulated data sets through the data grid, should be developed to help assess the degree to which the assumed wave set describes that data.

The code will run on many different computing systems, depending on which collaborator may be using it at any one time. Consequently, the portability of the running code will be important.

Record-keeping and Collaboration Interface

One key to operating an experiment with an active worldwide collaboration is to keep records (including the experiment "logbook") accessible to anyone in the collaboration at any one time. Such a portal can also be used as the basis for virtual meetings over the Internet, and a deposit for presentation materials, publications, internal notes, and other important avenues for information dissemination, both external and internal to the collaboration.

9.3.3 Software Model

An object-oriented framework will be established for all software that becomes an integral part of the GLUEX computing environment. The use of design patterns and other best practices from object-oriented design will encourage maintainable code. Unit testing, static analysis, and similar light-weight additions to the process will encourage a scalable software development and testing cycle.

Grid-based computing environments are in large part described by protocols, interfaces, and schema's. Software components built upon XML interfaces and metadata fit into the notion by

providing collaboration access to analysis, simulation, and visualization tools as "web services", a popular theme in current grid computing initiatives. Some work in this direction has already begun at Jefferson Lab [137, 138].

So long as the collaboration adheres to the above framework, it is not critical to decide on any specific programming language. Indeed, a language-agnostic approach will encourage the development of interface compliant, loosely coupled software components. Dependence on legacy code will be limited to the extent that XML interfaces exist (or are written by proponents) which hide the details of the code underneath.

A software distribution and revision control system needs to be set up and maintained. The system should be designed from the outset to not only include code for various purposes, but also documentation, dissemination materials, log books, and other archival information.

9.4 Organization

Clearly the successful development and implementation of the GLUEX computing environment will require extensive coordination between both the GLUEX collaboration and the JLab computing center and data-acquisition groups. Crucial to this is both the dynamic definition and the completion of various computing milestones. Figure 9.2 shows the currently identified milestones that need to be achieved to meet the computing requirements for GLUEX. Note that Monte Carlo simulations are already in progress and much progress has been made to date in developing the simulation code for detector, beam line, and trigger simulations. In addition, the collaboration is aggressively pursuing the development of the PWA codes and tools which will be crucial in extracting physics results from the data. While it is certainly true that the computing power per dollar invested continues to increase at a dramatic rate, it is not a viable option for the collaboration to wait until the last possible moment to purchase the necessary computing hardware infrastructure. The reason is that a large fraction of the software that will be needed to carry out the project must be developed by the collaboration. One cannot simply use a set of "canned" packages. In order to develop this software, as well as the associated physics analysis techniques, the computing infrastructure, both at JLab and at the university centers, must be at least partially in place well ahead of time. Thus, this infrastructure must be ramped up in the upcoming years. Indeed, a segment of the collaboration is in the process of securing funds to develop a dedicated center for PWA studies (Indiana University). As well, integration of several of the already existing and future computing clusters for initial grid computing studies (Carnegie Mellon, Connecticut, Indiana, JLab Regina) will be tested in the coming months.

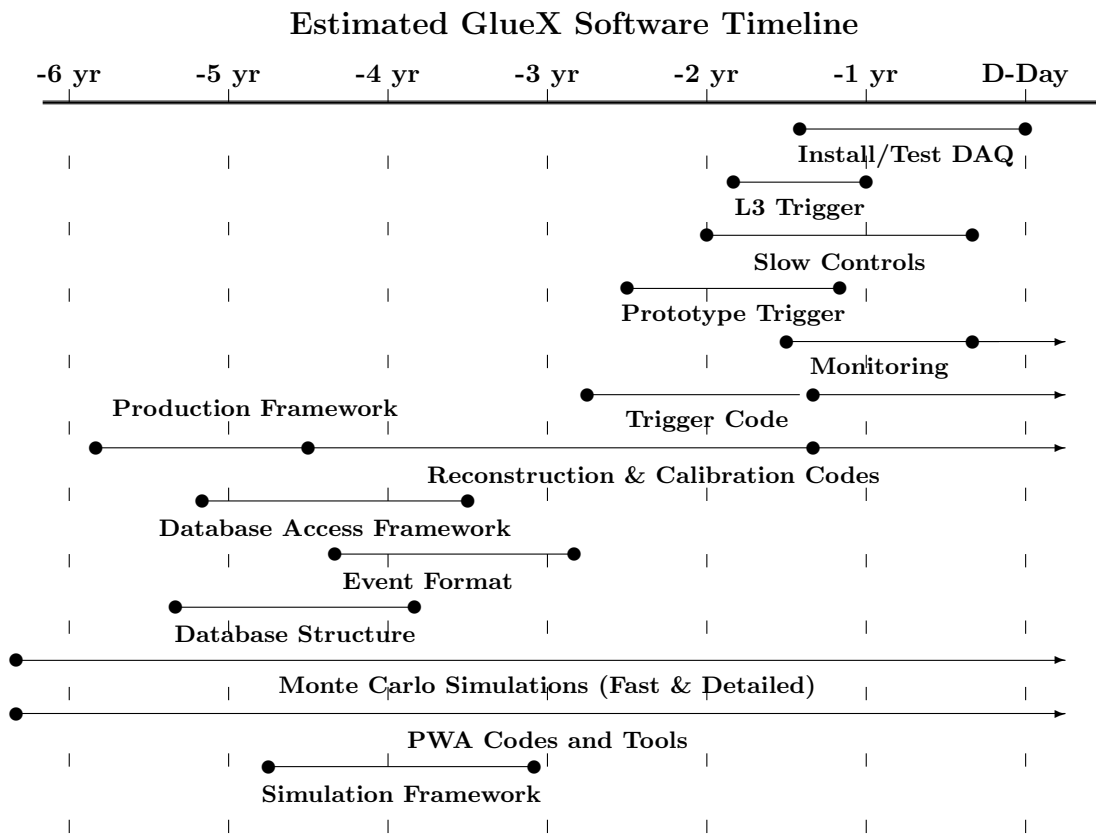


Figure 9.2: Milestones for GLUEX computing projects and tasks.

Chapter 10

Monte Carlo

Monte Carlo simulations of photoproduction reactions and the detector response are an integral part of data analysis for GLUEX. Monte Carlo data sets an order of magnitude larger than the real data for specific channels must be produced and analyzed within a unified analysis framework. The computer resources needed for this task were discussed in the previous chapter. This chapter describes how the simulation is to be carried out, the specific software components that exist at present, and some preliminary results regarding detector acceptance and resolution.

During the conceptual design phase of GLUEX two parallel paths of Monte Carlo development have been followed. The first has been focused on simulating reconstructed events for acceptance and resolution studies, and for tests of partial-wave analysis. On this path the simulation of particle interactions in the detector followed by track/cluster reconstruction is replaced by a model which accounts for the smearing of the final particle momenta according to detector resolution. This so-called *fast* Monte Carlo approach is computationally very efficient and permits the exploration of large regions of detector parameter space during design. In fact, important parts of the design evaluation can only be accomplished by this approach, before a full event reconstruction package is available.

When the event reconstruction package arrives, a different sort of simulation code will be needed. This so-called *physics* simulation relies on a detailed geometrical description of the detector and a library of known particle-material interactions to estimate the detector response to a given event as accurately as possible. From this response it forms a simulated event record that is analyzed by the reconstruction package in a similar way as real events. The physics simulation package should come first in the order of software development because it provides useful test data for debugging the rest of the analysis chain. The physics simulation is also useful at the design stage for estimating background rates in detector and trigger elements. This is the second path of Monte Carlo development being pursued by GLUEX.

These Monte Carlo simulation programs are the first components in what will grow to be a large body of code for the GLUEX experiment. It is useful to consider at the outset what pieces of these codes might be of broader use than strictly for simulation. For example, the reconstruction code will need access to the same alignment data as is used by the simulator. Some of the requirements for simulation can be met by incorporating existing software packages from other sources; however their use must be coordinated to avoid conflicts and unwanted dependencies in the future. Software developed at this early stage of the experiment must undergo numerous stages of evolution if it is to be of lasting usefulness. The incorporation of industry standards into the code wherever possible lays the groundwork for a smooth evolution in the foreseeable future. All of these things come together in the formulation of a software *framework* for the experiment.

In the sections which follow are discussed, first, the software framework, followed by a description of the individual components of the simulation package. The following three sections summarize the results from early design studies carried out with the fast Monte Carlo. The final section describes the general method how simulation results are incorporated into a partial-wave

analysis.

10.1 Monte Carlo framework

In this context, a framework refers to a set of specified interfaces through which the different software components in a system interact and exchange information, together with a set of common tools that facilitate access to information through these interfaces by application programs. Use of a framework allows builders of individual components to have a relative degree of independence in their implementation choices, knowing what requirements they must satisfy in order to work successfully with the other pieces. Before proceeding to the specifics, it is worthwhile to note two general principles that have been adopted for HALL D code development.

1. All data within the framework must be viewable in a well-formed xml document format that expresses the structure and relationships within the data.
2. All major interfaces should be implemented as web services, in addition to the normal API.

Not specified in this list is any mandated set of languages, operating systems, or disk file formats. While prudence suggests a restricted set of choices for each of these for developing new code, it was decided that the benefits of the freedom to borrow existing programs from a variety of sources outweighs the cost in complexity. Where necessary, legacy code can be wrapped in such a way that it provides its functionality through a protected interface. In any case, software technology is changing too fast at present to allow a final decision on such questions at this point in the life-cycle of the experiment.

The overall data-flow scheme for GLUEX is shown in Fig. 10.1. Data flows from the top to the bottom of the figure. On the right-hand side, digitized events come from the detector, are converted to hits by applying corrections derived from the calibration database, and are passed to the reconstruction programs for further processing. On the left-hand column, events start off as lists of particles and their momenta coming from a physics event generator and are converted to hits in the simulator, after which they follow the same path as the real events.

The remainder of this chapter is concerned mainly with what happens to the left of the vertical line in Fig. 10.1. For clarity, we will distinguish between event *generation* (first step) and *simulation* (next step) in the Monte Carlo process. As far as the framework is concerned, the only thing of concern is how programs (or people) can access what is inside the boxes. The details of how data is stored inside the boxes, or what happens inside the processing steps is beyond the scope of the framework. The generator needs to be able to find out what kind and how many events to generate. The simulator needs to be able to get from the generator a sequence of event specifications, and it must be able to provide its event hits to the reconstruction code in a format that it understands. Not shown in the figure but also important are the detector geometry information and the simulation control data which the simulator also needs. Within the GLUEX framework, all of these data have the common property that they are viewable in xml. When the software components are fully incorporated into the framework then each of the processing steps will be available on the GLUEX grid as a web service.

The formal specification of all of these interfaces is incomplete at present. The most complete specification is that of the detector geometry information, which has been published [139] on the web. It is described in more detail in a later section. A draft specification for the event description has also been published. [140]. Depending on the location along the data-flow pipeline, different pieces of event information are available. However it is decided that access to all event data by application code within the GLUEX framework is through a single interface. That interface must provide a mechanism for determining what kinds of information are available in an event and for providing what is available in a standard way to the client program.

This is all quite easy to do by specifying the interface in terms of an xml schema. However doing event input/output through xml libraries is very expensive for large data sets, not only

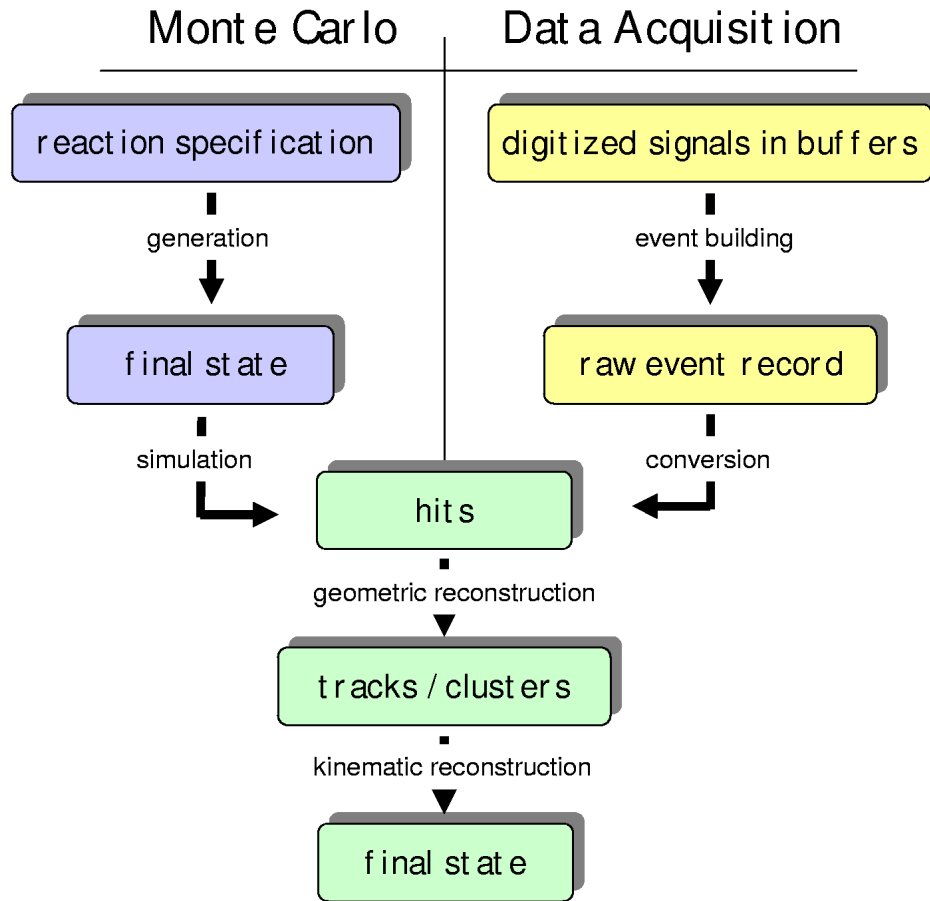


Figure 10.1: Data flow diagram showing the major software components responsible for data processing in HALL D.

in terms of data volume but also cpu overhead. This is why the framework specifies that all data should be *viewable* in xml, not necessarily *stored* in xml. No restrictions are placed on what data formats are actually used internally by applications, or how events are stored in disk files. In practice it proved convenient for the purposes of Monte Carlo to create a self-describing event data format that is very close to the underlying xml, called *hddm*. An *hddm* event stream (or file) begins with an event template in plain-text xml that describes the information that is available for each event, followed by the actual event data. The tags have been suppressed in the event data and the values written in binary format, so that the event record size is roughly equivalent to other binary formats. Framework tools exist which can automatically generate a miniature c or c++ library that contains the calls needed by an application program to access the event data, just by reading the first few lines in an *hddm* event file. Applications built with one of these libraries automatically verify that the data they require are present in the file before access is attempted. Finally, a single pair of translators called *hddm-xml* and *xml-hddm* exist which are capable of converting any *hddm* data stream to and from xml.

Thus the interface to the data in each of the boxes in Fig 10.1 is expressed in a xml specification that serves as an event template. The specification contains an inheritance mechanism that makes it easy to extend the event definition, so that producers and consumers of event data can decide to exchange additional information through the extended interface without interfering with the operation on the same data by older programs that rely on the base interface. All

of this is verified automatically by the framework API library without any need for checks by application code. Writers of application code have the choice of accessing the data through the API (currently provided in `c` and `c++` only) or by reading and parsing the `xml`. Use of the API is more efficient in that it eliminates the `xml` parsing step, but the choice of languages is restricted. On the other hand, standard tools are available in all major languages that make it easy to read and write `xml`. The advantage of this design is that anyone in any language that has the capability of reading `ascii` text has access to the event data in a standard way.

The `hddm` scheme is effectively an efficient mechanism for prototyping interfaces to event data. Eventually the information content of an event will stabilize to the point where the interface can be frozen, at least for the early stages of the pipeline. At that point the choice of the format for event data decouples from the interface. Different event formats at various stages along the data-flow path may be adopted based upon considerations of efficiency and prevailing technology. None of this has practical consequences for application code, provided that the interface remains everywhere the same.

10.2 Monte Carlo generators

There are two physics event generators available for use within the GLUEX Monte Carlo framework, known as *genr8* [87] and *cwrap* [141]. Both programs are capable of describing a complex decay chain of intermediate states, where decays into two or three bodies are supported at each step. The invariant masses of each particle produced is sampled from a Breit Wigner distribution, whose mass and width is taken from the PDG. A general t -channel process is assumed, with the distribution in t drawn at random from the standard form for a peripheral reaction

$$\frac{d\sigma}{dt} \propto e^{-b|t|}$$

where the b parameter is specified by the user. Both meson and baryon decay chains are allowed. In the case of *genr8* the user may specify the t -distribution in the form of a histogram in place of specifying a value for b in the above formula. b may be specified by an input histogram.

The angular distributions at each decay vertex are generated according to phase space. This may appear to be a severe restriction in an experiment whose goal is partial-wave analysis, but in fact that is not the case. To see how the physical model for particle spins and decay asymmetries are applied to phase-space Monte Carlo data, see section 10.8.

Both *genr8* and *cwrap* were imported from other experiments, and so write their output events in different and somewhat esoteric formats. To incorporate them into the GLUEX framework it was sufficient to provide translators from their private formats to a common `hddm` format that can be viewed as `xml`. The present draft specification for the standard `xml` interface to generated events is found in Ref. [140]. At present a second standard interface is also being supported known as *stdhep*. This somewhat archaic Fortran-based standard was in use by many HEP experiments over the last decade, and there are a number of useful Monte Carlo tools that rely on it, including *MCFast* (see section 10.5). Currently translators exist to supply generated events from either generator through either the `xml` or the `stdhep` interface.

Both generators use cryptic private formats for the input data that specify the reaction and desired number of events. At present there does not exist a single unified interface for specifying the reaction to be generated. The task of incorporating *genr8* and *cwrap* into the GLUEX framework will not be complete until that interface has been specified, and translators have been written to convert that information from `xml` to a form understandable to the generators.

10.3 Detector Geometry

One of the most basic requirements for the simulation is access to a detailed description of the geometry of the experiment. Included in geometry is the shape and location of all relevant components, their properties in terms of material composition, density, etc., and the map of the

magnetic field. Any objects with which beam particles may interact on their way to a detector are a part of the geometry, starting with the primary collimator and ending with the photon beam dump. Any application within the GLUEX framework that needs access to detector geometry data obtains that information through one unified interface. This interface is specified in the form of a xml *document type definition* (DTD) which details what tags exist in the document, what are their arguments, and their structural relationships. The basic structure of the DTD was borrowed from the ATLAS experiment at CERN and adapted for the needs of GLUEX. It describes the detector as a tree of volumes, each with specified shape, size, position and material properties. It allows elements to be grouped together and positioned as a unit, so that a survey datum can be expressed by a single element. More details on the interface can be found in Ref. [139].

Application code has access to geometry data through the standard xml libraries. Programs can scan the entire tree or ask for specific pieces of information, such as the position of the center of the target. At present the only consumers of geometry information are the simulation codes. The Geant simulator (see section 10.4) is capable of modeling any geometry, provided that the xml conforms to the DTD. The MCFast simulator (see section 10.5) supports a more limited geometrical description. A special set of tags in the geometry DTD have been created to describe the detector elements in simplified terms for MCFast, in places where the translation from the hierarchical description require some imagination. As more applications are created that depend upon access to specific pieces of geometry information, it will be necessary to extend the interface beyond the DTD to specify the presence and location of specific tags. Investigation is underway to determine if these more complex constraints might be better expressed using xml schema than the DTD.

At present the geometry description is implemented in a set of plain xml text files and organized under a sequential version system. In the future they will probably be stored in a database and indexed by date or run number.

10.4 Physics Simulation

The physics simulation for GLUEX is provided by a program called *HDGeant*. The simulator requires four data interfaces: an event source, detector geometry data, simulation control information, and event output. HDGeant is capable of simulating events from any one of three sources.

1. events from a Monte Carlo generator
2. coherent bremsstrahlung source generator
3. automatic single-track generator (for testing)

The first of the three is an external event source described in section 10.2. Events from the generator are distributed uniformly along the length of the beam-target interaction volume and final-state particles followed out into the detector from there. The other two sources are internal to the simulator, and are used for special purposes. The coherent bremsstrahlung source generates uncollimated photons with the energy, angle and polarization characteristics of bremsstrahlung from an oriented diamond radiator. These photons enter the setup upstream of the primary collimator and are followed through the collimator region into the experimental hall, where interactions in the detector are allowed to take place. This simulation mode is useful for estimating detector backgrounds, and for studying the systematics of the collimated photon beam. The single-track generator is used for development of various parts of the simulation, and will be useful later in debugging the event reconstruction package.

The choice of the source for input events is specified in an input file known as the *control* file. Also in the control file are a number of switches that control the simulation mode, such as the number of events to simulate, cutoffs for a variety of physics processes, and debug options. HDGeant obtains the detector geometry directly from the standard geometry interface. Input

uncollimated beam	44 ms
1GeV π^+ at 15°	55 ms
3GeV γ at 10°	200 ms
1GeV γ at 45°	90 ms
$\gamma p \rightarrow \pi^+ \pi^- p$	210 ms
$\gamma p \rightarrow \pi^+ \pi^- \pi^0 p$	430 ms
$\gamma p \rightarrow \eta \pi^0 \pi^0 p$	670 ms

Table 10.1: Average time required by HDGeant to simulate a single event of various kinds. The tests were carried out on a single Pentium III 1GHz processor. The times are reduced by about a factor of 1.8 on the Athlon MP 1800+ cpu.

events from the Monte Carlo generator are accessed through the the standard event interface implemented in the hddm library. Output events are likewise written out using the hddm library.

The output from the simulation is a list of *hits*, which are time and energy data from each detector element that received a signal during the propagation of the event through the detector. The hit data are stored in physical units appropriate to the signal (eg. ns, MeV) which is what the simulation directly produces. No provision is made in the simulator to convert these data back into ADC or TDC data in the form produced by the data acquisition hardware; that would require couple the simulation to the the detector calibration database, and introduces an unnecessary complication to the simulation. If events in that form were desired at some point, a separate converter could be written to generate simulated raw events from the simulator output.

The major effort in the ongoing development of the simulation is to have a reasonably accurate model of the detector response in each of the detector elements. A basic model presently exists in the code for each of the detector components. These must be improved by the incorporation of intrinsic resolutions for each of the detectors. For example, the impact parameter of tracks in a straw tube of the central drift chamber is converted to a hit time value using a simple linear model for the time *vs* radius. For another, for the response of the lead-glass calorimeter, the total energy loss of charged particles is reported as the hit energy, without taking into account the difference in the Čerenkov response between different kinds of particles. Nevertheless, in its present form the simulator is useful for estimating many aspects of detector performance.

In addition to the detector hits, the simulation is also capable of writing out certain kinds of auxiliary information about the simulated event, for example the actual 3-d points of track impacts on the planes of the forward tracker or the true energy of a photon creating a cluster in the barrel calorimeter. Such information is called *cheat* data because it is not available for real events. However it is invaluable for Monte Carlo studies prior to the development of event reconstruction code, and will be useful in that development for checking the fidelity of the reconstruction.

In Table 10.1 is shown the average time required to simulate a single event on a cpu that is available today, for a few sample reactions. The beam simulation uses the simulator's internal coherent bremsstrahlung generator, and exercises mainly the electromagnetic shower simulation in the collimator region upstream of the detector. The single-track case is included to show the cost of tracking charged particles through the the magnetic field. The gammas show the corresponding cost for photons. The two are put together in the reactions which follow.

In order to obtain a reliable simulation of backgrounds from the collimator region, two enhancements to the standard Geant simulation library were incorporated into HDGeant. The first of these is the addition of hadronic interactions by photons in materials, and the second was Bethe-Heitler muon pair production. The standard Geant electromagnetic shower simulation does not include hadronic photoproduction processes or muon pair production because their cross sections are several orders of magnitude less than the dominant electromagnetic processes and their presence is generally not important to simulating calorimeter response. For the purposes of HALL D however, the high intensities of showers in the collimator enclosure and the heavy

shielding against electromagnetic backgrounds makes them important. In particular there are two kinds of penetrating radiation that must be considered: neutrons and high-energy muons.

The incorporation of muon Bethe-Heitler production into Geant was straight-forward to do, simply by replicating the code for electron pair production with a changed mass, and the cross section reduced by the factor m_e^2/m_μ^2 . The inclusion of photonuclear processes is more daunting. Rather than launch a development of our own, it was decided to incorporate a package that was developed earlier for use by the BaBar experiment known as *Gelhad* [142]. This package breaks provides four models of hadronic photoproduction that are applicable at different scales: single nucleon knockout, two-nucleon knockout via the quasi-deuteron process, single pion photoproduction in the delta-resonance region, and diffractive vector production in the diffractive region. From the point of view of photonuclear physics, this model is far from complete. It will not be used by GLUEX to generate photoproduction events in the target. What it does provide is a starting point for estimating neutron fluxes in the hall from the collimator region.

The present HDGeant package is based on the widely-used version 3 of the CERN Geant library. Discussion has started regarding moving the development for GLUEXover to the C++ simulation package known as Geant4 that is being used by some of the LHC experiments. Given that the Geant-3 library is written almost entirely in Fortran and is no longer being actively supported by the CERN computer division, its long-term viability depends upon support by the user community. The LHC Alice experiment has taken the major components of Geant-3 and wrapped them for use in a C++ environment known as *AliRoot*. The choice of a long-term solution for a physics simulation for GLUEX has not yet been finalized.

10.5 Fast simulation

A fast Monte Carlo package has been developed to understand the performance of key aspects of the GLUEX detector systems. This package consists of a collection of modules, each serving some particular function. The modules consist of individual programs and library routines which use common event input/output formats. Figure 10.2 illustrates this modular structure.

First, a Monte Carlo four-vector generator is used to create phase-space distributed events. Next is the detector simulation, *HDFast*, which is a fast and flexible simulation program based upon the MCFast package developed by the simulation group at Fermilab. The Monte Carlo output includes (but is not limited to) the following data objects:

- generated event
- detector hits
- resolution modified (smeared) event
- time-of-flight information
- dE/dx information
- threshold Čerenkov information
- particle trajectory information

HDFast is a fast and flexible simulation program based upon the MCFast package developed by the simulation group at Fermilab[143]. MCFast consists of a set of modularized Monte Carlo library routines. It is designed to perform parameterized tracking by assembling a covariance matrix for each track that takes into account materials, efficiencies, and resolutions for all measurement planes, and use this matrix to smear the track parameters randomly. The covariance matrix is first diagonalized so as to properly account for effects due to correlations when parameters are smeared. In principle, the distribution of smeared tracks produced by this method would be similar to the distribution of real tracks that were measured by a real detector(with the same parameters) and analyzed with an idealized track fitting procedure[143].

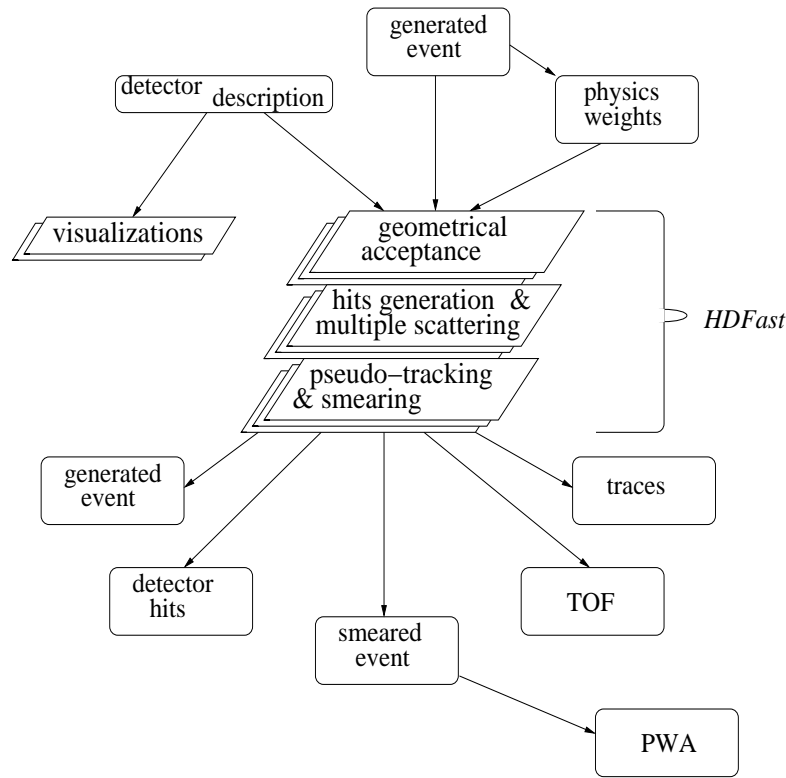


Figure 10.2: An illustration giving an overview of the GLUEX Monte Carlo software which emphasizes its modular nature.

HDFast is controlled via a set of user routines which act as an interface to the MCFast package. They control the tracking and smearing of the four-vectors, in addition to the booking and filling of monitoring ntuples and histograms. The detector geometry is controlled by an ascii file which is read in during program execution. This allows the user to quickly create or modify the detector geometry without the need to recompile the executable. In addition, ROOT[144] was used to develop an event display which reads in the ascii geometry file and displays a two-dimensional visualization (see Figure 10.8) of the detector configuration and event track projections.

10.6 Acceptance studies

In order to better understand the effects of finite acceptance of a proposed detector configuration, a simple study of the acceptance as a function of total meson effective mass for various final states has been performed. In doing the Monte Carlo acceptance studies we considered the following reactions: schematically shown in Figure 10.8. This configuration is composed of the following:

- 2.24 Tesla solenoid magnet –LASS magnet,
- 5-layer Vertex Chamber (VTX),
- 22-layer Central Drift Chamber (CDC),
- 5 6-layer Forward Drift Chambers (FDC),

- Barrel Calorimeter which also acts as central TOF(BCAL),
- Cerenkov Detector,
- Forward time-of-flight (FTOF),
- Forward Lead Glass Detector (LGD) 172x172 *cm* with 8x8 *cm* beam hole,
- target-beam vertex distribution at $r = 0.0$ *cm*, $z = 50$ *cm* with $\sigma_r = 0.3$ *cm*, $\sigma_z = 15.0$ *cm* (\hat{z} is along the magnet axis; the origin is located at the upstream face of the solenoid).

10.6.1 Acceptance performance

In the simulation, an event was accepted if the following minimum conditions were met:

- all charged tracks were found with a minimum of four hits per track, and
- all gammas were detected in either the BCAL and/or LGD.

The acceptance as a function of total effective meson mass is shown in Figure 10.3. It is important to note that at higher beam energies the forward boost results in more forward-going high-momentum tracks. And even though the mass acceptance seems good, the resolution of the forward-going higher-momentum tracks degrades. This issue has been studied in detail and is discussed in HALL D Note #7[88].

In Figure 10.4 through Figure 10.7, we show the acceptance for the Gottfried-Jackson decay angles (the particle decay angles often used in the partial wave analysis). It is clear that the Gottfried-Jackson angular acceptance is quite good. The acceptance for gammas is also rather high, but it suffers more from holes in the forward and backward regions. The hole in the backward region results from backward-going gammas, which is the dominant factor at lower beam energies. The forward hole, due to gammas passing through the beam hole in the LGD, becomes important for higher beam energies. Figure 10.8a displays an event for reaction $\gamma p \rightarrow p\eta\pi^0\pi^0$ at $Mass(X) = 2.0$ *GeV/c*² and beam of 5 *GeV* that was lost due to the upstream hole. For this channel 75% of the lost events were of this type. On the other hand, for a 12 *GeV* beam and the same final state about 50% of the lost events are due to the beam hole (See Figure 10.8b). While the beam hole is unavoidable, the hole in the backward region suggests the need at the lower beam energies for a backward gamma veto. Regardless of this, the acceptance for the Gottfried-Jackson decay angles is flat and not strongly dependent on $Mass(X)$ or the beam energy. This is important for partial wave analysis because, although the effects of acceptance distortions are accounted for in the method, large acceptance corrections can lead to large systematic errors in the results.

10.7 Monte Carlo Study of Photon Energy Resolution

In this study the GENR8 program was used to generate the events. Four different exclusive reactions were studied, two with photons produced at the baryon vertex:

$$\gamma p \rightarrow N^*(1500)\pi^+ \rightarrow (n\eta)\pi^+ \rightarrow n\pi^+\gamma\gamma \quad (10.1)$$

$$\gamma p \rightarrow X^+(1600)\Delta^0 \rightarrow (\pi^+\pi^+\pi^-)(n\pi^0) \rightarrow \pi^+\pi^+\pi^-n\gamma\gamma \quad (10.2)$$

The Δ^0 reaction (reaction 10.2) has a 3 π -meson mass of 1.600*GeV/c*², and a width of 300 *MeV/c*². The two meson vertex reactions are:

$$\gamma p \rightarrow X^+(1600)n \rightarrow (\eta\pi^+)n \rightarrow n\pi^+\gamma\gamma \quad (10.3)$$

$$\gamma p \rightarrow X(1600)p \rightarrow (\pi^+\pi^-\pi^0)p \rightarrow p\pi^+\pi^-\gamma\gamma \quad (10.4)$$

In both reactions 10.3 and 10.4, the meson systems were generated with a Breit–Wigner distribution of mass 1.6*GeV/c*² and a width of 0.3*GeV/c*².

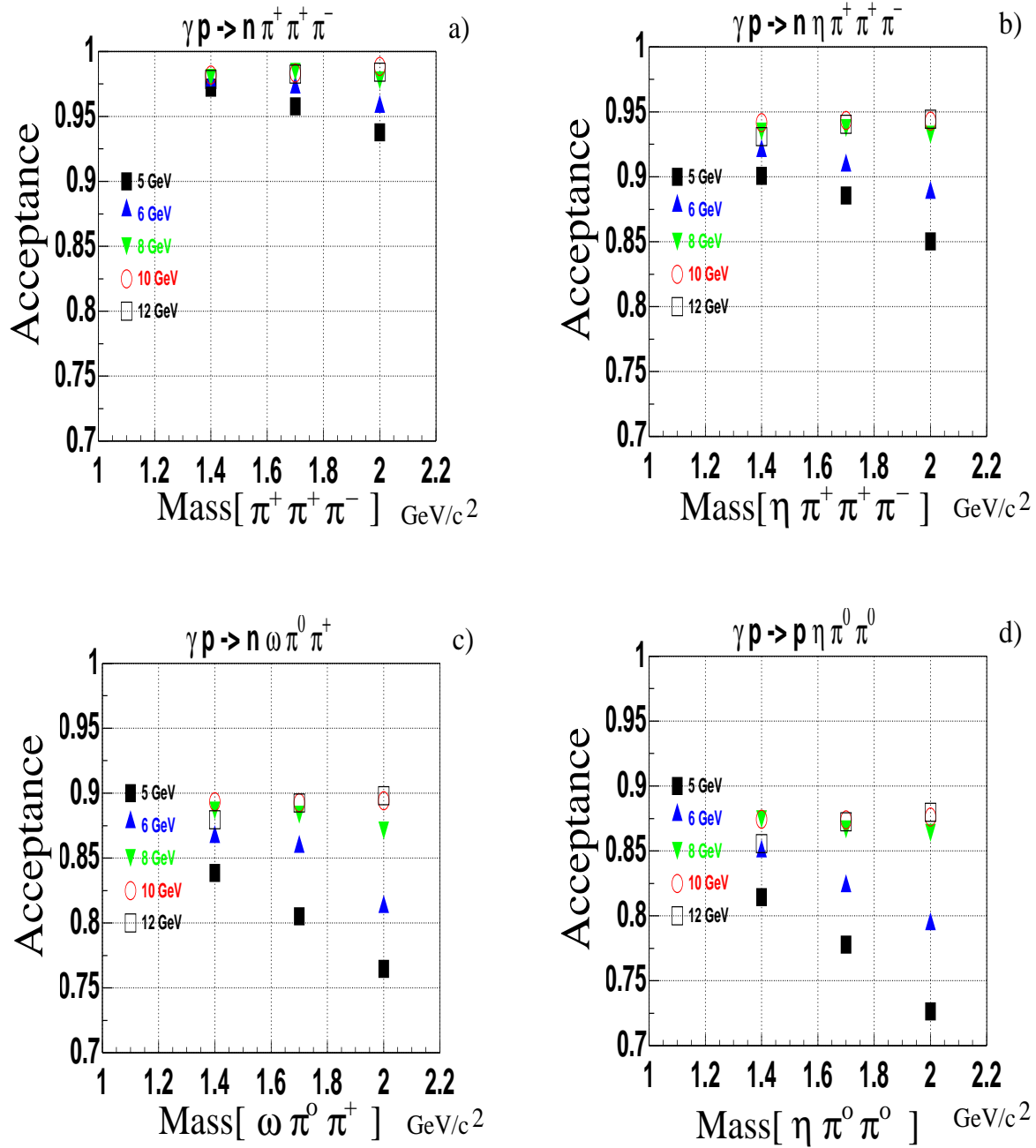


Figure 10.3: The acceptance as a function of total effective meson mass: a) $X^+ \rightarrow \pi^+ \pi^+ \pi^-$, b) $X^+ \rightarrow \eta \pi^+ \pi^- \pi^+$, c) $X^+ \rightarrow \omega \pi^0 \pi^+$, d) $X^0 \rightarrow \eta \pi^0 \pi^0$. The acceptance studies were performed for effective meson masses of 1.4, 1.7, and 2.0 GeV/c^2 , and at each mass point the photon beam energy was varied from 5 to 12 GeV .

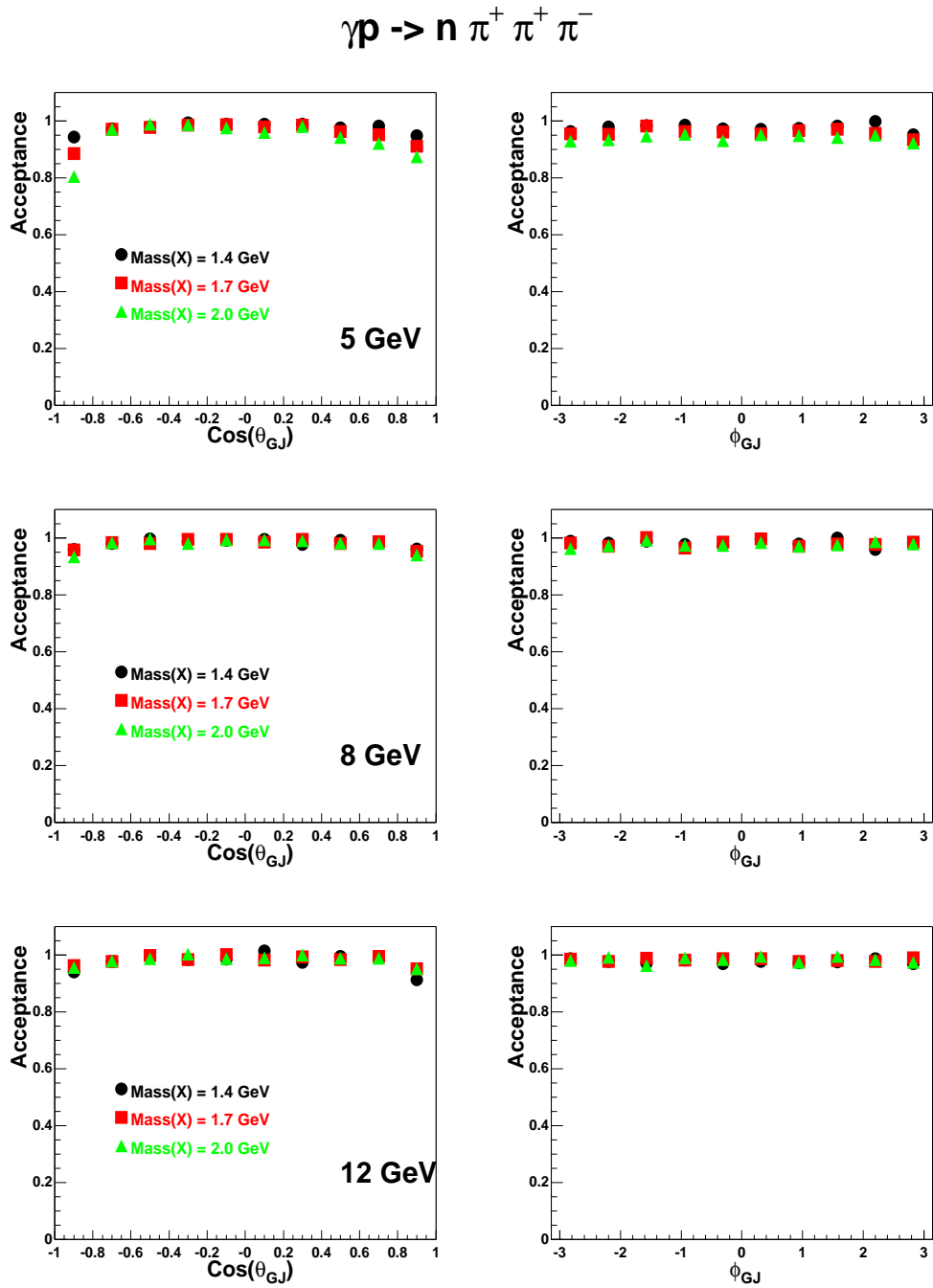


Figure 10.4: The acceptance in $\cos(\theta_{GJ})$ and ϕ_{GJ} for $X^+ \rightarrow \pi^+ \pi^+ \pi^-$. The acceptance was studied for X^+ effective masses of 1.4, 1.7, and 2.0 GeV/c^2 , and for different photon beam energies of 5 GeV (top), 8 GeV (middle), and 12 GeV (bottom).

$$\gamma p \rightarrow n \eta \pi^+ \pi^+ \pi^-$$

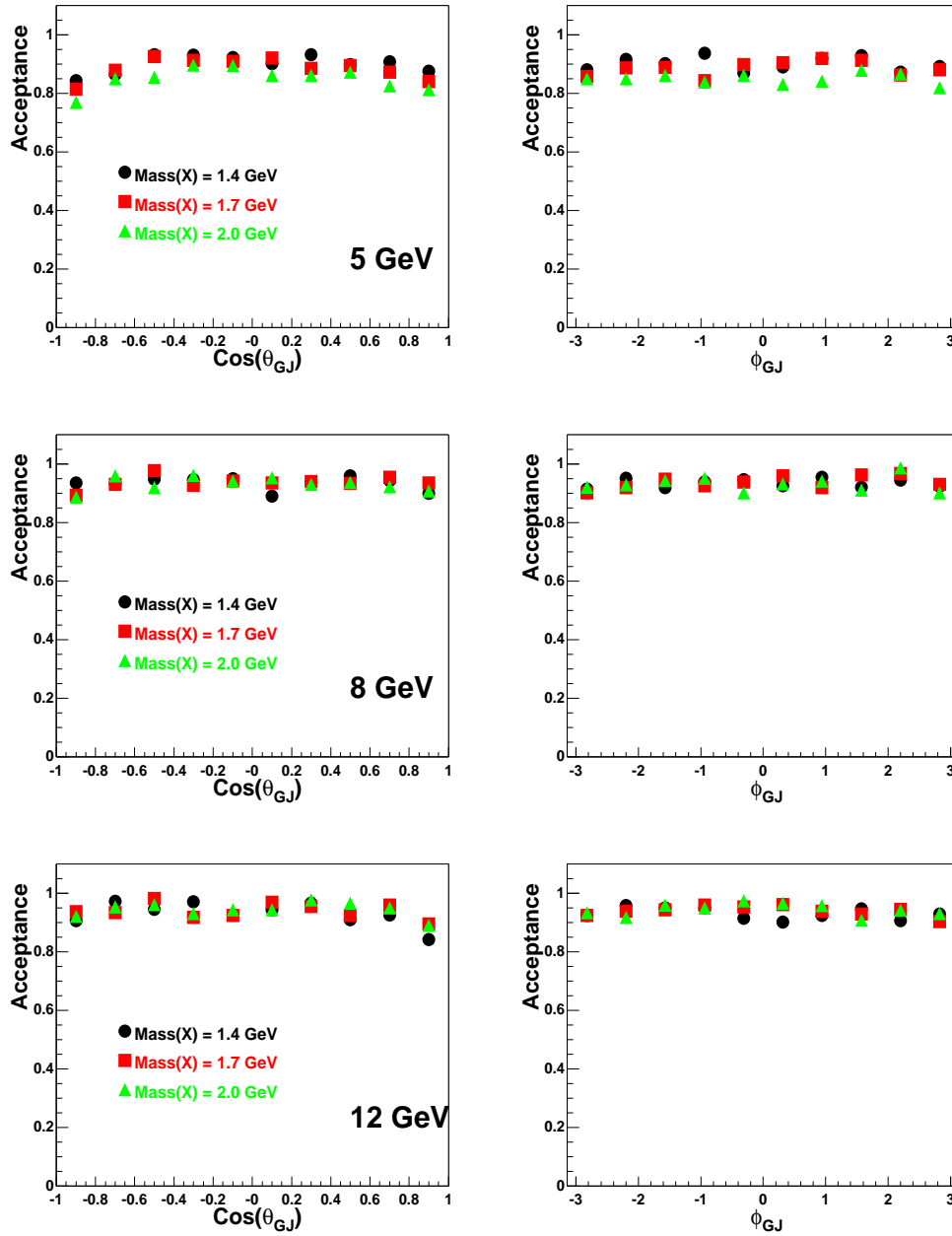


Figure 10.5: The acceptance in $\text{cos}(\theta_{GJ})$ and ϕ_{GJ} for $X^+ \rightarrow \eta \pi^+ \pi^+ \pi^-$. The acceptance was studied for X^+ effective masses of 1.4, 1.7, and 2.0 GeV/c^2 , and for different photon beam energies of 5 GeV (top), 8 GeV (middle), and 12 GeV (bottom).

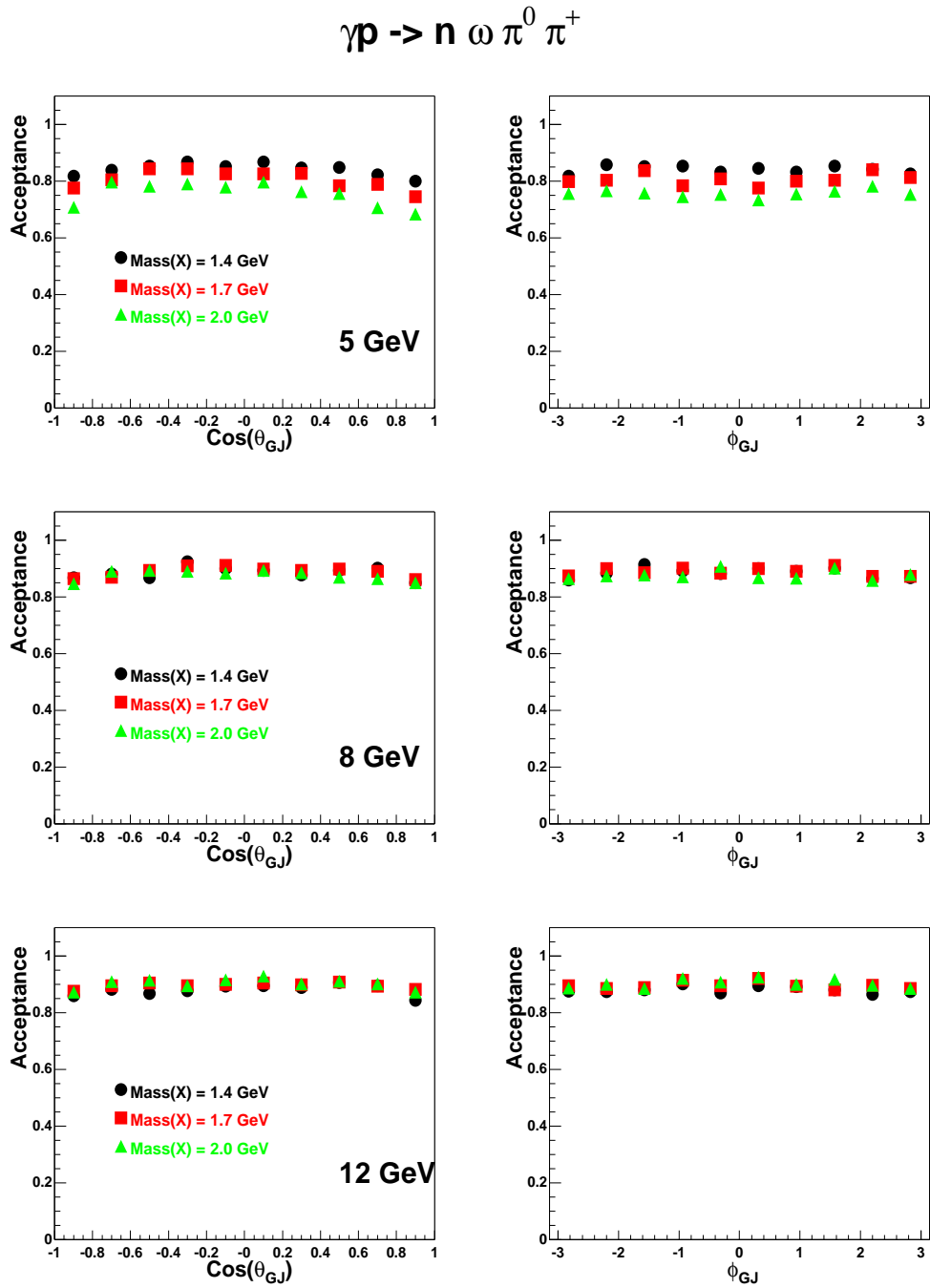


Figure 10.6: The acceptance in $\cos(\theta_{GJ})$ and ϕ_{GJ} for $X^0 \rightarrow \omega \pi^0 \pi^+$. The acceptance was studied for X^+ effective masses of 1.4, 1.7, and 2.0 GeV/c^2 , and for different photon beam energies of 5 GeV (top), 8 GeV (middle), and 12 GeV (bottom).

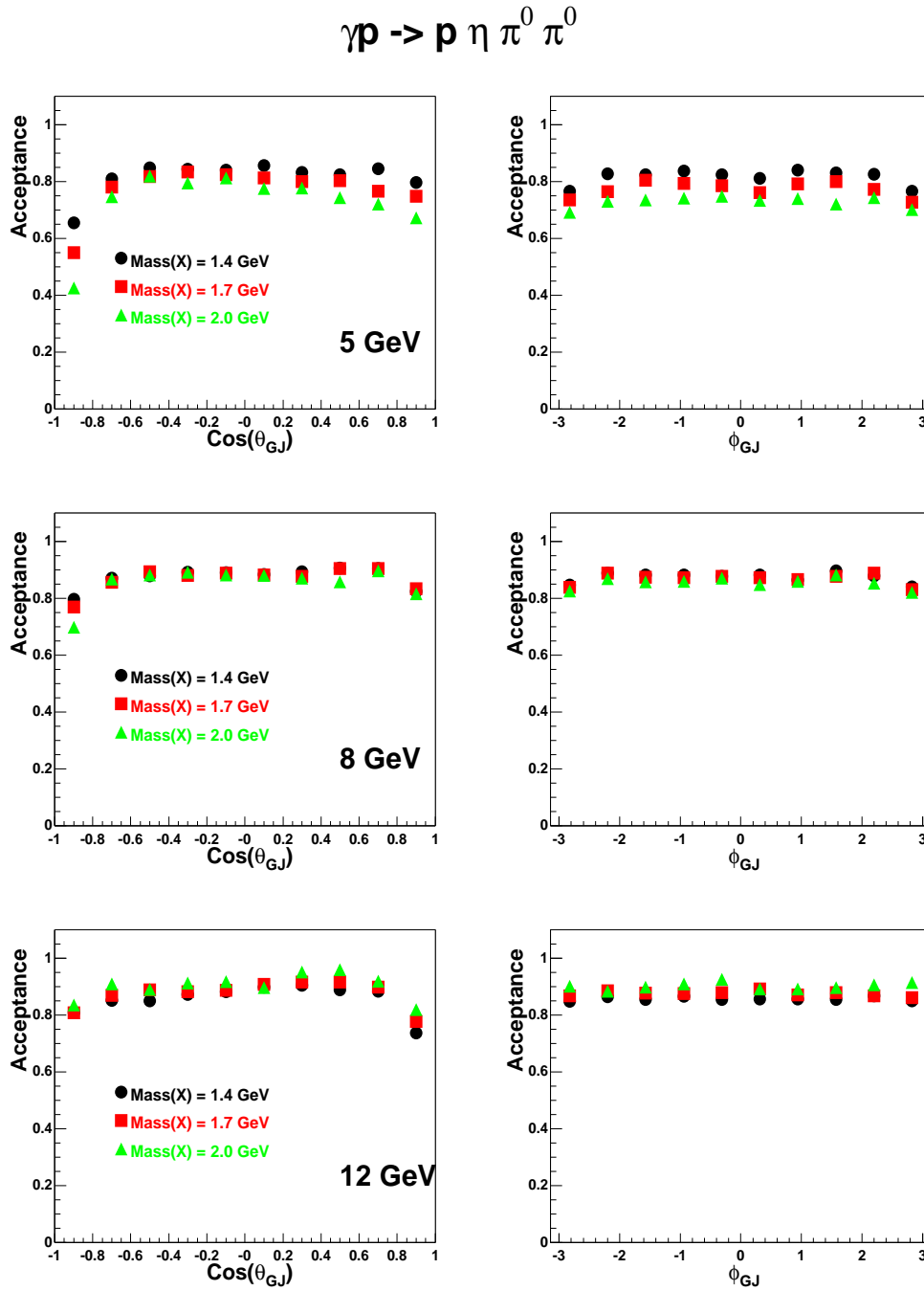


Figure 10.7: The acceptance in $\cos(\theta_{GJ})$ and ϕ_{GJ} for $X^0 \rightarrow \eta\pi^0\pi^0$. The acceptance was studied for X^+ effective masses of 1.4, 1.7, and 2.0 GeV/c^2 , and for different photon beam energies of 5 GeV (top), 8 GeV (middle), and 12 GeV (bottom).

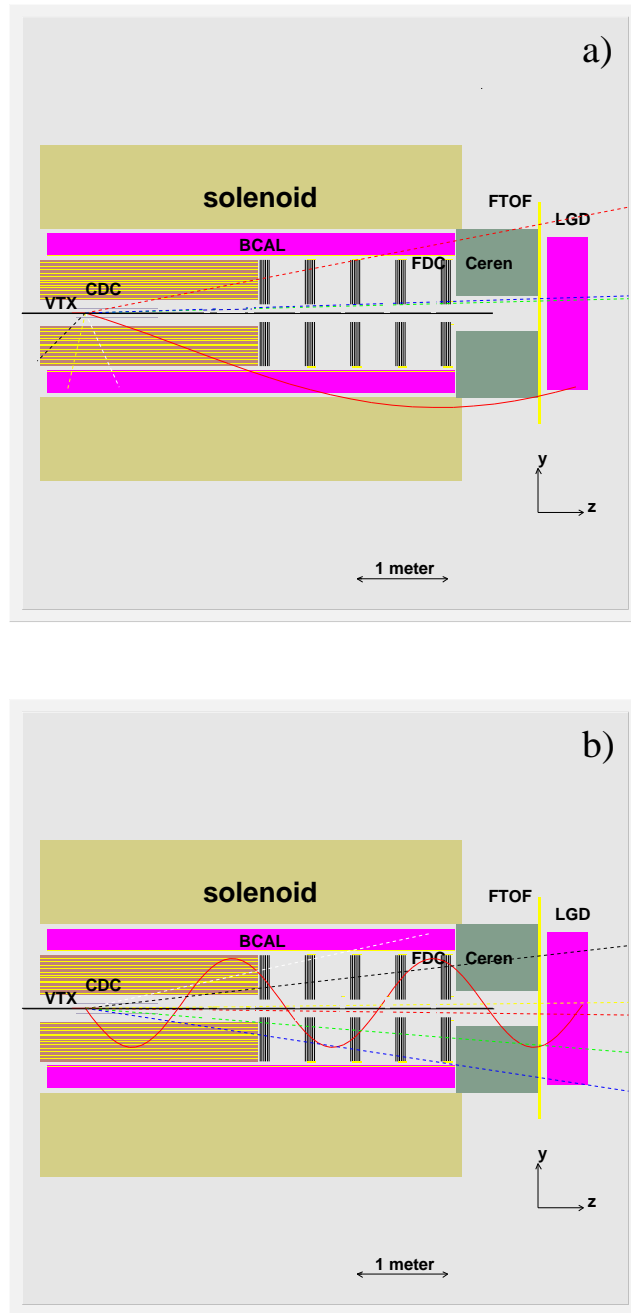


Figure 10.8: Event displays of lost events for $\gamma p \rightarrow p\eta\pi^0\pi^0$ for $Mass(X) = 2.0 \text{ GeV}/c^2$: (a) backward missed gamma at a beam energy of 5 GeV , and (b) forward missed beam hole gamma at a beam energy of 12 GeV . The events shown contain both charged particles (solid lines) and photons (dashed lines).

Each of the above reactions were simulated using a beam energy of 8GeV , and a t -channel slope of $5\text{GeV}/c^2$. The production and decay vertex was assumed to be at the center of the target. For each system, 10,000 events were generated. The direction and energy of the photons were recorded and analyzed.

10.7.1 Photon Detector Energy Resolution

The photons produced in the above decays were traced into the Barrel Calorimeter and the Lead Glass Detector. Figure 10.9 and 10.10 show the percentage of photons that would enter, but not be detected by the Barrel Calorimeter due to the minimum energy thresholds.

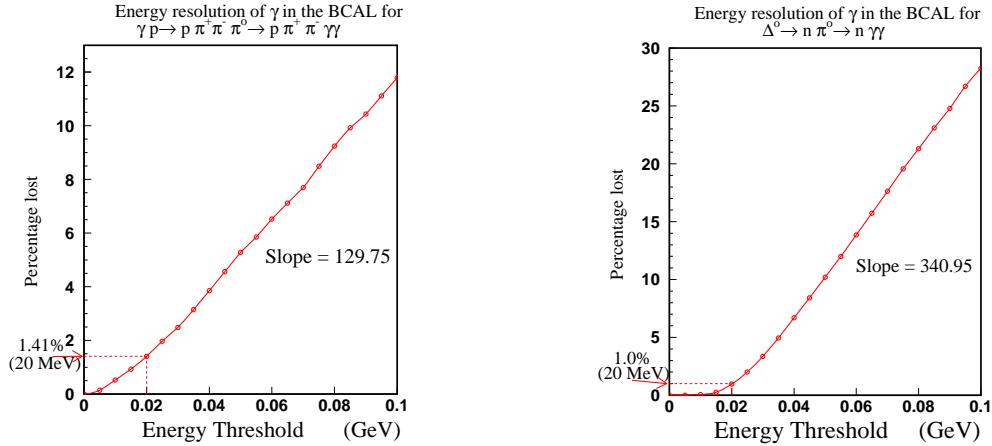


Figure 10.9: The percentage loss due to the energy threshold of the BCAL. Left is for reaction 10.4, while the right figure is for the Δ^0 decay from reaction 10.2. The percent of the total photons entering the Barrel Calorimeter for reaction 10.4 is 57% and reaction 10.2 is 87%.

Currently, the design calls for the energy sensitivity of 20 MeV for the Barrel Calorimeter. One can see that this results in around a 1% loss of photons which is quite acceptable. However, if this energy can not be met, the percentage of photons lost rises rapidly with the increased energy threshold, especially for the Δ^0 (reaction 10.2) decay. For example, if the threshold is 50 MeV, then 5% of the 3π reaction is lost, and 10% of the Δ^0 reaction is lost. The situation for the η reactions is not so severe, as would be expected from the higher energy photons in the η decay (figure 10.10).

The results for the Lead Glass Detector are similar, but the percentage rise is not so significant at higher energy thresholds. The only system with significant loss in the lead glass array is the 3π (reaction 10.4) decay. At the sensitivity threshold of 100 MeV, the lead glass detector will not see 0.718% of the photons. The design calls for a 150 MeV detection minimum in the LGD. At this energy, the detector will miss 1.86% of the photons (figure 10.11).

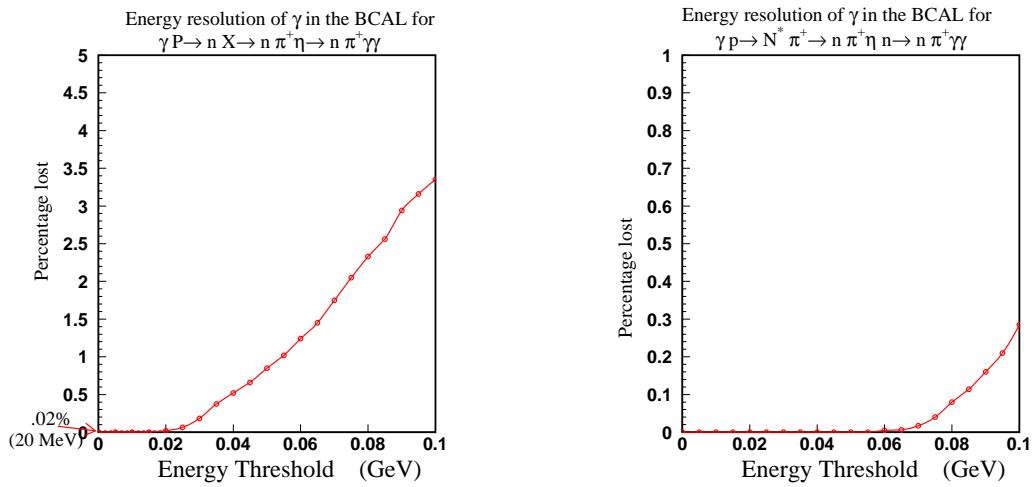


Figure 10.10: The percentage loss due to the energy threshold of the BCAL. The left plot is for reaction 10.3, and right is for reaction 10.1. The percent of all the photons entering the Barrel Calorimeter for the ηX (reaction 10.3) and the ηN^* (reaction 10.1) are 55% and 88% respectively.

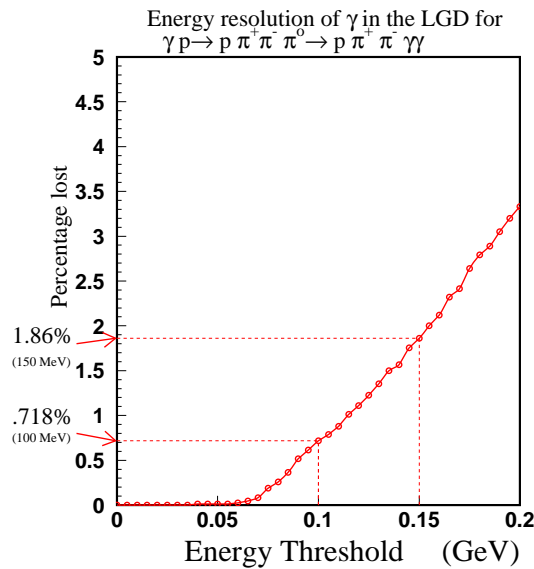


Figure 10.11: The percentage of undetected photons for a given energy threshold of the lead glass detector. From reaction 10.4.

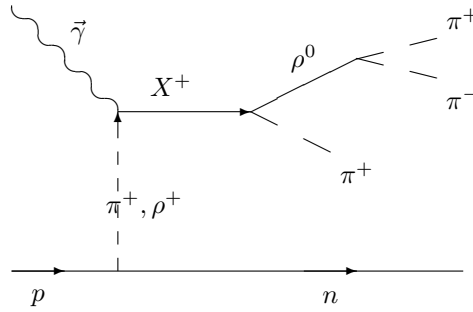


Figure 10.12: A schematic diagram of the photoproduction amplitude via one- π or ρ exchange. The state X^+ then decays via $\rho^0\pi^+$, and the ρ subsequently decays into $\pi^+\pi^-$.

10.8 Physics Event Weighters

Conceptually, what one would like to do in the analysis of any given reaction is to write down as complete as possible a set of diagrams leading to the final state and sum their amplitudes as a function of a minimal set of unknown parameters. This model would then be fed to the event generator to produce a Monte Carlo sample which could be reconstructed and compared to the data. By repeating this procedure for different values of the parameters through a fitting procedure, the best values of the parameters and an overall evaluation of the model could be derived.

Practically, this is not what is done because it is too expensive to recompute the entire Monte Carlo sample at every step in the fit. Instead a single Monte Carlo sample is produced using an initial crude approximation to the physics model distribution, and then corrections are applied using a weighting procedure after the sample has been simulated and reconstructed. The initial approximation is defined by the following three simple assumptions; (a) particles from high-energy photoproduction are produced independently from meson and baryon vertices; (b) the momentum separation between the two vertices is described by an exponential distribution in the Mandelstam variable t ; (c) within each vertex the particles are produced through a cascade of two- and three-particle decays which are each distributed according to a phase-space density function. If this approximation were an adequate model of the physics then there would be no need for the GLUEX experiment. Nevertheless it is a useful starting point because it can be used to produce a Monte Carlo sample of events with adequate coverage over the full kinematic range of interest.

Assuming the independence property of the Monte Carlo sampling technique, every event in the Monte Carlo sample is independent of the others. Each reconstructed Monte Carlo event carries with it the information about the original generated kinematics, from which the physics amplitudes can be calculated. For a given set of model parameters these amplitudes can be summed to form a probability for each event, which is called a *weight*. If all sums over the Monte Carlo sample during partial wave analysis are carried out including these weight factors then the foregoing conceptual procedure is recovered. Although the statistical errors in the weighted Monte Carlo sample are no longer simple Poisson factors, they are straightforward to calculate. In general these errors are larger for the weighted technique than for an unweighted procedure, but that is readily offset by generating a somewhat larger sample. Exactly how much larger depends on how different the weighted distribution is from the initial, but usually this factor is not larger than two. Ultimately it is not known until the final stages of the analysis how large a Monte Carlo sample is adequate for any given channel, but for the purposes of the design a conservative factor of 10 more Monte Carlo than real events has been adopted as a benchmark.

The above method is well-established for partial wave analyses in high-energy physics. To gain experience within the context of GLUEX it was decided to apply the procedure to a photoproduction reaction. To this end, an event generator for the 3π final state has been written

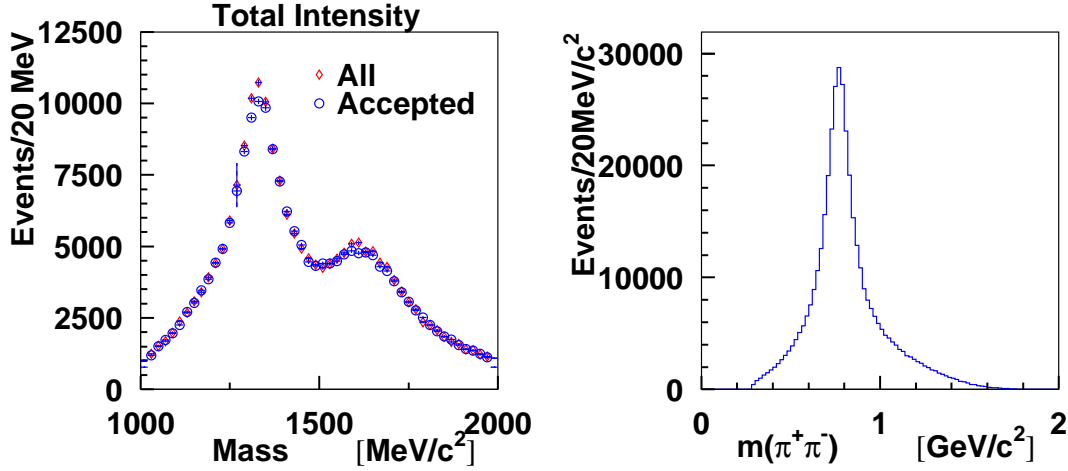


Figure 10.13: (Left) The generated 3π mass spectrum using four intermediate resonances, X^+ . The diamonds correspond to all generated events, while the circles correspond to events which have been run through the GLUEX Monte Carlo program. (Right) The $\pi^+\pi^-$ invariant mass from the 3π events. The peak corresponds to the $\rho^0(770)$.

using the one-pion charge-exchange mechanism as discussed in reference [38] for reaction 10.5.

$$\vec{\gamma}p \rightarrow X^+n \quad (X^+ \rightarrow [\rho^0 \rightarrow \pi^+\pi^-] \pi^+) \quad (10.5)$$

A schematic of this process is shown in Figure 10.12. One- π charge exchange requires both a spin-flip at the nucleon vertex, and that the X^+ particle carry the helicity of the incoming γ , ($M_X = 1$). Any number of resonances X^+ with different masses, widths and production strengths can be included in the generator. In addition, the photon beam can have any polarization desired. An extension to this program allows for ρ -exchange under the same conditions as the π exchange. These two amplitudes represent *unnatural* and *natural* parity exchanges respectively. Events produced using one of the phase space generators can then be weighted according to the physics weighter, and then passed through the GLUEX Monte Carlo program. These can then be used as input to the partial wave analysis as described in the next chapter.

A sample of the output of this generator is shown in Figure 10.13. These events have been generated with four resonances: $a_1(1260)$, $a_2(1320)$, $\pi_2(1670)$ and an exotic $\pi_1(1600)$. The masses and widths are all consistent with current accepted values. In addition, one can see the ρ^0 in the $\pi^+\pi^-$ invariant mass spectra. A full list of known resonances [145] that could be put in this generator is given in table 10.2.

Resonance	Mass	Width	$L_{\rho\pi}$
$a_1^+(1260)$	$1.230\text{GeV}/c^2$.250 to $.600\text{GeV}/c^2$	$L = 0, 2$
$a_2^+(1320)$	$1.318\text{GeV}/c^2$	$.105\text{GeV}/c^2$	$L = 2$
$\pi_1^+(1600)$	$1.593\text{GeV}/c^2$	$.168\text{GeV}/c^2$	$L = 1$
$a_1^+(1640)$	$1.640\text{GeV}/c^2$	$.300\text{GeV}/c^2$	$L = 0, 2$
$a_2^+(1660)$	$1.660\text{GeV}/c^2$	$.280\text{GeV}/c^2$	$L = 2$
$\pi_2^+(1670)$	$1.670\text{GeV}/c^2$	$.259\text{GeV}/c^2$	$L = 1, 3$
$a_2^+(1750)$	$1.752\text{GeV}/c^2$	$.150\text{GeV}/c^2$	$L = 2$
$a_4^+(2040)$	$2.014\text{GeV}/c^2$	$.361\text{GeV}/c^2$	$L = 4$
$\pi_2^+(2100)$	$2.090\text{GeV}/c^2$	$.625\text{GeV}/c^2$	$L = 1, 3$
$a_6^+(2450)$	$2.450\text{GeV}/c^2$	$.400\text{GeV}/c^2$	$L = 6$

Table 10.2: A list of known charged 3π resonances that could be produced in photoproduction and decay via $\rho\pi$. The column $L_{\rho\pi}$ are the allowed orbital angular momentum between the ρ and the π when the resonance decays. Because we require non-zero isospin, many states can not be produced.

Chapter 11

Partial Wave Analysis

11.1 Introduction

To identify the J^{PC} quantum numbers of a meson it is necessary to perform a *partial wave analysis* (PWA). In the simplest terms, a partial wave analysis determines production amplitudes by fitting decay angular distributions. The fit includes information on the polarization of the beam and target, the spin and parity of the resonance, the spin and parity of any daughter resonances and any relative orbital angular momenta. The analysis seeks to establish the production strengths, production mechanisms and the relative phase motion of various production amplitudes. Phase motion is critical in determining if resonance production is present.

While the implementation of a partial wave analysis is in principle straightforward, there are both empirical and intrinsic difficulties. Empirically, instrumentation effects, such as detector acceptance and resolution, can conspire to make one distribution look like another. These similar distributions lead to *leakage* in the partial wave analysis. Here, cropping, smearing, or incorrect acceptance corrections of two physically different distributions may lead to distributions which are apparently indistinguishable. These difficulties can be minimized by properly designing the experiment, (see section 11.4. Full angular coverage in the distributions can be achieved by using a nearly 4π detector with excellent resolution. In addition, high statistics are critical to be able to separate these partial waves with accuracy. Thus, thorough partial wave analysis requires nearly 4π coverage, excellent resolution, high statistics and a very good understanding of the detector.

The PWA method is subject to intrinsic mathematical ambiguities for certain final states. Two or more different choices of amplitudes lead to identical observables, *e.g.* moments. Here there are at least two approaches. The first assumes some *a priori* physics knowledge that allows one to choose one solution over another, *e.g.* at threshold low angular momentum waves should dominate high angular momentum waves. The second is to examine simultaneously several final states to which the resonance can decay. While the distributions may be confused in one final state, such as $\eta\pi$, they are likely to be different in a second such as $\rho\pi$. This latter approach assumes that the detector has been optimized for many different final states and that relative normalizations between these are understood.

This latter approach of looking at multiple final states not only allows one to separate different waves, but in itself yields key information about the relative decay rates of mesons. It is this latter information that is critical to understanding the underlying wave functions of the mesons — their content and mixing with other states. This ability to measure accurately many final states and to perform a simultaneous partial wave analysis is a key feature of the GLUEX spectrometer.

The use of photon polarization will also allow one to simplify the analysis and to access additional information on the production of mesons. This will provide key checks on the stability of the analysis itself. While a circularly polarized beam may yield some information in a few special cases, the true gain comes from linear polarization. Linear polarization defines a *new*

spatial direction beyond the photon direction, which is not the case for circular polarization. Linearly polarized light can be expressed as a coherent sum of helicity (circular polarization) states which leads to interference terms not present for unpolarized light. This yields additional angular dependence which simplifies the PWA analysis. Furthermore, linear polarization is necessary to discriminate between different production mechanisms.

Backgrounds are always a problem in a partial wave analysis. These limit one's ability to measure phase motion, and can be particularly severe in a region of dense overlapping resonances. Backgrounds involve a different final state accidentally reconstructing as the channel under study. Either a particle is missed by the detector or, when putting the final state back together, multiple interpretations are possible. This can be minimized with a good 4π detector with high efficiency for detecting all final state particles with good resolution. One needs all particles to be reconstructed well enough to allow for a complete kinematical identification of a specific final state.

Finally, while the PWA is in principle straight forward, the machinery itself can become rather cumbersome. There are several different equivalent bases in which the analysis can be done. In addition, small coding errors can lead to errors which may not be easily detected in the results. As such, the GLUEX collaboration is developing independent PWA packages. Currently two such packages have been implemented. These use two different formalisms (one uses the so called reflectivity basis and the other helicity basis), which can be used to cross check results of fits.

11.2 Beam and final state normalizations

It will be necessary to show, in the first results from GLUEX, that our experiment produces results that are consistent with previous investigations, albeit with much greater statistical precision. These will include total cross sections (at various photon energies) for various inclusive multi-particle photoproduction reactions [146], invariant mass distributions and differential cross sections for exclusive reactions [147, 32] and density matrix element determinations in processes for which polarized beams have been available [148].

Each of the measurements cited above has been carried out with relatively low flux photon beams (for which the beam normalization is rather straightforward) and using bubble chambers for particle detection (which therefore provide excellent, flat acceptance functions). Moving to high intensity beams and sophisticated electronic detectors, while leading to enormous gains in statistical precision, makes it more difficult to determine normalizations. Since one of our main goals is to determine such things as relative branching ratios and production cross sections of new states, it is important to establish consistent connections with these previous measurements. Furthermore, it is likely that our experiment will run with different triggers for different running periods, and these data sets need to be merged as seamlessly as possible. All of these goals will need accurate controls of beam normalization and detector acceptance, as well as a clear determination of their inherent systematic uncertainty.

Beyond demonstrating that earlier measurements can be reproduced, an accurate normalization plays a critical role in the physics of GLUEX. To measure relative decay rates of mesons it is critical to have accurate normalizations between different final states. This requires the ability to count incident photons and also the ability to understand systematics due to the trigger hardware and software on the event rates.

11.3 A partial wave analysis study

To study the design of the GLUEX detector, and to help in understanding the limits of the Partial Wave Analysis, a study was undertaken to perform a PWA on simulated data. The goals of the study are twofold: to both qualitatively and quantitatively understand the role of the photon polarization in the partial wave analysis and, to determine what limits are placed on the PWA due to the finite acceptance and resolution of the detector. The aim is to ultimately

perform such a study over many different final states but, to develop the tools to perform this, the initial studies have concentrated on the reaction 11.1 for $E_\gamma = 8.5 \text{ GeV}$.

$$\gamma p \rightarrow \pi^+ \pi^+ \pi^- n \quad (11.1)$$

This is a good candidate reaction for exotic π_1 searches. If a $\pi^+ \pi^-$ pair comes from the decay of a ρ^0 meson then the 3π final state has G -Parity = (-1) and is an isovector. Thus, a resonant $\rho^0 \pi^+$ P -wave would correspond to a charged member of the $J^{PC} = 1^{-+}$ exotic multiplet.

11.3.1 The Role of Linear Polarization

Monte Carlo studies have been made with unpolarized, 100% linearly polarized and fractionally polarized photons. The data can best be examined by looking at the 3π system in the Gottfried–Jackson (GJ) frame, (see Figure 11.1). The GJ frame is the rest frame of the 3π system with the z axis chosen to be along the photon beam direction. The y axis is defined as the normal to *neutron*– 3π production plane (which is invariant under boost to the rest frame of the 3π system). The photon polarization is fixed in the lab frame. However, in the GJ frame it is at some angle α with respect to the y axis (where α varies on the event-by-event basis). The 3π system decays into a 2π system, and a spectator π . In the GJ frame, the orientation of this decay is given by θ_{GJ} and ϕ_{GJ} as shown in Figure 11.1. In the case of linearly polarized photons, one expects there to be a dependence on both the angle α and the azimuthal angle ϕ . This would not be true for unpolarized photons.

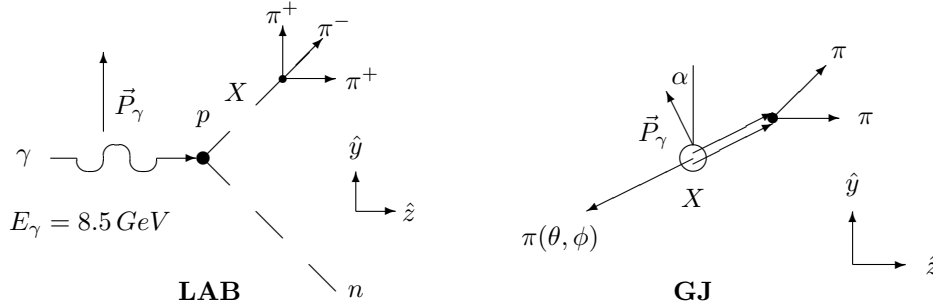


Figure 11.1: The reaction $\gamma p \rightarrow \pi^+ \pi^+ \pi^- n$ as seen in the lab frame and in the Gottfried–Jackson, (GJ), frames. The y direction in the GJ frame is defined as the normal to the reaction plane. The angle α locates the photon polarization direction with respect to the y axis in the GJ frame.

The 3π data have been generated using a phase-space Monte Carlo, and the events have been weighted using a one-pion exchange (OPE) production mechanism that includes 3π resonances decaying via $\rho\pi$ [38]. All known $\rho\pi$ resonances in the with mass less than $2\text{GeV}/c^2$ that can be produced in OPE have been included. (These are listed in Table 11.1). At low momentum transfer, OPE is expected to be the dominant production mechanism [147, 32].

		Resonance				J^{PC}	L	Wave
		Mass [GeV]	Width (Γ [GeV])	$\Gamma_{3\pi}/\Gamma$	σ_γ [nb]			
1	a_1	1260	400	99%	30	1^{++}	0	S
2				1%			2	D
3	a_2	1320	110	70%	500	2^{++}	2	D
4	π_2	1670	110	30%	20	2^{-+}	1	P
5				1%			3	F
6	π_1	1600	170	50%	20	1^{-+}	1	P

Table 11.1: The resonance contributions to the weighting function. The column labeled L corresponds to the relative angular momentum between the ρ and the π in the decay of the 3π resonance.

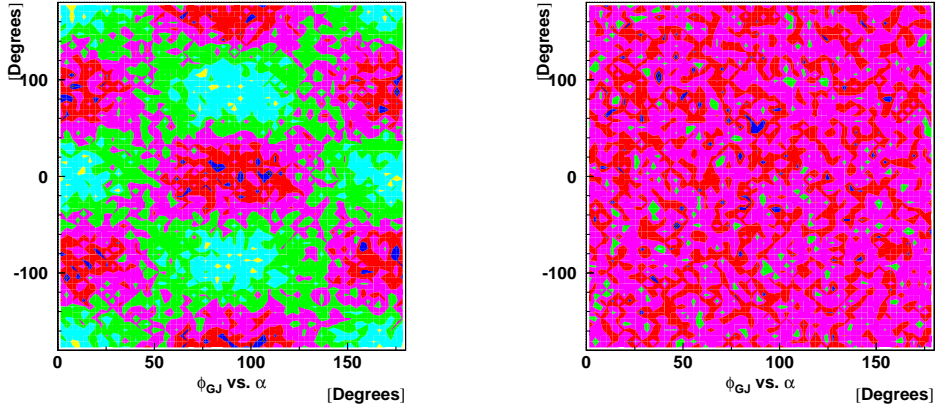


Figure 11.2: Plots of ϕ_{GJ} versus α in the Gottfried–Jackson frame for a band of 3π masses near the peak of the $a_2(1320)$. The left hand figure is for 100% polarized photons, while the right hand figure is for unpolarized photons.

The effect of polarization can be directly seen in Figure 11.2. In the absence of polarization, there is nothing to define a ϕ direction in the GJ frame. As such, a plot of ϕ versus α is flat, (in the unpolarized case, α is taken as the angle between the y axis in the GJ frame and the y axis in the Lab frame). However, if photon polarization is non-zero, there is clear structure in the ϕ versus α plots. Near $\alpha = 0^\circ$, the ϕ distribution is $\sin^2 \phi$, whereas near $\alpha = 90^\circ$, the distribution is $\cos^2 \phi$, consistent with the expected $(1 - \cos[2(\alpha - \phi)])$ dependence.

Because the only production mechanism used is OPE, all particles are produced, it is also possible to get additional information about the naturality of the produced resonances. Pion exchange corresponds to unnatural parity exchange, so depending on the naturality of the produced 3π system, the $\sin^2 \phi$ and $\cos^2 \phi$ will flip (the dependence on ϕ changes to that of $90^\circ - \phi$). For natural parity, $(0^+, 1^-, 2^+, \dots)$, it will be like the a_2 , while for unnatural, $(0^-, 1^+, 2^-, \dots)$, it will be opposite to that. This behavior can be seen in Figure 11.3 which shows ϕ versus the 3π mass for α near 90° , (left) and α near 0° (right). These figures show a clear band at the a_2 mass, which is $\cos^2 \phi$ in the left, and $\sin^2 \phi$ on the right. There is also a second band visible near a mass of $1.7 \text{ GeV}/c^2$, which if one looks carefully, has the opposite angular distributions as the a_2 . Since in this test, the exchange mechanism is known, the opposite structure means that the naturality of the particle at $1.7 \text{ GeV}/c^2$ is opposite that of the a_2 . In the real experiment the exchange mechanism will not be known. However, the PWA can determine the naturality of the produced particle, and this can then be used to determine the naturality of the exchange.

There is still additional information in these plots. For masses below that of the a_2 , there is a diffuse band that has the opposite angular distribution as the a_2 . This corresponds to the $a_1(1260)$ in the data. Finally, for masses just below the π_2 , there is an even more diffuse structure whose angular distribution is opposite that of the π_2 . This most likely corresponds to the π_1 . The fact that the photon beam is linearly polarized allows us to read significant information about the resonances and their production directly from such a plot.

11.3.2 The PWA Formalism and Results

There are several equivalent formalisms in which the PWA can be performed. All of these initially look at the decay of the meson state in the GJ frame, and require that the polarization be expressed in that frame. The spin density matrix of a linearly polarized photon in the helicity basis can be written in terms of the angle α in the GJ frame as in equation 11.2.

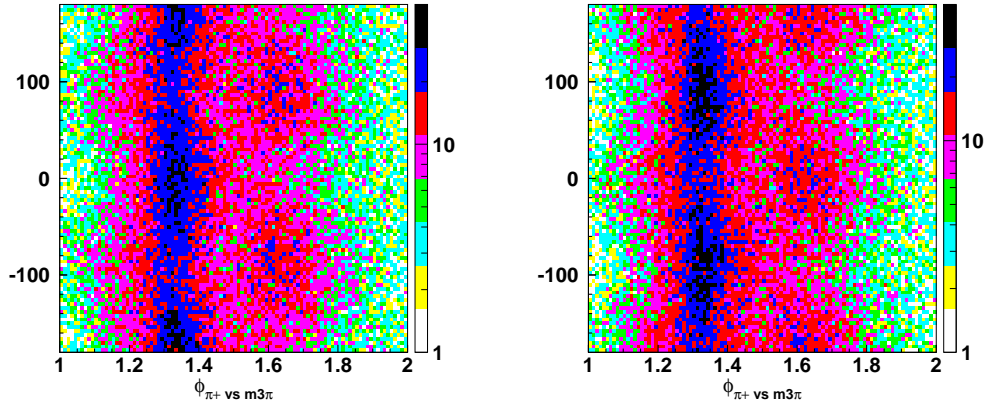


Figure 11.3: Plots of ϕ_{GJ} versus 3π -mass for 100% polarized photons. The figure on the left is for α near 90° , while that on the right is for α near 0° .

$$\rho_{\lambda_\gamma \lambda'_\gamma} = \begin{pmatrix} \frac{1}{2}(1 + P \sin 2\alpha) & \frac{P}{2} \cos 2\alpha \\ \frac{P}{2} \cos 2\alpha & \frac{1}{2}(1 - P \sin 2\alpha) \end{pmatrix} \quad (11.2)$$

$$\rho_{\epsilon_\gamma \epsilon'_\gamma} = \begin{pmatrix} \left(\frac{1}{2} - \rho_{1-1}\right) & \left(\frac{1}{2} - \rho_{-1-1}\right) \\ \left(\frac{1}{2} - \rho_{-1-1}\right) & \left(\frac{1}{2} + \rho_{1-1}\right) \end{pmatrix} \quad (11.3)$$

One particular choice for the analysis is the reflectivity basis. The eigenstates of reflectivity are eigenstates of reflection in the production plane. The density matrix of a linearly polarized photon in the reflectivity basis expressed in terms of the helicity basis elements is given in equation 11.3. In the reflectivity basis, photons polarized along either the x axis or the y axis in the GJ frame are eigenstates of reflectivity. However, photons that are polarized in some other direction are coherent mixtures of the two eigenstates. The eigenvalues of reflectivity depend on the naturality of particles involved in the reaction. For a given produced resonance, linear polarization enables one to distinguish between naturalities of the exchanged particles. This is the main handle on the production mechanism. Second, if the production mechanism is known (*e.g.* from momentum transfer or energy dependence), linear polarization enables one to filter resonances of different naturalities, as shown in the study of ϕ dependence discussed above. In the case of a known production mechanism, the same quality PWA can be done with about 50% as much polarized data as with unpolarized data.

To date, independent fits have been carried out using two different codes. One using the reflectivity representation, and the other using a moments fit. Both return the same results, and have provided a very good cross check of our understanding of the procedure. In fact, the development of two parallel versions of the PWA code, and cross checking results against each other will be an important handle on systematic errors in the GLUOX experiment. The results in Figure 11.4 are from the latter fit using the same formalism as in the weighting function. (These fits do not use input modified by the acceptance or resolution). What is of particular interest is the sensitivity limit in these data. The two extremely weak waves (at well less than 1% of the total intensity) are just at the limit of being resolved in this data set. This is seen in the $a_1 D$ wave in Figure 11.4. The data set used in these fits represents about 1% of the reconstructed statistics from one year of running at $10^7 \gamma/s$. The statistics of the experiment will clearly be large enough to resolve such small signals. They will also be large enough to provide statistically meaningful sample on much rarer final states. (The 3π mode chosen for this study is one of the largest contributors to the total γp total cross section.)

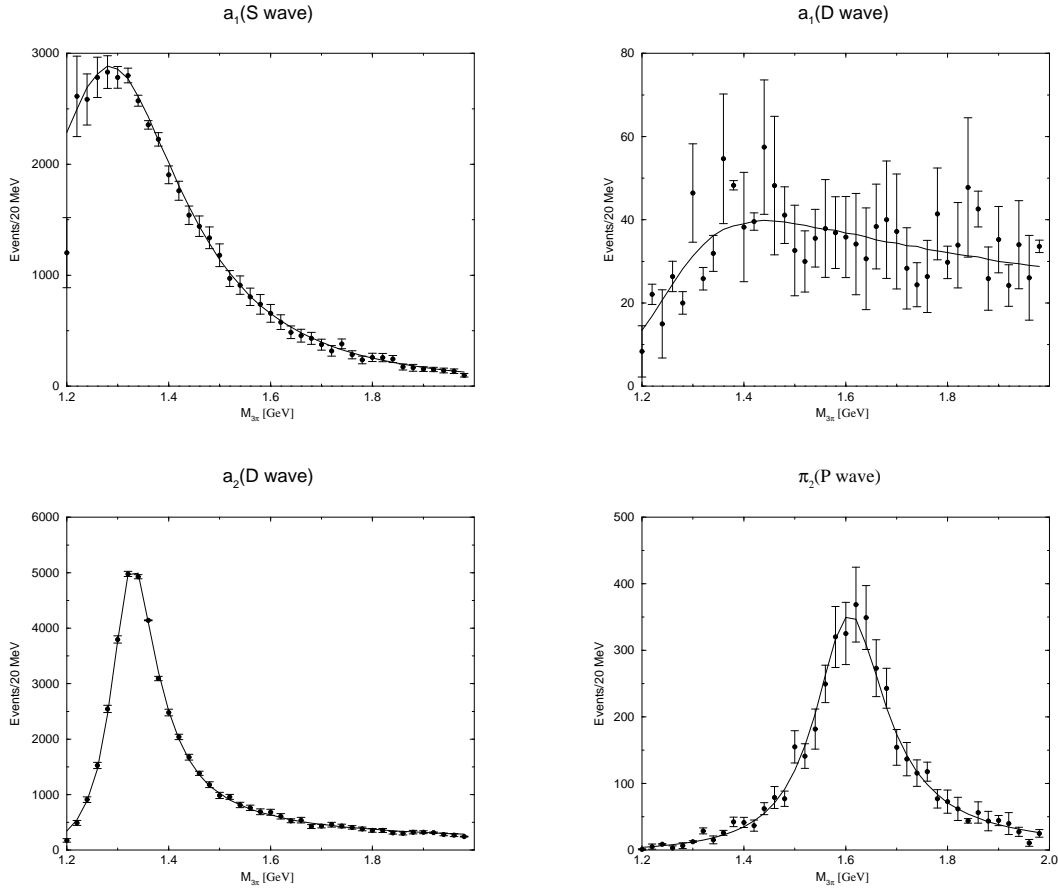


Figure 11.4: Fits to a 4π acceptance data set showing the four of the six partial waves from table 11.1. The error bars arise purely from the statistics of the data set which is about 1% of one year's running.

Figure 11.5 below shows the results of a double-blind Monte Carlo exercise that was performed to assess the ability to extract a small exotic signal from mix of various non-exotic waves. Specifically events corresponding to $\gamma p \rightarrow \pi^+ \pi^+ \pi^- n$ were generated assuming a mix of seven waves including the a_1 , a_2 , π_2 and the $J^{PC} = 1^{-+} \pi_1$. The latter was about 2.5 % of the total sample. The generated four-vectors were smeared and the sample was then put through the acceptance requirements. The acceptance assumptions were included in the PWA fitter. The statistics shown correspond to several days of running.

The second fitting procedure is done in the reflectivity basis. In the reflectivity basis, the total amplitude for some final state can be written as in equation 11.4. The subscript β refers to a given partial wave, $(J^{PC} M^e)$. The indices ϵ_x and ϵ_γ refer to the reflectivities of the state X and the γ respectively. The indices λ and λ' refer to the initial and final state nucleon spin-states. Parity reduces the total number of helicity amplitudes by a factor of two and connects the reflectivity of the beam and exchange particles to the reflectivity of the produced state ($\epsilon_\gamma * \epsilon_e = \epsilon_X$).

Additionally, in the case of OPE only the nucleon helicity-flip amplitude contributes and the λ and λ' indices are suppressed as in 11.4.

$$R_\beta^{\epsilon_x, \epsilon_\gamma} = V_{\beta, \lambda, \lambda'}^{\epsilon_x, \epsilon_\gamma} \times A_\beta^{\epsilon_x, \epsilon_\gamma} \quad (11.4)$$

The set of complex parameters, V 's, are known as the production strengths. These are usually determined by fitting to the data. The A 's are decay angular distributions which are functions

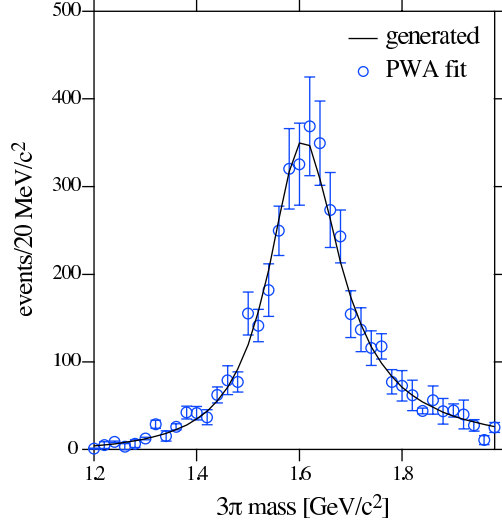


Figure 11.5: The results of a double-blind Monte Carlo exercise showing the $J^{PC} = 1^{-+}$ exotic wave after fitting (open circles) and the exotic wave input (curve) into the mix of $\gamma p \rightarrow \pi^+ \pi^+ \pi^- n$ events that were generated in this study. Details are given in the text.

of the angles in the various frames as well as resonance parameters of any daughter resonances into which the state X decays. The amplitude, A , for the decay of a particle with spin J and $|J_z| = M$ into two particles with helicities λ_1 and λ_2 ($\lambda = \lambda_1 - \lambda_2$) in the resonance rest frame is given by [149]:

$$A = \langle \vec{p}\lambda_1; -\vec{p}\lambda_2 | \mathcal{M} | JM \rangle = F_{\lambda_1\lambda_2}^J \mathcal{D}_{M\lambda}^{*J}(\phi, \theta, 0) \quad (11.5)$$

Calculation of the decay amplitudes for a resonance is done recursively within the isobar model, regarding the n -body final state as a result of a series of sequential, generally 2-body, decays through intermediate isobar states. The total decay amplitude is the amplitude for the resonance to decay into its intermediate daughters times the amplitude for each of its daughters to decay.

This total amplitude, R can then be used to predict the intensity distributions of the final state particles. For a particular point in phase space, τ , the intensity is given as in equation 11.6. Finally, for amplitudes that do not interfere, (denoted by α) *e.g.* from production via different initial and final spin configurations, a sum over these

$$I(\tau) = \sum_{\alpha} \text{Trace} \left[\sum_{\epsilon_{\gamma}, \epsilon'_{\gamma}} \left[\left(\sum_{\beta'} R_{\beta'}^{\epsilon_{x'}, \epsilon_{\gamma'}} \right)^{\dagger} \rho_{\epsilon_{\gamma}, \epsilon'_{\gamma}} \left(\sum_{\beta} R_{\beta}^{\epsilon_x, \epsilon_{\gamma}} \right) \right] \right] \quad (11.6)$$

gives the intensity.

The data are binned in mass of X and the momentum transfer t and a fit is performed for the full set of V 's in each bin. The results for such a fit for 100% linearly polarized photons are shown in Figure 11.6. In this fit, a comparison is made between the generated data and the Monte Carlo corrected data. In the 3π channel, the acceptance corrections are fairly small. The data shown are only for the positive reflectivity solutions, but a more or less identical set for the negative reflectivity are also produced. While visible, the acceptance effects are small, and do not hinder the extraction of the partial waves. It is also possible to extract the two rather small waves that are in the generated data set. These correspond to a second decay for each of 1^{++} and 2^{-+} waves. The main decays proceed with orbital angular momentum between the ρ and the π , $L_{\rho\pi}$ of 0, (S-wave), and 1, (P-wave) respectively. In addition, decays could occur via $L = 2$, (D-wave) and $L = 3$, (F-wave), respectively. The relative rates between the two decays of a given resonance is an important quantity which can be compared to several models.

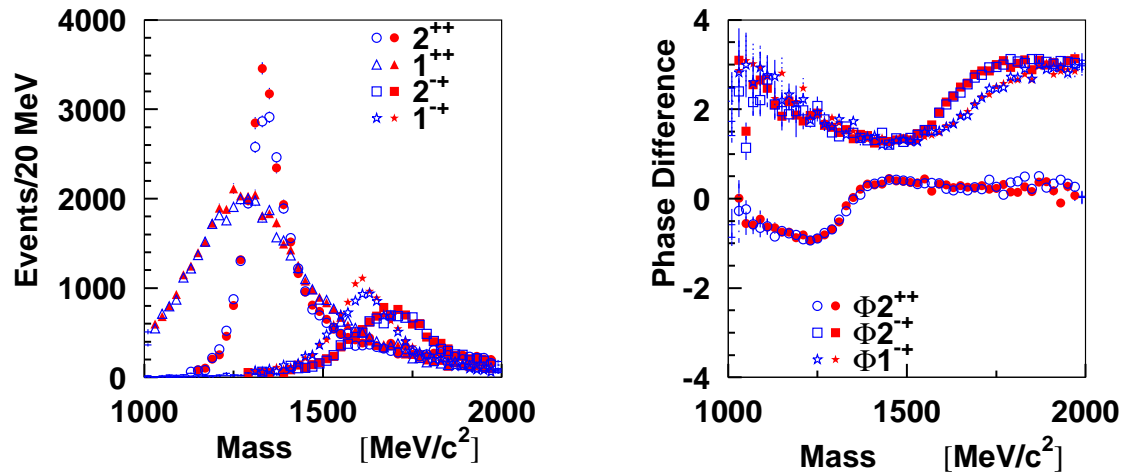


Figure 11.6: Fits to the weighted data using wave 1,3,4 and 6 from table 11.1. These fits compare generated data (solid shapes) to data that has been run through the GLUEX Monte Carlo, (open figures). The left figure compares the fits to the intensities of four waves, while the right figure shows the phase differences between the listed waves and the 1^{++} wave.

Its extraction will be an important GLUEX measurement. Figures 11.7 and 11.8 show the fits to these two waves. In each case, the left plot is the intensity of the positive reflectivity wave, while the right hand figure is the phase difference between the two decays of a given resonance. In the absence of final state interactions, the phase difference should be either 0° or 180° , which both fits show in the region where the intensity is non-zero.

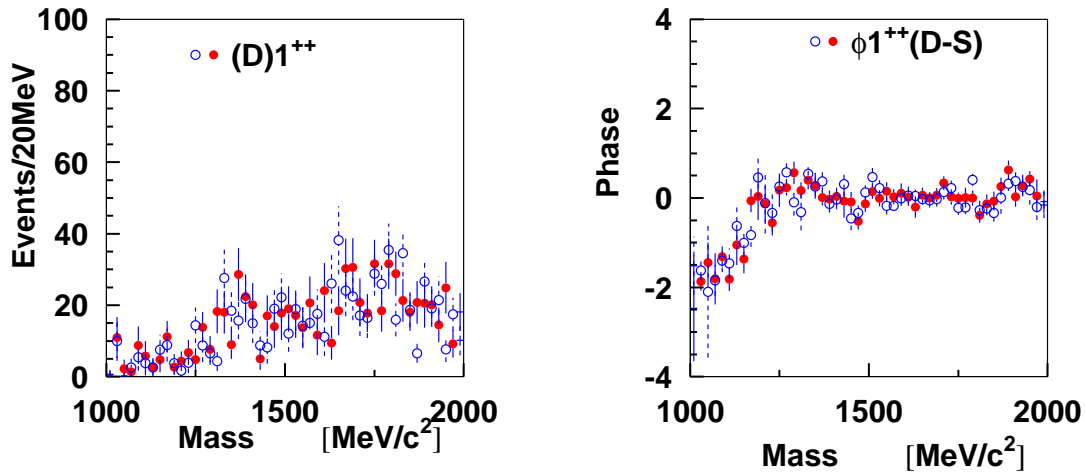


Figure 11.7: Fits to the D-wave decay of the 1^{++} wave from table 11.1. The figure on the left shows the intensity for the positive reflectivity wave. The right hand figure shows the phase difference between the S and D-wave decays. The open markers correspond to data that has been run through the GLUEX Monte Carlo, while the solid markers are the generated events.

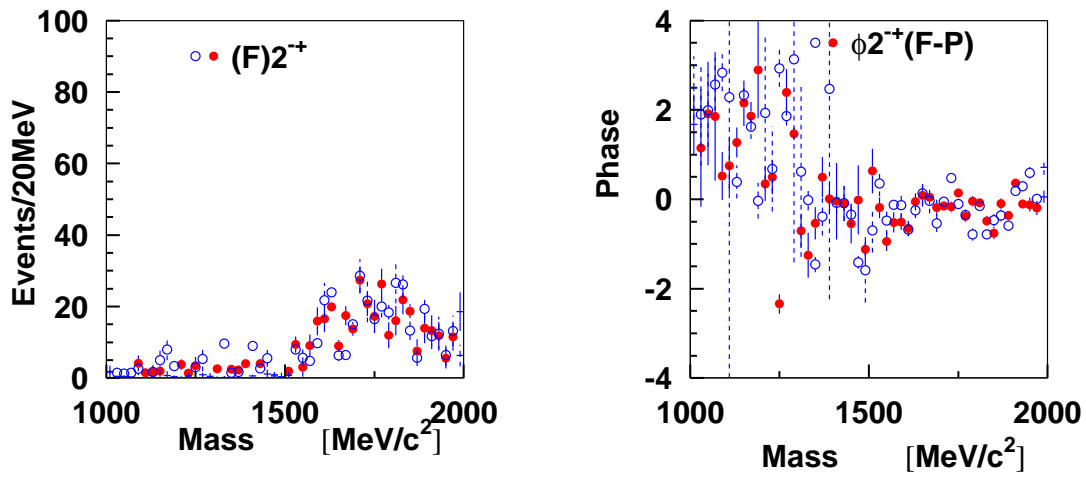


Figure 11.8: Fits to the F-wave decay of the 2^{-+} wave from table 11.1. The figure on the left shows the intensity for the positive reflectivity. The right hand figure shows the phase difference between the P and F-wave decays. The open markers correspond to data that has been run through the GLUEX Monte Carlo, while the solid markers are the generated events.

In addition to the small waves, another common problem in PWA is leakage from one wave into another wave. A small distortion in the acceptance that is not fully understood can cause one wave to look like a different wave. This has been examined by adding six additional waves which were not in the generated data set, and repeating the fits with these waves in them. These waves correspond to $J^{PC}(M^\epsilon)$ of $3^{++}(1^+)$, $3^{++}(1^-)$, $2^{++}(2^+)$, $2^{++}(2^-)$, $2^{-+}(2^+)$ and $2^{-+}(2^-)$. Figure 11.9 shows the results for two of these. The main point is that there is virtually no intensity in any of these waves, and certainly no structure leaking in from one of the strong waves in the events. At least in this study, the leakage appears to be an insignificant issue.

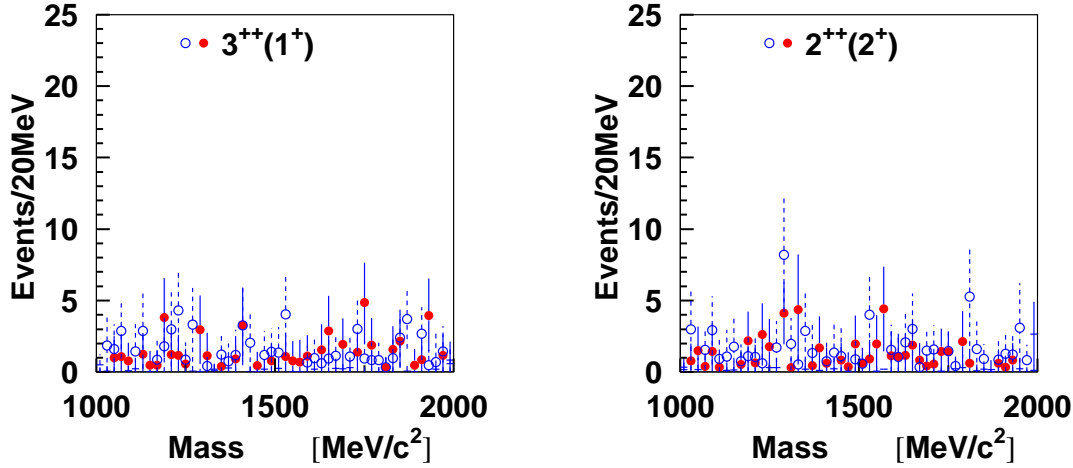


Figure 11.9: Fits to two partial waves which are not in the generated set. The figure on the left is a $J^{PC}(M^\epsilon) = 3^{++}(1^+)$ wave, while that on the right is a $J^{PC}(M^\epsilon) = 2^{++}(2^+)$ wave. There is virtually no leakage into these waves from resolution effects in the detector simulation. The open markers correspond to data that has been run through the GLUOX Monte Carlo, while the solid markers are the generated events.

A comparison can also be made between an unpolarized data set and a 100% polarized data set. Because the positive and negative reflectivity distributions do differ in their $\cos\theta_{GJ}$ distributions, it is possible to separate them with unpolarized data. The separation is just not as clean as it is for polarized data and in the absence of information on the production mechanism, this separation becomes more difficult, especially if multiple production mechanisms are present. The best way to view these results is to look at the errors in the wave intensities for both the polarized and the unpolarized data sets. These are shown in Figure 11.10. If one averages over all of the partial waves, the unpolarized errors are about $\sqrt{2}$ times larger than those for the polarized data set with the same number of events. Roughly speaking, in this test, the polarization reduces by a factor of 2 the statistics needed to achieve a given level of sensitivity. It should be pointed out that this is not the entire story as discussed below.

Finally we have examined the case of simultaneous production via unnatural (π) and natural (*e.g.* ρ) exchange. The point is to illustrate the need for linear polarization. As discussed earlier at the nucleon vertex OPE flips helicity and is proportional to $\delta_{\lambda',-\lambda}$. At the meson production vertex the helicity structure is given by $\delta_{\lambda',\lambda_X}$ for unnatural, and by $\tau_{\lambda',\lambda_X}^3$ for natural resonances respectively. For the spin-1 ρ exchange, the number of different helicity couplings is quite large, however, if the nucleon helicity is flipped then coupling is proportional to $\tau_{\lambda',-\lambda}^3$ and if the helicity in the photon-resonance vertex is conserved, natural exchange leads to the $\delta_{\lambda',\lambda_X}$ and $\tau_{\lambda',\lambda_X}^3$ dependencies for the natural and unnatural exchanges respectively, *i.e.* opposite to the case of unnatural exchange.

In an additional study a ρ exchange intensity that is about 50% of the π exchange has been

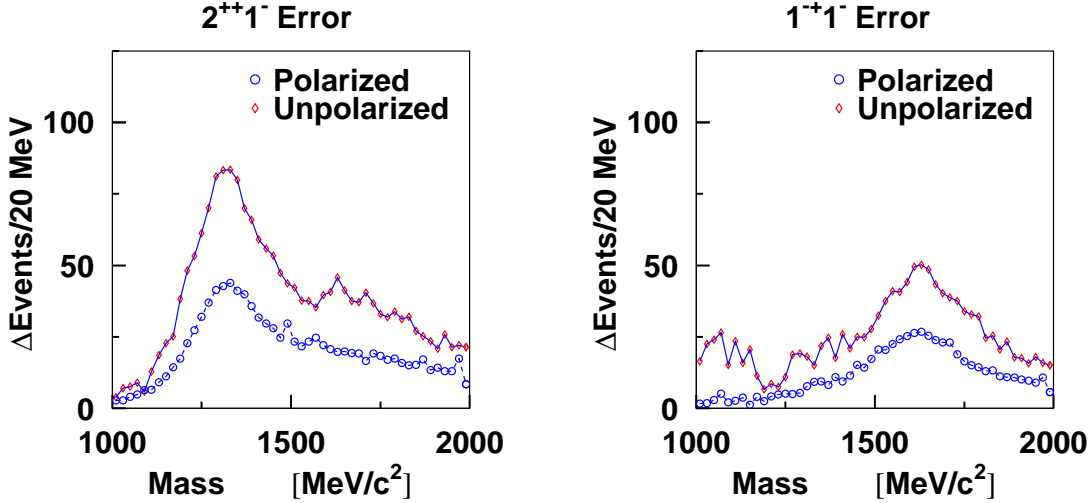


Figure 11.10: The errors in the fit results for two of the partial waves from the fit. The polarized and unpolarized data sets are the same size, and both sets are for generated data, (no acceptance corrections). The errors for the unpolarized data are on average about a factor of the $\sqrt{2}$ larger than those for the 100% polarized case.

added to all six partial waves given in Table 11.1 using Monte Carlo generated with 100%, 50%, 25% and 0% linear polarization. These two exchanges are incoherent, so the fit to the intensity is actually a fit to the sum of the two exchange mechanisms. As seen in Figure 11.11, this sum is well fit independent of the degree of linear polarization. One way in which the two can be separated is to fit the difference of the two exchanges (dashed curves in Figure 11.11). Here it is seen that the degree of linear polarization place a crucial role in a fit to this difference. With 100% polarization the difference is well fit, while for 0% polarization the difference is ambiguous. Any two values with the correct sum will work. Similar to this would be to examine the ϕ_{GJ} and α dependence of a given partial wave as in Figure 11.3.

To study on the effect of linear polarization in determining the production mechanism, data have been selected near $\alpha = 0^\circ$ and near $\alpha = 90^\circ$ in the Gottfried-Jackson frame of the resonance. These two states correspond to eigenstates of reflectivity. In the case of single pion exchange, (the naturality of the π is negative), the produced reflectivity state of the resonance is opposite to that of the photon. In the case of natural parity exchange, (such as ρ exchange), the two reflectivities will be the same. Partial wave analyses has been performed independently on the two data sets. Figure 11.12 shows the results for the 1^{-+} wave. The figure on the left shows the positive reflectivity 1^{-+} wave, $M^\epsilon = 1^+$. Only the events near $\alpha = 0^\circ$ contribute, while the $\alpha = 90^\circ$ gives nearly no contribution. The exact opposite happens in the $M^\epsilon = 1^-$ wave on the right. Had the production mechanism been of opposite naturality to the pion, these figures would have been reversed. If both mechanisms had been present, then the exact mixture could have been read directly off these plots as long as the degree of linear polarization in known. In the case of unpolarized photons, no such separation is possible. Of course the real data will involve a more general fit to this, but with linear polarization, the naturality of the exchange particle is trivially known, while for no linear polarization, there is no handle on this.

11.3.3 Joint production of excited baryons and mesons

In the kinematic region of GLUEX it is probable that baryon resonances will be produced in addition to the meson states we have been discussing. Processes such as the two shown in Figure 11.13 will interfere with each other and they must be taken into account in the analysis.

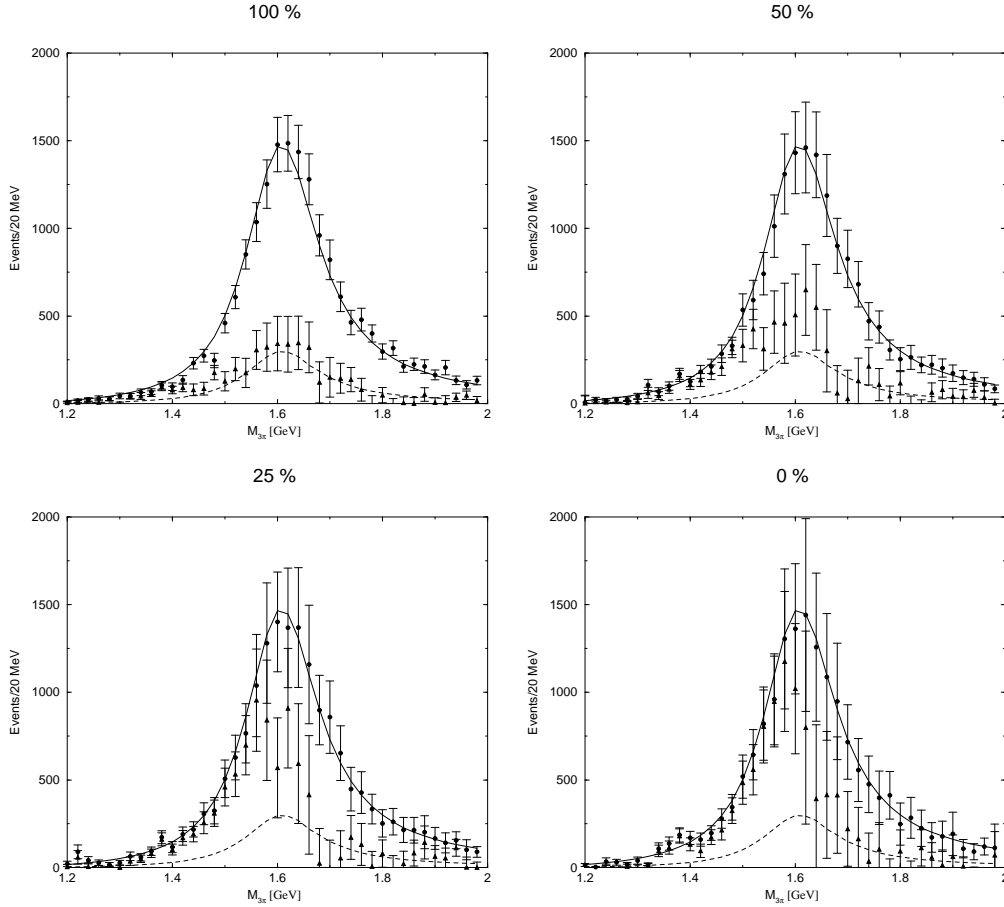


Figure 11.11: Fits to $\pi_1(1600)$, 4π acceptance data sets generated with a combination of π and ρ exchange mechanisms. The solid line is the sum of the two, while the dashed line is the difference. The four plots correspond to 100%, 50%, 25% and 0% photon linear polarization. The sum of the two is well fit for all values of polarization, while the difference becomes unclear as the polarization is decreased.

In general this could lead to ambiguities, since the baryon states can be described as an infinite sum over meson states. In practice, however, the sum over meson states is truncated to a finite number of resonances, and will not well describe the distribution due to the baryon resonance. Hence, in order to get a good description of the intensity distribution, the baryon resonances must be included explicitly. Effects of ambiguities are mitigated at the cost of requiring a physically motivated *ansatz* of states *i.e.*, truncating the set of waves to the minimal set required by the fit. The impact of any ambiguities created will vary with the reaction being studied, but can be well determined using Monte–Carlo methods.

11.4 Leakage studies

Of crucial importance in Partial Wave Analysis is the leakage or feed through from one partial wave to another. This leakage is usually caused by an imperfect understanding of the detector acceptance, and being able to minimize this is crucial in carrying out an excellent PWA. In order to study this in the GLUOX detector, a detailed study has been carried out using Monte Carlo simulations and the PWA code [150]. In this study, two 3π physics data sets were generated

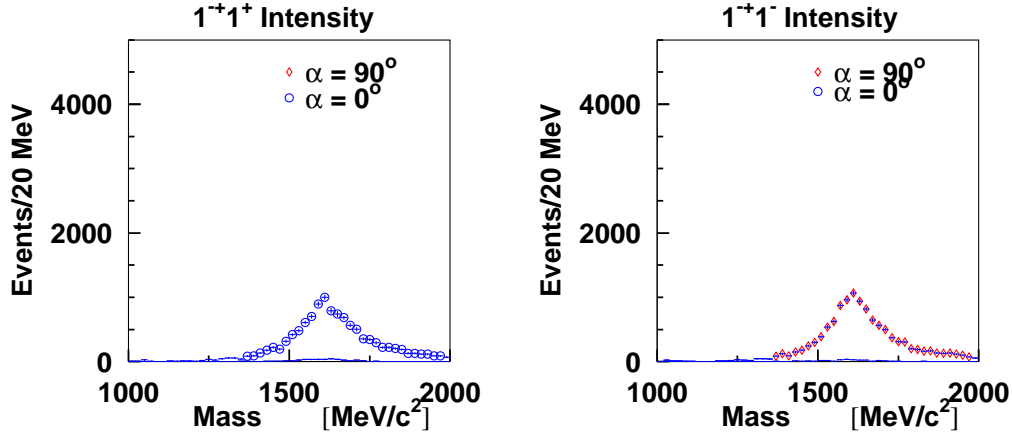


Figure 11.12: (Left) shows the fit to the positive reflectivity part of the 1^{-+} intensity for events near $\alpha = 0^\circ$ and 90° degrees. (Right) shows the same for the negative reflectivity waves. The key point is that for π exchange, (negative naturality), only the positive reflectivity wave is produced near $\alpha = 0^\circ$ while only the negative reflectivity is produced near $\alpha = 90^\circ$. If the exchange mechanism had opposite naturality, then exactly the opposite would have occurred. These fits can lead to an exact decomposition of the exchange mechanism as long as one knows the degree of linear polarization.

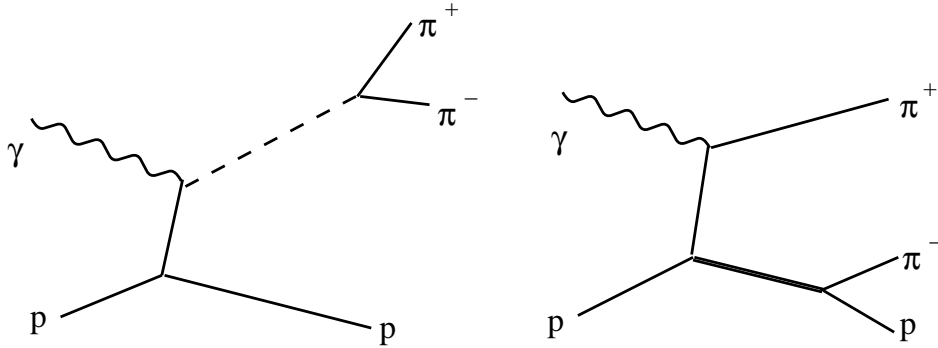


Figure 11.13: Example of interfering baryon and meson processes.

according to the reactions:

$$\gamma p \rightarrow \pi^+ \pi^+ \pi^- n$$

and the isospin related reaction

$$\gamma p \rightarrow \pi^+ \pi^0 \pi^0 n$$

. Included in the physics were the production of $a_1(1260)$, $a_2(1320)$ and $\pi_2(1670)$, but no exotic wave from the $\pi_1(1600)$. These events were then tracked through the GLUEX Monte Carlo program, and the output was then fed into a partial wave analysis. Additional sets of phase-space generated events were then produced for the normalization integrals in the PWA. These were tracked through a version of the GLUEX Monte Carlo in which the geometry description of the detector had been changed with respect to the physics samples. Examples of the types of changes made were distortions in the magnetic field, changing the location of the forward tracking chambers, changing the resolution of the tracking detectors, changing the low energy photon cut-off in both the forward and the barrel calorimeters, and changing the resolution of

the two calorimeters. The most striking result was that it was extremely difficult to produce leakage in the exotic π_1 channel with any of these changes. Figure 11.14 shows typical examples of the leakage from the study. While it is possible to induce 10% size leakages from the S-wave decay into the D-wave decay of some resonances, this is not the norm. In order to do this, resolutions need to be off by a factor of 2, or magnetic fields need 20% distortions.

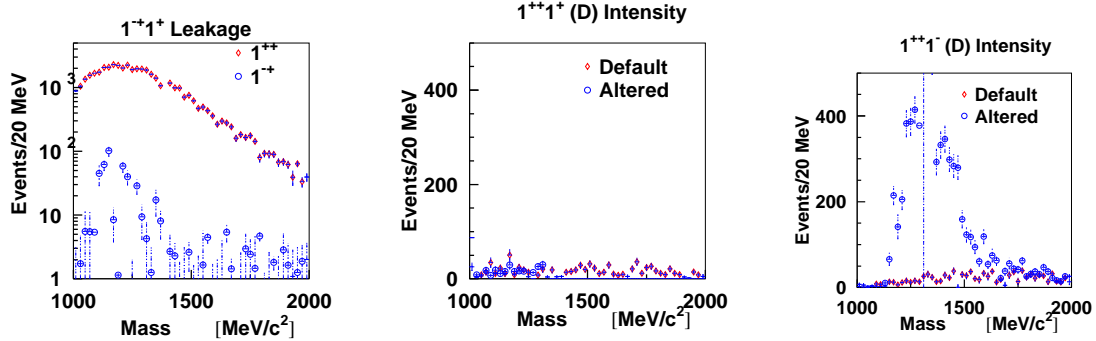


Figure 11.14: **Left:** Typical leakage induced in the exotic π_1 channel from the most extreme changes in the detector. It is difficult to get leakage larger than a few percent. **Center:** shows the typical leakage from the a_1 S-wave into the a_1 D-wave. **Right:** shows the most extreme leakage from the a_1 S-wave into the a_1 D-wave.

The most important conclusions of the study is that it is difficult to produce feed through into the exotic channel from other meson channels. For almost all changes made here, the amount of feed through was less than 1% of a strong channel, with the feed through for the nominal design values being something like 0.1%. However, it is possible to get significant leakage from the a_1 S-wave decay into the a_1 D-wave decay, with even small changes in the nominal detector design. This sort of feed through is fairly straight forward to understand. An S-wave decay is nominally flat, however, if we have losses near $\cos\theta = \pm 1$, the easiest description of this is with a D-wave component. In order to produce a P-wave component, it is necessary to produce a forward-backward asymmetry in the Jackson frame – something that appears fairly difficult to do with the GLUEX detector.

11.5 Summary

The GLUEX collaboration is currently performing partial wave analysis on data that have been run through the GLUEX detector simulation package. The initial studies have concentrated on the reaction $\gamma p \rightarrow \pi^+ \pi^+ \pi^- n$. The collaboration has two different software packages under development. These use different formalisms and fitting procedures to perform the PWA. The comparison of the results from the two efforts will allow us to better understand the systematic problems associated with the procedures.

Fits have been performed with varying degrees of linear polarization to understand the balance between polarization and raw statistics when the production mechanism is known and to demonstrate the need for linear polarization in disentangling the natural and unnatural exchange mechanisms in resonance production. These initial studies give us confidence that we are designing the appropriate detector with the capabilities needed to find and understand exotic mesons.

In order to continue to develop the partial wave analysis, both in terms of formalism, and its connection to phenomenology and to lattice QCD, some members of the GLUEX collaboration organized the first of what is hoped to be several workshops focused on this topic. This first workshop was held in June of 2002 at Carnegie Mellon University and was attended by approximately 35 experts in the field. The proceedings will be published in early 2003 [151].

The second workshop is expected to take place at Jefferson lab in the late spring of 2003.

Appendix A

Management Plan

A.1 Principles of the management plan

The task of the HALL D Collaboration, or simply the collaboration in this document, is to secure scientific approval and funding for the HALL D experiment at the Thomas Jefferson National Accelerator Facility (JLab) and to subsequently design, construct, and commission the beam-line and detectors and to complete the physics program leading to the publication of final results.

The governance of the collaboration is laid down in the Management Plan, MP, in such a way as to assure the timely and successful completion of the tasks above. It emphasizes teamwork and peer-review as essential to the successful execution of this plan. The framework is based on the formation of teams for each task with the autonomy and delegated authority needed for them to carry out their tasks within the integrated structure of the collaboration. Mechanisms of oversight and review of each team's work are implemented to assure that the goals of the collaboration are achieved in a timely, effective and coherent manner. An effective and unhindered liaison with JLab staff and management is paramount to the success of the project.

A collaboration is as good as the members that form it. The philosophy of the MP is to maximize the considerable talent and expertise available in its membership, while, at the same time, preserving a well defined order in decision making. Three principles guide this approach:

- First, the collaboration needs a strong and effective leadership. Such leadership ultimately resides with individuals who are identified with the physics and technical goals of the experiment and who have the confidence of their peers within the collaboration and the community beyond. The MP endorses a multi-tiered structure designed to encourage and recognize such leadership at all levels within the collaboration.
- Second, the collaboration needs a clear and transparent decision making process, one that is open to every member of the collaboration who wishes to participate. This is accomplished by the principle of representative democracy, where the collaboration and all the teams and groups within it elect their own representatives to the next higher level of decision making. In parallel, the MP makes provisions which safeguard the effectiveness of the structure by outlining the process of conflict resolution at the various levels where such conflict may arise.
- Third, the MP proposes a structure that is both simple and flexible and able to adapt and change as experience and circumstances dictate.

As the collaboration progresses through the various stages of its program, the MP is an adaptable and flexible instrument of governance and can change to best serve the membership based on experience and environment. The basic principles enumerated above provide a reliable basis upon which the MP and its future developments will be founded.

A.2 The Hall D collaboration membership

The HALL D Collaboration membership consists of physicists and engineers who have signed a Memorandum of Understanding (MoU) specifying the expected contributions within the scientific and/or technical objectives of the HALL D Collaboration. Such contributions may be defined as any component of hardware, software, or any aspect related to the scientific basis of the experiment, and which the collaboration deems important to the pursuit of its objectives.

Membership for researchers within either an institutional or a task oriented group will also carry individual membership status. The list of individual researchers within the group brought forward for membership is the responsibility of the group leader. The list, drawn in good faith by the group leader, is a commitment by the individuals named to fulfill the obligations outlined in the MoU and to be active members of The collaboration in all its aspects.

Membership entails specific contributions to the HALL D experiment in all its aspects. As such, a failure by any individual or group to meet the respective MoU commitments constitutes grounds for removal of the individuals or groups from the HALL D Collaboration membership list. The rules governing such matters will be defined in the appropriate sections of the MP and by the introduction of by-laws to be defined after the adoption of this MP.

Finally, all members in good standing will enjoy equal rights, opportunities for advancement, voting and decision making rights. the collaboration membership is the source of all decision making by elected representation and general voting procedures on the HALL D governance, as stated in the following sections. Even though the collaboration is a layered structure for organizational and functional efficiency, Collaboration members may bring concerns, ideas, and suggestions to any group, team, or representative within the collaboration. Thus, accessibility is an implied doctrine throughout this MP.

A.3 The Hall D governance structure

The governance structure of the HALL D Collaboration consists of five bodies. These are:

- The HALL D Collaboration Membership.
- The Working Groups (WG).
- The Technical Review Committee (TRC).
- The Executive Group (EG).
- the collaboration Board (CB).

The schematic diagram of the structure is shown in Figure 1.

A.3.1 The Hall D collaboration membership structure

Based on the general principles of the HALL D membership in Section 11.2, specific issues of membership structure are listed below which help define the membership, introduce grandfather clauses, and outline the mechanisms to be followed for introduction of new members. Purpose-specific by-laws may be added after the adoption of this MP to enhance and refine the process.

- When this MP is voted into existence by the existing membership, it will create the HALL D Collaboration by the current membership, as listed elsewhere in this document. This includes the posts of Spokesman, Deputy Spokesman, and HALL D Leader, as they are listed in this document. This article constitutes the formal grandfather clause of the collaboration.
- It is expected that all current members who wish to remain as Collaboration members will provide an MoU or equivalent document outlining undertaken commitments, for each individual or for each group of individuals, as stated above in Section 2.

- New applicants for membership, after the adoption of this MP, will be admitted into the HALL D Collaboration upon submission of an MoU, or equivalent, to the CB and Spokesman, and voted upon by both the CB and the Collaboration membership.
- The CB and/or the Spokesman may reject or return the application for further actions to be taken by the applicants. It is expected that the CB will communicate with the applicants the reasons of rejection or deferral.
- JLab physicists and/or technical staff will be assigned to HALL D tasks consistent with the objectives of the collaboration. This assignment will be done by JLab management in consultation with the CB Chair and the Spokesman.

A.3.2 The working groups

The WG s address themselves to the core of the reason of existence of the HALL D Collaboration and are the main means of reaching its objectives. The WG concept encompasses groups of Collaboration members working together on specific components of the experiment based on expertise, interest, and MoU obligations. The WG concept foresees an open architecture where members can contribute to more than one WG and where WG s may be added or dissolved as the need arises. Furthermore, members within a general WG may create sub-groups depending on need and work load.

Although new WG s may form as the needs arise and work progresses, it is clearly desirable to establish an initial structure of working groups to allow the installation of a critical structure to the HALL D project. Any changes in the structure and numbers of working groups after the MP is adopted will require the approval of the TRC in consultation with the EG. This will ensure that the needs of the project as a whole are taken into account in such restructuring. Each WG will select a representative to the next higher technical level, that of the TRC. The method of selection is left up to individual working groups.

The seven initial working groups upon approval of this MP are listed below:

- WG-M: is the group responsible for the assembly, installation and operation of the LASS/MEGA magnet and the liquid hydrogen target and their cryogenic infrastructure.
- WG-B: is the group responsible for the construction, installation and operation of the beam line elements, including the tagger, thin diamond radiator and the collimators leading to the delivery of tagged polarized photon beams of quality and intensity necessary to meet the objectives.
- WG-D: is the group responsible for the elements comprising the tracking, calorimetry, ToF, and all particle identification devices in the detector.
- WG-P: is the group responsible for the development and all related tasks necessary to pursue the PWA of the data. This is the working group developing and refining the scientific (Physics) case and looking into future experiments and new ideas that can be pursued by the collaboration. It is a natural working group for the theory group, but not exclusive to theorists.
- WG-C: is the group responsible for overall civil construction, the infrastructure needed to build the beam line, the end-station, control room, roads and radiation control procedures.
- WG-E: is the group responsible for coordinating the read-out electronics, trigger and DAQ hardware. Close cooperation with WG-D and WG-S will be needed.
- WG-S: is the group responsible for integration of all software issues, including simulations, data handling and online analysis. Close working relationships with WG-D and WG-P will be required.

A.3.3 The technical review committee

trc mandate

Although interaction between working groups is not only desirable but necessary, practical matters point to the necessity for a committee of representatives of the various WG s to form a review panel with the EG members and to oversee the total progress and integration, as it unfolds from the WG s. This is a very important committee on technical terms alone, since integration problems and solutions, element compatibility and delivery schedules of the total system will be examined and reviewed and recommendations will be made.

Other tasks may include the approval of prototypes before actual construction of the final elements begins, and addressing budget issues affecting construction and deliveries. Generally, the TRC is the body responsible for decision making on any and all technical and scientific issues concerning the HALL D experiment. The TRC will also act as a source of technical expertise to the EG members.

Finally, the TRC will also act as the panel of final technical judgement on actions to be taken if a WG or an MoU signatory fail to meet progress milestones which affect other WG s and/or the project overall. In such a case, the TRC will recommend to the CB whatever action is deemed necessary to rectify the situation, including loss of Collaboration membership status.

trc structure

The TRC consists of the representatives of each working group (chosen by their respective WG members) and the three members of the EG. The TRC will be chaired by the Spokesman, who can also invite any other member of the Collaboration to attend, based on a specific issue of need and expertise. In order to preserve flexibility and effectiveness, the Spokesman may invite experts outside the Collaboration to attend specific meetings.

All reasonable freedom of action should be given the TRC to accomplish the Collaboration's objectives. The Spokesman has the authority to replace the representative of a WG, for cause, with another member of the same WG selected by its members. Such action by the Spokesman must be preceded by consultation with the CB Chair and the membership of the TRC in an effort to resolve the issue prior to removal.

A.3.4 The executive group

The EG consists of three members, the Spokesman, the Deputy Spokesman, and the HALL D Leader.

The experiment spokesman

The experiment spokesman is the Collaboration's central scientific figure to the world. The spokesman is expected to act as the principal investigator (P.I.) on the main funding application, present most of the presentations (at least initially), and be familiar, but not necessarily an expert, with all physics and technical aspects of the experiment. Furthermore, and just as importantly, the Spokesman must provide leadership, encouragement, and continuity without undue interference, together with the ability to take charge of and motivate individuals.

As the P.I. of the experiment, the Spokesman is responsible for all scientific, technical, and financial affairs of the HALL D Collaboration. On financial matters, the Spokesman's duties must be consistent with all the requirements of the funding agencies and JLab structure. The Spokesman is the primary contact and ambassador between the HALL D Collaboration and JLab management and is expected to consult often and effectively with the CB Chair, the HALL D Leader, and the TRC. Finally, the Spokesman will chair the TRC and will nominate the Deputy Spokesman to the CB for approval.

The position of Spokesman is a term position. The initial stages of the HALL D Collaboration's objectives, such as the funding approval and the construction phases, require conditions of stability and continuity which are consistent with a longer term of tenure than later phases of

data taking and analysis. Thus, the initial term is fixed at four years from the date of adoption of this MP

The term for Spokesman is renewable without any restriction on number of consecutive terms served. Upon the expiration of the stated term, the CB will call for nominations among the collaboration. The CB will act as an initial search committee to select no more than two candidates, based on technical, scientific, personality traits and, most importantly, leadership qualities, from among the pool of nominees. The CB endorsed nominee(s) will be presented to the the Collaboration membership for final vote.

The deputy spokesman

The Deputy Spokesman is the Spokesman's load-sharing, stand-in during absence and close advisor. The Deputy Spokesman will generally carry duties and responsibilities assigned by the Spokesman. In case the Spokesman is either removed from office or resigns, the Deputy Spokesman will be assigned as Spokesman (acting) until the collaboration elects a new Spokesman.

The Deputy Spokesman will be selected by the Spokesman from among the Collaboration membership and presented to the CB and JLab management for confirmation only. In the case of the CB, there should be important and overriding concerns in order to reject the selection by the Spokesman. A rejection will require a two-thirds vote by the CB members.

The normal term for the Deputy Spokesman coincides with that of the Spokesman. There is no limit on the number of consecutive terms the Deputy Spokesman serves.

The Hall D leader

The HALL D Leader is a JLab staff physicist appointed by JLab management in consultation with the Spokesman, Deputy-Spokesman, and the CB Chair. The HALL D Leader must be either a Collaboration member, or become one immediately upon acceptance of the position.

The duties of the HALL D Leader are as diverse as they are important. The person will be the official representative of JLab management within the collaboration. The coordination of the civil construction and that for all elements necessary to deliver a high quality electron beam to the tagging facility, are primarily the responsibility of the HALL D Leader. All safety related administrative and engineering procedures and controls are also within the HALL D Leader's direct responsibility and authority.

The HALL D Leader is an important member of the TRC and is expected to interact and consult with members of the relevant Working Groups.

A.3.5 The collaboration board

The structure of the cb

The elected representative body of the collaboration is the CB. Its membership will consist of six voting members called CB Officers. The CB Officers will be elected directly by the Collaboration membership and they will choose their own chair. The Spokesman, Deputy-Spokesman, and the HALL D Leader, who cannot be elected to the CB, can attend CB meetings upon invitation by the CB Chair. No more than one voting member per institution or MoU group may serve on the CB. The CB membership tenure will be two years, with no more than two terms served consecutively for any member.

The mandate of the cb

The role of the CB is to address all issues related to the overall framework of the collaboration. It will decide on new membership applications in committee with the Spokesman. It will ratify the proposed by-laws for the collaboration and vote on proposed amendments. On major issues which affect the structure of the collaboration and the MP, both the CB and the general membership vote will be required. The exact mechanism will be defined in the by-laws, to be defined after the adoption of this MP.

Another important role of the CB is the management of issues related to graduate students. The very nature of the HALL D experiment, which is also a Collaboration as well as a facility, presents challenges and opportunities for the allocation of these material for graduate students among the university based members of the Collaboration. A set of by-laws will be needed to govern such matters and to ensure fairness and objectivity to students and faculty.

The CB represents the interests of the membership in all aspects relating to the objectives of the HALL D Collaboration. It is expected that the CB Chair will play an active role in the governance of the collaboration and will bring issues of interest and concern of the membership to the attention of the EG and JLab management. The CB may recommend to the membership the removal of either the Spokesman or Deputy Spokesman by a two-third majority in the CB vote. The CB will meet regularly as conditions and needs arise and not less than three times within a calendar year.

The CB, like the EG, is entrusted with essentially the well being of the collaboration. It is self evident that all avenues of communication and substantive exchange of views will be pursued among these two committees and that electronic polling and conference calls will be employed to enhance the time response and frequency of contact between these two groups, over and above formal CB meetings a few times a year.

The chair of the collaboration board

The Chair will be responsible for calling CB meetings. However, any CB Officer can request to the Chair that a meeting be held. The Chair will consult with the other Officers and decide on the merit of such a request. The Chair will announce general Collaboration meetings in consultation with the Spokesman.

The CB Chair, like the Spokesman, is a position of high responsibility and sensitivity because the role is primarily that of human interaction rather than technical aspects. It is expected that Robert's Rules of Order are followed. On the issue of voting, the Chair will not vote on routine matters where simple or absolute majority is required, thus eliminating the possibility of split decisions in the six member committee. If the Chair wants to vote on such matters, an alternate Chair from among the other CB Officers must chair the meeting. On issues that require two-thirds majority, all members of the CB are eligible to cast a vote.

General duties of cb officers

The assigned duties of the other five CB Officers, as delegated by the Chair in consultation with the Officers of the Board, reflect the mandate of the CB. Thus, CB Officers will be assigned one or more of the following duties:

- Dealing with membership issues.
- Dealing with nominations issues.
- Dealing with publication issues.
- Coordinating the speaker bureau.
- Keeping accurate records and minutes as the CB Secretary.
- Coordinating graduate student projects and theses.

If the need arises, either due to special circumstances or due to load factor, one or more Officers may request from the Chair the formation of subcommittees to assist in specific tasks. Such subcommittees are advisory to the CB and are to be recruited among Collaboration members. If necessary, non-Collaboration members may be invited to participate due to expertise and specific skills. Such subcommittees are of limited time duration and scope.

A.4 Summary

A management plan should create the minimum structure necessary to accomplish the ultimate objectives of the collaboration. It should preserve flexibility, while, at the same time, create a structure which is well defined and maximizes the individual talent and contribution of its membership. Due to the unique character, within the JLab structure, of HALL D as an experiment, but with a clear facility component, the MP could not necessarily be a direct or slightly modified copy of present models. The role of JLab management and structure for HALL D remains to be defined outside this MP, however, it should be an easy task to integrate new elements into this basic structure. Finally, the structure of the MP can be modified by the two-thirds majority vote rule in both the CB and the HALL D general memberships.

Appendix B

The report of the Cassel committee

Review of the Jefferson Laboratory “Hall D Project”: December 6& 7, 1999

Review Committee:

David Cassel	Cornell University
Frank Close	Rutherford Laboratory
John Domingo	Jefferson Laboratory
William Dunwoodie	Stanford Linear Accelerator
Donald Geesaman	Argonne National Laboratory
David Hitlin	California Institute of Technology
Martin Olsson	University of Wisconsin
Glenn Young	Oak Ridge National Laboratory

Report Date: January 12, 2000

Executive Summary

The Committee was asked to address three principal questions, whose answers were to be based on the answers to more detailed questions. This Report contains the Committee’s response to these questions, and advice to the Jefferson Laboratory management and the Hall D collaboration. Our answers to these questions are summarized in this Executive Summary and then given in more detail in the following Sections of this Report.

1. Evaluate the Scientific Opportunities Presented by the “Hall D Project”

This collaboration proposes to explore systematically the light mesons (with masses up to about 2.5 GeV) with capabilities far beyond those of previous experiments. The copious spin and flavor initial states produced by photon beams will be an extremely useful tool in this endeavor. Thorough study of the masses, spins, parities, and charge conjugation states of these light mesons will require a complete partial wave analysis. This will provide a much deeper understanding of quark-antiquark states, and will permit a definitive search for mesons with exotic quantum numbers, particularly hybrid states and glueballs. This search is very high priority physics; since the states involving excited glue, as well as quarkless glueball states, must exist if QCD is the correct theory of the strong interactions.

JLab is unique in being able to provide high quality, low emittance, CW photon beams that are required for this experiment. In addition, JLab and a significant segment of the JLab physics community are committed to this physics program. Together these provide a unique

opportunity for exploring light meson states and making definitive searches for exotic states in this mass region.

2. Review the Collaboration's Approach to the Realization of that Facility

The general design of the detector is technically sound. This is verified by a detailed comparison (included in the Appendix of this Report) of the capabilities of the proposed Hall D detector with those of the successful LASS detector. This comparison leads to the conclusion that the proposed detector and beam combination will be able to realize the physics goals of the Project.

However, substantial effort must be invested to optimize the detector design and minimize the cost. The items requiring optimization that we have identified are described in detail in Section 2 of this Report. These optimizations are part of the R&D required to prepare a Conceptual Design Report for the Hall D Project. Preparation of a CDR with the associated WBS and resource-loaded cost and schedule will require a Project Office at JLab with a Project Director and a well-structured organization designed to address the necessary R&D and optimization efforts.

3. Recommend R&D Needed to Optimize the Facility Design and to Minimize the Overall Project Cost.

The R&D item of greatest concern is ensuring that the magnet is still functional, particularly the fourth coil, which has not been used for at least 15 years. R&D should also include construction of prototypes to optimize detector design, to validate mechanical, electronic, and software choices; and ensure the feasibility of the proposed coherent bremsstrahlung system.

Conclusions

In conclusion we find that:

- The experimental program proposed in the Hall D Project is well-suited for definitive searches for exotic states that are required according to our current understanding of QCD.
- JLab is uniquely suited to carry out this program of searching for exotic states.
- The basic approach is advocated by the Hall D Collaboration is sound.
- The Collaboration will be ready to begin work on a Conceptual Design Report once a Project Office with a Project Director is in place.
- An R&D program is required to ensure that the magnet is usable, to optimize many of the detector choices, to ensure that novel designs are feasible, and to validate cost estimates.

1 Evaluate the Scientific Opportunities Presented by the “Hall D” Project

1.1 Is this High Priority Physics That Must Be Done to Understand QCD?

Low energy QCD confines quarks into hadrons. Monte Carlo simulations of QCD demonstrate that the gluonic field (glue) collapses into a flux tube at large distances. Due to its self-interaction the glue should possess excited states which can be thought of as vibrations of the flux tube. Mesons with excited glue are called hybrids. Their existence is a firm prediction of QCD which has not yet been experimentally verified. In addition, quarkless mesons, known as glueballs, must also exist if QCD is the correct theory of the strong interactions.

These additional meson states should be plentiful in the mass range from 1 to 3 GeV. It would be important and in fact a crucial step in hadron physics to find these unconventional meson states as well as to identify the numerous conventional ones in this mass range. The proposed Hall D upgrade offers a unique opportunity to explore this mass region. The use of a photon beam is another special feature of the proposal, particularly since the photon beam carries both spin and flavor, which allows a large number of states to be excited.

The most convincing demonstration of the existence of hybrids and glueballs is likely to involve identification of exotic mesonic states — those with quantum numbers that cannot be formed by a quark-antiquark pair. A number of such exotic mesons are predicted to lie in the mass range that will be thoroughly mapped out as a result of this initiative.

Because of the nature of QCD, many hadron states are approximately degenerate in mass, so a detailed partial wave analysis must be done to disentangle them. A photon beam at JLab is particularly well-suited for this task, and the proposed linear polarization would substantially enhance the partial wave analysis by separating natural and unnatural parity contributions to t -channel exchanges.

1.2 Will the Facility’s Capabilities be unique?

Photon beams bring the unique aspect of spin-aligned quarks to meson spectroscopy that is not available in the entrance channel with hadronic beams. This leads to the expectation of large cross sections for a number of states with exotic quantum numbers. While meson-production in baryon-baryon interactions, in principle, can populate the same states, the experimental situation is much more complicated.

The photon beam requirements for this project are initially 10^7 linearly polarized tagged photons per second in the energy range of 6–10 GeV with 100 percent duty factor and good emittance. The final goal is a tagged beam of 10^8 photons/s. JLab, with the energy upgrade, will be uniquely suited for providing such a beam. In particular, the excellent emittance of the JLab electron beam allows for strong collimation of the coherent bremsstrahlung radiation to enhance the polarization and ratio of tagged to untagged photons in the tagged photon beam. No other facility in the world will be able to provide a beam of this quality, with this combination of energy, duty factor, and emittance. If such a project were pursued at other existing high-energy facilities, either the data taking rate would be dramatically reduced, compromising the physics goals, or a much more complicated detector would be required. We do not see any project at an existing accelerator complex (*e.g.* SLAC, CESR, DESY) which is likely to be able to compete with the Hall D initiative in this area.

2 Review the Collaboration’s Approach to the Realization of that Facility

2.1 Is it Technically Sound?

- The technical solutions put forward in the proposal are, in the main, sound, but remain to be optimized
- It is worthwhile to spend time in optimizing individual component designs, in the context of the global scheme, rather than launching immediately into parallel prototyping efforts
- To this end, we recommend that, prior to assigning construction responsibilities, a set of “Task Force” efforts be launched to optimize the following detector systems:
 - Tracking
 - Calorimetry
 - Particle Identification
 - Trigger and Data Acquisition

- When specific approaches to detector design have been adopted, parametric studies should be carried out on items such as:
 - drift cell size,
 - support material distribution,
 - energy versus angular resolution in the barrel calorimeter,
 - particle ID capability, and
 - data acquisition concept and realization.
- Responsibility for each Task Force should be clear, and each Task Force should have an explicit charge and a definite reporting deadline.

2.1.1 Civil Construction

Since there was no detailed presentation of the civil construction, the Committee's comments are confined to the cost estimate and the brief outline in the document. The cost estimate provided by the JLab civil group appears reasonable for a project in this preliminary stage within the normal accuracy of 25% claimed by that group. We were more concerned by the 10–12 m of Fe shielding needed to range out the high energy muons from the photon collimator and the same amount probably required around the tagger dump. (The 1 m found in the document appears to be an error.) This suggest to the Committee that one should reexamine the decision to have a surface tagger dump and main building. By pointing the deflected electron beam downward and placing the dump in the earth one could probably substantially reduce the required Fe shielding. In the same manner, placing the level of the hall floor below grade might also considerably reduce the required Fe shielding from the photon collimator. We suggest reexamining these questions in order to optimize costs.

2.1.2 Photon Beam

- The proposed tagger is essentially the same as that for Hall B and does not constitute a problem.
- Linear polarization from coherent bremsstrahlung is a well-understood phenomenon and the kind of beam proposed for Hall D has been used routinely in earlier experiments. However, achieving a beam of the quality desired for this experiment (*i.e.*, the flux, the concentration into a narrow band of photon energies, and the collimation needed to adequately enhance the fraction of photons that are linearly polarized) will require ongoing R&D efforts in conjunction with JLab Hall B developments. The R&D efforts that will be required include:
 - growth of synthetic diamond crystals of suitable thickness,
 - thinning of natural diamond crystals to the relevant thickness ($\leq 50\mu\text{m}$), and
 - a collimator feedback system to regulate photon beam targeting an polarization.
- Hall B tests indicate that the proposed Hall D incident flux will result in drift chamber occupancies well within acceptable range.

We conclude that the proposed photon beam design is compatible with the goals of the experiment, contingent on a successful R&D outcome.

Should it prove impossible to achieve the proposed level of linear polarization, it will be necessary for the collaboration to make the appropriate modifications to the proposed physics program.

2.1.3 Solenoid

- It is extremely important to ascertain very soon whether the MEGA/LASS magnet is still functional - especially the fourth coil, which has not been operated since ~ 1982 . If the potential Los Alamos collaborators can make such tests in situ, this should be done soon.
- If the magnet cannot be used, a reliable replacement cost estimate is needed to see if the experiment could still be funded. For example, if a replacement would cost $\sim \$ 10$ million, would this be a showstopper?
- If the magnet is functional, experts, (*e.g.* John Alcorn, Steve Lorant) should be consulted to estimate anticipated lifetime and identify possible likely failure modes.
- A decision on coil configuration (*i.e.*, gaps or no gaps?) is needed, since this has an impact on *e.g.*, the length of the barrel calorimeter to the extent of 60-80 cm.

2.1.4 Target

The cost estimate for the 30 cm hydrogen target system is based on the replacement cost for the Hall B cyrotarget. However, since the maximum power delivered by the photon beam is limited to 15 W, and the only cryogenic target envisaged is hydrogen (or deuterium), a small commercial closed cycle helium refrigerator would probably be much simpler and cheaper. We suggest that the collaboration investigate this option.

2.1.5 Barrel and Forward Calorimetry

Forward Calorimeter

The forward calorimeter design is based on:

- repackaging of the Pb Glass used successfully in E852/RadPhi and
- replacement of the balance of the PMT bases with a Cockcroft-Walton design already used in RadPhi.

The carriage, restacking, and acceptance match to the solenoid are all straightforward. In addition, the required manpower is clearly in place. Hence we expect that the Forward Calorimeter will not be a serious technical challenge.

Barrel Calorimeter

- The concept is sound. JETSET calculations and more recently KLOE experience provide proof-in-principle and proof-of-performance at the appropriate scale.
- Prototyping is needed, partly for reasons of technology-transfer and partly to show that the groups responsible can obtain the projected energy, time, and spatial resolutions at this detector length. This is likely to lead to development of the needed manufacturing technique. It will lend urgency to choices of scintillator configuration, metal, and sampling fraction, as well as coupling of photosensors to the calorimeter and their integration with the solenoid magnet and tracking chambers.
- Calibration and monitoring concepts need to be addressed in order to ensure that energy, time, and spatial resolutions can be maintained throughout the duration of the experiment.
- Further development of the requirements for front-end electronics is needed
- Manpower and group sizes still seem low for this effort, and engineering support needs to be identified for the structure, module manufacturing, supports, and front-end electronics.

2.1.6 Tracking Chambers

The overall geometry and anticipated performance of the tracking system appears to be reasonable. However, much work needs to be done to optimize the tracking system. This includes:

- A definite decision between the TPC option and the Central Drift Chamber needs to be made as soon as possible.
- The study of the TPC option must include an understanding of the problems that will be encountered with the non-uniform magnetic field of the solenoid and consideration of the data rate and volume issues that will arise from the anticipated very high occupancy.
- The overall design of the tracking system must be optimized. This optimization should include: studying the possibility of reducing the number of different types of chambers, optimization of cell sizes, and optimization of chamber geometry and locations. In addition, options for eliminating the separate Beam Vertex Chambers by combining them with the Forward Drift Chambers should be studied carefully.
- Prototyping of the selected drift chamber option(s) should be included in the R&D effort for a Conceptual Design Report.
- The proposed Vertex Detector system will require serious R&D effort.

2.1.7 Particle Identification Systems: Time of Flight, Cherenkov and dE/dx

The basic detector technologies for the ToF and Cherenkov systems are not a concern.

- ToF system:
 - Coupling of the active region to photosensors needs development, particularly a decision whether the photodetectors will be in the magnetic field and the resulting requirements on photodetector design and magnetic shielding.
 - Prototyping of ToF elements would be useful to establish attainable timing resolution for chosen configuration and materials.
- Cherenkov system:
 - The proposed Cherenkov vessel would operate at pressures up to 5.6 atmospheres using an inert gas. This requires timely engineering attention to structural and safety issues.
 - The tradeoffs between threshold and imaging Cherenkov detectors should be examined.
- dE/dx system:
 - The proposed use of dE/dx information seems unsettled.
 - Extraction of dE/dx from straw tubes is possible but requires better understanding of the number of samples needed, electronics signal-to-noise, treatment of ambiguities in dE/dx versus momentum, and the resolution needed to obtain adequate $\pi/K/p$ separation without overdesigning this aspect of the spectrometer.
 - Prompt resolution of the choice of tracking system and whether a TPC would be employed will help in the timely resolution of these dE/dx issues.

Manpower is being addressed. Core institutions are identified for the ToF and Cherenkov detectors, while the effort on dE/dx is still a bit tentative.

2.1.8 Trigger System

- The basic concept for the Level-1 trigger is sound. This includes input from flash converters, a fully-pipelined formation of trigger primitives from several subsystems, appropriate front-end buffering during Level 1 latency, feature extraction from a settable time window, and local event buffering, zero-suppression, and packet formation in response to issuance of a global Level-1.
- The choice of pipeline architecture is not clearly motivated. Within a pipelined architecture, the choice of 250MHz for TDCs to preserve drift chamber spatial resolution is clear, but it remains to be shown if this is the optimum choice, both in terms of cost and performance, compared to other systems. Similarly, choices of ADC and TDC step size and bit count should be optimized.
- There is some reliance on continued commercial development of high-speed FADCs, memories, and gate-array logic, but this does not seem to be an area for present concern.
- The speeds proposed will require that fully functional prototypes be developed soon to ensure proper performance at speed, handling of pipeline synchronization, and noise immunity of front-end sections.

Core manpower is identified for this subsystem

2.1.9 Data Acquisition

- The general Online effort would benefit from early appointment of a manager to promulgate and ensure a uniform approach to front-end electronics; data transmission to the event-building stage; and distribution of trigger, timing, and exception (*e.g.* calibration) events. This will yield significant benefits over the life of the project.
- The basic readout and event building architecture is sound. It depends somewhat on continued applicability of Moore's Law. The challenge will be to flesh this out to a buildable design.

Core technical staff are identified, but added manpower, especially in areas of online software is likely to be needed.

2.1.10 Computing Hardware and Software

- The partial wave analysis software developed by the collaboration makes a significant contribution to understanding the physics potential of the proposed experiment.
- The projections of computer hardware requirements appear to be reasonable. However, economic realization of these requirements depends on the continued validity of Moore's law.
- The principal software effort required for the Conceptual Design Report is the development of a Monte Carlo simulation of detector options that can aid the process of optimizing detector components while providing an upgrade path to a full simulation of the detector for physics analysis.
- In developing software infrastructure, the collaboration should be aware of similar efforts in other collaborations and should utilize the resulting software that matches collaboration requirements whenever possible.

2.2 Will the Detector/Photon Beam Combination be Able to Realize the Physics Goals in Terms of Rates, Resolution, etc.?

The proposed Hall D detector instrumentation is compared to that used in the LASS experiment in a table in the Appendix. The primary goal of the latter was the performance of partial wave analysis in the same mass region up to ~ 2.4 GeV for forward-produced strange meson systems using incident K^\pm beams. It is generally acknowledged that this endeavor met with a significant degree of success. Consequently, it provides proof of principle for the configuration proposed for Hall D. However, the proposed instrumentation is superior or equal to that employed in LASS in almost every instance.

Therefore — if the proposed Hall D detector capabilities are realized — it should be eminently possible to acquire data of sufficiently high quantity and quality that the collaboration can achieve its analysis goals.

2.3 Can the Approach to the Facility and Its Physics Program Be Improved Significantly?

While the committee saw several issues where substantial optimization and cost minimization studies are required, it did not identify significant alternative approaches that the collaboration should investigate before proceeding. The collaboration should continue to remain alert to new ideas and technologies as the project proceeds.

2.4 Is the Approach to Cost Estimation Sound, and Are the Cost Estimates Reasonable for a Project at this Early Stage of Development?

The equipment and material cost estimates appear reasonable for a project at this stage except for the absence of contingency assignments. The Committee was more concerned with the accuracy of the manpower estimates, in particular, with the absence of any explicit engineering manpower, except for the chamber frame system. While some engineering jobs can probably be met by technicians, professional engineers will undoubtedly be required for many of the detailed designs. The collaboration should work to make a detailed estimate of the various manpower requirements in order to proceed to a CDR.

2.5 Is the Collaboration Ready to Begin Work toward a Conceptual Design Report?

The physics motivation, detector design concept, and status of data-analysis methods all are mature enough for the collaboration to proceed to develop a CDR. However, we feel that:

- The detector design is not yet optimized, and the Collaboration would benefit from appointing the Task Forces described above to carry out these optimizations.
- It is important for the collaboration to establish how the detector resolution requirements determine the quality of the physics output in order to have verifiable criteria to understand the costs versus performance optimization.
- The organizations need to be put into place to prepare a CDR. Both Collaboration and Project organizations need to be fleshed out to support this. The effort will benefit from early identification of a Project Director and formation of a Project Office at JLab to support preparation of the CDR and associated WBS with resource-loaded cost and schedule.
- The Collaboration should work closely with JLab management to define
 - a prioritized R&D funding plan and
 - a Conceptual Design Report, working to a budget envelope.

2.6 Comments on the Contents of the CDR

The Conceptual Design Report should contain:

- reasonably detailed descriptions of the individual detector systems;
- parametric optimization;
- relationship of detector performance to physics goals;
- budget and schedule;
- assembly and commissioning plans; and
 - project organization,
 - Collaboration organization,
 - funding profile,
 - contingency allocation and management procedure,
 - use of planning, scheduling and cost-tracking tools,
 - detailed budget with a year-by-year profile,
 - resource-loaded schedule, and
 - system integration.

3 Recommend R&D Needed to Optimize the Facility Design, and Minimize the Overall Project Cost

When system designs have been optimized, prototype construction should begin on items such as:

- mechanical prototypes
- electronics prototypes, and
- prototypes for online and offline software.

R&D objectives and their relation to the construction project should be clearly defined. These include:

- proof of principle of novel designs,
- establishment of the project schedule,
- refinement of fabrication techniques,
- validation of cost estimates, and
- measurement of actual system performance in test beams.

Appendix: Comparison of LASS and Proposed Hall D Detectors

System	LASS	Hall D
Target	85 cm LH ₂	30 cm LH ₂
Magnetic Field (solenoid)	22.4 kG	~ same field coil configuration may differ
Cylindrical Chambers	6 PWC's $5 \leq r \leq 50$ cm $\sigma \sim 600\mu\text{m}$ 2 mm wire spacing and cathode strip readout dE/dx: limited π/p separation below ~ 500 MeV/c Inner 2 cylinders used in definition of interaction trigger	Straw chamber $15 \leq r \leq 45$ cm $\sigma \sim 200\mu\text{m}$ dE/dx: capability proposed but needs optimization Dedicated start counter Scintillating fiber Immediately outside target
Planar Chambers	<i>Full Bore:</i> 6 PC's with 2 mm wire spacing 3 with (x,y,e) planes 3 with cathode strips $\sigma \sim 600\mu\text{m}$ (planes) $\sigma \sim 200\mu\text{m}$ (strips) <i>Beam Region:</i> 6 PC's with 1 mm wire spacing: all with (x,y,e) planes $\sigma \sim 300\mu\text{m}$ dE/dx: none First beam chamber package in trigger to close "target box"	5-6 drift chamber packages 6 planes in each package $\sigma \sim 300\mu\text{m}$ dE/dx: capability Configuration needs optimization
Cherenkov Counter	Segmented threshold counter Freon at atmospheric pressure π threshold ~ 2.6 GeV/c	Segmented threshold counter Capable of pressures up to 5 or 6 atmospheres in order to vary threshold momentum
ToF	Pie-shaped 1 PMT per counter $\sigma \sim 500ps$ Large hole on axis ($r \sim 20-25\text{cm}$) Downstream of Cherenkov Nothing in barrel region	Rectangular array 2 PMT's per counter $\sigma \leq 100ps$ Complete coverage except for small hole in beam region Downstream of Cherenkov EMC in barrel region capable of $\sigma \leq 250ps$
EMC	None	Barrel: Pb-scintillating fiber Downstream: Pb glass Almost hermetic coverage $\sigma(E)/E \sim 5-10\%$

Appendix C

Report of the Hall D Electronics Review Committee

Review Committee:

Andrew Lankford
Glenn Young
John Domingo

University of California - Irvine
Oak Ridge National Laboratory
Jefferson Laboratory

Date: July 23-24 2003

We have organized the report as a response to the questions posed in the charge to the committee.

Is the GlueX electronic design sound?

Although the GlueX electronics design has many features that differ from present JLab experiments, the design is fairly conventional relative to many other recent nuclear and high energy physics experiments. The GlueX electronics design is characterized by:

- Detector-mounted analog front-end electronics
- Pipelined data acquisition
- Crate-based TDC and Flash ADC modules
- Two stage trigger, with a hardware-based first level followed by software-based second level
- Parallel event building

All of these characteristics are sound and appropriate choices for GlueX (where “appropriate” assumes adequate human and fiscal resources). Although the GlueX electronics design parameters (e.g. data rates) exceed current JLab experiments, they do not exceed the performance of other contemporary experiments.

The committee notes that although its members are comfortable with the choice of pipelined electronics and data-acquisition systems, development of a compact justification for this choice might be advisable in preparation for a Lehman review of GlueX

The decision to standardize all detector readout on a single TDC module design and a single Flash ADC module design is good, and will help simplify the overall electronics system design in a constructive way and conserve valuable engineering resources. The Committee feels that it is desirable to locate these modules in a radiation-free area if possible, in order to improve access. Such a location is also likely to provide a cleaner and better cooled environment, which will also improve reliability. The Committee does not feel that there is a compelling reason not to use a crate and bus based system for the electronic modules.

Are there any special areas of concern that deserve special study?

More manpower will be needed in order to fully realize the GlueX electronics system. Considerable special (technical) expertise will also be required.

The requirements and specifications of the analog front-end electronics are not yet adequately defined. This is coupled to the tentative status of some detector designs. The lack of full definition of detector designs may soon limit progress on electronics design, although there are other issues on which progress can presently be made. Some issues deserving attention now are listed under the “Milestones” section.

Does the collaboration have a sensible plan for management?

Rudiments of a plan for management of the electronics system exist, although the plan needs further development. The Committee suggests creating a single organization covering front-end electronics of all detector subsystems, trigger, data acquisition, and online software.

The electronics organization should be put in place during the development of the CDR, and the electronics management plan included in that document

Are their estimates of manpower needs realistic?

The manpower resources shown during the review will be inadequate for developing an electronics system of the scope required by GlueX. A bottoms-up estimate of the necessary manpower should be derived from the manpower requirements for development of the electronics chain for each electronics subsystem, including packaging, grounding, shielding, and power issues.

The committee anticipates that the GlueX collaboration will need to discuss support for additional electronics and computing manpower with Jefferson Lab and the funding agencies.

Do they have a realistic milestones as we prepare for the Lehmann review and beyond to construction?

The Committee estimates that a project of the overall scale of GlueX will require about 6 years to complete after CD-3 is achieved. Approximately two years are available between obtaining CD-0 and CD-3, during which the CDR must be developed and all groups involved in the construction of GlueX be put in place. This requires that by FY2006, all major R&D issues should have been addressed.

The current good work on the flash TDC and ADC should continue. A multichannel FADC needs to be designed, fabricated, and tested. The Committee takes note that multichannel testing has started on the FTDC, with encouraging results on cross-talk and time-slewing due to hits in neighboring channels which overlap in time. The collaboration is developing strategies to record all needed data online to correct such dependencies during offline analysis. High-speed, densely populated pipelined systems are known to have such coupling issues, and a strategy should be developed to address them for all electronics and detectors.

Analog front-end requirements deriving from the detector should be settled; a good first summary of this was exhibited to the Committee. The resulting specifications for the electronics should be settled and used to drive further R&D work. Prototype work on the needed front-ends will require about one year once these specifications are settled. This suggests a review of progress in this area by Jefferson Lab management around the beginning of FY2005, covering the status of analog designs and prototypes.

The collaboration has experience with the needed fast discriminators and has started to explore options for tracking chamber front-ends. A program to develop the tracking chamber front-ends, either from a new design or by adapting an existing design, for example from among the family of ASD-8 ASICs developed at U. Pennsylvania, needs to be mapped out soon by the collaboration.

There is a concept for a pipelined LVL-1 trigger as an integral part of the pipelined online system. The link work shown should be completed. The general concept of local sums at the

front-end board level, followed by crate-level sums and subsequent transfer to a central Global LVL-1 processing area, is sound. A concept and proof-of-principle for crate backplane operation at the required high rate needs to be developed for the CDR. If high-speed serial operation proves challenging, the collaboration should explore possible parallel concepts to lower the bus-speed requirements. The global design concept for LVL-1 also needs to be developed for the CDR.

A concept for the timing system and trigger distribution system, as well as their synchronization (pipelined operation, exception injection), needs to be developed for the CDR. This should address establishing, maintaining and diagnosing the synchronization of the various pipelines. Similarly, a concept for the calibration system, and how it integrates with both the timing/trigger system as well as the analog front-ends and FADC/FTDC, needs to be prepared for the CDR.

The collaboration should start prototyping of the parallel event builder. Manpower needs to be identified at Jefferson Lab and elsewhere to carry this concept through to its execution. The LVL-3 concept is sound and the Committee applauds the opportunistic tests of it using CLAS. A concept for the software framework for algorithms needs to be established for the CDR as well as a method to test this using simulated events.

Finally, power management, grounding and shielding concepts need to be established for the CDR. These must address overall issues as well as those specific for each detector type. The Committee was pleased to hear the report about existing efforts in these areas at Jefferson Lab. GlueX is a large and complicated apparatus employing a demanding readout architecture, which in turn requires proper grounding and shielding be incorporated from the outset.

Are there any major items missing in their list of R&D tasks? Is the priority given to each appropriate at this stage?

The R&D tasks judged to be most pressing are noted above. It is critical that the choices made in readout architecture reflect requirements imposed by the physics and detector choices. We recommend that Jefferson Lab review the status of detector prototypes, with a key aspect of this review being the ability of each detector group to define their electronics needs. It is important to insure that the requirements on the electronics derive from the physics. For instance, momentum resolution requirements drive position resolution requirements, which drive time resolution requirements. Similarly, energy resolution and trigger sum selectivity requirements for the calorimeter drive choices about the number of bits in flash circuits. It must always be kept in mind that requirements are distinct from achievable performance and specifications. The review suggested above should examine these points so that design time and construction cost may be minimized while needed physics performance is preserved.

One example of an area of concern is the choice of barrel calorimeter photosensors. Familiarity with the chosen sensor and its implications for electronics requirements should be demonstrated. The Committee notes that CMS and ALICE have chosen to use custom Hamamatsu avalanche photodiodes to read out both crystal and lead-scintillator calorimeters and have developed appropriately matched preamplifiers and shapers. These APDs have moderate gain, around 50, are fast, and operate at modest voltages of less than 100 volts. These devices need to be studied by the collaboration to see if they would match the proposed barrel calorimeter light output levels. The CMS and ALICE groups use over 200,000 of these photodiodes and CLAS has several hundred of them and can probably supply samples.

Another area of some concern is the technology choice for the vertex tracker, particularly since its physics requirements seem to be undergoing some reconsideration. Present ideas center on tracking fibers and dense arrays of photosensors, such as the VLPC sensor array developed at FNAL. There are issues of VLPC suitability and availability which must be addressed in a timely manner if the collaboration is to pursue this option. Further remarks concerning the VLPC system are given below. If only vertex finding is needed and the fiber solution proves overly challenging, the Committee asks whether a modest silicon-strip array would serve the purpose. Various electronics designs exist, notably at SLAC and FNAL for Tevatron and LHC use.

In many of the above remarks we have stressed the relative priorities between design and prototyping for various items. The collaboration may choose to be more ambitious than sug-

gested, but the Committee feels the items noted should reach the state suggested before the CDR is deemed complete. Some of these efforts will likely require directed funding beyond present resources of the collaboration; thus a prioritized R&D program should be developed in consultation with Jefferson Lab and the funding agencies as soon as possible.

Are there technologies or developments which we have overlooked that may allow cost savings and/or improved technical performance?

The Collaboration should perform a systematic search for existing developments performed by other experiments that will facilitate the development of the GlueX analog front-end electronics. Some examples of interesting developments include:

- For anode wire readout in drift chambers, the family of amplifier/shapers and amplifier/shaper/discriminators developed at the University of Pennsylvania. These are generally referred to as the ASD-8 family and have been used successfully in experiments (ATLAS and PHENIX) in which two of the Committee members currently participate. If the ASD-Q, presented at the meeting, is chosen, then a pipelined TDC capable of recording pulse width is a must. The TMC chip developed by Y. Arai of KEK, also used in different manners by ATLAS and PHENIX, should be investigated.
- The Fermilab design for VLPC readout should be investigated for use in the vertex trackers fiber readout. The collaboration should consider the availability of VLPCs and whether elements of the Fermilab readout system are applicable within the context of the system design of the GlueX electronics. These considerations should be addressed soon, because significant development work may be required for this subsystem.
- For the forward drift chambers, the amplifier/shapers developed for the ATLAS, CMS, and PHENIX cathode strip chambers might provide a solution for the analog front-end. These ASICs are designed for strips up to over 200 pF in one case. The speed and packaging requirements differ among these experiments, thus the collaboration would need to study their suitability for the GlueX chambers, once the parameters are sufficiently well determined.

Appendix D

The GlueX Detector Review

Mike Albrow, Jim Alexander, Bill Dunwoodie, Bernhard Mecking
October 2004

D.1 Introduction

The GlueX Collaboration has proposed an experiment to produce hybrid mesons with a high energy linearly polarized photon beam incident on a hydrogen target, and to search for evidence of such mesons with an efficient, hermetic detector capable of charged particle tracking, electromagnetic shower reconstruction, and particle identification. At this review the Collaboration reported on the status of detector subsystems, which are presently in varying stages of development, ranging from conceptual design to full scale prototyping. This Committee evaluated the experiment according to the Charge which is included in Appendix A.

The Committee was satisfied overall with the detector concepts and the strategy the Collaboration has taken with respect to detector design. Designs are well based on prior experience which is either from local experiments (CLAS), or from elsewhere (LASS, KLOE), and on proven technology, which includes existing devices (LGD, magnet), or existing infrastructure (DAQ). Local experience with photon beams is also an important element which allows reliable estimates of rates and backgrounds.

The Committee was also impressed at the amount of R&D the Collaboration has managed to achieve over a period of years in which the prospects have been so uncertain. This speaks to strong physics motivation, coherent leadership, and a vibrant sociology within the Collaboration.

We begin this review with several comments of a global nature, and then proceed with a more detailed discussion of each subsystem.

D.2 Overall Comments

1. The collaboration urgently needs to take a global perspective in making design choices. Most critically, this implies that they should start as soon as possible using full GEANT MC with (a) real detector material (structural material, electronics, cables, etc) in place, (b) primary hit generation, (c) reasonable representations of noise levels (occupancy) in detectors, and (d) event reconstruction and analysis, in order to assess *combined* performance of all detectors. This analysis should include both signal *and* hadronic background. Some of the GEANT infrastructure appears to exist but it has not propagated to the detector designers, and pattern recognition and reconstruction software need yet to be written. Even rudimentary versions of a complete simulation will be helpful.
2. The Collaboration needs to develop a global perspective also in technology choices so that as much as possible common solutions can be adopted. Where differences are necessary to achieve performance goals or cost minimization, the choices should be clearly justified.

3. The open issue of downstream PID (threshold Cherenkov? DIRC? other?) is crucial to resolve soon. The Collaboration intends to do so by early spring 2005, but at present the DIRC option is the only one obviously on the table. In view of the considerable technical, cost, and schedule risk that a DIRC would involve, the Collaboration needs to develop at least one viable alternative so that they can make a genuine decision between options in order to avoid a Hobson's choice. The Collaboration should also study the impact of having no Cherenkov device downstream. If the outcome of the study confirms the need for such a device, the Collaboration should either be actively trying to revive the threshold Cherenkov option or should explicitly drop it; keeping a non-viable option on the table distorts decision making.
4. Tracking is not yet optimized. The Collaboration should explore ways to reduce the inner radius of the CDC and provide good z measurements at low radius. This will reduce the p_T threshold for tracking, improve vertex reconstruction, and K_S and Λ identification. It is not clear that the start counter is needed, and currently it occupies real estate that tracking might better use.
5. Current manpower levels are somewhat marginal. While sufficient for developing the main aspects of individual subsystems, the present staffing level is not sufficient to permit critical intersystem and global issues to be addressed. In particular there is the problem of the missing overall simulation, discussed in item 1, above. Even a single additional full-time person, for instance a post-doc, on each of the major subsystems could have a large impact.
6. Overall technical coordination is essential and the Collaboration or the Laboratory should appoint a Project Manager and give him or her sufficient authority to act decisively. A management structure *is* in place within the collaboration, and some formalities such as MOUs, leadership assignments for subsystems, and a system of regular teleconferences do exist. Nevertheless the system is largely informal, and mechanisms for resolving or enforcing global or intersystem issues are essentially absent. A more robust structure with a clear Project Manager will be critical for progress beyond this point.
7. Several individual subsystems showed schedules and milestones, but a fully integrated plan remains rather sketchy at this point. One clear starting task for a Project Manager would be to establish the schedule and plan, with milestones and a well-identified critical path.

D.3 Overview of Subsystem Status

D.3.1 Photon Beam and Tagging Spectrometer

The design of the photon beam line and the tagging spectrometer aims at taking full advantage of the small emittance of the 12 GeV electron beam to create a tagged photon beam with a high degree of linear polarization between 8 and 9 GeV. The layout of the beamline elements, especially the arrangement of collimators and sweeping magnets, seems to be optimized to support that goal. The tagging spectrometer consists of two separate dipole magnets, thus facilitating construction and installation. A potential concern is the high flux of electrons with energies close to the endpoint interacting with the mechanical structure of the vacuum chamber or the dump pipe. Because of the shallow bend angle of the spectrometer, downstream spray could cause background in the tagging detectors. The segmentation of the detectors into a lower resolution but broad coverage hodoscope and a high resolution system covering the region of the coherent peak is a sensible solution. The choice of scintillating fibers read out by Silicon photomultipliers (SiPMs) is well matched to the high rate environment.

Recommendation: Perform a Monte Carlo simulation of the tagging system with particular attention to background in the tagging counters caused by high-energy electrons.

D.3.2 Forward Calorimeter

The forward calorimeter design makes use of the availability of a large number of lead glass blocks which have seen prior service in the BNL E852 experiment. Segmentation, resolution, and rate capability are well matched to the GlueX requirements. A potential concern is the large electromagnetic background close to the central hole causing high rates and potential radiation damage in the lead glass elements.

Recommendation: Evaluate the benefits of covering part of the central region of the calorimeter with higher granularity, rad-hard detectors, e.g. lead tungstate crystals.

D.3.3 Barrel Calorimeter

The barrel calorimeter consists of scintillating fibers embedded in a lead matrix. This technique has been used successfully in the KLOE detector, and the present design follows that example very closely. The group has made good progress in constructing a prototype. An open issue is the choice of the readout for the scintillating fibers in the high-field environment. The newly developed SiPMs (Silicon photomultipliers) are presently favored by the group. The committee is concerned that due to their small active area SiPMs are not well matched to the large area of scintillating fibers.

Recommendation: Develop a good understanding of the light output budget of the calorimeter and evaluate the impact of different readout schemes on the energy and timing resolution of the calorimeter.

D.3.4 Start Counter

The function of the 40-element start counter was described as aiding the Level-1 trigger and the identification of the correct beam bucket in the final analysis. The committee was concerned that the benefits of using the start counter could easily be offset by negative aspects, like the start counter material (5mm of scintillator) causing multiple scattering and (occasional) particle conversion in front of the tracking system.

Recommendation: Make sure that the start counter has an essential role for triggering or event analysis. If it does not, then remove it; if it does, then look into a substantial reduction of the scintillator thickness.

D.3.5 Upstream Photon Veto UPV

The upstream region from polar angles 135° to about 160° is covered by a lead-scintillator sandwich electromagnetic calorimeter to provide offline rejection of events where the target proton has been excited, for example to a Δ^+ . Backward photons from π^0 s in this case are soft (20 to 120 MeV) and as the current plan is only to veto such events the simple detector they have proposed is adequate. On the other hand, it is conceivable that actual measurement of the photon momentum vector would be useful for physics, in which case a more elaborate detector is called for.

Recommendation: Study the physics impact of upgrading the UPV to provide real shower energy and position information.

There are also alternative technologies that could be considered. The scintillator paddles could be read out using embedded wavelength-shifting fibers, a technology that is now well established and enables one to put the photomultipliers clear of the magnetic field (and use smaller PMTs).

D.3.6 Time of Flight Counters

The time of flight TOF counters are x,y arrays of scintillation counter bars in the forward direction, used in the trigger and to identify charged pions, kaons and protons at lower momentum than the Cherenkov counter. The goal is 80 ps time resolution, which has been reached in tests. The Committee considers this to be a good design which is at an advanced stage of R&D, and it has no real concerns in this area.

D.3.7 Cherenkov Counter

The gas threshold Cherenkov counter, which was previously the default device for identifying hadrons with higher momenta than covered by the TOF, is not being actively worked on at the present time. An alternative technology, the DIRC Cherenkov ring imaging counter similar to that used in BaBar, is being considered. The DIRC is a powerful and compact approach to Cherenkov-based particle ID. The main components of the DIRC are synthetic quartz bars, a standoff tank containing water and an array of 1500 PMTs. There are groups from Oak Ridge National Laboratory and the University of Tennessee who are proposing to build this detector, and they bring with them valuable experience from BaBar.

The Committee notes that a DIRC detector would be technically challenging and demanding of manpower. If adopted as the choice for high momentum particle ID, it is likely to present considerable technical, cost, and schedule risk for the project. Simpler or more conventional alternatives do not appear to have been explored, at least not since the departure of members who had previously proposed building a threshold gas Cherenkov detector.

Recommendations:

1. Quantify the difference in physics capability of GlueX under various particle ID scenarios including: no Cherenkov device, a gas threshold Cherenkov, and a DIRC. If another technology could be competitive (for example a device exploiting K/π separation in the relativistic rise of dE/dx) include it.
2. Estimate the cost, timescale, and manpower requirements of each.
3. Investigate what kind of help might be available from SLAC for a DIRC project. This could include testing and evaluation equipment, spare bars, and consultation.
4. Identify collaborators who would build a non-DIRC particle ID system if the final decision goes against DIRC.
5. Based on the above, choose a particle ID technology prior to the CD1 review.

D.3.8 Central Drift Chamber

The primary goal for this system is to provide charged track reconstruction over the range of polar angle 10–150 deg. w.r.t. target center in z, with momentum resolution better than 4 % at all angles. In addition, particle identification (PID) information in the form of specific energy loss (dE/dx) measurements should be obtained with resolution ~ 0.10 (dE/dx).

A straw-tube Drift Chamber, referred to as the Central Drift Chamber (CDC), has been chosen as the technology to be used to attain these goals. Straw tubes (actually aluminized mylar) of diameter 1.6 cm. are assembled in 23 layers (8 stereo at $\pm 6^\circ$.) to form a cylindrical detector of length 1.7–2.0 m. to be mounted coaxial with the photon beam direction; the radial extent of the package is from 14 - 58 cm.

Simulation indicates that the required spatial resolution can be achieved, although the choice of gas mixture has yet to be optimized. A leak-proof feedthrough system has been designed, built and tested extensively, with excellent results. A full-scale prototype has been built, and wire-tension tests conducted. Pre-amps are being developed by Alberta and JLAB, and FADC's by Indiana and JLAB. HV, signal and structural tests will be performed in 2005. QC problems were encountered with the mylar straws, and the next prototype will make use of kapton (more expensive, but much more robust).

A concern with respect to the present design is that the first stereo layer does not occur until radius 24 cm. This means that charged tracks from the collision axis with transverse momentum (Pt) less than about 100 MeV/c cannot be reconstructed in the CDC. This seems like an unreasonably large loss. In addition, vertex resolution in z will be seriously impacted for tracks produced at small polar angle, and this in turn will make it difficult to clearly define event topology.

It is recommended at the very least that the first four layers of the CDC should provide stereo information; this would reduce the Pt limitation to about 60 MeV/c, and would provide first z information significantly closer to the production vertex. If the Start Counter is eliminated, the radial region down to about 6 cm becomes available to tracking, and it is recommended that the cylindrical tracking system be extended into this volume. This might be done by reducing the inner radius in the present design. However, if there were a need to incorporate a Start Counter at some future date (e.g. in the context of some specialized trigger), it might be better to introduce a separate vertex detector package which could then be removed without impact on the remainder of the CDC.

A further concern relates to the present thickness of the downstream end-plate (5 mm Al in the prototype). An effort should be made to reduce this material as much as possible. A reliable estimate of the impact on track and vertex resolution would benefit greatly from a detailed simulation involving coordinate generation, pattern recognition, track-fitting and event vertexing. The collaboration is moving to create such software, and is encouraged to give this effort high priority (see Section 3.11 below).

Charged tracks with Pt less than about 220 MeV/c cannot reach the Barrel Time-of-Flight (TOF) system. Such tracks which are either backward-going, or which stop or interact before reaching the Forward Drift Chambers and/or TOF system, rely on the CDC (or a kinematic fit) for PID information. It seems to be of high priority to demonstrate via the prototype that dE/dx information of the desired quality can in fact be obtained from the proposed straw-tube chamber design.

Recommendations:

1. Explore ways to obtain z information at the lowest radii possible in the CDC.
2. Explore ways to extend tracking into the volume presently occupied by the Start Counter.
3. Investigate designs that reduce the endplate material of the CDC as much as possible.
4. Study dE/dx resolution in prototypes soon to determine actual capability of the straw system.

D.3.9 Forward Drift Chamber

The primary goal for this system is to provide stand-alone charged track reconstruction for the region of polar angle less than 10° w.r.t. target center in z, and to contribute to joint CDC – FDC track reconstruction over the range of polar angle $10 - 30^\circ$.

The present detector design proposes to achieve these goals by means of four packages of planar drift chambers spread over a 2 m range in z, beginning at the downstream end of the CDC. Each package consists of six individual chambers, each individual chamber being rotated by 60° about the z axis w.r.t. the preceding (i.e. further upstream) chamber. An individual chamber consists of an anode wire plane, for which the design is not yet final, sandwiched between two cathodes with strip readout at $\pm 45^\circ$ w.r.t. the anode wires. For a 5 mm anode-cathode separation and a 5 mm strip pitch, the cathodes should yield $150 \mu\text{m}$ resolution for avalanche position along an anode wire, and drift time-to-distance conversion should yield similar position accuracy in the direction transverse to the wire orientation. Fast Monte Carlo studies indicate that momentum resolution better than 1.5% should be possible throughout the range 0.5 - 4.0 GeV/c for FDC stand-alone track reconstruction. There is a proposal for the On- and Off-chamber electronics which incorporates the same preamp being developed for the CDC; the

FADC clock speed has not yet been defined, since it may be possible to achieve significant cost savings by going to a lower clock speed. A serious prototyping effort is underway, and a well-considered Test Plan has been laid out. Future prototyping efforts aimed at addressing mechanical and electronics layout issues, gas system design, cathode measurement resolution, chamber failure modes, etc. are being planned in the context of a full-scale chamber.

Concern was expressed as to whether the resolution in the anode plane could be achieved in practice given the isochrone structure, Lorentz angle effects, etc. In this regard, has the Collaboration considered other possible technologies for the Forward Tracking System?

A second concern pertained to the possibility of obtaining dE/dx information from the proposed FDC system. Low P_t looping charged tracks may not yield sufficient PID information in the CDC, and may stop or interact before reaching the forward TOF counter. The possibility of supplementing the CDC information with dE/dx information from both the anode and cathode planes of the FDC system should be explored in the course of the prototyping efforts. In this regard, it might be worth noting that in the LASS experiment, useful dE/dx information was obtained from the cathode strip pulse heights from the cylindrical chambers, but nothing of use was obtained from the corresponding cathodes of the planar chambers. This was never understood, but it should be noted that the cylindrical chamber foils were mounted on hexcel cylinders (i.e. uniform anode-cathode spacing was maintained), whereas the planar chamber cathodes consisted of aluminized mylar which was susceptible to local wrinkling and sagging [aren't we all!]. In any prototyping effort concerning dE/dx, it might be worthwhile to investigate the possibility of using a rigid cathode in order to maintain more uniform anode-cathode gap size.

The present detector layout has equal spacing between the packages of the FDC system. Since low P_t , low P_z tracks loop rapidly in the strong field of the solenoid, it might prove better from the standpoint of pattern recognition and track reconstruction efficiency to have the second package quite close in z to the first, with the third and fourth packages spaced equally over the remaining total z range. As for the CDC, a detailed simulation package based on coordinate generation, and incorporating pattern recognition and track fitting would be invaluable for such a study (see Section 3.11 below).

Recommendations:

1. Explore the possible physics advantage and design implications of obtaining dE/dx information from the FDC.
2. Use a fully integrated GEANT based Monte Carlo with pattern recognition to optimize the spacing of the FDC planes.
3. Demonstrate that the isochrones of the present design provide adequate spatial resolution, or consider design modifications to improve drift properties.

D.3.10 Particle ID

The experiment relies on a diverse set of particle identification schemes, which include dE/dx in the straw tubes, time-of-flight in the BCAL and the downstream TOF wall. The choice of downstream PID for high momentum tracks remains uncertain though the Committee was shown rudimentary concepts for a DIRC detector. We discuss the key subsystems below.

1. dE/dx: In the present detector design, the CDC is the only source of dE/dx information. As discussed previously it is important to demonstrate by means of the prototype that dE/dx information of the required quality can be obtained, and also to explore the desirability of obtaining dE/dx information from the FDC system. This possibility should be investigated in the context of the ongoing prototyping effort.
2. TOF: Information on charged particle velocity is obtained from the Barrel Calorimeter, and also from the forward TOF wall located just upstream of the Forward Calorimeter.

The Barrel Calorimeter is very similar in design to that used in the KLOE detector, and so it is reasonable to expect that time resolution of 250 psec or better can be achieved. However, until the readout scheme has been finalized and prototype measurements carried out, the actual time resolution which can be obtained must be considered somewhat uncertain.

The forward TOF counter should be capable of achieving the desired time resolution (see Section 3.6). Systematic timing shifts which can result from hadronic interactions in the scintillator material should probably be investigated. Such interactions can yield large pulse height signals which result in an under-estimation of the time-walk correction.

3. Calorimetry: Electron identification, and photon detection and measurement, in the Barrel and Forward Calorimeters should be satisfactory for the proposed devices, although there is some concern about the impact of the readout scheme being considered for the Barrel Calorimeter (see Section 3.3).

The possibility of neutron and K_L detection should be considered, especially for the Barrel. For example, for events for which the kinematics yield a missing mass consistent with a neutron or K_L , a corroborating calorimeter cluster might be used to enhance signal-to-background at the expense of some loss in efficiency.

4. Cherenkov Counter: This is discussed in Section 3.7. The impact of the absence of such information should be investigated (e.g. in the context of kinematic fits to events in which all low momentum charged tracks are identified and any photons are detected), as should the effect of having the simpler threshold device instead of a DIRC. Again, such studies would be performed best in the context of a full detector simulation and track reconstruction program, as discussed in Sections 3.8 and 3.9.

D.3.11 Software

The brief overview presented indicates that the proposed software structure is well-conceived, and that the framework appears to incorporate those aspects of data-flow and data-management which will be essential to the handling of the very large data samples which the experiment is designed to produce. Code management and documentation schemes are being evaluated, and there is a significant ongoing effort to develop the complicated Partial Wave Analysis programs and procedures which are crucial to the success of the experiment.

A fast-simulation procedure exists, and work has begun on a more-detailed simulation at the coordinate generation and Calorimeter/TOF response level. As discussed already, it is the feeling of the review committee that this latter effort should be given very high priority, in particular with a view to the development of pattern-recognition and track- and vertex-reconstruction software, and the incorporation of Kalman fitting. As indicated in Section 2.1, this will be extremely important to the detailed design of the individual detector systems, and to an understanding of their impact on one another and upon the data quality which can be achieved under differing background conditions.

It is recommended that the collaboration consider a change from GEANT3 to GEANT4. The time scale for GlueX is rather long, and GEANT3 is already falling out of favor; in ten years there will likely be no support for it at all. In addition, as time moves on, it will become harder and harder to find young physicists willing or able to work in FORTRAN, which further argues for early migration to GEANT4. In any case, it might be of value to initiate discussions with e.g. Dennis Wright of SLAC (the BaBar expert on GEANT4) in order to evaluate the merits of such a transition. Similarly, the BaBar expert on the Kalman filter is Dave Brown of LBL, and he could prove to be a very useful resource with regard to GlueX software developments in this area. Ray Cowan of M.I.T. (but based at SLAC) is the BaBar Webmaster, and he could be of help to the expanding GlueX documentation and code management effort.

Recommendation: Evaluate merits of transitioning to GEANT4.

D.3.12 DAQ and Electronics

Although not requested to review DAQ and electronics, we note that design developments since the July 2004 electronics review have ameliorated or eclipsed some of the issues pointed out in that review. Notably, the vertex detector has vanished, removing all concerns about VLPCs; and the original plan to seek single TDC and FADC designs to serve all detector systems no longer appears optimal. With the addition of the Alberta group available manpower has grown, but still needs to grow more. Detector subsystems need to specify front-end electronics prior to the “Lehman Review”.

D.3.13 Integration and Milestones

Plans for civil construction of Hall D and provision of power, infrastructure, and utilities are in development. Although the choice of Cherenkov PID is still very much undecided, Hall D plans show the old gas Cherenkov device, which requires the rest of GlueX to stand on a platform. This concept may not be optimal if a more compact PID detector such as DIRC is ultimately selected. Strategies for detector installation, particularly for the installation and mounting of the massive BCAL, are in a conceptual stage but moving forward with appropriate engineering work. The need for interface documents specifying electronics paths was explicitly called out by the Collaboration, and is supported by this Committee.

Schedules and milestones are sketchy. This is true both for individual subsystems, where schedules and tables of milestones, if shown, were limited in depth, and it is true of the overall detector integration. The schedules seen by the Committee lack adequate detail to be used as effective management tools, *i.e.*, to be used prescriptively rather than merely descriptively, and it is not clear that critical paths can be accurately identified with existing information. In preparation for a “Lehman Review” the Collaboration and the Laboratory will have to evolve to a WBS-driven system, with managers in place at each level and a clear reporting structure.

Manpower levels throughout the Collaboration are minimal, as noted in the global overview at the front of this document, and this appears also to be true in the Laboratory-based staffing. A concept for Hall-D staff increase was shown but any underlying plan to achieve or approach that concept will be very funding-dependent and was outside the domain of discussion at this review. Nevertheless, Laboratory manpower for the GlueX project is important and will soon become critical. The Hall-D Coordinator position, which would be the same as the Project Manager position discussed above, is not yet officially filled.

Recommendations:

1. The Laboratory should move rapidly to confirm the Hall-D Coordinator and ensure the Coordinator is invested with broad authority and provided with sufficient supporting manpower to act decisively in all aspects of GlueX development, construction, integration, and commissioning.
2. The Hall-D Coordinator, when formalized, should bring standard management tools such as WBS organization fully into play and use these to drive the progress of the project.

Appendix A: Charge to Review Committee.

The scope of this review is to include the GlueX detector and the coherent breemmstrahlung/tagger system. It does not include the magnet, beamline, or civil systems. Nor does it include electronics or data acquisition per se (which were covered in a review held last year) except to the extent that this committee feels important for this review.

You are asked to address the following questions:

- Is the GlueX detector design sound? Are there any special areas of concern that deserve special study?
- Does the collaboration have a sensible plan for management and are their estimates of manpower needs realistic? Also, does the collaboration have realistic milestones as they prepare for the CD-1 Lehman review and beyond to construction?
- Are there design studies and/or prototyping efforts that, if undertaken in a timely manner, could strengthen the estimates of performance and cost of the planned experiment? Are each of the studies currently in progress given the appropriate priority at this stage?
- Does the collaboration have a plausible plan for assembly and maintenance of the detector? Is the collaboration properly addressing issues of subsystem integration?
- Are there technologies or developments which we have overlooked that may allow cost savings and/or improved technical performance?

Appendix E

The Report of The GlueX Magnet Review

Glue-x Magnet Review
Indiana University Cyclotron Facility
November 30, 2004

Review Committee:

Bob Kephart, Fermilab (chair)
Claus Rode, Jefferson Lab
John Alcorn (LASS Solenoid Engineer and JLAB retired)

The review was held at IUCF November 30, 2004. The charge is attached below including our specific response to each item in the charge.

The committee heard a presentation from Elton Smith on the purpose of the review and on the charge to the committee. The committee heard about the work done at IUCF from Jeff Self. Alex Dzierba presented an overview of the Glue-X experiment. Paul Brindza provided a long and detailed talk on the solenoid status, coil refurbishment, test results, planned yoke modification, new DC system, new controls, new instrumentation, planned testing at JLAB, and various possible alternatives to deal with the N₂ leaks and ground faults. The committee inspected coil 3 whose cryostat was open during the review. The LN₂ shields were exposed and the repairs done at Los Alamos were viewable.

Charge

- 1) **Provide advice to guide the decision to continue coil refurbishment as planned, or opt for a more complete cryostat remanufacture.**

The committee recommends a complete investigation of the nature of the observed ground faults before continuing the coil refurbishment. Inspection techniques including borescope, electrical measurements, attempts to clear the faults mechanically, pneumatically, or electrically should be completed and an evaluation of the situation should take place before further coil refurbishment continues.

If the faults are found to be systemic in nature an aggressive systematic remanufacture of the coils may be warranted.

- 2) **Review plans for tests in the Test Lab (at JLab), including manpower required, and all preliminary activities in advance of installation of the magnet in Hall D.**

The committee endorses the planned electrical retests after shipment of coils to JLAB. We consider the cryogenic tests to be of secondary priority in an era of tight budgets. To be successful these tests will need a small dedicated staff.

- 3) **Propose any near-term activities which could substantially reduce cost and/or risk to the project in the long-term.**

In addition to the items mentioned under charge # 1 it is important to ensure that the coil plumbing is continuously protected from moisture and oxygen to limit further corrosion which can lead to leaks.

Other Comments and Recommendations:

- 1) Leaks and corrosion in the LN₂ shield circuits: Coil number 1 had a LN₂ leak that was repaired. Subsequent to passing a leak test the LN₂ system was pressurized to 30 psi and failed due to a new leak that developed. The problem was a "pitted" region in the LN₂ tubing near a solder joint. This may point to systematic corrosion problems. Further evidence is provided by the fact that at some point coil 3 had its LN₂ supply and return pipes replaced at Los Alamos.

To date no leaks have been found in the copper shield panels themselves. Therefore a plan to replace the LN₂ shields with new stainless steel panels seems not to be justified.

The committee feels that it would be prudent to protect all the coil plumbing from moisture and air.

We also recommend that the return circuit be separated to produce two independent LN₂ circuits. This would allow isolation of one circuit at the junction box if a bad enough leak were to develop. The coil could still operate but with increased heat load.

- 2) Electrical Shorts to ground: Coil 1 has a short of approx 3 ohms to ground near the RH lead. Coil three has a short of .2 ohms close to the LH lead. The MEGA experiment ran with a low resistance short in coil 3. Operating the coil with one ground fault is risky but possible since the power supply can be floating. With two ground faults the result can be catastrophic. The observed new short in Coil 1 is a concern for two reasons. First, considerable current could now flow through the faults during a fast discharge of the coil. Second, one observed a change that may be due to contamination (e.g. metal chips) in the coil which has an open winding matrix. The shorts represent a significant risk for the long-term reliability of the magnet. It is worth considerable effort and possible risk to the coils to determine the nature of the ground faults.
- 3) It is worth considering if one can run the magnet without fast discharge. The magnet is designed to be cryostable. Thus it cannot quench so long as the conductor is immersed in liquid He. This is something that can be assured with carefully designed interlocks on the liquid level sensors and care to insure that the insulating vacuum never fails catastrophically. Provided one has current leads that can survive a loss of cooling incident, limiting the voltage during the discharge is probably a safer course of action than fast dumping the magnet if more than one ground fault is present. Consideration should be given to lowering the maximum operating current as an additional means of lowering the discharge voltage.

- 4) The fact that the resistance of the coil #1 fault has changed since its discovery is not reassuring. It is recommended that a careful inspection of the coil interior take place using a borescope. Particular attention should be paid to the lead area where it makes a right angle to enter the coil vessel. Our concern is that an insulating spacer may have broken or shifted in a way that results in the observed ground fault. In addition the coil pack should be inspected for metallic chips or debris.
- 5) The steel modifications that increase the forces on the axial support should not be considered. Opening the upstream end of the return yoke and filling the inter-coil gaps in the return yoke seems to have no negative effect on the coil forces. If modifications to the downstream end of the return steel are made, the option that adds steel to the outside is recommended.

Appendix F

The Report of the Hall D Tagging Spectrometer and Photon Beamline Review

Review Committee:

Juergen Ahrens, University of Mainz (chair)
Bernhard Mecking, Jefferson Lab
Alan Nathan, University of Illinois

Jefferson Lab, January 23-24, 2006

F.1 Charge

The scope of this review is the Hall D coherent bremsstrahlung beamline, including the photon tagging system. You are asked to address the following questions:

1. Is the conceptual design of the tagger magnet and hodoscope systems reasonable and adequate to achieve the Hall D physics goals?
2. Have the design parameters of the complete photon beamline been optimized for maximum physics impact? For example, will this design achieve maximal linear polarization up to the highest envisioned rates? Are the beamline diagnostics adequate?
3. Are the specifications for the incident electron beam sufficiently well-defined, reasonable, and consistent with achieving the Hall D physics goals?

F.2 Executive Summary

A review of the conceptual design for the Hall D Tagging Spectrometer and Photon Beamline was conducted at Jefferson Lab on January 23-24, 2006. The review committee consisted of Juergen Ahrens (University of Mainz, chair), Bernhard Mecking (JLab), and Alan Nathan (University of Illinois).

The Hall D bremsstrahlung tagging system will create a tagged photon beam with a high degree of linear polarization between 8.4 and 9.0 GeV. This beam will be used in combination with the GlueX detector in Hall D to search for mesons with exotic quantum numbers due to gluonic excitations.

The tagging system consists of two bending magnets, a large size vacuum chamber, electron detectors, collimators and sweeping magnets, and diagnostic equipment for the electron and photon beams.

At the review, the design philosophy and the technical features of all system components were presented in detail. The committee was impressed with the effort of the Collaboration to define the experimental requirements and to work out the optimal solution for the tagging system.

Based on the material presented at the review, the committee has come to the conclusion that the conceptual design of the tagger magnet and the hodoscope systems are well motivated by the Hall D physics goals, and are adequate to achieve those goals. The committee is also convinced that the design parameters of the photon beamline are optimized to achieve the highest possible linear polarization at the envisioned high tagging rates.

The specifications for the incident electron beam need to be better coordinated with the 12 GeV Accelerator Project Team to insure that the properties of the electron beam and the Hall D requirements are matched. Also, the planned assembly and alignment strategy for the tagging system components needs to be consistent with the layout of the tagger area and the capabilities and best practices of the rigging and alignment services available at JLab.

F.3 Introduction

A review of the conceptual design for the Hall D Tagging Spectrometer and Photon Beamline was conducted at Jefferson Lab on January 23-24, 2006. The review committee consisted of Juergen Ahrens (University of Mainz, chair), Bernhard Mecking (JLab), and Alan Nathan (University of Illinois). The charge to the committee and the agenda of the review are attached to this document.

The Hall D bremsstrahlung tagging system will create a tagged photon beam with a high degree of linear polarization between 8.4 and 9.0 GeV. This beam will be used in combination with the GlueX detector to search for mesons with exotic quantum numbers due to gluonic excitations.

The tagging system consists of two bending magnets, a large size vacuum chamber, electron detectors, collimators and sweeping magnets, and diagnostic equipment for the electron and photon beams.

At the review, the design philosophy and the technical features of all system components were presented in detail. The committee was impressed with the Collaboration effort in defining the experimental requirements as they impact the electron beam, the photon beam, and the tagging system. The committee would like to take this opportunity to thank the presenters for their well-prepared talks and for the frank and open discussions.

F.4 Experimental Requirements and Layout

The requirements for the electron beam, the photon beam, and the tagger are driven by the GlueX physics program, the goal of which is to map out the spectrum of hybrid mesons produced in photon-induced reactions on the proton and to identify their J^{PC} . Reaching a hybrid mass up to 2.5 GeV requires a photon beam in the energy range of (8-10) GeV, which requires a primary electron beam of energy 12 GeV. The J^{PC} identification requires a partial wave analysis, which in turn requires linearly polarized photons. To achieve these goals, the Hall D Collaboration proposes to use a tagged coherent bremsstrahlung beam in the energy range (8.4- 9.0) GeV with 40% linear polarization, an initial intensity of 10^7 tagged photons/s, with a clear upgrade path to 10^8 tagged photons/s. All these parameters were justified with convincing arguments.

The coherent bremsstrahlung photon beam is achieved with a diamond radiator which can be oriented to produce a peak in the photon energy spectrum between 8.4 and 9.0 GeV. Tight collimation of the photon beam (3.4 mm diameter opening at a distance of 80 m) reduces significantly the incoherent unpolarized photons without cutting into the coherent peak. Such tight

collimation places stringent (but probably realistic) requirements on the emittance, positioning, and stability of the primary electron beam. There was some discussion of the electron beam halo and its effect on the experiment, leading to the following recommendation:

Recommendation: The Collaboration should work closely with the 12 GeV Accelerator Project Team to insure that the electron beam emittance, positioning, stability, and halo match the requirements of the experiment.

An active collimator in the photon beam (outside of the beam-defining collimator) provides feedback to keep the virtual focus of the electron beam centered on the collimator. This active collimator uses known technology based on a tungsten “pin-cushion” detector.

In order to “tune” the orientation of the diamond crystal, it is necessary for the tagger to have a broad momentum acceptance so as to tag photons in the range (3-11) GeV (with a 12 GeV electron beam). The requirement of modest energy resolution over the (3-11) GeV range and the required much better resolution in the region of the coherent peak leads to the design of a two-hodoscope detector system. The design of the fixed broad-band hodoscope is driven by the requirement to align the crystal by identifying the characteristic structures in the photon energy spectrum expected from a diamond crystal; the hodoscope consists of 140 counters with a 60 MeV spacing. Convincing simulations were shown that such a hodoscope, along with the proposed goniometer, will allow adequate alignment of the crystal. The second hodoscope, which is called the “tagger microscope,” covers the photon energy range (8.4-9.0) GeV of the focal plane in 0.1% steps. The segmentation is mainly driven by the desire to count at high rates, up to 500 MHz/GeV. A clever design is proposed that utilizes scintillating fibers in a vertical stack read out by SiPM, leading to signals that will provide more than adequate signal-to-noise ratio. The vertical stack consists of one fiber in the horizontal plane plus two above and two below the plane. By considering only electrons in the central fiber, the tagging efficiency is improved by about 30%, since the outer fibers detect only electrons whose associated photons do not make it through the photon beam collimator. The outer fibers are necessary for alignment and monitoring purposes. A conceptual design for the detector readout exists. The detector and associated readout electronics should be capable of both high counting rate and good time resolution; this leads to another recommendation:

Recommendation: The Collaboration should revisit the time resolution requirement for the tagger hodoscope system to optimize the rejection of accidental coincidences ($\sigma=200$ ps seems to be a reasonable goal).

The Collaboration has done an excellent job simulating potential sources of background in the microscope counters and demonstrating that their experiment can tolerate those backgrounds. The committee would like these calculations to be extended to the entire tagging plane, leading to the recommendation:

Recommendation: Complete the Monte Carlo simulation of the background in the tagging counters caused by backscattering from the dump or the beam line.

F.5 Tagging System Design

The design of the tagger is fairly straightforward: it consists of two identical homogeneous rectangular magnets and a vacuum system in which the top and bottom pole pieces serve as parts of the vacuum enclosure.

F.5.1 Optics

The two-magnet system, in combination with the quadrupole in front, allows for a straight focal plane. It has a point-to-point focusing optics in the bend plane and it is defocussing vertically. The focusing properties, together with the segmentation required by the high tagging rates, easily allows for a resolution of 10^{-3} in photon energy.

F.5.2 Magnets

The two magnets are identical. They have rectangular pole surfaces and consist of parts that are simple to manufacture. No field clamps are required. The magnets weigh only 38 metric tons each.

F.5.3 Vacuum System

The pole shoes of the dipole magnets serve partly as top and bottom of the vacuum chamber. O-rings make a seal between a lip around the pole pieces and the corresponding surfaces of the vacuum chamber. Since the focal plane is a straight line which allows for a flat exit flange, the exit window for the electrons can be sealed with an O-ring, which can accommodate any window material. An aluminum foil will give better vacuum properties than Kapton. Note that a vacuum of 10^{-3} Torr in the chamber is sufficient.

Recommendation: Consider a clamped Al foil with an O-ring seal for the vacuum chamber exit window.

F.5.4 Detector System

The detector system consists of a fixed hodoscope with moderate resolution that covers the whole length of the focal plane (3-11.4 GeV photon energy) installed 20 cm away from the true focal plane, such that a second movable system with good resolution can be installed directly in the focal plane. This “microscope” has high granularity (5 horizontal rows of 100 detector elements each) which will help to measure the vertical electron distribution and, by excluding the outer channels, to increase the tagging efficiency. During commissioning, the detector system can be energy-calibrated relative to the incoming electron energy by means of the pair spectrometer in the photon beam (equipped with borrowed high granularity devices, e.g. silicon microstrip detectors).

Recommendation: To enable an online monitoring of the vertical electron distribution in the focal plane, the count rate distribution of (at least some of) the microscope detectors outside of the mid-plane should be read out, too.

Recommendation: Include the energy calibration of the tagging system in the commissioning plan.

F.5.5 Assembly, Alignment, and Disassembly

The optics calculations have shown that the relative positioning of the two magnets within 2mm does not have an impact on the properties of the instrument. Precise alignment (± 0.5 mm) is, therefore, needed only for one purpose: to make the vacuum chamber match the two magnets. The present procurement strategy is based on a single vendor taking responsibility for the entire tagging spectrometer. The simple design of the spectrometer permits the system to be put together with low risk at JLab. Therefore, the parts (magnets, vacuum chamber) could be produced by different manufacturers and put together at JLab for the first time. The strategy for supporting, assembling, and aligning the tagging system components has consequences for the beam height and the dimensions of the tagger area (including the access routes). Rigging and alignment strategy and procedures need to be discussed with the relevant groups. Potential disassembly needs to be included in the design studies.

Recommendation: Include as an option in the procurement strategy the possibility that different manufacturers produce the tagging spectrometer components, and that these components are assembled at JLab for the first time.

Recommendation: The Collaboration should work closely with the 12 GeV Civil Construction Project Team to make sure that the tagger area dimensions and the access to the area are consistent with the planned assembly and alignment strategy for the tagging system components.

Recommendation: Contact rigging and alignment services at JLab to make sure that the planned assembly and alignment strategy for the tagging system is feasible and consistent with the best practices of those groups.

Recommendation: The possibility that the system will have to be disassembled should be included in the design studies.

F.6 Summary

A review of the plans for the Hall D Tagging Spectrometer and Photon Beamline was conducted at Jefferson Lab on January 23-24, 2006. The system will create a tagged photon beam with a high degree of linear polarization between 8.4 and 9.0 GeV which will be used in combination with the GlueX detector to search for mesons with exotic quantum numbers due to gluonic excitations.

The major components of the tagging system are two bending magnets, a large size vacuum chamber, electron detectors, collimators and sweeping magnets, and diagnostic equipment for the electron and the photon beam.

At the review, the design philosophy and the technical features of all system components were presented in detail. The committee was impressed with the effort of the Collaboration to define the experimental requirements and to work out the solution for the tagging system.

Based on the material presented at the review, the committee has come to the conclusion that the conceptual design of the tagger magnet and the hodoscope systems are well motivated by the Hall D physics goals, and are adequate to achieve those goals. The committee is also convinced that the design parameters of the photon beamline are optimized to achieve the highest possible linear polarization at the envisioned high tagging rates.

The specifications for the incident electron beam need to be coordinated with the Accelerator Project Team to insure that the properties of the electron beam and the Hall D requirements are matched. Also, the planned assembly and alignment strategy for the tagging system components needs to be consistent with the layout of the tagger area and the best practices of the rigging and alignment services at JLab.

F.7 Summary of the Recommendations

1. The Collaboration should work closely with the Accelerator Project Team to insure that the electron beam emittance, positioning, stability, and halo match the requirements of the experiment.
2. The Collaboration should revisit the time resolution requirement for the tagger hodoscope system to optimize the rejection of accidental coincidences ($\sigma=200$ ps seems to be a reasonable goal).
3. Complete the Monte Carlo simulation of the background in the tagging counters caused by backscattering from the dump or the beam line.
4. Consider a clamped Al foil with an O-ring seal for the vacuum chamber exit window.
5. To enable an online monitoring of the vertical electron distribution in the focal plane, the count rate distribution of (at least some of) the microscope detectors outside of the mid-plane should be read out, too.

6. Include the energy calibration of the tagging system in the commissioning plan.
7. Include as an option in the procurement strategy the possibility that different manufacturers produce the tagging spectrometer components and that these components are assembled at JLab for the first time.
8. The Collaboration should work closely with the 12 GeV Civil Construction Project Team to make sure that the tagger area dimensions and the access to the area are consistent with the planned assembly and alignment strategy for the tagging system components.
9. Contact rigging and alignment services at JLab to make sure that the planned assembly and alignment strategy for the tagging system is feasible and consistent with the best practices of those groups.
10. The possibility that the system will have to be disassembled should be included in the design studies.

Appendix G

The NSAC Long Range Plan

The DOE/NSF Nuclear Science Advisory Committee (NSAC) of the Department of Energy and the National Science Foundation is charged with providing advice on a continuing basis regarding the management of the national basic nuclear science research program. In July 2000, the Committee was asked to study the opportunities and priorities for U.S. nuclear physics research, and to develop a long-range plan that will serve as a frame-work for the coordinated advancement of the field for the next decade.

The NSAC Long-Range Plan Working Group was formed to determine the overall priorities for the field and met in Santa Fe, NM during the week of March 25 , 2001. During this meeting, the scientific opportunities and priorities were discussed in depth and consensus was reached on the prioritized recommendations contained in the final report. This group looked at the output from the town meetings held during the previous six months, as well as many white papers and reports that were written. The outcome of this meeting was a list of four recommendations as well as a larger list of opportunities for the Nuclear Science community. During the next 10 months, the report which is submitted to both DOE and NSF was written and edited. The final report became available in April of 2002: **Opportunities in Nuclear Science, A Long-Range Plan for the next Decade** [3]. The following excerpts, which are particularly relevant to the GLUEX project, are taken directly from this final report .

The Four NSAC Recommendations

1. *Recent investments by the United States in new and upgraded facilities have positioned the nation to continue its world leadership role in nuclear science. The highest priority of the nuclear science community is to exploit the extraordinary opportunities for scientific discoveries made possible by these investments.*

Specifically, it is imperative to

- *Increase support for facility operations – especially our unique new facilities, RHIC, CEBAF and NSCL – which will greatly enhance the impact of the nations nuclear science program.*
 - *Increase investment in university research and infrastructure, which will both enhance scientific output and educate additional young scientists vital to meeting national needs.*
 - *Significantly increase funding for nuclear theory, which is essential for developing the full potential of the scientific program.*
2. *The Rare Isotope Accelerator (RIA) is our highest priority for major new construction..... RIA will require significant funding above the nuclear physics base. This is essential so that our international leadership positions at CEBAF and at RHIC be maintained.*

3. *We strongly recommend the immediate construction of the world's deepest underground science laboratory....*
4. *We strongly recommend the upgrade of CEBAF at Jefferson Laboratory to 12 GeV as soon as possible.*

The 12-GeV upgrade of the unique CEBAF facility is critical for our continued leadership in the experimental study of hadronic matter. This upgrade will provide new insights into the structure of the nucleon, the transition between hadronic and quark/gluon descriptions of matter, and the nature of quark confinement.

Elaboration in the Overview and Recommendations

Favorable technical developments, coupled with foresight in the design of the original facility, make it feasible to triple CEBAF's beam energy from the initial design value of 4 GeV to 12 GeV (thus doubling the "achieved" energy of 6 GeV) in a very cost-effective manner. The timely completion of the upgrade will allow Jefferson Lab to maintain its world leadership position, as well as to expand that leadership into new areas. The upgrade will provide an exceptional opportunity to study a family of "exotic mesons" long predicted by theory, but whose existence has only recently been hinted at experimentally. Equally important, the higher energy will open the door to the exploration, through fully exclusive reactions, of regions of high momentum and high energy transfer where electron scattering is known to be governed by elementary interactions with quarks and gluons.

Various Budget Scenarios

In discussing budget scenarios, the worst case considered was a constant dollar budget. There the report stated:

We should emphasize that smaller initiatives – even medium-sized initiatives such as the Jefferson Lab Upgrade – should be accommodated within a constant budget effort. However, the lost opportunity to build a major new facility, and the much slower pace of new initiatives, would be costly for the field.

There are also specific recommendations that the funding of the construction of RIA should not impact existing programs.

Resources. The long-range plan that we are proposing will require increased funding, first to exploit the facilities we have built, and then to invest in the new initiatives we have identified.

As noted in the detailed recommendation, construction of RIA will require significant funding above the nuclear physics base. Most of the current base funding in nuclear physics from the DOE supports researchers at universities, national laboratories, together with the operation of our two flagship facilities, CEBAF and RHIC. Redirection of funds away from areas where we are reaping the scientific benefits of recent investments would be inconsistent with our first recommendation.

Looking to the Future: The CEBAF 12 GeV Upgrade

Almost two decades have passed since the parameters of CEBAF were defined. During that period, the picture of how strongly interacting matter behaves has evolved dramatically, thus posing whole new classes of experimental questions best addressed by a CEBAF-class machine operating at higher energy. Fortunately, favorable technical developments, coupled with foresight in the design of the facility, make it feasible to triple CEBAF's beam energy from the initial design value of 4 GeV to 12 GeV (thus doubling the *achieved* energy of 6 GeV) in a very cost-effective manner. The cost of the upgrade is about 15% of the cost of the initial facility. Doubling the

energy of the accelerator has three major motivations, the first two of which are “breakthrough” opportunities to launch programs in completely new areas of research.

First, the higher beam energy will allow us to cross the thresholds for the production of states that are not currently accessible with CW beams. A prime example is the spectroscopy of “exotic mesons,” which will provide the data needed to determine whether the origin of quark confinement lies in the formation of QCD flux tubes. Not only general considerations and flux tube models, but also first-principles lattice QCD calculations require that these states exist in the accessible mass regime and demonstrate that the levels and their orderings will provide experimental information on the mechanism that produces the flux tube. Tantalizing experimental evidence has appeared over the past several years for both exotic hybrids and gluonic excitations with no quarks (glueballs). Through simple spin arguments, photon beams acting as virtual vector mesons are expected to be particularly favorable for the production of exotic hybrids. A definitive experiment to map out the spectrum of these new states required by the confinement mechanism of QCD will be possible at 12 GeV. These programs will be carried out in a new “photons only” experimental area, Hall D.

Equally important, the higher energy (coupled with the CW beam and appropriate detectors) will open the door to the exploration, by fully exclusive reactions, of regions of high momentum and high energy transfer where electron scattering is known to be governed by elementary interactions with quarks and gluons, not with hadrons. The original CEBAF energy did not allow full access to this critical regime, whereas at 12 GeV, researchers will have access to the entire “valence quark region.” This will be the first experimental facility that can measure the deep exclusive scattering (DES) cross sections in the kinematical regime where the three basic (“valence”) quarks of the proton and neutron dominate the wave function. The valence quarks play a big role over a large part of the nucleon, but it is only in this newly accessible regime that there are no significant contributions from more complicated components to the nucleon wave functions. With the energy upgrade, it will be possible to map out the quark distribution functions in the entire valence quark regime with high precision, which will have a profound impact on our understanding of the structure of the proton and the neutron. However, these structure functions are probabilities, not wave functions, and until recently the attempt to determine the quark-gluon wave functions of the nucleons has been seriously handicapped by the lack of a rigorous framework for making a connection between experimental measurements and these wave functions. The theoretical discovery of generalized parton distributions (GPDs) and their connection to certain totally exclusive cross sections have made it possible in principle to rigorously map out the complete nucleon wave functions themselves. The 12-GeV upgrade will make it possible to explore this new DES domain. This will allow exploration of the complete quark and gluon wave functions of the nucleons through measurements of quark momentum distributions, as well as through the novel framework of GPDs.

Finally, in addition to these qualitative changes in the physics reach of CEBAF, 12 GeV will also allow important new research thrusts in Jefferson Labs existing research campaigns, generally involving the extension of measurements to substantially higher momentum transfers (and thus to correspondingly smaller distance scales). An example of this is the measurement of the pion elastic form factor, one of the simplest quark systems. With the larger momentum transfers available, it should be possible to observe the transition from the strong QCD of confinement to perturbative QCD. Another example is the ability to probe the limits of the nucleonic picture of short-range correlations (SRCs), whose kinematics were first reachable at CEBAF at 4-6 GeV. The upgrade provides unique opportunities for measuring quark distributions over an even broader range of x and Q^2 , thus investigating the parton structure of bound nucleons. At this upgraded energy, we also cross the threshold for charmed-quark production. Another benefit is that most experiments that are approved to run at a currently accessible momentum transfer can be run more efficiently at higher energy.

The success of the original CEBAF design is one of the key features that make a cost-effective upgrade possible. First, the installed five-cell superconducting RF cavities have exceeded their design acceleration gradient of 5 MV/m by more than 2 MV/m and their design Q-value by a similar factor. Furthermore, seven-cell cavities have now been designed that are significantly

more powerful than the original design. Accordingly, 12 GeV can be reached by adding ten new modules in space available in the linac tunnels. However, this technological advance would not be so readily applied if it were not for the fact that the “footprint” of the CEBAF accelerator was, with considerable foresight, designed so that the recirculation arcs could accommodate an electron beam of up to 24 GeV. The basic elements of the CEBAF upgrade can thus be seen

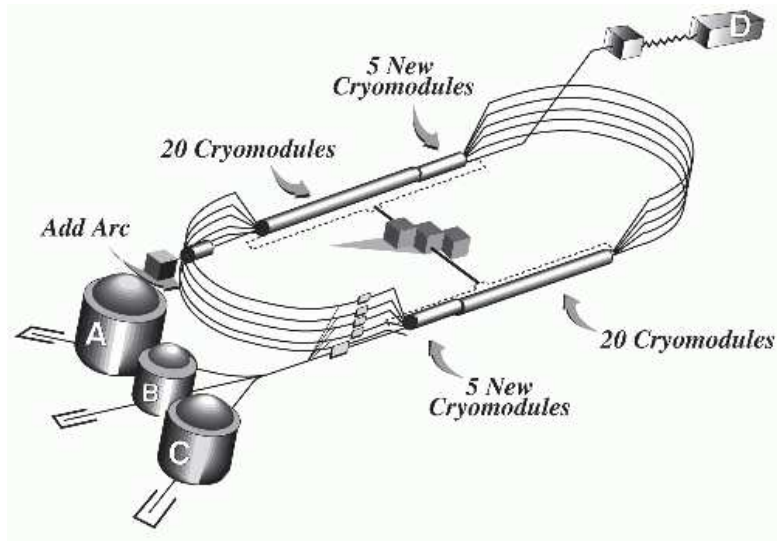


Figure G.1: Elements of the CEBAF upgrade. Increasing the beam energy at CEBAF from 6 to 12 GeV requires upgrades in four areas: (i) additional accelerating power, (ii) stronger magnets in the recirculation arcs, (iii) an upgraded cryoplant, and (iv) one additional recirculation arc. The higher-energy electrons can be directed to a new experimental area, Hall D.

in Figure G.1. The upgrade utilizes the existing tunnel and does not change the basic layout of the accelerator. There are four main changes: (i) additional acceleration in the linacs, as outlined above; (ii) stronger magnets in the recirculation arcs; (iii) an upgraded cryoplant; and (iv) the addition of a tenth recirculation arc, permitting an additional “half pass” through the accelerator (to reach the required 12-GeV beam energy), followed by transport to the new hall that will be added to support the meson spectroscopy initiative.

The timely completion of the CEBAF upgrade will allow Jefferson Lab to maintain its world leadership position, as well as to expand that leadership into new areas. The program of exotic mesons in Hall D is viewed by many as the definitive search for these states, and Jefferson Labs polarized photon beam will be the unique instrument to carry it out. The complete mapping of the nucleon wave functions is both interesting and of significant importance in other branches of nuclear physics, where these wave functions are important input to understanding higher-energy phenomena.

Appendix H

Civil Construction

The GLUEX experiment will reside in a new experimental hall (HALL D) located at the end of a new beamline off the stub at the east end of the North Linac. Figure H.1 gives a schematic view of the accelerator site and the proposed location for HALL D. The elevation of the beamline is 1.24 *m* below the nominal grade level. This height balances considerations of the beamline optics, radiation shielding issues, and civil construction cost. The figure in the foldout shows the plan and elevation views for the HALL D beamline and associated buildings.

Civil construction includes breaking through the accelerator stub, tunnel construction, beam transport system and instrumentation. The above ground facilities include the tagger building, HALL D, service buildings, beam dumps, control room, roads, and parking area. Basic infrastructure for all utilities is provided for all buildings [152].

We have had numerous meetings with JLab civil construction, accelerator, and RadCon staff, and conclude that there are no serious civil construction issues. The main problem is to minimize cost while satisfying GLUEX requirements. In particular, the beamline and buildings will fit on DOE/SURA land, building construction should be straightforward, and RadCon problems can be handled by standard techniques. A formal agreement to use a portion of land owned by SURA for the GLUEX project is under consideration.

H.1 General requirements

Requirements and specifications assuming a maximum electron beam energy of 12 *GeV* are given in Table H.1 and below:

- Single electron energy available for the D line
- HALL D is designed for a photon beam only (i.e. no primary electrons into HALL D)
- Civil construction compatible with 24 *GeV* beam (e.g. 80 *m* bend radius)
- Accelerator tangency point to radiator = 87 *m*
- Radiator to collimator distance = 75 *m*
- Tagger building = 7 *m* x 15 *m* x 3.5 *m* (height). Nominal beam height above tagger floor = 1.5 *m*. The beam is nominally 4.5 *m* from the south wall and 2.5 *m* from the north tagger wall.
- Housing for sideways electron beam dump = 3 *m* x 5 *m* x 3 *m* (height)
- Detector building = 17 *m* x 30 *m* x 9 *m* (clear hook height). The nominal beam height above the HALL D floor = 3.5 ± 0.3 *m*, 10 *m* from the south wall, and 7 *m* from the north wall in HALL D.

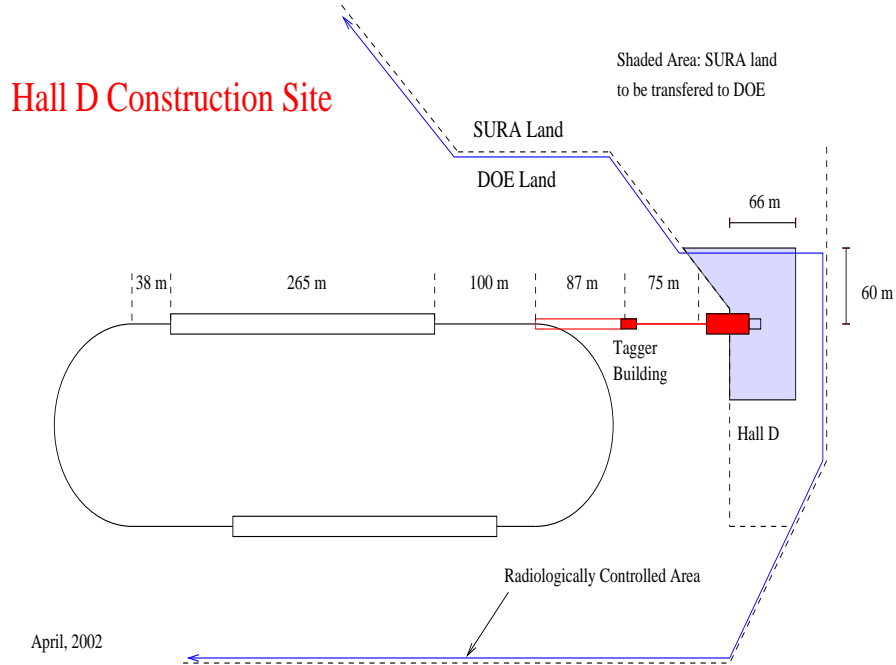


Figure H.1: An overall view of the accelerator site and HALL D.

Parameter	Operating Value	Design Goal
Max Electron Current	3 μA	5 μA
Min Electron Current	$\sim 0.0001 \mu\text{A}$	0.0001 μA
Electron Energy	12 GeV	12 GeV
Power	36 KW	60 KW
Photon Power (Collimator)	7 W	10 W
Photon Power (Detector)	1 W	1.5 W

Table H.1: Beam parameters for a 12 GeV electron beam.

- The collimator alcove is 4.5 m x 12 m x 3 m (height). The beam is nominally 1.5 m above the floor and 2 m from the north wall.
- Permissible building settlements: 1 *inch* initial; 2 *inches* max over lifetime

H.1.1 Compatibility with future upgrades

The allocation of space for the beamline instrumentation and layout of the site is designed such that an accelerator upgrade to 24 GeV would be possible using proposed buildings and tunnels. We assume that during 12 GeV operation HALL D would only receive 5.5-pass beam. For 24 GeV operation HALL D would receive 4.5, 3.5 or 2.5-pass beam; the number of passes will be switched at most annually. This implies that conditioning for the HALL D beam cannot start before the tangency point and no recombiner area is required. For 24 GeV operation, an east two-way RF separator would be used to extract the beam; the configuration could be changed during long shutdowns by relocating extraction and transport elements.

H.2 Personnel protection

The Jlab Beam Containment Policy requires that personnel be protected from accidental beam loss by at least three independent devices built using at least two different technologies.

H.2.1 Failure scenarios

The following failure scenarios were identified:

- Failure of vertical beam transport, shooting electron beam into the sky.
- Poor tuning or steering of electron beam.
- Excessive current in electron beamline.
- Tagger magnet failure, directing electrons down the photon line.
- Excessive photon flux (resulting from obstructions in the electron beamline, poor vacuum, etc).

H.2.2 Beam containment proposal

In the following we list the active and passive safety devices that assure the primary electron beam reaches the diamond radiator and the electron dump. We believe these devices satisfy the Laboratory beam containment rules as well as the SLAC beam containment rules, where there are currently two “above ground” primary electron beams in operation. See Ref. [153].

Electron beam on diamond radiator

1. There should be a beam current monitor near the exit from the linac which will turn off the beam if the current exceeds the Hall D requirement.
2. The bend string, which brings the beam up from the accelerator and back to horizontal, must be in series on the same power supply.
3. The bend string power supply should be equipped with a “meter relay” which shuts off the primary beam if the supply current varies by $\pm 10\%$ from its desired value.
4. Preceding the diamond radiator there should be a small aperture protection collimator with a burn-through monitor and a beam-loss detector, such as an ion chamber, which will shut off the beam if it hits the protection collimator.

Electron beam on the dump

1. There should be a meter relay on the tagger magnet power supply to turn off the beam if the supply current varies by more than $\pm 10\%$ from its desired value.
2. There should be a beam current monitor set to a low threshold in the photon beam line just downstream from the tagger magnet which will shut off the primary beam if it detects a charged beam in the photon line.
3. Following the current monitor there should be a permanent magnet to bend a charged beam downward.
4. There should be small aperture protection collimators with burn-through-monitors on either side of the permanent magnet with ion chambers or other type of beam loss detectors near the protection collimators.
5. There should be a beam current monitor just upstream of the 60 KW electron dump. This current reading can be compared to the current reading at the exit of the accelerator and shut off the beam if the readings differ by more than a few percent.

H.3 Environmental and radiation concerns

The civil construction includes shielding for all buildings which is sized based on preliminary, but conservative, estimates of expected radiation doses. Guidance was provided by the original calculations by Lewis Keller, who has served as a consultant on this project. The Jlab RadCon group has refined his estimates using GEANT based simulations and a realistic geometry for the buildings.

H.3.1 Site dose limits

On-Site The design goal at Jefferson Lab for a controlled area is 100 mrem/yr which may include occupancy as a factor and is based on guidelines from the Jefferson Lab RadCon Manual. Based on exposures of less than 2000 hours/yr, this sets an average dose limit of less than 50 μ rem/hour. There is also an instantaneous accident dose rate limit which is identified in the Jefferson Lab Beam Containment Policy as 15 rem/hour based on maximum credible beam loss conditions.

Site boundary The integrated dose limit at any point on the site boundary is 10 mrem/yr, or 2 μ rem/hour using an occupancy period of 5000 hours/yr.

H.3.2 Beam on radiator

For the purpose of estimating dose rates, RadCon assumes that losses along the transport line are of order 0.1%. Following the vertical bends, two burn-through monitors with small apertures preceding the radiator are needed. In addition there should be a 1-2 *m* steel wall downstream from the last vertical bend, as in the beam lines to existing halls. The surface is shielded from the tunnel by 4 *m* of earth. For comparison, we note that a similar vertical string configuration for the Hall B beamline is shielded by 2.3 *m* of earth.

H.3.3 Tagger building

Jlab rules require that the instantaneous dose rate in occupied areas (outside the building) during a beam accident be less than 15 R/hr, assuming the beam will be turned off in less than 1 second. Using a safety factor of 10-15, it was determined that 4 *m* of earth was required for the shielding against photons and neutrons.

H.3.4 Tagger hodoscope

Assuming the dump is 60 *m* from the hodoscope elements and that there is a 5 *cm* vacuum pipe leading to the dump, the neutron rate coming backward from the dump is 3×10^6 /s, and the photon rate is 0.9×10^8 /s for a 60 KW beam on the dump.

H.3.5 Electron beam dump

The electron beam dump proper will be based on a design similar to the existing BSY 120 kW dump¹ at Jlab. Beam dumps with similar characteristics are in use at SLAC [154]. We have extensive operational experience with the BSY dump and detailed calculations [155] of neutron production and ground water activation for this geometry. This dump is designed so that all the primary beam energy is dumped in solid metal. The closed water circuit for cooling sees only thermal energy, not beam energy, and there is no hydrogen generation. The dump will require regular service, which can generally be performed from outside the building itself. The absorption of longitudinal showers, including muons, will be accomplished with the beam dump

¹An identical dump is available, which is located in the north linac "stub" and was used in commissioning days, but must be removed during the construction of the HALL D transport tunnel. It has a closed circuit water system attached, along with steel shielding for neutrons.

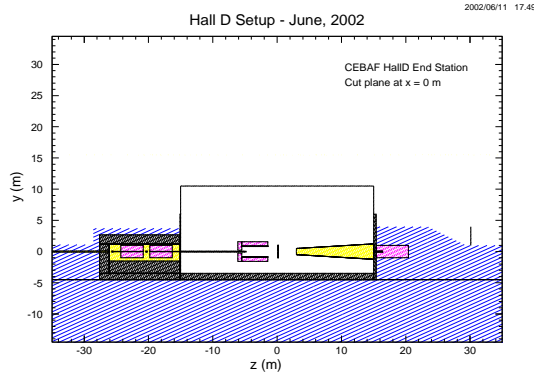


Figure H.2: Side view of the HALL D building and shielding. The upstream enclosure contains the photon collimator. The photon beam dump is downstream (right).

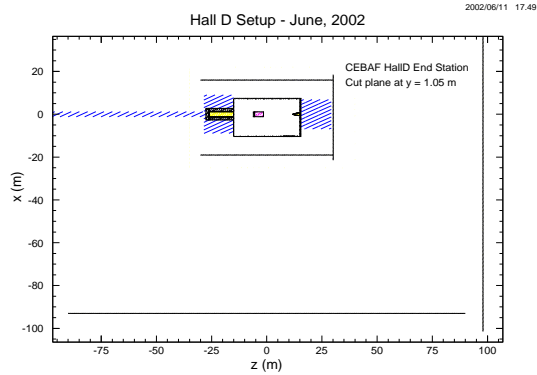


Figure H.3: Top view of shielding modeled in the simulations. Also shown are the scoring planes where radiation doses were recorded.

proper, aided by an additional 10 m of Fe downstream to insure containment. JLab requires that the dose rate must be less than 50 $\mu\text{rem}/\text{hour}$ in controlled areas. Therefore, the lateral containment of photons and neutrons resulting from the 60 KW beam, also requires 1 m of steel and 5 to 6 m of earth on the top and sides of the building.

H.3.6 Collimator enclosure

Assuming a dose limit of 50 $\mu\text{rem}/\text{hour}$ outside the building, a 10 W photon beam, and a safety factor of 10, 1.0 m of steel is needed on the top and sides of the collimators for high-energy neutrons, and 1.7 m of earth or concrete is needed in the backward direction for the giant-resonance neutrons. The design and specifications of the photon beam are given in Chapter 4.

H.3.7 Detector building

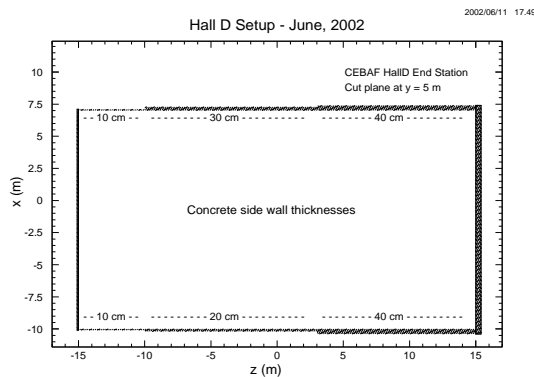


Figure H.4: Top view of the HALL D building showing the wall thickness used in the simulation.

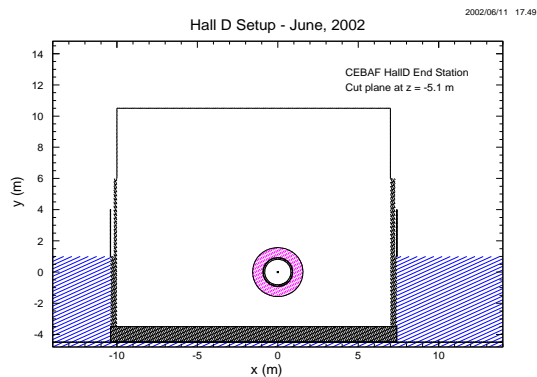


Figure H.5: Cross section of the HALL D building with the magnet.

The calculations of radiation dose for the HALL D building and site boundary were modeled with a GEANT code used by the JLab RadCon group. The program has been tested favorably

against data in existing experimental areas. The photon beam on target was generated using a $1/E$ spectrum for the incoherent flux plus a coherent spectrum representative of a typical crystal radiator. The total power in the beam was 1.5 W, which corresponds to a tagged rate of 10^8 photons/s. The upstream collimator enclosure, where 10 W of the beam is deposited, is assumed to have sufficient shielding so that it does not contribute to the resulting dose rates. The model for the building and shielding are shown in Figs. H.2-H.5.

The model for the HALL D building has concrete walls of different thickness from 10 cm upstream to 40 cm in the forward direction. The height of the walls is 5 m above the local grade level. Above the wall, we use a “tin box” construction of thin steel (0.6 mm thick walls; 0.8 mm thick roof). The target is 30 cm of liquid H₂, positioned inside the iron cylinder representing the coils and yoke, and the layers of lead representing the lead glass calorimeter (barrel portion, and forward portion). The photon beamline downstream of the detector is filled with He. The photon dump is 10 cm diameter and 1 m long hole in the dump iron. The truck ramp provides access to the building through a thin door. During accelerator operation, a fenced area is required 10 m from the truck ramp entrance.

The calculated radiation doses are shown in Fig. H.6 for various locations around the building. In all cases the dose rates are dominated by low energy neutrons which are not completely shielded. The estimated average dose rates are 10 $\mu\text{rem/hr}$ in the Counting House, 20 $\mu\text{rem/hr}$ in the parking lot, 5-10 $\mu\text{rem/hr}$ 15 m from the building, and 0.5 $\mu\text{rem/hr}$ at the site boundary.

The present solution appears to be acceptable both from the point of view of site boundary accumulated dose, and from the point of view of the dose rates around the building. The only additional safety measures would be the requirement to restrict access to the truck ramp area (if the entrance door is thin), and some restrictions on performing elevation work close to the Hall (roof of the counting house, light poles/fixtures, etc.)

H.3.8 Photon beam dump

The photon beam dump is required to absorb up to 1.5 W of photons which survive collimation and are used for experiments in HALL D. The photon beam must be transmitted to the interior of the dump in order to minimize the flux of secondaries scattering back into HALL D. A few meters of steel is adequate to contain the residual muon production, covered by earth to stop neutrons. Most of the muons produced in the collimation enclosure are absorbed before entering HALL D [156, 47].

H.3.9 Ground water activation

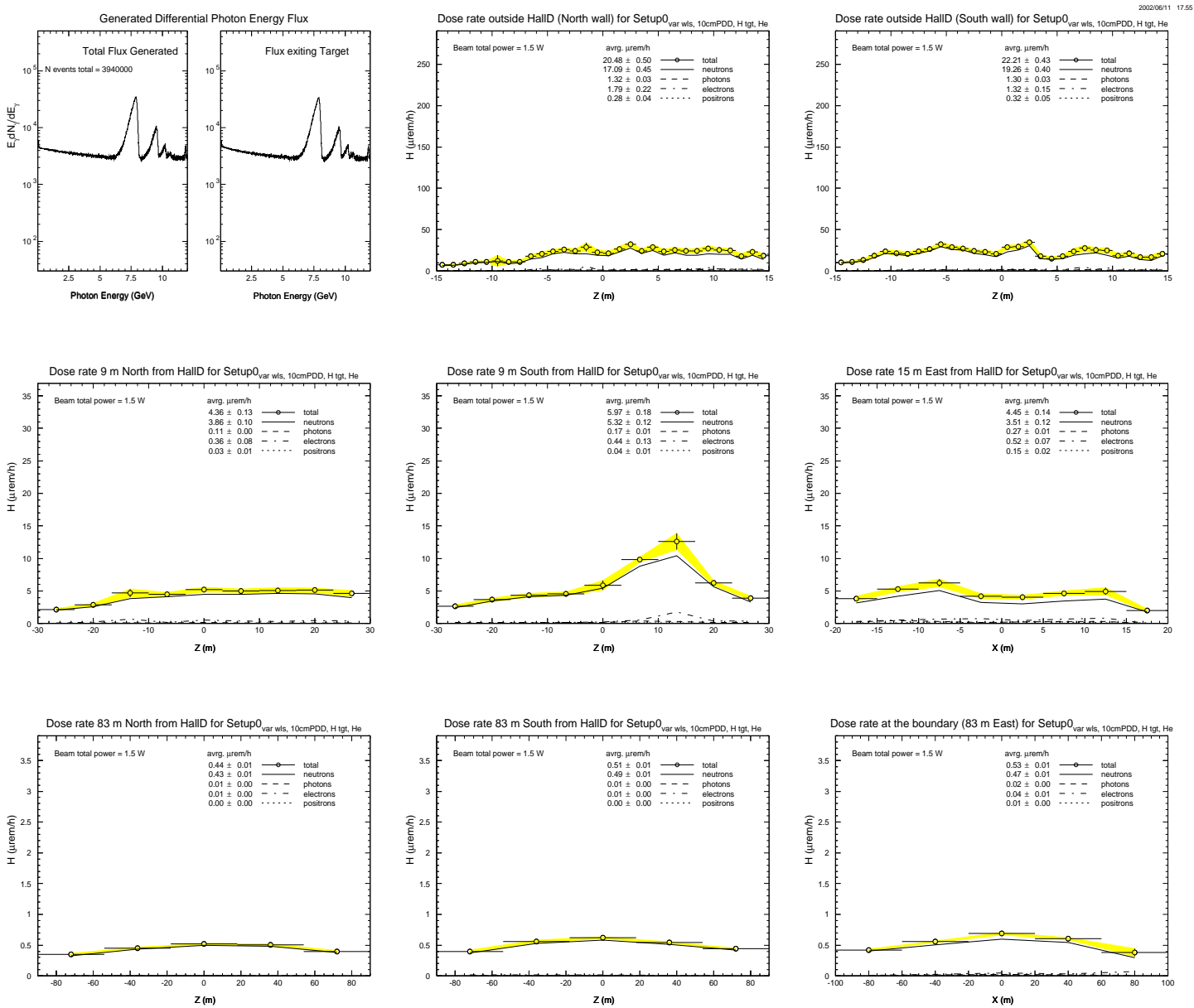
Based on the present design, there are no concerns about surface water, ground water, or soil activation in the vicinity of the end station itself. Any concerns for groundwater and soil activation are limited to the beam transport line up to and including the structures containing the photon tagger assembly and the electron beam dump. Procedures in place for current operation will be used to address these.

H.4 Geotechnical analysis

Engineering Consulting Services, Ltd. has completed a subsurface exploration and geotechnical analysis to understand the foundation conditions for building construction for the Hall D site on the east end of the accelerator. Details of their findings can be found in their report [157]. We briefly summarize their work and review their conclusions which are of direct interest to the project.

Eleven borings were taken which covered the intended construction site. Each boring obtained nine samples down to a depth of 10 m. The samples were analyzed and classified according to the unified soil classification system. In Figure H.7 we have summarized the composition of the soil from the samples. They indicate that the soil above the Yorktown Formation,

Figure H.6: Dose rates predicted by GEANT simulation code for various locations surrounding HALL D.



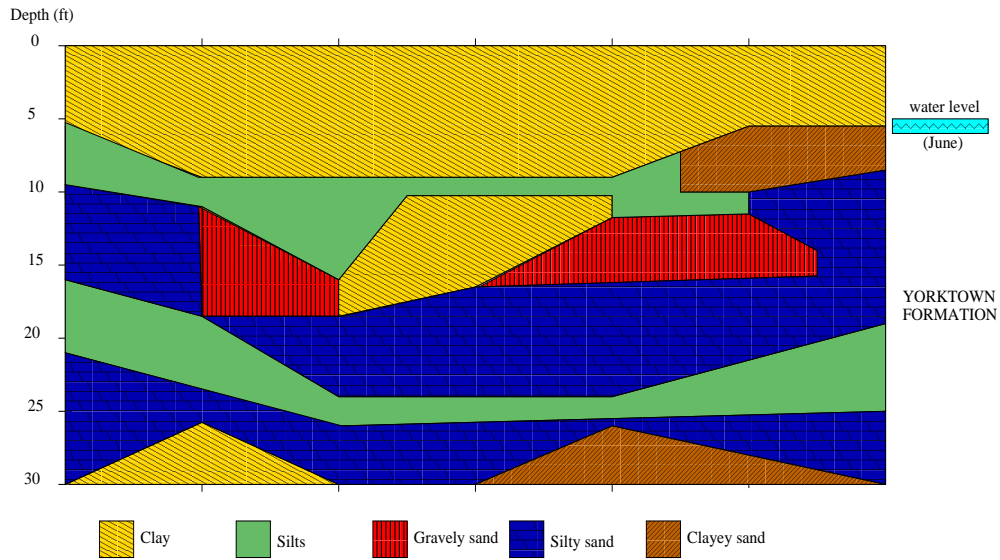
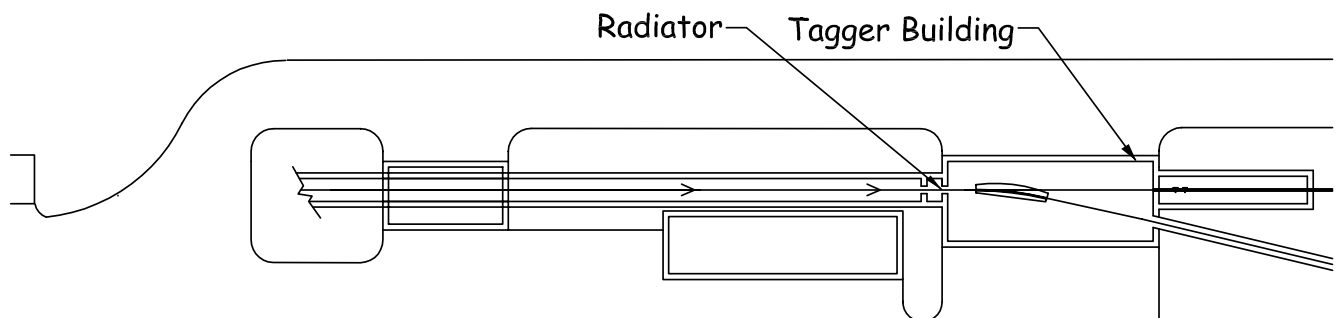
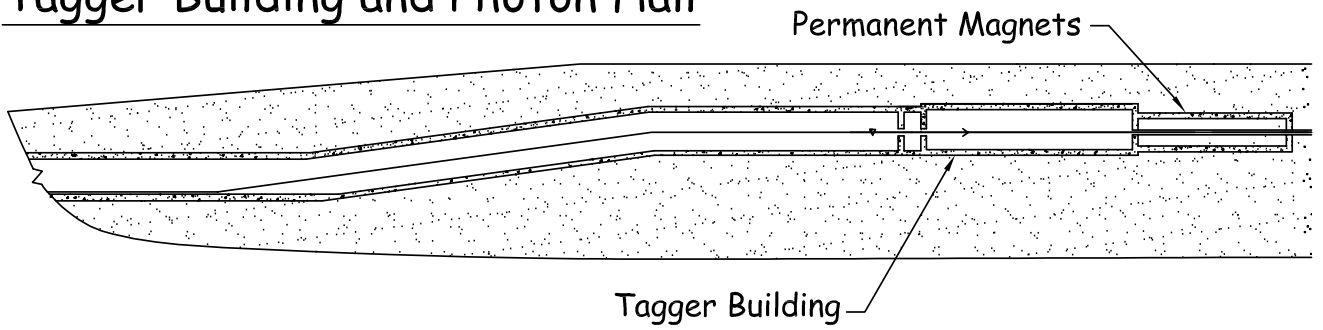


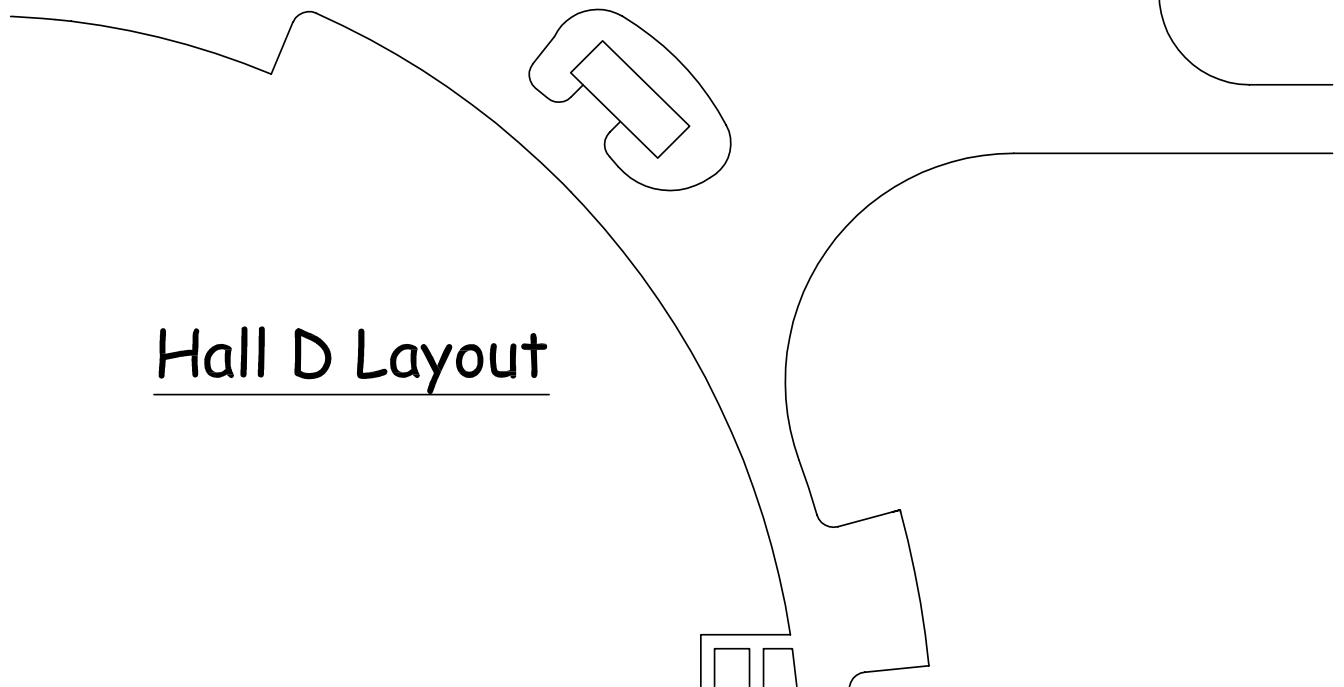
Figure H.7: Typical composition of soil under the HALL D construction site as a function of depth. Note that the horizontal dimension covers the distance from the accelerator to the building. The result of the geotechnical analysis shows that buildings at grade level will require support piles, driven approximately 15-20 *m* into the ground.

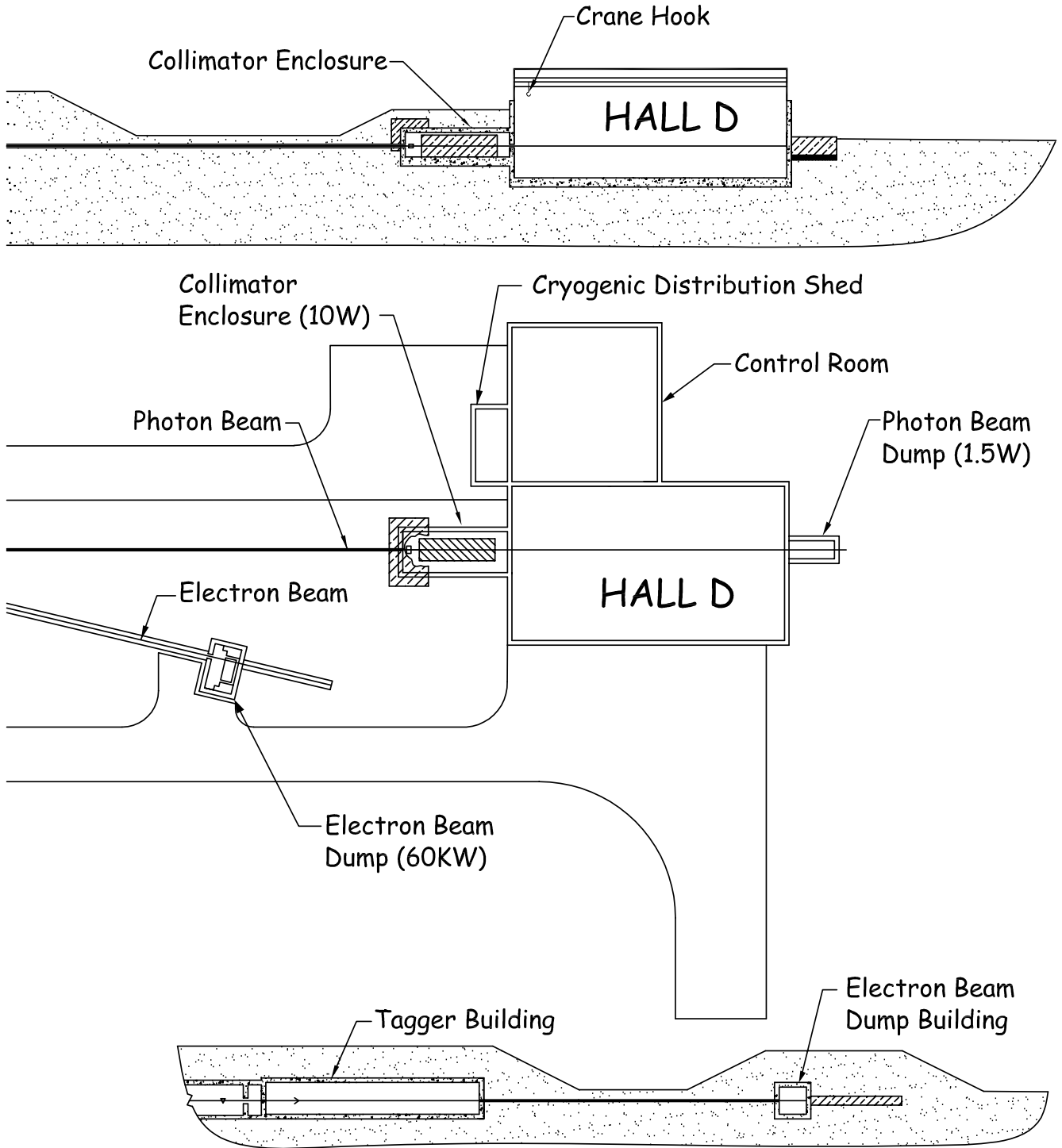
starting at depths of 5 to 6 *m* below grade, would not provide stable support for construction. The analysis shows that a mat foundation is an acceptable solution for the current design.

Tagger Building and Photon Hall



Hall D Layout





Tagger Building and Beam Dump

Bibliography

- [1] The Hall D Collaboration, R. Clark, *et al.* Hall D Design Report, Version 2. Technical Report GlueX-doc-19, 1999. <http://portal.gluex.org/>.
- [2] The Hall D Collaboration, R. Clark, *et al.* Hall D Design Report, Version 3. Technical Report GlueX-doc-44, 2000. <http://portal.gluex.org/>.
- [3] James Symons, *et al.* Opportunities in Nuclear Science, A Long-Range Plan for the Next Decade, April 2002. Available at <http://www.nsc1.msu.edu/future/lrp2002.html>.
- [4] A. R. Dzierba, C. A. Meyer and E. S. Swanson. The Search for QCD Exotics. *American Scientist*, **88**:406, 2000.
- [5] A. R. Dzierba and N. Isgur. Mapping quark confinement by exotic particles. *CERN Courier*, **40 No. 7**:23, 2000.
- [6] Y. Nambu. Univ. of Chicago report No. 70-70, 1970.
- [7] G. Bali *et al.* (SESAM Collaboration). Static potentials and glueball masses from QCD simulations with Wilson loops. *Phys. Rev.*, **D62**:054503, 2000. hep-lat/0003012.
- [8] C. Bernard *et al.* (MILC Collaboration). *Phys. Rev.*, **D56**:7039, 1997. hep-lat/9707008.
- [9] N. Isgur, R. Kokoski, and J. Paton. *Phys. Rev. Lett.*, **54**:869, 1985.
- [10] P. Lacey *et al.* (UKQCD Collaboration). *Phys. Lett.*, **B401**:308, 1997.
- [11] N. Isgur and J. Paton. Flux-tube model for hadrons in QCD. *Phys. Rev.*, **D31**:2910, 1985.
- [12] C.J. Morningstar and M. Peardon. Efficient glueball simulations on anisotropic lattices. *Phys. Rev.*, **D56**:4043, 1997.
- [13] G.S. Bali *et al.* *Phys. Lett.*, **B309**:378, 1993.
- [14] J. Sexton *et al.* (IBM Collaboration). *Phys. Rev. Lett.*, **75**:4563, 1995.
- [15] G. Bali *et al.* (SESAM Collaboration). *Nucl. Phys. Proc. Suppl.*, **63**:209, 1998. hep-lat/9710012.
- [16] C. Amsler and F.E. Close. *Phys. Lett.*, **B353**:385, 1995.
- [17] C. Amsler and F.E. Close. Is the $f_0(1500)$ a scalar glueball? *Phys. Rev.*, **D53**:295, 1996.
- [18] F. E. Close and A. Kirk. Scalar glueball- $q\bar{q}$ mixing above 1 GeV and implications for lattice QCD. *Eur. Phys. J.*, **C21**:531–543, 2001. hep-ph/0004241.
- [19] G. S. Adams *et al.* (E852 Collaboration). *Phys. Rev. Lett.*, **81**:5760, 1998.
- [20] E.I. Ivanov *et al.* (E852 Collaboration). Observation of Exotic Meson Production in the Reaction $\pi^- p \rightarrow \eta' \pi^- p$ at 18-GeV/c. *Phys. Rev. Lett.*, **86**:3977, 2001.

- [21] D. R. Thompson *et al.* (E852 Collaboration). *Phys. Rev. Lett.*, **79**:1630, 1997.
- [22] A. Abele *et al.* (Crystal Barrel Collaboration). Exotic $\pi\eta$ State in $\bar{p} - d$ Annihilation at Rest into $\pi^- \pi^0 \eta_{\text{spectator}}$. *Phys. Lett.*, **B423**:175, 1998.
- [23] D. Alde *et al.* *Phys. Lett.*, **B205**:397, 1988.
- [24] Yu. Prokoshkin, S. A. Sadovski. *Phys. Atom. Nucl.*, **58**:606, 1995.
- [25] G. M. Beladidze *et al.* *Phys. Lett.*, **B313**, 1993.
- [26] H. Aoyagi *et al.* *Phys. Lett.*, **B314**, 1993.
- [27] A. Afanasev and P. R. Page. Photoproduction and Electroproduction of $J^{PC} = 1^{-+}$ exotics. *Phys. Rev.*, **D57**:6771, 1998.
- [28] A. P. Szczepaniak and M. Swat. *Phys. Lett.*, **B516**:72, 2001.
- [29] J. Ballam *et al.* Vector-meson production by polarized photons from 2.8, 4.7, and 9.3 GeV. *Phys. Rev.*, **D7**:3150–3177, 1973.
- [30] K. Abe *et al.* *Phys. Rev. Lett.*, **53**:751, 1984.
- [31] Y. Eisenberg *et al.* *Phys. Rev.*, **D5**:15, 1972.
- [32] G. T. Condo, T. Handler, W. M. Bugg, G. R. Blackett, M. Pisharody and K. A. Danyo. Further results from charge-exchange photoproduction. *Phys. Rev.*, **D48**:3045, 1993.
- [33] M. Atkinson *et al.* (The Omega Collaboration). *Nucl. Phys.*, **B231**:15, 1984.
- [34] M. Davier *et al.* The reaction $\gamma p \rightarrow \pi^+ \pi^- \pi^+ \pi^- p$ at high-energy and γ dissociation into 4π . *Nucl. Phys.*, **B58**:31, 1973.
- [35] K. Abe *et al.* *Phys. Rev.*, **D32**:2288, 1985.
- [36] M. Atkinson *et al.* (The Omega Collaboration). *Nucl. Phys.*, **B243**:1, 1984.
- [37] G. R. Blackett *et al.* The Photoproduction of the $b_1(1235)\pi$ System. Technical report, August 1997. hep-ex/9708032.
- [38] A. V. Afanasev and A. P. Szczepaniak. Charge exchange $\rho^0 \pi^+$ photoproduction and implications for searches for exotic mesons. *Phys. Rev. D*, **61**:114008, 2000.
- [39] C. Keppel. Development of a Compton-backscattered photon source for Hall B at Jefferson Lab. In Alex Dzierba, editor, *Physics with 8+ GeV Photons Workshop*, 1997. Workshop in Bloomington IN, July 14-16 1997, proceedings available from Jefferson lab.
- [40] W. Kaune, G. Miller, W. Oliver, R.W. Williams, and K.K. Young. Inclusive cross sections for pion and proton production by photons using collimated coherent bremsstrahlung. *Phys. Rev.*, **D11**(3):478–494, 1975.
- [41] H. Bilokon, G. Bologna, F. Celani, B. D’Ettorre Piazzoli, R. Falcioni, G. Mannocchi, and P. Picchi. Coherent bremsstrahlung in crystals as a tool for producing high energy photon beams to be used in photoproduction experiments at CERN SPS. *Nuclear Inst. and Meth.*, **204**:299–310, 1983.
- [42] G. Diambrini-Palazzi. *Revs. Mod. Phys.*, **40**:611, 1968.
- [43] U. Timm. *Fortschr. Phys.*, **17**:765, 1969.
- [44] J. Kellie. Private Communication.
- [45] C. Sinclair. Private Communication.

- [46] J. Benesch. HallD Preliminary Optics Design. Technical Report JLab TN 00-011, Jefferson Lab., 2000.
- [47] L. Keller. Muon calculation results. Technical Report GlueX-doc-**33**, SLAC, 2000. <http://portal.gluex.org/>.
- [48] Anthony, *et al.* *Nuclear Inst. and Meth.*, **A301**:230, 1991.
- [49] J. Hall, *et al.* *Nuclear Inst. and Meth.*, **A368**:689, 1996.
- [50] D. Aston *et al.* The LASS spectrometer. Technical Report SLAC-Report-298, 1987. Copies available from the SLAC publications office, at <http://www.slac.stanford.edu/pubs/>.
- [51] J. S. Alcorn, H.O. Peterson, and S. St. Lorent. In *Applied Superconductivity Conference*, page 273, 1972.
- [52] A. Brunner *et al.* A Cockcroft-Walton base for the FEU84-3 photomultiplier tube. *Nuclear Inst. and Meth.*, **A414**:446, 1998.
- [53] B. B. Brabson *et al.* A study of two prototype lead glass electromagnetic calorimeters. *Nuclear Inst. and Meth.*, **A332**:419–443, 1993.
- [54] R. R. Crittenden *et al.* A 3000 element lead-glass calorimeter. *Nuclear Inst. and Meth.*, **A387**:377–394, 1997.
- [55] R. Jones *et al.* The Radphi detector. *submitted to Nucl. Instrum. Meth.*, 2004.
- [56] C. P. Steffen. PhD thesis, Indiana University, 2001.
- [57] J. Gunter. An analysis of the reaction $\pi^- p \rightarrow \pi^0 \pi^0 n$ at 18 GeV/c. Ph. D. Thesis - Indiana University, 1997.
- [58] J. Gunter *et al.* A partial wave analysis of the $\pi^0 \pi^0$ system produced in $\pi^- p$ charge exchange collisions. *Phys. Rev.*, **D64**:072003, 2001. hep-ex/0001038.
- [59] R. Lindenbusch. *An analysis of the reaction $\pi^- p \rightarrow \eta \pi^0 n$ at 18 GeV/c.* PhD thesis, Indiana University, 1997.
- [60] M. Swat. *Analysis of the $\eta \pi$ system.* PhD thesis, Indiana University, 2003.
- [61] A.R. Dzierba *et al.* A study of the $\eta \pi^0$ spectrum and search for a $J^{PC} = 1^{-+}$ exotic meson. *Phys. Rev.*, **D67**, 2003. hep-ex/0304002.
- [62] S. Teige *et al.* *Phys. Rev.*, **D59**:012001, 1999.
- [63] J. Manak *et al.* *Phys. Rev.*, **D62**:012003, 2000.
- [64] P. Eugenio *et al.* *Phys. Lett.*, **B497**:190, 2001.
- [65] M. Nozer *et al.* *Phys. Lett.*, **B541**:35, 2002.
- [66] J. Kuhn *et al.* *Phys. Lett.*, **B595**:109, 2004.
- [67] R. Fruhwirth *et al.* *Data Analysis Techniques for High-Energy Physics.* Cambridge University Press, 2000.
- [68] R. Wingman. *International Series of Monographs on Physics*, volume 107. Oxford University Press, 2000.
- [69] R. T. Jones and M. Kornicer. LGD Shower resolution. Technical report, 2003.
- [70] Graham McNicoll. A study of photon sensitivity in the Hall D detector. Technical Report GlueX-doc-**36**, Carnegie Mellon University, 2000. <http://portal.gluex.org/>.

- [71] Joachim Kuhn and Curtis A. Meyer. Acceptance Study for the GlueX detector system. Technical Report GlueX-doc-**264**, 2004. <http://portal.gluex.org/>.
- [72] C. A. Meyer. A study of timing resolutions on particle identification in the HALL D detector at Jefferson Lab. Technical Report GlueX-doc-**14**, Carnegie Mellon University, 1999. <http://portal.gluex.org/>.
- [73] C. A. Meyer and P. Eugenio. A Study of Combined $K-\pi$ Separation using Time-of-Flight Counters and a Gas Čerenkov Detector. Technical Report GlueX-doc-**15**, Carnegie Mellon University, 1998. <http://portal.gluex.org/>.
- [74] The GlueX Collaboration. Hall D Design Report, Version 4. Technical Report GlueX-doc-**58**, 2002. <http://portal.gluex.org/>.
- [75] D.W. Hertzog *et al.* *Nuclear Inst. and Meth.*, **A294**:446, 1990.
- [76] A. Antonelli *et al.* *Nuclear Inst. and Meth.*, **A370**:367, 1996.
- [77] M. Adinolfi *et al.* *Nuclear Inst. and Meth.*, **A494**:326, 2002.
- [78] Brian Klein *et al.* B-CAL Progress and Construction Report. Technical Report GlueX Technical Note **333**, 2004. <http://portal.gluex.org/>.
- [79] Brian Klein *et al.* B-CAL Progress and Construction Report. Technical Report GlueX Technical Note **333**, 2004. <http://portal.gluex.org/>.
- [80] Z. Papandreou, E.J. Brash, G.M. Huber, V.D. Kovaltchouk, S. Li, G.J. Lolos, L. Snook and S. Vidakovic. Attenuation Length and Timing Resolution of Scintillating Fibers for Hall D. Technical Report GlueX-doc-**50**, University of Regina, October 2001. <http://portal.gluex.org/>.
- [81] A. Antonelli *et al.* *Nuclear Inst. and Meth.*, **A354**:352, 1995.
- [82] B. Jasper and R. Filby. Degradation of Fibers with UV Exposure and Construction Aspects of the 4m Calorimeter Module. Technical Report GlueX-doc-**331**, University of Regina, April 2004. <http://portal.gluex.org/>.
- [83] B. Dolgoshein. *Nuclear Inst. and Meth.*, **494**:48, 2003.
- [84] D. Renker. Avalanche photodiodes now and possible developments. In *Vienna Conference on Instrumentation*, 2004. February 16-21 2004, conference web site: <http://vci.oeaw.ac.at/>.
- [85] V. Saliev. Private Communication.
- [86] T. Okusawa. *Nuclear Inst. and Meth.*, **459**:440, 2001.
- [87] P. Eugenio. *Genr8*: A general monte carlo event generator. Technical report, Carnegie Mellon University, 1998.
- [88] C. A. Meyer. Tracking Resolution Requirements in the Meson Spectroscopy Facility at Jefferson Lab. Technical Report GlueX-doc-**7**, Carnegie Mellon University, 1998. <http://portal.gluex.org/>.
- [89] Rob Veenhof. *The GARFIELD Program, Simulation of Gaseous Detectors*. CERN, 1984. <http://garfield.web.cern.ch/garfield/>.
- [90] H. Wirth. Particle Identification with the JETSET Straw Chambers. *Nuclear Inst. and Meth.*, **A367**:248-251, 1995. Prepared for 7th International Wire Chamber Conference (WCC 95): Recent Trends and Alternative Techniques, Vienna, Austria, 13-17 Feb 1995.

- [91] Zebulun Krahn and Mike Williams. Gas Composition Study for the Straw Tube Chamber in the GlueX Detector at Jefferson Lab. Technical Report GlueX-doc-62, 2003. <http://portal.gluex.org/>.
- [92] D. Barton, *et al.* (The EVA Collaboration). Color Transparency with EVA, October 1994. BNL-PROPOSAL-850.
- [93] Mike Williams, Zebulun Krahn and Curtis A. Meyer. A Study of the Straw Tube Detector for the GlueX Detector at Jefferson Lab. Technical Report GlueX-doc-54, Carnegie Mellon University, July 2002. <http://portal.gluex.org/>.
- [94] Curtis A. Meyer. Accuracy Measurements of the straw-tube chamber end plates. Technical Report GlueX-doc-61, 2003. <http://portal.gluex.org/>.
- [95] Curtis A. Meyer and Zebulun Krahn. A Summary of Straw-tube Chamber Tests. Technical Report GlueX-doc-280, 2004. <http://portal.gluex.org/>.
- [96] H. Fenker *et al.* *Nuclear Inst. and Meth.*, **A367**:285, 1999.
- [97] *ATLAS Collaboration*. ATLAS Technical Design Report, Chapter 6, June 1997.
- [98] *PHENIX Collaboration*. PHENIX Internal Note PN125.
- [99] D. Aston *et al.* (*The LASS Collaboration*). SLAC Internal Note SLAC-298.
- [100] A. Antonelli *et al.* A Pb SciFi EM calorimeter for an experiment on CP violation at DAPHNE. Technical Report LNF-91-073-P, Frascati, 1991.
- [101] S. Denisov *et al.* Timing characteristics of scintillation counters. *Nuclear Inst. and Meth.*, **A478**:440–443, 2002.
- [102] S. Denisov *et al.* Characteristics of the TOF Counters for the GlueX Experiment. *Nuclear Inst. and Meth.*, **A494**:495–499, 2002.
- [103] S. Denisov *et al.* Systematic studies of timing characteristics for 2-m long scintillation counters. *Nuclear Inst. and Meth.*, **A525**:183, 2004.
- [104] S. Denisov *et al.* Studies of magnetic shielding for phototubes. *Nuclear Inst. and Meth.*, article in press, 2004.
- [105] I. Adam *et al.* The DIRC Particle Identification System for the BaBar Experiment. 2004. accepted for publication.
- [106] P. Coyle *et al.* *Nuclear Inst. and Meth.*, **A343**, 1994.
- [107] B. Ratcliff. Technical report, 1992 and 1993. SLAC-PUB-5946 and SLAC-PUB-6047.
- [108] B. Aubert *et al.* Observation of Direct CP Violation in $B^0 \rightarrow K^+\pi^-$ Decays. 2004. hep-ex/0407057.
- [109] B. Aubert *et al.* The BABAR Detector. *Nuclear Inst. and Meth.*, **A479**, 2002.
- [110] *Status of the PEP-II B Factory*. talk given at the 14th Advanced ICFA Beam Dynamics Workshop: Beam Dynamics Issues for e^+e^- Factories “ (ICFA 97), Frascati, Italy, 1997.
- [111] E. Bloom *et al.* The PEP-II Asymmetric B Factory: Design Details and R&D Results. Technical Report SLAC-PUB-6564, 1994.
- [112] E. Bloom *et al.* PEP-II: An Asymmetric B Factory. Conceptual Design Report. Technical Report SLAC-R-418, 1993.

- [113] The BABAR Collaboration. The BABAR Physics Book. Technical Report SLAC Report 504, 1998.
- [114] The provider of fused silica: TSL Group PCL,
P.O. Box 6, Wallsend, Tyne & Wear, NE28 6DG, England.
Quartz Products Co., 1600 W. Lee St., Louisville, Kentucky 40201.
Manufacturer of quartz bars: Boeing, Rockedyne Division, 2511 C Broadbent Parkway
NE, Albuquerque, New Mexico 87107.
- [115] Manufacturer of photo-tubes: Electron Tubes Limited, (formerly: Thorn EMI Electron
Tubes), Bury Street, Ruislip, Middlesex HA47TA, U.K.
- [116] J. Cohen-Tanugi *et al.* *Nuclear Inst. and Meth.*, **A515**, 2003.
- [117] R. Brun *et al.*, 1986. GEANT3, CERN-DD/EE/84-1.
- [118] TOSCA 3D, software for electromagnetic design, Vector Fields Inc., Aurora, IL 60505,
USA.
- [119] M. Sivertz *et al.* A compact gas Čerenkov detector with novel optics. *Nuclear Inst. and
Meth.*, **A385**:37, 1997. hep-ex/9607013.
- [120] J. Va'Vra. *Nuclear Inst. and Meth.*, **A244**:391–415, 1986.
- [121] D.G.Cussans. *Nuclear Inst. and Meth.*, **A244**:277, 1995.
- [122] Signal Processing Technologies: <http://www.spt.com>.
- [123] Xilinx: <http://www.xilinx.com>.
- [124] More information on the FADC prototype can be found at
<http://dustbunny.physics.indiana.edu/~paul/hallDrd>.
- [125] CAEN: <http://www.caen.it>.
- [126] ATLAS ASD chip: http://bmc.bu.edu/bmc/asd/asd_chip.html.
- [127] Beamworks Spark 400: <http://www.beamworks.com>.
- [128] Armstrong *et al.* *Phys. Rev.*, **D5**:1640, 1972.
- [129] Caldwell *et al.* *Phys. Rev.*, **D7**:1362, 1973.
- [130] The Durham online database is located on the WWW at
<http://durpdg.dur.ac.uk/HEPDATA>.
- [131] R. Jones, 2001. The HDGeant Monte Carlo Program.
- [132] <http://monarc.web.cern.ch/MONARC/>.
- [133] <http://www.ppdg.net/>.
- [134] <http://www.griphyn.org/>.
- [135] <http://www.ivdgl.org/>.
- [136] Jim Gray and Prashant Shenoy. Rules of Thumb in Data Engineering. In *Proceedings
of the 16th International Conference on Data Engineering*, pages 3–12, 2000. Microsoft
Research Technical Report MS-TR-99-100.
- [137] Chip Watson. Web Services Data Grid Architecture, March 2002. PPDG documentation.

- [138] Ian Bird, *et al.* Common Storage Resource Manager Operations version 1.0, October 2001. PPDG documentation. http://www.ppdg.net/docs/documents_and_information.htm#Reports.
- [139] Richard Jones. HDDS - Hall D Detector Specification, 2001. <http://zeus.phys.uconn.edu/halld/geomerty/>.
- [140] Richard Jones. HDDM - Hall D Detector Specification, 2001. <http://zeus.phys.uconn.edu/halld/datamodel/doc/>.
- [141] S. Teige. A monte-carlo user guide. Technical report, Indiana University, 1998.
- [142] Art Snyder. GELHAD in BBSIM, 1995. <http://www.slac.stanford.edu/BFROOT/www/Computing/Offline/Simu>
- [143] Information on MCFast may be obtained via the WWW at <http://fnpspa.fnal.gov>.
- [144] Information on ROOT may be obtained via the WWW at <http://root.cern.ch>.
- [145] D. E. Groom, *et al.* (Particle Data Group). Review of particle physics. *Eur. Phys. Jour. C*, **15**:1, 2000.
- [146] ABBHHM Collaboration. Photoproduction of Meson and Baryon Resonances at Energies up to 5.8 GeV. *Phys. Rev.*, **175**:1669, 1968.
- [147] G. T. Condo *et al.* Charge-exchange photoproduction of the $a_2(1320)$ in association with Δ^{++} at 19.3 GeV/c. *Phys. Rev.*, **D41**:3317, 1990.
- [148] J. Ballam *et al.* Bubble-chamber study of photoproduction by polarized photons. *Phys. Rev.*, **D6**:454, 1972.
- [149] S.U. Chung. Spin formalisms. Technical Report CERN Report 71-8, Brookhaven National Lab., March 1971. Lectures given in the Academic Training Program of CERN 1969-1970.
- [150] Ben Zaroukian, Jeffrey Kaditz, Curtis A. Meyer and Paul Eugenio. A Study of leakage in Partial Wave Analysis for the HallD Detector at Jefferson Lab. Technical Report GlueX-doc-51, Carnegie Mellon University, December 2001. <http://portal.gluex.org/>.
- [151] C. A. Meyer and A. Szczepaniak, editors. *Partial Wave Analysis*, International Journal of Modern Physics A. World Scientific, 2003. <http://megux3.phys.cmu.edu/pwa.work/>.
- [152] Drawings of the Hall D site can be found at <http://www.jlab.org/Hall-D/civil/drawings>.
- [153] E.S. Smith L. Keller and E. Wolin. Beam containment proposal. Technical Report GlueX-doc-32, Jefferson Lab., 2000. <http://portal.gluex.org/>.
- [154] A. McFarlane D.R. Walz and E. Lewandowski. Beam dumps, stoppers and faraday cups at the slc. In *Physics with 8+ GeV Photons Workshop*, 1989. IEEE Particle Accelerator Conference, Chicago, IL, March 20-23, 1989 (SLAC-PUB-4967).
- [155] P. Degtiarenko. Neutron flux and ground water activation at bsy dump. Technical report, 1997. Intenal memo to R. May and G. Stapleton.
- [156] Muon Background in a 1.0-TeV Linear Collider. Technical Report SLAC-PUB-6385, SLAC.
- [157] Engineering Consulting Services Ltd. Report of subsurface exploration and geotechnical engineering analysis – hall d construction. Technical report, 1999.